



HAL
open science

Model and large-scale simulator of a biological retina, with contrast gain control

Adrien Wohrer

► **To cite this version:**

Adrien Wohrer. Model and large-scale simulator of a biological retina, with contrast gain control. Computer Science [cs]. Université de Nice - Sophia Antipolis, 2008. English. NNT: . tel-03300180

HAL Id: tel-03300180

<https://inria.hal.science/tel-03300180>

Submitted on 27 Jul 2021

HAL is a multi-disciplinary open access archive for the deposit and dissemination of scientific research documents, whether they are published or not. The documents may come from teaching and research institutions in France or abroad, or from public or private research centers.

L'archive ouverte pluridisciplinaire **HAL**, est destinée au dépôt et à la diffusion de documents scientifiques de niveau recherche, publiés ou non, émanant des établissements d'enseignement et de recherche français ou étrangers, des laboratoires publics ou privés.

PhD THESIS

prepared at
INRIA Sophia Antipolis

and presented at the
University of Nice-Sophia Antipolis
Graduate School of Information and Communication
Sciences

*A dissertation submitted in partial fulfillment
of the requirements for the degree of*

DOCTOR OF SCIENCE

Specialized in Control, Signal and Image Processing

Model and large-scale simulator of a biological retina, with contrast gain control

Adrien WOHRER

Advisor	Pr. Pierre Kornprobst	INRIA Sophia Antipolis, France
Reviewers	Pr. Jeanny Hérault Pr. Jonathan Victor	University Joseph Fourier of Grenoble, France Cornell University, USA
Examiners	Pr. Bruno Cessac Pr. Olivier Faugeras Pr. Guillaume Masson Pr. Adrián Palacios Pr. Simon Thorpe	INLN Nice / INRIA Sophia Antipolis, France INRIA Sophia-Antipolis, France INCM Marseille, France University of Valparaíso, Chile CERCO Toulouse, France

UNIVERSITÉ NICE-SOPHIA ANTIPOLIS - UFR Sciences

École Doctorale STIC

(Sciences et Technologies de l'Information et de la Communication)

THÈSE

pour obtenir le titre de

DOCTEUR EN SCIENCES

de l'UNIVERSITÉ de Nice-Sophia Antipolis

Discipline: Automatique, Traitement du Signal et des Images

présentée et soutenue par

Adrien WOHRER

Modèle et simulateur à grande échelle d'une rétine biologique, avec contrôle de gain

Thèse dirigée par Pierre KORNPBST

Date prévue de soutenance, 12 mars 2008

Composition du jury:

<i>Rapporteurs</i>	Pr. Jeanny Herault	Université Joseph Fourier de Grenoble, France
	Pr. Jonathan Victor	Université de Cornell, USA
<i>Examineurs</i>	Pr. Bruno Cessac	INLN Nice / INRIA Sophia Antipolis, France
	Pr. Olivier Faugeras	INRIA Sophia-Antipolis, France
	Pr. Guillaume Masson	INCM Marseille, France
	Pr. Adrián Palacios	Université de Valparaíso, Chile
	Pr. Simon Thorpe	CERCO Toulouse, France

Contents

Acknowledgments	9
Présentation générale (en Français)	13
Introduction	21
I The vertebrate retina	25
1 General anatomy and physiology of the retina	27
1 Anatomy of the visual system	28
1.1 The eye	28
1.2 The lateral geniculate nucleus (LGN)	30
1.3 The primary visual cortex	32
1.4 Ventral and Dorsal pathways of the visual system	33
2 The retina: a layered neural structure	35
2.1 Layered architecture of the retina	35
2.1.1 Five layers of cells	36
2.1.2 Synaptic connections between retinal layers	38
2.1.3 Parallel pathways	38
2.2 Functions of different retinal cells	40
2.3 Central vs. peripheral vision	41
3 General characteristics of the retinal output	44
3.1 Responses to light steps (ON and OFF cells)	45
3.2 Center-Surround architecture (concentric cells)	46
3.3 Temporal behavior (transient and sustained cells)	50
Conclusion	51
2 Linear approximations and modeling	53
1 Introduction: Linear receptive fields	54
2 Center-surround organization and the Difference of Gaussians	55
3 Linear models for temporal transients	59
4 Generalized spatio-temporal receptive fields	65
5 Reverse correlation and LN analysis	67
6 Linear models for electrical coupling	71
7 Conductance equation and other nonlinear filtering: The Linear ODE framework	75

3	Specialized functionalities in the vertebrate retina	77
1	Light receptors and horizontal cells	79
1.1	Phototransduction	79
1.1.1	Molecular basis of phototransduction	79
1.1.2	Modeling phototransduction	82
1.1.3	Functional implications	85
1.2	Further processing in light receptors and horizontal cells	85
2	Bipolar cells: the retinal turntable	86
2.1	ON and OFF pathways arise at the level of bipolar cells	86
2.2	Subtypes of bipolar cells	88
2.3	Center-surround architecture of bipolar cells	89
2.3.1	Center-surround receptive field in bipolar cells.	90
2.3.2	Controversial origin of the center-surround mechanism	90
2.3.3	Center-surround opposition in the OPL	92
2.3.4	Center-surround opposition in the IPL	93
2.4	Temporal shaping in bipolar cells	95
	Conclusion: A strong need for further exploration	97
3	Parallel pathways of the retinal output	97
3.1	Introduction: Ganglion cells and the Inner Plexiform Layer	97
3.1.1	Historical landmarks and bibliography	97
3.1.2	Architecture of the Inner Plexiform Layer	99
3.1.3	Amacrine cells	102
3.2	Physiology of the different visual pathways	104
3.2.1	Brisk sustained (X) cells	105
3.2.2	Brisk transient (Y) cells	107
3.2.3	Color-coding ganglion cells	115
3.2.4	The rod pathway	118
3.2.5	Direction-Selective (DS) cells	120
3.2.6	Local edge detectors (LEDs)	123
3.2.7	Other ‘sluggish’ ganglion cells	127
4	Properties of retinal spike trains	130
4.1	The problematic of spike coding in the retina	130
4.1.1	Spike as a simple means of physical transmission	132
4.1.2	Spike emissions lack a unified theoretical framework	132
4.1.3	A theoretical framework for spike coding in the retina	133
4.2	Spike-emission process for a single cell	134
4.2.1	The Poisson process	134
4.2.2	Gamma, and other simple modulated renewal processes (SMRP)	135
4.2.3	The statistics of retinal spike trains	136
4.2.4	Noisy leaky integrate-and-fire (nLIF) models and derivatives	144
4.3	Spike correlations between neighboring cells	146
4.3.1	Spike correlations and their anatomical origin	146
4.3.2	Stimulus-driven oscillations	149
4.3.3	Applications of information theory	153
5	Nonlinear adaptations in the retina	155
5.1	Adaptations to luminosity	156
5.2	Contrast gain control	158

5.2.1	Contrast, and the statistics of natural images	158
5.2.2	Multi-sinus experiments	159
5.2.3	Contrast gain control and LN analysis	162
5.2.4	Modeling contrast gain control	166
5.2.5	Perceptual impact of contrast adaptation	169
5.3	Slow adaptation and predictive coding	170
5.3.1	Adaptation of spatial receptive fields to background luminance	171
5.3.2	Predictive coding of spatio-temporal correlations in the stimulus	173

II A retina model: Definition, analysis and implementation **175**

4	A retina model, with contrast gain control	177
1	Introduction	179
2	General structure of the model	181
2.1	A layered model in three stages	181
2.1.1	Conception of the model	181
2.1.2	Spatio-temporal continuous maps	182
2.1.3	Three stages of the model	182
2.2	Mathematical framework and notations	184
2.2.1	Dimensional reduction	184
2.2.2	Notations for linear filters	185
3	First stage: The OPL filter	187
3.1	Equations of the system	187
3.2	Characteristics of the OPL filter	188
4	Second stage: Contrast gain control in bipolar cells	189
4.1	Motivations, and basic idea of the model	189
4.2	Equations of the system	190
4.3	Contrast gain control and Wiener kernels	192
5	Third stage: The IPL and ganglion cells	193
5.1	Synaptic current upon ganglion cells	193
5.2	Spike generation in ganglion cells	195
5.3	Ganglion cell sampling configurations	196
6	Physiological reproductions	197
6.1	X and Y cell responses to grating apparitions	197
6.2	Multi-sinus experiments	199
6.3	LN analysis	203
7	Large-scale simulations	205
7.1	Large-scale simulation of the model	205
7.2	Perceptual consequences of model architecture	207
7.2.1	Spiking pattern at image onset	207
7.2.2	Contrast enhancement through contrast gain control	208
8	Discussion	210
8.1	General discussion	210
8.1.1	Combining large-scale and plausibility	210
8.1.2	Spatial filtering in the model	212

8.1.3	Temporal transients and adaptation in the model . . .	213
8.2	Contrast gain control mechanism	215
8.2.1	Interpretation of the model	215
8.2.2	Other models of gain control	218
	Conclusion	219
5	A mathematical study of the gain control mechanism	221
1	Introduction	223
1.1	The underlying low-pass linear system	223
1.1.1	Characterizing the linear response to sinusoidal stimulation	223
1.2	Gain control through the nonlinear system	224
1.2.1	Characterizing the nonlinear response to sinusoidal stimulation	224
1.2.2	Reducing the system's dimensionality	225
2	General study of the gain control system	226
2.1	System definition and first properties	226
2.1.1	System definition	226
2.1.2	Notations	227
2.1.3	Periodic asymptotic solution of the system	228
2.2	Numerical simulation	231
2.2.1	General behavior of the system	232
2.2.2	Gain control on input amplitude	232
2.2.3	Parameter b defines the shape of the phase portrait	234
3	Asymptotic behavior $b = 0$	237
3.1	System definition	237
3.2	Dependence of V_{\max} and ϕ_{\max} w.r.t. system parameters	238
4	Asymptotic behavior $b = +\infty$	240
4.1	System definition	240
4.2	Integral formulations for partial derivatives in the system	242
4.3	Dependence of V_{\max} and ϕ_{\max} w.r.t. system parameters	246
4.3.1	Dependence w.r.t. A (Points (iii)-(vi)).	247
4.3.2	Dependence w.r.t. ω (Points (i)-(ii))	251
4.4	Local under-linearity of V_{\max} w.r.t. A	253
5	A track for the future: Perturbation analysis	255
5.1	Perturbation analysis near $b \rightarrow +\infty$	256
5.2	Perturbation analysis near $b \rightarrow 0$	259
	Conclusion	262
	Appendix: Periodic contracting system	262
6	Virtual Retina: a large-scale simulator	267
1	Introduction	268
2	Using <i>Virtual Retina</i>	269
2.1	The executables	270
2.1.1	The <code>Retina</code> executable	270
2.1.2	The <code>TestGanglionCell</code> executable	271
2.1.3	The <code>ReconstructRetina</code> executable	272
2.1.4	Other executables	272
2.2	The retina XML definition file	273

2.2.1	General architecture of a file	273
2.2.2	Sub-elements: Optional stages of the model	274
2.2.3	Microsaccade generation	279
2.3	Installing <i>Virtual Retina</i>	279
3	Implementation details	280
3.1	Synaptic inputs and connections	282
3.1.1	InstantSynapse: Model of synaptic transmission	282
3.1.2	CellPortHandler: Synaptic inputs to a cell	284
3.2	Implementing a foveated structure	285
3.2.1	RadialScheme and LogPolarScheme: defining the retinal scaling function	285
3.2.2	RadialFilter: spatially-variant recursive filtering	286
3.3	Continuous filtering	287
3.3.1	BaseRecFilter: Recursive temporal filtering	287
3.3.2	BaseMapFilter: Spatio-temporal filtering	292
3.3.3	RetinaMapFilter: Specific retinal specialization	294
3.3.4	CondCellMap: nonlinear, conductance-driven filtering	296
3.4	Spiking cells and arrays	297
3.4.1	<i>MvaSpike</i> in a nutshell	297
3.4.2	CondNeuron_cpm: Event-driven GIF neuron	300
3.4.3	IntegratorNeuron_cpm: ‘Pulsed’ integration of a time-varying signal	302
3.4.4	Various SpikingChannel objects	304
3.5	<i>xmlParameters++</i> : Loading/saving parameters with XML	305
3.5.1	Goals	305
3.5.2	Usage	306
3.6	Assembling and simulating a retina	308
3.6.1	The Retina object	308
3.6.2	Example of sub-stage object: The GanglionLayer	309
	Conclusion	313
	Conclusion générale (en Français)	319
	Appendix	321
	Convolution of Exponential filters	323
	Exact calculations	323
	An approximate two-parameter filter	325
	Bibliography	329

ACKNOWLEDGMENTS

My first thanks go to my advisor Pierre Kornprobst for scientific, professional and organizational guidance, for his savvy and (almost!) perpetual good humor. May your next PhD students have gaining watches, for a change! Special thanks also to Thierry Viéville for contributing to define the early tracks of my research, for his open ears and loud laugh. More general thanks go to everyone in the Odyssee Team for both their humor and professional competences.

Many grateful thanks to my reviewers Jeanny Herault and Jonathan Victor for taking time to read this work carefully –with special thanks to Prof. Victor for his numerous valuable comments under stressful conditions. Profs. Bruno Cessac, Olivier Faugeras, Guillaume Masson, Adrián Palacios and Simon Thorpe are also warmly thanked for accepting to examine this thesis, and are informed that the second part of the payment will be deposited only *after* the defense.

Last but not least, loving thanks are sincerely and non-exhaustively expressed to the following persons: My family for their everlasting presence in my heart (so I don't need to call too often!) ; All my friends from Paris, Côte-d'Azur and elsewhere (same remark about the phone...), and especially those who happened to also be colleagues: François for being my guru in oh so many ways, Sylvain for pulling me up in Verdon when he could have left me to the vultures, Beubeu, Christian, Claudio, Demian, Johnny, Maria-José, Max, various Nico's, PierreMomo, Romain and Sandrine for understanding that putting one specific sentence for each one of you would be too long ; My banker, my insurance agents, the university administrative department, etc., for every day that you *did not* try to contact me ; All musicians in my mp3 player for emotional support during the writing of this thesis, with special thanks to Steve Coleman, Herbie Hancock, Fela Kuti and Suprême NTM: I would never have made it without you ; Florina, for all preceding reasons, plus those that need not be written.

Présentation générale (en Français)

Contexte de ce travail

Il y a des liens historiques forts entre les neurosciences visuelles et la vision par ordinateur. Les deux disciplines ont émergé lors de la seconde moitié du XXème siècle, et se sont souvent mutuellement enrichies. Pour citer un unique exemple, la formalisation mathématique des principes de la vision biologique de bas niveau par David Marr (*Vision*, Marr 82 [104]) a donné naissance à une pléthore d'applications dans le domaine de la vision par ordinateur, et a fortement contribué à définir la méthodologie de cette science alors naissante.

En retour, la vision par ordinateur a noué des liens avec des disciplines plus abstraites (la vision mathématique, l'apprentissage) qui sont maintenant largement répandues en neurosciences: Le débruitage d'images cérébrales à l'aide d'algorithmes de régularisation, la modélisation d'aires corticales par des réseaux de neurones, les 'observateurs bayésiens' pour quantifier les capacités de codage d'un neurone biologique, en sont quelques exemples.

Cependant, tandis que la vision par ordinateur se développait rapidement autour de formalismes abstraits, elle a progressivement pris de la distance avec les neurosciences visuelles et leur bagage de connaissances sur le fonctionnement des systèmes visuels biologiques. Récemment, de nombreux chercheurs en vision par ordinateur se 'retournent' vers les neurosciences visuelles, à la recherche de nouvelles sources d'inspiration.

Le simulateur de rétine présenté dans cette thèse a précisément cette sorte d'origine. Il a été développé au sein du projet Odyssée de l'INRIA¹, dont le but est de confronter la vision par ordinateur 'traditionnelle' à de nouveaux algorithmes issus des neurosciences computationnelles. Plus précisément, le but de ma thèse a été de modéliser et d'implémenter une plate-forme de simulation de rétine qui puisse servir de point de départ pour différentes applications futures: Premièrement, fournir une entrée plausible à des modèles d'aires cérébrales de plus haut niveau. Deuxièmement, introduire un cadre de calcul et des objets informatiques qui puissent être réutilisés dans d'autres modèles d'aires visuelles. Troisièmement, offrir la possibilité d'études théoriques sur les propriétés de codage de la rétine elle-même, en tant que capteur sensoriel. Cette recherche a été effectuée dans le cadre de la participation de notre laboratoire au projet européen FACETS².

Tout en découvrant la vaste littérature consacrée à la rétine en neurosciences, il nous est apparu que les modèles détaillés du traitement rétinien *dans son ensemble* sont relativement rares. Du côté des chercheurs sur la rétine, de tels modèles sont peu requis car les recherches se portent généralement sur des points bien particuliers du traitement rétinien. Par opposition, du côté des chercheurs sur le système visuel de plus haut niveau (thalamo-cortical), on utilise généralement des modèles de rétine très simples, car ré-implémenter un modèle détaillé de rétine semble une tâche trop conséquente, en regard d'un intérêt pas toujours clair.

Cette dernière considération nous a amenés à créer et distribuer un simulateur, dénommé *Virtual Retina*, qui puisse être directement utilisé par les modélisateurs des aires visuelles thalamo-corticales. Pour ce faire, le simulateur répond aux exigences suivantes:

¹Institut National pour la Recherche en Informatique et Automatique

²Fast Analog Computing with Emergent Transient States, EC IP project FP6-015879, <http://facets.kip.uni-heidelberg.de/>

1. *Une bonne fidélité biologique*, en comparaison avec les modèles ‘minimaux’ de rétine habituellement utilisés (filtrage linéaire, génération poissonnienne de potentiels d’action, etc.), avec un accent sur les caractéristiques non-triviales de la rétine qui sont susceptibles de véhiculer d’importantes fonctionnalités.
2. *La possibilité de simulation à grande échelle*. Le simulateur peut reproduire les émissions de potentiels d’action de plusieurs milliers de cellules en un temps raisonnable (entre 10 et 100 fois le temps réel).
3. *Un usage simple*, condition obligatoire pour que le simulateur ait effectivement une chance d’être utilisé. Le modèle de rétine sous-jacent est modulaire, avec des niveaux de complexité facilement définissables par l’utilisateur.

Ma thèse est organisée en deux parties. La première partie présente en détail les nombreuses fonctionnalités des rétines biologiques. Ce travail de synthèse peut être vu aussi bien comme une contribution indépendante –nous n’avons pas trouvé dans la littérature ce genre de présentation à la fois ‘globale’ et détaillée– que comme un moyen de mieux cerner les enjeux et le ‘cahier des charges’ d’un simulateur de rétine à grande échelle. La seconde partie présente nos propres travaux: la conception du modèle, sa validation grâce à des reproductions expérimentales et à une analyse mathématique, et son implémentation au travers d’objets informatiques génériques.

Première partie – La rétine des vertébrés

Dans la première partie de notre travail, nous résumons les principales propriétés de la rétine –son organisation et le traitement du signal qu’elle réalise– telles qu’elles sont comprises de nos jours, après plusieurs décennies d’expériences et de modélisation. Cette synthèse est axée autour de la question de la *fonctionnalité* de la rétine: Quelles sont ses caractéristiques en termes de traitement du signal, et lesquelles sont suffisamment importantes pour être reproduites dans un simulateur à grande échelle?

Le **Chapitre 1** est introductif. Il présente les bases d’anatomie et de physiologie concernant la rétine, et son rôle dans le système visuel des vertébrés. La Section 1 contient une description anatomique de l’œil, puis une présentation d’ensemble du système visuel humain, à travers le thalamus et le cortex. La Section 2 décrit la structure anatomique de la rétine: l’information visuelle y est traitée par cinq couches successives de neurones spécialisés (les récepteurs, puis les cellules horizontales, bipolaires, amacrines et ganglionnaires), suivant une organisation anatomique très précise. Enfin, la Section 3 présente les notions de base concernant l’électrophysiologie des cellules ganglionnaires en sortie de rétine: ces neurones, qui émettent des potentiels d’action le long du nerf optique, peuvent être sensibles aux contrastes positifs (cellules ‘ON’) ou négatifs (cellules ‘OFF’). Spatialement, ils mesurent une opposition entre un signal *central* et un signal *périphérique*. Temporellement, leur réponse s’atténue rapidement face à une entrée constante (comportement ‘transient’).

Le **Chapitre 2** présente des éléments traditionnels de *modélisation* dans la rétine, en grande partie basé sur des formalismes linéaires. On y définit la notion de champ récepteur linéaire et de convolution (Section 1). Des modèles linéaires traditionnels pour la rétine sont ensuite présentés: modèle ‘différence-de-Gaussiennes’ pour les champs récepteurs spatiaux (Section 2), modèle ‘différence-d’exponentielles’

pour les champs récepteurs temporels (Section 3), et leur combinaison plus précise en une forme de filtre spatio-temporel non séparable (Section 4). Une extension classique du filtrage linéaire, le modèle ‘linéaire – non-linéaire’ (LN) est présenté en Section 5. Les dernières sections présentent des modèles plus spécifiques à la rétine: modélisation linéaire du couplage entre cellules voisines dû aux *synapses électriques* (Section 6), et présentation formelle d’une équation différentielle ordinaire, applicable à différents niveaux de la rétine, susceptible d’induire des effets *divisifs* dans le filtrage rétinien (Section 7).

Le **Chapitre 3** constitue le corps de cette première partie. On y énumère les principales propriétés organisationnelles et fonctionnelles de la rétine, à un niveau de détail relativement avancé. Les *récepteurs* et la phototransduction sont présentés en Section 1. Les récepteurs transmettent leur signal aux cellules *bipolaires* (Section 2). Ces cellules relai, de par leurs fortes interactions avec les cellules horizontales et amacrines (toutes deux inhibitrices), possèdent déjà la sensibilité spatio-temporelle ‘*passes-bande*’ propre au traitement rétinien. Le signal des cellules bipolaires est ensuite combiné de manière complexe et multiple par les nombreux sous-types de cellules amacrines et ganglionnaires, aboutissant à la création de nombreux *canaux parallèles d’information* en sortie de rétine, chacun caractérisé par des propriétés spatio-temporelles différentes (Section 3). De plus, les cellules ganglionnaires en sortie de rétine émettent leur signal sous forme de trains discrets de *potentiels d’action*, selon un processus à la structure statistique complexe qui intrigue toujours les spécialistes (Section 4). Enfin, nous finissons notre tour d’horizon de la rétine par une rapide présentation des nombreux mécanismes d’*adaptation*, rapide ou lente, qui permettent à la rétine de continuellement optimiser sa réponse en fonction des caractéristiques de son stimulus visuel (Section 5).

Cette première partie de notre travail, bien que principalement bibliographique, ne doit pas être vue comme le traditionnel ‘état de l’art’ introductif dans une thèse, mais bien comme une contribution à part entière. Dans le cadre de notre projet de thèse, un simulateur issu d’un laboratoire d’informatique et à l’attention de la communauté des neurosciences visuelles en général, cette synthèse apparaît comme un complément nécessaire à la partie de modélisation et d’informatique qui s’ensuit. Elle permet de comprendre les enjeux du simulateur, ses réussites et ses limites et, plus important encore à nos yeux, elle tente de transmettre au plus grand nombre certaines propriétés fondamentales de la rétine qui semblent peu connues en dehors des spécialistes du sujet. Le contrôle du gain au contraste, les nombreux canaux parallèles d’information en sortie de rétine, les synchronisations entre potentiels d’action, sont autant d’exemples de telles propriétés, à l’importance fonctionnelle certaine.

Par ailleurs, nous pensons que cette synthèse peut s’avérer utile aux étudiants en neurosciences souhaitant découvrir les propriétés fonctionnelles de la rétine à travers un panorama global, mais plus avancé que les traditionnelles descriptions ‘d’école’.

D’un point de vue plus personnel, cette première partie nous sert naturellement de justification pour le modèle implémenté dans notre simulateur, et nous y faisons souvent référence dans la seconde partie de notre thèse.

Deuxième partie – Un modèle de rétine: définition, analyse et implémentation

Dans la seconde partie de notre travail, nous présentons notre propre modèle de rétine et le simulateur informatique associé, *Virtual Retina*. Outre le modèle de rétine proprement dit, nous proposons un formalisme et des objets informatiques qui permettent d'implémenter facilement d'autres modèles de rétine. Nous consacrons une attention particulière au phénomène non-linéaire de contrôle de gain, pour lequel nous proposons un système dynamique simple, générique et justifié mathématiquement.

Le **Chapitre 4** présente notre modèle de traitement rétinien. Après des remarques et notations introductives (Sections 1 et 2), nous présentons le modèle proprement dit, qui consiste en trois étapes successives de filtrage. Premièrement, un filtre spatio-temporel linéaire et non-séparable modélise les interactions entre récepteurs et cellules horizontales (Section 3). Deuxièmement, une boucle de contrôle non-linéaire modélise le contrôle du gain au contraste, tel qu'il apparaît dans les cellules bipolaires (Section 4). Troisièmement, le signal des cellules bipolaires est transmis aux cellules ganglionnaires, avec différentes caractéristiques spatio-temporelles permettant de reproduire l'opposition classique entre cellules ganglionnaires de types 'X' et 'Y', ainsi qu'un processus plausible d'émission de potentiels d'action (Section 5). Le modèle est validé en reproduisant les réponses électrophysiologiques des cellules ganglionnaires à différents types de stimuli (Section 6). De premiers exemples qualitatifs de simulation à grande échelle sont donnés en Section 7, avec un accent sur l'impact perceptif des différentes composantes de filtrage incluses dans le modèle. Enfin, la Section 8 propose une discussion générale sur le modèle, et plus particulièrement sur la plausibilité du mécanisme de contrôle du gain au contraste. En effet, ce mécanisme, quoiqu'inspiré de précédents modèles, est une contribution originale de notre travail.

Le **Chapitre 5** est une étude mathématique plus poussée du mécanisme de contrôle de gain que nous proposons. La haute dimension du système original (où l'espace et le temps sont couplés) est réduite pour obtenir un système purement temporel, défini par l'évolution (non autonome) d'un système à deux dimensions (Section 1). De plus, le courant en entrée du système est choisi comme une sinusoïde $I(t) = A \cos(\omega t)$, une expression simple qui permet de mener des calculs exacts tout en ayant le contrôle sur le contraste A et la fréquence temporelle ω du stimulus. Le système ainsi défini est étudié empiriquement en Section 2, via des simulations numériques qui révèlent les propriétés attendues de contrôle de gain: Sous-linéarité de la réponse du système par rapport à A , et avance de phase lorsque A augmente. La preuve mathématique de ces propriétés n'est faite que dans deux cas particuliers, aux bornes du domaine de définition pour le paramètre b du système qui mesure la rapidité de l'adaptation au gain. Ces deux limites asymptotiques sont les cas ' $b = 0$ ' (Section 3) et ' $b = +\infty$ ' (Section 4), pour lesquels le système à deux dimensions vit dans une sous-variété de dimension 1, où les calculs sont simplifiés. Enfin, nous terminons ce chapitre par une ébauche d'analyse dans le cas général où b est un réel positif quelconque (Section 5). Le développement de la solution en série par rapport à b autorise une analyse de perturbations près des bornes ' $b = 0$ ' et ' $b = +\infty$ ', et même probablement un développement analytique de la solution 2D pour n'importe quel paramètre b .

Le **Chapitre 6**, enfin, détaille l'implémentation informatique du modèle à travers

le logiciel *Virtual Retina* (sous licence open-source CeCILL C de l'INRIA³). Ce logiciel peut simuler jusqu'à environ 100 000 cellules ganglionnaires en 100 fois le temps réel, ce qui en fait un bon outil pour les simulations à grande échelle du cortex visuel primaire ou du LGN qui nécessitent une entrée rétinienne réaliste. Le chapitre est divisé en deux sections distinctes. La Section 2 présente rapidement l'utilisation du logiciel: ses différents programmes, ainsi que le fichier au format XML qui permet de définir l'ensemble des paramètres du modèle simulé. Ensuite, la Section 3 présente les détails de l'implémentation, *via* des objets C++ au fonctionnement assez générique pour pouvoir être réutilisés comme 'briques élémentaires' d'autres modèles d'aires visuelles de bas niveau.

Concluons par quelques quelques mots concernant l'esprit dans lequel cette recherche a été menée. Produire un simulateur fonctionnel du traitement rétinien dans son ensemble a nécessité un travail bibliographique important ainsi qu'une large part de programmation. Logiquement, le contenu de la thèse reflète cette importante partie méthodologique de notre travail: la Partie I est un résumé bibliographique des fonctionnalités de la rétine, et le Chapitre 6 une documentation des objets informatiques implémentés. Nous espérons que ces deux présentations s'avèreront utiles aux lecteurs désireux d'utiliser le logiciel, ou simplement de découvrir plus en détail le fonctionnement de la rétine.

La contribution la plus originale de ce travail est sans doute l'analyse mathématique du système de contrôle de gain (Chapitre 5). Nous pensons que ces résultats sont un 'plus' pour justifier la forme particulière donnée au contrôle du gain au contraste dans notre modèle, qui est à la fois simple et plausible.

Enfin, remarquons qu'une partie du matériel pour cette thèse a déjà été publié dans de précédents travaux. Le Chapitre 4 est adapté d'un article de journal (Wohrer-Kornprobst 08, accepté pour publication dans le *Journal of Computational Neuroscience*). L'étude mathématique du Chapitre 5 est partiellement adaptée d'un précédent rapport de recherche (Wohrer 07 [182]). Enfin, la Section 2 du Chapitre 6, sur l'utilisation du logiciel, vient du tutoriel écrit pour *Virtual Retina* et inclus dans la distribution du logiciel. Nous espérons cependant que cette thèse pourra être lue comme un ensemble cohérent.

³numéro IDN IDN.FR.001.210034.000.S.P.2007.000.31235.

Introduction

Context of this work

There is traditionally a strong interplay between computer vision and visual neuroscience. Both disciplines really emerged during the second half on the twentieth century, and served each other as mutual inspirations. As a striking example, David Marr’s mathematical formalization of early visual processing, based on traditional physiological knowledge of the visual pathway (*Vision*, Marr 82 [104]), spawned a whole field of applications in computer vision, strongly contributing to define the goals and means of this –by then– emerging science.

In return, computer vision has developed a link with more abstract domains (mathematical vision, machine learning) which are now widely used in the field of neuroscience: Denoising of brain imaging data via advanced regularization techniques, neural network models of cortical areas, bayesian ‘ideal observers’ to quantify the coding capabilities of real neurons, are only a few examples.

However, as computer vision rapidly developed based on abstract formalisms, it progressively took some distance with visual neuroscience, until researchers in both fields could be specialized enough to ignore most of the other domain. Recently, many computer scientists are starting to ‘rediscover’ visual neuroscience, in quest of new sources of inspiration from the biological world.

The retina simulator presented herein has precisely this sort of origin and motivations. It has been developed inside the Odyssee Laboratory at INRIA⁴, whose goal is to confront a strong ‘computer vision’ background to novel algorithms in computational neuroscience. More precisely, the goal of my PhD was to model and implement a retina simulation platform, which could be used as a first step towards different possible directions: First, to provide input to further models of cortical processing. Second, to introduce a framework and computer tools which could be reused for other purposes, e.g., other models of low-level visual areas. Third, to be studied for itself, as an example of neural encoding system. This research was part of our lab’s contribution to the FACETS⁵ European research project.

While discovering the complexity of retinal processing through its wide literature, it occurred to us that precise, integrated models of retinal processing are relatively rare in the visual neuroscience community. Also, the models which *do* exist are not widely used as input to higher level models of visual processing, because potential users are generally not convinced of the need to use such a detailed model. Instead, modelers of thalamo-cortical areas often use over-simplified retina models, because they either ignore subtle features of retinal processing, or do not wish to spend time on re-implementing an existing retina model.

These considerations led us to implement a retinal simulator that could be easily used by modelers of thalamo-cortical areas, and to distribute it as an open-source software. The resulting simulator, termed *Virtual Retina*, intends to fulfill the requirements of thalamo-cortical modelers through three particular points:

1. *Increased biological precision*, as compared to minimal retina models (e.g., a simple filtering by a differences-of-Gaussians, or a simple spike generation process, or even a simple transmission of the input luminosity profile), with a

⁴Institut National pour la Recherche en Informatique et Automatique

⁵Fast Analog Computing with Emergent Transient States, EC IP project FP6-015879, <http://facets.kip.uni-heidelberg.de/>

focus on non-trivial features of retinal processing that could still be associated to important functionalities.

2. *Large-scale simulations.* The simulator is able to produce the spikes of an assembly of several thousands of ganglion cells in reasonable time.
3. *Convenient usage,* so that the simulator has a chance to be effectively used. The model implemented is modular, allowing for more or less complexity, and it can easily be defined and changed by the user.

This thesis is organized in two parts. First, we propose a detailed review of processing in biological retinas, in order to understand what we need –or can– model in a large-scale simulator. Second, we describe the conception of the simulator’s underlying model, its validation through experimental reproductions and mathematical analysis, and the computer implementation of the simulator through generic C++ objects.

Part I – The vertebrate retina

In the first part of our work, we summarize the major properties of retinal filtering and organization, as understood by numerous experiments and models over the last decades. For this review, we take a *functional* approach. Our underlying goal is to answer the question: ‘What are the main characteristics of the retinal output?’, to better define the requirements of a retina simulator.

In Chapter 1, we present an overview of retinal processing, including anatomy of the retina, and its place in the larger structure which is the visual system. In Chapter 2, we take a modeler’s standpoint, and present various classical tools, derived from linear analysis, which have been used to account for signal processing in the retina. Once these preliminary facts and tools are settled, we enter in Chapter 3 the details of retinal function. This detailed chapter proceeds to the review of prominent features in the retina, from phototransduction to emitted spike trains, including the organization of the retina in parallel pathways, and various mechanisms of nonlinear adaptation.

This first part, although focused on state-of-the-art knowledge, should not be viewed as the traditional ‘state-of-the-art’ chapter of a thesis, but as a full contribution in our work. It has been written in the same spirit as our simulator, aiming at the whole ‘visual neuroscience’ community rather than only at retinal specialists – a type of approach which we could not find in the literature. Our hope is that this review will shed light on some intriguing features of retinal processing which are not universally known outside of the ‘retina’ community itself, even though they may convey advanced functionalities. Contrast gain control, numerous parallel pathways at the retinal output, or spiking synchronies, are some of these intriguing features. We also believe that this integrated presentation will prove useful to students wishing to discover the retina at a general level, yet more advanced than classical ‘textbook’ descriptions.

Naturally, from a more personal standpoint, this first part also provides several landmarks and justifications for the model implemented in our simulator, that we present in the second part of our work.

Part II – A retina model: Definition, analysis and implementation

In the second part of our work, we present our retina model, and its associated simulator *Virtual Retina*. The model itself is presented in Chapter 4: It is mostly a state-of-the-art model, whose formulations have been adapted to large-scale simulation. It takes its inspiration and justification from the review made in Part I. The model is primarily based on linear filters, but with added nonlinearities which include contrast gain control, Y cells, and spike generation. We insure ourselves of its good behavior by reproducing different experimental measurements on real ganglion cells, from the literature.

Contrast gain control, more precisely, is implemented here in an original framework, although it bears strong similarities with various existing models. The proposed mechanism is based on a very simple feedback loop, whose general formulation could also be used elsewhere than in the retina. To better assess its behavior, this model of gain control is mathematically analyzed in Chapter 5. This analysis reveals more arduous than could be expected from the simple form of the system, but we eventually prove some interesting results, which confirm the *gain control* properties of our feedback loop.

Finally, Chapter 6 focuses more specifically on the computer *simulator*, *Virtual Retina* (under INRIA CeCILL C open-source license⁶). This software can emulate up to around 100,000 cells with a processing speed of about 1/100 real time, which makes it a good choice for large-scale simulations of the visual cortex (and possibly LGN) that require a realistic input from the retina. This last chapter is divided into two sections. The first section presents the general principles of use of the software. The second section focuses on the underlying implementation, with an accent on its computational ‘building blocks’, that can be reused in other models of low-level visual areas.

Before moving on, let us add a few words about the spirit in which this research was pursued. In order to produce a relevant retinal platform, our work was largely methodological, including strong components of documentation and coding. Logically, the content of our thesis reflects this important part of methodology, through a detailed presentation of retinal processing (Part I), and of our simulation tools (Chapter 6). We believe that these two presentations can provide many useful informations to potential readers, and users of the software.

Presumably, the most original contribution of this work is the mathematical analysis of the gain control system (Chapter 5). We believe that these results are a ‘plus’ to justify the use of our particular form of contrast gain control mechanism.

To conclude, let us note that a part of the material herein has already been published in previous work: Chapter 4 is adapted from a journal article (Wohrer *et al.* 08, accepted for publication in *Journal of Computational Neuroscience*). The mathematical study of Chapter 5 is partially adapted from a previous research report (Wohrer 07 [182]), while the ‘usage’ section of Chapter 6 comes from the tutorial written for *Virtual Retina*. We hope nevertheless that the resulting thesis can be read as a coherent ensemble.

⁶IDDN number IDDN.FR.001.210034.000.S.P.2007.000.31235.

Part I

The vertebrate retina

CHAPTER 1

GENERAL ANATOMY AND PHYSIOLOGY OF THE RETINA

In this chapter, we present general properties of the retina. In Section 1, an overview of the eye and visual system is given, to situate the role of the retina in a wider processing structure. In Section 2, focus is given to the anatomical structure of the retina: Its different types of cells and their generic connectivity. Finally, Section 3 presents the general characteristics of the retinal output (center-surround organization, temporal band-pass behavior). The notions presented here provide landmarks for Chapters 2 and 3, where the retinal function is described in more detail.

Contents

1	Anatomy of the visual system	28
1.1	The eye	28
1.2	The lateral geniculate nucleus (LGN)	30
1.3	The primary visual cortex	32
1.4	Ventral and Dorsal pathways of the visual system	33
2	The retina: a layered neural structure	35
2.1	Layered architecture of the retina	35
2.2	Functions of different retinal cells	40
2.3	Central vs. peripheral vision	41
3	General characteristics of the retinal output	44
3.1	Responses to light steps (ON and OFF cells)	45
3.2	Center-Surround architecture (concentric cells)	46
3.3	Temporal behavior (transient and sustained cells)	50
	Conclusion	51

1 ANATOMY OF THE VISUAL SYSTEM

The visual system is very developed in humans and primates (see Figure 1.1), and vision is by far the most processed sensory modality in terms of number of neurons involved: In the human brain, almost 30% of the cortical surface processes an information which is mostly related to vision [30]. Here, we provide an overview of the low-level visual system: First, the visual organ itself (the eye), and second the thalamo-cortical pathway that starts the processing of visual information in the brain. We hope that this overview can help non-specialist readers to situate retinal processing in the wider scheme of visual perception as a whole. Furthermore, the specific visual pathways and areas introduced here have a close relation to retinal processing, and we will sometimes mention them further in this work.

Our main sources for description of the visual system are the reference books *Principles of Neural Science* (2000, Kandel, Schwartz and Jessell, editors) [87], *Neuroscience* (2004, Purves *et al.*, editors), and *The Visual Neurosciences* (2004, Chalupa and Werner, editors) [30]. This last book offers an important and comprehensive documentation on most aspects of visual processing. Concerning anatomy of the eye, our main source is the website Webvision [95].

1.1 The eye

A human eye is about 2,5 cm in diameter. One is represented in Figure 1.2, along with its anatomical components. We rapidly present the main components and features of the mammalian eye.

Cornea and crystalline lens: An adapting converging lens. The eye contains two successive lenses, the cornea and the crystalline lens, which project incoming light on the back of the eye. The most powerful lens is the cornea (convergence of about 40 diopters), which accounts for roughly 70% of the eye's total convergence power¹. The crystalline is a deformable lens controlled by zonule fiber muscles, that dynamically provides additional convergence so that the retinal image is always precise at the back of the eye, independently of the distance of the considered object. As we browse the visual space, our eyes constantly undergo this mechanism, known as *accomodation*. The converging power of the crystalline lens is of about 10 dioptries, but varies drastically with age (which can lead to presbytia in elderly individuals). Its accomodation range is of 2-3 dioptries, depending on age [136].

Retina: The neural captor. The retina is a thin (0.5 mm) sheet of neural tissue at the back of the eye, that transforms the incoming light into a neural message suitable for transmission to the brain. Amongst other cells, the retina contains *photoreceptors* that absorb a part of the light hitting the back of the eye, and convert the absorbed light signal into electrical activity, through a complex chemical process known as *phototransduction*. In many mammal species, the retina has a central zone (called the *fovea* in primates and humans) where a high density of cells allows

¹This strong convergence is due to the large difference in refraction index between the air and the cornea. In fact, the convergence index of the cornea is closer to that of water, so that underwater the cornea is much less convergent, explaining the unfocused and distorted visual perception [136].

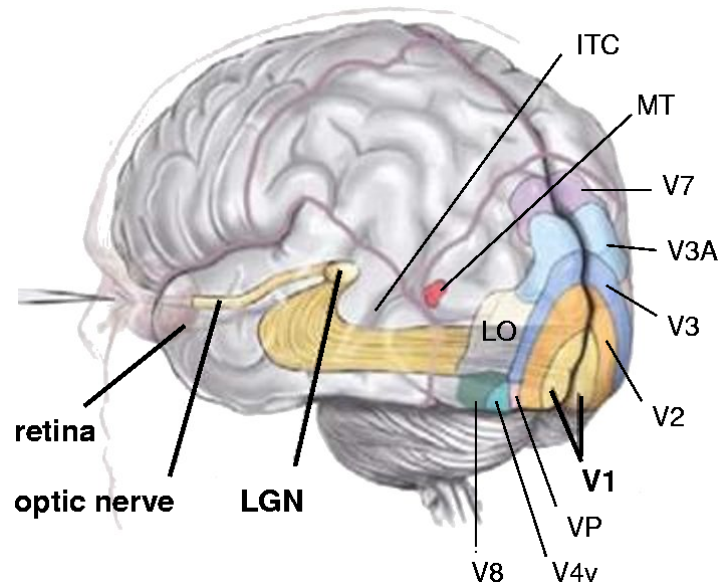


Figure 1.1: Visual pathway in the human brain. Visual signal from the retina travels along the optic nerve in the form of spike trains, to the Lateral Geniculate Nucleus (LGN) in the thalamus. Visual signal is then transmitted to the Primary Visual Cortex (V1), and is further processed in terms of shapes (V2,V3,V4...), color (V4,V8...) and movement (V2, MT, MST, IT...). Reproduced from Logothetis, Scientific American 99.

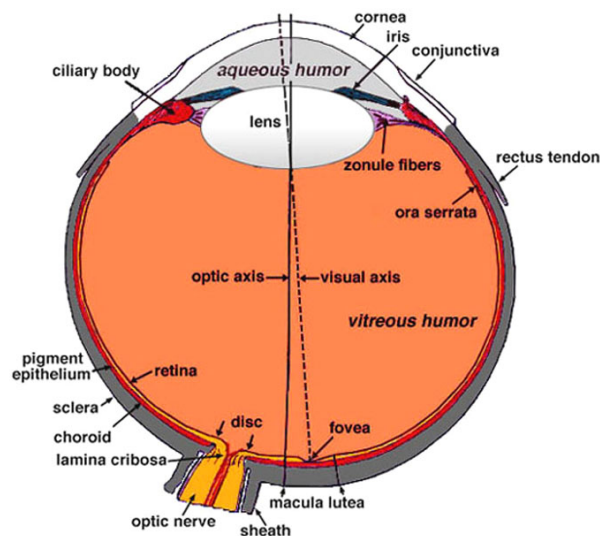


Figure 1.2: A human eye. The cornea and crystalline are lenses that allow the image at the back of the eye to be well-focused, especially at the *fovea* which is the central and most precise zone of the retina.

a high spatial resolution. The crystalline lens dynamically adapts its strength for the image to be most precise at this central zone.

The convergence power of the cornea and crystalline lens defines the projection ratio from the visual field to the retina. Typically, one degree of visual angle can correspond to 290 (human), 210 (macaque) or 170 (rabbit) μm on the retinal surface. As with any converging lens, the image projected on the retina is reversed: The left visual field is projected on the right side of the retina, the upper part of the visual field is projected on the lower part of the retina, and conversely. Naturally, this has no effect on our perception, because the visual perception is only defined by the neural connectivity, not the physical organization of the neurons.

Iris: An adapting diaphragm. The iris is the circular membrane whose colorful pigments define the color of our eyes. It plays the role of an optic diaphragm, with a variable aperture: the pupil. Through this variable aperture, the iris provides a first adaptation to the incoming levels of light in the eye. To account for the variation of pupil aperture, a psychophysical measure of illuminance at the back of the eye has been introduced: the photopic troland (tr). The retinal illuminance T in photopic trolands is defined through $T = Lp$, where L is the photopic luminance from the visual world, in cd/m^2 , and p is the pupil aperture, in mm^2 . Depending on their experimental protocols, neuroscientists use photopic trolands, or directly the input photopic luminance, which is much easier to measure ².

Epithelium: An absorbing medium. Behind the retina is layer of cells called the epithelium. It contains visual pigments that absorb the light which has not been absorbed by photoreceptors. This prevents any diffuse light from being reflected at the back of the eye, which would make the retinal image less precise. The epithelium is always absorptive. However, in many nocturnal mammal species (such as cats and dogs), the epithelium is lined with a reflective layer called the *tapetum*, allowing the retina to absorb twice as much light because the light ‘comes back’. This provides a better vision in weak illumination conditions, at the expense of a loss in retinal precision. In these animals, the pupils seem to glow at night, because the back of the eye reflects incoming light.

1.2 The lateral geniculate nucleus (LGN)

From the two retinas, the visual signal is transferred along the optic nerves to the lateral geniculate nucleus (LGN, see Figure 1.3), a specific nucleus in the thalamus (a part of the diencephalon). Information (from both eyes) concerning the left visual field is transferred to the right hemisphere LGN, and conversely. A key feature of retinal processing is that there is no backward projection from the LGN or other visual areas onto the retina³. As a result, unlike most areas of the brain, retinal processing can be studied as a closed problem involving solely the retina itself.

Traditionally, the LGN has been seen as a simple relay for the visual signal, to provide input to the visual cortex. This assumption was based on the fact that

²In scotopic (‘night-time’) conditions, the psychophysical measure used is rather the *scotopic troland*, that includes a supplementary measure of the spectral composition of the incoming light, to account for the strong preference of our rod receptors to ‘greenish’ spectral light. See e.g. Lance Hahn’s retina page at <http://retina.anatomy.upenn.edu/lance/modelmath/units.photometric.html>

³In fact, some backward connections from LGN to the retina have already been reported anatomically, but rarely and with no known functionality.

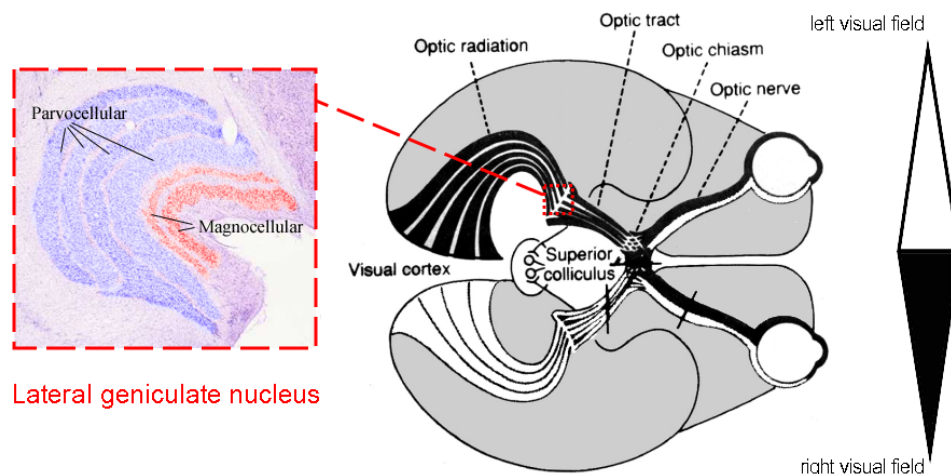


Figure 1.3: *The lateral geniculate nucleus (LGN) in the visual pathway.* The visual signal from the left visual field of both eyes (in white) is transmitted to the right hemisphere of the brain, while the visual signal from the right visual field (in black) is transmitted to the left hemisphere. The LGN is a thalamic nucleus that relays the visual signal before transmission to the cortex. It is a layered structure, and each layer *maps* the whole visual field, for a single eye. In the primate, some layers are associated to the Parvocellular pathway, and other layers to the Magnocellular pathway (see Chapter 3). The LGN is mostly a relay of the retinal signal, but there is strong evidence that it also has more complex and less well understood roles.

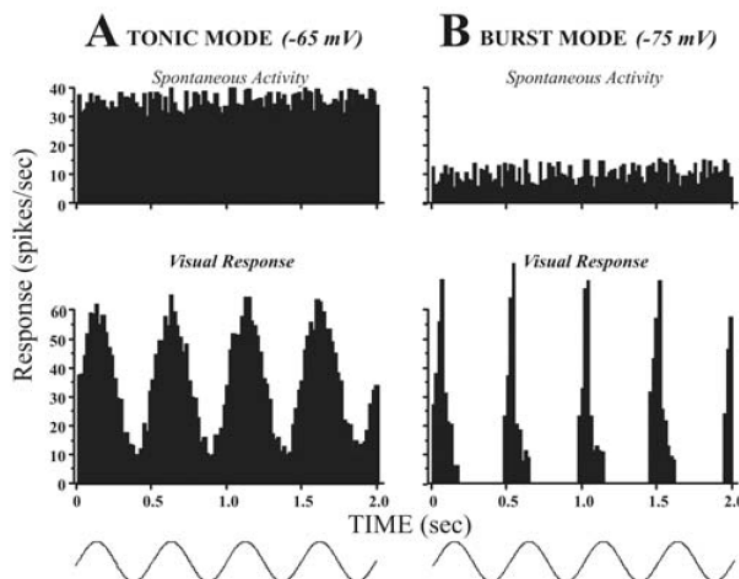


Figure 1.4: *Tonic and bursting activity in the LGN.* According to the value of their resting membrane potential (imposed by their synaptic entries), LGN relay cells can respond to a signal whether in a *tonic* fashion (large, regular activity) or in a *bursting* fashion (irregular activity with alternating bursts of spikes and silent periods). Cortical feedbacks are largely responsible for putting LGN cells in either spiking mode. From Sherman and Guillery [158].

LGN cells respond to stimuli in a way very similar to the ganglion cells that form the output of the retina, with a strong *center-surround* opposition (Section 3.2). The center-surround opposition of LGN cells was found in many studies: For references, see e.g. the LGN chapter of Sherman and Guillery [158] in the reference book *The Visual Neurosciences* [30].

At some places of this manuscript, we will refer to specific works on the LGN that confirm its similarities with the retinal output organization. For example, we mention the works of Cai *et al.* [26] on LGN receptive fields (Chapter 2), or the works of Neuenschwander *et al.* [121] on spiking synchronies in the retina and LGN (Chapter 3).

However, it is now well established that by some aspects, the LGN is much more than a simple relay. Indeed, retinal inputs constitute only about 10% of the total inputs of the LGN. The remaining input comes as a *feedback* from different areas of the visual cortex, and as recurrent connections made with inhibitory interneurons in the LGN itself [158]. Such connectivity is not that of a relay, but rather of a *platform* for visual information, somehow integrating the high-level processings that occur in the different visual cortical areas.

In particular, a specific functionality is present in the LGN and absent from the retinal output: An LGN relay cell can achieve two distinct spiking modes, the *tonic* and the *bursting* mode. This property is illustrated in Figure 1.4. The cell's tonic or bursting behavior depends mostly on the resting potential imposed on the cell by its synaptic inputs, and involves specific transient Calcium channels. It is believed that cortical feedbacks are largely responsible for the 'choice' of putting LGN cells in either of the two spiking modes. Possibly, the tonic mode could be more linked to attentional processes, while the bursting mode could allow the strong transmission of sudden unexpected visual cues. Sherman and Guillery 04 [158] are our reference for this whole paragraph.

To conclude, cells in the LGN display typical receptive fields very close to retinal receptive fields. Yet the LGN is clearly more than a simple relay and, as all areas of the brain, it displays complicated behaviors which are badly understood.

1.3 The primary visual cortex

From the LGN, the visual signal is mostly transmitted to the primary visual cortex, generally termed V1 (or area 17). The cortex is a two-dimensional, layered 'sheet' of neurons, which is strongly developed in primates and humans and responsible for high-level perception and abstraction.

Both cerebral hemispheres display symmetric visual areas, each one in charge of one side of the visual field. V1, the entry of the visual cortex, is probably the most studied area of the visual pathway. In humans and primates, V1 has been found to display a variety of neurons that form retinotopic maps of the visual field in a log-polar mapping, with many more neurons associated to the central region of the visual scene (see Figure 1.5). This predominance of the central region of the visual field reflects the architecture of the retina: in primates and humans, the center of the retina, termed the *fovea*, has a much greater spatial resolution than the periphery, with a greater density of retinal cells (see Section 2).

A striking feature of V1 is that several different types of visual informations are simultaneously mapped on the surface of the cortex. At each location of the visual

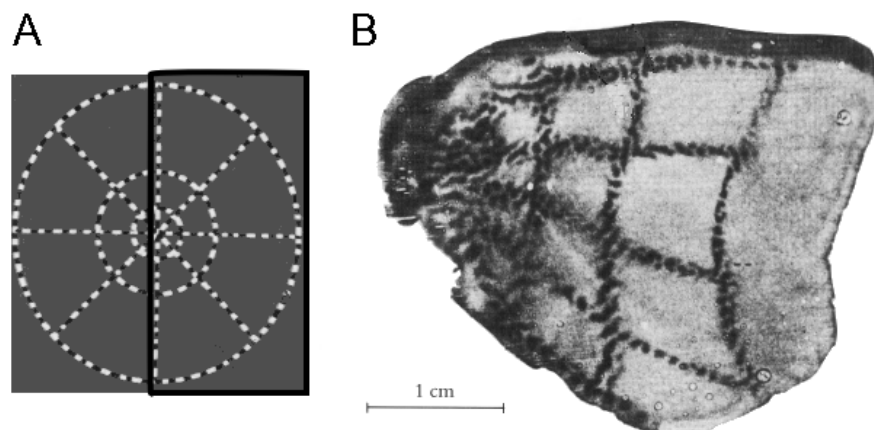


Figure 1.5: Retinotopic organization of the primary visual cortex (V1): The visual field is continuously mapped onto the visual cortex. *A*: A grid pattern made of concentric circles is presented to a macaque. The black box corresponds to the right visual field, that will be transferred to the left hemisphere of the brain. *B*: The grid pattern is reproduced at the level of the primary visual cortex (V1). The mapping from visual field to V1 is termed *retinotopic*, because it continuously preserves the topology of the retina. The central zone of the visual field is processed with great precision: It is processed by many neurons in V1, comparatively to the periphery. Mathematically, the mapping from visual field to V1 is well approximated by a log-polar scheme. From Tootell et al, 88 [168].

field, the activity pattern at the corresponding location in V1 codes simultaneously for different features:

- The orientation of image contours at this location. If a contour is present at this location of the visual field, some cells in V1 will respond preferentially, but only if the contour is along their preferred orientation.
- Ocular dominance. Many V1 cells are only sensitive to input from one specific eye. Some cells are equally sensitive to both eyes.
- Color information. Specific cells in V1 code for red/green and blue/yellow color oppositions.

The spatial organization of these different maps on a single two-dimensional surface of cortex is achieved through a complex multi-dimensional organization of V1 neurons around typical structures called ‘pinwheels’ [87], as illustrated in Figure 1.6.

1.4 Ventral and Dorsal pathways of the visual system

From V1, the primary cortical input, several other cortical areas proceed to more advanced processing of the visual information. These cortical areas can be associated to two distinct pathways of visual processing, largely independent. The *ventral* pathway, which involves areas such as V2, V4, V8, etc. is mostly dedicated to precise analysis of shape, texture, color, object recognition, etc. It has been termed the

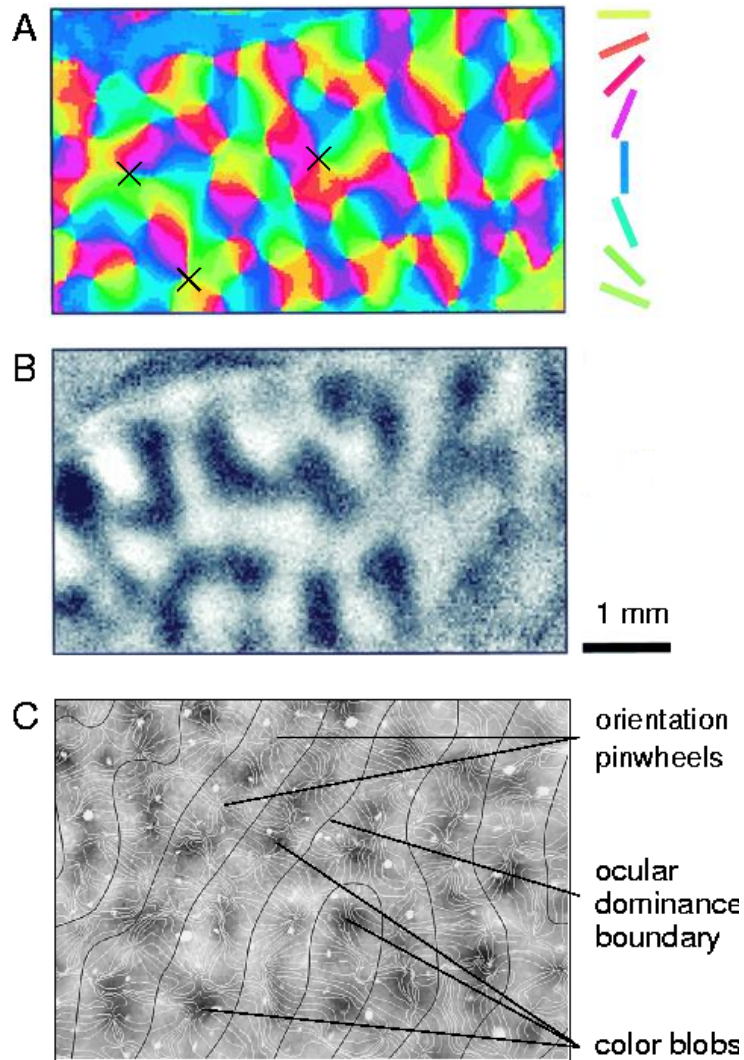


Figure 1.6: Simultaneous mapping of different visual features in the primary visual cortex. *A*: Orientation preferences in V1. Most V1 neurons respond preferentially to image edges in a particular orientation. Neurons are organized around ‘orientation pinwheels’, which are the singularities in the mapping of preferred orientations (examples marked with a cross). From [83]. *B*: Ocular dominance. Neurons in V1 respond preferentially to stimulation from one eye or the other. Scale for *A* and *B* represents 1 mm of visual cortex. From [83]. *C*: Color blobs, orientation preferences and ocular dominance. Aside from ocular dominance and orientation, V1 codes for color oppositions in special zones called cytochrome-oxydase (CO) *blobs* (in darker shade). Cells in the blobs are sensitive to color, and less sensitive to edges of high spatial frequency. Cells in interblobs (lighter shade) do not code for color, but respond to edges of high spatial frequency. The three simultaneous mappings (orientation, ocular dominance, color) have very correlated spatial structures. From [16].

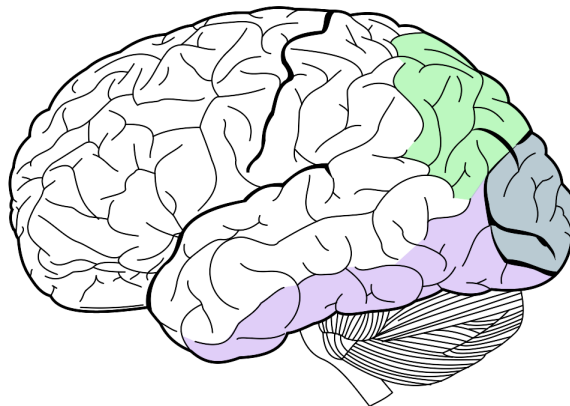


Figure 1.7: Ventral (purple) and dorsal (green) pathways schematically represented in the brain. Areas in the ventral - or 'What' - pathway are involved in precise form analysis and object recognition. Areas in the dorsal - or 'Where' - pathway are involved in general scene and motion analysis.

'Form', or 'What', pathway of the brain. By opposition, the *dorsal* pathway, involving areas such as V2, MT(V5) or MST, is dedicated to rough analysis of the visual scene as a whole, and of various movements in the visual field (objects, self-motion, etc.) It has been termed the 'Motion', or 'Where' pathway. These two distinct pathways are schematically represented in Figure 1.7.

The connections between various visual areas in the cortex are not obvious, and are less and less well understood as one gets to higher levels of processing. Many modulation feedbacks and thalamic relays strongly participate to the processing of visual information.

2 THE RETINA: A LAYERED NEURAL STRUCTURE _____

The retina is the neural entry of the visual system: It contains the first visual neurons, that convert the incoming light into an electrical signal sent to the brain. Here, we present a general anatomy of the retina. The main functions of the different types of retinal cells are evoked, providing landmarks for the detailed analysis that follows in Chapters 2 and 3.

2.1 Layered architecture of the retina

Visual cells in the retina are organized following a layered architecture, from light receptors responsible for the acquisition of incoming light, to ganglion cells that send the visual information to the brain in the form of *spike trains*. The successive layers of cells naturally define a functional architecture for the retina.

2.1.1 Five layers of cells

The retina contains five different types of visual neurons, that convey visual information thanks to their electrical activity. Figure 1.8(a) shows a section of a real mammalian retina and its anatomical interpretation. Cells of the same type are organized along layers, paving the whole retina. Layers are connected as described in Figure 1.8(b), and summarized in Figure 1.9. The five types of cells are:

- Light receptors
- Horizontal cells
- Bipolar cells
- Amacrine cells
- Ganglion cells

Their respective roles are briefly exposed in Section 2.2. We start by a general description of these cells and how they are organized in the retina.

Signal transmission in the retina

A first issue concerns the mode of electrical transmission used by neurons in the retina. In the brain, most neurons fire action potentials, or *spikes*, which are stereotyped electrical impulses well suited to relay the neural signal over long distances, along the neurons' axons (an axon is a typical elongated structure possessed by many cortical neurons to project their message far from their cellular body). Spikes form the basis of the neural code in the cortex.

By opposition, most retinal cells do not fire spikes. They are very localized cells, and most types do not possess any well-defined, elongated axon. Rather, retinal cells form organized mappings, with only local connections between neighboring cells, which occur mostly through dendrites or small axonic processes. Instead of displaying spike trains, most retinal neurons respond through graded, 'continuous' electrical signals. Such graded transmission is well-suited for a structure like the retina, where the cells form very local connections.

As an exception, the output cells of the retina, called ganglion cells, have long axons which form the optic nerve to the brain. These cells fire spikes, in order to rapidly transmit the electrical information to the brain, along the long distance of the optic nerve.

An organization in layers

Retinal cells are organized in *layers*: Cells of the same type pave the whole visual field by forming a homogeneous and dense array of cells. As a strong expression of this layered architecture, neighboring cells of the same layer are linked one to another through **electrical synapses**, also called **gap junctions**, small ionic channels allowing the bidirectional circulation of ions between the cells' two cytoplasm. These junctions are present with different strengths in each of the five layers, and result in a local sharing of the information between cells of the same type. Functionally, this local sharing of information has many advantages, as detailed in Chapter 2, Section 6.

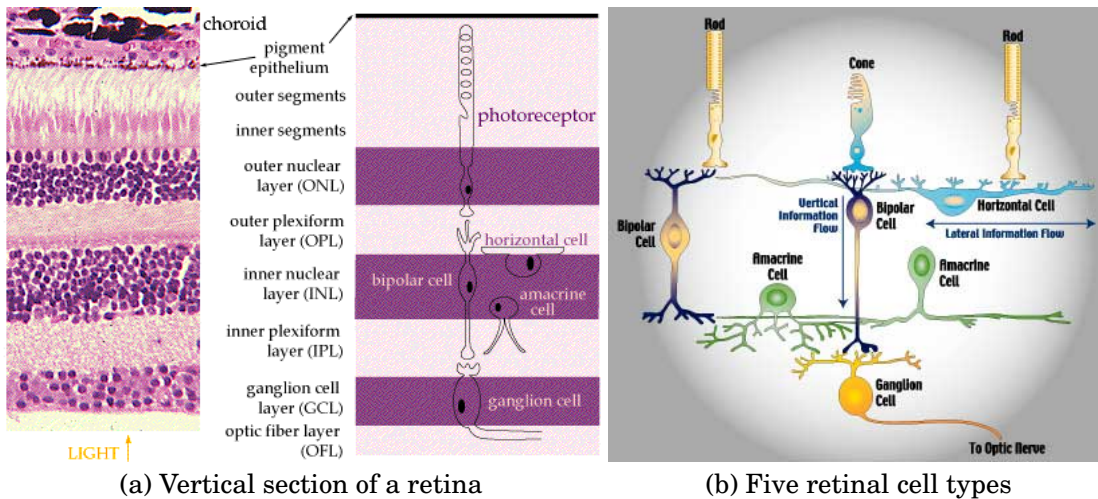


Figure 1.8: (a) Vertical section of a retina. There are five cell types, whose nuclei are located in three layers, and that make their synaptic connections in two plexiform layers. From [115]. (b) Schematic view of the five cell types and their connections. Found at [35].

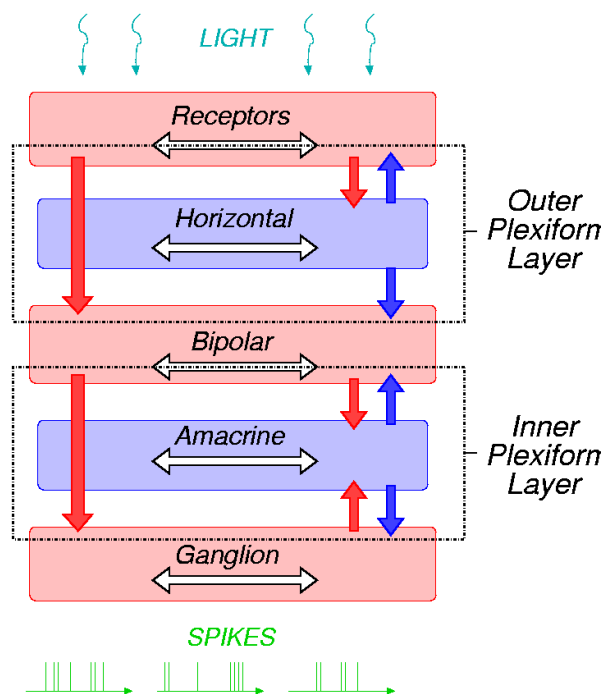


Figure 1.9: Schematic representation of retinal architecture. Excitatory cells are in red, inhibitory cells in blue. The direct excitatory pathway from light receptors to ganglion cells (thick arrows on the left) is modulated by the interstitial, inhibitory cells (small arrows on the right). Neighboring cells of the same type are generally linked through gap junctions (white horizontal arrows). Two distinct synaptic layers, the OPL and the IPL, define two successive filtering stages with similar excitatory-inhibitory patterns.

2.1.2 Synaptic connections between retinal layers

Neighboring cells from different layers are also linked one to another, this time through **chemical synapses**, i.e., mono-directional junctions involving neurotransmitter release from a pre-synaptic cell to a post-synaptic cell. Amongst neurons, some are *excitatory*, releasing neurotransmitters that tend to depolarize, or excite, their post-synaptic cells. Others are *inhibitory*, releasing neurotransmitters that tend to hyperpolarize, or inhibit, their post-synaptic cells. In the retina, both types of neurons are present.

Excitatory pathway. In the retina, light receptors, bipolar cells, and ganglion cells are excitatory neurons. They are represented in red in Figure 1.9, and their synaptic connections are depicted by red arrows. The synaptic pathway defined by the transmission *receptors*→*bipolar*→*ganglion* is thus a ‘direct’ excitatory pathway, that transmits the visual signal from the first cells of the processing (receptors) to the last (ganglion cells).

Inhibitory modulation. By opposition, the retina contains two types of inhibitory neurons: horizontal cells and amacrine cells. They are represented in blue in Figure 1.9, and their synaptic connections are depicted by blue arrows. As seen in Figure 1.9, inhibitory neurons are involved in ‘indirect’ signal transmission, in particular in feedback connections: horizontal cells onto light receptors, or amacrine cells onto bipolar cells.

Both horizontal and amacrine cells mediate modulation mechanisms, which serve to control and shape transmission through the ‘direct’ excitatory pathway. They have very important functional roles in the retina. They also have very *diverse* roles, especially amacrine cells which exist under various subtypes with different functionalities, not always well understood.

Two synaptic stages. All chemical synapses occur in two distinct layers, formed only of synaptic processes (Figure 1.8-a): the Outer Plexiform Layer (OPL) and the Inner Plexiform Layer (IPL)⁴. These two layers of synapses define *two (almost) independent processing stages*. The two layers are also represented functionally in Figure 1.9.

The OPL defines a first filtering structure through the interaction of light receptors, horizontal cells and bipolar cells. It is thought to mediate spatial oppositions that allow the retinal output to enhance image edges. The IPL defines a second filtering structure through the interaction of bipolar cells, amacrine cells and ganglion cells. It is thought to mediate additional spatio-temporal shaping of the visual signal.

2.1.3 Parallel pathways

Each type of retinal cell (receptor, horizontal, bipolar, amacrine and ganglion) exists under a variety of sub-types, with different morphological and physiological characteristics: Typical sub-types in a mammalian retina are represented in Figure 1.10. These sub-types are not connected to their neighboring cells randomly. Rather, distinct sub-types of cells connect into distinct pathways, and make the retinal output a

⁴Their name refers to the network (*plexus*) organization formed by the numerous synapses.

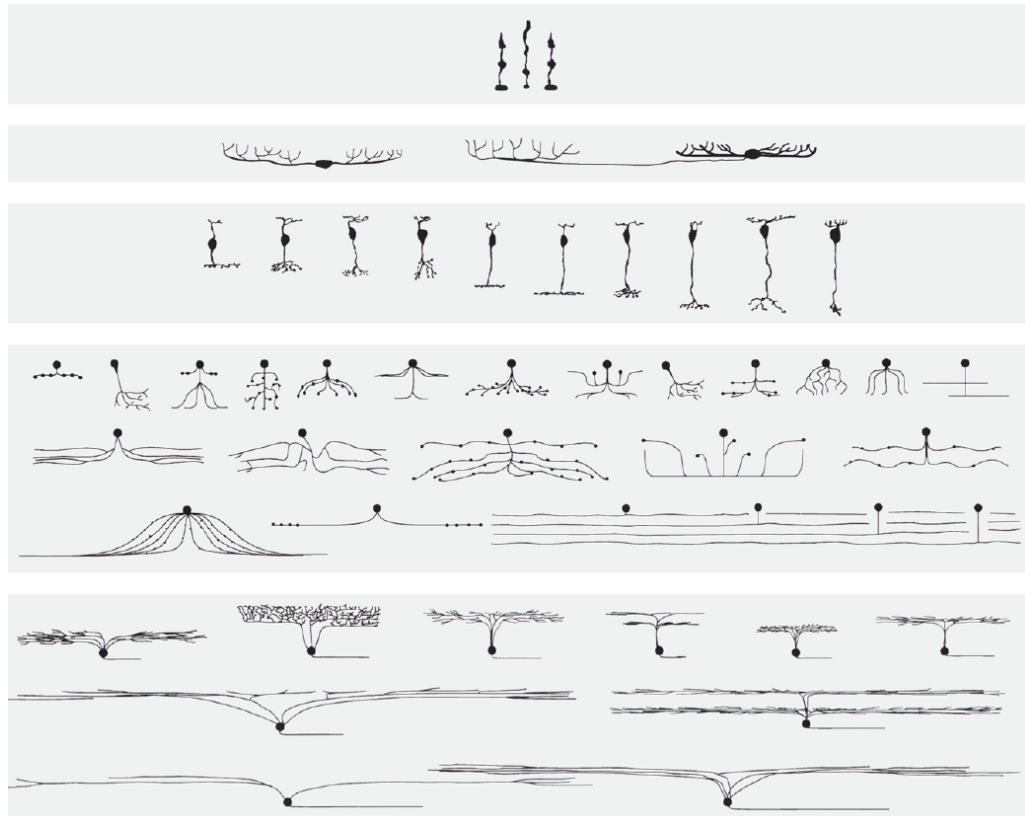


Figure 1.10: *Major types of cells in a typical mammalian retina.* From top to bottom: *Photoreceptors* are rods and two types of cones (three in some primates including humans). *Horizontal cells* exist in two major morphological subtypes termed *A* and *B*. *Bipolar cells*, present under 11 subtypes in primate retinas, have a typical elongated structure. *Amacrine cells* are the most various type of cell: 29 subtypes have been reported [107] that fall into two broad categories: small-field and wide-field cells. *Ganglion cells*, the output spiking cells of the retina, exist in 10 to 15 morphological subtypes in mammals. Images from the rabbit retina, except bipolar cells (rat retina). From Masland 01 [107].

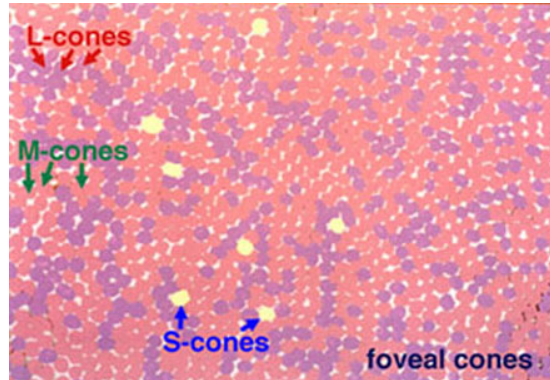


Figure 1.11: Paving of a primate fovea by cones. Notice how sparse short wave-length ('Blue') cones are. From [95], reproduced from *Lall and Cone, 1996*.

combination of several parallel signals with different spatio-temporal properties. In terms of filtering, this means that the diagram in Figure 1.9 exists in several, parallel versions involving different sub-types of cells. Examples of different coexisting retinal pathways include ON or OFF cells, parvo- and magno- cells, color opponent cells. . . The main retinal pathways are detailed in Chapter 3, Section 3.

2.2 Functions of different retinal cells

We now provide a first, very general presentation of the different types of retinal cells, without mentioning the various sub-types and pathways. We just present the main roles of each type of cell.

Receptors

Receptors receive, sample and integrate the light arriving at the back of the eye. They are of two kinds: *cones* and *rods* (both represented on top of Figure 1.8-b).

- Cones are activated at high illumination levels (daytime, termed *photopic* light conditions). They are the most useful source of information for the 'form' pathway of the visual system (involved in precise shape analysis and object recognition, see Section 1.7). In primate and human retinas there are three types of cones, sensitive to different wavelengths (Red, Green and Blue): cones encode color. Figure 1.11 shows a paving by cones in a primate retina.
- On the contrary, rods exist in a single version: They only see 'in black and white'. Rods are very sensitive to luminosity, and their response saturates at high illumination (daytime). They are much more numerous than cones. The rod signal is most useful at night (*scotopic* light conditions), and for the 'motion' pathway of the visual system (Section 1.7). Phylogenetically, rods seem to have appeared later in the evolution.

The integration of light by receptors is known as *phototransduction*. The output signal of the receptors is then transmitted to horizontal cells and bipolar cells, in the OPL.

Horizontal cells

Horizontal cells relay the signal from the receptors (through chemical synapses in the OPL), and are also highly coupled to their neighboring horizontal cells (through electrical synapses). This intra-layer coupling makes a horizontal cell sensitive to the *average* illumination in its neighborhood. Thanks to this measure of average luminance, horizontal cells modulate the transmission from light receptors to bipolar cells, in order to create invariance to luminance in the retinal output. Horizontal cells make feedback connections to receptors, and also feed-forward connections to bipolar cells.

Bipolar cells

In the OPL, bipolar cells are connected with both receptors and horizontal cells. But the sign of these two types of connexions are always different: If a bipolar cell is depolarized by the signal of receptors, it is hyperpolarized by the signal of horizontal cells, and vice-versa. Hence, a bipolar cell is always sensitive to a difference between the signal from receptors and its averaged version by the horizontal cells.

Such excitatory/inhibitory interaction is called a *synaptic triad*. The synaptic triad makes bipolar cells spatial and temporal *band-pass* filters: they behave like edge detectors. According to the respective signs of the connexions from receptors and horizontal cells, there will be ON-center cells and OFF-center cells (Chapter 3, Section 2).

Bipolar cells are also the input to the second filtering stage of the retina, the IPL. They possess an elongated structure with two dendritic trees (Figure 1.8-b), that gave them their name of 'bipolar'.

Amacrine cells

Synaptic transmissions in the IPL are relatively similar to those in the OPL, but less well understood. Indeed, amacrine cells, that play the same interstitial role as horizontal cells in the OPL, are a very *diverse* class of cells. They exist with various sizes, physiology and functions that are not all well understood.

Generally speaking, amacrine cells can be classified in two broad categories: Small-field and wide-field amacrine cells. Small-field amacrine cells are more involved into a temporal shaping of the retinal responses. Wide-field amacrine cells, some of which emit action potentials, are supposed to be involved in long-range synchronizations between the spike trains of neighboring ganglion cells.

Ganglion cells

Ganglion cells receive signal from bipolar and amacrine cells. They are the output of the retina, and they all fire *spikes* to the brain. They are the only retinal cells to possess a well-defined axon. The axons from ganglion cells form the optic nerve, and make their axonal terminations at the level of the LGN (Section 1.2).

2.3 Central vs. peripheral vision

When one wants to have a precise look at an object, one needs to move the eyes on it, so as to have the considered object projected at the very center of the retina. This

is because in several species, the retina exhibits a particular radial structure, with a central region that displays a much higher density of cells and, subsequently, a much better image resolution than the periphery. This central region is known as the *area centralis* in cats and dogs⁵. In primates and humans, the central region is even more specialized and precise: It is called the *fovea*. In humans, it covers about 6 degrees of visual field, the size of a fist at arm length. Humans even possess a more precise zone in the very center of the retina (diameter of 1.5 degrees, one or two fingers at arm length) called the *foveola*, at the core of our ability to execute very precise visual tasks such as reading.

Radial densities of photoreceptors

Figure 1.12 shows the densities of both types of receptors in a human retina, as a function of eccentricity r (distance from the center of retina). The fovea is packed with cones, which are the most spatially and temporally precise type of light receptors. Then, the density of cones follows a typical power law, proportional to r^{-1} . This translates into our decreasing ability to precisely see objects far from the center of our retina.

On the contrary, rods are virtually absent from the fovea. The density of rods reaches its peak at around 20 degrees of eccentricity. Then it decreases slowly, but no power law exists as obviously as for cones. Rods are much more numerous than cones, especially in peripheral regions. The great number of rods allows the retina to detect subtle illumination changes through *population coding*, even in the daytime when they are mostly saturated. It makes rod signal a good basis for movement detection. The counterpart of rods' population coding is the loss of spatial acuity. For this reason, the fovea doesn't contain rods: It is dedicated to precise, daytime, shape analysis based on cone signals.

The organization of rods and cones in our retina is well-adapted to the way we use the fovea and periphery of our eyes. Thanks to the high sensitivity of rods, the retinal periphery is useful for coarse detections of movement or salient image features. In a second time, the detected feature can be analyzed more precisely by cones in the fovea, after an appropriate eye movement.

Radial structure of the whole retinal scheme

The density decrease with eccentricity r is not only observed for receptors, but also for all subsequent retinal cell types, including ganglion cells. At the same time, the sizes of the cells' dendritic trees (the arborescence of synapses connecting a cell to its pre-synaptic cells) increase with r . An example is given for ganglion cells the primate retina, in Figure 1.13.

The increase of dendritic trees with r is very coherent from the point of view of signal sampling: If receptors are seen as the discrete sampling of a continuous illumination signal, then a decrease in the density of receptors means a decrease of the sampling frequency. To avoid aliasing, the subsequent retinal cells must integrate the receptor signal from a larger region, which the cells insure by increasing the

⁵Many mammalian retinas display an alternative structure known as the *visual streak*: A quite narrow horizontal zone that spans the whole width of the retina, and roughly corresponds to the projected location of the horizon on the retina. The density of cells and subsequent resolution is greater in this horizontal strip. For example, rabbits, horses and some species of dogs possess a visual streak. Cats, and some other species of dogs, possess *both* a visual streak and an even more precise *area centralis*.

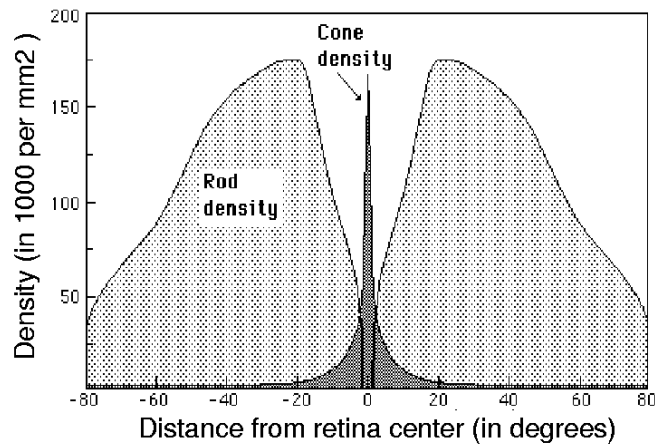


Figure 1.12: Density of receptors found in human retina. Reproduced from Osterberg 35 [127].

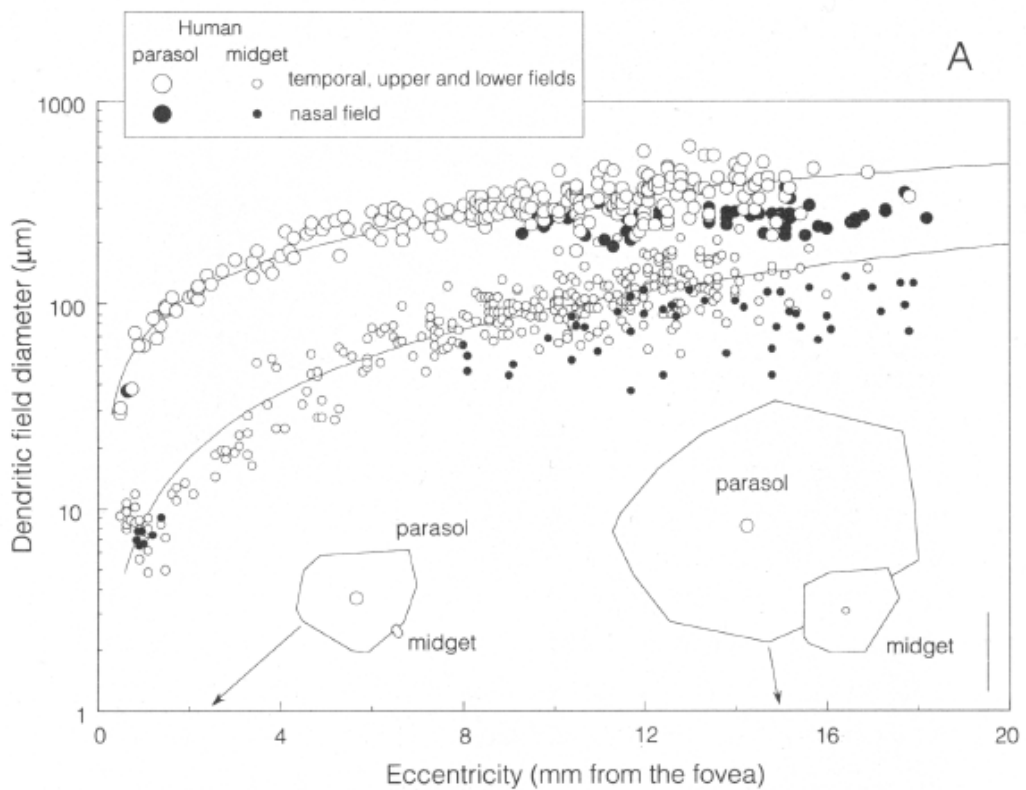


Figure 1.13: Measurements of ganglion dendritic tree sizes with respect to eccentricity, in the primate. The two sets of curves correspond to two distinct sub-types of ganglion cells, respectively Midget and Parasol cells. From Dacey-Petersen 92 [39].

size of their receptive fields. Perceptually, the image becomes less precise far from the fovea.

Figure 1.13 illustrates the global scaling of dendritic trees with eccentricity r . The two types of ganglion cells measured here, Midget and Parasol, are discussed in Chapter 3. For the current discussion, it is sufficient to know that Midget cells take their input mostly from cones, whereas Parasol cells take a mixed input from cones and rods. The authors [39] estimate the average Midget dendritic trees to approximately scale with r , while Parasol cells' dendritic trees rather scale with $r^{0.65}$. These power laws are interesting to compare with the receptor densities illustrated in Figure 1.12, and in particular with cone density that grossly scales with r^{-1} . Midget cells receive their inputs mostly from cones, and their dendritic trees follow a law inversely proportional to cone density: this suggests that the whole cone pathway might scale with r . Conversely, Parasol cells receive a mixed input of rods and cones, and rod density decreases much slower than cone density. As a result, the Parasol receptive field size increases more slowly with eccentricity, with a power law approximated by $r^{0.65}$.

3 GENERAL CHARACTERISTICS OF THE RETINAL OUTPUT

In this last Section, we present the main characteristics of retinal filtering: First, retinal cells are divided in ON and OFF pathways. Second, retinal cells display a preference for stimuli with a strong spatial structure (edges), thanks to a *center-surround* organization of their receptive fields. Finally, retinal cells can be distinguished according to their temporal behavior: Some cells, termed *transient*, respond by short peaks of activity and remain silent otherwise, while other cells, termed *sustained*, have a longer lasting activity in response to stimuli.

When light hits the back of the eye, it is absorbed by specific photopigments in the outer segments of the first retinal neurons, the light receptors. The subsequent mechanism, phototransduction, involves a complex cascade of catalyzed reactions, which end up in the creation of a light-induced electrical current, or *photocurrent*, through the membranes of light receptors.

After phototransduction has given rise to the photocurrent, connectivity of the subsequent layers of cells serves to shape and transform the visual signal, defining what we could term the retinal code. Finally, ganglion cells, which form the last layer of the retina, send the signal to the brain in the form of spike trains.

Historically, this spiking output has been the first and privileged subject of study for experimentalists. Naturally, a first reason is that the retina's functional importance lies precisely in the output of ganglion cells, as received and processed by the brain. A second, practical reason is that measurements were much easier than elsewhere in the retina: Ganglion cells are much larger than other retinal cells, whose small sizes make experimental measures difficult, in particular in mammalian and primate retinas. Also, ganglion cells fire spikes that are easily captured by extra-cellular recordings, whereas other retinal cells can only be studied by intra-cellular techniques.

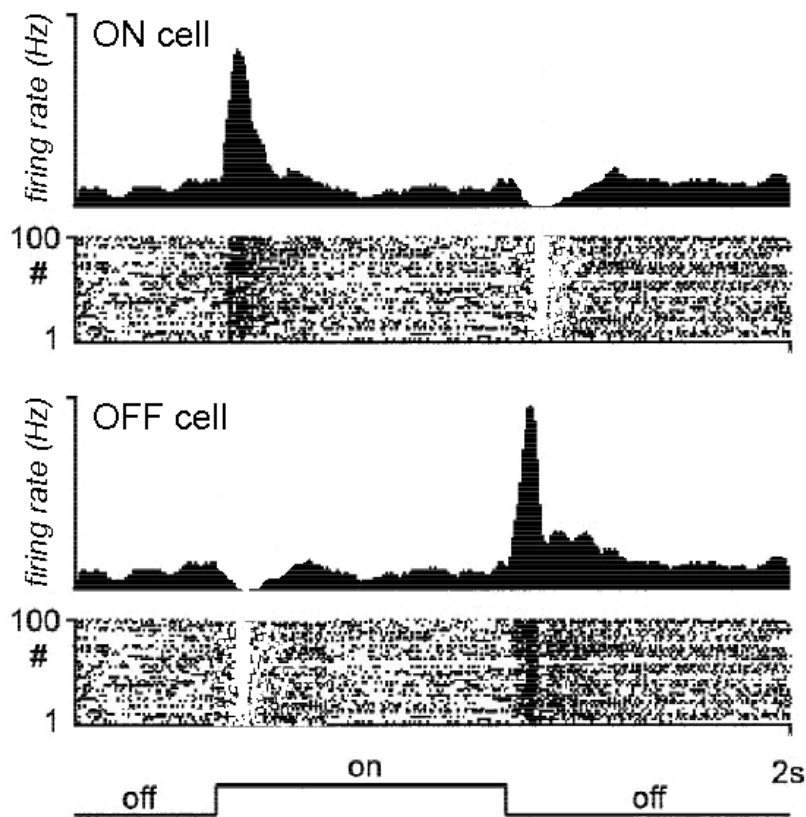


Figure 1.14: *Schematic behavior of ON and OFF cells.* In response to a uniform flash of light (of approximately 1 second, schematically represented in lower trace), ON cells (upper panel) respond at light onset while OFF cells (lower panel) respond at light offset. For each cell, the spike trains resulting from different trials can be considered separately as a raster plot, or summed in a histogram to consider the *average mean firing rate* in response to the stimulus. Figure is modified from real data: Two artificial ON and OFF raster plots are derived from the firing of a single perigeniculate ON-OFF cell in the cat thalamus, from [67].

In this section, we only focus on the properties of the retina's output, as measured from the emitted spike trains of ganglion cells. Physiological properties of the intermediate signals are discussed more thoroughly in Chapter 3.

3.1 Responses to light steps (ON and OFF cells)

The first distinction that can be made between retinal cells is their behavior in response to a sudden steps of light in their receptive field. Some cells respond strongly to light increments, while others respond strongly to light decrements. The first are termed 'ON', and the second 'OFF' cells. This property is illustrated in Figure 1.14, that presents schematized responses of ON and OFF cells.

ON-OFF symmetry. A first observation from Figure 1.14 is that qualitatively, ON and OFF cells seem to respond symmetrically: Their behaviors seem identical,

except the response of an ON cell to a light increment is that of an OFF cell to light decrement, and reciprocally. In fact, the relative symmetry between ON and OFF cells also holds for more complex stimuli: As a first approximation, *an OFF cell responds to an image as an ON cell would respond to the image with inversed luminosity* (as a photograph negative).

ON-OFF asymmetries. At a more detailed level, several asymmetries exist between ON and OFF pathways. Examples of these asymmetries can be found in Chapter 3, Section 3.2.2.

Spontaneous firing activity. In the absence of visual stimulation (for example, in the dark), an important proportion of retinal cells already have a spiking activity, which is generally termed ‘spontaneous’. By opposition, other cells are totally silent in the absence of a strong visual stimulation. Spontaneous activity can be observed in Figure 1.14, where the considered cells fire spikes throughout the whole stimulation, even when there is no specific stimulus to trigger them. A cell’s spontaneous activity during an experiment can depend on the cell’s intrinsic properties, but also on the general state of the network in the given experiment. It is thus a complex and ill-defined phenomenon.

Trial-to-trial variability and average firing rate. Finally, Figure 1.14 is the occasion for us to remind the concept of *average firing rate* for a spiking neuron: When the same experimental protocol is repeated several times on a neuron, the emitted spike trains show some variability between the trials, due to internal noise etc. The average firing rate is obtained by counting the emitted spikes over several repetitions of the same experiment, to obtain an ‘average instantaneous activity’ for the neuron in response to the stimulus. The average firing rate provides a more intuitive, and likely reliable, measure of the neuron’s response. However, important information lying in the precise times of the spikes might be lost in the process. The problematic of spike coding is presented in Chapter 3, Section 4.

3.2 Center-Surround architecture (concentric cells)

Receptive field

As a necessary foreword, let us remind the notion of a cell’s receptive field: The *classical receptive field* of a retinal cell is the area of the visual field where a light stimulation has an influence on the firing of the cell, when the rest of the visual field is not stimulated (gray field). Generally, in the literature, this is the notion referred to when using the term ‘receptive field’.

By opposition, the *non-classical* receptive field describes the visual region that has potential influence on the firing of the cell, although a light stimulation in this region does not modify the firing if the rest of the scene is a gray field. It is a secondary influence, requiring stimulation on the classical receptive field (see e.g. the LED cell in Chapter 3, Section 3.2.6).

In the retina, the (classical) receptive field of most ganglion cells displays a characteristic *center-surround* architecture.

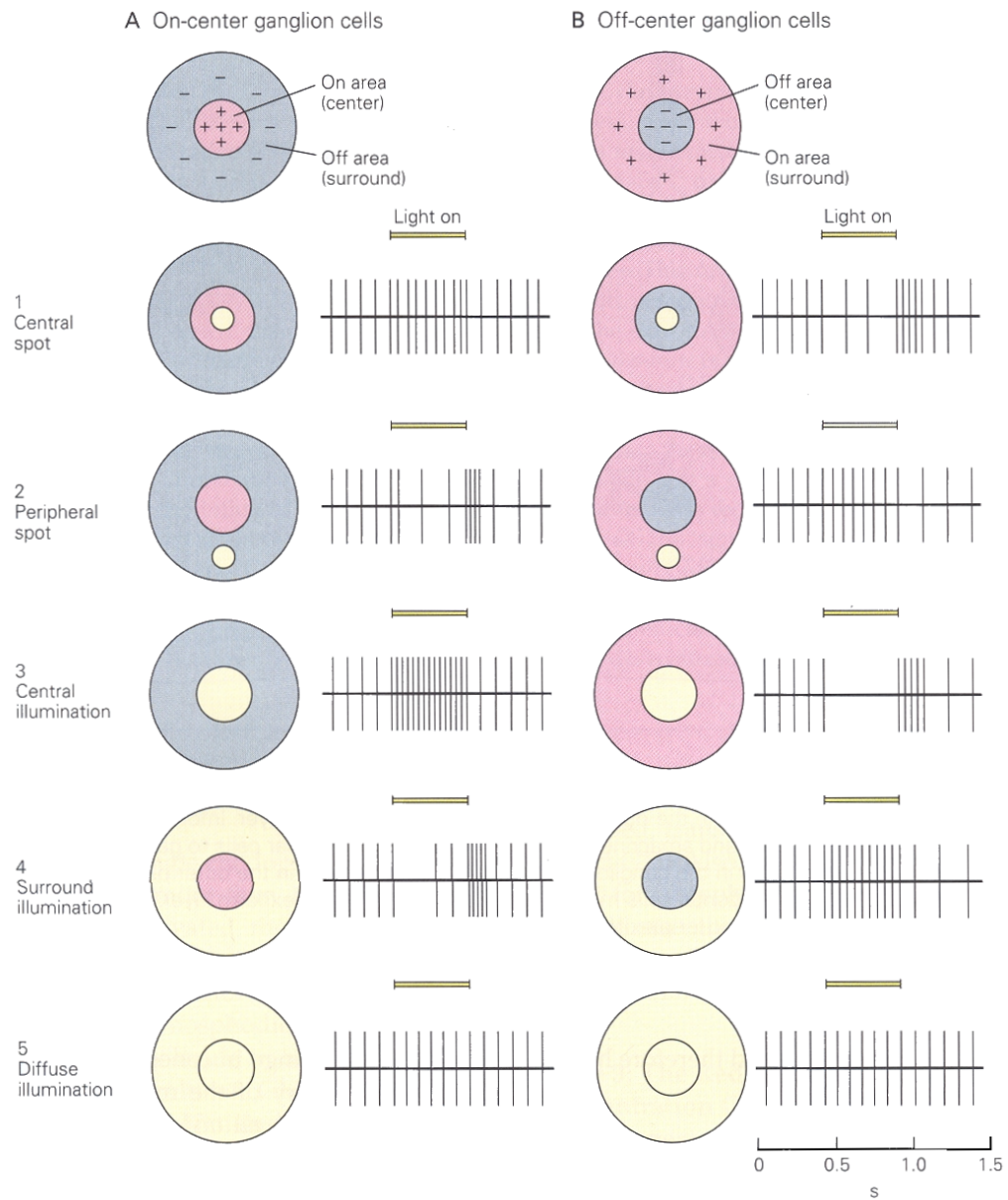


Figure 1.15: Response of ON and OFF retinal cells, with a center-surround architecture. Figure from [87], after the works of Kuffler [96].

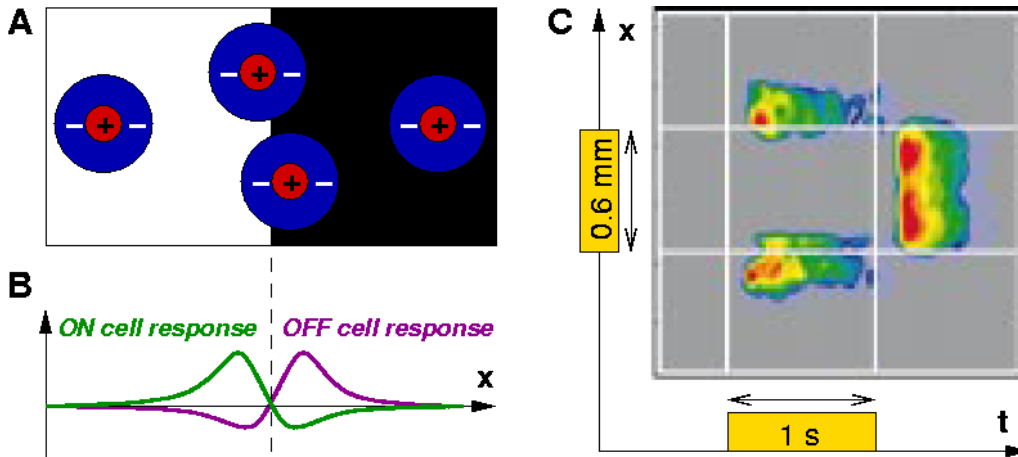


Figure 1.16: Edge detection via the center-surround architecture. *A*: Different locations of a center-surround receptive field, near an image edge. *B*: corresponding spatial profile of activity for ON and OFF cells, along a one-dimensional line perpendicular to the edge. *C*: *Edge detection in OFF-center ganglion cells of the rabbit*. The average firing rate of a one-dimensional line of cells (vertical axis), in response to a square spot of light, is represented at each time t (horizontal axis). From Roska-Werblin 01 [146], activity pattern inferred from the responses of a single cell (see text).

Center-surround opposition

The center-surround architecture is probably the most well-known fact about retinal filtering. It was first observed in the mammalian retina by Kuffler in the 50's [96]. When a small spot of light is presented in front of a ganglion cell's receptive field, it evokes different reactions according to the precise location of the spot:

- If the spot is at the *center* of the receptive field, it elicits a positive response of the ganglion cell - that is, an increased firing of spikes.
- If the spot is at the *surround* of the receptive field, then it inhibits the ganglion cell: If the cell has a significant spontaneous firing rate, then this firing rate decreases when the spot is in the surround. If the cell has no spontaneous firing rate, the spot still has an inhibitory effect, making the cell harder to excite by a second simultaneous stimulus.

Both ON and OFF cells display a similar opposition. This is represented in Figure 1.15. Note that we have just enounced the center-surround behavior for an ON ganglion cell, stimulated by a spot of light brighter than the ambient illumination. For an OFF cell to have the same reaction, the spot should be *darker* than the ambient illumination. On the contrary, when an OFF cell is stimulated with a spot of bright light, it displays an opposite behavior: Stimulation in the center inhibits the cell, while stimulation in the surround excites it.

Edge detection

The center-surround architecture is well-known because of its important functional consequences: As a result, retinal ganglion cells act as detectors of *strong spatial*

contrast, such as object edges. Indeed, the *surround* signal provides an average of the illumination in the neighborhood of the cell, to which the more precise *center* can be compared, thus increasing retinal sensitivity to small details.

For example, when an edge is present in the image, the strongest responses are for cells located near the edge, such that:

- The *center* receptive field lies on a single side of the edge, providing strong excitation to the cell.
- The *surround* receptive field lies *across* the edge, providing little inhibition on the cell.

This property is schematized in Figure 1.16 *A* and *B*. As an illustration of edge detection in real retinas, Figure 1.16 *C* presents a reconstructed recording for an array of rabbit OFF-center ganglion cells, in response to an appearing square spot of light. The simultaneous activity of a one-dimensional array of ganglion cells was recorded over time⁶. The square spot of light was on for a second. The size of the square was 600 μm on the retina, which corresponds roughly to the size of two fingers at arm length. Two simultaneous properties of OFF ganglion cells can be simultaneously observed in this recording.

First, during the presence of the square on the retina, these ganglion cells indeed have a strong response near to the square's edges. More precisely, strong responding cells are on the *dark* side of the square's edges, since they are OFF cells (see Figure 1.16 *B*).

Second, all cells have a strong activity at offset of the square (after one second), including cells which are not near the edges of the square. Indeed, all cells observe a sudden temporal light decrement at that instant, and respond to it because they are OFF cells.

This experiment is a good illustration of the *dual* coding, spatial and temporal, that simultaneously occurs in most ganglion cells.

Concentric vs. non-concentric receptive fields

Cells with a receptive field displaying a center-surround architecture are often termed *concentric*. In most mammalian retinas, concentric receptive fields form an important proportion of the retina's output cells (although the exact proportion is not well established, and varies according to the species considered).

However, non-concentric cells are also present in the retina, probably in a 'comparable' proportion. Such cells are generally less well understood. In most of them, a center-surround architecture still underlies their behavior, although modified or masked by subsequent interactions: See Chapter 3, Section 3.

A complex phenomenon

As we present in Chapter 2, a simple model of linear filtering, based on Difference-of-Gaussians (DOG) filters, accounts for several aspects of the center-surround opposition in retinal receptive fields. However, many questions remain unsolved concerning the center-surround architecture:

⁶In fact, the authors [146] used a smart experimental protocol where a *single* ganglion cell provided the whole reconstructed array: It was the square stimulus that was moved between successive trials, to obtain the response of the cell at each position relative to the square.

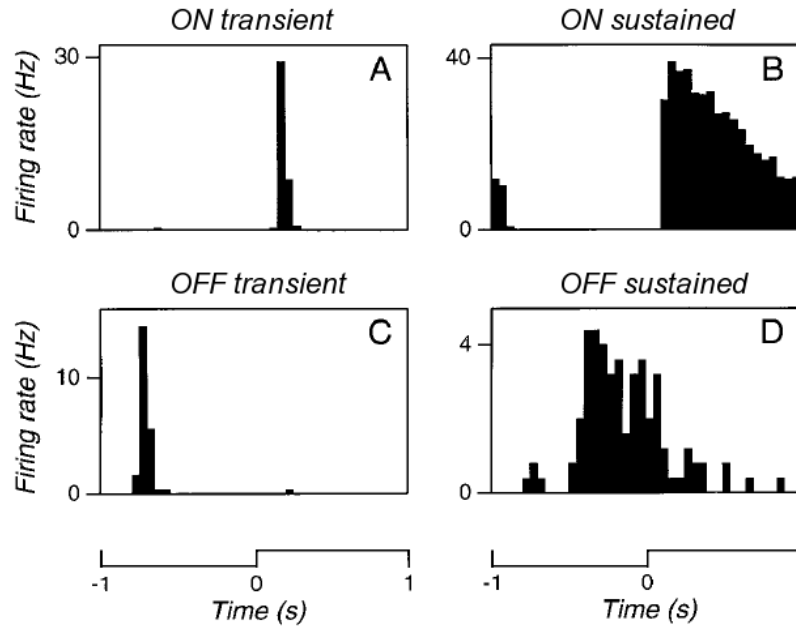


Figure 1.17: *Transient and sustained cells in the retina.* In response to a continuous stimulation, some retinal cells have a sustained response (right-hand side), while others have only a short response at stimulus onset (left-hand side). Sustained cells are termed *tonic*, and transient cells are termed *phasic*. Mouse retina, from [122].

- The biological origin of the phenomenon is still controversial. The opposition is known to arise, at least in part, through synaptic interactions in the OPL. However, for many types of ganglion cells, interactions in the IPL have been found to largely contribute to the phenomenon (Chapter 3, Sections 2.3 and 3).
- Center-surround opposition is not a static feature in our retinas. For example, the relative size and influence of the *surround* varies according to the ambient level of luminosity, through the influence of a particular class of dopaminergic amacrine cells. This particular adaptation effect is supposed to improve the signal-to-noise ratio (SNR) in dark conditions where the photocurrent is particularly noisy (Chapter 3, Section 5).
- The center-surround architecture is often associated to edge detection. But at a more detailed glance, the perceptual correlate of center-surround oppositions is not evident. According to the sizes and relative weights of *center* and *surround* receptive fields, the activity pattern of the cells can vary drastically (see Figure 2.2).

3.3 Temporal behavior (transient and sustained cells)

In Figure 1.14, it can be observed that the considered cells, ON or OFF, do not respond throughout the whole presence of their preferred stimulus, but only at *onset*. In other words, the depicted cells seem to be preferentially sensible to *temporal change*. This is in fact a very intrinsic behavior, shared by virtually all sensory neurons. This behavior is strongly related to the notion of information transmission,

and can be explained intuitively: *If a stimulus is kept constant, then information transmission about this stimulus is redundant because it has already been transmitted in the past. As a result, after an initial phase of coding, the neuron needs not keep on coding for a constant stimulus.*

However, in the retina, strong differences exist between ganglion cells, concerning the shape and time scales of their temporal behavior. Figure 1.17 illustrates these differences, between *sustained* -or *tonic*- cells, and *transient* -or *phasic*- cells. The tonic-phasic opposition is a general concept in physiology that can be described in simple words: *“A tonic process is one that continues for some time or indefinitely after being initiated, while a phasic process is one that shuts down quickly”* [61]. Figure 1.14 displays two ‘extremes’ for transient and sustained cells: The transient cells (left column) respond for one or two hundreds of milliseconds only, while the sustained cells (right column) respond for a whole second.

Multiple origins of temporal transients

When considered in detail, the temporal response of retinal cells is an extremely complex phenomenon. Between the two extremes depicted in Figure 1.14, there is a huge variety of possible temporal behaviors, according to the type of cell, the stimulus it undergoes, and the species considered.

The explanation for this complexity is simple: Each biological relay of signal transmission (cellular integration, synaptic transmission, membranar ionic channels, control mechanisms. . .) has its typical temporal behavior, and internal time scale. The temporal behavior of retinal processing as a whole, results from the addition of all these successive processing stages, and is thus a very complex and *distributed* phenomenon.

For example, the fast shutting down (a few hundreds of milliseconds) of the *transient* cells in Figure 1.14 results largely from a network architecture: These cells receive a delayed inhibition from other cells, that helps to cut their response. By opposition, the slow decrease in the response of the *sustained* cells in Figure 1.14 is largely due to slow cellular adaptation: A general ‘calming down’ of all neurons in the pathway due to the stationarity of their responses. We refer to the next chapters for more details.

As a result of the distributed nature of the retina’s temporal behavior, a large-scale model must introduce some drastic simplifications regarding temporal processing. Some functional principles must be found, that yield both conceptual simplicity and a relative similarity with the real retinal output. In particular, we believe that temporal behaviors in the retina could be better understood if they were related to information-theory calculations and interpretations.

CONCLUSION

In this chapter, we have presented an overview of retinal filtering and its role in the larger scheme of our visual system. The two following chapters study in more details the retinal properties introduced here. Chapter 2 takes the modeler’s point of view by introducing linear filtering, an unavoidable tool to model retinal function. By opposition, Chapter 3 takes the experimentalist’s point of view, going further into the architecture and physiology of real retinas. Both chapters must be seen

as serving a common purpose: Find a model that can encompass the *functionality* embedded in the retina's complex physiology.

LINEAR APPROXIMATIONS AND MODELING

In this chapter, we present the linear tools which are widely used to account for retinal filtering. Linear filtering is a necessary tool for a retinal model. First, it is a conceptually simple and mathematically well-defined framework for which a powerful theory is available, e.g., thanks to Fourier analysis. At the same time, linear models have a lot of experimental successes, yielding many correct predictions of real data. As a result, linear filtering is a strong component of virtually all retinal models, including those which possess additional nonlinear properties.

Contents

1	Introduction: Linear receptive fields	54
2	Center-surround organization and the Difference of Gaussians	55
3	Linear models for temporal transients	59
4	Generalized spatio-temporal receptive fields	65
5	Reverse correlation and LN analysis	67
6	Linear models for electrical coupling	71
7	Conductance equation and other nonlinear filtering: The Linear ODE framework	75

1 INTRODUCTION: LINEAR RECEPTIVE FIELDS _____

Consider a retinal cell centered in (x_0, y_0) on the retina, with a receptive field RF having (x_0, y_0) as its spatial origin. A linear approximation of its activity consists in finding the spatio-temporal kernel $K(x, y, t)$ for which the following equation is best verified:

$$A(t) = \int_{u=0}^{+\infty} \int_{(x,y) \in \text{RF}} I(x_0 - x, y_0 - y, t - u) K(x, y, u) dx dy du, \quad (2.1)$$

where $I(x, y, t)$ is the luminosity profile of the image, and $A(t)$ is a measure of activity appropriate to the type of cell (its membrane potential if it is a non-spiking cell, or its firing rate if it is a spiking cell). This is a formal way to write that $A(t)$ depends linearly on all past values for the input image I located in the cell's receptive field RF. By extent, K is often described as the *linear receptive field* of the cell.

Convolution

In fact, the operation performed in (2.1) corresponds to the well-defined mathematical concept of *convolution*. Accordingly, (2.1) can be rewritten:

$$A(t) = (I * K)(x_0, y_0, t), \quad (2.2)$$

where symbol $*$ denotes spatio-temporal convolution. Fourier analysis is particularly suitable for the study of that kind of filter, because convolution corresponds to multiplication in the Fourier space.

Separating time and space

Often, one desires to study separately the spatial and temporal properties of filtering for the cell. For example, one can craft a input sequence whose spatial structure at each time t is entirely defined by a single number $I(t)$ (for example, a uniform flickering screen, or a static image whose illumination is modulated in time). In this case, the temporal behavior of the cell can be studied linearly by:

$$A(t) = \int_{u=0}^{+\infty} I(t - u) K_{\text{temp}}(u) du.$$

Conversely, one can only be interested in some measure of the cell's activity, in response to a static image $I(x, y)$. This can be linearly modeled by:

$$A = \int_{(x,y) \in \text{RF}} I(x_0 - x, y_0 - y) K_{\text{spat}}(x, y) dx dy.$$

However, in this case, the exact nature of activity A is more ambiguous, and depends on the nature of the experiment. It can be an equilibrium activity for the cell (after waiting for sufficiently long – but remember that in most cases, cellular activity to a static stimulus declines over time). Rather, it can be a peak of activity, soon after image onset. Also, it can be some integrated measure of activity over time.

In fact, linear kernels for retinal cells are generally *non-separable* in time and space: The best-fitting linear kernel $K(x, y, t)$ cannot be written as a product

$K_{\text{spat}}(x, y)K_{\text{temp}}(t)$. As a result, all reductions to either temporal or spatial properties only necessarily imply a loss of information: Measuring separately filters of the form $K_{\text{spat}}(x, y)$ or $K_{\text{temp}}(t)$ through specific experiments, does not allow to reconstruct the best spatio-temporal filter.

To conclude, many magnitudes measured in different experiments can be approximated by linear models. Such magnitudes include: Average firing rate, peak of activity for a cell, synaptic inputs to a cell, etc. According to the experiment, the accent can be put on the whole spatio-temporal pattern of the stimulus, or on simpler expressions of the stimulus that are temporal only or spatial only. In the second case, information is lost about the ‘real’ spatio-temporal kernel, because retinal receptive field is generally not separable.

Whatever the experiment, the best-fitting linear kernel will always be an approximation that depends on the particular experimental conditions. A different experiment, especially at different illumination levels, will provide a different best-fitting linear kernel, although probably related to the first one. This is because many nonlinear adaptation factors influence retinal processing (Chapter 3, Section 5).

In Sections 2 and 3, we present separately spatial and temporal linear approximations for the retina. In Section 4 and 5, we present more general tools of linear modeling.

2 CENTER-SURROUND ORGANIZATION AND THE DIFFERENCE OF GAUSSIANS

The DOG model

In the 60’s, Rodieck [143] and Enroth-Cugell and Robson [59] showed that the spatial center-surround opposition is well approximated by a filter consisting of a Difference of Gaussians:

$$K_{\text{spat}}(x, y) = w_C G_{\sigma_C}(x, y) - w_S G_{\sigma_S}(x, y), \quad (2.3)$$

where w_C and w_S are the respective weights of the *center* and *surround* components of the receptive field, and $G_{\sigma}(x, y)$ is a normalized, two-dimensional Gaussian function of standard deviation σ :

$$G_{\sigma}(x, y) = \frac{\exp\left(-\frac{(x^2 + y^2)}{(2\sigma^2)}\right)}{2\pi\sigma^2}. \quad (2.4)$$

By ‘normalized’, we mean that the spatial integral of G_{σ} is 1: When applied as a filter, it has a linear gain of 1, so that the linear gains are only fixed by w_C and w_S . The DOG approximation of retinal receptive fields is illustrated in Figure 2.1 A.

Figure 2.1 B shows an application of the DOG model to predict the response of a primate ganglion cell to gratings of different spatial frequencies [37], measured as the amplitude of variation in the cell’s firing rate. This type of study is closely related to Fourier analysis: The output log-log curves in Figure 2.1 B represent the

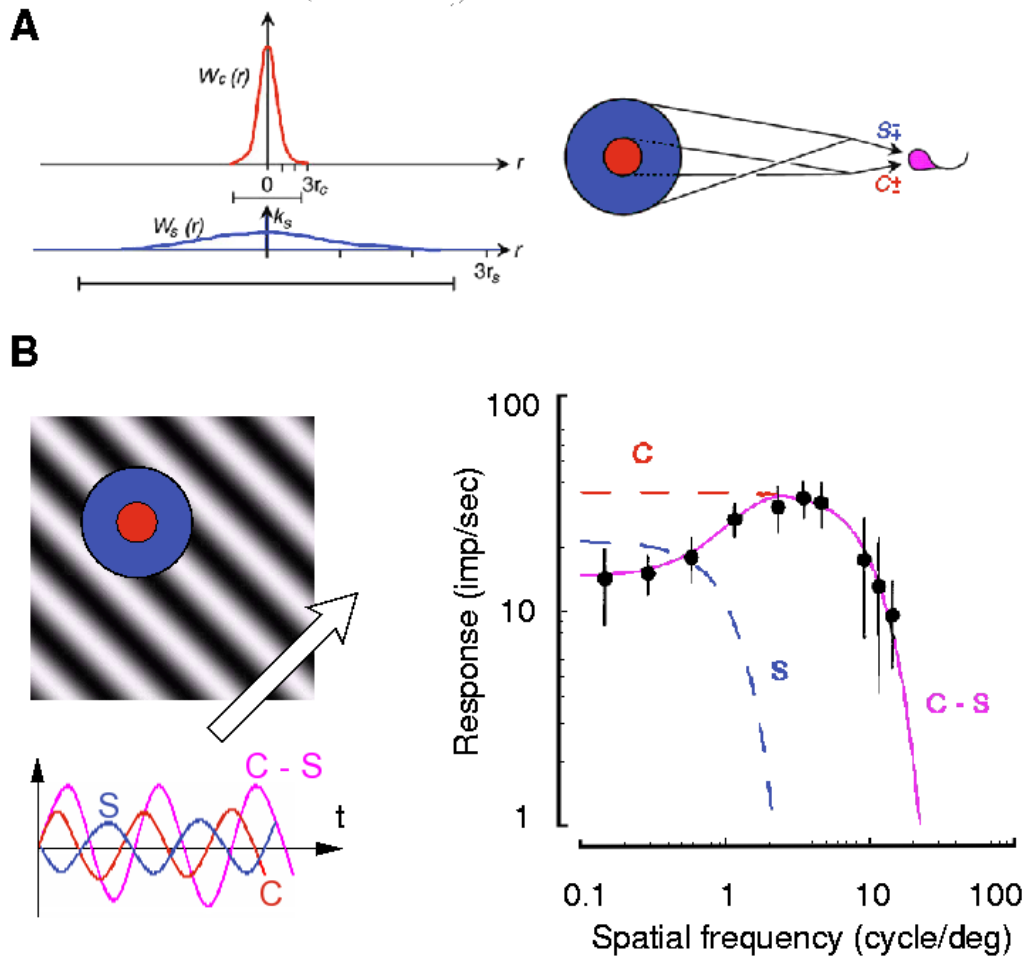


Figure 2.1: A: The Difference-of-Gaussians (DOG) approximation for center-surround receptive fields. Reproduced from [95], and the original works of Enroth-Cugell and Robson 66 [59] B: Response of a primate ganglion cell to drifting gratings of different spatial frequencies is by a DOG model. The measured output is the amplitude of the cell's center, surround, and total response. Drift frequency of 4 Hz. From Croner-Kaplan 95 [37].

amplitude of the Fourier transform of the cell's best fitting linear kernel $K_{\text{spat}}(x, y)$. In this particular experiment, the fit is very good.

Not all retinal cells are well fit by a DOG model. Some cells have a very linear spatial behavior (X cells in cat, Parvo cells in primate...). They generally coincide with the spatially precise cells, that provide input to the *Form* pathway of the brain. Other cells display a strong spatial nonlinearity (Y cells in cat, M cells in primate...). They generally coincide with the temporally precise cells, that provide input to the *Motion* pathway of the brain (see Chapter 3, Section 3).

Remark: Note that in the experiment of Figure 2.1 B, this particular measure of 'spatial' response also relies on temporal properties, since the grating *drifts* in front of the cell with a temporal frequency of 4 Hz. It allows to directly calculate the 'spatial amplitude' of the cell's response with a single trial, since the output amplitude of response directly accounts, through temporal integration, for all possible spatial phases of the grating in front of the cell.

By opposition, one could get another measure of a spatial linear kernel, from the responses of the cell to purely static images. This would be more complicated, because: (i) In response to a static image, the cell's response is transient at image onset, then declines; so the measure of activity is less reliable (e.g. amplitude of the transient peak). (ii) One would have to do several trials with different spatial locations of the grating in front of the cell, to reconstruct a 'two-dimensional map' of the cell's responses to the grating, and measure amplitudes of variations among this map.

Whatever the experimental protocol chosen to do this, some temporal information (phases for the cell's responses) interferes with the 'purely spatial' information sought by the experiment, because the cell's real receptive field is not separable (see Section 4). As a result, the 'spatial' linear filters measured through both experiments would surely display slight, but relevant, differences. ■

Parameter fitting in the DOG model

The DOG model in (2.3) is driven by four parameters. Here, we review the functional importance of each of these parameters, and compare it with its experimental estimations. Our goal is to illustrate how hard it is to link a cellular model with functional and perceptual consequences, even using a simple retinal model such as the DOG (linear, and with a spatial behavior only). From the point of view of functional image transmission by whole layer of cells, the parameters of the DOG model have the following interpretation:

- **Spatial resolution** σ_C . This is a measure for the 'fundamental' blur applied to the light image hitting the retina. From a signal processing point of view, it defines the spatial frequency cut-off of retinal filtering. The width of the *center* signal has several biological origins, starting with the sampling frequency of light receptors. Furthermore, a local sharing of information between neighboring light receptors (Chapter 3, Section 2.3), helping to prevent aliasing and reduce phototransduction intrinsic noise, also contributes to the width of σ_C .

A fundamental difference between the retinas of different species lies in their spatial resolution, as measured from the extent of their *center* signal. For example, in the mammalian retinas, cells with the smallest receptive fields have different scales according to the species considered: σ_C can be as small as 0.03 deg in the primate[37], but is rather around 0.3 deg in the cat[59], reflecting that the cat vision is several times less precise than our central foveal vision.

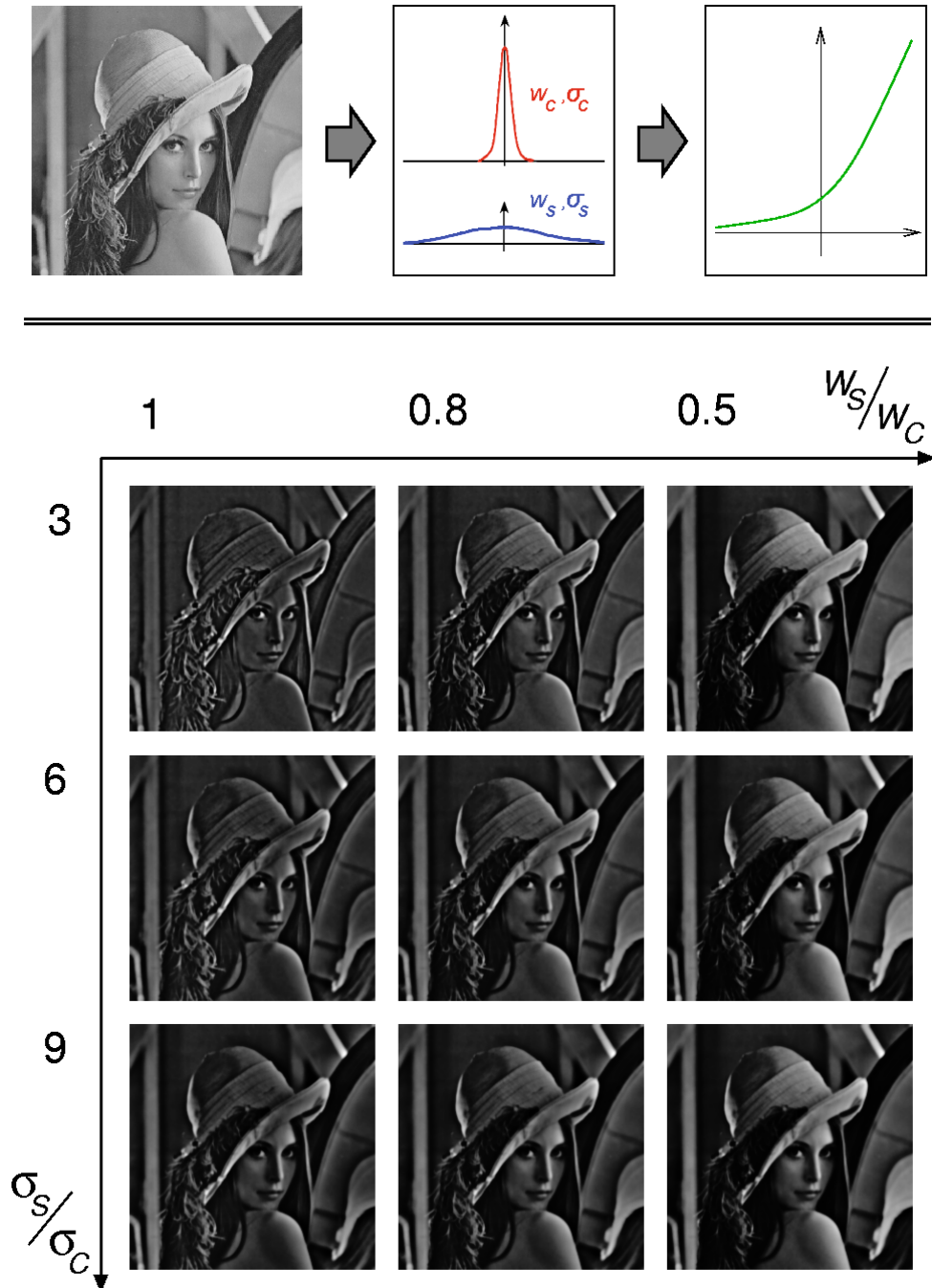


Figure 2.2: Perceptual impact of parameters in the DOG model. *Up*: Input image is convoluted with a DOG filter of parameters $w_c = 1$, $\sigma_c = 2$ pix, and with various values for σ_s and w_s . To provide a ‘biological’ output for ON cells, the resulting images are normalized between -1 and 1 , and passed in a smooth static rectification, as inspired by LN models (see Section 5). *Down*: Results, for various sets of biologically-plausible *surround* parameters. When large-scale filtering is inferred from a DOG model, the perceptual output can vary a lot depending on the parameters chosen. In particular, edge detection can be obvious (upper left image) or not (lower right images).

- **Linear gain** w_C . This gives the orders of magnitudes for retinal amplification, from input luminosity (various possible units) to a spiking activity (generally in impulses/sec). In fact, this ‘linear gain’ is all but a constant: It is highly controlled, in a nonlinear fashion, by statistics of the input image such as luminosity or contrast. All these nonlinear mechanisms are generally termed *gain controls*, and are an expression of retinal *adaptation* (Chapter 3, Section 5).
- **Relative surround extent:** $\frac{\sigma_S}{\sigma_C}$. Expressed relatively to the ‘fundamental’ precision of the retina as measured by σ_C , the extent of the best-fitting Gaussian for the *surround* is highly variable across retinal ganglion cells, even across cells supposedly of the same sub-type. For example, Enroth-Cugell and Robson 66 [59] measured relative extents of the *surround* that ranged roughly from 3 to 10.

Biologically, this fact probably has a moderate importance: after all the DOG model is just an approximation. Combined with a natural cell-to-cell variety, a three-fold variation in the ratios is not so surprising. However, when pasted into a functional model, the extent of the *surround* has strong perceptual consequences: see Figure 2.2. In particular, it raises the question to what extent the *surround* signal allows edge detection, or simply increased invariance to luminosity.

- **Relative surround weight:** $\frac{w_S}{w_C}$. Similarly, the best-fitting weights for *center* and *surround* are biologically measured to display a strong cell-to-cell variability. For example, in Figure 2.1 B, the weights w_C and w_S can be measured in response to a ‘uniform screen’ stimulus, i.e, for low spatial frequencies (left of the diagram). One thus reads $w_C \simeq 12.5$ and $w_S \simeq 11$, so that they are in a ratio of approximately 0.9.

Amongst cat X cells, Enroth-Cugell and Robson 66 [59] measure relative weights ranging from 0.8 to 0.95. An even stronger variability can be observed in other species/pathways (Chapter 3, Section 3). Again, this raises questions about these cells really being edge detectors, as illustrated in Figure 2.2.

Whatever these perceptual issues, the DOG model remains a strong and important influence throughout all retinal models. Also, it presents an excitation-inhibition structure that has a direct equivalent at the level of temporal filtering, and temporal linear models.

3 LINEAR MODELS FOR TEMPORAL TRANSIENTS _____

Exponential and Gamma functions

The linear modeling of temporal delays and transients in the retina is very close to the spatial DOG modeling, except that the base filter is not the Gaussian, but the

Exponential and/or Gamma filters:

$$E_\tau(t) = \frac{1}{\tau} \exp(-t/\tau), \quad (2.5)$$

$$E_{n,\tau}(t) = \frac{(nt)^n}{(n-1)!\tau^{n+1}} \exp(-nt/\tau), \quad (2.6)$$

if $t > 0$, and zero otherwise. We refer to filter (2.5) as the Exponential filter, and to filter (2.6) as the Gamma of order n . These filters are normalized to have a temporal integral of one. Unlike Gaussian filters, these filters are null for $t < 0$, which means that they are *causal* filters: This insures that, in the linear model, the present state for the cell is linearly calculated only from the past values of the input stimulus.

These filters also have the nice property to all result from self-convolutions of an Exponential filter. One has:

$$\underbrace{E_\tau \overset{t}{*} E_\tau \overset{t}{*} \dots \overset{t}{*} E_\tau}_{n+1}(t) = \frac{t^n}{\tau^{n+1} n!} \exp\left(-\frac{t}{\tau}\right) = E_{n,n\tau}(t). \quad (2.7)$$

where sign $\overset{t}{*}$ denotes temporal convolution. The Gamma filter can thus also be termed an ‘*Exponential Cascade*’ filter: It is obtained as a succession of low-pass Exponential filters with similar time scales. Conversely, the Exponential filter is the Gamma filter of order 0. In fact, any succession of Exponential filtering stages – even with inhomogeneous time constants – is reasonably approximated by a single filter $E_{n,\tau}$. The more homogeneous the different time constants in the cascade, the better the fit by filter $E_{n,\tau}$. We refer to Appendix 3.6.2 for more details.

This composition property is interesting, since it allows to encompass in a single linear filter the distributed low-pass stages that occur along the retinal pathway (synapses, cellular integrations, etc). An illustration of the filters and of the composition property is shown in Figure 2.3.

In formula (2.6), rather than defining $E_{n,\tau}$ as the n -fold auto-convolution of the Exponential filter, we preferred to divide the time-scale by n . As a result, all filters E_τ and $E_{n,\tau}$ have the same first-order approximation for their Fourier transform: At first order, each of these filters induces a temporal delay of magnitude τ to the signal. The parameter n is just a secondary influence, allowing more liberty in fitting the filter’s shape to experimental data. In the Fourier domain, higher values for n induce a steeper frequency cut-off after frequency $1/\tau$.

A transient filter: The Difference of Exponentials (DOE)

Just as the center-surround opposition can be modeled as a difference of two low-pass Gaussian filters, linear transients in the retina can be modeled as the difference of two low-pass Exponential (or Gamma) filters:

$$K_{\text{temp}}(x, y) = w_1 E_{n_1, \tau_1}(t) - w_2 E_{n_2, \tau_2}(t), \quad (2.8)$$

where τ_2 is bigger than τ_1 .

This is a band-pass temporal filter, which displays a strong functional resemblance with the DOG model:

- Filter E_{n_1, τ_1} reflects the low-pass properties of the considered filtering stage,

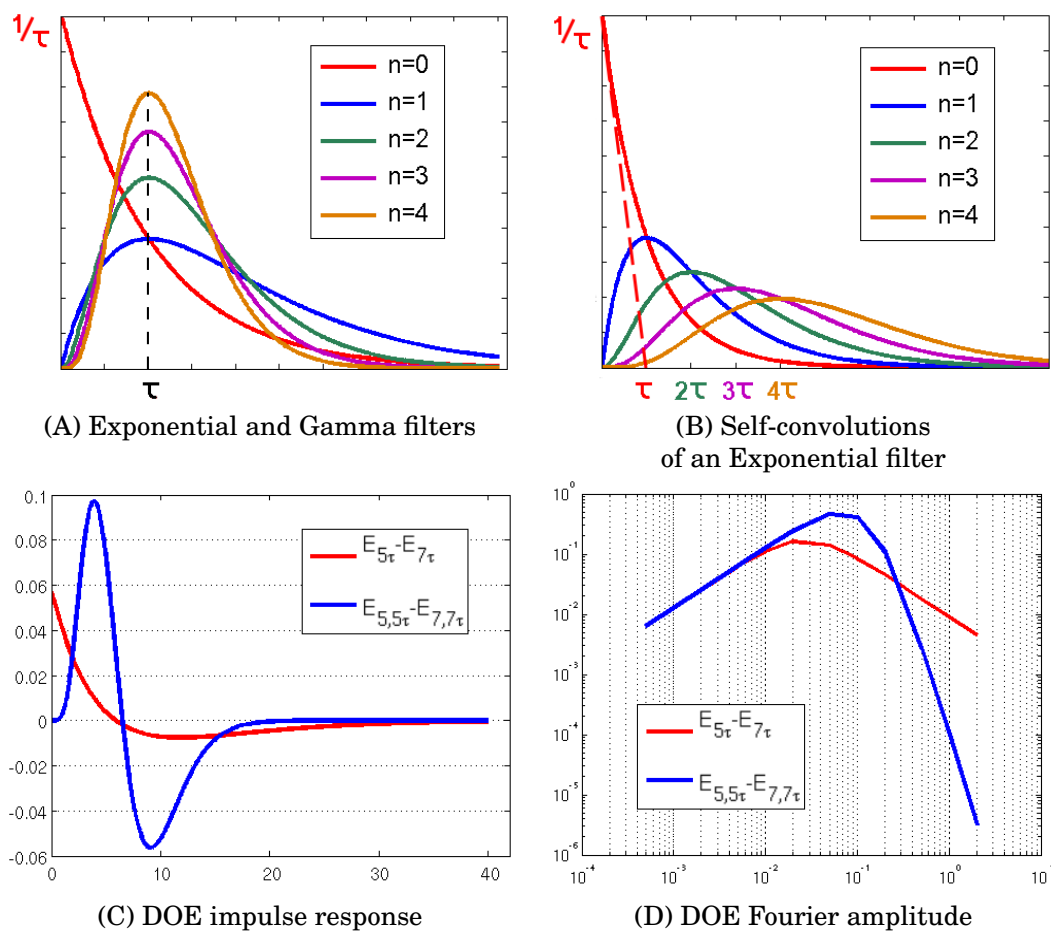


Figure 2.3: Exponential, Gamma and Differences of Exponentials (DOE) filters. **A:** The first five Gamma filters ($n = 0$ being the Exponential filter). They all peak at time τ and induce a temporal delay of order τ when applied on a signal. The bigger the exponent n , the more ‘concentrated’ the filter is around time τ . In the Fourier domain, higher values for n induce a steeper frequency cut-off after frequency $1/\tau$ (curves not shown). **B:** Filters $E_{n,n\tau}$ defined the successive auto-convolutions of the Exponential filter E_τ . **C:** Two different DOE filters with similar time scales and first-order behavior in the frequency range. The Cascade DOE is closer to experimentally measured shapes. Parameter $\tau=1$. **D:** Corresponding amplitudes for the Fourier transform. The Cascade DOE displays a stronger frequency cut-off.

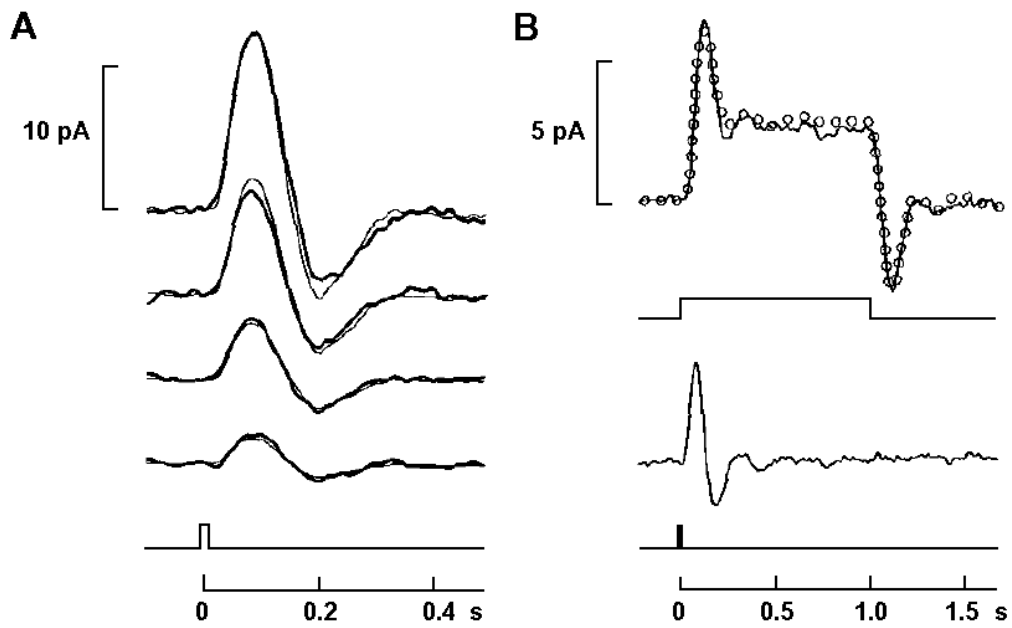


Figure 2.4: *Linear filtering in primate cones.* At small illuminations, the temporal response of cone light receptors is well modeled by a linear filter. Note the resemblance with a Difference-of-Exponentials (DOE) filter. *A:* The impulse response of a single macaque cone is tested, by applying short pulses of light (approximation for a Dirac input). *B:* The response of a cone to a step of light is well modeled by linear convolution with its impulse response. From Schnapf et al 90 [151].

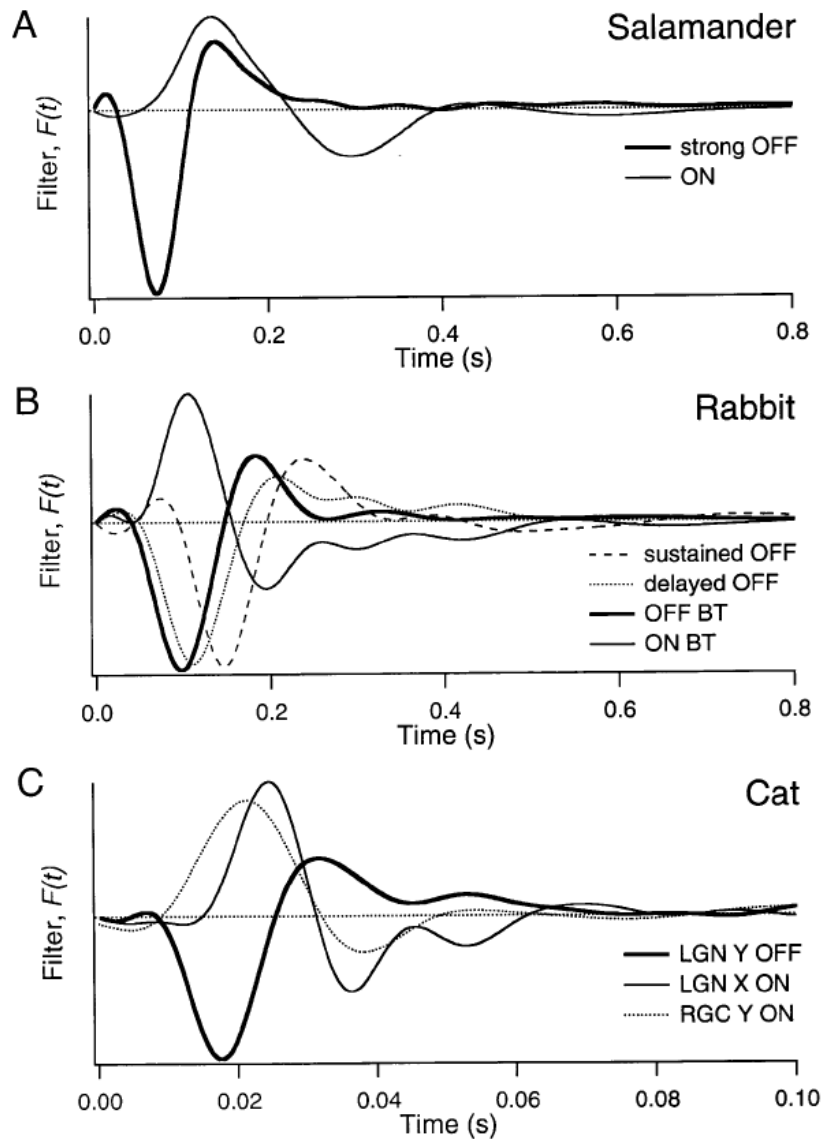


Figure 2.5: Best-fitting linear temporal filters, for different ganglion cells (and LGN cells) stimulated by a random flickering screen. For most cells, the best-fitting filter is biphasic, reflecting the *transient* behavior of retinal ganglion cells (see text). Approximation by a DOE is generally a suitable approximation. However, real cell impulse responses can sometimes display slow oscillations, reflecting the internal complexity of a distributed temporal processing. Also, these linear filters reflect the cells' behavior *for this specific experiment*, with spatially uniform stimuli. From Keat *et al.* 01 [89].

due to successive delays in the internal transmission of the signal. It defines the frequency cut-off of the filtering stage: Temporal variations faster than $1/\tau_1$ Hz are attenuated in the transmission.

- Filter E_{n_2, τ_2} represents the delayed inhibition that makes the response *transient*: In response to an input step function, filter (2.8) displays a peak of activity, and then a decrease of activity as the inhibition, of time scale τ_2 , ‘catches up’ with the direct signal of time scale τ_1 . This behavior is illustrated in Figure 2.4 B.
- The ratio $\frac{w_2}{w_1}$ defines the *strength* of the transient. For a ratio of 1, the filter is totally transient: Its response to an input step displays a peak of activity, and then returns to zero. For a ratio smaller than 1, a residual activity remains after the peak of activity: see Figure 2.4 B.

However, a major difference exists with the DOG model: Temporal filtering in the retina is distributed along many filtering steps, from phototransduction to spike emission. As a result, the DOE model applies to many different stages of retinal filtering, with different precision, and different time scales:

- First, consider Figure 2.4: The photoresponse of cones to input light is well-modeled by a linear DOE filter with a typical time scale of 100ms (the impulse response resembles $E_{5,100} - E_{7,140}$: compare with Figure 2.3 C, taking $\tau = 20$ ms).
- Then, consider Figure 2.5: Best-fitting temporal kernels are calculated for ganglion cells of various species, in response to a uniform flickering screen. In Figure C, a cat ganglion cell (RGC Y ON, same temporal behavior as a primate cell) is well modeled with a DOE of typical time scale 20 ms.

So, the best-fitting DOE filter for a ganglion cell is about five times faster than the best-fitting DOE filter for the cones, which are upper in the pathway. This counter-intuitive result is due to successive high-pass transients in retinal processing, that enhance fast frequencies in the retinal output.

This example illustrates how DOE filters are a much more ‘relative’ modeling than DOG filters, and strongly depends on which filtering structure is being modeled, and at what precision. As a result, the fitting to experimental data is generally looser than for the DOG model: For example, see how ganglion cell impulse responses (Figure 2.5) can display attenuated oscillations, not accounted for by a DOE filter.

Also unlike the Gaussian filters, a supplementary liberty is given for the two low-pass Exponential filters used: The choice of their exponents n_1 and n_2 . This liberty is convenient to provide better fit to data (see Figure 2.3 D), but the resulting choices for n_1 and n_2 are often arbitrary, and not necessarily useful from a functional point of view.

A simplified transient filter

The high number of parameters (5) in the generalized DOE filter somewhat ‘drowns’ the main functional role of the DOE filter, which is to provide high-pass (‘transient’)

behavior. A simpler DOE filter can be introduced to model transients in the simplest functional way:

$$T_{w,\tau}(t) = \delta_0(t) - wE_\tau(t), \quad (2.9)$$

This filter is a simple extrapolation on the DOE filter (2.8), except that the fast exponential is ‘removed’ by taking its limit when $\tau_1 \rightarrow 0$, becoming a Dirac $\delta_0(t)$, and that the slow exponential takes its simplest form with exponent $n = 0$. When filter (2.9) is applied to an input $X(t)$, its output simply corresponds to

$$Y(t) = T_{w,\tau} * X(t) = X(t) - wE_\tau * X(t).$$

The two parameters are sufficient to model the ‘high-pass’ functionality of a DOE filter:

- τ fixes the time delay between the initial signal and its ‘removed average’.
- w fixes the relative weights of original signal and ‘removed average’ in the output.

Temporal convolution and ODEs

Remark that temporally, convolution by E_τ in (2.5) or $T_{w,\tau}$ in (2.9) amounts to passing the signal through specific linear ordinary differential equations (ODE). Let us remind these results:

$$Y(t) = E_\tau * X(t) \quad \iff \quad \tau \frac{dY}{dt} = X(t) - Y(t) \quad (2.10)$$

$$Y(t) = T_{w,\tau} * X(t) \quad \iff \quad \tau \frac{dY}{dt} = \tau \frac{dX}{dt} + (1-w)X(t) - Y(t), \quad (2.11)$$

these relations being true once that the initial condition of the ODE is forgotten. Convolution by $E_{n,\tau}(t)$ is equivalent to an n -th order ODE, obtained by cascading (2.10) n times.

4 GENERALIZED SPATIO-TEMPORAL RECEPTIVE FIELDS

After the first DOG models, several specific works have revealed other subtleties in the spatio-temporal structure of retinal filtering. Amongst these new properties, most concern nonlinear behaviors, which we address more specifically in Chapter 3. Also, some new properties were found, that can be well modeled linearly as enhancements of the DOG model. We review them here.

Delayed surround

As mentioned already, the best-fitting linear kernel for a cell is generally not separable in time and space. One of the first observations of the phenomenon was by Enroth-Cugell *et al.* 83 [60]: They found that measures of spatial sensitivity using drifting grating (as in Figure 2.1 *B*) were different according to the temporal frequency used for the grating – which would not be the case for a separable filter.

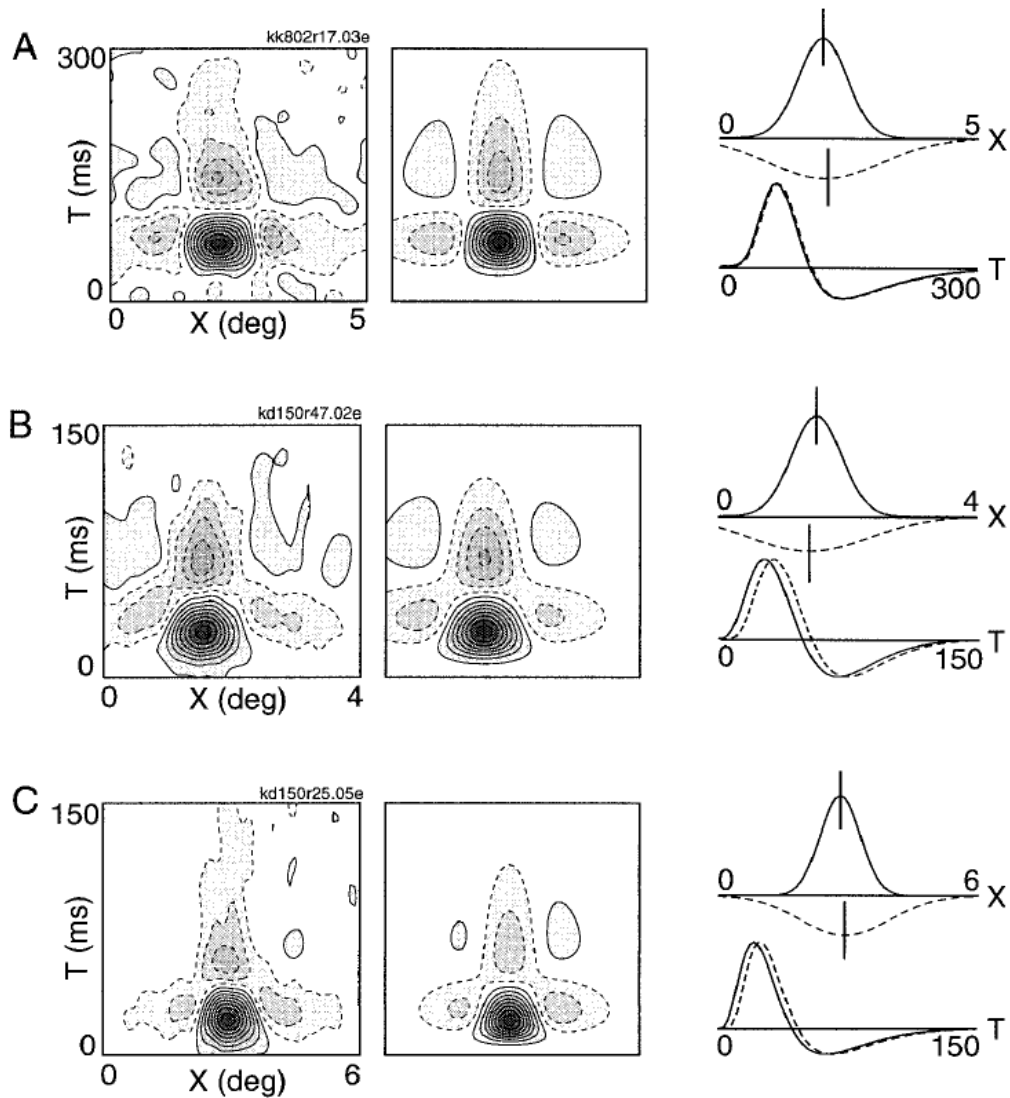


Figure 2.6: *Non-separable receptive fields and generalized DOG models in the cat LGN. Left column: Spatio-temporal receptive fields (with a single spatial dimension) revealed through reverse correlation analysis. Middle column: Fit by a generalized DOG model. The $X - T$ profile is rather separable for cell A, but not for cells B and C. Right column: Parameters of the generalized DOG models. The surround signal (dotted lines) is associated to a different DOE filter than the center signal (continuous line). Best-fitting DOE filter for the surround reveals a supplementary time delay. Note also that the center and surround Gaussians are allowed to have different offsets. From Cai *et al.* 97 [26].*

Furthermore, the authors found that the non-separability is well accounted for by a linear model where the spatial *surround* signal is transmitted with a supplementary delay, of a few milliseconds. This is illustrated in Figure 2.6, which displays non-separable kernels, from cat LGN cells [26]. Although very small (3 – 7 ms in cat [60, 26] and primate [12]), this delay may have important perceptual consequences, as we illustrate in the simulations of our model (Chapter 4).

In the case of cat LGN cells, Cai *et al.* 97 [26] suggest that the total receptive field structure is well encompassed by a modified Difference-of-Gaussians, where both Gaussians are associated to a different DOE temporal profile:

$$K(x, y, t) = w_C G_{\sigma_C}(x, y) \text{DOE}_C(t) - w_S G_{\sigma_S}(x, y) \text{DOE}_S(t), \quad (2.12)$$

where both filters DOE_C and DOE_S are DOE filters as in 2.8, with slightly longer time scales for the *surround*. This is the type of linear model that we kept in our model (Chapter 4).

Modified Gaussians

Other detailed studies have revealed that ganglion cells' *center* and *surround* can display geometrical asymmetries. First, the *center* and *surround* filters may display a small relative offset in their respective spatial positions. This fact can be introduced in a linear DOG model by adding a spatial offset to the *surround*. Second, the receptive fields are generally not perfectly spheric: The *center* and *surround* receptive fields can have slightly ellipsoidal profiles (see e.g. DeVries-Baylor 97 [55] in the rabbit retina). In our model, we did not include such asymmetries, whose functional interest is not clear.

5 REVERSE CORRELATION AND LN ANALYSIS _____

Reverse correlation

We now give a few words on *reverse correlation* methods, which are widely used nowadays to study linear receptive fields in low-level visual areas (see e.g. Ringach and Shapley 04 [141] for review). Consider a ganglion cell centered in (x_0, y_0) and driven linearly by its input, through formula (2.1). Reverse correlation studies the statistical dependence of the cell's activity at time t , on all past values of image I in the cell's receptive field. For a spatio-temporal offset (a, b, s) , the reverse correlation $C(a, b, s)$ is formally defined as:

$$C(a, b, s) = \frac{1}{T} \int_{t=-\infty}^{+\infty} I(x_0 - a, y_0 - b, t - s) A(t) dt, \quad (2.13)$$

where $[-\infty, +\infty]$ is the formal notation for the real recording period $[0, T]$, where T is supposed 'long enough'.

The reverse correlation $C(a, b, s)$ is very interesting in neuroscience because it is a quantity experimentally measurable, which allows to find back kernel $K(x, y, t)$

under a variety of models and experimental conditions. It can be calculated spatio-temporally (Figure 2.6 was obtained with this procedure), or simply temporally, forgetting the two first coordinates.

To prove the interest of function C , rewrite (2.13) with the linear expression (2.2) for $A(t)$:

$$C(a, b, s) = \frac{1}{T} \int_{t=-\infty}^{+\infty} I(x_0 - a, y_0 - b, t - s) (I * K)(x_0, y_0, t) dt. \quad (2.14)$$

This expression is problematic because it involves only a specific spatial location (x_0, y_0) on the retina, which prevents from doing well-suited spatial averages and subsequent Fourier analysis. So, to continue the reverse-correlation analysis from (2.14), the input stimulus must necessarily have some form of translational spatial invariance, so that ‘all spatial locations are statistically equivalent’ over a long run of stimulus. Mathematically, this writes

$$\forall (x_1, y_1, x_2, y_2, \delta), \int_{t=-\infty}^{+\infty} I(x_1, y_1, t) I(x_2, y_2, t + \delta) = F(x_1 - x_2, y_1 - y_2, \delta), \quad (2.15)$$

dependent only on the spatial *offset* (translational invariance). Relation (2.15) is verified for three particular experimental conditions:

- If the input image is spatially uniform at each time t . In this case, one focuses only on the temporal properties of the cell, through some filter $K_{\text{temp}}(t)$.
- The stimulus is created as a pseudo-random sequence with translational invariance. This is the case, for example of white-noise stimulus, which is often used. Also, random bar apparitions can be used to test the summation properties along a single spatial direction (e.g., by Cai et al 97, Figure 2.6).
- The stimulus is a natural scene movie sequence, long enough for property (2.15) to be approximately true.

If (2.15) is verified, one can check that (2.14) becomes independent of the choice of (x_0, y_0) , so that one can ‘artificially’ express $C(a, b, s)$ as an average over the whole spatial domain:

$$\begin{aligned} C(a, b, s) &= \frac{1}{TM} \iiint_{x,y,t} I(x - a, y - b, t - s) (I * K)(x, y, t) dx dy dt \\ &= \frac{1}{TM} I^- * I * K(a, b, s), \end{aligned}$$

where M is the spatial area of summation, and $I^-(x, y, t) = I(-x, -y, -t)$. Then, switching to the Fourier domain:

$$\tilde{C}(\xi_x, \xi_y, \xi_t) = \frac{1}{TM} \tilde{I}(-\xi_x, -\xi_y, -\xi_t) \tilde{I}(\xi_x, \xi_y, \xi_t) \tilde{K}(\xi_x, \xi_y, \xi_t),$$

so that one has an exact access to filter K , through the formula

$$\tilde{K}(\xi_x, \xi_y, \xi_t) = TM \frac{\tilde{C}(\xi_x, \xi_y, \xi_t)}{|\tilde{I}(\xi_x, \xi_y, \xi_t)|^2}, \quad (2.16)$$

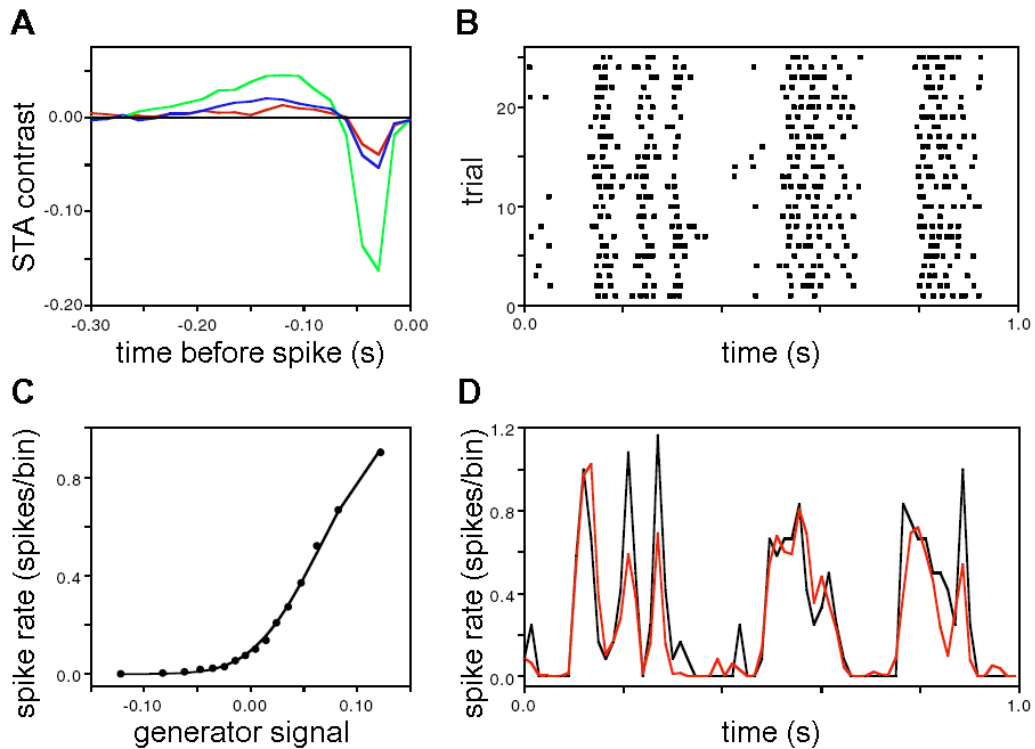


Figure 2.7: *The LN model applied to a macaque OFF cell.* An LN analysis is derived from the spiking response of a ganglion cell to white noise stimulus (in color). *A:* The reverse correlation, here, is a Spike-Triggered Average (STA). The chromatic structure of the input allows to separate the cellular responses to Red, Green and Blue components. *B:* The best-fitting static nonlinearity N is then calculated (see text). *D:* Comparison of the real cell's firing rate (black, reconstructed from the various trials in *C*), and of the output of the LN model. From Chichilnisky 01 [31].

an equation which can be understood, whether as a spatio-temporal relation, whether only through its temporal part in the case of a spatially uniform stimulus.

White noise

The only condition to find K back from C with (2.16), is to know precisely $|\tilde{I}(\xi_x, \xi_y, \xi_t)|^2$, called the *power spectrum* of the input stimulus (it is the Fourier transform of the auto-correlation of I). A good experimental way to get rid of this problem is to have I as close as possible to *white noise*, which verifies $|\tilde{I}(\xi_x, \xi_y, \xi_t)|^2 = \sigma^2$ for all frequencies.

Remark: In experiments, white noise is just an abstraction, that can be built experimentally only up to a certain cutting frequency ξ_0 (possibly a vector), which determines the spatial and temporal precision of the measure for K . Problematically, to elicit a fixed response of the cell, the power σ^2 of the white noise should be kept constant; But in order to keep a constant σ^2 , the amplitude of the white-noise should tend to $+\infty$ when ξ_0 tends to zero. This is unrealizable, so ξ_0 cannot be made too small: The precision obtained by reverse correlation with a white noise is limited in practice. ■

LN models

Aside from experimental limitations, formula (2.16) can be tested on any cell, in response to any stimulation, and thus provide a linear filter K for the cell. However, one might argue that given the many nonlinearities in retinal processing, the obtained filter K may not be very relevant for a real cell. How can one measure the information lost when approximating the cell by a linear model?

The simplest answer is to compare the real response of the cell $A(t)$, with the linear prediction $I * K(t)$. Even for cells termed *linear*, there is of course a discrepancy between the two signals. *LN* models try to compensate for part of that of that discrepancy by adding a supplementary stage to the model. *LN* models have become an increasingly popular model for low-level visual processing over the last decade: They have even been termed the *standard* model for retinal processing by Carandini *et al* [29].

The initials LN stand for *Linear - Nonlinear*. In this ‘enhanced’ linear model, cellular filtering is supposed to consist of a linear filter, followed by a static nonlinearity accounting for part of the inherent nonlinearities in retinal processing. With the same notations as before, the activity of the cell becomes

$$A(t) = N(I * K(x_0, y_0, t)), \quad (2.17)$$

where N is a static nonlinear function. Note that there is an undetermined parameter in this model: Multiplying K by λ and dividing the input scale of N by λ yields the exact same behavior.

Introducing this nonlinearity is a natural, and often mandatory, idea. First, all ganglion cells are limited in the negative range of signal transmission, because their output firing rate cannot be negative. Typically, a cell with a low spontaneous firing rate cannot code linearly when it is inhibited. A simple rectification $N(r) = [r]_+$ (positive part) will naturally provide a better fit to the cell’s real response! But rectification is also a *distributed* phenomenon, which does not only concern spike generation. In fact, any stage of transmission relying on a physical magnitude that cannot get negative (synaptic transmission, conductance opening. . .) is likely to display a signal rectification.

Experimentally, the best-fitting couple (K, N) for the cell is found from its real response $A(t)$, as a two-step procedure:

- First, a reverse correlation analysis yields the best-fitting linear kernel K (formula 2.16).
- Second, the linear reconstruction $r(t) = I * K(t)$ is calculated, and a two-dimensional map is constructed with the ensemble of points $(r(t), A(t))$ at all simulation times. Through various methods, the best fitting static curve $r(t) = N(A(t))$ is then derived from the map.

A mathematical result (sometimes known as Bussgang’s Theorem [25]) insures that if a cellular model really behaves as equation (2.17), then the preceding two-step procedure, with white-noise input stimulus $I(x, y, t)$, finds the exact K and N back. Note that this result is not trivial, because the nonlinearity N prevents from doing the linear analysis that led to (2.16).

Remark: Naturally, real cells do not follow an exact LN model either. There is still a discrepancy between the LN model's prediction and output spikes. Even with our simulator (though close in conception to an LN model, see Chapter 4), when an LN analysis was applied to the output spikes, we sometimes found a strong dispersion of the maps $(r(t), A(t))$ around the theoretical line $A = N(r)$. ■

The LN model can also be enhanced to a spiking model, where $A(t)$ in (2.17) serves to generate the spikes with an inhomogeneous Poisson process (LNP model, see Section 4). In this case, the reverse correlation can be done directly from the spike train, considered as a discrete series of Dirac pulses: The reverse correlation is then called a *Spike Triggered Average* (STA).

Because Poisson spike trains are statistically 'transparent' (see Chapter 3, Section 4.2.1), the two-step reconstruction from the STA also provides back the exact K and N of an LNP model [31].

6 LINEAR MODELS FOR ELECTRICAL COUPLING _____

We now present linear models which have been proposed to account for electrical coupling between neighboring cells of a same layer through *gap junctions*. Gap junctions are ionic channels between two cells' cytoplasms, which allow the circulation of ions - generally in both directions. Whatever unsolved questions remain concerning the arousal of center-surround opposition in the retina, there seems to be a consensus that gap junctions between neighboring cells of the same type are responsible for a good part of the spatial extent of *center* and *surround* signals.

Electrical coupling in horizontal cells

Gap junction coupling is particularly strong and well assessed in horizontal cells, which provided some of the first intracellular recordings of retinal neurons (Svaetichin 53 [164]). Morphologically, this has been revealed by experiments such as that of Figure 2.8 A: Dye injected in one horizontal cell's cytoplasm spreads to all neighboring horizontal cells through the gap junctions.

The effect of horizontal cell coupling is also well understood: Photoreceptors transmit the visual information to horizontal cells through excitatory synapses. Then, electrical coupling between horizontal cells results in a local *averaging* of this visual information, so that horizontal cells are sensitive to the sum of visual inputs over a wide spatial range. This is verified in the rabbit retina, in Figure 2.8 B: Horizontal cell responses grow linearly with the size of a stimulating light spot, over a 'long' distance (relatively to the response of photoreceptors).

From the standpoint of image processing, horizontal cells thus 'see' an image much more blurred than photoreceptors. From a physiological standpoint, gap junctions create wide receptive fields in horizontal cells, which probably contribute significantly to the creation of the *surround* signal (Chapter 3, Sections 2 and 3).

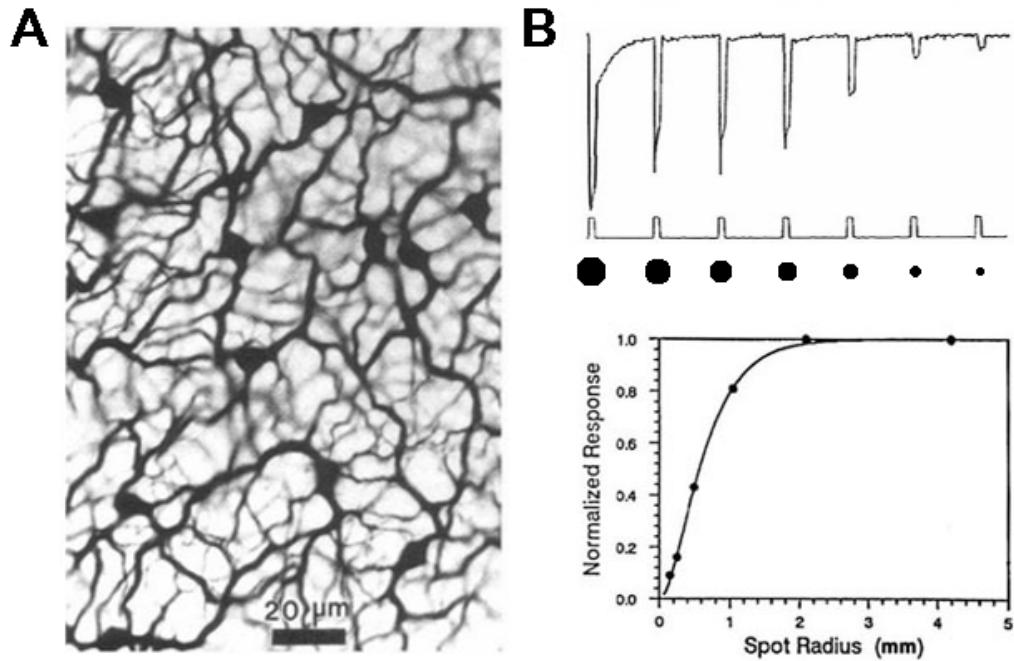


Figure 2.8: Spatial coupling in horizontal cells. A: Gap junctions between neighboring horizontal cells are revealed: Dye injected in one cell's cytoplasm propagates to the neighboring cells through gap junctions. Rabbit cells, from [113] B: The responses of a horizontal cell to spots of increasing size reveal spatial summation over a wide distance, due to gap junctions. Note that horizontal cells are always hyperpolarized by increased light ('OFF' behavior, see Chapter 3, Section 1). Turtle cells, from [129].

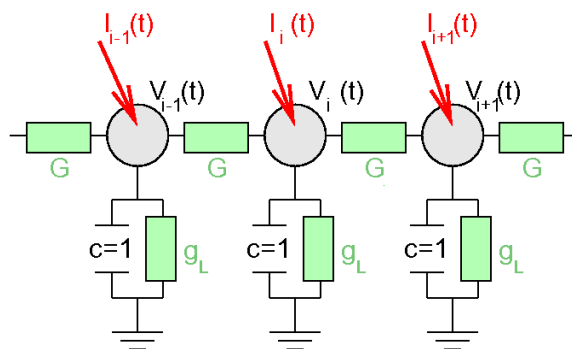


Figure 2.9: An electrical model for coupling through gap junctions. Cells with potentials V_i are modeled as linear capacitors linked to their nearest neighbors by static conductances G (gap junctions), and integrating an input synaptic current I_i .

Linear models for electrical coupling

Coupling through gap junctions is well modeled in a linear framework, as proposed by Naka-Rushton 67 [116] for horizontal cells (see also Lamb 76 [97]). In these models, a layer of cells with membrane potentials V , modeled as leaky membranes, integrate a current I , with static conductances G linking neighboring cells. According to the framework, the model can involve a discrete array of cells (here, a one-dimensional array):

$$c \frac{dV_i}{dt}(t) = I_i(t) - g^L V_i(t) + G(V_{i+1}(t) + V_{i-1}(t) - 2V_i(t)), \quad (2.18)$$

or rather a continuous framework involving Partial Derivative Equations (PDEs):

$$c \frac{dV}{dt}(x, y, t) = I(x, y, t) - g^L V(x, y, t) + \mathcal{G} \Delta V(x, y, t), \quad (2.19)$$

where $\Delta V = \partial_x^2 V + \partial_y^2 V$ is the Laplacian of potential V , and the leak conductance g^L is associated to a rest potential E^L taken as 0.

Formulation (2.18) is written for a one-dimensional array of cells with membrane potentials $V_i(t)$, integrating their input current as a current $I_i(t)$ (see Figure 2.9). The gap junctions are modeled as static conductances G , and are supposed to only occur between closest neighbor cells. This formulation is well suited for hardware implementations of coupling, as proposed by Mahowald and Mead 91 [101] to produce one of the first ‘retina-inspired’ chips. This discrete model has a simple equivalent for two-dimensional arrays, and has been tested with connections more complex than just closest neighbors: See, e.g., the works of Herault [76, 79] and Beaudot 94 [11]. The properties of the resulting filter are best expressed in the Fourier domain.

By opposition, formulation (2.19) can be seen as the continuous limit of (2.18) (or its two-dimensional version) when the step between the discrete units tends to zero and the neurons can be seen as a continuum: Suppose that cells are separated by a spatial step s , and that the (serial) conductances G behave as $G = \mathcal{G}/s$, while the (parallel) conductance g^L , capacity c and input currents scale with s . Then, leading s to zero in (2.18) yields (2.19).

For our model (Chapter 4) which uses a formalism of continuous maps, we find formulation (2.19) better suited. We often refer to (2.19) as a ‘leaky heat equation’ (without the leak term $-g^L V$, it would be a simple heat equation). It bears the analytical solution:

$$V(x, y, t) = H \overset{x, y, t}{*} I(x, y, t), \quad (2.20)$$

where H , impulse response of the filter, is given by:

$$H(x, y, t) = \frac{1}{c} G_{\sigma \sqrt{t/\tau}}(x, y) \exp(-t/\tau). \quad (2.21)$$

In (2.21), G_σ is the normalized Gaussian kernel of standard deviation σ and integral 1, as in (2.4), and σ and τ are the typical spatial and temporal extent of the impulse response:

$$\sigma = \sqrt{2\mathcal{G}/g} \quad (2.22)$$

$$\tau = c/g. \quad (2.23)$$

Similarities and discrepancies w.r.t. Gaussian filtering

Filtering by (2.20)-(2.21) has a close relation to the Gaussian kernels introduced in Section 2 to model *center-surround* interactions. When a signal is convoluted by filter H in (2.21), it is low-passed as with a Gaussian kernel. However, filter H is not separable in time and space: The spatial blur through $G_{\sigma\sqrt{t/\tau}}$ spreads in time. Such spread of the signal has indeed been observed in the responses of some ganglion cells to static squares by Jacobs-Werblin 98 [85], probably imputable to gap junction diffusion of the signal.

However, the ‘spreading’ gap junction filter (2.21) is not widely used in the field of retinal models. Often, a layer of electrically coupled cells is rather associated to a simple separable filter:

$$H_{\text{sep}}(x, y, t) = \frac{1}{c} G_{\sigma}(x, y) \exp(-t/\tau), \quad (2.24)$$

with σ and τ still defined in (2.22)-(2.23). There are several conceptual advantages in this simplification:

- Filter H_{sep} in (2.24) can also account for static pooling of a pre-synaptic signal as caused by the spread of a cell’s dendritic tree.
- If filters of the form H_{sep} are successively applied to the signal at successive stages of the retinal pathway, the resulting filter keeps a simple expression: Since filters like H_{sep} are separable in time and space, their successive convolutions remain separable in time and space, and their spatial component remains a Gaussian, as the convolution of Gaussians. By opposition, convolutions of filters of the form H in (2.21) have no simple expression, except in the Fourier domain.
- At the same time, filter H_{sep} in (2.24) remains close to filter H in (2.21): In the Fourier domain, they have the same asymptotical expression for small spatio-temporal frequencies (see equations (2.25)-(2.26)).

It is not clear to our mind, whether the original ‘spreading’ filter in (2.21), probably closer to biological reality, has specific functional interests which are lost in the simplification to (2.24). This is indeed possible, because filter (2.24) displays a much stronger frequency cut-off at high spatial frequencies. To verify this, express the respective Fourier transforms of the two filters:

$$\tilde{H}(\xi_x, \xi_y, \xi_t) = \frac{1}{c \left(1 + \frac{\sigma^2}{2} (\xi_x^2 + \xi_y^2) - i\tau\xi_t \right)} \quad (2.25)$$

$$\tilde{H}_{\text{sep}}(\xi_x, \xi_y, \xi_t) = \frac{1}{c(1 - i\xi_t\tau)} \exp\left(-\frac{\sigma^2}{2} (\xi_x^2 + \xi_y^2)\right), \quad (2.26)$$

so that the spatial frequency cut-off is exponential for H_{sep} , versus a simple power law for the ‘real’ H . Furthermore, the typical spatial cut-off frequency of H_{sep} is constant: $\sqrt{2/\sigma}$, whereas in the case of H , it depends on the temporal frequency ξ_t^0 of the stimulus: $\tau\xi_t^0\sqrt{2/\sigma}$.

This is an interesting feature because it means that, for similar typical parameters σ and τ (which can be experimentally measured), the filtering through gap junctions might allow higher spatio-temporal cut-offs than what is generally believed. As a result, the simulator *Virtual Retina* allows to choose any of the two filtering schemes H and H_{sep} at the level of the Outer Plexiform Layer. In experiments involving frequency kernels, we did find improved results when the ‘spreading’ filter H was used.

7 CONDUCTANCE EQUATION AND OTHER NONLINEAR FILTERING: THE LINEAR ODE FRAMEWORK

To conclude this chapter, we give a few words on the *conductance* driving equation for a neuron:

$$\frac{dV}{dt} = \sum_i I_i(t) + \sum_j g_j(t)(E_j - V(t)), \quad (2.27)$$

where currents in the neuron’s membrane can be modeled either as currents $I_i(t)$, or more precisely as conductances $g_j(t)$ associated to Nernst potentials E_j .

If only currents are present in (2.27), then it subtends a *linear filtering* relation between the neuron’s input currents and the subsequent potential $V(t)$. By opposition, time-varying conductances induce a nonlinear filtering relation between the neuron’s inputs and $V(t)$.

However, even if it induces nonlinear *filtering*, (2.27) is still a *linear ODE* w.r.t. V (if V_1 and V_2 are solutions, so is $V_1 + V_2$), and it can be solved. Let us introduce the general solution of a 1d linear ODE.

Linear ODE. Consider the variable $X(t)$ driven by a stable linear ODE:

$$\frac{dX}{dt} = A(t) - B(t)X(t), \quad (2.28)$$

where $B(t)$ is supposed to be always positive and to accept a strictly positive lower bound $B_0 > 0$ (This condition insures stability of the ODE; In a cell membrane model, the inert leaks play the role of B_0).

Once that initial conditions are forgotten (with time constant no longer than B_0^{-1}), the solution to (2.28) writes

$$X(t) = \int_{u=0}^{t=+\infty} A(t-u) \exp\left(\int_{s=t-u}^t B(s)ds\right) du, \quad (2.29)$$

$$= \int_{u=0}^{t=+\infty} \frac{A(t-u)}{B(t-u)} \left(B(t-u) \exp\left(\int_{s=t-u}^t B(s)ds\right) \right) du. \quad (2.30)$$

The second line (2.30) is a simple rewriting of (2.29) which puts forth the dual functional implications of ODE (2.28):

1. $V(t)$ is driven by the *driving potential* $A(t)/B(t)$.
2. Kernel $\left(B(t-u) \exp\left(\int_{s=t-u}^t B(s)ds\right) \right)$ is a *normalized kernel* (integral of one), which *averages* the driving potential, with a typical time extent proportional to

$B^{-1}(t)$. It can thus be seen as a low-pass filter, but with varying time constant ($V(t)$ sticks closer to the driving potential when $B(t)$ is large).

The linear ODE in neuroscience. In the case of conductance equation (2.27):

1. The driving potential is $\frac{A(t)}{B(t)} = \frac{\sum_i I_i(t) + \sum_j g_j(t)E_j}{\sum_j g_j(t)}$,
2. The instantaneous time constant is $B(t)^{-1} = (\sum_j g_j(t))^{-1}$.

Through Point 1, conductances have a divisive effect on the values taken by $V(t)$. Through Point 2, conductances make the response of $V(t)$ faster. This effect is more and more explicitly taken into account by modelers, as it provides interesting normalization behaviors.

But linear ODEs have other fields of applications in neuroscience and biology in general. For example, catalyzed reactions –as occurring during phototransduction in the retina– can also be modeled following a linear ODE (Chapter 3, Section 1.1.2), and with the same double effect of divisive behavior and time constant modulation. Linear ODEs also occur in precise models of synaptic transmission (Dayan and Abbott [45]), and more generally in all biological stages that imply chemical equilibriums between different chemical species.

The linear ODE in our work. In our model (Chapter 4), we use an explicit conductance equation to account for contrast gain control. We mathematically study the behavior of the resulting feedback loop (Chapter 5), and we implement a general computer object that can account for any equations of the form (2.28) at the level of retinal maps (the `CondCellMap` object, Chapter 6, Section 3.3.4).

This means that our model and software *Virtual Retina* can easily be extended to incorporate any specific nonlinear filtering effects relying on linear ODEs.

CHAPTER 3

SPECIALIZED FUNCTIONALITIES IN THE VERTEBRATE RETINA

In this chapter, we go deeper into the retina's internal architecture and physiology. After a rapid presentation of light receptors and phototransduction (Section 1), we present the physiology of bipolar cells (Section 2), which are a functional turntable in the retina, being at the interface of the two plexiform layers (OPL and IPL). In particular, we report how the 'traditional' characteristics of retinal filtering (center-surround organization, temporal band-pass) are already present at the level of bipolar cells. We then report the diversity of ganglion cells at the output of the retina (Section 3), which proceed to different spatio-temporal transformations of the signal from bipolar cells. This diversity suggests the existence of parallel channels of information at the output of the retina, with different roles in cortical processing. In Section 4, we question the nature of spike emission, and its possible specific roles in retinal coding. Finally, we mention the different processes of adaptation that constantly help to shape and adapt the retinal output in a nonlinear fashion (Section 5).

Contents

1	Light receptors and horizontal cells	79
1.1	Phototransduction	79
1.2	Further processing in light receptors and horizontal cells . . .	85
2	Bipolar cells: the retinal turntable	86
2.1	ON and OFF pathways arise at the level of bipolar cells . . .	86
2.2	Subtypes of bipolar cells	88
2.3	Center-surround architecture of bipolar cells	89
2.4	Temporal shaping in bipolar cells	95
	Conclusion: A strong need for further exploration	97
3	Parallel pathways of the retinal output	97
3.1	Introduction: Ganglion cells and the Inner Plexiform Layer . .	97
3.2	Physiology of the different visual pathways	104
4	Properties of retinal spike trains	130
4.1	The problematic of spike coding in the retina	130

4.2	Spike-emission process for a single cell	134
4.3	Spike correlations between neighboring cells	146
5	Nonlinear adaptations in the retina	155
5.1	Adaptations to luminosity	156
5.2	Contrast gain control	158
5.3	Slow adaptation and predictive coding	170

1 LIGHT RECEPTORS AND HORIZONTAL CELLS

Light receptors are in charge of converting the incoming light into variations of their membrane potential and thus, into synaptic activity. The process by which this happens, known as *phototransduction*, occurs in light receptors' *outer segments* (Figure 3.1). It is a complex cascade of molecular reactions which involves several intermediate catalyzers, and many feedback loops.

In turn, the *inner segments* of the receptors act as a 'traditional' layer of retinal cells, spatio-temporally integrating the current provoked by phototransduction. The inner segments are in strong interplay with horizontal cells, which provide modulatory feedback.

The whole architecture forms a very complex mechanism. This complexity serves a difficult goal: Allow the retina to function under the wide variety of illuminations in our environment. From dark night to bright sunlight, the light hitting the back of the retina can vary in ratios of order 10^{10} , requiring powerful and distributed control mechanisms.

However, modeling light adaptation in its complexities is not mandatory in the scope of our simulator (Chapter 4), which aims at working on normalized computer images. For this reason, phototransduction and light adaptation are presented here only succinctly. Yet, it seemed impossible not to say a few words about this strong initial stage of visual processing.

1.1 Phototransduction

1.1.1 Molecular basis of phototransduction

Phototransduction is the conversion from an input light, consisting of photons, into an electrical current. More precisely, a cation current (85 % Na^+ , 15 % Ca^{2+}) constantly circulates between the receptor's outer and inner segments (Figure 1.11). In the inner segments, the current flow is created by ionic pumps: The famous (2 K^+ /3 Na^+) exchanger (not shown) produces the Na^+ outflow, while the (4 Na^+ / Ca^{2+} , K^+) exchanger (Figure 3.2, top right) produces the Ca^{2+} outflow¹.

In the outer segment by opposition, ionic channels (Figure 3.2, bottom right) insure the inflow of Na^+ and Ca^{2+} . These ionic channels are the ultimate target of phototransduction: Incoming light results in a closing of these channels, and thus in a *reduction* of the circulating current, which allows the receptor to code for its light stimulus.

Figure 3.2 presents the main steps of phototransduction. Panel A, reproduced from Burns and Lamb [24], presents the main chemical species involved in the process. Panel B takes a more functional approach, oriented around four 'crucial' steps, and associated chemical species. Let us present the principles of phototransduction through successive description of these four steps.

1. Light absorption. Rhodopsin (R) is the photosensitive molecule. Numerous rhodopsin molecules are inserted in the membranes of the stacked sacs (in cones) or disks (in rods) which form the receptor's outer segment. Absorption of an incoming

¹At the expense of an Na^+ inflow, so it seems...

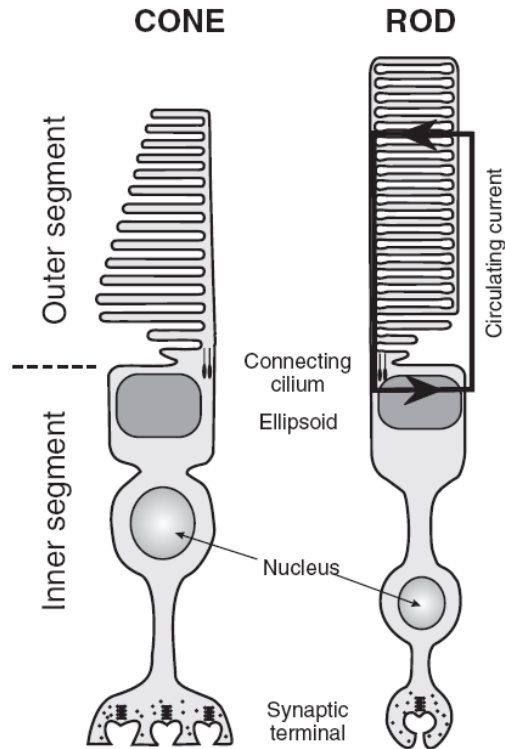


Figure 3.1: *Anatomy of cone and rod receptors.* Both types of receptors possess two distinct segments. The *inner segment* is in charge of conventional cellular metabolism. The *outer segment* is in charge of phototransduction. It contains *rhodopsin* molecules that can capture incoming photons, thus initiating a molecular cascade which leads to a *reduction* of the ionic current flowing through the outer segment. From Burns and Lamb [24].

photon produces a change in the rhodopsin's 3d structure, transforming it into its activated form R^* .

2. Disc membrane cascade. Each activated rhodopsin R^* repeatedly contacts transducin molecules G (a G-protein) and thus catalyzes their transition to an active form G^* . In turn, two activated G^* can bind to an effector protein PDE also inserted in the disk membrane, transforming it into its activated form PDE^{**} . The whole reaction occurs on the 2d surface of the disk (or sac): The freely moving intermediate molecule, the G-protein, rarely dissociates from the membrane's surface.

The catalyzed reaction allows very high gains of response (detection of down to single quanta of lights in dark adapted rods). But because of this high gain, the cascaded reaction is also under control of various inactivation mechanisms. The most important inactivation is naturally that of R^* , at the root of the cascade. This shutting off is a complex mechanism which occurs through different mechanisms and different time scales, not all understood (see Burns and Lamb [24] for reference).

3. Channel opening and photocurrent. Activated PDE^{**} acts as a catalyzer on the destruction of cyclic guanosine monophosphate cGMP (noted cG in Figure 3.2), a soluble molecule. In turn, the variations of concentration $[cGMP](t)$ are directly linked to the photocurrent, because the target ionic channels open only when bound to cGMP (Figure 3.2, bottom right).

Remark: Note that guanosine is a crucial transmitter involved at other locations of the process in its di- (GDP) and tri- (GTP) phosphate forms. ■

4. Calcium and adaptation to light. Calcium is the number one mediator of adaptation to light during phototransduction (Torre *et al.* 86 [169], Polans *et al.* 96 [131], and Burns and Lamb [24] for supplementary reference). When the photocurrent is reduced by light absorption, following the previous explanations, the influx of Ca^{2+} decreases because of the closure of the ionic channels. Because Ca^{2+} is continually expelled by the exchanger (Figure 3.2, top right), the intracellular concentration $[\text{Ca}^{2+}]$ rapidly decreases, so that $[\text{Ca}^{2+}]$ becomes a *marker of the receptor's recent level of response*.

Exploiting this property, a number of feedback gain controls are based on Ca^{2+} . A major effect of Ca^{2+} is to inhibit GCAP molecules (Figure 3.2, Panel A). By opposition, at low $[\text{Ca}^{2+}]$ concentration, the inhibition on the GCAP disappears and they start to regenerate cGMP, thus counterbalancing the effects of light. This effect allows:

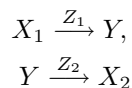
1. To speed up the recovery from a light pulse (thus reducing the low-pass properties of the cascade).
2. To prevent channel saturation by divisively controlling the levels of [cGMP], thus providing adaptation to the level of light.

In Figure 3.2 Panel B, we show the functional equivalent of this property: Calcium contributes to the deactivation of cGMP. Besides, calcium also has strong modulatory effects on the disk membrane cascade, including its inactivation mechanisms (Pugh *et al.* 99 [135]).

1.1.2 Modeling phototransduction

The number of reactions involved, including feedbacks, makes the detailed modeling of phototransduction a difficult task. However, nice quantitative reproductions are now obtained, at least to reproduce responses to simple stimuli such as pulses of different intensities.

Catalyzer equations. The key type of mathematical calculation involved appears to be catalyzer equations. As an example, consider this simple case of catalyzed reaction:



where a single molecule of each species is involved in the reactions. We focus here on the dynamics of $Y(t)$, a measure (possibly normalized) of the concentration of species Y . We consider two reactions: A creative and a destructive one, which is the strict minimum to define a dynamic concentration equilibrium for Y . The evolution of $Y(t)$ is then well modeled by

$$\frac{dY}{dt} = \alpha X_1(t) Z_1(t) - \beta Z_2(t) Y(t), \quad (3.1)$$

where α and β are constants. More complex chemical equilibria can be modeled, but the concept is similar: Catalyzers serve as multiplicative factors for the destruction of reactives (sign -) and the creation of products (sign +).

Remark: Linear ODE framework

Interestingly, equation (3.1) (or any other simple catalyzed reaction) is formally similar to the *conductance* driving equation in a neuron: It is a linear ODE (Chapter 2, Section 7), with specific effects on the time constant and gain with which the reaction product Y evolves.

Because linear ODEs are generically implemented in software *Virtual Retina*, it can easily be extended to incorporate the dynamics specific of phototransduction. ■

Responses to pulses of light. A direct cascade of catalyzer equations can successfully reproduce the *rising phase* (so, before the apparition of inactivation reactions) of receptors' response to pulses of light (Pugh and Lamb 93, [134]).

In addition, inactivation reactions have also been modeled, as well as Calcium adaptation to levels of illumination. We give the single example of the recent model of Van Hateren and Lamb 06 [175], which reproduces correctly the responses of cones to pulses of different intensities (Figure 3.3). Here are the main components of the model:

1. Inactivations in the disk membrane cascade are simply modeled as linear exponential decays, meaning that [PDE**] is obtained as a linearly low-passed version of the input luminosity.
2. Concentration of [cGMP] is driven by a catalyzer equation involving [PDE**] and the feedback Calcium current. The model relies on variable $\beta(t)$ which sets simultaneously the gain and time constant for the evolution of [cGMP], as arises from the general formula of a linear ODE such as (3.1) (see Chapter 2, Section 7).
3. Activation steps which require the simultaneous binding of multiple reactives are modeled with the introduction of a Hill exponent.
4. The feedback arising from variations in $[Ca^{2+}]$ is obtained as a low-passed version of the circulating current, followed by a static function with a Hill exponent, modeling the binding of calcium to GCAP molecules.

Analysis, and links with linear modeling. Analyzing in details the shape of the various pulse responses (Figure 3.3 A) and how they relate to different elements of the model, is beyond our scope here. Let us simply note that the model behaves quite linearly at low intensities, with a typical monophasic shape.

This linear behavior at low intensities is in agreement with the previous findings of Schnapf *et al.* 90 [151] (Figure 2.4). However, note that in these previous recordings, the impulse response was biphasic. A possible explanation for this discrepancy with Figure 3.3 is the level of extracellular calcium between the in-vivo conditions of Figure 3.3 and the in-vitro conditions of Figure 2.4. The Van Hateren *et al.* model of Figure 3.3 does start to become bi-phasic when the Calcium feedback time constant is set at longer values [175].

At higher intensities, nonlinear behaviors occur:

- Intrinsic saturation due to the limited number of channels.
- Shorter time constant for the rising time, as resulting from the catalysis by [PDE**] ('linear ODE' framework, see above description of the model).

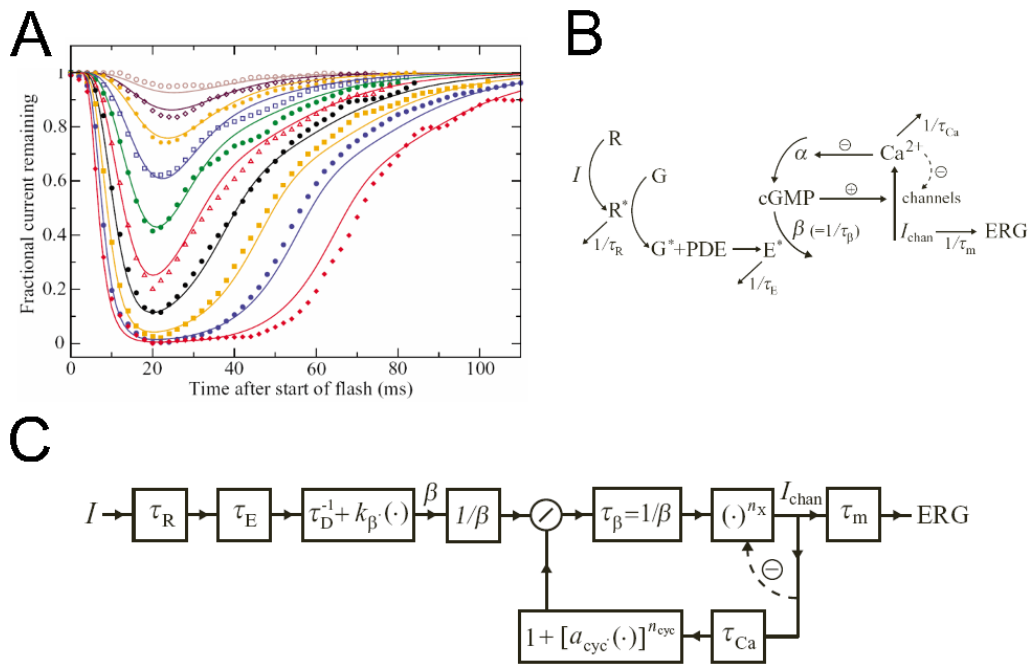


Figure 3.3: *A model for cone responses to pulses of increasing intensities. A: Responses of a real cone from the squirrel retina, and fit by the model. B: Link of the model with phototransduction cascade, and C: Functional architecture of the model. Boxes marked τ_X symbolize low-pass exponential filters ($E_\tau(t)$ in our notations). Boxes marked $a + b(\cdot)^n$ implement the transform $x \rightarrow a + bx^n$, where n is a Hill coefficient, often introduced to account for activation steps that require the simultaneous binding of several molecules. Finally, signal $\beta(t)$ models the nonlinear catalyzer effect of PDE**, like variable Z_2 in our equation (3.1). From Van Hateren and Lamb 06 [175].*

- An increased plateau before the decay, at high illuminations. We have not investigated how model equations account for this phenomenon, very typical of phototransduction responses.

1.1.3 Functional implications

To conclude, we mention the functional implications of the phototransduction process for subsequent retinal processing.

Rods and cones. The rod and cone pathways function with very similar principles, but the rods' phototransduction cascade is many orders of magnitude more sensitive than the cones', for reasons which are not totally understood (different concentrations of the chemical species involved, organization of the outer segments in dissociated disks rather than sacs, rapidity of the inactivation mechanisms, etc. [24]). In this chapter and in the sequel, we rather focus on the cone pathway, at the base of our precise daytime vision. The rod pathway, more useful at night and for movement detection, is mentioned specifically in Section 3.2.4.

Light receptors and horizontal cells have 'OFF' polarity. Due to the nature of phototransduction, incoming light reduces an incoming cation current, and thus lowers (hyperpolarizes) the cell's membrane potential, which corresponds to an 'OFF' behavior. This is true for rods as well as cones. Coherently with their single type of polarity, all light receptors express a single type of neurotransmitter: glutamate, which is an *excitatory* neurotransmitter.

In turn, horizontal cells post-synaptic to receptors are depolarized by glutamate (the natural response to this excitatory transmitter), and thus inherit from receptors' OFF polarity.

Adaptation to light. The main effect of phototransduction is the adaptation to various levels of luminosity, mostly thanks to the modulatory effects of Calcium (and also pigment bleaching –pure inactivation of rhodopsin– at very high light levels).

To a first approximation, this adaptation can simply be modeled by the divisive effect of Calcium on [cGMP], as in the Van Hateren *et al.* model, without taking into account the supplementary effects of Calcium on the disk membrane cascade (in the model, a simple linear conversion from incoming light to [PDE**]). In this case, the divisive effect of Calcium on the steady-state level of [cGMP] allows to find back the parallel shift of photoreceptor response curves with increasing background light (Section 5.1).

1.2 Further processing in light receptors and horizontal cells

After phototransduction, light receptors' inner segments behave as 'traditional' retinal cells. They are linked to their neighbors by gap junctions, and have a complex interaction with horizontal cells and bipolar cells.

Gap junctions between receptors.

Light receptors are coupled through gap junctions, although not as strongly as horizontal cells (see e.g. Raviola-Gilula 73 [137] who demonstrate the results in primate,

rabbit and turtle retinas). These gap junctions are partly responsible for the spread of the retinal *center* signal. Likely, they play a fundamental role in the retina's robustness to noise, by homogenizing the phototransduction noise between neighboring receptors, prior to any subsequent treatment.

Horizontal cells.

Light receptors make feed-forward connections to horizontal cells, and receive feedback from these. Modalities of the feedback are not totally understood, neither its global functional effects (supplementary adaptation to the local luminosity and/or beginning of the *surround* opposition signal). This issue is discussed in the next section, where we present bipolar cells and the arousal of the center-surround organization.

2 BIPOLAR CELLS: THE RETINAL TURNTABLE _____

This section is devoted to bipolar cells, the intermediate excitatory cells which make synaptic connections both in the OPL and IPL (see Figures 1.8 and 1.9 in Chapter 1). The 'take-home message' of this section is that bipolar cells already display the typical spatio-temporal sensitivity evoked in the two preceding sections: They exist in ON and OFF versions (Section 2.1), have a center-surround architecture of their receptive field (Section 2.3), and exist in transient and sustained versions (Section 2.4). Furthermore, bipolar cells exist in several different subtypes, which mark the beginning of differentiation of the retinal output into various parallel pathways (Section 2.2).

One might ask then, what is the precise role of the many amacrine and ganglion cells which interact with bipolar cells in the IPL. Are all these diverse cells only dedicated to generating a spiking output from the signal of bipolar cells?

Nowadays, the current opinion [107, 146] is that the bipolar signal is a 'basis' signal, for which the typical spatio-temporal band-pass operations have already been performed, and that is combined by cells in the IPL in various ways – often nonlinearly – to produce parallel flows of information at the retinal output, with different properties. The combination of the bipolar signal into various retinal pathways, at the level of the IPL, is developed in Section 3.

2.1 ON and OFF pathways arise at the level of bipolar cells

Unlike photoreceptors and horizontal cells that exist in a single polarity (OFF), bipolar cells exist under ON and OFF versions, marking the initiation of the 'ON' and 'OFF' cellular pathways. At each cone synaptic terminal, the receptor's signal is transmitted to both an ON and an OFF bipolar cell, through different synaptic interactions :

- OFF bipolar cells make 'basal' junctions with their presynaptic cones (Figure 3.4). There, OFF bipolar cells express ionotropic receptors to glutamate, which tend to depolarize ('excite') the cell when glutamate is released by the cone. As

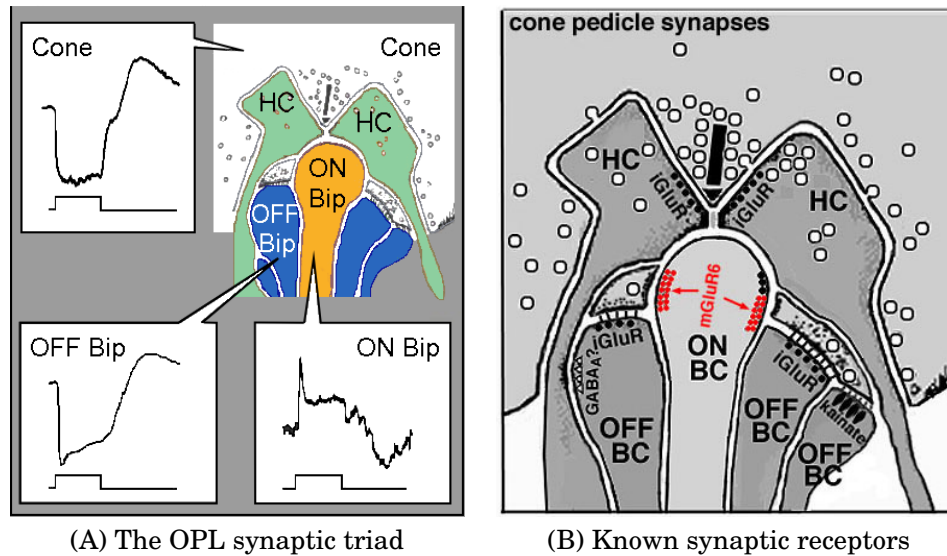


Figure 3.4: *Signal transmission from a cone to ON and OFF bipolar cells occurs at the cone's pedicle synapses. A: In response to a step of light, cones are hyperpolarized and diminish their release of glutamate. OFF bipolar cells make basal junctions with the cones, while ON bipolar cells make invaginating junctions, and display an inversion of polarity w.r.t. cones. B: Known synaptic receptors expressed at the level of the cone pedicles. Horizontal cells and some OFF bipolar cells express the ionotropic receptor iGluR to glutamate, preserving the polarity of signal transmission. ON bipolar cells express the metabotropic receptor mGluR6 that allows a hyperpolarization by glutamate (polarity inversion). From [95].*

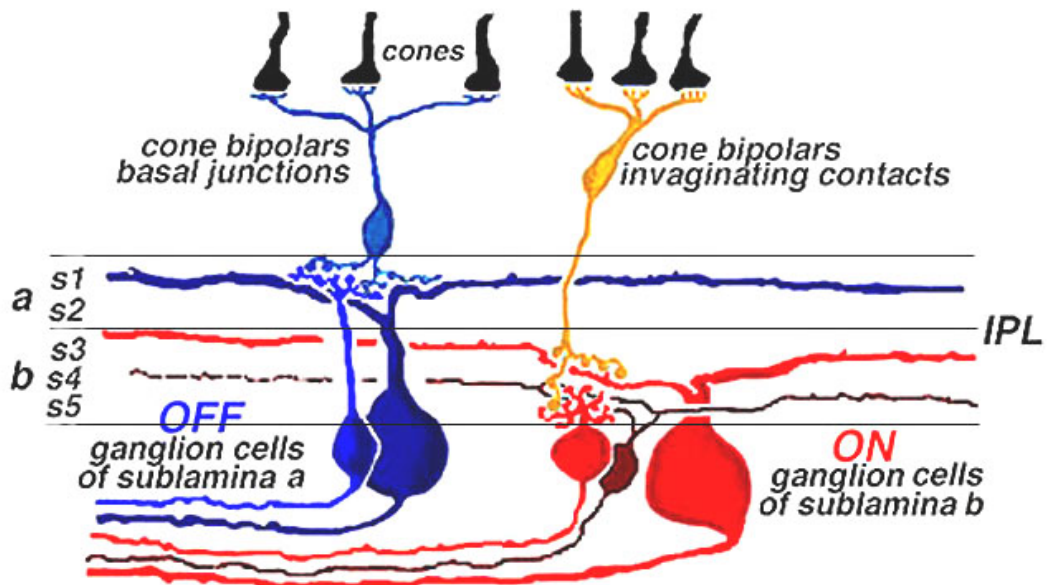


Figure 3.5: *Synapses in the IPL occur in two distinct laminae involving respectively the ON and the OFF pathways (with different bipolar, amacrine and ganglion cells). The laminae are further divided into five strata, denoted s_1 to s_5 (see Section 3). From Nelson *et al.* 78 [118], found at [95].*

a result, these synapses preserve the polarity of the cones' response, making the bipolar cells 'OFF' type.

- ON bipolar cells make 'invaginating' junctions with their presynaptic cones (Figure 3.4). Unlike OFF bipolar cells, ON bipolar cells must invert the polarity of their response to light, and be inhibited by the cones' released glutamate, although this is a typically excitatory neurotransmitter. To achieve this, ON bipolar cells express a specific *metabotropic* receptor to glutamate, termed mGluR6, which in turn activates a G-protein, causing the cell to hyperpolarize in response to glutamate [117].

2.2 Subtypes of bipolar cells

Unlike photoreceptors and horizontal cells which exist in relatively few subtypes in mammalian retinas (3-4 subtypes of receptors, including color sensitivity, and 2-3 types of horizontal cells), bipolar cells exist in around 10 different subtypes.

Primate retina. In the primate retina, Boycott and Wässle 91 [19] have established the morphological classification of 11 subtypes of bipolar cells (Figure 3.6). Here are the main subtypes identified:

- A single ON cell is dedicated to integration of the rod signal (see Section 3.2.4).
- A single ON cell is dedicated to integration of the signal from 'Blue' (S-type) cone receptors (see Section 3.2.3).
- One ON and one OFF type, known as '*Midget*' bipolar cells, are the most numerous, and spatially precise. Each midget cell connects only a small number of cones: In the fovea, cones and midget bipolar cells are even in a one-to-one connection (Masland 01 [107]). In turn, midget bipolar cells connect 'midget' ganglion cells (Section 3), also in a one-to-one connection at the level of the fovea.
- The remaining cells, known as '*Diffuse*' bipolar cells, connect more cones, so that they have less spatial precision. 'Diffuse' is a rather generic term which applies to all 'non-midget' bipolar cells of the primate. Several different types of diffuse bipolar cells make contact with the wide α ganglion cells which form the basis for the 'Movement' pathway in the brain (Section 3.2.2). But diffuse cells also provide input to other, less well known ganglion cells. Globally, little is known about the specificities and roles of each different type of diffuse cell.

Other mammalian retinas. In other mammals also, there are around 10 different subtypes of mammalian cells (see e.g. Boycott and Wässle 74 [18] or McGuire *et al.* 84 [110] in the cat retina). The classification previously given for primate retinas holds, with one difference: Other mammals do not possess such specialized and precise cells as primate 'midget' cells. However, distinct subtypes still display different sizes of dendritic trees, implying different levels of spatial precision and different functions [110].

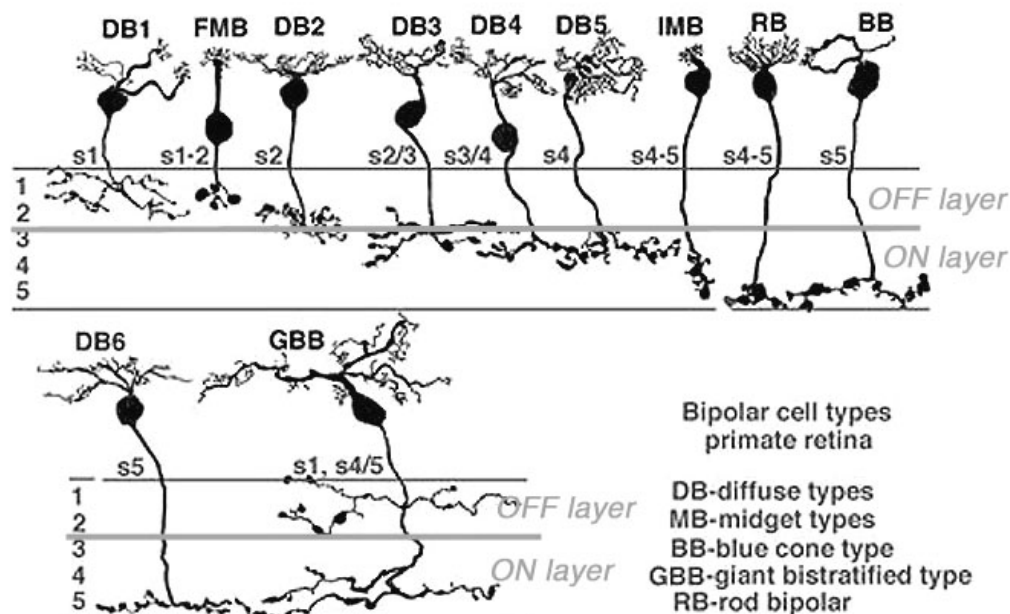


Figure 3.6: Morphological classification of bipolar cells in the primate retina. From Boycott-Wässle 91 [19], found at [95].

Bipolar cell axons in the IPL. The IPL is a thick (as compared to the OPL) and very ordered synaptic structure. Several parallel pathways of information emerge there, each involving different bipolar, amacrine and ganglion cells, and the corresponding synapses of the different pathways are segregated vertically (see Section 3). As a result, various sub-types of bipolar cells have their axonic arborization at different depths in the IPL.

First, ON and OFF pathways are anatomically segregated: The IPL is divided in two *laminae*, termed *a* and *b*, and each of these laminae is specifically concerned with all the synaptic interactions of only one polarity: *a* is the OFF lamina, and *b* the ON lamina (see Figure 3.5). Second, the two laminae are further divided into five specific synaptic *strata*, termed *s1* to *s5*, and different sub-types of bipolar cells have their axon terminals in different strata (Figure 3.6).

2.3 Center-surround architecture of bipolar cells

It is now well established that bipolar cells already display the center-surround spatial opposition so typical of retinal processing. In this section, we first present the characteristics of bipolar cells' center-surround filter: Most bipolar cells display the center-surround sensitivity, but the size of their receptive field depends on the subtype considered. Then, we question the nature of bipolar cells' center-surround opposition: Does it arise from synaptic interactions in the OPL (as caused by horizontal cells), or in the IPL (as caused by amacrine cells)? Also, does it rely on synaptic feedbacks, or on feedforward transmission from horizontal cells? To these last questions, only partial answers exist.

2.3.1 Center-surround receptive field in bipolar cells.

Bipolar cells have long been suspected to display center-surround organization of their receptive fields. The result was proved a long-time ago for the salamander retina (Werblin and Dowling 69 [181]) where the cells are fairly large (see also Hare and Owen 90 [72, 73]). By opposition, mammalian and especially primate bipolar cells have been subject to much more interrogations, because intracellular recordings were much harder in these cells with a very small soma: As a result, some ‘old’ recordings reported little or no *surround* component in the receptive fields of mammalian bipolar cells (Nelson and Kolb 83 [119]).

Though, recent studies tend to prove that a center-surround opposition is also present in mammalian bipolar cells (see Dacey *et al.* 00 [38] for the primate retina, and supplementary reference). In the primate, both diffuse and midget cells display a center-surround opposition, but with much larger receptive fields in the case of diffuse cells, in particular concerning the *center* signal (Figure 3.7).

Relative weight of center and surround. The authors in [38] measured the relative weights of *center* and *surround* signals: These relative weights were close to 1 in average, but with a certain variability, especially for diffuse bipolar cells (some relative weights were close to 3). By this aspect too, midget bipolar cells appear to form a homogeneous class well suited for precise vision, while diffuse bipolar cells appear more heterogeneous, and possibly mediating other visual features. In the salamander retina also, some variability is seen in the relative weight between *center* and *surround*: Hare and Owen 90 [72] find it around 0.6 for ON cells and 0.9 for OFF cells.

Relative sizes of center and surround. An even more striking feature is the relative sizes of *center* and *surround* signals: The authors in [38] found that, for midget bipolar cells, *center* and *surround* sizes are in an average ratio of 10. This result compares relatively well to the average ratios of 7-8 found between *center* and *surround* for primate midget *ganglion* cells by Croner and Kaplan 95 [37]. This intriguing number raises important issues concerning the edge detection capabilities of our retinas: We have seen in Section 2 how a linear model with such a ratio between *center* and *surround* is likely *not* to be able to detect edges.

2.3.2 Controversial origin of the center-surround mechanism

Although center-surround opposition is probably one of the best known properties of retinal filtering, its biological origins are still somewhat controversial. The basis principle is relatively well-settled: Some inhibitory interneurons – horizontal cells and/or amacrine cells – compute a local average of the excitatory cells’ signal, and transmit it back to excitatory cells through inhibitory synapses, thus creating the *surround* signal.

It is also well settled that the spatial extent of the *center* and *surround* signals is due in good part to gap junctions between neighboring cells – although naturally, the morphological spread of dendritic trees (and even axons, for some amacrine cells) also plays a role in the spatial extent of receptive fields. Actually, gap junctions between neighboring cells of the same type have been observed for all types of retinal cells (see e.g. Kolb 79 [94] in the IPL).

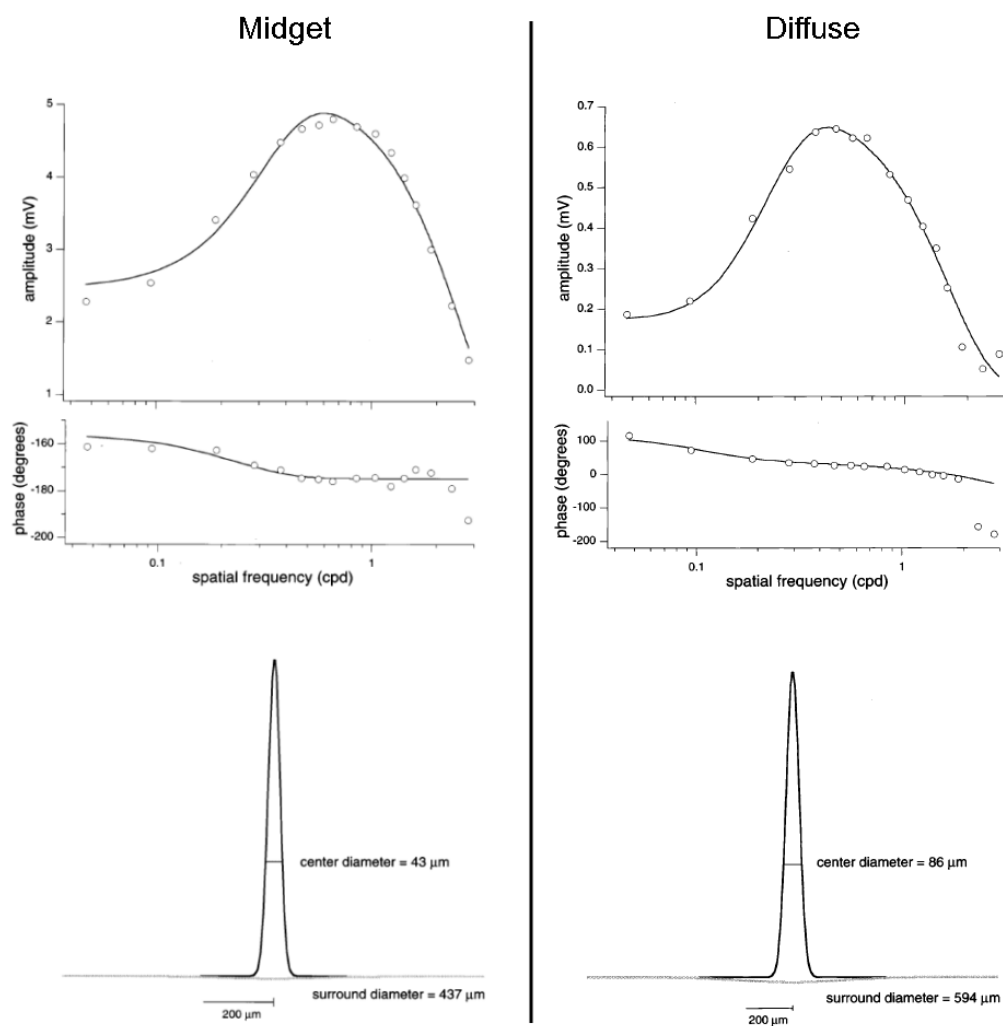


Figure 3.7: *Center-Surround structure in primate bipolar cells.* Sensitivity to drifting gratings and DOG approximation for one 'midget' and one 'diffuse' bipolar cell in the primate retina. Note that the cells are from the retinal periphery: In central retina, all scales would be much smaller. From Dacey *et al.* 00 [38].

But a distinct question is the nature and location of synaptic interactions that mediate the *opposition* between *center* and *surround*. The existence of two successive layers of inhibitory cells in the retina raises strong questions concerning their respective roles in spatial (and temporal) oppositions, especially since the traditional center-surround opposition could be theoretically explained by a single layer of inhibitory cells.

Bipolar cells are at the core of these intriguing questions, since they receive synaptic inputs from both horizontal and amacrine cells.

2.3.3 Center-surround opposition in the OPL

The ‘mainstream’, or ‘historical’, view is that the center-surround mechanism arises mostly due to the synaptic opposition between receptors and horizontal cells, in the synaptic triad onto bipolar cells.

Feedback to receptors. Feedback synapses from horizontal cells onto receptors are traditionally cited as the primary origin of center-surround opposition. For example, a strong feedback has been shown from horizontal cells to cones in non-mammalian retinas such as salamander or turtle². However, the precise medium for this feedback is not known: GABA synaptic inhibition is the traditional assumption, yet it lacks experimental evidence [180]. Other models have been proposed that do not involve feedback synapses, but rather electrical gradients at the synaptic terminal of cones (work of Kamermans and colleagues [86]).

Also, the ‘main’ functional role of the feedback is not clearly assessed. Rather than creating a linear surround, the main role could be to provide nonlinear *divisive invariance* to cones, based on the local level of light in the neighborhood as measured by horizontal cells. A ‘linear ODE’ formalism (e.g., conductance feedback) could account for this phenomenon, pretty much like the contrast gain control loop used in our model (Chapter 4, Section 4). See for example the model of Van Hateren of cone/horizontal coupling [174]. In this case, the linear center-surround observed in cones may be only a secondary effect, due to the synaptic conductances’ hyperpolarizing Nernst potential.

Feedforward to bipolar cells. Furthermore, a *feedforward* transmission from horizontal cells to bipolar cells has also been observed, both in mammalian and non-mammalian species, that very likely adds its effects to the feedback mechanism onto receptors. Interestingly, the best candidate for synaptic transmission between horizontal and bipolar cells is also GABA, traditionally an inhibitory transmitter, which is supposed to provide simultaneously inhibition to OFF bipolar cells and excitation to ON bipolar cells: It is believed that ON and OFF bipolar cells express different chloride transporters, to achieve different equilibrium potentials for ion Cl^- that is associated to the GABA receptors (works of Vardi and colleagues)³.

Whatever the medium (feedforward or feedback), there is undeniably a *surround* influence of horizontal cells at the level of bipolar cells. It should be noted that, when solely a *linear* feedback is implemented between cones and horizontal cells,

²Many references can be found at website Webvision [95], more precisely at the page of horizontal cells: <http://webvision.med.utah.edu/HC.html#Feedback>

³We refer to the ‘horizontal cell’ page of website Webvision [95] for further details and references: <http://webvision.med.utah.edu/HC.html#Functional%20Roles>

it produces a relative weight of *center* and *surround* signals strictly smaller than 1. So, relative weights of *center-surround* equal or bigger than 1 (as observed in many bipolar cells by Dacey *et al.* [38]) necessarily imply feed-forward transmission and/or nonlinear feedback enhancements of the *surround* signal.

Remark: Linear feedback from horizontal cells

Let us prove that a linear feedback cannot achieve a relative *center-surround* weight of 1: Let $V_R(x, y, t)$ and $V_H(x, y, t)$ be the respective potentials of receptor and horizontal layers. The excitatory current on receptors provoked by phototransduction is noted $I^{exc}(x, y, t)$. Then, the feedback couples linearly $V_R(x, y, t)$ and $V_H(x, y, t)$, through two equations similar to (2.19):

$$\frac{dV_R}{dt}(x, y, t) = \mathcal{G}_R \Delta V_R(x, y, t) - g_R V_R(x, y, t) + I^{exc}(x, y, t) - (aV_H(x, y, t) + b) \quad (3.2)$$

$$\frac{dV_H}{dt}(x, y, t) = \mathcal{G}_H \Delta V_H(x, y, t) - g_H V_H(x, y, t) + (cV_R(x, y, t) + d), \quad (3.3)$$

where $cV_R(x, y, t) + d$ represents the (linear) excitatory current from receptors to horizontal cells, while $aV_H(x, y, t) + b$ represents the (linear) feedback current from horizontal cells to receptors, which is always inhibitory. \mathcal{G}_R and \mathcal{G}_H model gap junctions between receptors and horizontal cells respectively.

Through subtraction of the static solution of this system, we can always suppose $b = 0$ and $d = 0$. Then, $V_H(x, y, t)$ and $V_R(x, y, t)$ bear Fourier transforms, for which the coupled system can be solved, yielding:

$$\tilde{V}_H(\xi_x, \xi_y, \xi_t) = \tilde{H}_H(\xi_x, \xi_y, \xi_t) \tilde{I}^{exc}(\xi_x, \xi_y, \xi_t),$$

with

$$\tilde{H}_H(\xi_x, \xi_y, \xi_t) = \frac{c}{ac + (g_R + \mathcal{G}_R(\xi_x^2 + \xi_y^2) - \mathbf{j}\xi_t)(g_H + \mathcal{G}_H(\xi_x^2 + \xi_y^2) - \mathbf{j}\xi_t)}. \quad (3.4)$$

This is also the asymptotical expression found by J. Hérault in the case of a discrete array of cells (forthcoming book Hérault 08 [78], see also Hérault 01 [77]).

Equation (3.4) involves the total gain of the feedback loop, ac . By studying the partial derivatives of $\tilde{H}_H(\xi_x, \xi_y, \xi_t)$ w.r.t. ξ_x , ξ_y and ξ_t , one finds that \tilde{H}_H is always a spatial low-pass, but that it can become temporally band-pass if the gain of the feedback loop gets too high, possibly implying undesired oscillations.

More importantly, when the horizontal signal is transmitted back to cones through (3.2), it creates a *surround* component in the cone response whose Fourier transform is $a\tilde{H}_H(\xi_x, \xi_y, \xi_t)$, so that the relative weight of *surround* w.r.t. *center*, measured at the DC output of cones (null frequencies in the Fourier transform), is $w = ac/(ac + g_R g_H)$, a number always strictly smaller than one. Furthermore, in real retinas, the gain of the feedback loop ac cannot get too high, in order to avoid strong temporal oscillations (see Hérault 08 [78]).

Hence, in the case of a linear model, a supplementary feedforward transmission from horizontal cells to bipolar cells is mandatory to obtain a relative gain of 1 or more. ■

2.3.4 Center-surround opposition in the IPL

In parallel to the ‘textbook’ version of center-surround interactions arising between light receptors and horizontal cells, different considerations speak in favor of a contribution of amacrine cells to the observed *surround* of ganglion cells, and also possibly of bipolar cells through feedback interactions.

The various roles of amacrine cells in shaping ganglion cells’ responses are rather discussed in Section 3 when presenting the different retinal output pathways. Here, we take a different, more generic approach: What is known concerning the compared

contributions of OPL and IPL processes to the overall center-surround organization in ganglion cells?

Amacrine surround in bipolar cells. In our readings, we have not come across the unambiguous proof of an amacrine *surround* component in bipolar cells. However, anatomical considerations (and, likely, articles unknown of us) speak in favor of such a fact: Several identified types of amacrine cells are linked by gap junctions to their neighbors (bipolar and/or amacrine and/or ganglion, according to they type of amacrine cell considered), possibly implying a consequent extent of their receptive fields⁴. Simultaneously, several amacrine cells make feedback connections to bipolar cells, through gap junctions or chemical synapses⁵. Should one type of amacrine cells display both features simultaneously (spatial extent and feedback to bipolar cells), it would naturally provide their target bipolar cells with an extended *surround*.

Horizontal cells have too big receptive fields. Various physiological measurements directly on ganglion cells add direct or indirect evidence to the roles of some amacrine cells in spatial oppositions. In the rabbit retina, typical receptive fields for horizontal cells have been measured between 2 and 3 mm (Dacheux and Raviola 82 [43]), whereas brisk sustained (X) ganglion cells (Section 3.2.1) *surround* receptive fields, in response to drifting gratings, are often measured at less than 1 mm (DeVries and Baylor 97 [55]). It is thus possible that the ‘overall’ *surround* of these cells rather arises from inhibition by neighboring amacrine cells⁶.

Still in the rabbit, the most spatially precise retinal cells, the local edge detectors (LEDs, Section 3.2.6) can have inhibitory *surround* receptive fields markedly smaller than 1 mm, and in this case the effect has been demonstrated to arise from amacrine cells.

Experimental comparisons of OPL and IPL contributions. Experimentalists have recently started to question the respective impacts of OPL and IPL with more quantitative tools, at the ganglion cell output. In the primate retina, Mc Mahon *et al.* 04 [112] found that GABA-ergic amacrine cells (generally wide-field) have a minority influence on parasol cells’ classical *surround*. In rabbit cells however, Flores-Herr *et al.* 01 [65] measured an influence (moderate) of amacrine cells on the *surround* of most ganglion cells.

Nature of the amacrine surround. In conclusion, the spatial effects of amacrine cells are far from being well understood, and two strong questions remain. First, is the amacrine-related *surround* a specificity of particular sub-types of ganglion cells? Second, to what extent do amacrine *surround* oppositions correspond to the ‘traditional’ *surround* observed in receptive fields and reverse correlation analysis, or to secondary ‘silencing’ effects modulating the already spatially band-pass signal of bipolar cells?

⁴ From website Webvision [95], more precisely at the page of amacrine cells: <http://webvision.med.utah.edu/amacrine1.html>

⁵idem as footnote 4

⁶The discrepancy can also possibly be explained without amacrine cells: By differences of experimental protocols, or by an ‘attenuation’ of weak signals from horizontal cells’ remote *surround* due to successive synaptic rectifications from horizontal cells to ganglion cells.

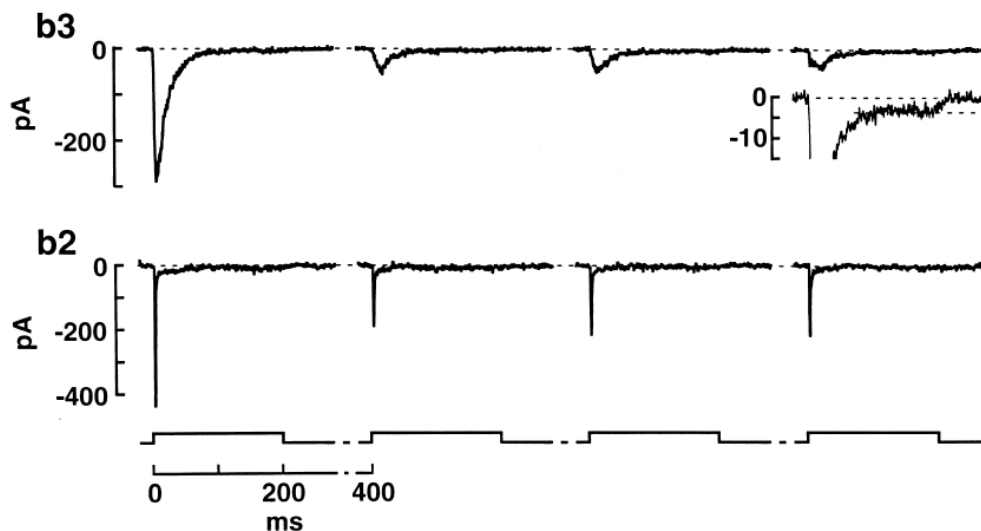


Figure 3.8: *Temporal band-pass properties of various bipolar cells.* Synaptic input currents of two types of bipolar cells (from ground squirrel retina). According to the type of synaptic receptor to glutamate they express, different bipolar cells filter the input cone signal with different time constants. For b2 bipolar cells (morphologically close to a primate DB3 diffuse bipolar cell [54]), a fast transient response arises from the fast alternation of desensitization and recovery in their AMPA receptors to glutamate. For b3 cells, kainate receptors to glutamate are *permanently* desensitized because of a longer recovery time constant, so their response reflects only the slow transient of the cone's response. From DeVries 00 [54].

Partial answers can be found in the presentation of the different types of ganglion cells, in Section 3.2.

2.4 Temporal shaping in bipolar cells

To finish this presentation of bipolar cells, we mention their temporal behavior: All bipolar cells have a rather *transient* response to light stimulation, which arises simultaneously from different origins, and can have different time scales according to the sub-type of bipolar cells considered.

Slow phototransduction transients

Phototransduction in cones may already display a partially transient response, with a time scale of approximately 100 ms, as we have shown in Figure 2.4, from the experiments of Schnapf *et al.* 90 [151] on single cones. However, more recent results (Van Hateren and Lamb 06 [175], Section 1.1) tend to show that the photoresponse in humans (in vivo!) is actually monophasic and much faster (time constant around 10 ms): The authors suggest that the slow biphasic shape previously observed [151] was due to the *in vitro* conditions.

Horizontal cell opposition

Whether resulting from feedback or feedforward opposition, the *surround* signal provided by horizontal cells to bipolar cells can induce temporal transients because it is delayed in time, due to the supplementary membranar integration in horizontal cells. The strength of the horizontal cell opposition is probably dependent on the spatial structure of the image: the opposition should be rather strong in the uniform zones of the image, where the horizontal signal is as strong as the cone signal. Near image edges, where the cone signal is stronger than the horizontal signal, the temporal influence of horizontal cells is probably weaker.

Band-pass filtering by synaptic receptors

More importantly, it has been recently shown that the synaptic transmission from cone to bipolar can also induce intrinsic transients on the visual signal. DeVries and Schwartz 99 [56, 54] showed that the synaptic transmission from cones to OFF bipolar cells is very affected by rapid *desensitization* of the synaptic receptors to glutamate in the membrane of the bipolar cells: In a few tens of milliseconds, the *effective* synaptic transmission is reduced in a factor of 10, by a complex desensitization of most of the synaptic receptors.

The effect is represented in Figure 3.8: When a presynaptic cone undergoes a series of voltage steps (alternatively stopping and starting the glutamate release by the cone synapse), the synaptic current induced in the bipolar cells is a series of transient waves, whose amplitude is high during the first glutamate release of the experiment (left of the Figure), but consequently smaller during the next synaptic releases, because the synapse is *desensitized*. These ‘reduced’ responses are in fact the ‘normal’ responses of the synapse, because glutamate is continuously released by the cone in normal visual conditions.

Furthermore, as demonstrated by DeVries 00 [54], different bipolar cells express different synaptic receptors to glutamate, with different time constants for *recovery* from desensitization. Some cells, that have fast-recovering AMPA receptors, have a synaptic transmission that continuously undergoes alternate desensitization and recovery in response to the cone’s glutamate release, and thus provide a very *high-pass* temporal filtering of the cone signal (b2 cells in Figure 3.8). Other cells, that have slow-recovering kainate receptors, are continuously desensitized during ‘normal’ visual stimulation, and thus provide a more low-pass filtering of the cones signal (b3 cells in Figure 3.8).

As argued by the author, very likely, the ‘fast’ AMPA cells are rather ‘diffuse’ bipolar cells specialized in temporal sensitivity, while the ‘slow’ kainate cells rather correspond to the primate ‘midget’ bipolar cells, less sensitive temporally but with a stronger spatial resolution. However, it should be remarked that even the ‘slow’ b3 cells display a *transient* synaptic current, although with a slower time scale: According to the author, this transient shape directly reflects the cone’s synaptic release.

Band-pass filtering by amacrine cells

The preceding experiment concerned only cone synaptic inputs to bipolar cells (the bipolar cells’ axons had been removed). A supplementary source of temporal transient has been found in bipolar cells, through the reciprocal inhibition of some

amacrine cells in the IPL. Amacrine cells are known to be involved in the temporal shaping of ganglion cells' responses (Nirenberg *et al.* 97), and part of their temporal cutting effects are done by feedback connections to bipolar cells. These results were demonstrated for example by Euler and Masland 00 [63] in the rat retina.

Conclusion: A strong need for further exploration

In conclusion, the combined effects of synapses in the OPL and IPL provide bipolar cells with the spatio-temporal band-pass structure typical of retinal processing: ON and OFF cells, center-surround oppositions and temporal transients.

Also, separation of the visual signal into distinct pathways starts at the level of bipolar cells: The distinction is mostly between midget-like and diffuse-like bipolar cells ('midget' and 'diffuse' being a terminology reserved to the primate retina). Midget-like bipolar cells are the most precise spatially, and display temporal responses which are relatively sustained (or rather, transient with a longer time scale). By opposition, diffuse-like bipolar cells are less precise spatially, but display a series of temporal transients (including a very fast desensitization and recovery at their synaptic receptors) that helps to shape and enhance fast temporal variations in their input.

Bipolar cells, with their role of 'turntable' between OPL and IPL, are a fundamental key to understand the complex nature of further filtering in the IPL, and the functional 'task repartition' between OPL and IPL. Bipolar cells are still in a strong need of further exploration, and particularly the response characteristics of their different subtypes. Unfortunately, experimental exploration is made difficult by their small somata and 'hidden' locations in the Inner Nuclear Layer.

3 PARALLEL PATHWAYS OF THE RETINAL OUTPUT —

3.1 Introduction: Ganglion cells and the Inner Plexiform Layer

3.1.1 Historical landmarks and bibliography

Concentric X and Y cells

Kuffler 53 [96] was the first to measure the center-surround, or concentric, receptive field architecture shared by many ganglion cells. Hubel and Wiesel 60 [82] also measured the concentric architecture, in their seminal series of papers on the receptive fields of low-level visual processing.

A few years later, Enroth-Cugell and Robson 66 [59] revealed the distinction between two distinct types of ganglion cells in the cat retina, which they named X and Y cells, that had markedly different physiological properties (detailed in the sequel). Since then, many subsequent pieces of work have reinforced knowledge on these two types of cells in different ways: Equivalents for X and Y cells have been found in other species, models have been proposed for the particular nonlinearity in the responses of Y cells, and the distinction between the two cell types has been

further investigated in the light of other specific retinal effects such contrast adaptation, connectivity, temporal behavior, synchronies, etc.

Sluggish and non-concentric cells

In parallel, other work has revealed several types of ganglion cells which could not be labeled 'X-like' or 'Y-like'. In the 60s, Barlow, Levick and colleagues started a systematic study of ganglion cell types encountered in the rabbit retina, which revealed interesting new types of ganglion cells: Direction-selective (DS) cells (Barlow-Levick 65 [8]), local edge detectors (LED) and suppressed-by-contrast cells (Levick 67 [99]). Further studies have then revealed similar cells in the cat retina (Cleland and Levick 74 [33, 34], Stone and Fukuda 74 [163], Rowe and Stone 76 [147]). These cells were long thought marginal because rarely encountered. Only recently, it became increasingly clear that they all possess important and distinct functional roles.

For the occasion, Cleland and Levick also introduced the concept of *brisk* and *sluggish* cells, accounting for the fact that some ganglion cells ('brisk') have strong, fast and rather transient responses to light stimuli, while others ('sluggish') have slow responses, of smaller amplitude and which can develop over several seconds [33]. In this alternative classification, the X and Y cells of Enroth-Cugell and Robson were the *brisk* cells (X cells as 'brisk sustained' and Y cells as 'brisk transient'): Likely, it is the 'brisk' nature of their response (very reactive) that has made them the privileged targets of first physiological measures in the retina. Originally, Cleland and Levick reserved the 'brisk'-sluggish terminology to *concentric cells* only (with a clear center-surround architecture), but the terminology seems to have switched to a more general signification of 'sluggish', since some non-concentric cells (LED, suppressed-by-contrast) also have rather sluggish responses. Stone and Fukuda 74 [163] introduced the terminology of 'W cells' to designate all these sluggish, non-X and non-Y cells of the cat retina.

The primate retina

As opposed to other mammal species, primate retinas possess a much greater number of ganglion cells, due to the existence of a specialized pathway formed by the tiny and numerous 'midget' cells (see Section 3.2.1). As a result of the overwhelming statistical predominance of midget cells, non-concentric cells have been much less encountered and studied in the primate retina. However, non-concentric cells have occasionally been found (see e.g. De Monasterio-Gouras 75 [46]), and there is now an increasing certitude that all the typical mammalian concentric and non-concentric cells also exist in the primate retina, in numbers similar to other mammals (Masland 01 [107]).

Morphology of ganglion cells

In parallel to the study of ganglion cells' various physiological properties, their *morphology* has been subject to a detailed analysis, especially in cat and rabbit retinas. Morphological studies, through various staining techniques, have long been favored as a relevant medium to classify the various types of ganglion cells, for two striking reasons:

1. The morphology of retinal cells is very stable across mammalian species. Although the sizes and relative proportions of ganglion cells vary from one species to another, there is an overall correspondence of morphological types across species.
2. There is a striking correspondence between morphology and physiological behavior: Both criteria (morphology and physiology) lead to the same classification of ganglion cells (see Masland 01b [108] for review).

Both facts tend to prove that the various morphological types of ganglion cells serve very precise, and distinct, functional roles.

Boycott and Wässle 74 [18] led the first ‘modern’ morphological study of the cat retina, distinguishing four morphological types that they referred to as α , β , γ and δ cells. It soon appeared that α cells correspond to the physiological Y cells, β cells to the physiological X cells, and that these two morphological-physiological associations hold across most mammalian species.

More recently, new techniques have provided accurate and systematic description of ganglion cells in the rabbit (Amthor *et al.* 89 [3], Rockhill *et al.* 02 [142]) and cat (works of Berson’s lab, as cited in O’Brien *et al.* 02 [124]). In the primate retina, morphological descriptions also exist (Rodieck and Watanabe 93 [144], works of Dacey and colleagues as cited in Dacey 99 [40]). Although less systematic than in cat or rabbit, both these works are particularly interesting because they back-propagated a cellular staining from different visual areas onto the retina, thus giving insights on the cerebral projections -and hence of the function- of the different ganglion cells. However, their results remained partial and purely morphological.

Intracellular recordings

For electrophysiological measurements, intracellular recordings of ganglion cells are more and more favored. Where extracellular recordings allow only to measure a cell’s emitted spikes, intracellular recordings also provide good approximations of *the excitatory and inhibitory synaptic inputs to the neuron* (thanks to voltage clamps at different potentials). These techniques allow to gain insight on the connectivity of the measured cells, and they have recently provided interesting new results (some detailed in the sequel).

Interesting examples of such recordings in the rabbit retina are the work of Roska, Werblin and colleagues [146, 145], the work of Taylor, Vaney and colleagues (on DS cells [167] and on LED cells [177]), the work of Fried, Münch and Werblin on DS cells [66].

3.1.2 Architecture of the Inner Plexiform Layer

We now report more specifically what morphological studies have revealed concerning the spatial organization of the various subtypes of ganglion cells and amacrine cells in the IPL. First, the synaptic processes of cells from different morphological types are strongly segregated into different strata of the IPL. Second, all retinal cells of a same morphological type provide a continuous *paving* of the visual space. These two observations confirm the functional unity formed by cells of the same morphological type, and hence the notion of *parallel visual pathways* forming the retinal output.

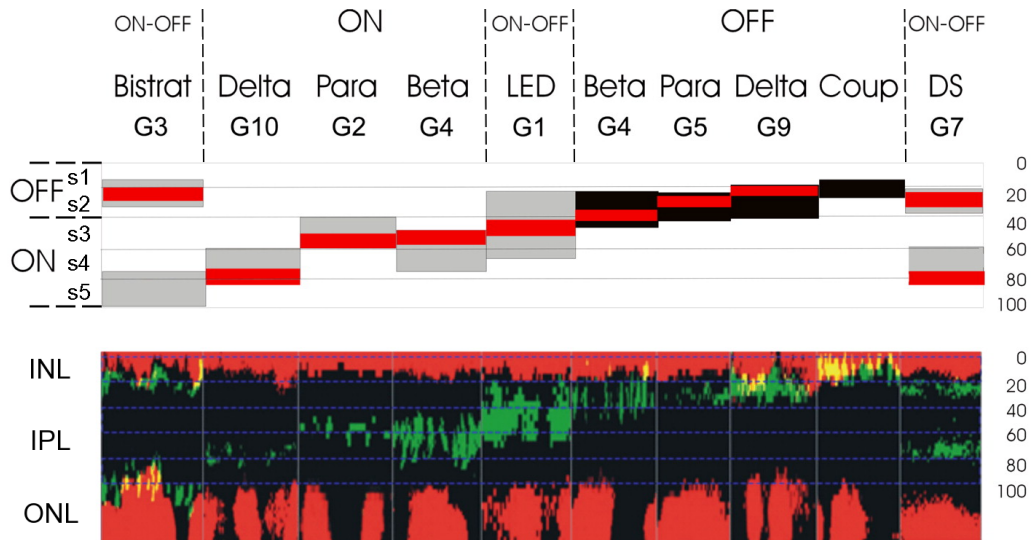


Figure 3.9: *Different pathways use different synaptic strata in the IPL. Up: Correlation between ganglion types (morphological and physiological) and the locus of dendrites in the IPL. ON cells have their dendrites in sublamina b of the IPL, OFF cells in sublamina a. Three types represented here are ON-OFF cells having dendrites in both layers: Bistratified cells, local edge detectors (LEDs) and direction selective (DS) cells. From Roska *et al.* 06 [145]. The ‘Gx’ notations are the morphological classification of Rockhill *et al.* 02 [142]. Down: Corresponding microscopic images from the IPL (one different image per cell type), with the dendrites stained in green. All cellular bodies are in red (up: bipolar and amacrine cells in the INL, down: ganglion cells in the ONL). From Roska *et al.* 06 [145].*

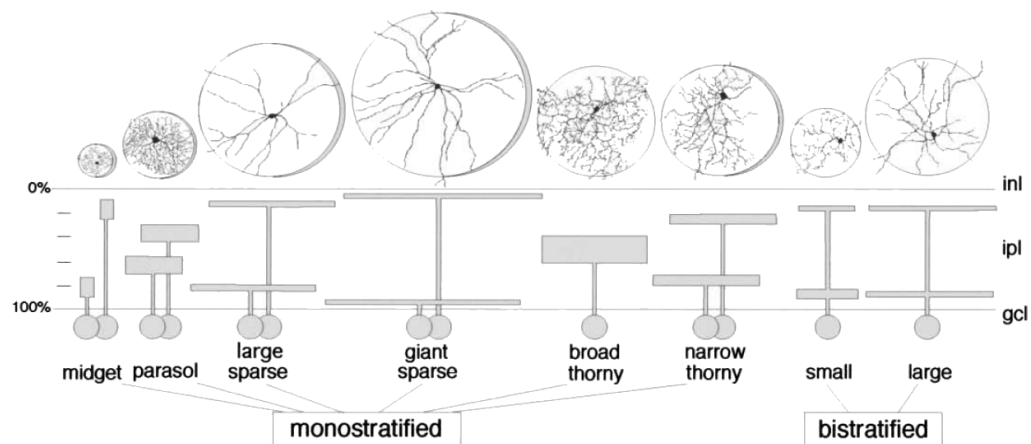


Figure 3.10: *Morphological types of primate ganglion cells that project to the LGN. In addition to ‘traditional’ LGN-projecting cells (midget cells projecting to the P layers, parasol cells to M layers and small bistratified cells to the K layers), other subtypes of ganglion cell seem to provide input to the LGN, and possibly to our conscious perception. From Dacey *et al.* 03 [42].*

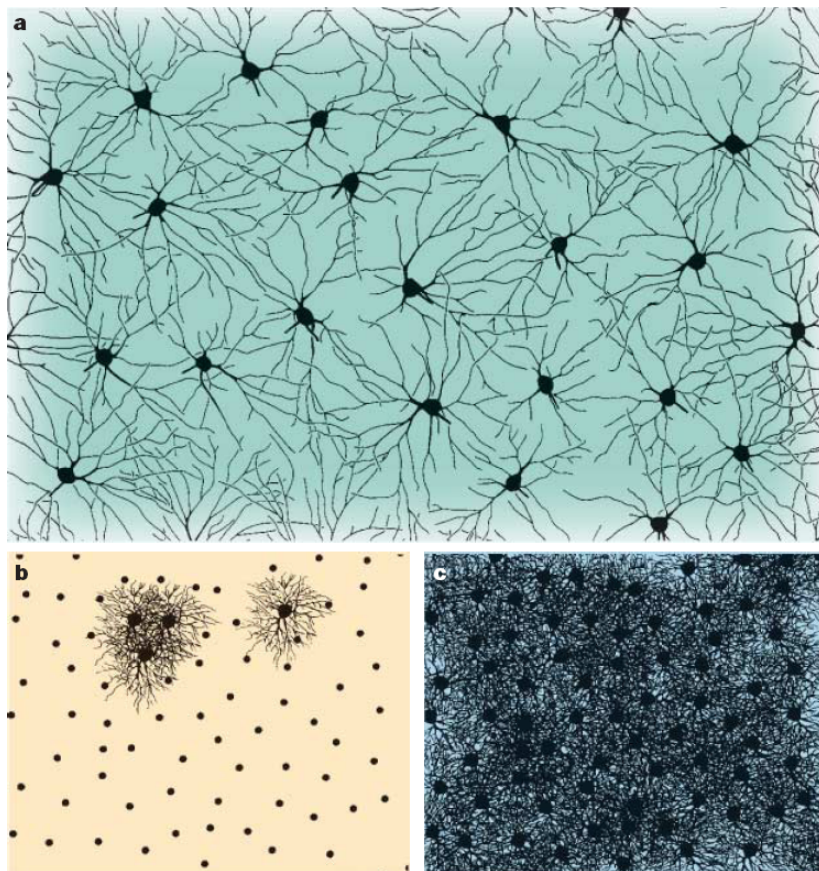


Figure 3.11: *Tiling of the visual space by α and β cells.* *a:* ON α ganglion cells in a 1.2 x 1.8 mm patch of cat retina. *b:* ON β ganglion cells in the cat retina, with roughly the same scale. The dots indicate the cell's locations. *c:* Computer reconstruction of all dendritic trees from the data in b. From Wässle 04 [180].

Synaptic strata in the IPL define different pathways

We have already presented in Section 2 how the IPL is divided in two laminae involving respectively OFF and ON pathways (Figures 3.5 and 3.6). These laminae are further divided into five strata, termed s1 to s5, and different types of bipolar, amacrine and ganglion cells make their synaptic connections in different strata of the IPL (see Figure 3.6 for bipolar cells).

The dendrites of different subtypes of ganglion cells are represented in Figure 3.9. The first obvious vertical segregation is between the ON and OFF pathways, in the two sublaminae a and b. But there is also a clear vertical segregation between the different physiological pathways of ganglion cells⁷.

However, although their synapses are spatially segregated, the various ganglion cell pathways are not independent. It has recently been demonstrated that many vertical flows of information between different pathways are present, likely mediated by amacrine cells: See Section 3.1.3.

Different pathways tile homogeneously the visual space

In addition to this ‘vertical’ architecture, the IPL should be well organized ‘horizontally’: If the various types of morphological cells really correspond to different functional pathways, then cells of the same type should be present at all locations of the retina, with receptive fields that provide a tiling, without holes, of the whole visual space. And indeed, this property of regular tiling has been proved for most morphological types of ganglion cells, and likely holds for all morphological types. Figure 3.11 shows the tiling of α (Y) and β (X) cells in the cat retina.

Note that this tiling property implies an inverse dependency between the size of a morphological cell type’s dendritic tree, and the number of such cells present in the retina. This inverse dependency is well verified by most known types of cells (De Vries and Baylor 97 [55], Wässle 04 [180]).

To conclude, the spatial organization of synapses in the IPL allows various pathways of cells to simultaneously tile the visual space, thanks to a vertical segregation of their dendrites in the different strata of the IPL. These various pathways form parallel flows of information at the output of the retina, most likely with different and specific functions.

3.1.3 Amacrine cells

Amacrine cells are the most diverse class in the retina: Around thirty different subtypes have been reviewed morphologically (Masland 01 [108]). They are also, by far, the less well-understood type of cell. Although they are putatively associated to many different tasks of signal shaping in the IPL, there are only few examples for which the role of a particular subtype of amacrine cell has been rigorously proved, in association with a precise description (morphological or physiological) of the subtype in question.

⁷The central strata (close to the boundary between ON and OFF sublaminae) are sometimes said to involve more transient pathways than the exterior strata (close to INL or ONL), which involve more sustained pathways (Awatramani and Slaughter 00, Roska *et al.* 06 [145]). We personally did not find this division very obvious in our readings.

Throughout the following presentation of ganglion cells (Section 3.2), amacrine cells will be mentioned several times as playing an important role. Here, we give general landmarks on the nature of amacrine cells, and a summary of their presumed functionalities, with pointers to the corresponding sections in the sequel.

Narrow-field and wide-field amacrine cells. The major distinction in the amacrine cell population can be done between *narrow-field* and *wide-field* amacrine cells. The two types possess fundamentally different roles. Narrow-field amacrine cells are involved in local calculations, providing a constant shaping of the bipolar and ganglion signals (for example, through delayed inhibitions). Wide-field amacrine cells, by opposition, are involved in transmitting remote inhibitions to ganglion cells, and likely contribute to create the wide, nonlinear inhibitions generically referred to as the *non-classical surround* of ganglion cells (Troy and Shou 02 [171]). As an additional particularity, many wide-field amacrine cells fire spikes, and can thus be involved in complex synchronization effects.

GABA and glycine. An alternative criterion to distinguish amacrine cells is according to the type of neurotransmitter they release. Amacrine cells use two main⁸ neurotransmitters: GABA and glycine. Interestingly, the resulting classification of amacrine cells has strong overlaps with the wide/narrow field classification: All wide-field cells are GABA-ergic, and most narrow-field cells are glycinergic, although some narrow-field GABA-ergic cells also exist.

This provides a good experimental means to assess the different roles of narrow- and wide- field amacrine cells, through the use of chemical antagonists: Picrotoxin blocks all GABA-ergic amacrine transmissions, while strychnine blocks all glycinergic amacrine transmissions (see, e.g., Caldwell *et al.* 78 [28] for a more detailed description of the effects of these antagonists).

Presumed roles of amacrine cells. Here are the different presumed roles of narrow-field and wide-field amacrine cells, as presented in the sequel:

- Temporal shaping (transient) of ganglion cells responses, especially Y cells (Section 3.2.2). Narrow-field amacrine cells likely play the strongest role in this shaping.
- Contribution to the spatial *surround* of the most ‘precise’ ganglion cells. Narrow-field amacrine cells are responsible for the strong and narrow inhibitory *surround* of LED cells (Section 3.2.6). Likely, similar inhibitions also occur in X cells (Section 3.2.1).
- Suspected ‘vertical’ transmission of information between the ON and OFF pathways, otherwise segregated. A ‘push-pull’ transmission of ‘negative’ signals to ON ganglion cells by OFF amacrine cells, and reciprocally, has been hypothesized (Figure 3.29), probably relying on narrow-field amacrine cells.
- Inhibition related to global movements of the background is likely provided by wide-field spiking amacrine cells to ‘object motion sensitive’ ganglion cells, such as ON Y cells (Section 3.2.2).

⁸Rarer neurotransmitters (acetylcholine in DS cells) and neuromodulators (dopamine) are also released by some amacrine cells.

- Stimulus-dependent spike synchronies (Section 4.3) very likely rely on wide-field amacrine cells.

Inhibition as the dominant shaping factor of the IPL. To conclude on the general importance of amacrine cell inhibition, we review this intriguing observation (Brivanlou *et al.* 98 [23], salamander retina): When *all* synaptic transmission (excitatory and inhibitory) was blocked in the IPL (so that ganglion cells were, so to speak, ‘left on their own’), the net number of emitted spikes *augmented*. This observation can be explained by intrinsic depolarizing conductances in ganglion cells’ membranes.

Even if these results are possibly linked to the given experimental setup, they suggest that ganglion cells undergo a constant and strong inhibition from amacrine cells during normal visual stimulation (see also Figure 3.29). So likely, amacrine inhibition has a fundamental role in shaping ganglion cell responses, comparable or even superior to direct excitation from bipolar cells.

3.2 Physiology of the different visual pathways

In this central section, we present the physiological properties of the various types of ganglion cells forming the retinal output. We try as much as possible to link these properties to specific functional roles of the associated visual pathway in further cerebral processing. However, for most types of cells, the precise functional roles are still hypothetical, based on inferences from their physiological type of response.

We start by presenting the classical ‘brisk’ retinal cells, respectively ‘brisk sustained’ (X) (Section 3.2.1) and ‘brisk transient’ (Y) (Section 3.2.2) cells.

The two following sections review how the initial diversity of photoreceptors (various color cones and rods) is relayed at the retinal output. Cells involved in the coding of color are specifically mentioned in Section 3.2.3, and the integration of the rod signal to the retinal output, by various pathways, is mentioned in Section 3.2.4.

Section 3.2.5 is dedicated to a short presentation of direction-selective (DS) cells in the retina, whose working principles and function in visual processing remain somewhat mysterious after 40 years of intensive studies.

The remaining sections are devoted to the description of ‘sluggish’ ganglion cells, which have been subject to much less investigation until recent years. These ganglion cells were once termed ‘rare’ because they were less numerous than β cell, and less remarkable than α cells. It now appears likely that some of them are more numerous than α cells, and have important but badly established roles in visual processing. Without entering too much details, we specifically present one such type of sluggish cell, the local edge detector (LED), in Section 3.2.6. Section 3.2.7 then evokes other observed types of sluggish cells, and hints for their roles in visual processing.

Throughout this presentation, we try to provide references to relevant bibliography which can serve as an ‘entrance door’ to these different types of cells. Before we move on, let us review here some especially important references of our work: A general review of most types of retinal cells can be found in Troy and Shou 02 [171], and compared to the very interesting and visual work of Roska *et al.* 06 [145] presenting response patterns for most types of rabbit ganglion cells.

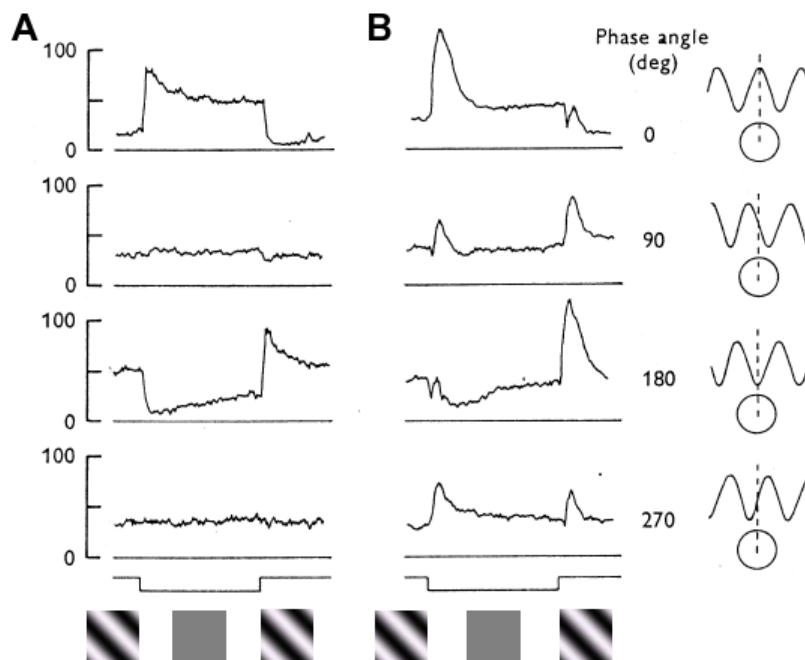


Figure 3.12: *Response of X and Y cells to a flashed grating.* Trial-averaged firing rates of a cat OFF-center X cell (A) and OFF-center Y cell (B), in response to the disappearance and reappearance of a static grating with different spatial offsets (right). If the cell proceeds to linear summation of its input, there is an offset of the grating for which the cell has a null response, when the positive and negative parts of its signal counterbalance each other. The 'null position' exists in X cells but not in Y cells, revealing a nonlinearity. Also, Y cells are more transient than X cells. Total time 2s. From Enroth-Cugell and Robson 66 [59]

A good introduction to DS cells is provided by the recent works of Fried *et al.* 02 [66], and the review of Taylor and Vaney 03 [167].

Finally, most types of sluggish cells are very well presented in the classic work of Levick 67 [99]. Caldwell *et al.* 78 [28] provide interesting insights on the roles of amacrine cells in shaping the complex and slow responses of these cells. More recently, the dynamics and sensitivity of sluggish cells have been studied by Xu *et al.* 05 [183]. Hendry and Reid 00 [74] have reviewed the projections of sluggish cells to the koniocellular layers of the LGN, implying possible perceptual roles - yet unknown.

3.2.1 Brisk sustained (X) cells

These cells, originally termed 'X cells' by Enroth-Cugell and Robson 66 [59] in the cat retina, are the 'archetypal' ganglion cells. Their mode of response, illustrated for a static grating in Figure 3.12 A, correspond to what could be termed the 'generalist' vision of retinal processing:

- They have fast and strong ('brisk') responses to changes in contrast of the input image.
- Their response to a change in contrast is rather sustained, consisting of a

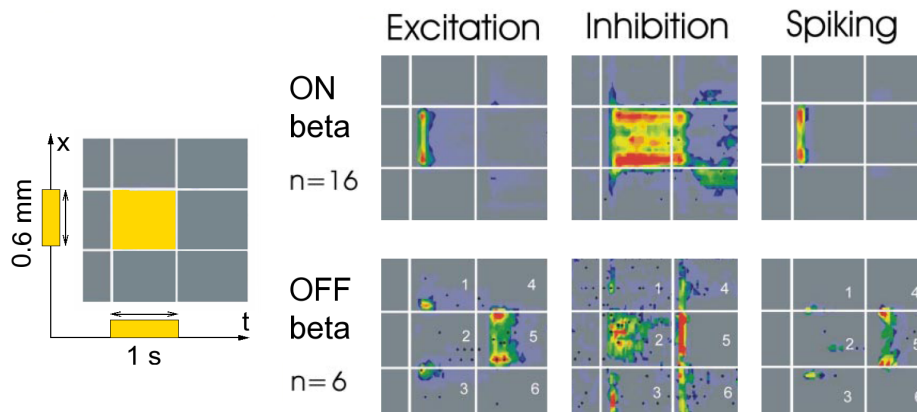


Figure 3.13: *Rabbit β (X) cells respond to a static square.* *Left:* Stimulus is the apparition of a static square of light for one second, here represented along time and one spatial dimension. *Right:* Reconstructions of the response of ON and OFF rabbit β (X) cells to the stimulus, with the same space-time representation. Excitatory and inhibitory input conductances to the cells are represented, and the resulting spiking activity for the cells. Both ON and OFF β cells have rather transient responses (although they are known as *sustained* cells), and respond preferentially to the square's edges, as predicted from a DOG model. Each reconstruction is obtained from a single cell in response to different offsets of the square stimulus. Then, reconstructions are averaged over the indicated number n of cells of the same type. From Roska *et al.* 06 [145].

strong initial transient that slowly declines over several hundreds of milliseconds.

- Their response is fairly linear with the spatial profile of the input image, and their linear receptive field is well modeled by a DOG, reflecting a strong center-surround organization. This is illustrated by the 'null position' test of Figure 3.12 A, or by responses to a drifting grating, as in Figure 2.1 which displays the response of a primate 'midget' cell.
- They have small receptive fields, resulting in a sensitivity to image details at fine scales (sensitivity to high spatial frequencies).
- They exist in ON and OFF versions, allowing the separate detection of light and dark contrasts.

Morphologically, brisk sustained cells correspond to the β type, which is observed in all mammalian retinas. The β type is characterized by its small dendritic tree, in good adequation with the small receptive fields observed physiologically. As expected from the tiling principle presented above, β cells are therefore numerous, providing a dense tiling of the retinal space (see Figure 3.11). They account for around 50 % of ganglion cells in the cat retina (Wässle 04 [180]).

Functionally, the brisk sustained (X) cells are well suited for providing the 'precise' vision pathway of the animal. Their small receptive fields and rather long-lasting responses make them a suitable source of information to transmit precise, static image contours. As an argument for this 'precise' role, β cells are particularly small and numerous in the *area centralis* of cats and in the *fovea* of primates

(‘midget’ cells). In the primate retina, midget cells are connected to the Parvocellular pathway of the LGN, and they constitute the primary source of information for the ‘Form’ pathway of visual processing.

In dichromat mammals (most mammals, with only two different types of cones), brisk sustained (X) cells are achromatic: They only see ‘in black and white’. Indeed, in dichromat mammals, a strong majority of cones are of the ‘L’-type (long wavelength), and thus provide a monochromatic input to β cells. See Section 3.2.3 about color pathways for more details.

It should be noted that β cells are not the only candidate for precise vision in mammalian retinas. The much less understood local edge detectors (LEDs, see Section 3.2.7) play a role very similar, with small dendritic trees and responses to fine contrast. In the rabbit, β cells seem to be *less* precise than LEDs. In cat and primate, β cells seem to be the most precise cells.

Finally, β cells are generally renowned as ‘simple’ retinal cells, with a simple center-surround architecture quite similar to that presumed in their presynaptic bipolar cells. Figure 3.13, in the rabbit retina, illustrates how even β cell can possibly receive a strong inhibition from amacrine cells, whose role is not clear yet (possibly, a ‘tightening’ of the cells’ spatial sensitivity, as mentioned in Sections 2.3 and 3.1.3). Also note that, in spite of their ‘brisk sustained’ denomination, the β cells represented in Figure 3.13 have a markedly transient response to that type of stimulus.

Midget cells in the primate retina

A few words should be said specifically about primates’ ‘midget’ cells. These cells have been termed the ‘P’ cells, because they project to the Parvocellular (‘small cells’) layers of primates’ LGN. In the common opinion, these cells correspond to a specialization of other mammals’ β cells, but driven to a spatial precision unequaled in other species. In the fovea, the midget pathway has even reached its upper-limit precision, where a single cone contacts a single ‘midget’ bipolar cell, which in turn contacts a single midget ganglion cell. As a result, the very numerous midget cells constitute more than 70-80 % of the roughly 1,000,000 ganglion cells in a primate retina (compared to the 200,000 ganglion cells of a cat retina)(Masland 01 [107], Wässle 04 [180]).

It is still controversial whether midget cells are an evolution of other mammals’ β cells, or a ‘new’ type of cells (Masland 01 [107], Wässle 04 [180]). Morphologically, midget cells are relatively close to the β archetype. However, midget cells display some physiological specificities. For example, unlike cat X cells, midget cells are very little subject to contrast gain control (as measured by Bernadete and Kaplan 99 [12], see Section 5.2). Also, unlike other mammals’ X cells, midget cells are sensitive to a special color opposition, as we explain in Section 3.2.3 (color pathways).

3.2.2 Brisk transient (Y) cells

These cells were originally introduced as ‘Y cells’ by Enroth-Cugell and Robson 66 [59] in the cat retina, to designate cells that did not fit into the ‘linear DOG framework’ of X cells. Indeed, Y cells display a typical nonlinearity, whose most famous expression is the absence of a ‘null position’ in their response to a static grating (see

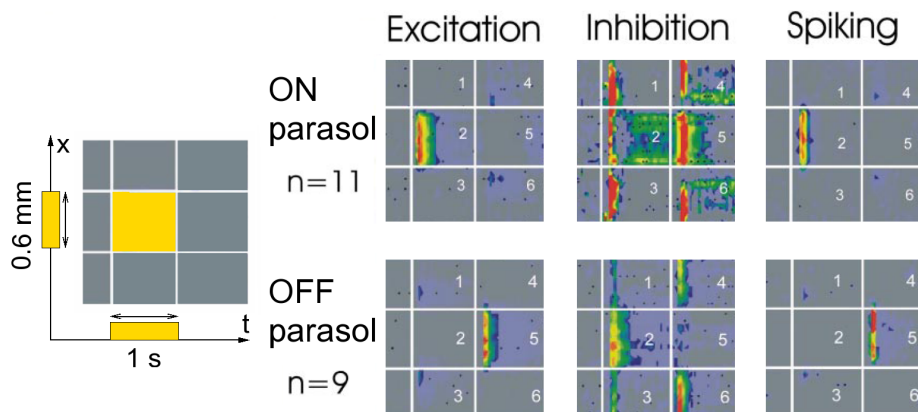


Figure 3.14: *Rabbit 'parasol' (Y) cells respond to a static square.* Same experimental protocol as in Figure 3.13. Both ON and OFF 'parasol' cells (a name usually reserved to primate retina) have transient responses, with no significant preference for edges, due to the relatively big size of their receptive fields, as compared to the size of the square stimulus. Notice the long-range inhibitory connections, likely mediated by wide-field amacrine cells, and the quantitatively stronger inhibitory patterns in ON cells (see text). From Roska *et al.* 06 [145].

Figure 3.12 B). More generally speaking, the physiological characteristics of Y cells are the following:

- They have fast and strong ('brisk') responses to changes in contrast of the input image, with a higher sensitivity to contrast than X cells.
- Their response to a change in contrast is strikingly transient: Y cells fire strongly to a change of illumination in their stimulus, but their response totally shuts down in a few hundreds of milliseconds if their input remains constant.
- Y cells generally have a lower spontaneous firing rate than X cells: Many Y cells are virtually silent in the absence of an image change in their receptive field (This is not the case, however, of the Y cell depicted in Figure 3.12 B).
- They have wide receptive fields, resulting in a bad spatial resolution (sensitivity to low spatial frequencies only).
- They exist in ON and OFF versions, allowing the separate detection of light and dark contrasts.
- Their response displays a strong spatial nonlinearity, as detailed in the sequel. However, Y cells are still 'concentric cells', in the sense that they possess an excitatory *center* and an inhibitory *surround*.

Morphologically, brisk transient cells correspond to the α type, observed in all mammalian retinas. Quite opposite to the β type, the α type has a big cell body and a wide dendritic tree, in adequation with its wide receptive field. Following the tiling principle, α cells are very sparse cells, but their dendritic trees still tile the whole visual space (see Figure 3.11). α cells are thought to account for only 3 - 8

% of ganglion cells in the retina (with some variation between species) (Masland 01 [107], Webvision [95]). However, these cells were rapidly remarked because of their brisk responses (early experimentalists localized cells thanks to the sound produced by their spike trains through an amplifier), and of their large cell bodies that were often found by the electrodes.

Brisk transient cells are movement detectors

Physiologically, the brisk transient (Y) cells are well suited to be the animal's primary 'movement detection' pathway. Indeed, they are very transient cells who only respond to sudden illumination changes – most often produced by movement, in the animal's everyday life. Furthermore, these cells have been measured to have the highest gain of response to contrast (see Croner and Kaplan 95 [37] in the primate): They can detect strongly small variations in intensity over their receptive fields. Likely, this high sensitivity results from their wide dendritic trees, implying that they have many more synaptic inputs than X cells (for example, Chichilnisky and Kalmar 03 [32] found a correlation in the primate retina between receptive field size and full-field sensitivity). Conversely, the wide receptive fields lead to a decrease in the spatial precision of the cells: This is why one often speaks of the *trade-off* between spatial accuracy and sensitivity to contrast.

In the primate retina, brisk transient cells are termed 'Parasol' cells because of their large dendritic trees, or 'M' cells because they connect to the 'Magnocellular' ('big cell') layers of the LGN. From there, they are the privileged input for the 'Motion' pathway of visual processing.

The Y cell spatial nonlinearity

Enroth-Cugell and Robson 66 [59] observed that Y cells could not be well modeled by a linear kernel. A classical expression of the nonlinearity is the absence of a 'null position' for the cell when a static grating is presented in front of it (Figure 3.12 B): If the cell responded linearly, there would be a spatial offset for the grating for which the positive and negative contributions to the cell's response cancel each other out, resulting in a null response of the cell (as is the case with X cells). Instead, at what should be its 'null position' (90 deg and 270 deg experiments in Figure 3.12 B), a Y cell still responds, both at onset and offset of the grating.

Equivalently, the Y cell nonlinearity results in a *frequency doubling* when the cell is presented with a drifting grating of small spatial frequency, whereas a linear filter always responds to a drifting grating with a frequency equal to the drift frequency (see e.g. the experiments of Hochstein and Shapley 76 [80]).

Hochstein and Shapley 76 [80] found that both experiments (no 'null position' for a static grating and frequency doubling for a drifting grating) could be accounted for by a same model, in which (part of) the Y cell's response is spatially pooled from a rectified set of smaller, linear receptive fields, which they termed 'subunits'. Their idea was later extended into a functional model by Enroth-Cugell and Freeman 87 [58], amongst others. The underlying idea of this model is depicted in Figure 3.15.

The natural biological candidates for the 'subunits' are bipolar cells: We have seen how bipolar cells already have the *center-surround* architecture, with small receptive fields, and are well modeled by linear filters. And indeed, it has been proved by Demb *et al.* 01 [48] that the spread of the dendritic tree of Y-type cells is large

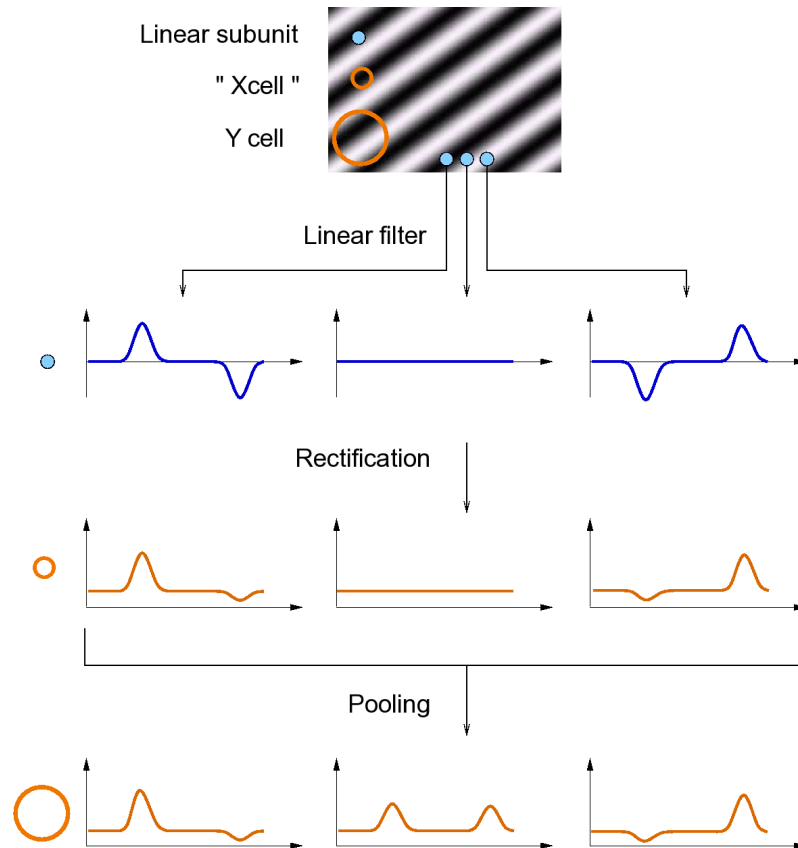


Figure 3.15: *A subunit model for Y cells' spatial nonlinearity.* In this model, 'subunits' with small receptive fields compute a linear filtering over the input sequence. The nonlinearity of Y cells in response to a static grating apparatus (Figure 3.12 B) can be explained if their response is obtained by spatially summing the rectified versions of subunit responses over a broad spatial neighborhood. By comparison, the responses of X cells are well modeled only by a rectification of the subunits' response, without the final pooling. However, note that Y cells do not pool their responses from X cells, but directly from input bipolar cells and amacrine cells, which are the likely biological correspondence of the 'subunits'. This model, schematically inspired from Enroth-Cugell and Freeman 87 [58], may be an oversimplified representation of real Y cells, which also have a purely linear component in their response (Hochstein and Shapley 76 [80]).

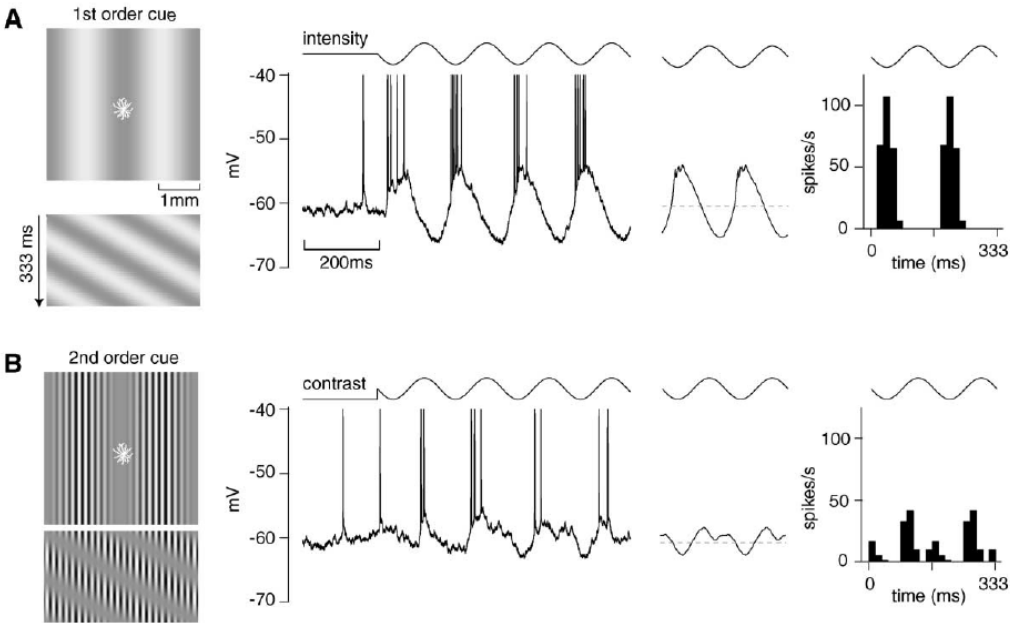


Figure 3.16: *Y* cells respond to first- and second- order motion cues. *A*: First order motion (drifting grating) in front of a *Y* cell (represented by its dendritic tree). *B*: Second-order motion, consisting of a contrast modulation (with same spatial scale as the previous first-order motion) drifting over a finer and static spatial structure. Thanks to their rectification and pooling, *Y* cells respond to both movements. There would be no response in *B* if *Y* cells had the same size of receptive fields, but responded linearly. From Demb *et al.* 01b [50]

enough to account for the functional pooling in the subunit model. However, many amacrine cells also interact with Y-type cells, and likely contribute to the nature of Hochstein and Shapley's functional 'subunits'.

Remark: Other explanations have been proposed to account for the nonlinearity of Y cells. For example, Hennig *et al.* [75] find that part of the nonlinearity might be due to the spatial integration by Y cells of a temporal nonlinearity due to phototransduction. Although they propose a different model, their explanation is also based on a wide spatial pooling at the level of Y cells. ■

Y cells detect second-order motion

Whatever its biological origin, it is not clear if the spatial nonlinearity of Y cells has a specific functional role or not. The argument has been given that the rectification-pooling architecture of Y cells provides them with an ability to detect second-order motion: Movements based on the contrast information rather than on the luminance information (see Demb *et al.* 01b [50] and their associated references). This is illustrated in Figure 3.16: Because they pool and rectify the signal from subunits with smaller receptive fields, Y cells can respond to 'contrast movements' created by the contrast modulation of a fine, underlying grating whose stripes remain static.

However, this presumed functionality raises some questions. First, it is not clear what kind of natural stimulus indeed creates this sort of second-order movement. Second, the detection of second-order contrast is made possible only by the finer spatial resolution of the subunits: The subsequent spatial pooling by Y cells is not the key feature of detection, it only leads to a loss in spatial precision!

We rather believe that the rectification-pooling scheme must be seen as an 'economical' feature: It allows a small number of output cells with wide receptive fields (remember that α cells account for only 5 % of retinal cells) to transmit a movement information without losing the fine *spatial sensitivity* of the subunits. The *precise location* of the stimuli are lost in the pooling operation, but this information is probably not mandatory to the 'movement' pathway initiated by Y cells.

The surround of Y cells

Although they display a singular nonlinearity, Y cells still possess a marked inhibitory surround (Enroth-Cugell and Robson 66 [59]). This raises questions, especially when one keeps in mind the rectification-pooling model: When the *surround* of a Y cell is stimulated by a small spot of light, it probably inhibits the presynaptic bipolar cells -the presumed subunits- for which the spot is in the *surround* (since bipolar cells already display a center-surround sensitivity, see Section 2). However, this inhibition signal should be greatly lost in the rectification from bipolar cells to the Y cells, and intuitively the observed *surround* of Y cells should be greatly reduced through the rectification-pooling operation. Likely, the observed *surround* of Y cells also reflects an interaction with different types of amacrine cells.

And indeed, recent results of Ölveczky *et al.* 03 [126] suggest the presence of a strong amacrine-related *surround* in some brisk transient cells, allowing them to detect object motion from global eye movements. Their results are illustrated in Figure 3.17. When the center of a rabbit brisk transient (Y) ON cell is stimulated

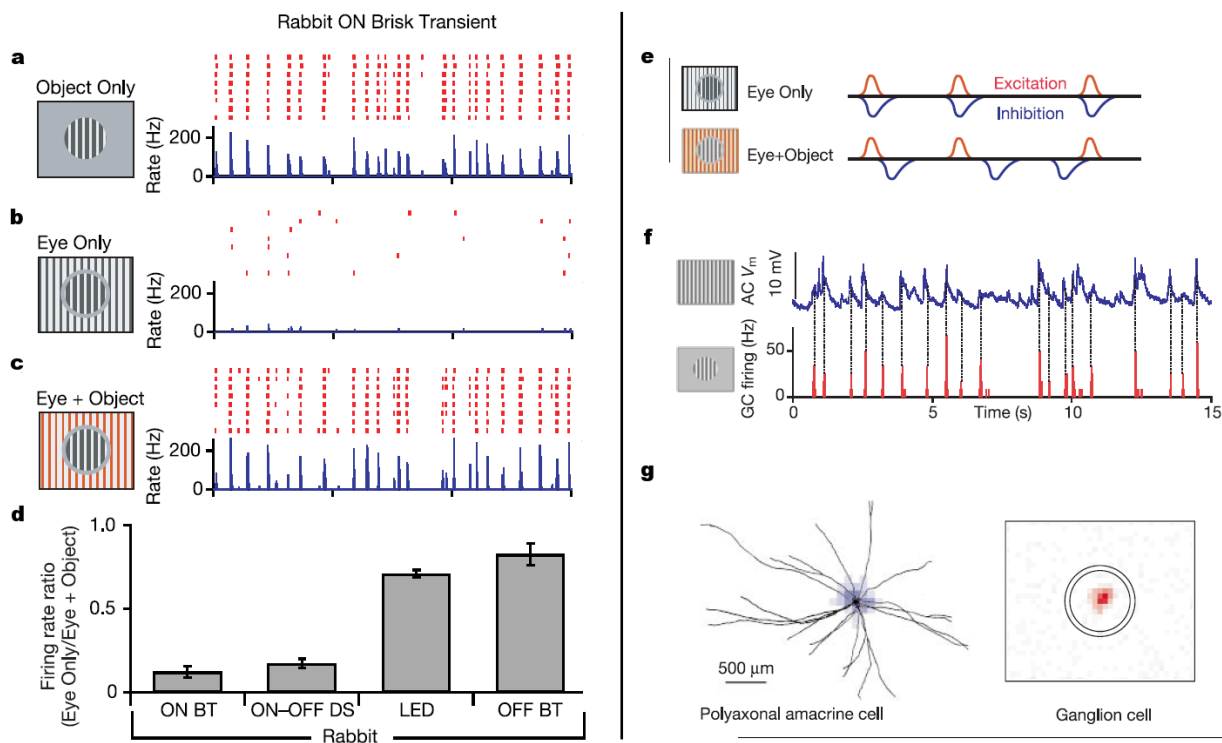


Figure 3.17: *Inhibition of movement detection by coherent background motion.* *a*: A small patch of grating moves in front of a rabbit ON α cell, with a trajectory typical of small fixation eye movements, eliciting a strong response. *b*: When the grating is made full-field, the response is abolished. *c*: If the background grating undergoes a different motion than the center's, the response is not suppressed. However, if the background undergoes a movement *exactly opposite* to the center's, the response remains suppressed (not shown). *d*: Strength of the effect in various rabbit cells. Note the asymmetry between ON and OFF α (BT) cells. *e, f, g*: Presumed explanation of the phenomenon, by synchronous inhibition of amacrine cells from the *surround*, when *center* and *surround* movements are synchronized. From Ölvécsy *et al.* 03 [126].

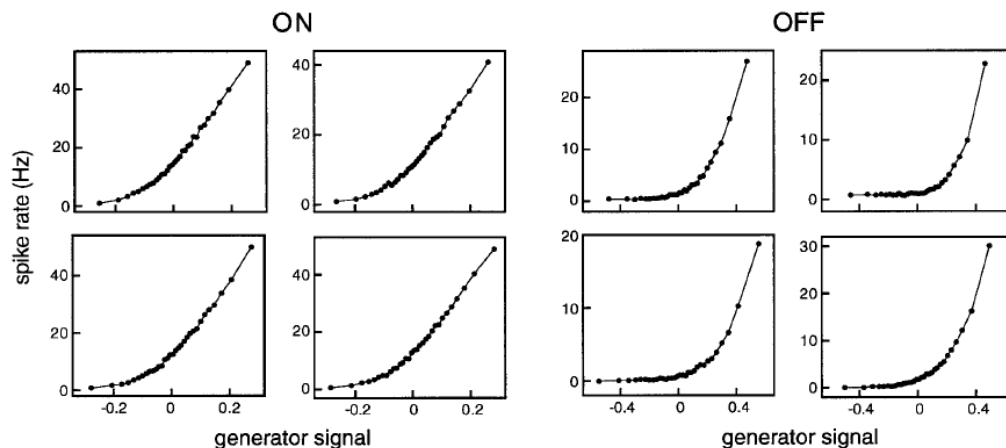


Figure 3.18: *Asymmetries between ON and OFF cells.* OFF cells are more rectifying than ON cells, as observed from an LN analysis of their receptive fields. From Chichilnisky-Kalmar 03 [32].

by random movements of a grating, it fires vigorously and reproducibly. However, when the stimulus becomes full-field, the response of the ganglion cell is totally suppressed. Furthermore, this suppression occurs only if the background's motion is synchronized with the central motion. The authors suggest that this mechanism is mediated by wide-field 'polyaxonal' amacrine cells outside the ganglion cell's receptive field (so, in the background), whose synchronous response serves to shut down the ganglion cells' response when movement is similar in its receptive field and in the background.

As a result, the brisk transient ON cell, coupled with polyaxonal amacrine cells, might implement the equivalent of a center-surround mechanism, but on a very broad spatial scale, and applied on an already transformed version of the image: The rectified, spatio-temporal band-pass image from bipolar cells. The resulting ganglion cells would detect (very coarsely) the edges of moving objects, but not global background motion, which is 'uniform' from the point of view of bipolar cells' rectified spatio-temporal band-pass signal.

Asymmetries between On and Off pathways

The selectivity to object motion was observed by Ölviczky *et al.* 03 [126] only in a subset of ganglion cells (see Figure 3.17 *d*).

Interestingly, as for 'Y-type' cells are concerned, On brisk transient (Y) cells were affected, but not Off brisk transient (Y) cells, suggesting that On and Off 'Y' cells might play a different perceptual role. Previous studies had already found evidence for a strong asymmetry between On and Off 'Y' type cells: In the primate retina, Chichilnisky and Kalmar 03 [32] find that On parasol cells are faster than Off cells, have markedly larger receptive fields (20 % on average), display more contrast gain control (see Section 5.2) and have a more linear input-output response, as measured through LN analysis (see Figure 3.18).

This asymmetry may seem surprising at first, but consider the following argument: If On and Off 'Y' cells both functioned along a simple 'rectification-pooling'

scheme, then their signals would be very redundant. Indeed, most image edges are dark on one side and bright on the other, so their motion should activate both On and Off ‘Y’ pathways. But after a relatively large spatial pooling, the On and Off ‘Y’ signals would then end up very similar, raising questions about the usefulness of having both pathways. Instead, if the On pathway segregates background from motion, both On and Off ‘Y’ cells gain different functional roles.

3.2.3 Color-coding ganglion cells

Color processing in the retina is a wide problem, subject to complex phenomena – especially of adaptation – that we do not discuss in detail here. We only mention the existence of two very distinct pathways for color information in mammalian retinas: The first pathway is that of ‘blue/yellow’ oppositions, which is shared by all mammals and relies on a specific circuit that involves sparse ‘color cones’ (‘S’, or blue) whose information is relayed by the similarly sparse ‘blue On’ bipolar and ganglion cells. The second pathway, specific to some trichromat primates including humans, is that of ‘red/green’ oppositions which are transmitted by midget cells. This presentation focuses on the primate retina, based on the reviews of Martin 98 [105] and Dacey 99 [40].

Blue-yellow color-coded cells

Most mammals are dichromats, having only two types of cones: The numerically dominant ‘L’ cone, sensitive to low spectral frequencies, and a much sparser ‘S’, or ‘blue’, cone sensitive to higher spectral frequencies. Then, similarly sparse bipolar and ganglion cells calculate color opponents based on the ‘S’ signal. These cells only exist with an ‘On’ polarity and account for the totality of color perception in most mammals, resulting in a ‘blue-yellow’ dichromatic vision.

In the primate retina, the ‘blue-yellow’ opponent cell is called the ‘small bistratified’ cell (since its discovery by Dacey and Lee 94 [41])⁹. Thanks to its bistratified dendritic tree, it opposes a ‘blue-on’ signal, from ‘blue-on’ bipolar cells, to an Off signal from a diffuse non-chromatic bipolar cell (see Figure 3.19 *B*, in the case of a primate retina). As expected from its active role in conscious vision, this cell projects to the LGN (see Section 1.2), mainly to one of the koniocellular layers (Hendry and Reid 00 [74]), and also probably to the parvocellular layers (Rodieck and Watanabe 93 [144]).

In cat and rabbit, the color-coded cell has often been observed in early studies, but only in small samples because of its sparseness, and not all records agree on its properties. The main opinion seems to be that this cell is rather ‘brisk’ (Cleland and Levick 74b [34]), possibly with the spatial and temporal characteristics of X cells (Caldwell and Daw 78 [27] in the rabbit). We have not come across the specific structure of this cell in our documentation, but it must likely be bistratified, like its equivalent in the primate retina.

Red-Green oppositions in primate midget cells

In parallel to the increased precision of their midget cells, some primates (humans and Old World primates) have developed a trichromatic vision, thanks to the divi-

⁹A ‘large bistratified’ cell, with similar ‘blue on’ opposition, has recently been discovered, see Figure 3.10.

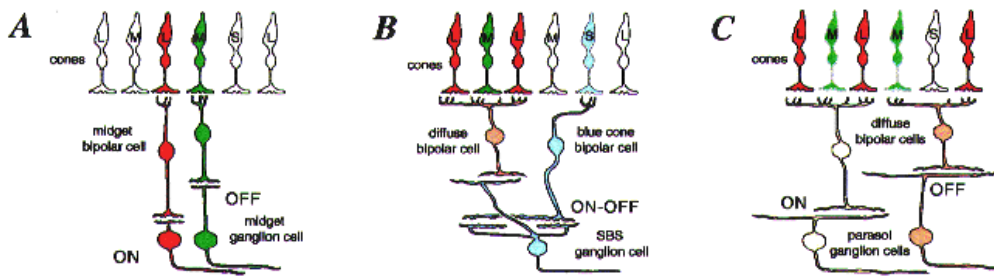


Figure 3.19: *Color pathways in the primate retina.* A: Midget cells connect randomly a ‘L’ or a ‘M’ cone, and thus fall into two distinct categories of color sensitivity. B: The bistratified blue-yellow opponent cell, typical of all mammalian retinas. C: Parasol ganglion cells have no specific color sensitivity. From Martin 98 [105].

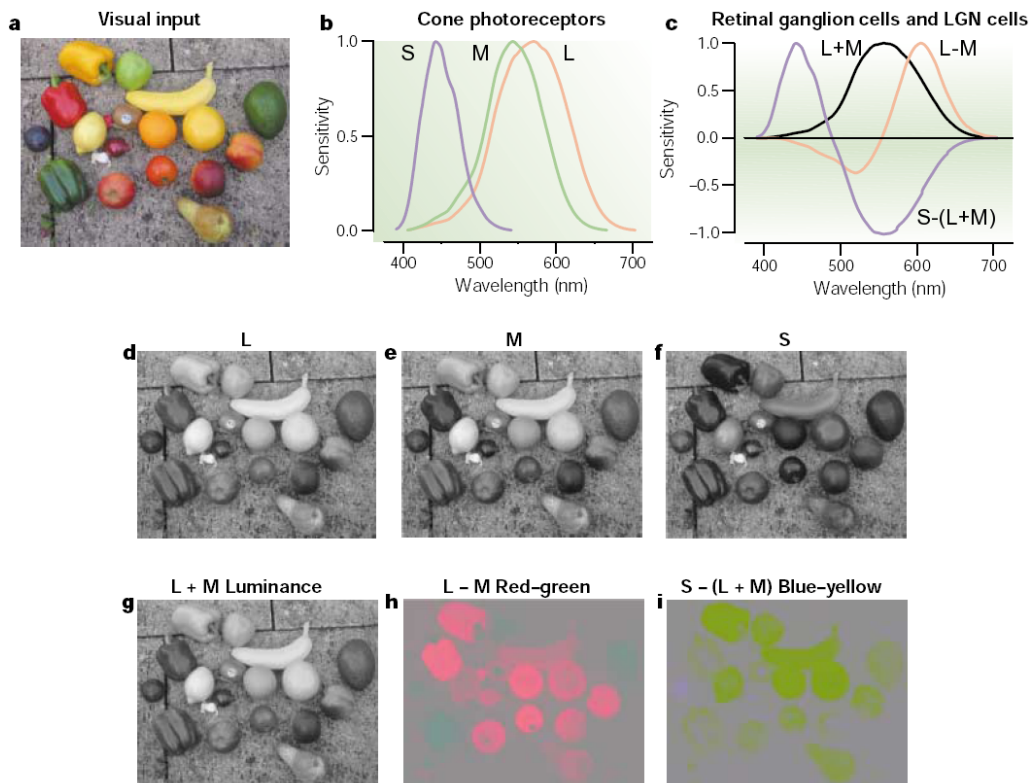


Figure 3.20: *Perceptual luminance and color opposition signals of the primate retina* a: Original color image. b: Spectral sensitivities of the three types of cone. c: Spectral sensitivities of the signals L+M (luminance), L-M (red-green signal) and S-(L+M) (blue-yellow signal). d,e,f: Response components of the three cone sensitivities S,M and L. g: Resulting L+M luminance image. h,i: Resulting color signals, if the luminance and other color channel are set at zero. Notice how we fail to find spatial precision in these iso-luminant color images. From Gegenfurtner 03 [70].

sion of the predominant type of cone into two distinct types, the ‘L’ (low wavelength, or ‘red’) and the ‘M’ (middle wavelength, or ‘green’) type. The resulting scheme of cones in trichromats consists of two dominant types of cones (‘red’ and ‘green’) randomly distributed, and a third type of cone (‘S’ or ‘blue’, the original color cone of dichromat mammals) distributed along a sparser, but more regular, sampling. This is illustrated in Figure 1.11 of Chapter 1.

Midget cells are the relays of this new color information specific to trichromats. The most usual interpretation of their color sensitivity is the ‘random wiring’ hypothesis (Martin 98 [105]): Because midget cells are directly connected to a single cone (at least in the fovea), they gain *de facto* a color sensitivity, with a *center* signal respectively sensitive to ‘L’ or ‘M’ wavelength according to the cone they connect (Figure 3.19 A). By opposition, the *surround* of midget cells arises in good part of horizontal cells, which contact ‘L’ and ‘M’ (and sometimes ‘S’) cones indifferently. As a result, half of the midget cells code for the color opposition R-(R+M) while the others code for the opposition M-(R+M). In this ‘random wiring’ hypothesis, trichromacy probably appeared in the evolution *after* the spatial specialization of midget cells into a one-to-one connection from cones. Yet, this wiring hypothesis raises issues concerning our color perception in the peripheral retina, where midget cells starts to contact many cones (Wässle 04 [180]).

Interestingly, this color opposition remains a *secondary* source of information for midget cells: The wavelength sensitivities of ‘L’ and ‘M’ cones remain very close one from another, so that a strong luminosity contrast will always be favored by midget cells, whatever the colors in opposition. This double carrying of information (edges and color) through a single signal is called *multiplexing*. It is intriguing, how the brain manages to exploit both sources of information simultaneously. Since information from a single midget cell is ambiguous, and dominated by the edge information, it is likely that red-green oppositions carried by midget cells are integrated over a wider spatial range, for the brain to grasp the ‘color-related bias’ in the output of a population of neighboring cells (see e.g. the color demosaicing model of Alleysson *et al.* 05 [2]).

With this necessary spatial integration to ‘demultiplex’ the midget signal, the red-green opposition pathway might end up with a spatial sensitivity comparable to the blue-yellow opposition mediated by the sparse blue-yellow color-coded cells (This last supposition is made without precise references).

Color pathways and perception

To conclude, both our color vision pathways (sparse ‘blue-on’ cells and multiplexed ‘red-green’ midget cells) have a spatial acuity much lower than the luminosity image carried by midget cells (see the respective dendritic tree sizes in Figure 3.10). So, the fact that our color percepts are always linked to observed objects, even at very fine spatial resolution, probably results from an efficient multi-modal sensory integration in our brain, and remains an exciting and intriguing phenomenon.

Figure 3.20 presents the respective spectral sensitivities of our three types of cones, and how they can be decomposed in a luminance image, and two iso-luminant red/green and blue/yellow images. Very little shape information subsists in the iso-luminant color images (especially in the blue-yellow image¹⁰), reflecting the poor

¹⁰and yet more especially if you have printed this thesis in black and white!

spatial resolution of our color pathways. We refer the interested reader to the review of Gegenfurtner 03 [70] on color pathways in the cortex.

3.2.4 The rod pathway

Rods are by far the most numerous light receptors in mammalian retinas, especially in nocturnal species (see the density diagram of Figure 1.12 in Chapter 1). A detailed study of their light response is not in the scope of this work. We will only remark the following characteristics of phototransduction in rods:

- An increased sensitivity allowing very efficient detection of light in dark-adapted (scotopic) illumination conditions: Reliable detection of flashes of ~ 20 incident photons over the whole retina, and better-than-chance response to single photons [154, 152].
- In scotopic illumination, a monophasic and long-lasting (typically between 0.5 and 1 sec, Baylor *et al.* 84 [9]) impulse response to dim flashes of light.
- In scotopic illumination, a saturating and nonlinearly delayed response to stronger pulses of light (Baylor *et al.* 84 [9]).
- A general and progressive saturation at higher illumination levels, starting at around 100 scotopic trolands (typically, the luminance of a very cloudy sky¹¹).

There is phylogenetic evidence that rods have appeared later than cones in the course of evolution. In coherence with this fact, there is no specific ganglion cell associated to rods. Instead, the rod signal is transferred back to the traditional, cone-dominated pathways, by two distinct mechanisms represented in Figure 3.21. Interestingly, these two pathways have different spatio-temporal characteristics, that allow to use the rod information in two different functional ways.

1. A ‘slow, sensitive’ pathway of transmission transits through the specific ‘rod bipolar’ cells (see Figure 3.6), which in turn synapse onto dedicated amacrine cells, termed ‘AII’. From AII amacrine cells, the signal is transferred back onto both ON and OFF cone pathways, respectively thanks to gap junctions with On bipolar cells (‘ON1’ pathway of Figure 3.21) and inhibitory synapses to Off bipolar cells (‘OFF1’ pathway of Figure 3.21).

This pathway, rod-specific up to AII cells, displays a very strong convergence ratio from rods to ganglion cells (see Figure 3.22). Furthermore, rod bipolar cells integrate the rod signal with a high gain and slow response kinetics (Dacheux and Raviola 86 [44]). In the end, this results in a pathway that displays: (i) a high sensitivity and rapid saturation as background illumination increases, (ii) slow response kinetics, and (iii) poor spatial resolution.

2. By opposition, a ‘fast, insensitive’ pathway transits directly from rods to cones, through gap junctions between the receptors’ inner segments (‘ON2’ and ‘OFF2’ pathways of Figure 3.21). And indeed, a delayed ‘rod contribution’ of small amplitude can be observed in the responses of individual cones (Schneeweis and Schnapf 95 [152]). Gap junction coupling is the only source of spatial convergence for this rod pathway. Afterward, this pathway benefits of the specific

¹¹See e.g. Lance Hahn’s retina page at http://retina.anatomy.upenn.edu/~lance/modelmath/units_photometric.html.

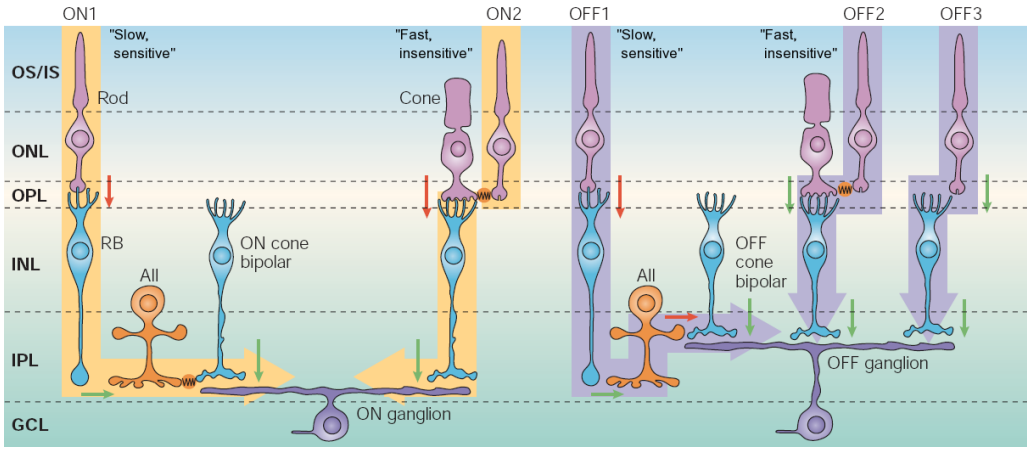


Figure 3.21: *Rod pathways in the mammalian retina.* The rod signal is grafted on the cone-dominated retinal output by two main pathways with sensibly different spatio-temporal characteristics (see text). A third ‘OFF3’ pathway of transmission, with ‘fast, insensitive’ characteristics, has also been observed in rodent retinas (see Sharpe and Stockman 99 [157]). From Wässle 04 [180], adapted from Demb and Pugh 02 [49].

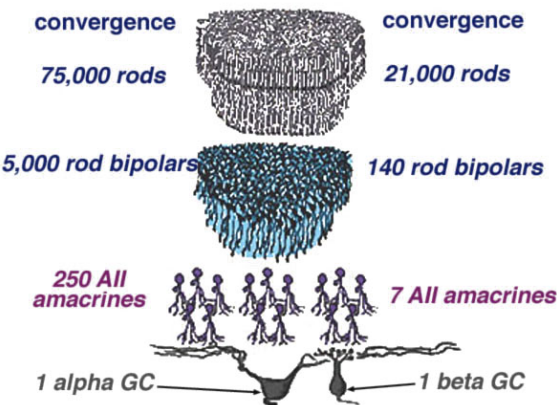


Figure 3.22: *Convergence of the ‘slow sensitive’ rod pathway.* The strongly convergent scheme of rods onto ganglion cells confers the ‘slow sensitive’ pathway with a strong sensitivity to light (better-than-chance detection of individual photons in dark-adapted conditions), at the expense of a loss in spatial and temporal precision. From Webvision [95].

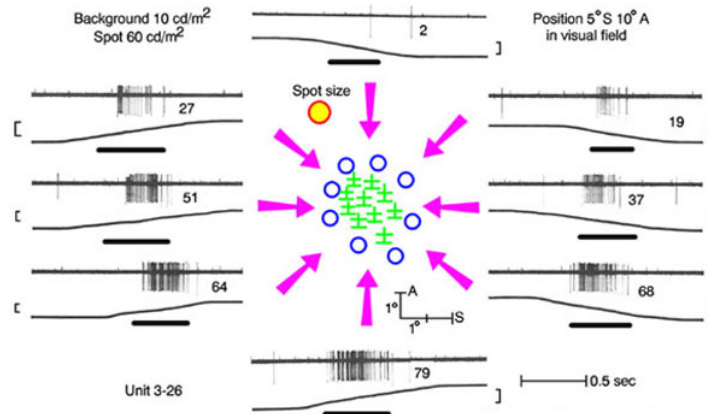


Figure 3.23: *On-Off direction selective (DS) cells in the rabbit retina.* DS cells respond to the movements of contrasted targets in their preferred direction (here, upwards), but not in their ‘null’ direction (here, downwards). From Barlow *et al.* 64 [7].

properties of cone bipolar cells, including precise spatial treatment and high-pass temporal transmissions.

In the end, this pathway is thus characterized by: (i) a poor sensitivity to light increments, that prevents from saturation until strong photopic illuminations, (ii) fast response kinetics, and (iii) relatively good spatial resolution.

As a result, the two dominant rod pathways are well suited for an optimal exploitation of the rod signal over a broad range of intensities: The ‘slow, sensitive’ pathway allows to cover dark scotopic ranges, while the ‘fast, insensitive’ pathway covers a higher illumination range (up to dark daylight), likely providing an important component of our ‘precise’ vision in mesoscopic conditions (nightfall, moonlight, etc.).

An interesting evidence for the two rod pathways can be found in Sharpe and Stockman 99 [157], through psychophysical experiments on human subjects: Destructive temporal interferences between the ‘fast’ and the delayed ‘slow’ rod pathways result in a ‘blind’ zone in the perception of light flickers at 15 Hz, at contrasts well above the absolute psychophysical detection threshold.

3.2.5 Direction-Selective (DS) cells

On and On-Off DS cells

Direction-Selective cells have been observed more than forty years ago in the rabbit retina by Barlow and colleagues [7, 8], but their specific circuitry is not fully understood yet. Two main types of DS cells have been found, the On DS cell and the On-Off DS cell. The On DS cell is a monostратified cell (with dendrites only in sublamina b of the IPL) that projects to the accessory motor system, where it drives optokinetic eye movements, that allow the eyes to compensate for head movements during fixation (Oyster *et al.* 72 [128], Masland 01b [108]).

The second type, the On-Off bistratified cell (with two dendritic trees, in both sublaminae a and b of the IPL), has been subject to much more studies concerning

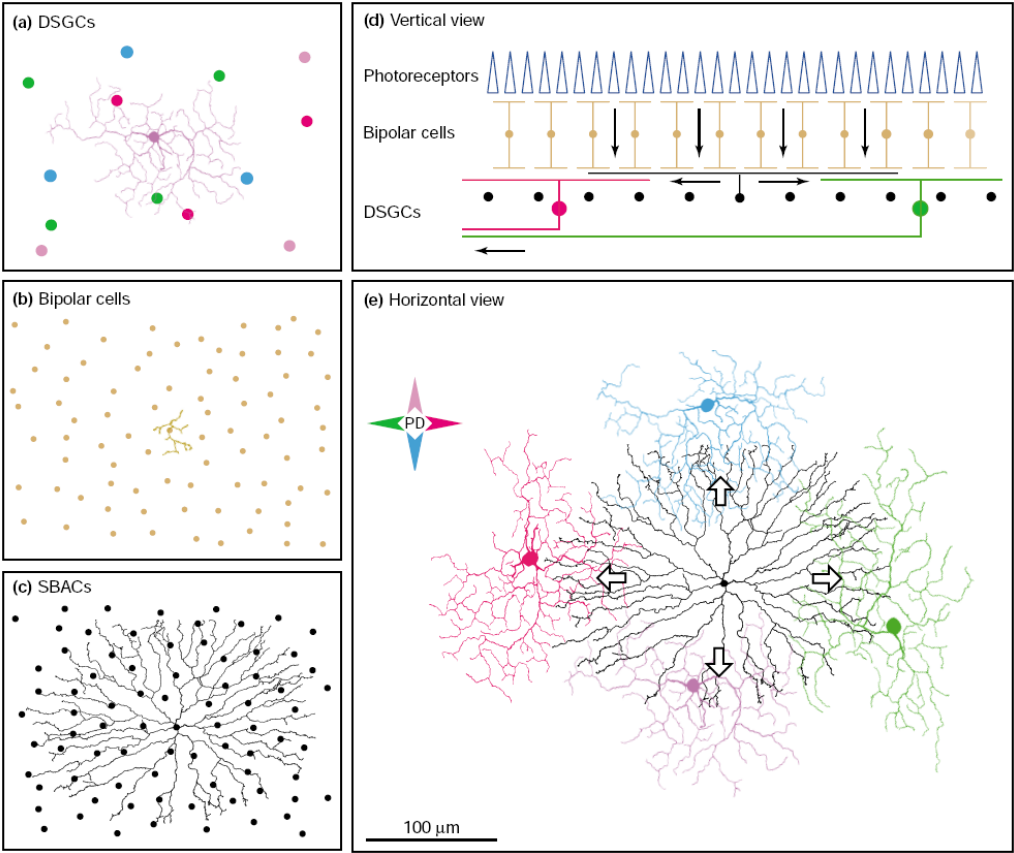


Figure 3.24: *On-Off direction selective (DS) cells, and their interaction with starburst amacrine cells.* *a:* Tiling of the visual space by On-Off DS cells. Four parallel populations of cells respond preferentially to each of the four cardinal directions (color code as in *e*). *b,c:* Tiling of the visual space respectively by bipolar cells and starburst amacrine cells. *d:* Vertical schema of the interaction. Notice the centrifugal sensitivity of starburst amacrine cells. *e:* A single starburst amacrine cell has dendrites which are largely independent, and each respond preferentially to centripetal motion from the amacrine cell's center (thick arrows), for a reason yet to be discovered. Asymmetric connections then transmit this directional sensitivity to DS cells (see text). From Taylor and Vaney 03 [167].

its architecture and the arousal of movement selectivity. It is a very important type of cell, which constitutes around 10 % [167] of ganglion cells in the rabbit retina (other studies have met it even more often [27, 55]). An example of tiling by On-Off DS cells is provided in Figure 3.24 *a*.

Physiology and function of the On-Off DS cell

When a small contrasting shape (light or dark) passes in front of them, On-Off DS cells display an opposition between a ‘preferred’ direction of movement, and the opposite (180 deg) ‘null’ direction, for which the cells remain totally silent (Figure 3.23). The typical range of speeds thus detectable is 1 to 10 deg s⁻¹ [99, 128]. In the rabbit, four parallel tilings by DS cells have been observed, corresponding to the main four cardinal directions for motion sensitivity [167]: See Figure 3.24 *e*.

To our knowledge, it is not known with certainty to which regions of the brain On-Off DS cells project, and what their main function in visual processing is. However, by comparing the respective sensitivity curves to motion speed of On-Off DS cells and of the optokinetic reflex, Oyster *et al.* 72 [128] have suggested that On-Off DS cells may have the same functional role as On DS cells: Driving optokinetic eye movements. In their optic, On DS cells could provide the control signal for slow movements (0.01 to 5 deg s⁻¹), and On-Off cells for faster movements (1 to 10 deg s⁻¹), thus requiring a denser tiling of the retina.

By opposition, direction-selective cells have never been observed in the LGN to our knowledge. So, it is likely that DS cells do not constitute a source of input for cortical calculations, but rather directly for motor control areas.

Starburst amacrine cells and their role in direction selectivity

It is now understood that the directional selectivity of On-Off DS cells strongly relies on the properties of particular glycinergic amacrine cells: The *starburst* amacrine cells, which densely tile the visual space (equivalently to bipolar cells, see Figure 3.24 *b-c*). As a proof of the important role of starburst amacrine cells, direction selectivity ceases when they are blocked by picrotoxin (Caldwell *et al.* 78 [28]).

Starburst amacrine cells have very dense and circular dendritic trees. Very intriguingly, their dendrites at different locations behave independently one from another, and are strongly excited by *centrifugal* movement, from center of the amacrine cell to its periphery (Euler *et al.* 02 [62], and for review Taylor and Vaney 03 [167]). It is not known what mechanism –electrotonic or resulting from a network interaction– creates this centrifugal sensitivity of starburst cells’ dendrites.

In turn, On-Off DS cells receive inhibition from starburst amacrine cells with a strong directional bias: Most of the ‘starburst to DS’ inhibitory synapses are located only on the ‘null’ side of the DS cell (Fried, Münch and Werblin 02 [66], and for review Taylor and Vaney 03 [167]). As a result, movement in the DS cell’s null direction will first reach the presynaptic starburst, that will inhibit the DS cell before a response can be elicited by the stimulus. By opposition, movement in the DS cell’s preferred direction first excites the cell and produces its firing, while the starburst amacrine cell *does not* provide inhibition since the input movement is centripetal for the starburst’s dendrites at contact with the DS cell. More controversially, this mechanism is also suspected to be enhanced by an excitatory acetylcholine release

from the starburst cells on the *preferred* side of the DS cell [167]. Indeed, it has been proved that the excitatory input to the cell is also direction selective [66].

Figure 3.24 *e* represents how a single starburst amacrine cell can make inhibitory connections and provide directional sensitivity simultaneously to four DS cells with different preferred directions, according to the mechanism explained above.

DS cells are an intriguing feature of the retina that still puzzles neuroscientists after forty years of studies. Their synaptic inputs are not fully understood yet (for example, they also display an inhibitory *surround*, Troy and Shou 02 [171]). Knowing to which regions of the brain they project is an important functional issue.

3.2.6 Local edge detectors (LEDs)

We now come to the best-described ‘sluggish’ retinal cell, the local edge detector (LED). LEDs were first observed by Levick in the rabbit retina, and his work (Levick 67 [99]) is likely the first reference to be checked. Later studies found LEDs in the cat retina as well (Cleland and Levick 74b [34]). These cells are now thought to constitute a functionally very important pathway: They account for 15 % of ganglion cells in the rabbit retina, which makes them one of the most present types (Van Wyk *et al.* 06 [177]), and their receptive fields are of a size comparable to the brisk transient (X) cells: Around 1 or 2 degrees of visual angle in cat [34] and rabbit [99] (or equivalently, 170 to 350 μm of retinal surface, in the rabbit).

Sluggish, On-Off detector of localized contrast

Levick 67 [99] termed the cells ‘local edge detectors’ because they respond only to contrasts of small objects, whether brighter (On behavior) or darker (Off behavior) than the surround. The ‘On-Off’ behavior, typical to these cells, is likely due to their thick dendritic tree which spans both the On and Off laminae of the IPL (see Figure 3.9). However, when a reverse correlation analysis is performed, LEDs appear as Off-sensitive cells (Van Wyk *et al.* 06 [177]), revealing an asymmetry in the strengths of On and Off inputs.

Temporally, LEDs could be termed ‘sluggish sustained’ cells (but do not confuse with the concentric sluggish sustained type, Section 3.2.7). Quite incredibly, their response develops over several seconds after a contrasting stimulus: In Figures 3.25 A or 3.26, even the offset of a pattern elicits a response over several seconds, even though the light stimulus has just ‘switched back’ to a uniform screen! The lengthy responses of LEDs is reflected in their excitatory inputs (most likely from bipolar cells), and yet enhanced by their high membranar resistance (M. Van Wyk, personal communication).

Strong inhibitory surround

A specificity of LEDs is their reduced responses whenever the immediate surround of the cell is also stimulated. This translates in the rapid apparition of inhibition in the LED response (On and Off) to spots of light with increasing diameter (Levick 67 [99], Cleland and Levick 74b [34], Van Wyk *et al.* 06 [177]), as depicted in Figure 3.25.

The underlying mechanism for this strong inhibitory surround is not well understood yet, but it clearly involves the specific contribution of glycinergic (small-field)

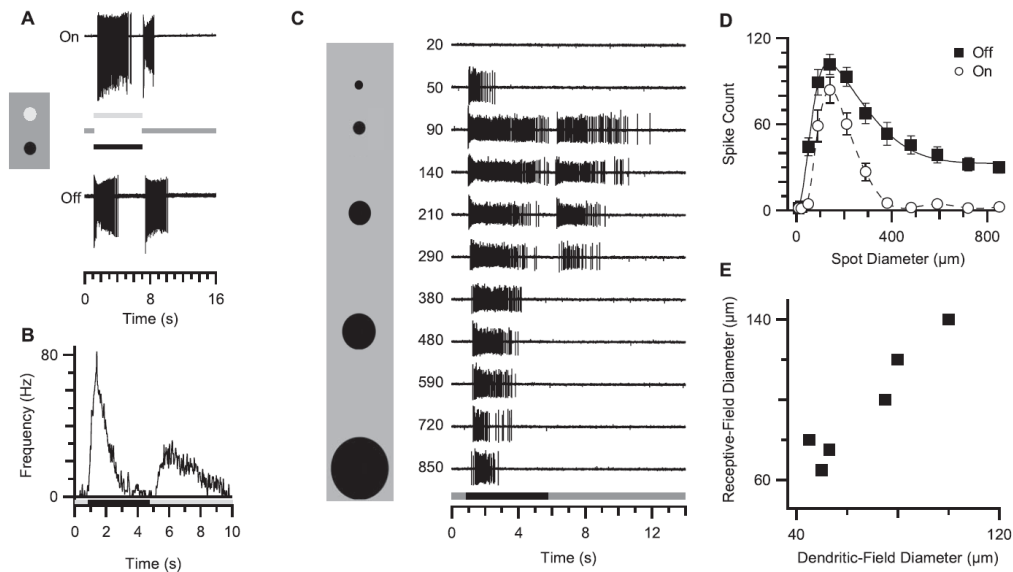


Figure 3.25: *Local edge detector (LED) in the rabbit retina.* A: LEDs display On and Off responses, both at onset and offset of small contrasting spots (light or dark). B: Corresponding spike-triggered average, for the dark spot stimulus. C: Both the On and Off components of the cells' response rapidly fail to detect stimuli of increasing sizes: A strong inhibitory surround provides LEDs with a strong spatial band-pass property. D: Tuning of the 'On' and 'Off' components of the LED's response depicted in C. E: Correlation between the cells' dendritic tree and receptive fields sizes. From Van Wyk *et al.* 06 [177].

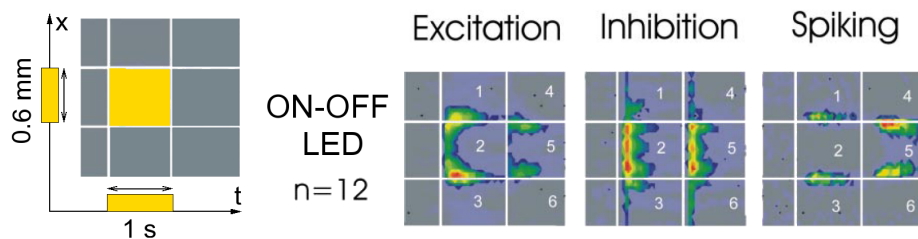


Figure 3.26: *Rabbit LEDs respond to a static square.* Same experimental protocol as in Figure 3.13. A broadly band-pass and sluggish excitatory input is shaped by a strong amacrine inhibition, resulting in an increased sensitivity to image edges at the spiking output of the cell. From Roska *et al.* 06 [145].

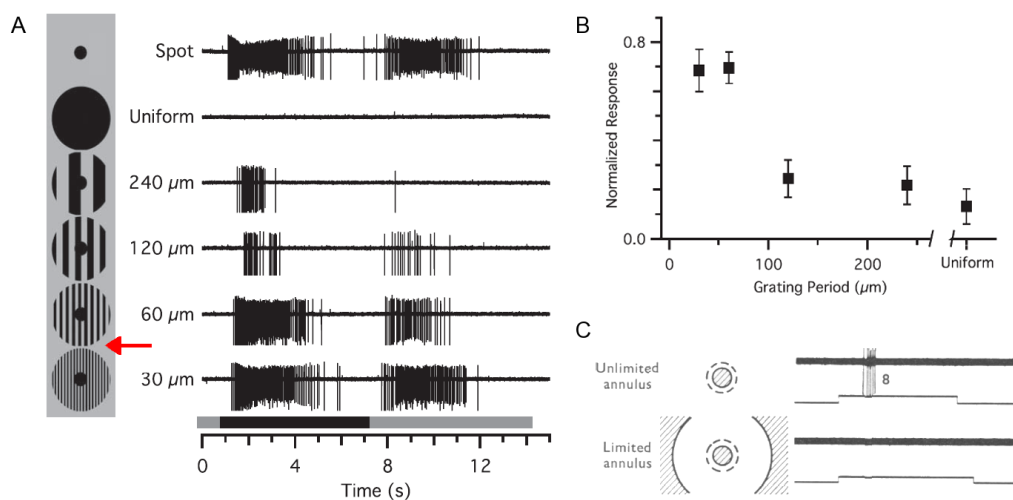


Figure 3.27: *Properties of the LED surround.* *A:* Between the extreme responses to small ($100\ \mu\text{m}$) and large spots ($850\ \mu\text{m}$) (first two lines), the strength of the LED's surround inhibition depends on the spatial frequencies it contains. The reduced inhibitory effect as the spatial frequency augments reveals the intrinsically *low-pass* properties of the surround, reflecting the spatial sensitivity of the presynaptic bipolar cells. Coherently, the last spatial frequency where surround inhibition is visible ($60\ \mu\text{m}$ ' line, red arrow) also corresponds to the psychophysical detection threshold of gratings in rabbits. This experiment does not allow any conclusion on possible band-pass preferences of the surround. *B:* Quantified data from *A*. *C:* An experiment suggesting a band-pass sensitivity in LEDs' surround: The response of a central spot ($85\ \mu\text{m}$) is reduced when an annular structure ($500\ \mu\text{m}$) introduces edges in the cell's surround. But all results in this figure cannot provide any definitive conclusion until the tuning properties of presynaptic bipolar cells are better known. From Van Wyk *et al.* 06 [177] (*A,B*), and Levick 67 [99] (*C*).

amacrine cells: Caldwell *et al.* 78 [28] observed that when glycine amacrine cells were inhibited with strychnine, the LEDs' specific sensitivity to small spots disappeared. The important effect of amacrine inhibition in shaping the LED response is also obvious in Figure 3.26: It results in a spiking pattern much more concentrated on edges than the cells' presynaptic excitatory signal is.

In particular, there is still debate over the spatio-temporal preference of the LEDs' inhibitory surround. Levick 67 [99] suggested that the inhibitory surround was stronger when it contained itself edges (implying that LEDs perform a center-surround operation on a presynaptic signal where edges are already enhanced). Indeed, the response to a dark spot is inhibited when an annulus structure creates edges in the *surround* (Figure 3.27 C). But by opposition, in response to a square pattern (Figure 3.26), the inhibitory inputs to the LED do not appear to display any preference for the squares' edges. Finally, another recent experiment (Figure 3.27 A and B) has provided some partial insights on the nature of the LED surround. However, to understand unambiguously all these experiments and the general organization of LEDs' receptive field, a better knowledge of their presynaptic bipolar cells' spatial tuning is still required.

Remark: The LED's inhibitory surround mentioned here is generally considered a part of the *non-classical* receptive field of this cell, because direct stimulation in the surround elicits no response from the cell. But to our minds, this fact is simply due to the low spontaneous activity of LEDs, implying that pure inhibition cannot have any visible influence on their spiking output. ■

Excitation and inhibition patterns typical of 'sluggish' cells

There are interesting and significant discrepancies between the respective behaviors of the excitatory and inhibitory synaptic inputs received by a LED: The excitatory input is sluggish, developing over several seconds, while the inhibitory input displays both a sluggish and a brisk component, particularly strong at stimulus onset (Van Wyk *et al.* 06 [177], not shown). Likely, LEDs receive different simultaneous sources of inhibition. This can also be seen in the patterns of excitation and inhibition in Figure 3.26.

The strong inhibition, with a fast initial transient, is largely responsible for the 'sluggish' nature of LEDs, because it totally shuts down their response during the few first hundreds of milliseconds following stimulus onset. Very likely, similar strong inhibitory transients exist in other 'sluggish' cells with complex responses (Xu *et al.* 05 [183]), and might be a common feature of these cells.

Furthermore, the experiments of Van Wyk *et al.* 06 [177] (their Figures 8 E and 12) provide strong hints of an interplay between the LED's excitation and inhibition, one possible explanation being that the rapid inhibition also acts directly on the presynaptic excitatory inputs to the LED.

Comparison with brisk sustained (X) cells

In the rabbit retina, it has now been demonstrated (Roska *al.* 06 [145], Zeck *et al.* 05 [184]) that LEDs are more spatially precise cells than brisk transient (X) cells. This can be seen by comparing the response of the β (X) cells and of the LEDs in response to a static square (respective 'Spiking' responses in Figures 3.13 and 3.26):

The response of the LED is very localized on the edges of the square, whereas the responses of the β cell displays a consequent width.

By opposition, LEDs in cat and primate retina have been less studied, but they are supposed to be less precise than β cells. For example, Figure 3.10 (from Dacey *et al.* 03 [42]) displays a plausible candidate for the LED in the primate retina: Their ‘broad thorny’ cell, with the typical ‘thick’ dendritic tree overcrossing the On and Off sublaminae. If this cell is indeed a LED, then its typical dendritic tree is far bigger than those of midget cells. In fact, it is even larger than the dendritic trees of parasol cells. However, note that the cells in Figure 3.10 are cells projecting to the LGN, so that our ‘presumed LED’, the ‘broad thorny’ cell, likely plays a role in cortical processing and thus in ‘conscious’ visual perception.

3.2.7 Other ‘sluggish’ ganglion cells

To conclude, we mention here the remaining types of ganglion cells that have been observed. Most of these remaining cells have small somata and slow, ‘sluggish’ responses, which have contributed to their ‘discrete’ place in the field of retinal physiological studies. However, all these cells now appear to constitute distinct, functional pathways, with cellular densities that can be comparable to those of α cells.

The origin of these cells’ sluggish response remains quite enigmatic. It seems attributable to the combined effects of (i) slow presynaptic bipolar cells, (ii) strong inhibitory shaping by amacrine cells (Xu *et al.* 05 [183]), possibly including a fast initial transient inhibition, and (iii) a high membranar resistance that implies a very long time constant for the cells. All these points have been mentioned previously through the detailed presentation of the local edge detector (LED, Section 3.2.6).

Importantly, it should be noted that although sluggish cells are less reactive and fire less spikes than ‘brisk’ cells, they display the same absolute sensitivity to contrast (Xu *et al.* 05 [183]), so they are also able of carrying an important quantity of information. They appear to saturate faster than brisk cells at high levels of contrast.

Possible cortical roles (LGN koniocellular layers)

The nature and importance of sluggish cells have recently been re-estimated, as it now appears that many of them likely provide input to the LGN, and from there to cortical processes. Indeed, in addition to the best-known Parvocellular and Magno-cellular layers, the LGN displays interstitial layers of cells with very small somata: The *Koniocellular* (K, ‘sand-like’) layers. In the macaque LGN, there is one layer of koniocellular cells ventral to each of the four Parvo and two Magno layers (see Figure 3.28). Likely, each of the six resulting Konio layers displays a full map of the visual receptive field, and is associated to a precise functional treatment (see Hendry and Reid 00 [74] for an interesting review).

It is now well established that the medial K layers relay the blue/yellow color oppositions arising from retinal bistratified cells. By opposition, much less is known concerning the physiology of the ventral and dorsal K layers. A few studies have revealed their sensitivity to broader spatial stimuli than Parvo and Magno layers (Hendry and Reid 00 [74]). It is likely that some retinal sluggish cells constitute the main source of input to these K layers, with a possible associated role in cortical

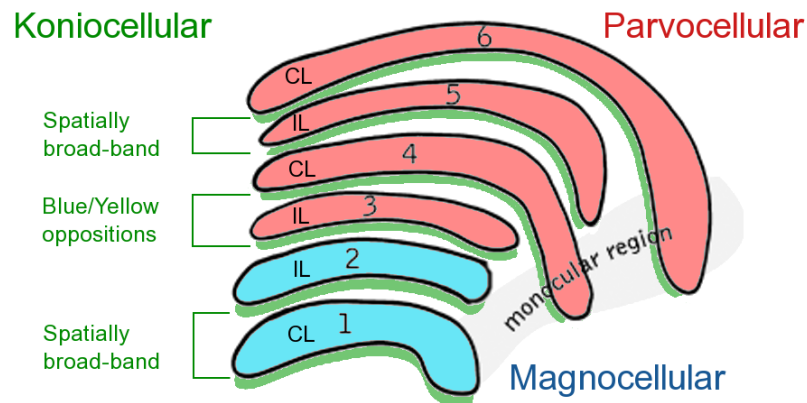


Figure 3.28: *Koniocellular layers in the macaque LGN.* Schematic view of a macaque LGN: The layers go in functional pairs, respectively associated to the ipsilateral (IL) and contralateral (CL) eye. Magnocellular (M) cells map the visual field once (one layer per eye) and Parvocellular (P) cells map the visual field twice (two layers per eye). Ventral to each of the P and M layers is a layer of koniocellular (K) cells. The medial K cells relay the blue/yellow oppositions from retinal small bistratified cells, making the resulting medial P/K complex the primary source of color information to the CO blobs of V1. The dorsal and ventral K layers arise from distinct retinal cells, most likely sluggish cells. These K cells are supposedly sensitive to broad spatial frequencies, but their physiology and functional role is still badly known (Hendry and Reid 00 [74]).

processing (especially because specific neural projections exist from the K layers to V1 and V2 [74]).

Unfortunately, in the retina, documentation on sluggish cells remains rare and often ambiguous: To date, the unification between morphological and physiological classifications has not been realized (see Troy and Shou 02 [171]), while the functions of these cells remain globally unknown. We now rapidly present what we have identified as the most important types of sluggish cells in mammalian retinas. Interested readers are referred to the review of Troy and Shou 02 [171] for further details and references on these cell types.

Sluggish concentric cells. The term of ‘sluggish’ cells was originally introduced by Cleland and Levick 74a [33], to designate cells with a marked center-surround architecture and responses of small amplitude. Just like concentric brisk cells, they were reported to enter four possible categories, being either ‘On’ or ‘Off’ and ‘sustained’ or ‘transient’. Although these cells have been termed ‘sluggish’ because of their low response rates, they appear to have a fairly good temporal precision, discriminating signals up to 15 Hz (Troy and Shou 02 [171]). We now present both types, sustained and transient.

Sluggish-sustained concentric (Q) cells. Sluggish-sustained cells have a relatively linear *center-surround* behavior, as ‘brisk sustained’ (X) cells, but with a low spatial precision, an order of magnitude smaller than X cells. Their wide dendritic trees and receptive fields are rather comparable to those of Y cells. Their spiking

activity is sustained and regular (Cleland and Levick 74a [33]). In the cat, they probably correspond to the linear ‘Q’ cells of Enroth-Cugell *et al* 83 [60], and to the respective δ (On sluggish-sustained) and ε (Off sluggish-sustained) morphological types (Troy and Shou 02 [171]).

Their functional role or cerebral projections are not known with certitude, but the On sluggish-sustained cells have been observed to project to the LGN in the cat (Pu *et al.* 84 [132]). This remark is interesting because the dual functionality of the Q and X cells, with qualitatively the same linear behavior but different scales of filtering, is reminiscent of multi-scale techniques used in image processing. Q cells could thus help to cortical interpretation of uniform zones, in addition to the precise ‘edge-dominated’ signal of X cells. In particular, it would be interesting to know whether ‘Q-like’ cells contribute input to the K cells of the LGN in primates.

Sluggish-transient concentric cells. These are the other type of sluggish concentric cells first classified by Cleland and Levick [33]. They also exist in On and Off version, and have low and irregular firing patterns that show a transient wave of activity at stimulus onsets. They are an intriguing class of cell, because while little is known about their functionality, they seem to be a very frequent type of cells with small dendritic trees (between β and α), that would account for around 10 % of cells in the cat retina [171].

We now present other types of non-concentric cells, which we have also termed ‘sluggish’ in allusion to their small and relatively slow response rates.

Suppressed-by-contrast (SbC) cells. Found in rabbit (Levick 67 [99]), cat (Cleland and Levick 74b [34], Troy *et al.* 89 [170]) and primate (De Monasterio and Gouras 75 [46]) retinas, these cells seem to have the exact opposite behavior of LEDs: They have a sustained firing in the presence of uniform light, which decreases whenever a contrasting stimulus (light or dark) appears in their receptive field. Temporally, the responses are sluggish and can be rather sustained or transient according to the type of cell studied (it has been argued that ‘SbC’ cells may in fact consist of two or more cell types with different physiologies: See [34, 171]). Spatially, there is a striking similarity between the SbC receptive fields and those of Y cells: They have the same typical sizes, and the same tuning to drifting gratings at different frequencies, including the doubled harmonic response typical of Y cells’ spatial nonlinearity. It is not known to what extent this similarity is significant of a common input.

We ignore the functional roles of these cells and the nature of their cerebral projections. We note that such ‘uniformity detectors’ (an alternative name for this class of cells) could have a useful function in computational models of diffusion processes in the visual cortex, as markers of zones where visual diffusion can be important.

Orientation selective cells. In the rabbit, orientation selective cells with particularly elongated receptive fields have often been reported (Levick 67 [99], Caldwell *et al* 78 [28]). Again, amacrine cells play a large role in this selectivity, which disappears when GABA-ergic (so, likely, wide-field) amacrine cells are inhibited by picrotoxin. Both their excitatory and inhibitory receptive fields were reported to be oriented along parallel bars [28].

We have not come across the cerebral projections of these cells. Their biological role remains mysterious, since directional selectivity is rather a strong attribute of cortical V1 and V2 areas, where it arises through specific connectivity patterns.

Photosensitive ganglion cells. To conclude this presentation of the diversity of retinal ganglion cells, a rare (1-3 %) ganglion cell has recently been found which expresses melanopsin, a particular photopigment. As a result, this cell possesses an intrinsic photosensitivity, independently of its retinal connectivity. It is supposed to play a strong role in the regulation of circadian rhythms and pupillary reflexes (Wässle 04 [180]).

Conclusion: Diversity of ganglion cell responses

To conclude this presentation, we reproduce in Figure 3.29 the very interesting inventory of ganglion cell responses by Roska *et al.* 06 [145], to their ‘static square’ stimulus. Amongst their sample population of ‘classic’ (β , parasol) and more ‘original’ ganglion cells, a striking feature is the fact that excitation and inhibition are often anticorrelated.

The spatial anticorrelation of inhibitory and excitatory inputs is best seen in the ‘Region of Interaction’ column of Figure 3.29. At most spatial locations (corresponding to successive trials on the same cell, with different offsets for the input stimulus), the cell receives an input where either excitation or inhibition is largely dominant.

In the authors’ interpretation, this observation reflects the fact that some short-range amacrine cells transmit inhibitory information vertically between the ‘On’ and ‘Off’ pathway, in a ‘push-pull’ manner: For example, an ‘On’ β cell could receive its inhibitory inputs from an amacrine cell relaying the signal of ‘Off’ bipolar cells. This mechanism would allow to enhance the dynamic range of the ganglion cell in both ‘On’ and ‘Off’ directions, and thus counteract the compression of the ‘Off’ signal due to rectification in the direct synaptic transmission from ‘On’ bipolar cells to the ganglion cell.

However, we remark that the anticorrelated pattern of excitation and inhibition could also be explained by amacrine cells providing an inhibition simultaneously to ganglion cells and to their presynaptic bipolar cells.

4 PROPERTIES OF RETINAL SPIKE TRAINS _____

4.1 The problematic of spike coding in the retina

Spike emission by ganglion cells is a particular subject in the general scope of retinal studies. Historically, although spikes were discovered very early as being the manifestation of retinal output activity, their individual role for coding was long overlooked, in favor of some more continuous information integrated from the spike trains (whether temporally, or over successive trials). There have been two main reasons for neglecting individual spikes: First, the role of spikes in retinal coding is

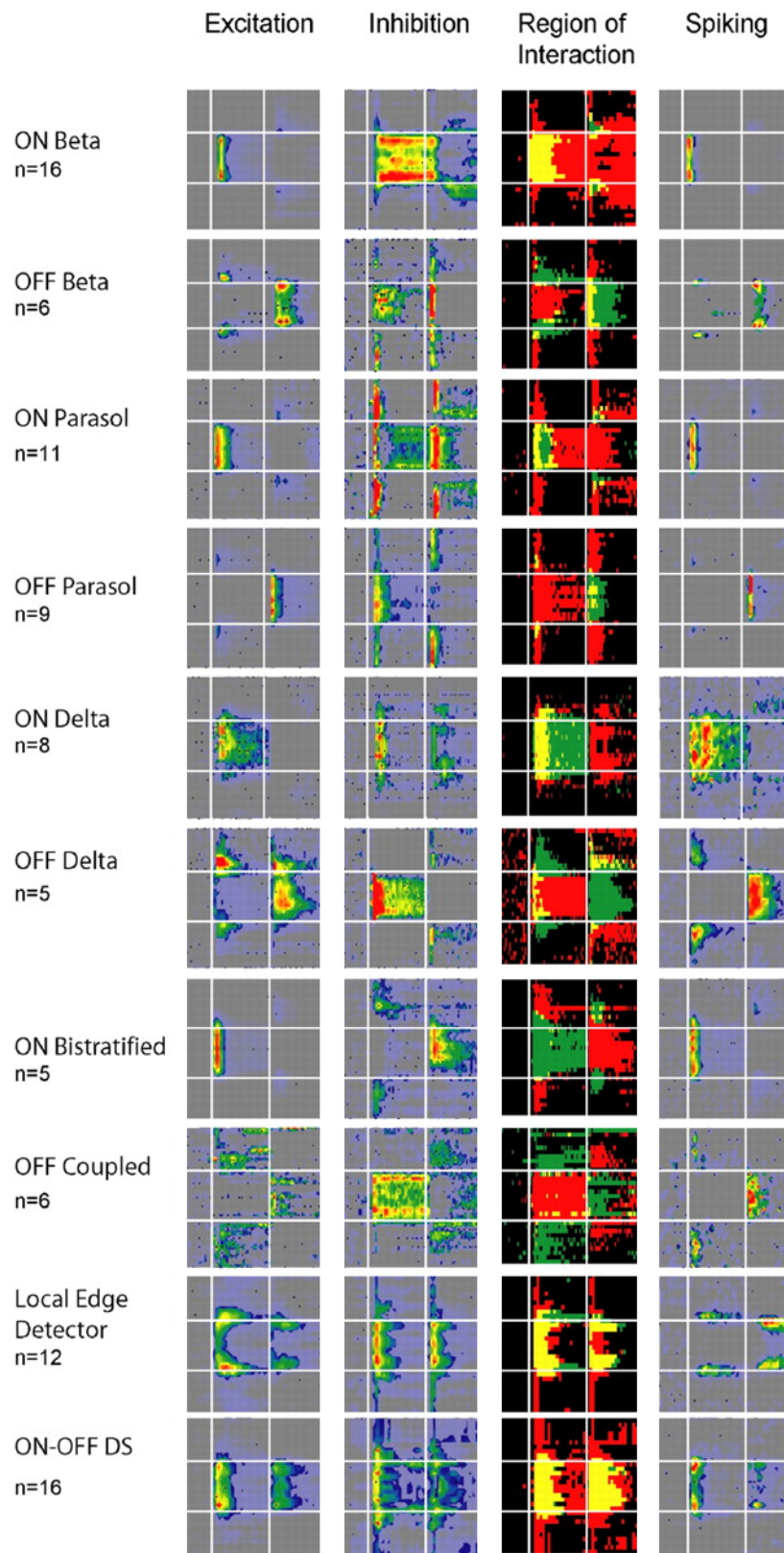


Figure 3.29: *Different ganglion cells respond to a static square stimulus. Same stimulus and representation as in Figure 3.13. In most cells, the output spiking pattern strongly resembles the input excitatory pattern, because the excitatory and inhibitory inputs show little overlap (as indicated by yellow regions in the ‘Region of Interaction’ column). This suggests a ‘push-pull’ organization of excitation and inhibition (see text). From Roska *et al.* 06 [145].*

not obvious, as they could logically be seen only as a means of physical transmission. Second, the precise study of spike trains requires a theoretical framework which is not totally grounded yet.

4.1.1 Spikes as a simple means of physical transmission

The first reason to neglect individual spikes is an Occam's razor argument: Retinal spikes have an obvious physical role that has nothing to do with coding efficiency. The axons of ganglion cells, thanks to their myelinated sheath and Ranvier nodes, allow the transmission of spikes over long distances, whereas a continuous graded signal would be transmitted slowly and with strong attenuation. With this obvious physical role of spikes, their existence needs not be explained by a role in *coding* as well. A basic working assumption can then be, that spikes are only sources of noise in the retinal code, imposed by the need for transmission over long distances.

Following this assumption, the nature of retinal coding is best studied through some averaging over the spikes, to wipe-out the noise added by the spike generation: This justifies the study of trial-averaged firing rates as the most informative output. The argument that 'spikes are only coding noise' has strong theoretical links with the modeling of spikes as Poisson processes (see Section 4.2.1).

4.1.2 Spike emissions lack a unified theoretical framework

A second and more prosaic reason to neglect individual spikes is that the question of spike coding is theoretically difficult: Defining a correct framework is not obvious, and deriving mathematical results from this framework is accordingly hard.

The fundamental problem is that spike emission involves very rapid and nonlinear variations of the underlying physical magnitudes (membrane potentials, synaptic release, etc.). To account for this intrinsic complication, two options are available, which result into fundamentally different mathematical frameworks.

If one really wishes to stick to physical nature of the spike, it can be modeled as a fast oscillation resulting from specific, very nonlinear dynamic systems (models of Hodgkin and Huxley, FitzHugh-Nagumo, or more recently of Izhikevich and others). However, these equations become very hard to interpret, and the functionality attached to the spikes becomes hard to study.

Rather, one can consider the spikes as discrete stereotyped events associated to precise times, and claim that the retinal code is totally contained in this discrete set of events. This is a strong and fundamentally *interpretative* claim, which does not reflect a physical reality, but an intrinsically human segmentation procedure¹².

Maybe because spikes are such a subjective interpretation of the physical reality, their mathematical analysis is difficult, as classical tools (L^2 distance, Fourier analysis, ODEs) are not available anymore. Naturally, strong theoretical frameworks for

¹²It could be replied that any physical observation and measure is fundamentally human and interpretative, and eventually depends on our mental representation of the perceived world. Here, we mean that 'visually' segmenting a signal into discrete spikes is a much stronger interpretative leap, than simply associating physical quantities (charge, intensity, etc.) to phenomena. In other words, there is no simple and rigorous mathematical definition of a spike, and yet least of a spike train, or spike burst. Instead, spikes can only be defined through specific threshold criteria on the underlying continuous signal, derived from our perceptual analysis. This is quite anecdotic, but an epistemologist might remark that there is some paradox in claiming that the cerebral code is associated to spikes, when spikes themselves do not have a precise physical definition, but rather result from our own human interpretation capabilities.

spikes also exist. From the point of view of an *emitting* cell, a spike train emission is well accounted for by the formalism of *point processes*. From the point of view of a *receiving* cell, a spike is often modeled as a Dirac function¹³. However, the junction of these two formalisms (emission and reception) in network models generally leads to complex frameworks where mathematical analysis is difficult. As an example, note such a simple notion as that of a *distance* between two spike trains, so intuitive in the continuous case, becomes a challenging problem (see Victor 05 [179] for review).

4.1.3 A theoretical framework for spike coding in the retina

In its most general expression, the question of spike coding in the retina amounts to finding the relation –necessarily statistical, because of the intrinsic trial-to-trial variability of the cells– between a visual stimulus and a cell’s spiking output. Given the particular functional spaces for the input (a three dimensional vectorial space) and for the output (discrete trains of temporal Dirac functions), this is a mathematical problem for which very few tools are available.

As a result, the theoretical framework must again be considerably reduced. In the retina, all models are based on the same theoretical simplification by a two-step procedure:

1. First, some continuous activity $A(t)$ (possibly multi-dimensional) is calculated for each ganglion cell, which reflects all continuous filtering prior to spike generation.
2. Second, each ganglion cell generates a discrete train of spikes from its activity $A(t)$, plus possibly from previous spikes of other spiking cells, following some specific *spiking procedure*.

This two-step model architecture is the simplest extension of ‘continuous’ models, for which only the first step is present. In the retina, this two-step model is rather well justified, since cells prior to ganglion cells do not fire spikes. Roughly speaking, the activity $A(t)$ may be associated to the synaptic inputs of the ganglion cell. It may be multi-dimensional if one wants to model both excitation and inhibition on a ganglion cell. Note however that, even in the retina, this is a reduced model of the biological reality (for example, the spikes from ganglion cells could have an influence on bipolar cells, through amacrine cell feedback).

The most classical example of such a two-step spike coding is the LNP model (Chapter 2, Section 5). Because it is conceptually simple, this sort of model is also used to model the spiking activity of other low-level visual areas (LGN, V1...), but in that case the model is less justified biologically, since many successive spiking layers are modeled through a single spiking step.

In the retina, most work has been done on two main aspects of the spike emission. The first aspect (Section 4.2) is the characterization of the spiking procedure for a single cell, and how it can be modeled by specific point processes. The second aspect (Section 4.3) is the study of correlation between the spike trains from neighboring cells, in the dark and under visual stimulation, and how they could mediate advanced coding schemes.

¹³By Dirac, we mean ‘the distribution that, when applied to any signal, returns the value of this signal at one particular instant in time’, a definition which applies to both continuous and discrete time scales.

4.2 Spike-emission process for a single cell

Here we review models that have been proposed to understand the spike emission of a single ganglion cell in response to a visual stimulus, and the experiments on which these models rely. For the models presented here, the underlying framework is the two-step spiking procedure presented in the preceding paragraph, with the added supposition that *ganglion cells do not exchange spiking information*: The spiking of a single ganglion cell is totally determined by its input $A(t)$. We will now refer to such models as ‘single-cell models’.

In Section 4.2.1, we rapidly present the Poisson model and its implications in terms of spike coding. A classical extension, the ‘simple modulated renewal process’ (SMRP) is presented in Section 4.2.2, that allows to take more biological constraints into account. We then switch to real retinal measurements (Section 4.2.3) and compare them to Poisson and SMRP models. This allows us to understand which alternative and more efficient model of spike generation can be proposed, in Section 4.2.4.

4.2.1 The Poisson process

The non-homogeneous Poisson process is the simplest way to generate a discrete and random set of events (the spikes) from an underlying continuous variable. Mathematically, it can be defined in several equivalent ways, and it has several properties, which it is not our goal to explore here. For this report, we choose a presentation which allows direct extension to SMRPs (next paragraph).

Let $\lambda(t)$ be a strictly positive function of time, defining the *instantaneous rate* of the Poisson process. Let $U(t)$ be the transformed time scale

$$U(t) = \int_{s=0}^t \lambda(s) ds. \quad (3.5)$$

A Poisson process of instantaneous rate $\lambda(t)$ is a random distribution of discrete and growing event times $\{T_n\}$, such that for any spike time T_n , the probability of occurrence of the next spike in the Poisson process is defined by:

$$P(T_{n+1} \in [T_n, t]) = \int_{U(T_n)}^{U(t)} \exp(-\tau) d\tau. \quad (3.6)$$

One can check that the process defined by (3.6) fires on average $U(b) - U(a)$ spikes in any interval $[a, b]$, so that $U(t)$ can be called the *average spike count measure*: On average, one spike is emitted every $\Delta U = 1$. Coherently, the temporal derivative of the spike count $U(t)$ is the instantaneous firing rate $\lambda(t)$ (equation (3.5)). The bigger values $\lambda(t)$ takes, the faster $U(t)$ grows, so the more spikes are emitted.

It should be noted (although we do not prove it here) that a Poisson process verifies the Markov property (conditional independence of past and future), which is a strong theoretical advantage.

A ‘transparent’ process

In the optic of transforming a continuous firing rate into a discrete and random set of spike trains, the Poisson process is the most ‘transparent’ possible, in terms of the

statistical links between the spike train and the underlying firing rate. This link can be resumed as follows:

1. **Maximum entropy process:** Of all renewal processes which share the same trial-averaged firing rate $\bar{\lambda}(t)$, the Poisson process of instantaneous firing rate $\bar{\lambda}(t)$ is the one which has the maximum Shannon entropy. So, if no other information is known about a spike train than its trial-averaged firing rate, it should be modeled as Poisson to minimize artificial, model-related correlations.
2. **Reciprocally,** if a spike emission procedure is based on a Poisson model, the underlying continuous processing $\lambda(t)$ can be reconstructed from the averaged firing rate $\bar{\lambda}(t)$ (over an infinity of trials): $\bar{\lambda}(t) = \lambda(t)$.

This property is particularly interesting for the LNP model (Chapter 2, Section 5): When a spike-triggered average (STA) is performed on the output, the spikes are ‘transparent’, so the STA amounts to performing a ‘classical’ reverse correlation analysis which allows to find back the best-fitting linear kernel and nonlinearity (Chapter 2, Section 5).

To sum up, being ‘transparent’ confers a strong theoretical advantage to Poisson processes, but also a lack of interest as far as spike coding is concerned: No information is embedded in the precise spike emissions of a Poisson process.

Rather, the only effect of a Poisson process in the transmission of a signal, is the addition of a specific stochastic *noise*: If the successive emitted spikes are considered as Diracs localized at successive times T_n , then the Poisson emission transforms the continuous signal $\lambda(t)$ into signal $O(t) = \sum_{n=0}^{+\infty} \delta(t - T_n)$. On a trial-average, $O(t)$ and $\lambda(t)$ have the same integral in each interval (e.g., the average number of spikes in this interval), but in the case of $O(t)$ the power is randomly re-concentrated on a discrete set of points.

4.2.2 Gamma, and other simple modulated renewal processes (SMRP)

Real neurons show deviation from the exponential inter-spike interval (ISI) distribution of Poisson models, as defined by (3.6). In particular, in a particular realization of a Poisson emission, two successive spikes can be very close one from another: If a short interval of time dt is considered, (3.6) implies that $P(T_{n+1} \in [T_n, T_n + dt]) = \lambda(T_n)dt + o(dt)$. Taking $\lambda(T_n)=100$ Hz and $\Delta t = 1$ ms, the probability of a second spike being separated by less than 1 ms is around 0.1. This behavior is in contradiction with the *refractory* behavior of real neurons, which ensures that two successive spikes can never get closer than a few milliseconds (typically 5 ms, but with consequent variation between neurons).

The Poisson model can thus be extended to the more general class of ‘simple modulated renewal processes’ (SMRPs, using the terminology of Reich *et al.* 98 [138]), to impose a more biological ISI distribution. In SMRP models, the underlying continuous variable $\lambda(t)$ still defines the instantaneous firing rate, so the model is still based on the average spike count measure $U(t)$ in (3.5). However, one now has the choice of the probability distribution for the interspike intervals (ISI):

$$P(T_{n+1} \in [T_n, t]) = \int_{U(T_n)}^{U(t)} f(\tau)d\tau, \quad (3.7)$$

where f defines the *probability density function (pdf)* of the ISI, with the properties that $\int_0^\infty f(\tau) = 1$ (probability distribution) and

$$\mathbb{E}(T_{n+1} - T_n) = \int_0^\infty \tau f(\tau) d\tau = 1,$$

to respect the definition of $U(t)$ as an average *spike count*. This liberty allows a better fit to experimentally measured ISI distributions.

A particular parametric class of functions allows a direct extension of Poisson models: They are Gamma processes, based on ‘Gamma’ *pdfs*:

$$E_{\alpha,\tau}(t) = \frac{(\alpha t)^\alpha}{\Gamma(\alpha)\tau^{\alpha+1}} \exp(-\alpha t/\tau), \quad (3.8)$$

where α is the parameter of the function (necessarily positive with the definition chosen here), and Γ is the Gamma function (the traditional interpolation of the integer factorial, which has improperly given its name to these ‘Gamma’ functions).

We have already met such functions when modeling linear temporal kernels in the retina (equation (2.6) and Figure 2.3, for *integer* parameter $\alpha = n$). For $\alpha \rightarrow 0$, they tend to a decaying exponential, and thus a Poisson process. By opposition, the bigger α gets, the more regular and deterministic the spike emission, as resulting from the more peaked shape of the *pdf*¹⁴.

In particular, Gamma processes account better for the cells’ refractory period, since for the Gamma process of parameter α , one now has $P(T_{n+1} \in [T_n, T_n + dt]) = \lambda(T_n)dt^{\alpha+1} + o(dt^{\alpha+1})$, which greatly minimizes the probability of successive spikes being too close.

However, the increased biological plausibility allowed by generalized SMRP processes has a theoretical price: The Markov property does not hold anymore for such processes, since it resulted exclusively from the exponential expression of the *pdf* in the case of Poisson processes. Also, the link between the instantaneous firing rate $\lambda(t)$ and the trial-averaged firing rate $\bar{\lambda}(t)$ which can be measured becomes slightly more complicated, but as a correct approximation, one still has $\bar{\lambda}(t) = \lambda(t)$ as in the Poisson process¹⁵.

4.2.3 The statistics of retinal spike trains

Along with proposed models for retinal spiking, comes the need for theoretical and mathematical tools to confront the models to experiments. For example, how can one quantify to what extent a real ganglion cell follows or deviates from a Poisson behavior? This question is in strong relation to the remarks we made previously about the theoretical difficulty of studying spike trains: A spike train as itself is not very informative visually, and many of its characteristics are stochastic. As a

¹⁴For $\alpha = n$ integer, the Gamma process can also be generated from a Poisson process with an n -fold bigger instantaneous firing rate, but where only one spike every n is kept. Each resulting ISI is thus the average of n Poisson ISIs, providing another intuitive interpretation of the increased regularity.

¹⁵After reconsidering this problem in the spike-count time scale $U(t)$, one can get persuaded that the only possible discrepancy between $\lambda(t)$ and measure $\bar{\lambda}(t)$ comes from the initial condition of the SMRP process, if it is imposed that the process starts at time $t = 0$ as if a spike had just been emitted. If the first time in the SMRP process is initialized with a correct random probability, or if one considers the system only long after onset (ergodic conditions), then $\bar{\lambda}(t) = \lambda(t)$ becomes true with exactitude.

result, more than in any other domain of the retina, a strong theoretical framework is necessary even at the experimental level, to produce meaningful results from the raw data.

Here, we present the classic tools which have been used to quantify the response and stochastic variability of ganglion cells, and what properties of retinal spiking have thus been revealed. As an illustration of the difficulty of theoretically grasping spike trains, any one of these tools only provides a partial view of the spiking phenomenon as a whole.

Trial-averaged firing rate

This is obviously the first statistical indicator which can be derived from sets of spike trains. It grasps the whole information available in a Poisson process, and almost all the information available in a SMRP (see Section 4.2.2), but significant information can be lost for other spiking procedures.

Inter-spike interval (ISI) histogram

This measure is obtained by constructing a histogram of all interspike times $T_{n+1} - T_n$ emitted during the process. In the case of a *homogeneous* spiking procedure (if the statistical properties of the process are stationary over time), the ISI histogram gives access to the *pdf* of the renewal process $dP(T_{n+1} = T_n + \tau)$.

Unfortunately, a real retinal spike emission is generally not homogeneous, since it depends strongly on the temporal evolution of the visual input. As a result, ISI histograms have a very limited signification, except in the case of cells receiving a temporally constant input. It is possible to compensate for (part of) this input-related variability by plotting the ISI histogram in the spike-count reduced time scale as in equation (3.5) (see next paragraph).

Interval maps

Reich *et al.* 98 [138] proposed a two-dimensional representation of spike trains allowing to represent simultaneously trial-averaged firing rates, ISI histograms, and supplementary statistical information, in a single representation that they called the *interval map*. This map is constituted of a plot of all couples $(T_n, T_{n+1} - T_n)$, over successive trials. Interestingly, the projection of this map on the abscissa is the average firing rate, and the projection on the ordinates is the ISI histogram. Such ‘interval maps’, in response to a drifting grating, are represented in Figure 3.30, left column.

A striking feature is that, even after averaging over all stimulus cycles, strong peaks remain in the average firing rate. A natural explanation of these peaks is that the precise spike times are relatively deterministic over the cycles, at odds with Poisson or other simple modulated renewal processes (SMRP, see Section 4.2.2). And indeed, a spiking procedure based on a noisy integrate-and-fire model (see Section 4.2.4) allows to reproduce this statistical ‘phase locking’ between the spikes and the stimulus cycles.

Remark: Note however that such an experiment cannot prove *a priori* that these oscillations come only from a statistical phase locking of the spiking response to the stimulus: Theoretically, they could also arise from ‘real’ oscillations in the IPL, followed by a simple

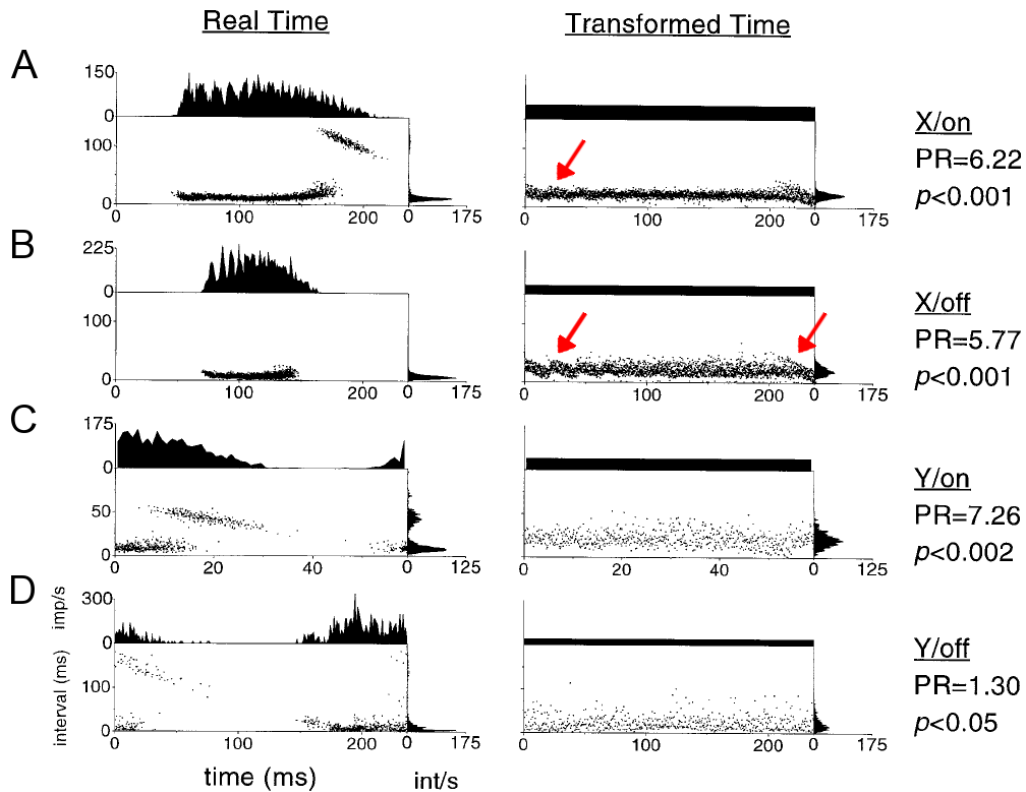


Figure 3.30: *Interval maps of cat ganglion cells over one cycle of drifting grating.* *Left column:* Plots of the couples $(T_n, T_{n+1} - T_n)$ for different ganglion cells, averaged over the repeated cycles of a drifting sinusoidal grating at 4.2 Hz (except C: 16.9 Hz). Average firing rate (top) and ISI histograms (right) can be derived from the interval map by simple projection. Longer intervals at the end of the cycle correspond to the time to wait before first spike of the next cycle (too big to be represented in B). *Right column:* Same data in a spike count time scale, using the empirical average firing rate. These cells differ strongly from Poisson or SMRP behavior, as marked by the bumps in the rescaled maps (see text). From Reich *et al.* 98 [138].

Poisson spike emission. The results of the following paragraph prove that, independently of the shape of the average firing rate, the spike statistics *are not* Poisson.

Still, ‘continuous’ oscillations in the IPL might be *coupled* to the spiking procedure, and account for part of the oscillations seen in Figure 3.30 (see the results of Sakai and Naka, Figure 3.36). Such oscillations cannot be accounted for by the two-step procedure of Section 4.1.3. In the end, the interpretation of Figure 3.30 remains very dependent on the underlying ‘frame of modeling’, a sort of problem often encountered when dealing with precise spike models. ■

More precise properties of the cells’ spiking procedure appears when the interval map is replotted in the empirical spike count time scale given by

$$\bar{U}(t) = \int_{s=0}^t \bar{\lambda}(s) ds, \quad (3.9)$$

where $\bar{\lambda}(s)$ is the empirical average firing rate measured over the trials. Replotted interval maps are presented in Figure 3.30, right column. They allow to estimate the relation of the cell’s spiking procedure to a SMRP, independently of its average firing rate. Indeed, in a SMRP, the rescaled interval map is by definition translationally invariant, and its associated *pdf* can be found by measuring the ‘rescaled’ ISI histogram, after projection along the abscissa axis.

As a result, the rescaled interval map provides both:

1. A measure for the ‘best-fitting *pdf*’ if the cell was to be modeled as a SMRP.
2. The discrepancy between the cell’s actual emission and a SMRP model, visible in deviations of the interval map from translational invariance.

And indeed, the interval maps of real cells often display significant bumps (arrows in Figure 3.30), with a typical diagonal orientation. This diagonal orientation indicates an anti-correlation between the time of the current spike and the next spike time, and it has a typical slope of -1 . Such bumps appear when the ‘next spike following the bump’ (quite an approximate definition!) is more deterministic than what would be predicted by Poisson. For example, if the next spike $T_{n+1} = t_0$ was totally deterministic, then the cluster would be a single diagonal line, consisting of all points $(T_n, t_0 - T_n)$.

The authors [138] then propose an empirical measure called the *power ratio* (PR), based on the Fourier transform of the rescaled interval map, to measure the strengths of such clusters, and hence deviations from SMRP behavior. Typically, the PR of Poisson or Gamma SMRPs is smaller than 1, whereas most cells have a PR significantly higher: See Figure 3.30, on the right.

The authors show that a noisy leaky integrate-and-fire spiking model (nLIF, Section 4.2.4) has a high PR in response to sinusoidal stimulation, and the same characteristic ‘diagonal bumps’ in the rescaled interval map.

Fano factor, and other spike count measures

Alternatively, many authors have been using the *Fano factor* (FF) to measure the variability of spike trains. The Fano factor is defined on any time interval W from the statistics of $N(W)$, stochastic number of spikes falling into interval W during a

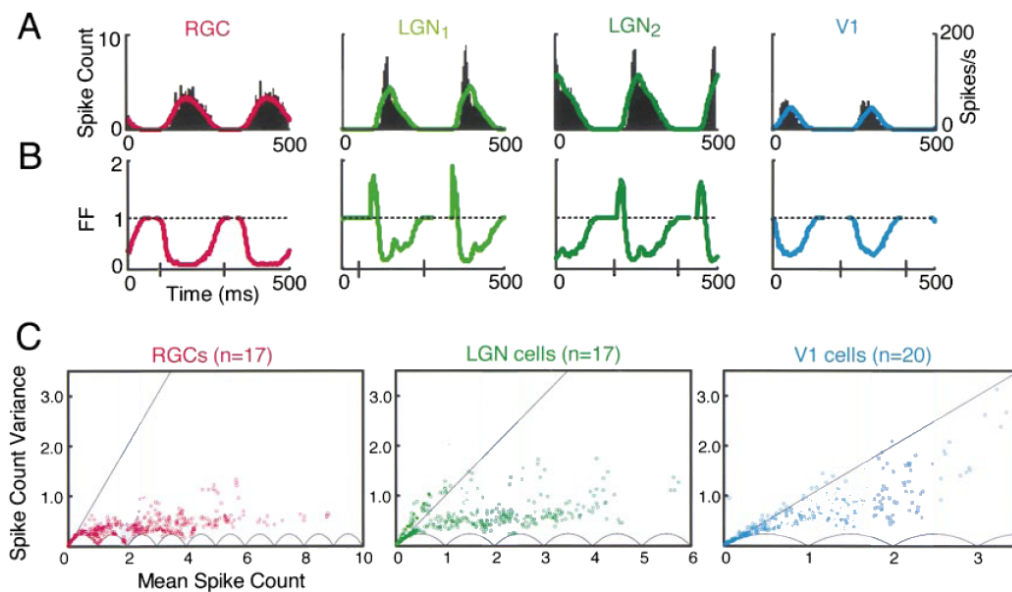


Figure 3.31: *Fano factors in the cat visual system, responding to a drifting grating.* **A:** Mean spike count (firing rate) of different cat visual cells, using binning windows of 50 ms. **B:** Corresponding Fano factors (FF) calculated from the same 50 ms intervals. The clear anti-correlation between spiking activity and Fano factor reveals that spikes are relatively ‘more regular’ at high firing rates. The high FF of LGN cells is attributable to spike bursts (Chapter 1, Section 1.2). **C:** Mean spike count versus variance, for all 50 ms intervals and all measured cells from each area. The scalloped curve at the bottom is a theoretical lower bound for the spike count, due to the fact that it can only take integer values. From Kara *et al.* 00 [88].

trial:

$$FF(W) = \frac{\text{Var}(N(W))}{\mathbb{E}(N(W))}. \quad (3.10)$$

Interestingly, a non-homogeneous Poisson process always verifies $FF(W) = 1$, independently of W and of the instantaneous firing rate $\lambda(t)$. Unfortunately, for other processes, the FF has no simple expression. For a SMRP, calculations derived from the central limit theorem insure that asymptotically

$$FF(W) \rightarrow \frac{\sigma^2}{\mu^2} \text{ when } L(W)\mu^{-1} \rightarrow +\infty, \quad (3.11)$$

where $L(W)$ is the time length of interval W , and μ and σ^2 are the respective mean and variance of the *pdf* of the ISI for the process. This is true only when the average number of spikes $L(W)\mu^{-1}$ tends to infinity. It thus appears that the Fano Factor is linked to the *coefficient of variation* σ/μ , another traditional statistic on interspike intervals. Hence, for a Gamma process of order α , one has:

$$CV = 1/\sqrt{\alpha}, \text{ and } FF(W) \rightarrow 1/\alpha \text{ when } L(W)\mu^{-1} \rightarrow +\infty.$$

In real ganglion cell spike trains, the Fano factor is not constant: There is a striking anti-correlation between the value of the FF on short intervals (typically, 50 ms) and the average firing rate in these intervals (Figure 3.31). This means intuitively that spike trains get more deterministic – even relatively to their firing rate – at high firing rates. To account for this fact, some models such as Gazères *et al.* 98 [69] have introduced enhanced LNP models, where the choice of the spiking process depends on the strength of the instantaneous firing rate $\lambda(t)$: It is Poisson for small values of $\lambda(t)$, and switches to a higher-order Gamma process, with lower FF, when $\lambda(t)$ crosses a threshold.

However, in the case of a real cell, the Fano factor is not at all the intrinsic characteristic which it is for a theoretical Poisson spiking procedure¹⁶. Due to its definition, the FF depends not only on the state of a cell at a given time t_0 , but also strongly on the length of the measuring interval W around t_0 . As a result, we believe that FF-related studies should rather be taken as benchmarks to test the plausibility of a spiking procedure, than as an interpretative tool to directly derive parametrized models, as in Gazères *et al.* 98 [69].

Furthermore, as we present in the next paragraph, the particular nature of retinal coding might be such that spike counts, and thus Fano factors, are not the most relevant statistic to estimate the reliability of the retinal code.

Firing events: A strong coding principle?

Another line of work has investigated how the nature of the input stimulus could dramatically change the statistics of the spiking output. In the recent years, it has become clear that grating stimuli -so often used as experimental input- elicit very unnatural responses from retinal cells¹⁷, due to their strong regularity. When white noise stimuli or, better, natural image stimuli are tested on ganglion cells, they generally elicit much *sparser* responses from these cells than a drifting grating.

¹⁶And for SMRPs to a lesser extent, with the asymptotic limit (3.11).

¹⁷And more generally, from the whole visual system.

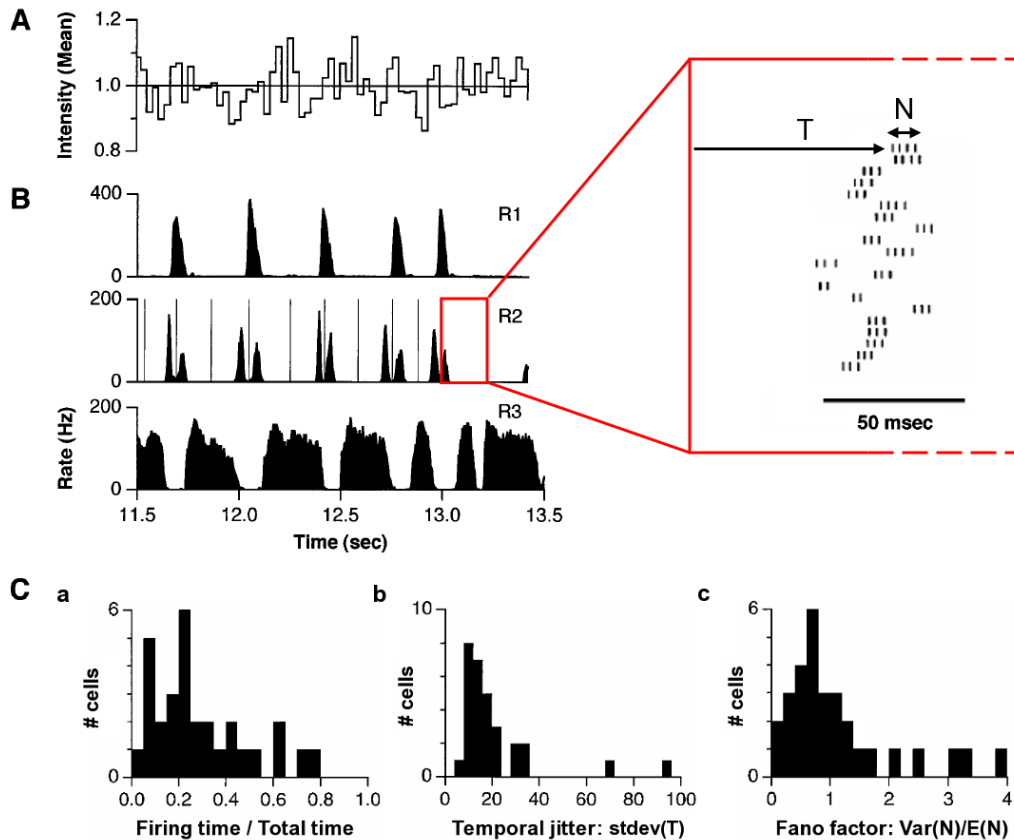


Figure 3.32: *Firing events in the rabbit retina.* A: Input stimulus is a uniform flickering screen following a temporal white noise. B: Firing responses of three rabbit cells. The responses naturally define *firing events* separated by long periods of silence. Automatic segmentation can be performed, as shown for cell R2. In each event, two random variables are studied: The time of first spike T and the number of spikes N in the event. C: *Statistical properties of a population of 30 rabbit cells.* Three ‘statistical indicators’ are derived for each cell, and respectively stored in three population histograms. a: Fraction of total time occupied by spiking events. Most cells (like R1 or R2) spend most of the time silent. b: Jitter in the time of the first spike in an event. A single indicator is calculated for each cell, as the median of $\sigma(T)$ over all its firing events. As compared to the typical time between successive events, this jitter is strikingly small. c: Variation in the number of spikes per events. A single indicator is calculated for each cell, as the average of the Fano factor over all events. The average FF is 0.7 over the whole population, markedly lower than for a Poisson process. Adapted from Berry *et al.* 97 [15].

The responses of rabbit ganglion cells to a white noise stimulus are represented in Figure 3.32: Most cells, such as the depicted R1 and R2, fire strongly only at precise moments of the stimulation, which are rather sparse, and stable over trials. (By opposition, cell R3 has a strong ongoing spiking activity, suggesting that it might be one of the ‘suppressed-by-contrast’ cells discussed in Section 3.2.7.). In front of natural image stimuli, retina and LGN cells also display the same sort of peaked activity, although the peaks are not always as sparse as in Figure 3.32 (see for example Carandini *et al.* 05 [29]).

Berry *et al.* 97 [15] proposed the term *firing event* to describe these specific bursts of activity for the cells, and suggested that these events, rather than their individual constitutive spikes, could be the fundamental ‘brick’ of retinal coding. To justify this claim, they designed an automatic segmentation of the average firing rate into a discrete set of events (bumps of strong activity separated by zones of silence, illustrated for cell R2 in Figure 3.32), and measured for each event the statistics of T , time of the first spike, and N , number of spikes in the event (see Figure 3.32). Over a population of 30 rabbit cells, they found that:

1. Most cells spend a lot of time silent, with a small or null spontaneous firing rate, and sparse firing events (Figure 3.32 *C,a*). These observations are at odds with typical responses to drifting gratings, as in Figure 3.12, where some cells have a high spontaneous firing activity.
2. The precision of the first spike time, measured by the variance of T over all trials and events (Figure 3.32 *C,b*), is very small (10 or 20 ms for most cells) as compared to the typical time interval between two successive events (generally, several hundreds of ms). As a result, a lot of information is likely to be carried by the timing T of successive events: The authors estimated roughly this information to be $I_T = 7.3$ bits per spiking event, for a particular cell [15].
3. The number N of spikes per event has a relatively large variation across trials, but still less than a Poisson process (Fano factor of 0.7 on average over cells and events, against 1 for Poisson). A rough information measure yielded $I_N = 1.7$ bits per spiking event, on the same cell as in point 2.

Both information measures were based on the same estimation: Given their typical average and variance, how many different configurations of stimulus is the cell able to discriminate on the single basis of T (I_T , point 2) or N (I_N , point 3). Although very rough calculations, these results suggest that the strongest information carried by the cell in response to this sort of white noise stimulus, is in the successive timings of the events rather than in the total number of spikes in each event.

Remark: Could it be possible that a mathematical formalism should focus on firing events rather than individual spikes? Likely, taking such a wide step in modelization requires more experimental knowledge than is available at present time, and our retina simulator will of course retain spikes at the elemental bricks of signal transmission. However, it should be remarked that there is nothing more ‘complicated’, or ‘integrated’, in the notion of firing event than there is in the notion of individual spike: In the end, both criteria rely strongly on our visual segmentation and interpretation capabilities, when we look at the underlying continuous signal. ■

4.2.4 Noisy leaky integrate-and-fire (nLIF) models and derivatives

When it comes to modeling the specific statistical structure of single cell firing patterns as presented in Section 4.2.3, the leaky integrate-and-fire model (LIF, see e.g. Rieke *et al* 97 [140]) has generally been presented as the good alternative to Poisson or SMRP models. Indeed, both interval map measures (Figure 3.30) and firing event measures (Figure 3.32) relied in the end on the same fundamental remark: When the cell has been silent for a while and that it undergoes a sudden augmentation of activity (rising phase of a sinusoidal cycle, or sudden strong response to white noise), the first following spike is more deterministic than predicted by SMRP models.

A LIF model precisely allows this first spike to be quite deterministic. The most basic ¹⁸ LIF neuron receives its input continuous signal as an excitatory current $I(t)$, from which it generates spike trains with the following procedure:

$$\left\{ \begin{array}{l} \frac{dV}{dt} = I(t) - g^L V(t) \\ \text{Spike when threshold } \theta \text{ is reached: } V(t_{\text{spk}}^-) = \theta \\ \text{Reset: } V(t_{\text{spk}}^+) = V_R, \\ \text{and (3.12) again.} \end{array} \right. \quad (3.12)$$

Interestingly, the LIF model can be made a *stochastic* firing process if noise sources are added in its generation. We will term the resulting models nLIF procedures. They are generally much more deterministic than a Poisson model concerning the ‘first spike in a firing event’. Indeed, when $I(t)$ undergoes a sudden raise of its values, marking the beginning of a firing event for the cell, the next spike t_{spk} always follows quickly, following (3.12), rather independently of the added noise.

A typical nLIF has been proposed by Reich *et al.* 98 [138], that can reproduce the non-stationary bumps in real cells’ rescaled interval maps (Figure 3.30, right column). The noise source they used was an input Poisson shot noise (Diracs fired following a Poisson process) added to the input current $I(t)$.

Similarly, Keat *et al.* 01 [89] have proposed a model very strongly inspired by a LIF, to reproduce the typical statistics of *firing events* in response to a white noise temporal signal, as presented in the preceding section (Figure 3.32). A summary of their model is presented in Figure 3.33. Importantly, their model uses two sources of noise:

- A correlated Gaussian noise $a(t)$ added to their generator potential (equivalent of $V(t)$ in the LIF model (3.12)), that can account for variations in the time of the first spike T in each spiking event.
- A noisy refractory after-potential $P(t)$ following each spike, that can account for variations in the number N of spikes in each firing event.

Their model strongly relates to a nLIF model, their variable $g(t)$ (see Figure 3.32 and caption) corresponding to the integrated current $I(t) \ast \exp(-g^L t)$ in (3.12). Although we have preferred to stick to a pure nLIF formalism, the model we have

¹⁸The LIF model can then undergo several improvements: It can include a refractory period, absolute ($V(t)$ held at V_R for a fixed amount of time after each spike) or relative (a kernel is added after each spike to the threshold $\theta(t)$, which becomes dynamic). It can also be based on conductances rather than currents (see e.g. Tao *et al.* 04 [166]), etc.

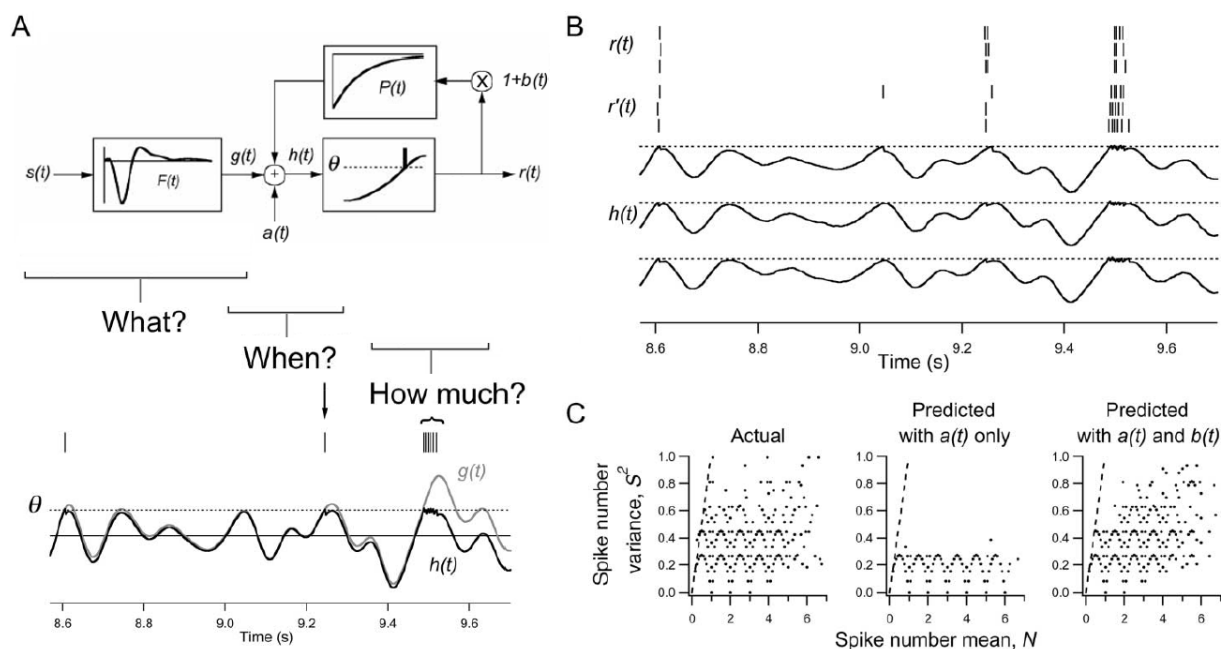


Figure 3.33: *A noisy LIF-inspired model of spike generation.* The model of Keat *et al.* 01 [89] is purely temporal, and reproduces the statistics of firing events for ganglion cells stimulated with white-noise modulated uniform screens. **A: Architecture of the model.** A response $g(t)$ is derived from the input $s(t)$ thanks to the optimal linear kernel $F(t)$. The generator signal $h(t) = g(t) + a(t) - \sum_i (1 + b(t_i))P(t - t_i)$ generates a spike t_i every time it crosses threshold θ . A refractory kernel $-(1 + b(t_i))P(t - t_i)$ is added after each spike. The model includes a Gaussian auto-correlated noise $a(t)$, and a noise $b(t_i)$ on the strength of each refractory period. **B:** Compared spikes of a real cell ($r(t)$) and of the model ($h(t)$) producing $r'(t)$ for three trials. **C:** Spike count statistics ($\mathbb{E}(N)$, $\text{Var}(N)$) over firing events for a real cell, the model with noise source $a(t)$, and the model with both noise sources $a(t)$ and $b(t)$. When only noise $a(t)$ is present, the jitter $\sigma(T)$ in the time of first spike is well reproduced ('When' criterion of Panel A), but the spike count N in each event is too deterministic. The addition of $b(t)$ allows to produce better statistics for N , by adding more noise in the intervals between the successive spikes in an event ('How much' criterion of Panel A). From Keat *et al.* 01 [89].

implemented (Chapter 4) also has two sources of noise, inspired by the Keat *et al.* model.

This concludes our presentation of single-cell models for spike generation. In a schizophrenic tentative to explain retinal spike coding, we have assumed in this section that all ganglion cells could be modeled as independent spiking encoders, whereas in the following section, we explain how neighboring ganglion cells' spike trains *are not* independent. The theoretical link between these two sections is not evident, since spikes from neighboring cells may possibly influence the spiking statistics at the level of a single cell. We will not enter such considerations, and only present experimental evidence for correlations in neighboring cells' spike trains.

4.3 Spike correlations between neighboring cells

The spike trains emitted by neighboring ganglion cells are generally not statistically independent. Two neighboring cells may have a tendency to fire synchronously, more often than by chance: Then, there is a positive correlation between their spiking outputs. Conversely, some cells (typically, an ON and an OFF cell) may have a tendency to never fire synchronously, implying a negative correlation between their spiking outputs.

Although some pioneering works had already been pursued long before (e.g., Laufer and Verzeano 67 [98], Mastronarde 83 [109]), the subject of correlations between ganglion cells has strongly arisen only in the last decade. This recent trend has different explanations¹⁹:

- Technical progress: Multi-electrode arrays now allow to record simultaneously from many tens of ganglion cells, rather than from pairs only, as was the case before.
- The introduction into neuroscience of new theoretical tools, such as information theory, allowing a deeper interpretation of experimental data.
- Increasing suspicion that correlations may carry a strong functional role in retinal transmission, as some recent experiments have suggested (see Figure 3.35). However, the functional importance of correlations is not well assessed either, which probably contributes to making this subject so attracting.

Because the subject is quite fresh, a state-of-the-art presentation appears difficult. However, we also feel the possible importance of these correlation mechanisms between ganglion cells, and thus try to provide an overview of current issues in the subject, by presenting some recent and relevant pieces of work.

4.3.1 Spike correlations and their anatomical origin

Correlograms

Correlations between spiking cells are well represented by using correlograms. A correlogram between two cells A and B is the histogram of all differences $\{t_A^{(i)} -$

¹⁹Others than its being a trend!

$t_B^{(j)}\}_{i,j}$ between the spikes emitted by the two cells. It will be termed an *auto-* correlogram if $A = B$, and a *cross-* correlogram otherwise. If enough samples are available, the correlogram eventually represents $f(\tau) = dP(t_A^{spk} = t_B^{spk} + \tau | t_B^{spk})$, density of probability to have a spike from A at time τ before/after a spike from B .

As a result, two independent cells necessarily have a flat correlogram. By opposition, two *correlated* cells can be either:

- Positively correlated, with a peak in their cross-correlogram near $\tau = 0$.
- Negatively (anti-) correlated, with a dip in their cross-correlogram near $\tau = 0$.

Examples of cross-correlograms with positive correlation are depicted in Figure 3.34, Panel A. Note how different ‘zooms’ (e.g., insets on the right column) allow to reveal the properties of the correlation on different time scales.

Cross-correlograms are not necessarily symmetric. For example, if a spike from B always elicits a spike from A with a time delay τ_0 , the correlogram will have a peak around $\tau = \tau_0$. Conversely, if a spike from A always elicits a spike from B with delay τ_1 , there will be a peak around $\tau = -\tau_1$, etc.

Correlations of ON and OFF pathways during spontaneous activity

Correlations can be recorded in the absence of visual stimulation (‘spontaneous activity’). This is an interesting experimental protocol, since it reveals the intrinsic biological structures giving rise to correlations, without the additional structure arising from the spatial coherence of an input stimulus.

A first strong observation during spontaneous activity is that neighboring cells of opposite polarity (e.g., On and Off BT cells in the rabbit) are generally *anti-correlated*, with a dip in their cross-correlogram near $\tau = 0$. (Mastrorarde 83 [109], not shown). This reveals subtle interactions between the two pathways, generally renown as being segregated. We have not read much about such anti-correlations, but they can clearly lead to interesting synchronization effects: See e.g. the results of Sakai and Naka reproduced in Figure 3.36.

By opposition, neighboring cells from the same pathway are very often *positively* correlated, meaning that they have a tendency to fire in close synchronies. In the next paragraph, we detail the plausible anatomical origins of these positive correlations.

Origins of correlations amongst cells of the same polarity

Correlations between the spike trains of ganglion cells are mediated by different anatomical structures. In salamander retina, Brivanlou *et al.* 98 [23] found that pairs of correlated cells fell in three distinct clusters, according to the typical time scale for the peak in their cross-correlogram, and the resistance of the peak to synaptic blockade (Figure 3.34, Panel B). Here are the three types of correlations they reviewed:

- ‘Short’ correlations occur on the time scale of a few milliseconds, and are characterized by a *double peak* in their correlogram (like the one observed in rabbit On BT cells, Figure 3.34 A, top right). They likely arise from **gap junctions between neighboring ganglion cells**. Indeed, these correlations persist in

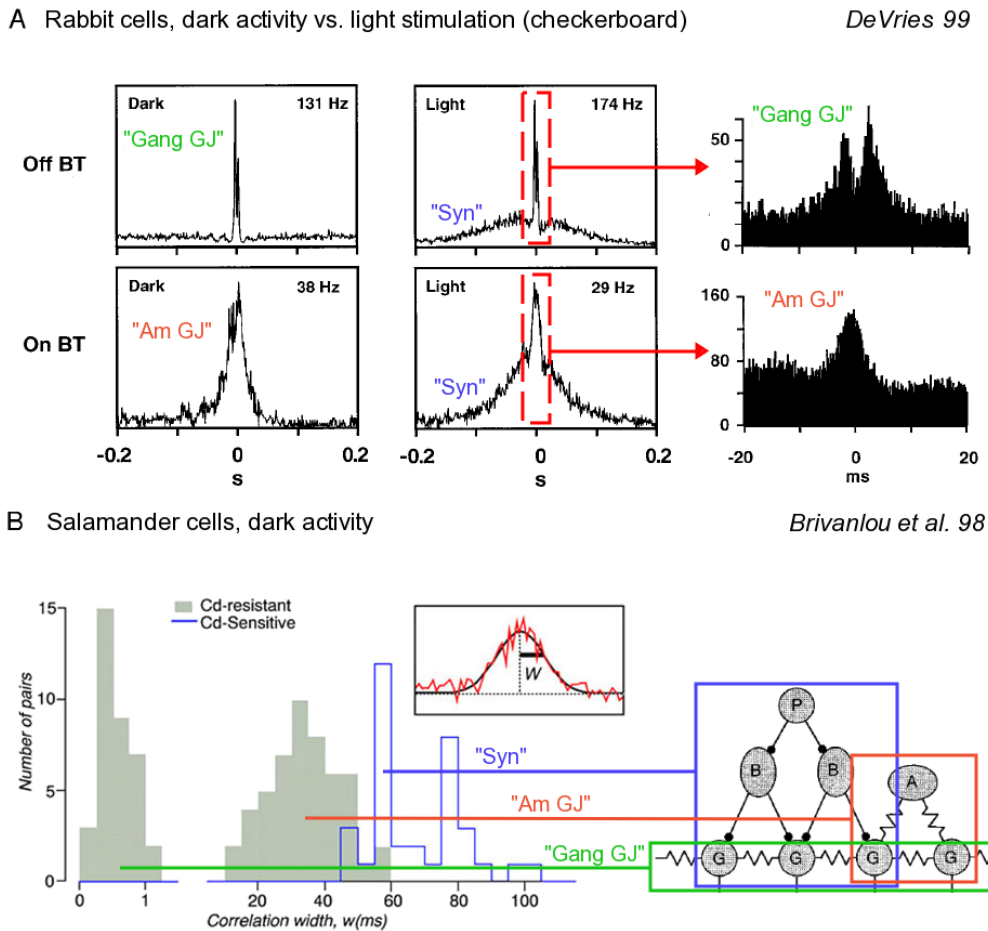


Figure 3.34: *Different temporal scales, and origins, of spike correlations. A: Rabbit On and Off brisk-transient (Y) cells exhibit different types of spontaneous and input-driven correlations. Short time-scale correlations in Off BT cells reveal direct coupling through gap junctions, as indicated by the double peak (bidirectional transmission, delay of 1-2 ms). Short and medium time-scale correlations in On BT cells reveal a common input from pre-synaptic neurons, likely amacrine, through gap junctions and/or chemical transmission. In the presence of a visual stimulus (checkerboard), broad correlations appear superimposed. Numbers in Hz give a measure for the width of the central peak. Magnified insets are from different cells. Notations “Syn”, “Am GJ” and “Gang GJ” refer to Panel B; They are schematic interpretations, hypothesized by us, not by the original authors. From DeVries 99 [53]. B: Different scales of correlations, and presumed biological origins, in salamander retina. When their correlograms are fitted by a Gaussian of deviation w ms, salamander cell pairs fit into three distinct clusters, according to the biological connections that dominate their correlations. Short and Medium time scale clusters are still observed in the presence of cadmium, a blocker of virtually all synaptic transmissions, so they likely arise from gap junctions. Conversely, the Broad time-scale cluster appears mediated by chemical synapses. Right: Hypothesized biological origins of the three types of correlations. We also marked their plausible correlates in rabbit retina, in Panel A. From Brivanlou et al. 98 [23].*

the presence of Cadmium which blocks all synaptic transmission. Furthermore, the symmetric peak indicates a fast, bidirectional connection between the two cells. Such correlations were found by [23] in about 10 % of the cells studied.

- ‘Medium’ correlations occur on the time scale of 20-50 ms and are marked by a single, symmetric peak in the correlogram (like the one observed in rabbit Off BT cells, Figure 3.34 A, bottom right). They likely arise from **gap junctions with amacrine cells**. Indeed, the larger time scale of the correlation indicates an indirect effect from non-spiking cells, and the persistence of these correlations in the presence of Cadmium suggests that gap junctions are involved. This effect formed a *majority of the correlations* studied by [23], accounting for ~ 50 % of all emitted spikes during spontaneous activity!
- ‘Broad’ correlations occur on the time scale of 50-100 ms and are also marked by a single, symmetric peak in the correlogram (like the one observed in rabbit Off BT cells, Figure 3.34 A, bottom right). They likely arise from **synaptic connections** from amacrine cells and/or bipolar cells. Indeed, unlike the preceding two types of correlations, these are blocked by Cadmium.

In the overall scheme depicted by the study of Brivanlou *et al.*, amacrine cells are suspected to play a fundamental role in the apparition of correlations, through gap junctions and/or synaptic interactions with neighboring cells. And indeed, studies and models concerning *stimulus-driven* correlations (Section 4.3.2) suggest that an important synchronization is provided by specific populations of amacrine cells.

In the rabbit retina, De Vries 99 [53] has led a similar study with comparable results, depicted in Figure 3.34 A. Interestingly, On BT cells (top line) rather displayed the sharp (frequency ~ 150 Hz) double peaked correlogram typical of direct gap junctions, while Off BT (bottom line) displayed the broader (frequency ~ 30 Hz) simple peaked correlogram typical of correlation through intermediate cells. This adds supplementary evidence to the possible different functions of On and Off types of ‘Y’-like cells (Section 3.2.2).

In addition, a much broader peak appeared in the presence of a visual stimulus, denoting the synaptic origin of broad correlations, and the increased complexity of the correlation structure in the presence of a visual stimulus, as we now present.

4.3.2 Stimulus-driven oscillations

Although studies of correlations during spontaneous activity are best designed to reveal an underlying biological architecture, the real impact of correlations on retinal coding must be measured in the presence of visual stimulus.

Phase locking

The strong characteristic of spike correlations under visual stimulation is the possible apparition of a *phase locking* between the spike trains of two cells, or two populations of cells (Neuenschwander and Singer 96 [121], Neuenschwander *et al.* 99 [120]). In the cross-correlogram, this phase locking translates in fast oscillations, as depicted in Figure 3.35. The properties of the phase locking are the following:

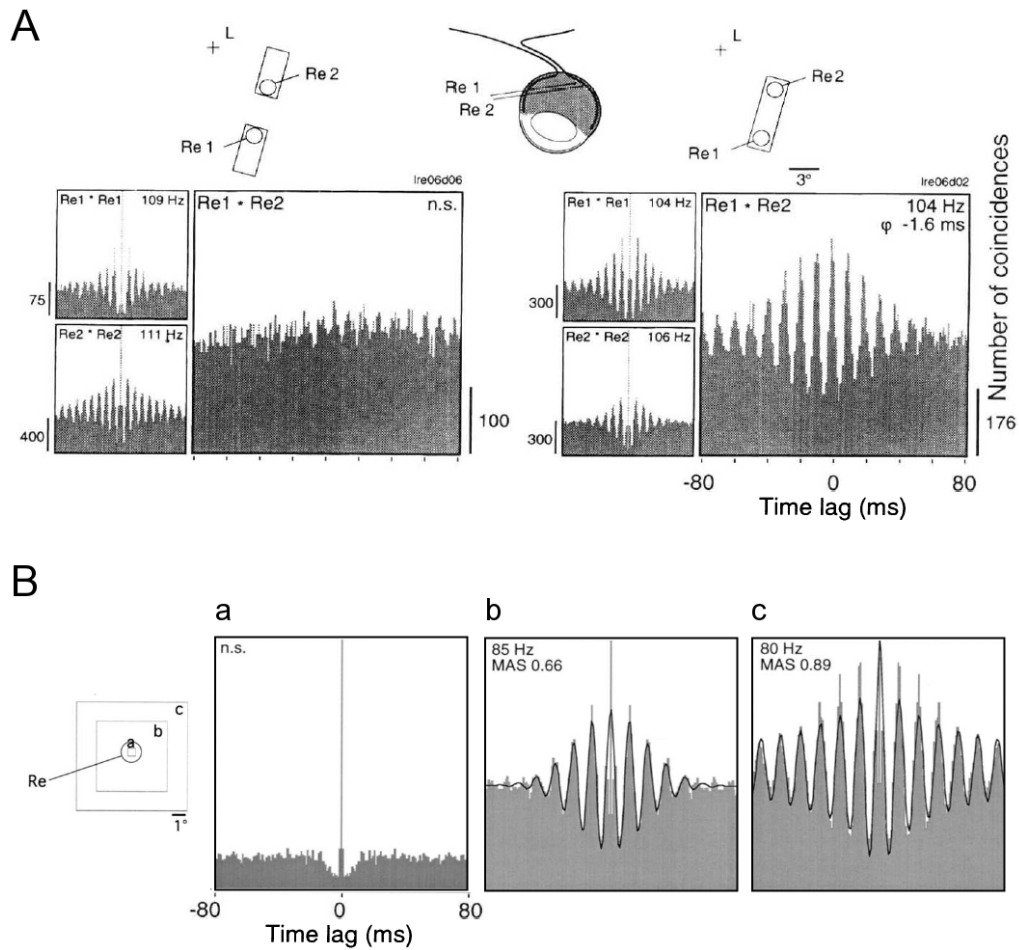


Figure 3.35: *Stimulus-dependent oscillations in the primate retina.* **A:** Two populations of cells, separated by 3 degrees, have uncorrelated spike trains (flat correlogram) when their receptive fields are lit by two discontinuous bars (left). By opposition, their spike trains are phase locked (oscillations in the correlogram) if they are lit by a single continuous bar (right). From Neuenschwander and Singer 96 [121]. **B:** Autocorrelogram of a single population of cells, for different sizes of a square stimulus. Oscillations, and thus phase locking amongst cells in the measured population, augments with stimulus size. From Neuenschwander *et al.* 99 [120].

1. It can occur even between distant cells (separated by several degrees), depending on the spatial structure of the underlying visual stimulus. Phase locking will be present between two cells only if their two receptive fields are located on a single spatial structure of homogeneous luminosity (Figure 3.35 A). Also, the bigger the homogeneous structure around the cell, the stronger the phase locking (Figure 3.35 B).
2. It is not locked to the onset of the visual stimulus (not shown). At onset of a stimulus, the first spikes are locked to the onset time: For each cell, the averaged firing rate right after stimulus onset displays peaks because the first spikes are quite deterministic. But soon after stimulus onset, the ‘internal’ phase locking of the retina takes over: The average firing rate for each cell becomes flat (spikes fall anywhere over the trials), but the cross-correlograms of neighboring cells remain strongly peaked (all spikes are still synchronized).
3. It involves ensembles of cells rather than individual cells. Most of the cross-correlograms of Neuenschwander *et al.* were made directly on populations of cells. When cells are studied at the level of a population, oscillations are even revealed during spontaneous activity [120] (unlike the single-cell correlograms presented in Figure 3.34).

This phase locking is a very intriguing phenomenon. Since it depends on the spatial structure of the stimulus, it could provide a strong and early preprocessing for subsequent *object segmentation* procedures in the brain.

Including some simple model for this phase locking is one of our goals concerning future evolutions of software *Virtual Retina*.

Oscillations and amacrine cells

Because direct gap junctions between ganglion cells appear to make up only for a minority of correlations in the retina (Section 4.3.1, Paragraph “Origins of correlations...”), amacrine cells are the most likely candidate to account for the synchronies.

Speaking in favor of this fact, the results of Sakai and Naka 90 [149, 150] in the carp retina suggest that strong oscillations are induced by interactions with amacrine cells. More precisely, they studied the complex connections between two types of ganglion cells (On-type GA and Off-type GB) and two types of amacrine cells (On-type NA and Off-type NB), by injecting current pulses in one cell and simultaneously recording the voltage response in another cell. Let us comment their main findings with the help of Figure 3.36:

1. On-type ganglion and amacrine cells (GA and NA) are linked by strong gap junctions (see the effects of reciprocal current injections, in Panel B), resulting in very similar responses to light (Panel A, left column). The same coupling is observed between the Off-type ganglion and amacrine cells (GB and NB), as assessed from current injections (Panel D) and similar responses to light (Panel A, right column).
2. By opposition, strong anti-correlations (not shown) exist between NA and NB amacrine cells, with the apparition of specific oscillations around 30 Hz. More precisely, a current pulse injected in an NA cell induces strong oscillations in

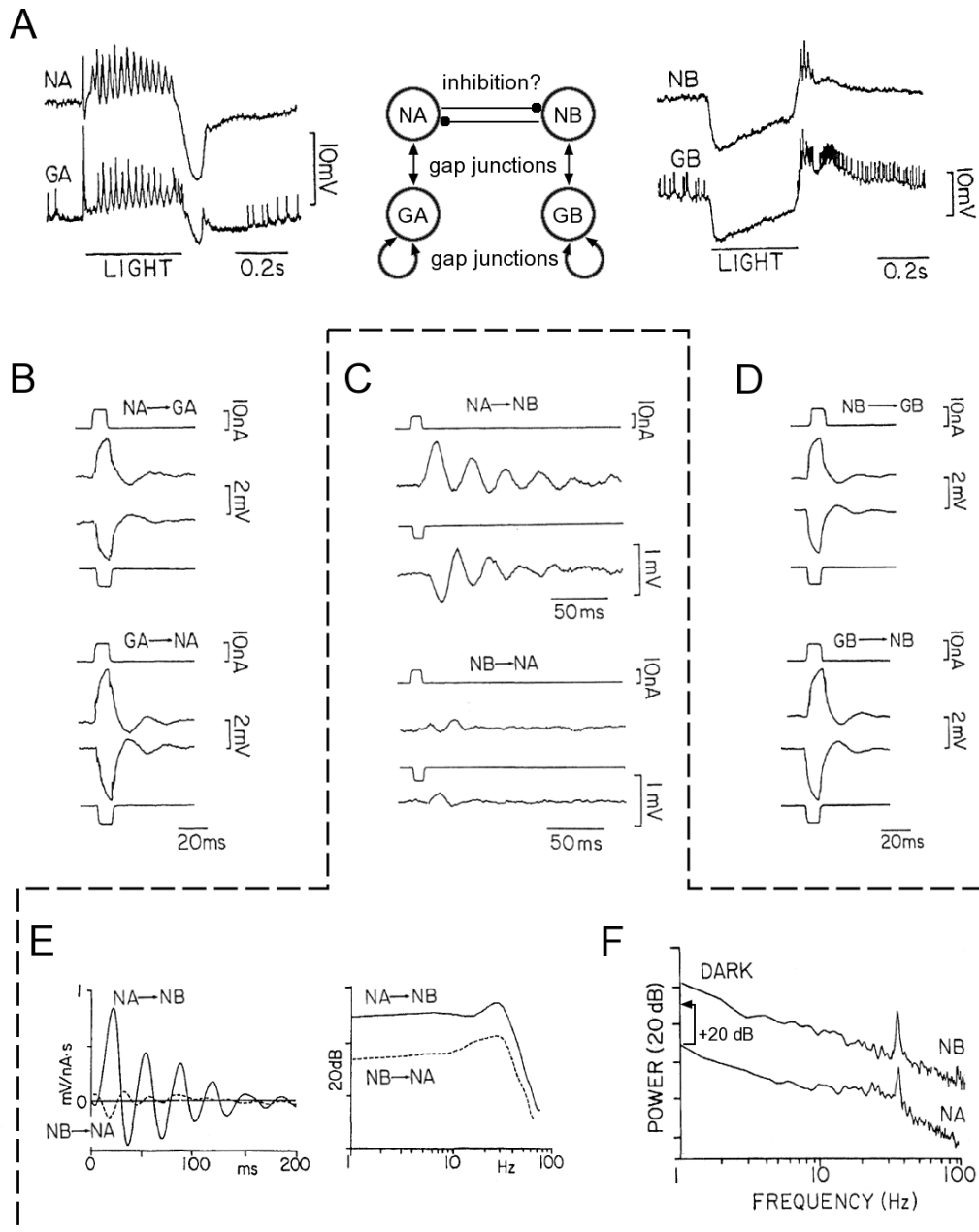


Figure 3.36: *Oscillations between On and Off pathways in the carp retina.* The On pathway (GA ganglion and NA amacrine cells) and the Off pathway (GB ganglion and NB amacrine) are anti-correlated, with the apparition of intrinsic oscillations at around 30 Hz in the responses of the cells. In Panel *F*, the NA curve is shifted of 20 dB downwards for visibility. See text for more details. From Sakai and Naka 90 [149, 150].

an NB cell, lasting for several hundreds of milliseconds (Panel C). Oscillations around 30 Hz are revealed, both in the linear kernel derived from reverse correlation between NA and NB (Panel E) and from the spectrum of the cells' spontaneous activities (Panel F). Interestingly, the effect is non-symmetric, as current injected in NB elicits much less response in NA (Panels C and E).

In the middle of Panel A, we propose the type of architecture suggested by these interesting results. The oscillations, which appear somehow intrinsic to the NB amacrine cells (Panel C), may serve as a vector for large-scale synchronizations. Unfortunately, by many ways these results are only partial, and difficult to interpret without supplementary research in the same direction.

Modeling stimulus-driven synchronizations

As far as modeling is concerned, the work of Kenyon *et al.* [91, 92, 90] is to our knowledge the most advanced reproduction of the synchronization results of Neuenschwander *et al.* (Figure 3.35). Logically, their model relies on amacrine cell populations, and involves a complex interplay between ganglion cells, short-range inhibitory amacrine cells, and long-range amacrine cells which provide synchronization to ganglion cells through gap junctions.

An interesting question to address is whether stimulus-related synchronizations could arise *without* explicit modeling of amacrine cells, by allowing short-range excitatory / long-range inhibitory connections between model spiking units. Such a simplifying leap from the true structure of a retina (short-range excitation from ganglion cells and possible long-range inhibition from amacrine) could help to better understand the underlying functionality of spiking correlations.

The following results (Section 4.3.3), based on information theoretical measures, provide (amongst other things) informations concerning the feasibility of a model where all interactions would occur directly between the output spiking units. Interestingly, these results suggest that the whole structure of ganglion cell correlations, including negative correlations mediated by amacrine cells, can be accounted for by pairwise interactions between ganglion cells, possibly with negative weights (anti-correlation). However, the exact structure of the weights appears to depend on the type of stimulus used for the experiment, so that the correlation structure may not be directly usable in a generic model.

4.3.3 Applications of information theory

The increasing popularity of information theory in neuroscience has recently allowed to consider spike correlations with a more functional approach, questioning their impact on the statistical structure of the population spike trains. We here review two particular applications.

Pairwise correlations account for the whole correlation structure

For technical reasons, most recordings of spike correlations have only been pursued between pairs of cells. Yet, there is no *a priori* reason why retinal correlations should be understood simply by considering pairwise interactions. Recent studies (Schnei-

dman *et al.* 06 [153], Shlens *et al.* 06 [160]) have questioned whether pairwise correlations are sufficient to account for the statistical structure of the retina.

Maximum entropy distribution. Their approach was based on the *maximum entropy* method, allowing to find the ‘most random’ probability distribution for a system, given a set of constraints on the observed output of the system:

1. At order 1, this method takes as only constraints the average firing rate measured for each cell. The resulting maximum entropy distribution is that of independent uniform encoders (tending to *Poisson* encoders when the discretization time step tends to zero), where the probability of firing of each cell i is based on a single constant number h_i .
2. At order 2, pairwise correlations are also taken into account. In this case, the maximum entropy distribution is a variation on Ising models: The probability of firing for each cell is coupled to the spikes simultaneously emitted by all other cells, being determined by $h_i + \sum_j J_{ij}\sigma_j$, where $\sigma_j = +1$ if cell j also fires a spike, and -1 otherwise. J_{ij} measures the coupling from cell j to i , so that a high J_{ij} tends to imply positive correlation between i and j (although the overall correlation between i and j depends on the whole structure h, J).

Pairwise correlations explain the statistical structure. Both Schneidman *et al.* 06 [153] and Shlens *et al.* 06 [160] found that the statistical structure of the population spike trains is very well accounted for by an Ising model, depending only on pairwise correlations. This finding is especially interesting, because it gives hope to implement easily spike-based correlations. Indeed, the Ising model is closely related to simple Hopfield neural networks [160].

What cells, what stimulus? However, it should be noted that important differences appear in the conclusions of both studies, due to the different experimental procedures.

- In Shlens *et al.* 06 [160], the authors used artificial stimuli with no strong correlations (uniform light, and occasionally white noise), tested on a *single population of cells* (e.g., salamander OFF transient). In their resulting maximum entropy distribution, all the J_{ij} were found positive²⁰, meaning that each cell only influences the others positively. Also, they could take only nearest neighbor correlations into account (imposing $J_{ij} = 0$ otherwise) and still reproduce well the whole statistical structure.

So, the statistical structure for the spikes of a single ganglion pathway under simple stimulation, is totally explained by reciprocal excitations between close neighbors. This finding is consistent with the nature of correlations during spontaneous activity (Section 4.3.1).

- In Schneidman *et al.* 06 [153], by opposition, natural stimuli were used (forest scenes, etc.) and the different cell types in the population were not distinguished. This time, a meaningful percentage of the resulting J_{ij} were negative²¹, indicating anti-correlations in the population.

²⁰Remark in their Section “Materials and methods”, paragraph “*Maximum entropy*”

²¹Their Figure 3, Panel *b*

So, inhibitory spiking interactions *do* exist at the scale of a whole retinal population under visual stimulation. This finding is consistent with the presumed roles of wide-field amacrine cells in creating stimulus-driven synchronizations (Section 4.3.2).

Redundancy and the role of correlations

Another application of information theory is to measure the overall *redundancy* in the retinal code. This has been done recently by Puchalla *et al.* 05 [133]. Based on measures of mutual information between a neuron and the input stimulus, they could derive a global *overrepresentation* factor for the retina, giving an estimate for the number of times the information carried by one neuron is also represented in the spikes of its neighbors. They found this factor to be around 10, suggesting that the retina is a highly redundant transmitter of information.

And indeed, it should be remembered that from an information-theoretic point of view, any deviation from independent spike encoding necessarily leads to a global diminution of the information transmitted by the retina. One can then wonder how spike correlations may still serve a functional role. However, several works attest the efficiency of correlation-based coding (e.g., Kenyon *et al.* 04 [90] in the retina, or Singer 99 [161] for general references).

Very likely, the resolution of this paradox lies in the dual fact that

- Not all ‘information’ has the same value for the retina. Cues for object segmentation, movement detection, etc., are clearly more valuable than telling the exact shade of gray in the sky, whereas ‘information’ is a much more abstract concept, especially in the absence of good generative models for natural scenes.
- Constraints in biological architecture probably make the most ‘efficient’ coding schemes impossible for implementation.

A better formalization of these issues, possibly in an information-theoretic framework, would help to better quantify the *functional* importance of correlations in the retina.

5 NONLINEAR ADAPTATIONS IN THE RETINA _____

The retina, as most biological organs, is not a static structure. Several mechanisms constantly adapt and regulate the successive stages of signal transmission, through complicated molecular control loops. In this last section, we mention some of the most important expressions of this adaptation.

Amongst various mechanisms of adaptation, a particular distinction can be made between ‘fast’ and ‘slow’ ones. The ‘fast’ adaptations are almost instantaneous mechanisms which allow to control the gains of signal transmission and thus avoid saturation of the system. Two major phenomena enter this category: Rapid adaptations to light and rapid contrast gain control. The term of ‘adaptation’ may be ill-suited for these mechanisms, because it evokes a somewhat secondary effect to improve

performance, whereas these fast gain controls are simply necessary for the system to avoid total saturation and uselessness.

By opposition, ‘slow’ adaptations are mechanisms which occur in the range of seconds or even minutes. These are truly secondary effects which allow to optimize image processing in terms of acuity and economy of energy. Both types of phenomena will be evoked here.

In Section 5.1 we mention the most fundamental type of adaptation: Adaptation to luminosity, which allows our eyes to see from dark night to bright sunlight. However, the huge complexity and numerous mechanisms underlying this functionality are only rapidly evoked, by lack of time and because adaptation to luminosity is not in the scope of our simulator for the moment. In Section 5.2, we spend more time describing the phenomenon of *contrast gain control* (or ‘contrast adaptation’) which is of direct concern to our simulator.

Both adaptations to luminance and contrast possess at the same time fast and slow components. In Section 5.3 we present supplementary examples of slow adaptations, and how they can be interpreted in the theoretical framework of ‘predictive coding’.

5.1 Adaptations to luminosity

Adaptation to luminosity has been a large subject of research in physiology and psychophysics for more than fifty years. The most important site of adaptation is obviously the photoreceptors, but horizontal cells are supposed to also play a role in the process, as well as some specific modulatory amacrine cells. It is not our goal here to review all these mechanisms which we have not investigated in detail.

We simply mention the fundamental effect of adaptation as observed in photoreceptors. The effects of background illumination on the transfer properties of ganglion cells are also evoked in Section 5.3, along with Atick’s decorrelation hypothesis. Readers interested in the classical psychophysics of light adaptation are referred to the review of Shapley and Enroth-Cugell 84 [154].

Phototransduction and light adaptation. The main effect of light adaptation is to shift the whole response curve of the photoreceptors, in such a way that response to the background light is always close to the receptor’s point of optimal sensitivity (maximum slope in the response function). This effect is illustrated in Figure 3.37. This process of ‘response shift’ remains efficient on a large range of background luminosities (especially in cones), and is sufficient to account for our ability to see at all levels of illumination, regardless of subtler adaptation effects.

From a molecular standpoint, the calcium modulatory feedback of phototransduction (Section 1.1) plays a fundamental role in the ‘response shift’. It accounts for most of the receptors’ adaptation until very high luminosities, where pigment depletion (massive deactivation of a majority of rhodopsin molecules) is required as an additional mechanism (Valeton and Van Norren 83 [172]).

The calcium modulatory feedback seems to be a rather ‘fast’ adaptation effect: To provide a good fit to data, Van Hateren and Lamb 06 [175] (Figure 3.3) must use values $\tau_{Ca} = 3\text{--}12$ ms for their calcium feedback. Experimentally, Schnapf *et al.* 90 [151] report ‘fast’ adaptation to fully develop within one second after a sudden change of

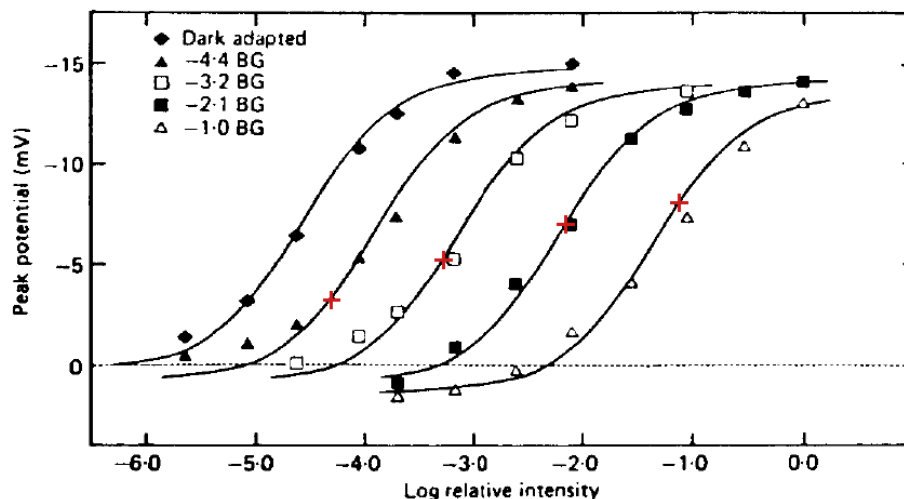


Figure 3.37: *Adaptation to background illumination in turtle cone receptors.* Each point plots the peak of response of a turtle cone receptor to a step of light of 0.5 s (in ordinates), versus the luminous intensity of the step (abscissa, log units). The retina was adapted to different levels of background illumination before the responses were measured, providing different ‘response curves’. Through light adaptation mechanisms, the receptor’s response curve is shifted so that response to the adapting illumination (red crosses) be always in the ‘middle’ of the curve. From Normann and Perlman 79 [123].

illumination²². By opposition, pigment depletion clearly enters the ‘slow’ category, with depletions and recoveries occurring in the order of one minute [151, 172].

Remark: Weber and Fechner laws

A classical experiment in psychophysics consists in finding, for a given background intensity I , the threshold difference of intensity ΔI which can be detected by an observer. In fact, a relation of proportionality holds over a large range of background illuminations:

$$\frac{\Delta I}{I} = cst, \quad (3.13)$$

a relation known as *Weber’s Law*. The physiological correlate of Weber’s law can be seen in the receptor responses of Figure 3.37: The slope of the receptors’ response curve, in a logarithmic scale, is relatively independent of the adapting background luminosity I , meaning that the threshold ΔI inducing a fixed amount of response remains proportional to I .

Relation (3.13) is often integrated to derive a formula where the receptor’s instantaneous response is

$$R \sim \log(I),$$

I being the instantaneous incident luminosity. This relation, known as *Fechner’s Law*, is true only if one supposes that adaptation to light is an *instantaneous* phenomenon. In the log representation of Figure 3.37, Fechner’s law would predict a single, linear response curve. As can be seen in Figure 3.37, the real instantaneous response to an incident luminosity I_2 is also determined by the ‘recent’ value I to which the receptor has been adapted. The receptor

²²This duration of one second seems somewhat at odds with the faster adaptation constant τ_{Ca} required by Van Hateren and Lamb 06 [175]. Again, this raises questions concerning the respective extracellular concentrations of calcium between the two experiments (see Section 1.1.2).

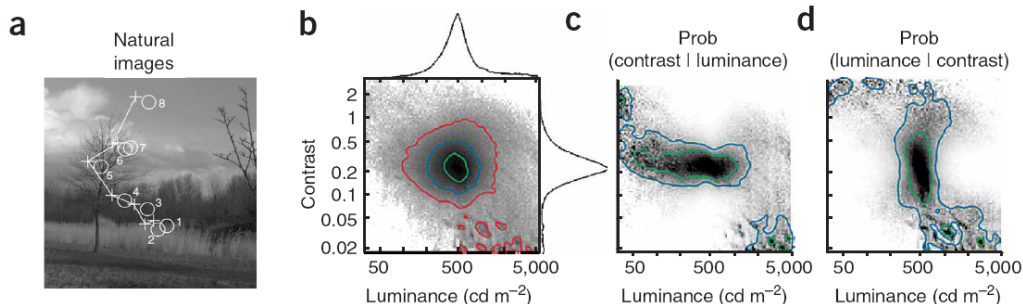


Figure 3.38: *Luminance and contrast have independent statistics in natural images.* The statistical distribution of luminance and contrast across small image patches from natural scenes (a) reveals a factorial distribution (b) and thus, statistical independence. This is confirmed by a representation of the conditional distributions $P(\text{cont}|\text{lum})$ (c, data from b normalized by its projection along vertical slices) and $P(\text{lum}|\text{cont})$ (d, data from b normalized by its projection along horizontal slices). From Mante *et al.* 05 [102].

can possibly saturate if I_2 is very different from I , at odds with Fechner’s law. ■

5.2 Contrast gain control

In this section we present the phenomenon of *contrast gain control*, or *contrast adaptation*, a particular nonlinearity in the responses of retinal cells to stimuli of different contrasts. A scheme of contrast adaptation has been implemented in our model and simulator (Chapter 4), so we spend some time presenting the effect, quite universal in vertebrate retinas.

5.2.1 Contrast, and the statistics of natural images

Contrast. The precise definition for the ‘contrast’ of a stimulus is variable. The underlying idea, though, is always the same: The ‘contrast’ seen by a cell located at (x_0, y_0) on the retina is derived from the values of

$$c(x, y, t) = \frac{|I(x, y, t) - \hat{I}|}{\hat{I}}, \quad (3.14)$$

where (x, y) belongs to some neighborhood of (x_0, y_0) (typically, the cell’s receptive field), $I(x, y, t)$ is the instantaneous luminosity at point (x, y) and time t , and \hat{I} is some ‘average’ value for luminosity in the sequence, generally defined as a spatial and/or temporal linear average. Generally also, the ‘contrast’ seen by the cell is defined as an average, spatial and/or temporal, for $c(x, y, t)$ over the simulation. We refer to Shapley and Enroth-Cugell 84 [154] for more rigorous definitions (Rayleigh contrast, Michelson contrast).

Contrast, luminance, and retinal responses. The level of contrast is an easy measure to define in artificial images such as drifting grating (amplitude of the sinus divided by the mean luminance), moving bars (difference of intensity between bar and background, divided by background intensity), etc.

In natural images and sequences, by opposition, contrast is not a global feature anymore, but rather a local value depending on which part of the image/sequence is considered. Mante *et al.* 05 [102] have recently led a study on the statistics of luminance and contrast in randomly chosen patches of natural images (Figure 3.38). They found that the distributions of contrast and luminance are generally *independent*, whatever the nature of the observed natural scene (clouds, forest, etc.).

In parallel, Mante *et al.* 05 [102] have recorded the responses of ganglion cells to these various patches of images. Interestingly, they found that retinal responses are well explained by a model with two *independent* stages of gain control: The first providing only independence to luminance, and the second only to contrast. So, retinal processing apparently ‘sticks’ to the independence of luminance and contrast in natural scenes. These results suggest that invariances to luminance and contrast are provided by distinct stages of retinal processing, as it has long been suspected from physiological observations: Adaptation to luminance is supposed to occur mostly in receptors and horizontal cells, while adaptation to contrast occurs in bipolar cells and on (see the next sections).

In the scope of our model, the results of Mante *et al.* –regardless of necessary experimental limitations on their reach– confirm that even in a simulator bound to function on normalized digital sequences (thus greatly removing issues of luminance adaptation), a nonlinear stage of contrast adaptation is still mandatory to produce correct magnitudes for the responses of the modeled cells.

In the rest of this section, we further characterize the expression of contrast gain control and its possible perceptual consequences, through the presentation of fundamental experimental results.

5.2.2 Multi-sinus experiments

We start by presenting the Shapley and Victor 78 [155] multi-sinus experiments, which gave the first quantitative measures of contrast gain control in the retina. These experiments were pursued on an ON-center cat X cell. Input stimulus $L(x, y, t)$ was a static grating of fixed mean luminance $\bar{L} = 20 \text{ cd/m}^2$, temporally modulated by a sum of sinusoids with adjustable contrasts:

$$L(x, y, t) = \bar{L} \left(1 + \text{Gr}(x, y) \sum_{i=1}^8 c_i \sin(\xi_i t) \right), \quad (3.15)$$

where $\text{Gr}(x, y)$ is a sinusoidal grating function with normalized amplitude (between -1 and 1). The ξ_i are a set of eight temporal frequencies that logarithmically span the frequency range from about 0.2 Hz to 32 Hz, respectively associated to contrast strengths c_i .

Recordings were made for different distributions of the c_i . For each recording, the cell’s output firing rate was Fourier-analyzed at each of the input frequencies ξ_i , thus yielding a set of eight amplitudes and eight phases. This set provided a measure for the linear kernel (first-order Wiener kernel) that best fits the cell’s response, *in the given contrast conditions*.

Influence of the mean level of contrast

This first experiment measures how the mean level of contrast changes the best-fitting first-order Wiener kernel for the cell. The c_i are all fixed at the same value $c_i = c$, global level of contrast for the stimulus. The experiment is repeated for four values of contrast, c being doubled each time.

Remark: When $\forall i, c_i = c$, the temporal part of signal (3.15) is related to a *pink noise* stimulus (with similar power in each frequency octave, so that for a 1D signal the power spectrum is $\sim |\xi|^{-1}$). Indeed, the power spectrum of (3.15) is uniformly distributed in logarithmic scale, just like pink noise. However, the spectrum of (3.15) is concentrated on eight discrete values, unlike a real pink noise. The ‘pink’ spectrum plays a privileged role in natural stimuli (for example, *spatially*, natural images have similar power in each octave (Field 87 [64]). ■

The resulting amplitude and phase diagrams for the cell’s output, represented in Figure 4.8- A and B, reveal deviations from linearity: If the ganglion cell responded linearly to its input, the modulations in its response would simply be proportional to c . Successive amplitude curves in Figure 4.8-A would be parallel, spaced by $\log(2)$ as contrast is doubled, and all phase curves in Figure 4.8-B would superimpose, since the phase portrait depends only on the nature of the linear filter.

Instead, the cell responds under-linearly to contrast at low temporal frequencies, where successive amplitude curves are spaced by less than $\log(2)$. In the phase portrait, strong contrasts induce a phase-advance of the response (phase curve shifted upwards), meaning that the cell responds *faster* at high contrasts. As resulting from these experiments, contrast gain control is thus characterized by the double behavior:

- Amplitude compression at low frequencies,
- Phase advance with increasing contrasts.

The authors found the two phenomena to be highly correlated in their experiments, probably resulting from a common mechanism. In our model (Chapter 4), we will take both phenomena into account in the simplest of ways, through a variable resistance in an ‘RC’ circuit.

The basic role of contrast gain control is obviously to limit the response of the system at high input contrasts, thus avoiding saturation at high contrasts, and providing a relative enhancement of small contrast stimuli. However, behind this simplified formulation, it is not so clear how the physiological measurements of contrast gain control are reflected in functional and perceptual effects. The issue is presented in more details in Section 5.2.5.

Frequencies that induce contrast gain control

For the moment, we present a second experiment that was crafted by the authors [155] to further investigate the origin of the gain control mechanism. It reveals that the contrast gain control mechanism is preferentially triggered by stimuli with fast temporal variations, in the range of 3 – 10 Hz. It thus constrains models that can be used to reproduce the effect.

Each input frequency ξ_{i_0} is successively chosen as a ‘carrier’ frequency with $c_{i_0} = 0.2$, while the other frequencies are added as perturbation terms: $c_i = 0.0125$ for

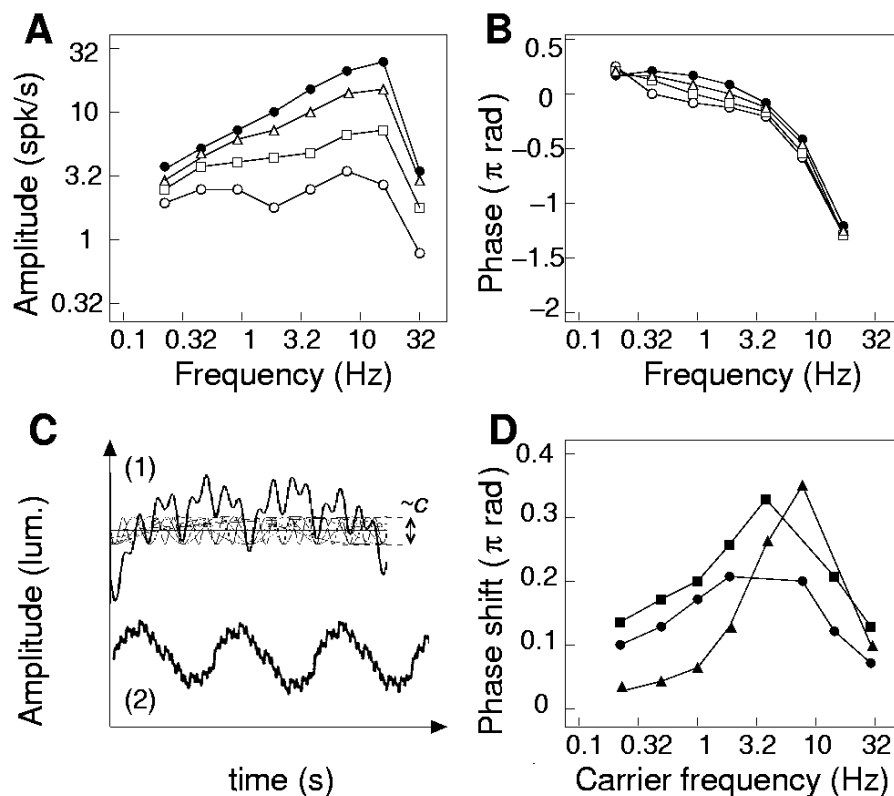


Figure 3.39: Contrast gain control in a cat ON-center X ganglion cell. A and B: Response to multi-sinus stimuli of different contrasts c (sample input signal depicted in panel C-1). Amplitude curves (A) reveal under-linearity at low temporal frequencies. Phase curves (B) reveal time advance for high contrasts (see text). Successively, c was 0.0125 (white circles), 0.025 (\square), 0.05 (\triangle) and 0.1 (filled circles). D: Strength of the gain control effect depends on the dominant frequency ξ_{i_0} present in the input (stimuli with a carrier frequency ξ_{i_0} , as depicted in Panel C-2). The three curves represent indicators $\phi_5(\xi_{i_0})$ (filled circles), $\phi_6(\xi_{i_0})$ (\blacksquare) and $\phi_7(\xi_{i_0})$ (\blacktriangle) which measure the strength of the gain control (see text). Frequencies that elicit the most gain control are $\xi_{i_0} = 3\text{--}10$ Hz. From Shapley and Victor 78 [155].

$i \neq i_0$ (see equation (3.15)). Results are compared to a ‘low contrast’ test condition where $c_i = 0.0125$ for all i .

For each carrier frequency ξ_{i_0} three phase advance indicators $\phi_5(\xi_{i_0})$, $\phi_6(\xi_{i_0})$ and $\phi_7(\xi_{i_0})$ are measured, respectively associated to *assay frequencies* $\xi_5 = 3.9$ Hz, $\xi_6 = 7.8$ Hz and $\xi_7 = 15.6$ Hz. $\phi_5(\xi_{i_0})$ is obtained by measuring output phase at the assay frequency ξ_5 when ξ_{i_0} is the carrier frequency, and subtracting the output phase at ξ_5 in the low-contrast test condition; similarly for $\phi_6(\xi_{i_0})$ and $\phi_7(\xi_{i_0})$.

Since contrast gain control can be measured by a phase advance (previous paragraph), $\phi_5(\xi_{i_0})$, $\phi_6(\xi_{i_0})$ and $\phi_7(\xi_{i_0})$ provide three indicators, hopefully highly correlated, of the strength of the gain control induced by ξ_{i_0} .

Figure 4.8-D represents experimental measures for $\phi_5(\xi_{i_0})$, $\phi_6(\xi_{i_0})$ and $\phi_7(\xi_{i_0})$. As predicted, the three indicators are highly correlated, consistently with the global time advance induced by contrast gain control. Phase advance is strongest when the carrier ξ_{i_0} is around 3 – 10 Hz. This reveals that the underlying mechanism for the contrast gain control measured here has a ‘band-pass’ sensitivity, being preferentially triggered by temporal variations around 3 – 10 Hz.

Contrast gain control in different types of cells

Retinal cells in most species are subject to contrast gain control. Shapley and Victor 78 [155] measured the effect in both X and Y cat cells (but stronger in Y cells), and measurements in salamander cells (next section) also reveal contrast gain control in different subtypes of cells, although with certain asymmetries, e.g., between ON and OFF cells (Chichilnisky and Kalmar 03 [32], and next section).

However, a notable exception seems to be the case of primate midget cells, which have been reported to display little contrast adaptation (Bernadete *et al.* 92 [13]).

5.2.3 Contrast gain control and LN analysis

Let us now present more recent experiments, which have provided new insights on the nature of contrast gain control. A good number of these experiments (plus the Mante *et al.* 05 [102] experiment presented in Section 5.2.1) are based the application of LN analysis to a cell at different levels of contrast, to measure contrast-related changes in the LN structure.

‘Fast’ and ‘slow’ contrast adaptations

Two independent experiments (Kim and Rieke 01 [93], Baccus and Meister 02 [5]) have recently revealed that different (at least two) mechanisms contribute to contrast adaptation in ganglion cells. More precisely, a distinction can be made between ‘fast’ and ‘slow’ adaptations to contrast.

The experiment reproduced here (Figure 3.40) is that of Baccus and Meister 02 [5]. They exposed salamander ganglion cells to alternative epochs of high and low contrast white noise stimulus (one ‘adaptation epoch’ is represented in Figure 3.40-A – note the beginning of a new epoch at the far right), and performed LN analysis on a few seconds’ periods of firing for the cell, at different instants during the adaptation epoch (Figure 3.40-A, bottom). First, LN analysis could be performed on the cell whether during high (H) or low (L) contrast stimulation. Second, the period used for analysis could either be at the *beginning* of a new contrast epoch (periods noted H_{early} and L_{early}), or at the *end* (H_{late} and L_{late}).

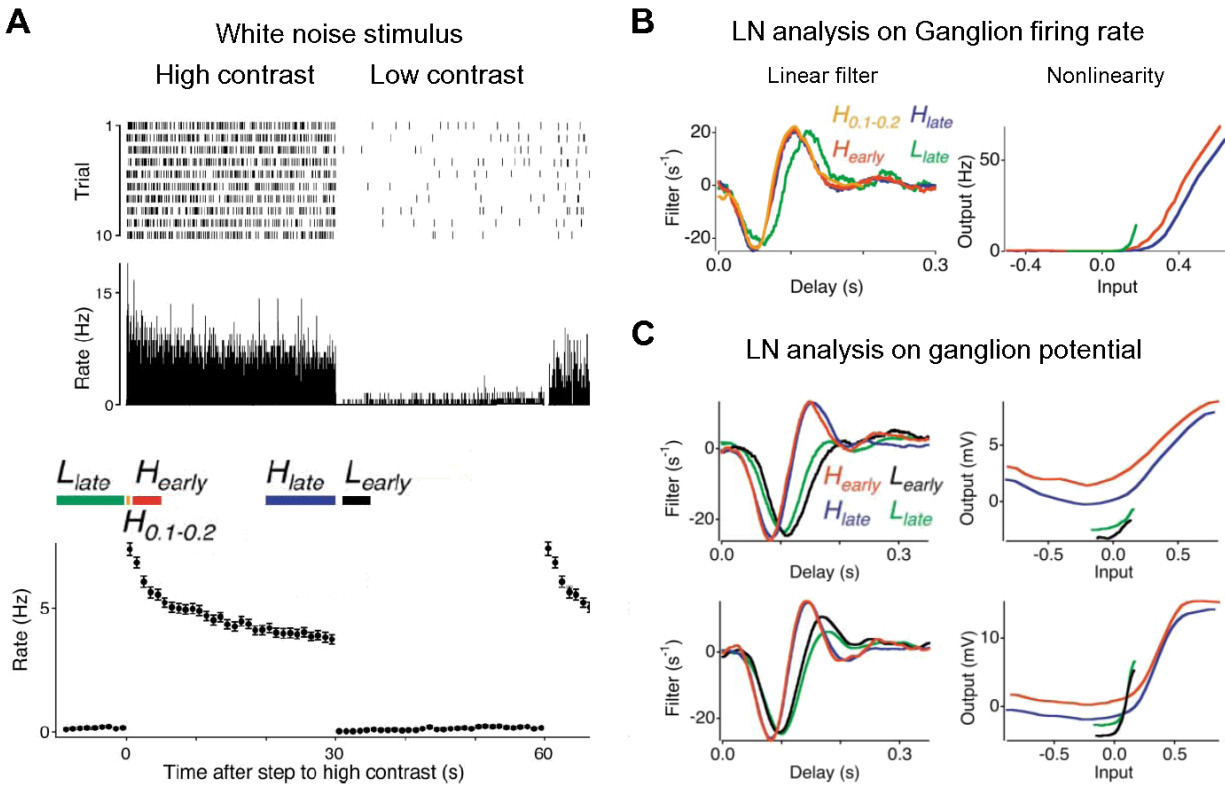


Figure 3.40: *‘Fast’ and ‘slow’ contrast adaptation in the salamander retina.* When a cell undergoes an alternation of high and low contrast epochs, its filtering properties continuously change, as measured from LN analysis performed at different instants of the cycle (Panel A, see text). The LN results (Panels B and C) reveal two speeds of adaptation. ‘Fast’ adaptation lowers the amplification gain of the cell (smaller slope in the ‘Nonlinearity’ panels) and speeds up filtering (time advance in the ‘Linear filter’ panels), in a few hundreds of milliseconds. ‘Slow’ adaptation progressively shifts the cells’ baseline potential downwards, over several tens of seconds, as reflected in the ‘Nonlinearity’ panels.

The resulting analysis was performed for different cells throughout the whole retinal pathway. Here, we only show results of LN analysis obtained from ganglion cells' firing rates (Figure 3.40-B) and intracellular potentials (Figure 3.40-C). They reveal two distinct components of adaptation.

'Fast' component. The strong difference in LN characteristics for the cell between periods right before and after a change of contrast (L_{late} to H_{early} , and H_{late} to L_{early}) reveals a 'fast' component of contrast adaptation. It is characterized by a double impact on the LN characteristics for the cell:

1. A reduction of the filtering gain at high contrasts, as measured by the lowered slope of the LN static nonlinearity in the 'H' modalities as compared to the 'L' modalities (Figure 3.40-B, 'Nonlinearity' panel).
2. A reduction of the time scale of filtering at high contrasts, as measured by the time advance of the best-fitting LN linear filter between the 'H' and 'L' modalities (Figure 3.40-B, 'Linear filter' panel).

These two effects precisely correspond to the dual mark of contrast gain control, as measured by Shapley and Victor 78 in their original experiments (Section 5.2.2).

Further evidence for the speed of apparition of the fast gain control is provided by the response of the cells during the 100-200 ms period right after onset of the high contrast (period noted $H_{0.1-0.2}$ in Figure 3.40): The best-fitting linear filter is already characteristic of 'high' rather than 'low' contrast behavior (Figure 3.40-B, 'Linear filter' panel).

'Slow' component. By opposition, a more subtle change occurs between the beginning and end of an epoch of same contrast (H_{early} to H_{late} , and L_{early} to L_{late}), revealing a 'slow' component of contrast adaptation. The main expression of the slow adaptation is a progressive downwards shift of the LN static nonlinearity between beginning and end of the epoch, which can be observed both at the level of firing rates (Figure 3.40-B, 'Nonlinearity' panel) and of intracellular potentials (Figure 3.40-C, 'Nonlinearity' panel). The downwards shift suggests an effect intrinsic to the spiking ganglion cell, such as the opening of specific conductances that would shift the cell's baseline potential downwards.

Biological origins of fast and slow gain controls

Another study in salamander cells was pursued in parallel by Kim and Rieke 01 [93, 139], which has led to similar conclusions as the study of Baccus and Meister 02 (preceding paragraph). Furthermore, thanks to comparative study of the effect in ganglion cells (Kim and Rieke 01 [93]) and bipolar cells (Rieke 01 [139]), their study provided supplementary insights on the biological origins of gain controls.

We here review their results, and those from previous work, which have started to clarify the underlying mechanisms of contrast adaptation in bipolar and ganglion cells.

Fast adaptation in bipolar cells. Interestingly, fast contrast adaptation is already observed to a large extent in bipolar cells (Mao *et al.* 98 [103], Shiells and

Falk 99 [159], Nawy 00 [117], Rieke 01 [139]), whereas it is absent from the previous layers of cells (receptors and horizontal, Rieke 01 [139], Baccus and Meister 02 [5]).

However, the origin of the gain control in bipolar cells is still controversial. Here are the main possible hypothesis, and how they have been infirmed / confirmed by recent experiment:

- *Feedback inhibition from amacrine cells* has been the ‘historical’ claim. However, this hypothesis has been infirmed by recent studies (Rieke 01 [139], and also Beaudoin *et al.* 07 [10] in mammalian retina), as contrast gain control is still observed under blockade of all amacrine synapses.
- *Voltage-gated conductances* can easily account for the time advance and gain reduction typical of contrast gain control (see the discussion in our model, Chapter 4, Section 8.2). Mao *et al.* 98 found that current injected into salamander bipolar cells could elicit contrast gain control depending on the strength of the average input current, and that adaptation was eliminated after blockade of a potassium current, suggesting that the adaptation might be elicited by voltage-gated potassium (inhibitory) currents. On the other hand, Rieke *et al.* 01 [139] found no effects of voltage nor current clamps on the adaptation properties of the cells, in contradiction with a voltage-dependent origin for the adaptation. In the end, the role of voltage-gated conductances remains controversial.
- *Calcium adaptation in bipolar dendrites* has been observed as another plausible candidate. In ON salamander bipolar cells, Nawy 00 [117] found that contrast adaptation in bipolar cells is associated to a rise in intracellular $[Ca^{2+}]$, and that the adaptation was largely suppressed when Calcium was buffered from the intracellular medium²³ (see also Shiells and Falk 99 [159]). Oddly, still in the salamander, Rieke 01 [139] also found that calcium buffering affected adaptation in bipolar cells, but rather in OFF type than ON type. Anyway, it seems likely that calcium plays a crucial role in contrast adaptation.
- *Feedforward control from horizontal cells* has sometimes been hypothesized. However, Rieke 01 [139] demonstrated that contrast gain control persists in bipolar under blockade of horizontal cells.
- The fast *desensitization/recovery* of bipolar cell AMPA receptors at the cone synapses (De Vries 00, Section 2.4) is also an intrinsically nonlinear phenomenon. Its modalities should be studied in more detail to investigate its possible role in contrast gain control.

Slow adaptation in ganglion cells. By opposition, the ‘slow’ adaptation effect seems rather weak in bipolar cells (Rieke 01 [139]), although some slow changes have also been reported (Baccus and Meister 02 [5]).

Rather, slow adaptation seems to be particularly strong at the level of the ganglion cells themselves. Kim and Rieke 01 [93] have suggested that spike-frequency

²³This observation may recall calcium adaptation in photoreceptors. In fact, the whole scheme of activation of ON bipolar cells through the metabotropic receptor mGluR6 and a messenger G protein – as imposed to produce a hyperpolarization in response to the excitatory transmitter glutamate (Section 2.1) – is strikingly similar to that occurring in phototransduction (1.1).

adaptation (inhibitory conductance which slowly builds up with repeated spikes) may be largely responsible for the process. In their proposed scheme, bipolar cells would account for most of the fast adaptation, and ganglion cells for most of the slow adaptation.

Undoubtedly, the arousal of contrast adaptation is not a closed subject yet, especially in bipolar cells, for which experimental data is still relatively rare.

5.2.4 Modeling contrast gain control

Many models of temporal contrast gain control rely on the original ideas introduced by Shapley and Victor 81 [156] (general form for linear temporal filtering in ganglion cells) and Victor 87 [178] ('neural measure of contrast' applied as feedback). We present their model in a 'general' form, and some of its subsequent applications / simplifications in other model.

The Shapley and Victor 81 model

In Shapley and Victor 81 [156], the authors proposed a general form for temporal linear filtering in ganglion cells, from input signal $X(t)$ to output signal $Y(t)$. This filter involves a cascade of low-pass filters followed by a single high-pass stage. In our terminology for linear filters introduced in Chapter 2, Section 3, the general form writes:

$$Y(t) = AT_{w_H, \tau_H} * E_{n_L, \tau_L} * X(t). \quad (3.16)$$

Shapley and Victor 81 [156] fitted the parameters of this formula to reproduce the response curves of ganglion cells at different contrasts (as in Figure 3.39 A-B). However, they did not provide equations to link the various parameters to the levels of contrast, so that (3.16) was used only in a descriptive, not predictive, fashion.

The Victor 87 model

In Victor 87 [178], the author proposed an enhancement of (3.16) allowing to reproduce the curves at different contrasts from a single set of parameters (Figure 3.41-A). Naturally, some dynamic nonlinearity must be introduced in the system to reproduce the nonlinear responses of Figure 3.39 A-B. The 'minimal' solution proposed by Victor, in order to reproduce the responses of X cell *center* signals, is to make the high-pass time constant τ_H in (3.16) a dynamic value of the cell's own recent level of response:

$$X_L(t) = E_{n_L, \tau_L} * X(t), \quad (3.17)$$

$$\tau_H(t) \frac{dY}{dt} = \tau_H(t) \frac{dX_L}{dt} + (1 - w_H)X_L(t) - Y(t), \quad (3.18)$$

where $\tau_H(t)$ is now an instantaneous time constant, whose value is determined by the recent values of contrast, as measured from the cell's own recent activity $Y(t)$:

$$c(t) = E_{\tau_C} * |Y|(t), \quad (3.19)$$

$$\tau_H(t) = \tau_H^0 \frac{c_{1/2}}{c_{1/2} + c(t)}. \quad (3.20)$$

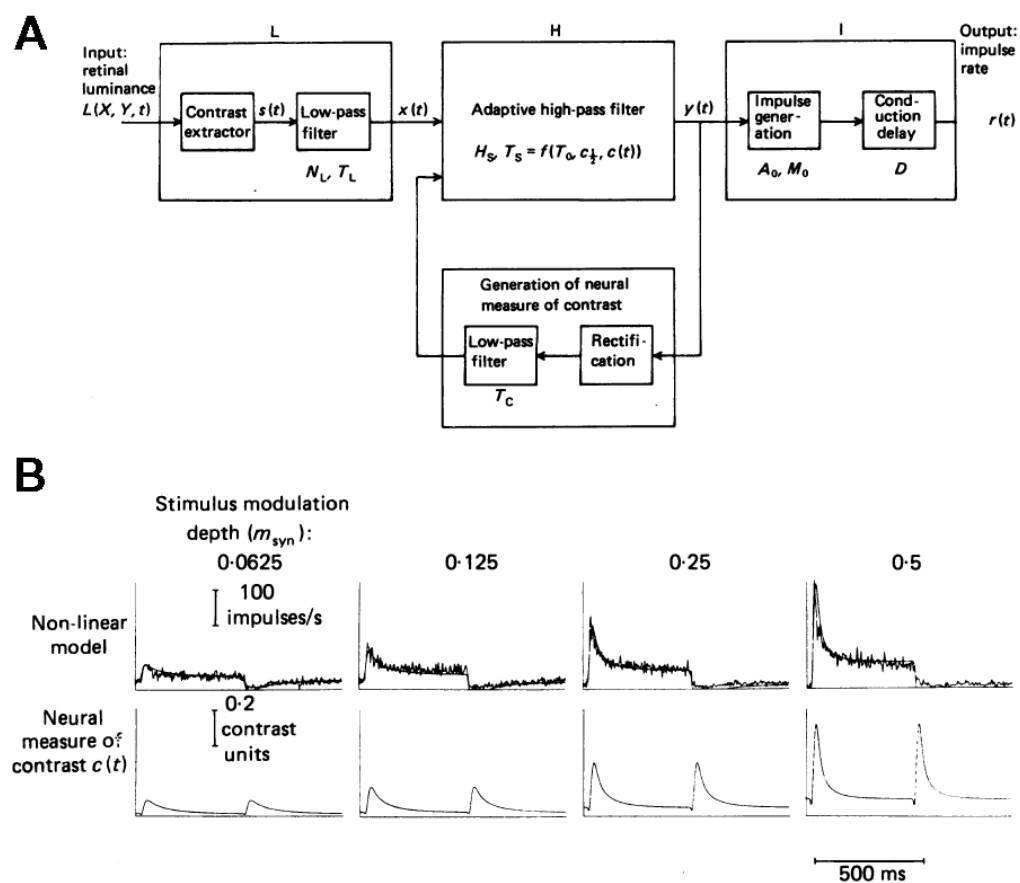


Figure 3.41: *The Victor 87 model for temporal gain control.* A: Schematic representation of the model. After a traditional stage of low-pass linear filtering (box L), a high-pass stage is added (box H), whose instantaneous time constant $\tau_H(t)$ depends on the recent values of contrast, as measured by feedback from the cell's own recent levels of response. B: The model successfully reproduces the progressive shortening of real cells' response time, in response to grating reversals of increasing contrasts. The 'neural measure of contrast' $c(t)$ is derived from the cell's own recent levels of activity, positive or negative (typically, with time constant $\tau_C=15$ ms). From Victor 87 [178].

Note that (3.18) is directly linked to filter T_{w_H, τ_H} in the linear system (3.16). If τ_H was constant, (3.18) would simply be the linear ODE implementing convolution by T_{w_H, τ_H} (see Chapter 2, Section 3). Here, the ODE formulation allows extension to the nonlinear case where $\tau_H(t)$ depends on the current estimation of contrast $c(t)$ (3.20), as measured by an average (3.19) of $|Y(t)|$ over recent time, with time constant τ_C (typically small, around 15 ms).

Finally, the cells' response (firing rate) is derived from $Y(t)$ through amplification, rectification, etc. (Figure 3.41-A).

The Victor model performs well on reproducing responses of an X cell to grating reversals at different contrasts, including the progressive speeding-up of the transient as contrasts get higher (Figure 3.41-B).

Derived and alternative models

Feedback measure of contrast. A strong idea of the Victor 87 model was to introduce contrast gain control thanks to a feedback derived from the cell's own recent levels of activity. Several models of gain control have been built on the same principle: See e.g. the Y cell model of Enroth-Cugell and Freeman 87 [58], or the Van Hateren *et al.* 02 model for primate Parasol cells [173].

Explicit dependence of filtering gain. In the original model of Victor 87, the contrast gain control mechanism only acts on the temporal scale τ_H of the high-pass stage: Contrast does not explicitly modify the *gain* of filtering, as defined by A in (3.16). In fact, such a dependence of A is not mandatory for the Victor model to reproduce frequency kernels as in Figure 3.39 A-B, because the cut-off frequency τ_H^{-1} of the high-pass stage augments with input contrast, strongly 'cutting off' low temporal frequencies only in the case of high input contrasts.

However, an explicit dependence of A on input contrast is more intuitive, and often convenient for modelers. Some models explicitly add a control on A , based on recent values for the cells' activity (Van Hateren *et al.* 02 [173]). Finally, some modelers totally forget the dependence of the time scale τ_H on contrast (possibly even, forget the totality of the high-pass stage), and simply implement a feedback control on A . This is for example the case of the gain control model in Figure 3.42.

Varying resistance in an RC model. In an old model for light adaptation in horseshoe crab photoreceptors, Fuortes and Hodgkin 64 [68] proposed that both time advance and gain reduction (which are linearly anti-correlated during light adaptation) could arise from a simple extension of a first-order RC equation, but with an adaptable resistance. This gives, in reduced units:

$$\frac{dY}{dt} = X(t) - Y(t)/\tau_L(t), \quad (3.21)$$

where $\tau_L(t)$ (obtained as $\tau_L(t) = R(t)C$) is a function of recent illumination levels (model reviewed in Enroth-Cugell and Shapley 84 [154]).

If τ_L remained constant, (3.21) would be the ODE expression of convolution by $\tau_L^{-1}E_{\tau_L}$ (Chapter 4, Section 3). It is thus the direct extension of a low-pass filter. Such a scheme is likely the simplest implementation allowing to reproduce the dual

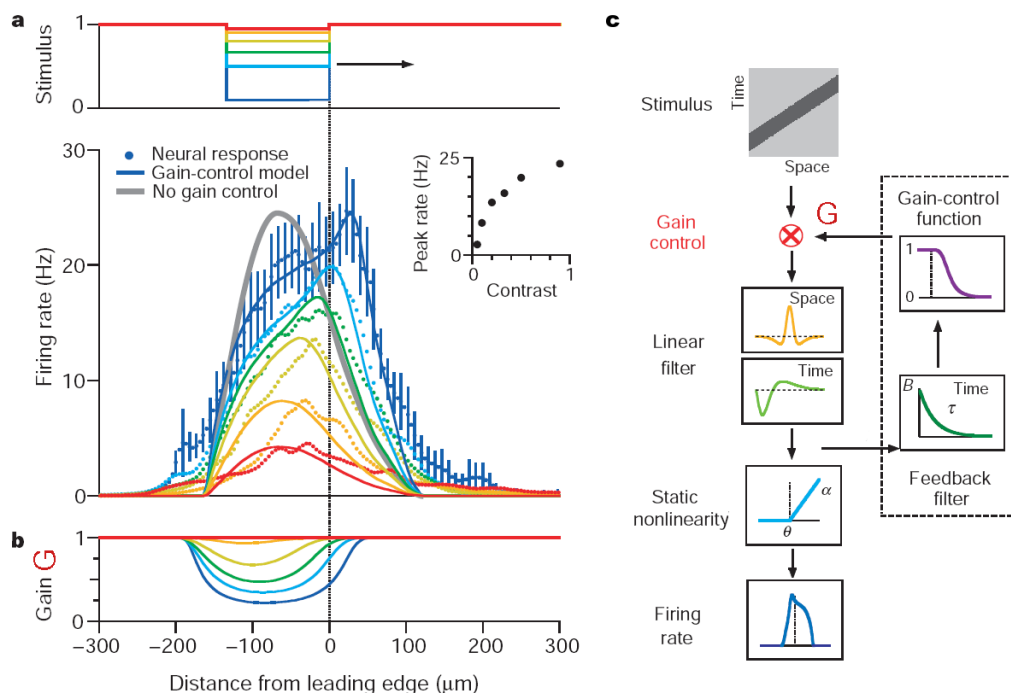


Figure 3.42: *The leading edges of a moving bar are enhanced at high contrast.* *a:* In response to a drifting bar (width $133 \mu\text{m}$, speed 0.44 mm s^{-1}) at different contrasts, salamander ganglion cells progressively shift from a ‘linear’ response profile at low contrasts, with the peak lagging behind the bar’s leading edge, to an ‘enhanced’ profile at high contrasts, with the peak lying ahead of the bar’s leading edge. *b* and *c:* A simple model of contrast gain control, where the cell’s gain $G(t)$ is driven by a dynamic feedback (Panel *c*), is sufficient to account for the effect (Panel *a*, plain curves). The corresponding profile for $G(t)$ is given in Panel *b*. From Berry *et al.* 99 [14].

mark of contrast gain control: Gain reduction (because of the multiplication by τ_L^{-1}) and phase advance for high contrasts.

In our model (Chapter 4, Section 4), this is the implementation retained to account for contrast gain control. Its simplicity allows to rigorously track some of its mathematical properties (Chapter 5). However, such a scheme cannot by itself account for the high-pass behavior observed in Figure 3.39-A. It must thus be included in a broader model of retinal processing, as we perform in Chapter 4.

5.2.5 Perceptual impact of contrast adaptation

To conclude this presentation of contrast gain control, we question its possible functional, and even perceptual, roles. The first obvious answer is that it avoids saturation of bipolar and ganglion cells in response to high contrast stimuli. Or, put in another way, that it allows to enhance the response to low contrasts, relatively to the response to high contrasts.

However, characterizing with more precision the perceptual effects of the mechanism is not evident, because the strength of contrast gain control apparently depends strongly not only on ‘contrast’ (a rather vague definition, see Section 5.2.1),

but more precisely on the temporal (and possibly, spatial) composition of the input stimulus. As a single example, we refer to the various strengths of contrast gain control observed according to the dominant temporal frequency in the input (Figure 3.39-D).

Global repartition of contrast levels in the retinal image. In our model (Chapter 4, Section 7.2.2), we study the possible impacts of the gain control mechanism on the global repartition of contrasts in the output retinal image, especially when the local measure of contrast (function $c(t)$, eq. (3.19), in Victor’s model) is allowed to operate with a spatial extent.

These results suggest that contrast gain control may help to locally equalize the levels of contrast in the retinal output ‘image’, an effect which reminds some classical techniques in image processing.

Enhancement of moving object’s leading edges. However, the strongest presumed perceptual role for contrast gain control, supported by recent experimental data, is to allow enhancement of the leading edges of moving objects. This work of Berry *et al.* 99 [14] in the salamander retina is illustrated in Figure 3.42. For a moving bar of high contrasts, the lateral profile of activation for the cells is typically displaced towards the bar’s leading edge, at odds with the simple output of a linear filter (whose normalized profile is represented a single time, in gray).

This effect can be explained by a simple model of temporal contrast gain control, implemented by a varying gain G on the response of the cells. In this simple model, when cells at the leading edge are first reached by the advancing bar, they are adapted to the background’s low contrast, and thus respond with a high gain. As the bar advances over the cell, contrast gain control sets in, contributing to lower the response of cells once the leading edge has passed.

This effect might be an important perceptual role of contrast adaptation. Indeed, mammalian ‘Y-like’ cells, the presumed movement detectors, are the cells which are most subject to contrast gain control (Section 5.2.2, Paragraph “Contrast gain control in different types of cells”).

5.3 Slow adaptation and predictive coding

We have seen in the preceding sections that both adaptations to luminance and contrast presented at the same time fast and slow components. We argued that fast adaptations likely have a fundamental role in avoiding system saturation. The slow adaptations, conversely, seem to be precision mechanisms allowing to *optimize* the retinal response to its current type of stimulus, following different possible criteria.

Possibly, the optimizations provided by slow adaptation mechanisms serve an *economical* purpose, such as limiting the amount of fired spikes in response to strong stimulations, static stimuli, etc.

More precisely, it has been suggested that slow adaptation may help to optimize the *information transfer* in the retina, an idea obviously linked to the economical optimization mentioned above, since each fired spike provides additional information to the brain, but costs some energy to the cell.

The sort of coding schemes allowing the retina to optimize its information transfer are often referred to as examples of *predictive coding*. This denomination, some-

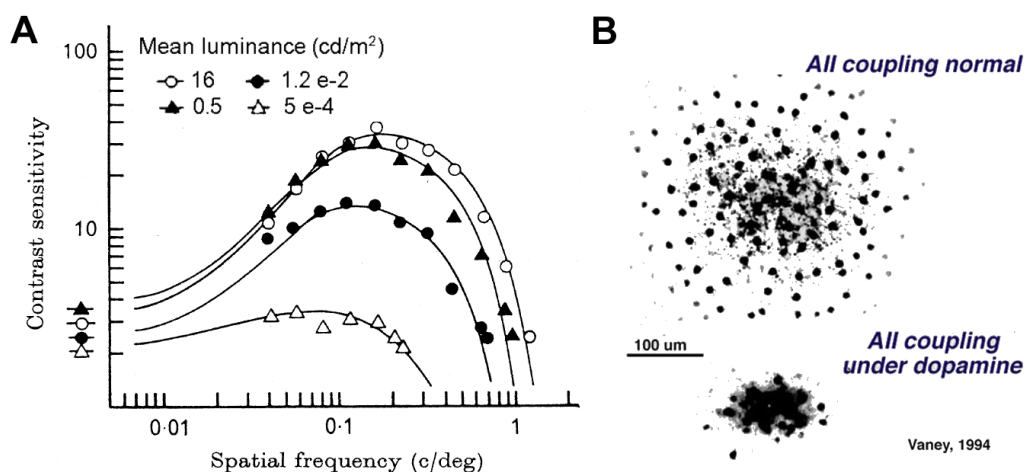


Figure 3.43: *Adaptation of retinal spatial filtering to background illumination.* A: The response (sensitivity) curves of ganglion cells become relatively more low-pass spatially at low illuminations, implying that spatial couplings likely become stronger at low illuminations (see text). From Enroth-Cugell and Robson 66 [59]. B: The modulatory effects of dopamine have been found to reduce the amount of gap junction spatial coupling, in various retinal cells, at high illuminations. From Vaney 94.

what frightening, comes from the fact that generally speaking, each cell should ‘remove’ from its response the part which can be *predicted* from the responses of its neighbors, in order to optimize independence of the various sources and thus, the output information rates.

We finish this presentation of nonlinear adaptations by two accounts of slow adaptation phenomena, which can be interpreted in terms of predictive coding.

5.3.1 Adaptation of spatial receptive fields to background luminance

Modulatory changes in the spatial structure of the retina. A particularly interesting slow modulatory effect is the dynamic change in the spatial structures of receptive fields for different levels of background illumination. Figure 3.43-A depicts the sensitivity of ganglion cells (inverse of the threshold contrast detectable by the cell) at different background intensities. At low illuminations, the sensitivity to contrast of the retina is globally diminished. Furthermore, the spatial cut-off frequency is lower for low illuminations, and there is no band-pass behavior anymore. All these observations can be resumed by saying that filtering in the retina becomes *more low pass spatially* under low illumination.

In fact, correlates to these physiological effects have been found anatomically, and appear particularly linked to the effects of dopamine. Dopamine is a neuromodulator of crucial importance in the brain. In the retina, it is believed to be released by specific *dopaminergic* amacrine cells, possibly directly in the extracellular medium, without the need for synapses²⁴. Importantly, dopamine is released in the presence of light. It has several modulatory effects at different stages of retinal processing. In particular, it is known to *uncouple* cells linked by gap junctions: Hor-

²⁴For references, we refer to the Webvision page <http://webvision.med.utah.edu/amacrine3.html#A18>

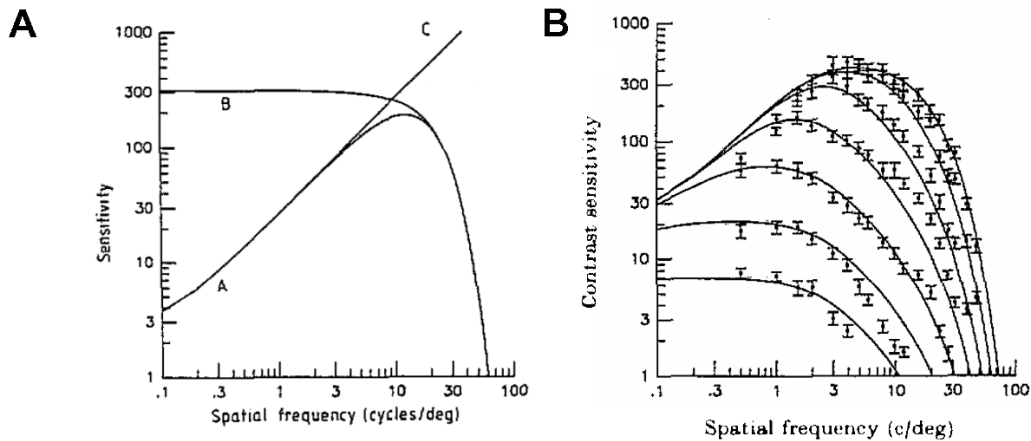


Figure 3.44: *Adaptation to background illumination and the decorrelation hypothesis.* *A:* Modeling by Atick 92 [4] of the trade-off between optimal decorrelation of ganglion cells' signals (high-pass filter 'C') and noise removal based on pooling from neighboring receptors (low-pass filter 'B'). The optimal filter 'A' is influenced by both behaviors. *B:* The formalism of Atick 92 [4] allows to find back the change of shape of real cells' sensitivity curves. Original data are psychophysical measures from Van Nes *et al.* 67 [176]. Background intensities range from $9 \cdot 10^{-4}$ to 900 photopic td, each time multiplied by 10.

izontal cells and various amacrine cells (such as the rod system's AII amacrine cell, Figure 3.43-B). As a result, dopamine contributes to make receptive fields smaller at high illuminations, with the likely physiological correlates of Figure 3.43-A.

Predictive coding. Interestingly, theoretical considerations (Srinivasan *et al.* 82 [162], Atick 92 [4]) allow to interpret illumination-related changes in spatial receptive fields. Both pieces of work have somewhat different formalisms, but the same underlying idea: To optimize information transmission in the presence of noise, ganglion cell receptive fields implement a trade-off between noise removal and statistical decorrelation of neighboring cells' outputs. More precisely:

1. To optimize *statistical independence* with their neighbors (and thus optimize information transmission, Atick 92 [4]), ganglion cells tend to perform a spatial opposition between their 'direct' signal and some neighborhood signal. Because of the typical amplitude spectrum of natural images ($\sim 1/|f|$, Field 87 [64]), the optimal decorrelating filter has a Fourier transform proportional to $|f|$ (line 'C' in Figure 3.44-A)(Atick 92 [4]). This sort of filter requires to use an 'infinitely small' neighborhood to perform the spatial opposition.
2. By opposition, to optimize *noise reduction*, the cells must proceed to spatial pooling over a *finite* neighborhood, whose extent depends on the typical length of spatial correlations in the noiseless input image, and on the signal-to-noise (SNR) ratio in the real, noisy image. The resulting pooled signal can be viewed as the best prediction by the cell of its own value, based on the values of its neighbors (Srinivasan *et al.* 82 [162]). In Atick's formalism, this 'optimal noise reduction pooling' is modeled as a low-pass filter (line 'B' in Figure 3.44-A), whose cut-off frequency depends on the SNR in the input image.

In the Fourier domain, the optimal retinal filter must then achieve a trade-off between decorrelation and noise removal. In Figure 3.44-A, Atick's optimal filter (line *A*) is thus constructed from the two preceding filters *B* and *C*.

Interestingly, the mean illumination I_0 of a scene has a profound influence on the SNR ratio. Indeed, the input of retinal processing, the photocurrent, is subject to an intrinsic 'phototransduction noise', with an incompressible background level (the 'dark noise') that does not scale with I_0 . So, the SNR in the photocurrent becomes significantly lower (more noise) at low illuminations. According to the preceding argumentation (point 2), this implies that spatial poolings must get larger at low illuminations.

Conversely, the value of I_0 does not change the nature of spatial correlations in an image (simply, the whole autocorrelation function is multiplied by I_0^2).

Figure 3.44 presents the formalization of these issues by Atick 92 [4], and an application to the reproduction of retinal sensitivity curves from the psychophysical literature. Because SNR changes, the pooling for optimal noise removal becomes more low-pass, following the same trend as real retinal processing (Figure 3.44 -*B*).

This is a very interesting result linking retinal physiology to advanced functional interpretations.

5.3.2 Predictive coding of spatio-temporal correlations in the stimulus

Recent work by Hosoya *et al.* 05 [81] has suggested that cells in the retina are even capable of adapting their receptive fields in response to much more complex spatio-temporal correlations in their input. An example of their results is presented in Figure 3.45. When presented with a 'complex' spatial structure (here a checkerboard, but see the whole article) for several seconds, a cell slowly adapts its receptive field to counteract the persistent correlations in the input. The resulting effect in terms of information transmission would be, here also, to increase independence of the responses of neighboring ganglion cells. The authors suggest that short-term synaptic plasticity in the IPL may be involved in this phenomenon.

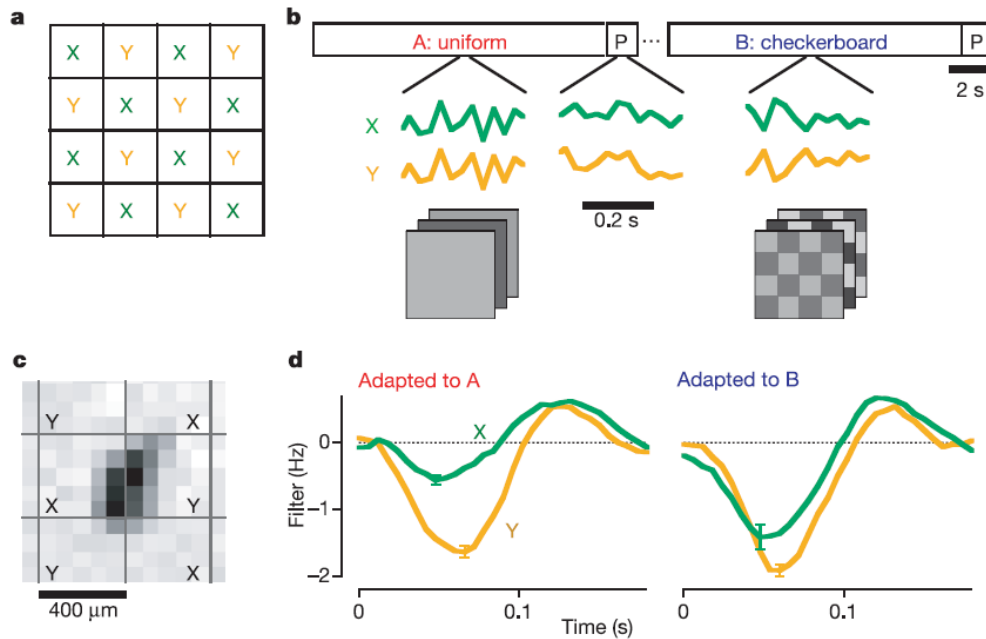


Figure 3.45: *Dynamic adaptation in the salamander retina.* *a:* Simple stimuli are based on a partition into two regions X and Y of homogeneous luminosity, following a checkerboard pattern. *b:* The cell is alternatively adapted to two environments A and B based on white noise. In A , the stimuli for regions X and Y are totally correlated (flickering uniform screen) while in B , regions X and Y are totally anti-correlated (flickering checkerboard). The cell's adapted response to both environments is measured by reverse correlation with an independent probe P , providing a kernel with only two spatial components: Response to X and response to Y . *d:* Adapted to environment A , the cell reveals a kernel with asymmetric weights between zones X and Y . When applied to environment B , this kernel would produce a response strongly biased towards the signal of zone Y . However, slow adaptation to environment B counteracts this bias, by enhancing the gain over zone X . As a result, the cell's response to environment B after adaptation is more centered around zero mean. From Hosoya *et al.* 05 [81]

Part II

A retina model: Definition, analysis and implementation

A RETINA MODEL, WITH CONTRAST GAIN CONTROL

In this chapter, we present the model we have chosen to implement in our simulator *Virtual Retina*. Our goal is twofold: Allow large scale simulations (up to 100,000 neurons) in reasonable processing times and keep a strong biological plausibility, taking into account implementation constraints. The model is mostly based on state-of-the-art knowledge about retinal processing, as described in Part I, with formulations adapted to large-scale simulation. Here, we focus on the chosen model and how it relates to experimental data. The organization of the simulator and its implementation are discussed in Chapter 6.

After introductory remarks and an overview of our model, we detail its three successive stages. The first stage (Section 3) is a linear filter that reproduces the center-surround architecture arising from the interaction between light receptors and horizontal cells. The second stage (Section 4) is a contrast gain control mechanism at the level of bipolar cells, driven by feedback conductances. The third stage (Section 5) provides additional temporal shaping of the signal, and then a spike generation process. Based on this model, we present two different types of results. First, we test the pertinence of the model against recordings of ganglion cells in different experiments (Section 6). Then, we show large-scale simulations and more qualitative results (Section 7), obtained with the large-scale software *Virtual Retina*. Finally, in Section 8, we discuss the nature of the model, and in particular of its contrast gain control stage.

Contents

1	Introduction	179
2	General structure of the model	181
2.1	A layered model in three stages	181
2.2	Mathematical framework and notations	184
3	First stage: The OPL filter	187
3.1	Equations of the system	187
3.2	Characteristics of the OPL filter	188
4	Second stage: Contrast gain control in bipolar cells	189
4.1	Motivations, and basic idea of the model	189

4.2	Equations of the system	190
4.3	Contrast gain control and Wiener kernels	192
5	Third stage: The IPL and ganglion cells	193
5.1	Synaptic current upon ganglion cells	193
5.2	Spike generation in ganglion cells	195
5.3	Ganglion cell sampling configurations	196
6	Physiological reproductions	197
6.1	X and Y cell responses to grating apparitions	197
6.2	Multi-sinus experiments	199
6.3	LN analysis	203
7	Large-scale simulations	205
7.1	Large-scale simulation of the model	205
7.2	Perceptual consequences of model architecture	207
8	Discussion	210
8.1	General discussion	210
8.2	Contrast gain control mechanism	215
	Conclusion	219

1 INTRODUCTION

Retina (and LGN) models are very numerous, ranking from detailed models of a specific physiological phenomenon, to large-scale models of the whole retina. However, interestingly, the category of large-scale models appears under-represented in retinal literature. The reason is simple: On one side, experimental researchers on the retina are not very interested in large-scale models that require mostly a compilation of already well-established results. On the other side, researchers that seek a retina/LGN input for further modeling (typically, of V1) often overlook the complexity of processing in the retina, and use very simplified retina models.

Our primary goal is to provide a better retinal input to modelers of the visual cortex. We hope that Part I of this work was a convincing illustration of the actual complexity of retinal processing, and of its functional importance for subsequent treatment: Band-pass filtering, gain controls, spiking synchronies, etc., form a pre-processing which is likely fundamental for further cortical interpretation. It is those *functional* implications of retinal processing that we wish to keep in our large-scale model. Reproducing biological complexity is not our primary goal. However, because the retina is an efficient machinery, a functional model to reproduce retinal specificities must *de facto* have an architecture quite close to that of a real retina, to allow the same sort of filtering operations.

Amongst models of retinal processing as a whole, some focus on a detailed reproduction of retinal connectivity in successive layers, each layer being modeled with a full set of cellular and synaptic parameters (see e.g. Balya *et al.* 02 [6] with an accent on retinal connectivity, or Hennig *et al.* 02 [75] with an accent on phototransduction). Other models take a more functional approach, built on a series of specific filtering stages, to produce a functionally efficient retinal output. In this group, another distinction can be made between models that aim at strong biological precision (see e.g. Hateren *et al.* 02 [173] for primate cells, Gazères *et al.* 98 [69] or Bonin *et al.* 05 [17] for LGN cells), and models more oriented towards signal processing and computer vision, with a consequent reduction of model parameters (e.g. the works of Herault and co-workers [79], or Thorpe and co-workers [47]).

As we have seen in Chapter 2, functional models of the retina often follow an *LN* architecture based on three successive stages: Linear filtering on the visual stimulus, static nonlinearity and then spike generation (Chapter 2, Section 5). Because of their generality and wide use, LN models have even been termed the retinal *standard model* by Carandini *et al* [29].

For *Virtual Retina*, we propose a model somewhere in-between all models cited above. It is definitely a functional model, with consequent simplifications regarding the complexity of retinal physiology. Still, it aims at a relative biological precision: This is verified by reproducing different experimental recordings on real retinal ganglion cells, including experiments not accounted for by linear models.

Also, LN models are a strong inspiration to the model we propose here: The first stage of our model consists of a spatio-temporal linear filter, and we make use of static nonlinearities. However, as opposed to LN models, we also incorporate a nonlinear mechanism of contrast gain control, inspired from retinal physiology and existing models. Furthermore, most LN models have an empirical architecture,

designed to fit some experimental ganglion cells recordings (see Chichilnisky 01 [31], Keat *et al.* 01 [89], Baccus and Meister 02 [5] etc.). Instead, we propose here a functional model suitable for large-scale simulation.

More generally, our model keeps an architecture strongly related to retinal physiology, in a desire to reproduce specific effects which are functionally important, and often discarded by large-scale models:

- *Non-separability of the center-surround filtering.* It is well-known that most ganglion cells have a *center-surround* receptive field organization which makes them more sensitive to image edges. In real retinas, the *surround* signal is transmitted with a supplementary delay of a few milliseconds (Chapter 2, Section 4). This delay is included in our model, since it yields consequent effects for the perception of uniform screens, or appearing images. A qualitative, large-scale illustration of this fact is provided in this chapter (Section 7.2.1).
- *Contrast gain control.* This specific nonlinear dependence of retinal filtering on the mean level of contrast (Chapter 3, Section 5.2) is modeled in an original framework, inspired by previous models, that can account simultaneously for gain controls due to the *temporal* and *spatial* structure of the stimulus. This contrast gain control model is carefully discussed, justified mathematically, and its perceptual consequences are suggested through qualitative simulations.
- *Adaptable band-pass temporal filtering.* To account for both sustained (tonic) and transient (phasic) cells, and the specificities of temporal shaping in the retina, we make use of successive difference-of-exponentials (DOE) filters.
- *Reproduce the parallel output pathways.* The model allows for the reproduction of the X-like and Y-like retinal pathways (Chapter 3, Section 3), which provide different outputs to the brain. The model for Y-like cells is inspired by previous modeling of cat Y cells (e.g. by Enroth-Cugell and Freeman 87 [58]). The possible implementation of other types of ganglion cells is also discussed at the end of this chapter.
- *Spike generation mechanism.* A possible spike generation process is proposed at the output of the software, with a model derived from experimental fitting of ganglion cell outputs by Keat *et al.* 01 [89] (Chapter 3, Section 4.2.4), that yields more realistic spike trains than a Poisson process.

None of the previously cited models of retinal processing displays simultaneously all these elements. In addition, our simulator can possibly include a log-polar scheme modeling the large-scale organization of primate retinas.

Let us start by a general presentation of the model's architecture, before entering the details of its successive stages.

2 GENERAL STRUCTURE OF THE MODEL ---

2.1 A layered model in three stages

2.1.1 Conception of the model

When it comes to modeling a retina on a large scale, two major issues have to be dealt with. The first issue is to grasp the functionality of the different filtering stages in a real retina: Phototransduction, synaptic interactions in the OPL, in the IPL, and spike generation. Grasping this functionality is not easily done, because it is very *distributed*: Elements such as synaptic poolings, signal rectifications, and various temporal transformations of the signal occur all along the retinal pathway, as we have presented in Chapter 3. Furthermore, feedback mechanisms occur at different levels, and there is no real certitude regarding the strength and location of these feedbacks. Some modulatory feedbacks, e.g. by dopanimergetic amacrine cells, are likely to affect all previous processing, up to photoreceptors.

By opposition, one would like a large-scale model to have functionalities much more *concentrated*, in order to remain conceptually simple. We tried to keep some of this conceptual simplicity by defining the model as a feedforward series of distinct stages, with distinct functions. This necessarily implies some sacrifices regarding biological plausibility, especially feedbacks.

However, the retina is an ordered structure that naturally provides these successive ‘stages’: Synaptic interactions in the OPL and in the IPL are largely independent, only linked by the turntables that are bipolar cells. Following this biological inspiration, we made our three stages the crude models of successively the OPL, bipolar cells, and the IPL. In the sequel, biological terms are applied to many of our modeling elements: ‘OPL current’, ‘bipolar current’, etc. We always keep in mind how these terms refer to our simplified model architecture, rather than the complex biological reality.

The second issue for a large-scale model is to account for the diversity of the retinal output. Sections 3 and 4 of Chapter 3 have illustrated how this output in fact consists of several parallel pathways of information, with strongly different properties of filtering and spiking. Which of these pathways should be kept in a large-scale model is not an easy question: It depends more on the requirements of potential users, than on some absolute measure of ‘utility’ of the different pathways, which is still a controversial subject amongst retinal specialists. It can be argued that some cells such as direction-selective cells, although very interesting, may not be of crucial interest for modelers of the cortex, since there is no evidence that they provide input to thalamo-cortical circuits. But if they did? And what about sluggish cells which likely constitute a source of input to the LGN: Local edge detectors, orientation-selective cells, or sluggish concentric ‘Q’ cells? We have rapidly evoked how some of these cells might play a computational role in diffusion processes, or multi-scale signaling.

As a first step towards this biological diversity, we have implemented the two best-known types of cells, the ‘brisk’ X-like and Y-like ganglion cells. We limited ourselves to these two cellular types because a large bibliography has made some

‘state-of-the-art’ model available for them, and not for the rarer cell types aforementioned. Also, as newcomers to the field of retinal processing, we did not question the predominance of X and Y cells found in the literature until quite recently. However, because our model and software have tried to reproduce the division in successive stages of real retinas, we believe that the computational framework is present to build models for many of the rare, ‘other’ types of retinal cells. The subject is discussed in the Conclusion of this thesis.

2.1.2 Spatio-temporal continuous maps

Figure 4.1 presents the global architecture of our model. The layered architecture of a retina suggests a model made of successive continuous spatio-temporal maps that progressively transmit and transform the incoming signal. The incoming light on the retina is the luminosity profile $L(x, y, t)$, defined for every spatial point (x, y) of the retina at each time t . It can have any units in our model; for our simulations we used digitalized intensities between 0 and 255. The subsequent layers of cells are also modeled as spatial continuums (no discrete cells, except the output ganglion cells), driven by specific differential equations.

This choice to use spatial continuums reflects our desire for a functional approach, that keeps strong links with computer vision. It allows to model spatial couplings (gap junctions, synaptic poolings) as operators which are both simple to implement, and fast (recursive filtering, Chapter 6, Section 3.2.2). Furthermore, for most known types of retinal interactions, the transition from discrete cell-to-cell interactions to continuous differential equations is well-defined mathematically: See discussion in Section 8.1.2.

2.1.3 Three stages of the model

The first stage of our model deals with signal processing done in the outer plexiform layer (OPL). It involves the two first layers of cells in the retina: Light receptors and horizontal cells. This stage is modeled as a simple spatio-temporal linear filter based on experimental recordings [60, 26] and previous models [101, 76]. We detail this OPL filter in Section 3. When applied to the input sequence $L(x, y, t)$, the OPL filter defines a band-pass excitatory current $I_{\text{OPL}}(x, y, t)$ which is fed to bipolar cells.

The second stage of the model is an instantaneous, nonlinear contrast gain control through a variable feedback shunt conductance $g_A(x, y, t)$, applied on bipolar cells in our model. This interaction is represented by the two small arrows between bipolar cells and the ‘fast adaptation’ signal in Figure 4.1. The contrast gain control mechanism is the subject of Section 4.

The third stage (Section 5) models signal processing in the inner plexiform layer (IPL) and ganglion cells. First, additional spatio-temporal shaping of the signal is provided, modeling some synaptic interactions in the IPL. It produces the excitatory current $I_{\text{Gang}}(x, y, t)$, which is fed to our model ganglion cells. Second, ganglion cells themselves are modeled as a discrete set of noisy integrate-and-fire (nLIF) cells paving the visual field, and generating spike trains from input current I_{Gang} . The cells that we model can be either X-type (the blue arrow in Figure 4.1, representing a one-to-one connection from bipolar cells) or Y-type (the blue cone, representing a synaptic pooling of the excitatory current).

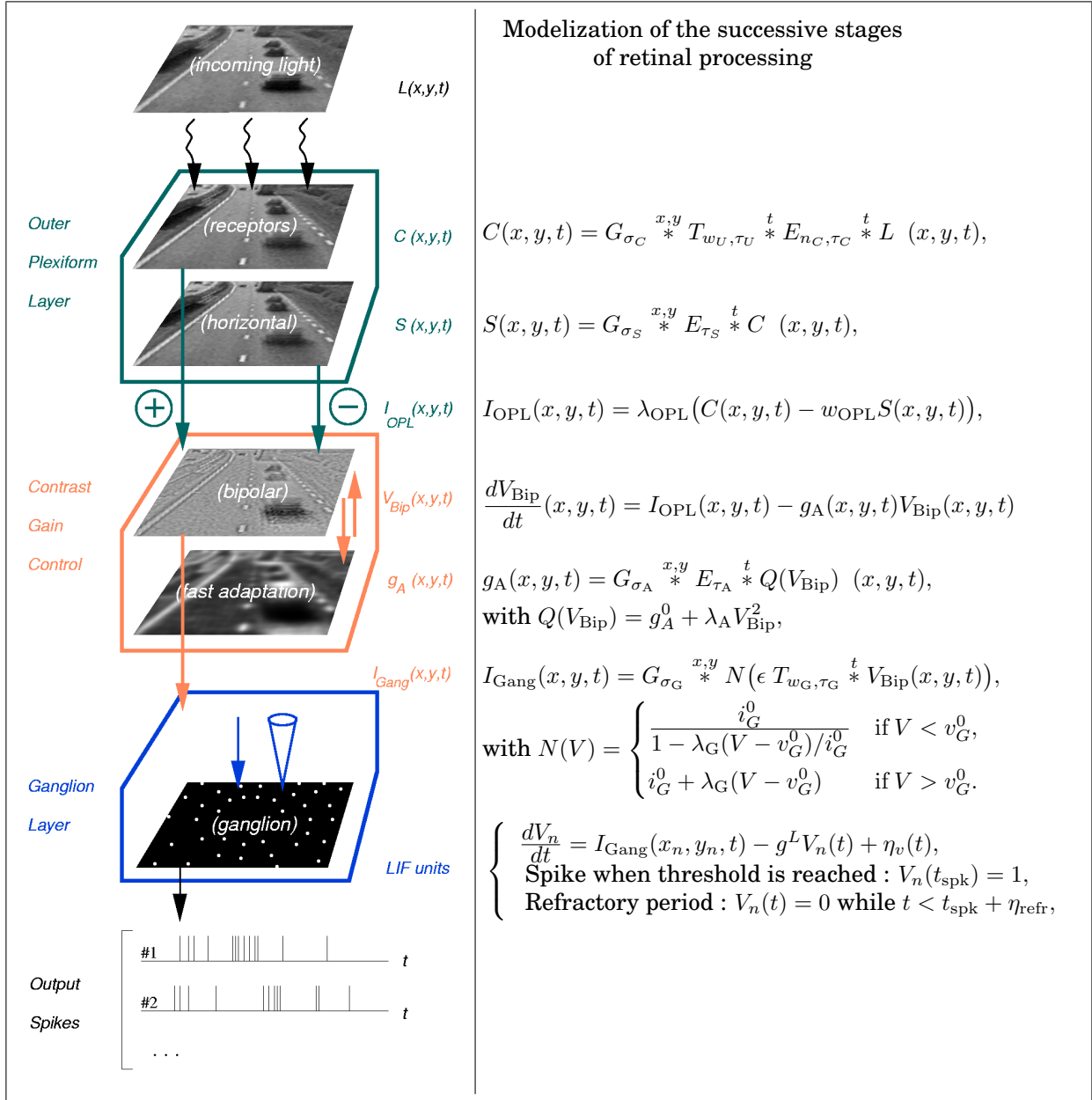


Figure 4.1: Schematic view of the model, inspired by the layered structure of the retina. Three boxes indicate the three stages of the model. Corresponding mathematical notations are indicated in the right-hand side. Except for the last layer (ganglion cells), successive signals are modeled as spatially continuous maps.

All along this presentation of the model, we try to justify and discuss its constitutive elements, on the basis of the general presentation of the retina we have made in Part I.

2.2 Mathematical framework and notations

2.2.1 Dimensional reduction

Let us first introduce the units which we use in our model. All parameters and variables presented in the sequel are expressed in reduced units, according to the following explanation. Biologically, membranar integration for a point neuron can be modeled in the general form

$$c \frac{dV}{dt} = \sum_i I_i + \sum_j g_j (E_j - V), \quad (4.1)$$

which is the typical equation for a capacitor. V is the cell's membrane potential in Volts, c is the membranar capacity in Farads. Synaptic inputs (and other intrinsic membranar currents) can either be modeled as currents I_i in Amperes, or more precisely as synaptic conductances g_j in Siemens associated to reversal potentials E_j in Volts.

Since our model does not focus on physiological precision, but on the functional output of the retina on a large scale, we are solely concerned with the *temporal* evolution induced by (4.1). Hence the following reduction of dimensionality:

$$V \rightarrow (V - V_R)/\Delta V, \quad I \rightarrow I/(c\Delta V), \quad g \rightarrow g/c, \quad (4.2)$$

where c is the membranar capacity of the neuron, V_R its resting potential, and ΔV a 'typical' range of variation for the neurons' potential. Through this reduction, constant c disappears from (4.1), V and the E_j become dimensionless with typical values the order of unity, and I_i and g_j , expressed in Hertz, directly give scales for the temporal evolution of V .

Constants c , V_R and ΔV generally depend on the type of neuron measured. In the present work, we needed to estimate these parameters only for bipolar cells and ganglion cells (see model in the sequel). We here suggest 'typical' values for c , V_R and ΔV , which can hold both for ganglion cells and bipolar cells at first approximation:

$$c \equiv 0.1 \text{ nF}, \quad V_R \equiv -70 \text{ mV (gang)}, -40 \text{ mV (bip)}, \quad \Delta V \equiv 20 \text{ mV}. \quad (4.3)$$

The approximation for c comes from the works of O'Brien *et al.* 02 [124], who measured the intrinsic electrical properties of virtually all populations of ganglion cells in the cat's retina. Amongst many other results, they find a ratio τ/R (τ , membranar time constant and R , membranar resistance of the cell) quite constant over cellular types, roughly amounting to $c = 0.1 \text{ nF}$ (except maybe for α cells, which have particularly large somata). This measure being quite constant over all small-bodied ganglion cells, we can take the same typical capacity for bipolar cells, whose somata have comparable sizes.

The approximation for resting potentials comes from O'Brien *et al.* 02 [124] (for ganglion cells) and Euler and Masland 00 [63] (for bipolar cells). These potentials

Magnitude	V (potential)	I (current)	G (conductance)
Reduced Units	1 (no unit)	1 Hz	1 Hz
Physical Units	20 mV	2 pA	0.1 nS

Table 4.1: Rough conversion between physical and reduced units in the model, based on (4.2)-(4.3).

actually vary over cells, and their precise values are not very important for scale conversions. They only define the potential baseline of our reduced equations.

The approximation $\Delta V=20$ mV allows roughly a simultaneous fit to the typical observed range of variation of mammalian bipolar cells (Euler and Masland 00 [63]), and to the typical distance between a ganglion cell' resting potential (typically -70 mV) and its spiking threshold (typically -50 mV). Note that with these conventions, our model ganglion cells emit a spike when their potential reaches value 1 in reduced units.

Using the typical scales in (4.3), Table 4.1 sums up the conversion factors between reduced and physical units in our model. Although these conversions are only indicative, they can help to verify whether or not our model parameters stay in a biological range.

2.2.2 Notations for linear filters

We have seen in Chapter 2 how linear filtering is a basic and unavoidable tool to model retinal processing, both on the spatial (Section 2) and temporal (Section 3) aspects. As all retinal models, we thus use linear filters at several locations of our model, to approximate signal transformations that occur in the successive layers of the retina. Here, we introduce our notations for the different types of linear filters used in the model.

These filters have been kept as simple as possible, because our simulator is focused on functional efficiency: Low-pass temporal filters are simple exponential filters, low-pass spatial filters are Gaussian filters, and band-pass oppositions are created by the simple subtraction of a low-passed signal to the original signal. All these filters have already been presented in Chapter 2, so we spend little time commenting them. They are all represented in Figure 4.2.

Low-pass temporal filters

As presented in Part I of this work, temporal low-pass occurs throughout retinal processing, starting at the level of photoreceptors with the complicated phototransduction cascade, and continuing in subsequent layers because of synaptic delays and membranar integration of synaptic currents.

We will use exponential filters to model low-pass temporal filtering (Chapter 2, Section 3), or possibly exponential cascades (Gamma filters):

$$E_{\tau}(t) = \exp(-t/\tau)/\tau, \quad (4.4)$$

$$E_{n,\tau}(t) = (nt)^n \exp(-nt/\tau)/((n-1)!\tau^{n+1}), \quad (4.5)$$

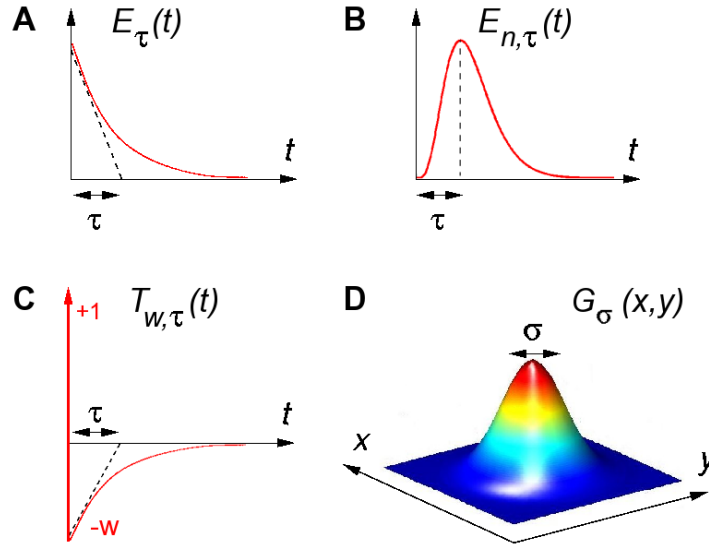


Figure 4.2: Linear kernels used in the model. *A*: Exponential kernel $E_\tau(t)$ (temporal, low-pass). *B*: Gamma (exponential cascade) kernel $E_{n,\tau}(t)$ (temporal, low-pass). *C*: Partially high-pass kernel $T_{w,\tau}(t)$ (temporal, high-pass). *D*: Gaussian kernel (spatial, low-pass).

if $t > 0$, and zero otherwise (causal filters). These are normalized filters summing to one, meaning that they are only *averaging* filters, without a linear gain. The exponential cascade filter (4.5) peaks at time τ (not $n\tau$), and offers more variability in the shape of the filter thanks to parameter $n > 0$.

Partially high-pass temporal filters

Temporal high-pass behavior is present at various locations of the retina (Chapter 3, Section 3.3) with many different time scales. It can result from synaptic oppositions between excitatory and inhibitory cells (horizontal and amacrine), but also from different phenomena intrinsic to each cell: Control loops during phototransduction (Chapter 3, Section 1.1), desensitization of synaptic receptors (Chapter 3, Section 2.4), fast and slow gain adaptation (Chapter 3, Section 5), etc.

We will model high-pass stages in the simplest functional way, as the difference between a Dirac representing the original signal, and an exponential filter representing the low-pass average removed from the original signal:

$$T_{w,\tau}(t) = \delta_0(t) - wE_\tau(t). \quad (4.6)$$

This filter has already been presented in Chapter 2, Section 3, as a particular case of DOE filter.

Low-pass spatial filters

We take these filters as normalized two-dimensional Gaussians:

$$G_\sigma(x,y) = \exp(-(x^2 + y^2)/(2\sigma^2))/(2\pi\sigma^2), \quad (4.7)$$

a traditional modeling element to account for dendritic pooling or electrical coupling through gap junctions (Chapter 2, Sections 2 and 6). $G_\sigma(x, y)$ is again a normalized filter that only performs spatial *averaging* on the input signal.

Convolution

All filtering kernels are applied as convolution operators on their input signals. In this chapter, $\text{sign} \overset{t}{*}$ denotes temporal convolution, and $\text{sign} \overset{x,y}{*}$ denotes spatial convolution.

3 FIRST STAGE: THE OPL FILTER

The first stage of our model consists of a spatio-temporal linear filter, which encompasses most of the band-pass behavior typical of retinal ganglion cells. We have seen the general characteristics of this band-pass behavior: Spatial as well as temporal, it is well modeled by a ‘modified’ difference of Gaussians (DOG) where the *center* and *surround* components are associated to two different difference-of-exponential (DOE) temporal filters, with a small supplementary delay for the *surround* component (as measured by Cai *et al.* 97 [26], Chapter 2, Section 4). We have also reviewed evidence that this type of band-pass architecture is already present at the level of bipolar cells (Chapter 3, Section 2).

Our modeling hypothesis is that, apart from mechanisms of adaptation to ambient luminosity, the input current received by bipolar cells is rather linear w.r.t. the input luminosity profile, and that the center-surround opposition of bipolar cells arises mostly from the synaptic triad in the OPL, with light receptors and horizontal cells. Our first filtering stage is thus termed the ‘OPL filter’.

3.1 Equations of the system

The OPL filter takes the luminosity profile $L(x, y, t)$ as input, and results in a synaptic current $I_{\text{OPL}}(x, y, t)$ (in reduced units of Hertz), received by bipolar cells from light receptors and horizontal cells, which already displays the typical center-surround characteristics:

$$C(x, y, t) = G_{\sigma_C} \overset{x,y}{*} T_{w_U, \tau_U} \overset{t}{*} E_{n_C, \tau_C} \overset{t}{*} L(x, y, t), \quad (4.8)$$

$$S(x, y, t) = G_{\sigma_S} \overset{x,y}{*} E_{\tau_S} \overset{t}{*} C(x, y, t), \quad (4.9)$$

$$I_{\text{OPL}}(x, y, t) = \lambda_{\text{OPL}}(C(x, y, t) - w_{\text{OPL}}S(x, y, t)), \quad (4.10)$$

where successive convolutions are applied from right to left. $C(x, y, t)$ represents the *center* signal, associated to light receptors, and $S(x, y, t)$ the *surround* signal, associated to horizontal cells. Let us comment these three equations.

Center signal [Equation (4.8)]

Temporally, the phototransduction process is modeled as a partially transient linear cascade: the exponential cascade $E_{n_c, \tau_c}(t)$ is modulated by a partially transient filter $T_{w_U, \tau_U}(t)$ (U standing for ‘undershoot’). Such filter provides an impulse response close to that measured by Schnapf *et al.* 90 [151] in macaque cone receptors: See Figure 2.4. But more generally, since (4.8)–(4.10) is a linear filter, the high-pass effects of $T_{w_U, \tau_U}(t)$ spread to $I_{\text{OPL}}(x, y, t)$: They are designed to account for all ‘inherent’ temporal transients prior to synaptic integration in bipolar cells, due to cellular mechanisms (for example, desensitization of bipolar cells’ synaptic receptors, Chapter 3, Section 2.4).

Spatially, $G_{\sigma_C}(x, y)$ encompasses the spatial blur due to gap junctions between light receptors’ inner segments, thus creating the ‘fundamental’ low-pass cut-off in the retina, which contributes to noise robustness (Chapter 2, Section 2).

Surround signal [Equation (4.9)]. The *surround* signal is obtained through a supplementary low-pass on the *center* signal. Indeed, horizontal cells receive their input from light receptors, so their signal develops with one more synapse and one more cellular integration than receptors. Spatially, horizontal cells are very low-pass (meaning big σ_S), due to the added effects of synaptic pooling and a strong electrical coupling through gap junctions (Chapter 2, Section 6).

Temporally, the supplementary delay $E_{\tau_S}(t)$, modeling membranar integration in horizontal cells, makes the whole filter (4.8)–(4.10) non separable, and potentially mediates strong perceptual effects, as we discuss right after.

OPL signal [Equation (4.10)]. Constant λ_{OPL} is the overall gain of the center-surround filter, expressed in Hertz per unit of luminance. Constant $w_{\text{OPL}} \in [0, 1]$ is the relative weight of *center* and *surround* signals. Physiologically, this relative weight has been measured close to 1 in mammalian ganglion and bipolar cells (Chapter 3, Section 2.3), but we have also discussed how even relatively small variations in its value could make strong perceptual differences in a model (see e.g. Chapter 2, Figure 2.2).

3.2 Characteristics of the OPL filter

A non-separable spatio-temporal filter. Spatially, the center-surround filter (4.8)–(4.10) can be associated to a classical DOG filter. Temporally, it is biphasic. As a result, our OPL filter acts at the same time as an edge detector and a movement detector. However, note that the center-surround filter is *not separable* in time and space: It cannot be written as the product of a spatial kernel by a temporal kernel. Indeed, the *surround* signal is more delayed than the *center* signal because of $E_{\tau_S}(t)$ in (4.9).

This delay, although estimated to only a few milliseconds in mammalian retinas (Chapter 2, Section 4), has significant perceptual consequences. As a result, the center-surround filter is able to detect temporal variations of luminosity even in a spatially uniform zone. This would not be the case for a separable filter, like a spatial DOG multiplied by a temporal DOE. Indeed, the response of such a separable filter on a uniform region would *always* be zero because of the DOG properties, even if the luminosity does vary in time.

Also, the delay between *center* and *surround* probably implies that the first retinal spikes after onset of a new image do not code for image edges, but simply for the luminosity signal, independently of the strength and precision given to the *surround* signal (through parameters σ_S , w_{OPL} , etc.). This result is illustrated in Section 7.2.1.

Phototransduction. We have seen in Chapter 3, Section 1.1 that the typical impulse response of the phototransduction cascade has the ‘blobby’ shape of a Gamma filter (4.5) (Figure 3.3). As a result, our model accounts for phototransduction in a linear way, thanks to filter $E_{n_C, \tau_C}(t)$. This is the only place of our model where a Gamma function is used, because a simple exponential approximation (4.4) would appear too crude.

The phototransduction process is in fact hardly linear, since it displays fast and slow adaptation to the ambient level of luminosity, mediated by different nonlinear processes, where calcium plays a fundamental role (Chapter 3, Section 1.1). Advanced models of light adaptation could easily be implemented in the simulator if required (see Conclusion of the thesis).

The linear approximation, used here for simplicity, remains relatively valid as long as the luminosity range of the input image remains constant: Room with artificial light, monitor screen. . . For this reason, our simulator in its present state is designed to take only normalized sequences as input, such as movies coded between 0 and 255.

4 SECOND STAGE: CONTRAST GAIN CONTROL IN BIPO-LAR CELLS

4.1 Motivations, and basic idea of the model

Contrast gain control, or contrast adaptation, is the usual term to describe the influence of the local contrast of the scene on the transfer properties of the retina. We have seen the main characteristics of this intrinsically nonlinear phenomenon (Chapter 3, Section 5.2): Contrast adaptation occurs both on a fast time scale (tens to hundreds of ms), and also on a much longer time scale (1-10 s). The slow effect enters the more general realm of slow adaptations in the retina, which are not encompassed by our model. By opposition, the fast contrast gain control is an intrinsically dynamic feature of the system, which has a strong and constant influence on the shape of retinal responses, and very likely on our percepts (Figure 4.13, and also Chapter 3, Section 5.2.5). We thus wished to include such an effect in our large scale simulator.

To our knowledge, the precise biological origin of the fast gain control is yet unknown (Chapter 3, Section 5.2.3). However, although the effect is likely distributed at several locations in the retina (like most other filtering features), recent findings have marked bipolar cells as key players in the phenomenon.

The dual mark of fast contrast adaptation appears to be a decrease of the instantaneous linear gain of transmission, and a shortening of the cells’ temporal response,

in the presence of strong contrasts. We reflected that both effects could be accounted for by a dynamic variation of the membranar resistance of an ‘RC’ circuit: In an RC circuit, the output potential $V(t)$ is a low-passed version of the input current, following $V(t) = E_\tau *^t RI(t)$, with $\tau = RC$ and $E_\tau(t)$ the exponential kernel as defined in (4.4). So, R defines both the gain and the time constant of the integration.

In real neurons, the total membranar resistance R is indeed dynamic, since it results largely from the openings and closings of numerous ionic channels, synaptic and others, in the course of the neurons’ activity: See equation (4.1). The nonlinear influence of these channels, through their weight on the neuron’s total membranar resistance, is generally termed *shunting inhibition* (‘inhibition’ because it decreases the neurons’ gain of integration), and it has been proved to be highly present in the cortex (see e.g. Destexhe *et al.* 01 [52]).

As a result, we proposed a model of gain control where a variable shunt conductance $g_A(x, y, t)$ (still defined on a spatial continuum) dynamically changes the resistance of membranar integration in bipolar cells. The resulting model is interesting for its simplicity, and the way it allows to account for various physiological measurements of contrast gain control (Section 6). Also, it yields equations that are rather tractable mathematically, insuring that the control loop behaves well under simple stimuli (Chapter 5).

We do not claim our model to directly reflect the biological reality. Fast contrast adaptation in bipolar cells can arise from many types of nonlinear mechanisms, for example from nonlinear desensitization of AMPA synaptic receptors (DeVries 00 [54], Chapter 3, Section 2.4). However, at least two particular biological mechanisms (voltage-gated conductances, calcium adaptation) can lead to a system close to our model, as we discuss in Section 8.2.

4.2 Equations of the system

In our model, bipolar cells with potential $V_{\text{Bip}}(x, y, t)$ integrate the linear signal $I_{\text{OPL}}(x, y, t)$ from the model’s first stage (OPL filter), and are controlled by a feedback from shunt conductances in their membranes:

$$\frac{dV_{\text{Bip}}}{dt}(x, y, t) = I_{\text{OPL}}(x, y, t) - g_A(x, y, t)V_{\text{Bip}}(x, y, t) \quad (4.11)$$

$$g_A(x, y, t) = G_{\sigma_A} *^{x,y} E_{\tau_A} *^t Q(V_{\text{Bip}})(x, y, t), \quad (4.12)$$

$$Q(V_{\text{Bip}}) = g_A^0 + \lambda_A V_{\text{Bip}}^2, \quad (4.13)$$

where g_A represents a variable leakage (‘shunt’) term in the membranes of our model bipolar cells, which is activated through the static function Q (Figure 4.3). All physiological magnitudes are reduced dimensionally, as detailed in (4.2).

The total membranar resistance is the inverse of the total membranar conductance g_A . Following the argument above, g_A thus has a divisive effect on the evolution of V_{Bip} in (4.11) and at the same time, g_A defines the ‘time constant’ (not constant, here) of equation (4.11). In our model, g_A depends dynamically on the recent values taken by bipolar cells (feedback mechanism), with a typical time scale

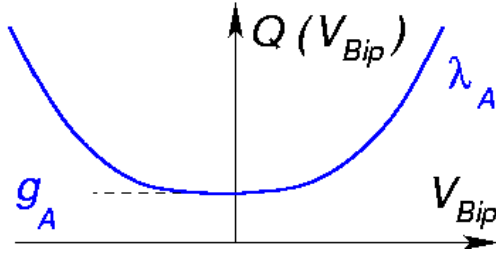


Figure 4.3: Activation function $Q(V_{Bip})$ for shunt conductances g_A in bipolar cells.

τ_A and spatial extent σ_A , as described by equation (4.12). These two parameters determine the size of the spatio-temporal neighborhood used by g_A to determine a local measure of contrast.

The possible values and biological origin of parameters σ_A and τ_A are discussed in Section 8.2. They cannot be directly fixed from experimental data, due to the hypothetical nature of the stage (4.11)-(4.13). In the experiments of Section 6, best reproduction was obtained for a small adaptation time constant (typically, $\tau_A = 5$ -20 ms). As for parameter σ_A , we make no assumption on its possible values: It could be absent ($\sigma_A = 0$), or present with the typical spatial extent of diffusion processes in the retina (e.g. through gap junctions, see discussion in Section 8.2).

A static activation function $Q(V_{Bip})$ links values of V_{Bip} to the activation of leak conductances g_A , through equation (4.13). Q is defined as an even function, so that the activation of g_A depends only on the absolute value of V_{Bip} . Parameter g_A^0 in (4.13) represents the inert leaks in membranar integration (4.11) (because filters G_{σ_A} and E_{τ_A} in (4.12) have a gain of 1). It does not depend on the mean level of V_{Bip} . On the contrary, λ_A in (4.13), also in Hertz, fixes the strength of the gain control feedback loop.

Furthermore, Q is assumed to have a *convex* shape, implying different behaviors of the system, depending on the contrast:

- At small contrasts, the system has a quasi-linear working range. Indeed, when the input current I_{OPL} has small variations, it translates into small variations of the bipolar potential, so that V_{Bip} remains in the ‘central region’ of function Q , where $V_{Bip}^2 \simeq 0$. As a result, g_A^0 remains the principal, constant, leaking force in equation (4.11), and integration remains quasi-linear at the level of bipolar cells.
- At high contrasts, by opposition, as $|V_{Bip}|$ enters the ‘big value’ range of function Q , the leakage term g_A in equation (4.11) becomes truly subject to dynamic variations. As a result, bipolar cells start responding under-linearly to the input current I_{OPL} .

Note that the precise choice of function $Q(V_{Bip})$ is arbitrary in our model (a linear-by-parts version was successively tested, but required an extra parameter, see discussion in Section 8.2). The only important constraint for our model to reproduce experimental curves, was that function Q be *strictly convex*, in order to enhance the contrast gain control effect (multi-sinus experiments in Section 6.2).

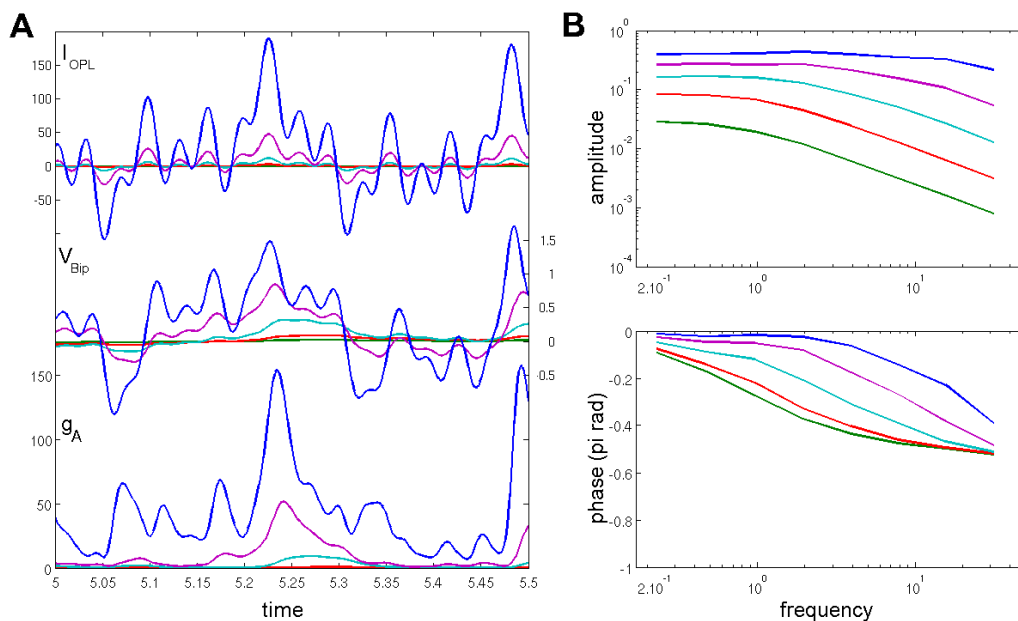


Figure 4.4: *Temporal response of the gain control loop at different input modulation strengths*, measured for multi-sinus input currents such as that of Shapley and Victor 78 [155] (Chapter 3, Section 5.2.2). *A*: Extract from the temporal signals for $I_{OPL}(t)$, $V_{Bip}(t)$ and $g_A(t)$. *B*: Corresponding Fourier transforms for $V_{Bip}(t)$ (*top*: amplitude, *bottom*: phase). Input currents: $c = 0.15625$ to 40 Hz, each time multiplied by 4. Gain control and phase advance (higher frequency cut-off) are observed for strong input currents.

4.3 Contrast gain control and Wiener kernels

As an illustration of the temporal properties of our gain control mechanism (4.11)-(4.13), we show in Figure 4.4 its response to multi-sinus input currents of different amplitudes, inspired from the multi-sinus experiments of Shapley and Victor 78 [155] (Chapter 3, Section 5.2.2). This gives a measure for the best-fitting linear kernels for the system, at different strengths of input modulation ('contrast'). There is no spatial structure in this simulation (as would be the case, e.g., in response to uniform flickering screens).

A first observation is that (4.11)-(4.13) always keeps a low-pass sensitivity, like the traditional linear 'RC' circuit from which it is derived (Section 4.1).

A second observation is that the dual mark of contrast gain control (Chapter 3, Section 5.2.2) appears at high input modulations: Successive amplitude curves become spaced by less than $\log(4)$ (input current being multiplied by 4 between two successive curves) and their cut-off frequency shifts to the right for high modulation inputs, while the phase curve shifts upwards for high modulation inputs. In the temporal domain (Figure 4.4-A), the system's increased cut-off frequency is reflected in a better following of the input signal's modulations.

This confirms empirically that our gain control model is efficient in reproducing under-linearity and phase advance in response to strong input currents. We will see in Chapter 5 how such a behavior can be mathematically proved in simple cases (reduced dimensionality, and simple sinusoidal stimulation).

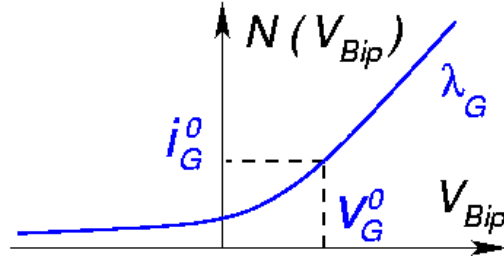


Figure 4.5: Synaptic rectification $N(V_{\text{Bip}})$ from bipolar to ganglion cells.

5 THIRD STAGE: THE IPL AND GANGLION CELLS

The last stage of our simulator is the generation of spike trains, modeling how retinal ganglion cells produce spikes from bipolar cells' activities. First, bipolar signal V_{Bip} is rectified, and possibly receives additional spatio-temporal shaping, to produce an excitatory current on ganglion cells I_{Gang} (Section 5.1). From $I_{\text{Gang}}(x, y, t)$, an array of noisy leaky-integrate-and-fire neurons (nLIF), modeling ganglion cells, produces the sets of output spikes. The nLIF procedure is described in Section 5.2, while Section 5.3 shows how to define a whole retina as an assembly of nLIF. Two possible retinal organizations are discussed, log-polar or homogeneous.

5.1 Synaptic current upon ganglion cells

In real retinas, additional and complex transformations of the signal are provided by the synaptic structures in the *Inner Plexiform Layer* (IPL), the second layer of synapses in the retina which is the locus of synaptic interactions between bipolar cells, amacrine cells, and ganglion cells. Our simulator uses a single, empirical formula to model signal shaping in the transition from bipolar cells to classical center-surround ganglion cells (cat X and Y cells, primate parvo- and magnocellular cells):

$$I_{\text{Gang}}(x, y, t) = G_{\sigma_G} \overset{x,y}{*} N(\varepsilon T_{w_G, \tau_G} \overset{t}{*} V_{\text{Bip}}(x, y, t)), \quad (4.14)$$

with

$$N(V) = \begin{cases} \frac{i_G^0}{1 - \lambda_G(V - v_G^0)/i_G^0} & \text{if } V < v_G^0, \\ i_G^0 + \lambda_G(V - v_G^0) & \text{if } V > v_G^0. \end{cases} \quad (4.15)$$

Equations (4.14)–(4.15) do not aim to explain the biological complexity of the IPL, but to allow functional reproduction of some ganglion cells' specific responses. Parameters in these formulas will vary according to the subtype of ganglion cell being modeled. Equations (4.14)–(4.15) comprise four modeling elements:

Polarity. 'ON' and 'OFF' ganglion cells are simulated simply by the simulator, by setting parameter ε in (4.14) to respective value 1 or -1 .

Biologically, ON and OFF cellular pathways diverge earlier in retinal processing, involving different types of bipolar cells. From the level of bipolar cells and on, there are physiological and anatomical disparities between ON and OFF cells, such as reaction time, sensitivity to contrast gain control, or density of cells. These dis-

crepancies are not explicitly taken into account by our model that considers a single, symmetric signal up to bipolar cells. However, model parameters allow to reproduce either population, when required.

Rectification. Equation (4.14) rectifies signal V_{Bip} through the static nonlinear function N , defined in equation (4.15) and represented in Figure 4.5. Parameters λ_G and i_G^0 have, again, the dimension of ‘reduced currents’ expressed in Hertz. v_G^0 is the ‘linearity threshold’ of the cell, i.e. the value after which transmission becomes linear. Note that $N(v_G^0) = i_G^0$.

Such rectification is a very common feature in neural modeling and in retinal models [29, 31, 69]. It reflects static nonlinearities observed experimentally in the retina [31, 93, 5], e.g., through LN analysis of retinal cells (Chapter 2, Section 5). Biologically, static nonlinearities in signal transmission can occur for different reasons: Saturations, synaptic transmissions, etc. Equation (4.15) defines a *smooth* rectification with a shape close to experimental curves observed when performing an LN Analysis.

Additional transient. The temporal filter T_{w_G, τ_G} allows to control how much the simulated ganglion cells are *phasic* or *tonic*. For primate Magnocellular cells or cat Y cells, response to a constant stimulation shuts down quickly after one or two hundreds of milliseconds (Chapter 3, Section 3.2.2), requiring the use of a transient weight w_G close to 1. For our simulations of cat X cells, the supplementary transient was fixed at an intermediate balance ($w_G = 0.7$) in order to reproduce correct Wiener kernels in Section 6.2, and correct responses to gratings in Section 6.1.

There are several plausible biological explanations for the transient properties intrinsic to ganglion cells. Likely, one main reason is the existence of specific amacrine cells in the IPL that were found to cut the responses of ganglion cells [122, 107, 95], whether through a feedback to bipolar cells, whether by direct inhibition on ganglion cells.

Locating this transient *before* the static nonlinearity N is a convenient, empirical choice. First, it provides better reproduction of Y cells’ spatial nonlinearity (see next paragraph and Section 6.1) by creating fully band-pass units before the rectification and pooling. Second, it allows undershoots possibly generated by the transient filter T_{w_G, τ_G} to be attenuated by the compression N .

Additional pooling. The spatial filter G_{σ_G} aims at reproducing a typical non-linear effect observed in cat Y cells [59] (Chapter 3, Section 3.2.2). The simplest explanation of this spatial nonlinearity is a spatial pooling that would occur *after* the synaptic rectification onto these ganglion cells. This explanation, first proposed by Hochstein and Shapley [80], is at the base of the Freeman and Enroth-Cugell model for Y-type cells [58]. Furthermore, the biological basis was justified experimentally [48, 95]: The spread of the dendritic tree of Y-type cells is large enough to significantly average the synaptic input from bipolar cells over a consequent spatial extent (Chapter 3, Section 3.2.2).

X and Y ganglion cells. The simulator has been fitted to reproduce the responses of cat X and Y cells, with the introduction of a supplementary pooling G_{σ_G} required for Y cells. Due to the relatively strong constancy of X-like and Y-like types across

Parameter	Cat X	Cat Y	Parasol	Midget
(*) σ_C (deg)	0.15–0.8	0.15–0.8	0.03–0.1 (fov)	0.03–0.1 (fov)
(*) σ_S (deg)	0.8–6	0.8–6	0.2–0.7 (fov)	0.2–0.7 (fov)
(?) σ_A (deg)	0–1.5	0–1.5	0–0.2 (fov)	0–0.2 (fov)
(+) σ_G (deg)	0	1.5	0–0.15 (fov)	0 (fov)
(+) λ_A (Hz)	50–100	50–100	50–100	0
(+) g_A^0 (Hz)	5	5	5	50
(+) w_G	0.7	1	0.7–1	0.7
(+) λ_G (Hz)	100	300	100–300	100

Table 4.2: Model parameters that vary according to species (cat and primate) and pathway. Plausible values for other parameters are in caption to Figure 4.7. (*) Values taken from [59] (cat) and [37, 111] (primate). (+) Values which provided good fit to the model. Most of these parameters have equivalents in other retina models, with comparable values. (?) The adaptation spatial scale σ_A is a free parameter of the model, for which no data is available, only plausible orders of magnitude.

species (Chapter 3, Section 3.2), we can thus also reproduce primate Parasol cells (whose behaviors are generally Y-like, possibly overcrossing to X-like), and Midget cells (in their achromatic features).

Table 4.2 summarizes plausible orders of magnitude for the model parameters that must vary between cat and primate retinas. Values for σ_C and σ_S are taken from the literature ([59] for cat, [37, 111] for primate). Other parameters for cat cells are plausible orders of magnitude that provided good fit to data. Other parameters for primate cells are suggestions respecting the scaling from cat to primate retina, and the known specificities of primate cells: Parasol cells can behave like cat X or Y cells, and Midget cells display no contrast gain control (Chapter 3, Sections 3.2.1 and 3.2.2). Note that typical spatial scales for the primate retina are given in the fovea.

A discussion concerning the possible implementation of other, less well-known types of ganglion cells is provided in the thesis' Conclusion.

5.2 Spike generation in ganglion cells

This Section is about the transformation of the continuous signal $I_{\text{Gang}}(x, y, t)$ into discrete sets of spike trains. Let us consider N ganglion cells C_n ($n = 1 \dots N$) paving the retinal space (see Section 5.3 for their repartition and parameters) and let us denote by V_n the potential of cell number n ($n = 1 \dots N$) centered at position (x_n, y_n) .

Our simulator simply generates the output of cell C_n with a standard nLIF model

(Chapter 3, Section 4.2.4):

$$\left\{ \begin{array}{l} \frac{dV_n}{dt} = I_{\text{Gang}}(x_n, y_n, t) - g^L V_n(t) + \eta_v(t), \\ \text{Spike when threshold is reached: } V_n(t_{\text{spk}}) = 1, \\ \text{Refractory period: } V_n(t) = 0 \text{ while } t < t_{\text{spk}} + \eta_{\text{refr}}, \\ \text{and (4.16) again,} \end{array} \right. \quad (4.16)$$

where $\eta_v(t)$ and η_{refr} are two noise sources that can be added to the spike generation process in order to reproduce the trial-to-trial variability of real ganglion cells, following the experimental results of Keat et al [89] 01 (Chapter 3, Section 4.2.4). $\eta_v(t)$ is taken as a Brownian movement that has the dimension of a current. Integration of this current through equation (4.16) is equivalent to adding to $V_n(t)$ a Gaussian auto-correlated process with time constant $1/g^L$ (typically, 20 ms), and variance σ_v . The amplitude of $\eta_v(t)$ is chosen for σ_v to be around 0.1. η_{refr} is a stochastic absolute refractory period that is randomly chosen after each spike, following a normal law, typically $\mathcal{N}(3 \text{ ms}, 1 \text{ ms})$.

Note that spike generation is the only source of noise in our model, following the model of Keat *et al.* 01 [89] for trial-to-trial variability in ganglion spike trains. Recent findings (Dhingra and Smith 04 [57]) have confirmed that the spiking mechanism is an important contribution to the overall noise in retinal processing.

Remark: Link with the Keat et al. 01 model. Although Keat *et al.* 01 is our reference work to define the nature of the two sources of noise, we implemented a real nLIF model rather than their integrated procedure. Indeed, their own procedure is strongly inspired by the LIF model, but it displays less convenient mathematical properties (it is not Markov, etc.), and is harder to implement in the event-driven formalism which we use for spike generation (Chapter 6, Section 3.4).

As a result, our two sources of noise are not exactly defined as in Keat *et al.* 01, but mathematical analysis reveals that they have strong links, and similar effects. ■

Remark: Spike correlations between neighboring cells. Note that for the moment our simulator does not include any model of spike correlation between neighboring cells, as we have presented in Chapter 3, Section 4.3. This is a promising future extension of the model. (see Conclusion of the thesis). ■

5.3 Ganglion cell sampling configurations

The whole model presented above holds when modeling a small region of the retina, in which the density of retinal cells can be considered uniform. In that case, all filtering scales and parameters are constant and do not depend on the spatial position of each cell. Our simulation software can easily handle such a uniform distribution of cells. And in most mammalian species, the whole retina has a fairly uniform density of cells.

However, the *primate* retina taken as a whole is not uniform at all. Density of cells and filtering scales depend on the position considered in the retina. One needs to distinguish the *fovea* in the center, from the surround of the visual field where precision is less. A simple way is to define a scaling function, that describes at the

same time the local density of cells and the spatial scales of filtering in the different regions of the retina.

Our simulator implements a radial and isotropic density function that depends on the distance r from the center of the retina. We define a one-dimensional log-polar scaling function $s(r)$ as

$$s(r) = \begin{cases} 1 & \text{if } r < R_0, \\ 1/(1 + K(r - R_0)) & \text{if } r > R_0, \end{cases} \quad (4.17)$$

where R_0 is the size of the fovea and K is the speed of density decrease outside of the fovea. When $K = 1/R_0$, this amounts to a traditional log-polar scaling. The density of cells in a given region of the retina at eccentricity r is then given by $d_0 s(r)^2$, d_0 being the 2d-density of cells in the fovea. Conversely, all spatial filtering scales of the model presented before (σ_C , σ_S , σ_{Am} , σ_{Gang}) scale with $s(r)^{-1}$.

The choice of such a scaling function is biologically justified: Dendritic trees for primate ganglion cells have experimentally been found to scale with a positive power of r , between $r^{0.7}$ and r according to the type of cell (Dacey and Petersen [39], Chapter 1, Section 2.3).

6 PHYSIOLOGICAL REPRODUCTIONS

Now that our model is totally defined, we test it on classical physiological experiments, led on single ganglion cells. These experiments, with various protocols, demonstrate that the model induces linear kernels close to those measured physiologically, and can also account for two typical nonlinear effects: Contrast gain control and spatial nonlinearity of Y-type ganglion cells.

A first experiment (Section 6.1) is devoted to reproduction of the physiological difference between X- and Y- type cells. The two following experiments (Sections 6.2 and 6.3) are devoted to the phenomenon of contrast gain control in the retina. We show that our gain control loop (4.11)–(4.13), along with the rest of the model, reproduces qualitatively the dynamic changes in retinal filtering linked to the average level of contrast.

6.1 X and Y cell responses to grating apparitions

Grating apparitions are a classical stimulus when experimenting on the low-level visual pathway. We reproduce here one of the first recordings of that kind, on cat ganglion cells in 1966 by Enroth-Cugell and Robson [59], which led to the distinction between cat X type and Y type cells (already presented in Chapter 3, Figure 3.12).

Description of the experiment

Cat ‘OFF’ ganglion cells are presented with the alternation of a static grating and a uniform screen of same luminance, at a frequency of about 0.5 Hz, and their spiking output is measured extracellularly. The experiment is repeated for different spatial phases of the grating, so as to test the summing properties of the cells’ receptive

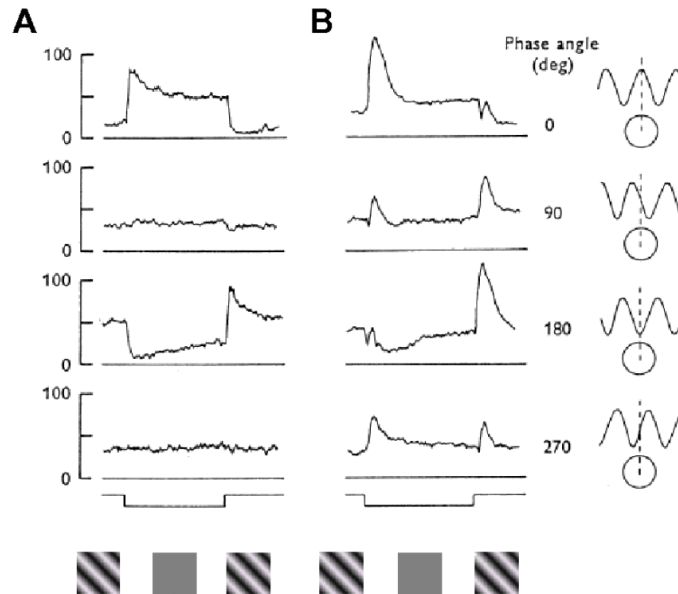


Figure 4.6: *Response of cat OFF-center X and Y ganglion cells to the disappearance and reappearance of a sinusoidal grating with different spatial offsets, reproduced from Enroth-Cugell and Robson 66 [59]. A: typical X-type ganglion cell. B: typical Y-type ganglion cell (see details in the text). Grating spatial frequencies of 0.13 deg^{-1} (A) and 0.16 deg^{-1} (B). Mean luminance 16 cd/m^2 , grating contrast of 0.32.*

fields. Typical responses (averaged instantaneous frequencies) for an X cell and a Y cell are presented in Figure 4.6.

The experiment reveals that X cells have a relatively *tonic* behavior, since their response to a static stimulus lasts for a long time, whereas Y cells are totally *phasic*, only responding for a few hundreds of milliseconds after stimulus onset, and returning to silent.

The experiment is also an illustration of the ‘null position’ test: For X cells, a spatial phase exists for which the cell has roughly no response to the grating (here, 90 and 270 deg), when the ‘positive’ and ‘negative’ parts of the grating exactly compensate one another thanks to linear summation. For Y cells such a position does not exist, revealing a spatial nonlinearity (Chapter 3, Section 3.2.2).

Interestingly, the X cell curves in Figure 4.6-A also reveal a slow, nonlinear adaptation of the cell to its own level of response. Consider the responses of the cell at the end of the ‘uniform screen’ period. Linear approximation would predict similar levels of response in the four experimental conditions, since the uniform screen has already been on for a whole second, which exceeds the latency of the cell’s linear response.

However, real cell responses at the end of the ‘uniform screen’ period are bigger in the experiment with the ‘0 deg’ grating, and lower with the ‘180 deg’ grating. This can be explained by a slow adaptation of the cell’s gain to its global level of response (Chapter 3, Section 5.3), which is stronger in the ‘180 deg’ experiment because the cell responds strongly when the grating is on.

Simulation with our model

Our modeled X and Y cells are tested in Figure 4.7. Parameters σ_C and σ_S (see caption to Figure 4.7) are chosen to fit the receptive fields measurements for the original X cell in Figure 4.6, by the authors. Other parameters are chosen to produce a good, simultaneous fit to these experiments and the following (multi-sinus, LN analysis).

The model reproduces the ‘null position’ typical of X cells, and the absence of such ‘null position’ for Y cells, due to the post-synaptic pooling added in equation (4.14). Reproduction of Y cell curves required that the three modeling elements in equation (4.14) be in the right order: Temporal transient T_{w_G, τ_G} , rectification N and pooling G_{σ_G} .

The slow decay of X cell responses to static stimuli is also reproduced, with the correct time scale. This is due to the added effects of the two transient filters in our retinal scheme: slow transients with T_{w_U, τ_U} in (4.10), and fast transients with T_{w_G, τ_G} in (4.14).

Note however that in our model, in any of the four experimental conditions, the X cell sets back to the same firing rate at the end of the ‘uniform screen’ period: its ground firing rate. Parameters i_G^0 in (4.15) and g^L in (4.16) were fixed to obtain a ground firing rate of around 50 Hz. Our model does not encompass the slow cellular adaptation of the cell to its own level of response, observed in Figure 4.6-A and explained in the previous paragraph. Slow adaptation is discussed in Section 8.1.3.

6.2 Multi-sinus experiments

To test and calibrate our contrast gain control loop (4.11)-(4.13), we reproduced two of the Shapley and Victor [155] multi-sinus experiments, which gave the first quantitative measures of contrast gain control in the retina (already presented in Chapter 3, Figure 3.39).

Description of the experiment

The experimental protocol has already been described in detail in Chapter 3, Section 5.2.2. In short, the stimulus was a grating temporally modulated by a sum of sinusoids with adjustable contrasts:

$$L(x, y, t) = \bar{L} \left(1 + \text{Gr}(x, y) \sum_{i=1}^8 c_i \sin(\xi_i t) \right),$$

such that the ξ_i logarithmically span the frequency range from about 0.2 Hz to 32 Hz.

Two different experiment protocols were made for different distributions of the c_i . In the ‘general’ protocol, a global level of contrast c is imposed for all the cells $\forall i, c_i = c$, yielding the best-fitting Wiener kernel for the cells at this level of contrast. The resulting kernels display an under-linearity with contrast at low temporal frequencies (Figure 4.8-A) and a phase advance at high contrasts (Figure 4.8-B).

In the ‘carrier frequency’ protocol, a carrier frequency ξ_{i_0} is chosen to concentrate most of the power of the stimulus, with $c_{i_0} = 0.2$, while the other frequencies are added as perturbation terms: $c_i = 0.0125$ for $i \neq i_0$. An empirical measure for the ‘strength’ of the gain control effect in this particular case can then be derived, in

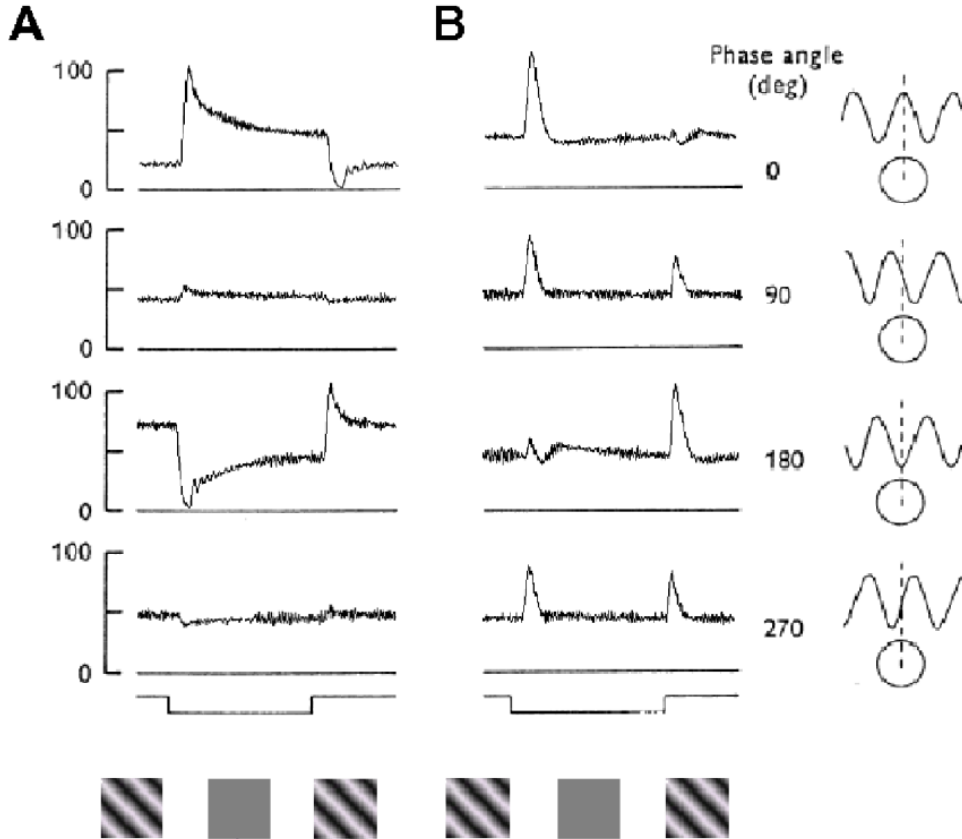


Figure 4.7: *Reproduction of the experiments in Figure 4.6 by our retina model. A: X cell model, B: Y cell model. Average firing rates generated from 80 trials with noise in the spike generation. Test grating: Normalized mean luminance of 0.5, contrast 0.32, spatial frequency of 0.13 deg^{-1} . OPL parameters: Center, $\sigma_C = 0.88 \text{ deg}$, $\tau_C = 10 \text{ ms}$, $n_C = 2$. Surround, $\sigma_S = 2.35 \text{ deg}$, $\tau_S = 10 \text{ ms}$. Slow linear transient, $w_U = 0.8$, $\tau_U = 100 \text{ ms}$. Global amplification, $\lambda_{\text{OPL}} = 1000 \text{ Hz}$ per normalized luminance unit. Gain control parameters: $g_A^0 = 5 \text{ Hz}$, $\lambda_A = 50 \text{ Hz}$, $\tau_{\text{Am}} = 5 \text{ ms}$, $\sigma_{\text{Am}} = 2.5 \text{ deg}$. X cell parameters: IPL transients, $w_G = 0.7$, $\tau_G = 20 \text{ ms}$. Synaptic transmission, $\sigma_G = 0$, $\lambda_G = 150 \text{ Hz}$, $v_G^0 = 0$, $i_G^0 = 80 \text{ Hz}$. Y cell parameters: IPL transients, $w_G = 1$, $\tau_G = 50 \text{ ms}$. Synaptic transmission, $\sigma_G = 1.8 \text{ deg}$, $\lambda_G = 300 \text{ Hz}$, $v_G^0 = 0$, $i_G^0 = 80 \text{ Hz}$. Spike generation: $g^L = 50 \text{ Hz}$, $\sigma_v = 0.2$, $\eta_{\text{refr}} \sim \mathcal{N}(3 \text{ ms}, 1 \text{ ms})$.*

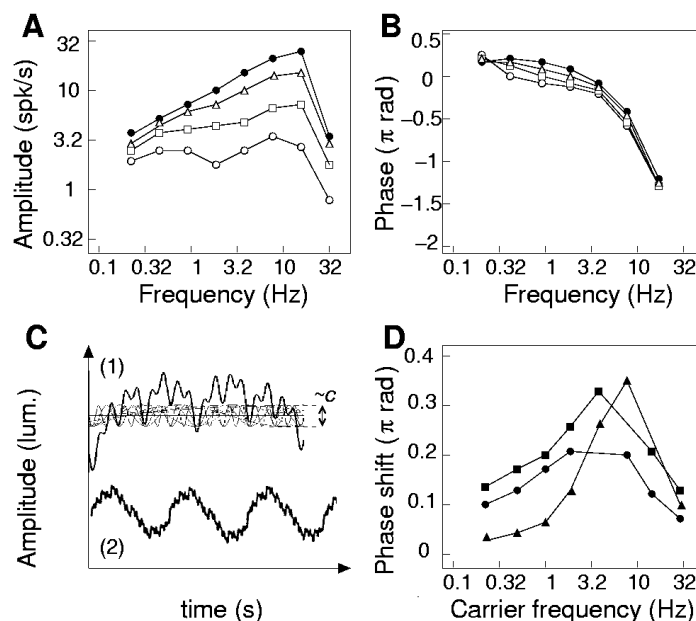


Figure 4.8: *Contrast gain control in a cat ON-center X ganglion cell*, reproduced from Shapley and Victor 78 [155]. *A and B*: Response to multi-sinus stimuli of different contrasts c (sample input signal depicted in panel C-1). Amplitude curves (A) reveal under-linearity at low temporal frequencies. Phase curves (B) reveal time advance for high contrasts (see text). Successively, c was 0.0125 (white circles), 0.025 (\square), 0.05 (\triangle) and 0.1 (black circles). *D*: Strength of the gain control effect depends on the dominant frequency ξ_{i_0} present in the input (stimuli with a carrier frequency ξ_{i_0} , as depicted in Panel C-2). The three curves represent indicators $\phi_5(\xi_{i_0})$ (circles), $\phi_6(\xi_{i_0})$ (\blacksquare) and $\phi_7(\xi_{i_0})$ (\blacktriangle) which measure the strength of the gain control (see text). Frequencies that elicit the most gain control are $\xi_{i_0} = 3\text{--}10$ Hz.

the form of three (correlated) indicators $\phi_5(\xi_{i_0})$, $\phi_6(\xi_{i_0})$ and $\phi_7(\xi_{i_0})$. High values for these numbers indicate that frequency ξ_{i_0} induces a lot of gain control.

Figure 4.8-D, which represents the three indicators as a function of ξ_{i_0} , thus reveals that the underlying mechanism for the contrast gain control measured here has a ‘band-pass’ sensitivity, being preferentially triggered by temporal variations around 3-10 Hz.

Simulation with our model

‘General’ protocol. Reproduction by our model of the ‘general’ protocol is shown in Figure 4.9- A and B. The model reproduces the typical time advance of ganglion responses at high contrasts (Figure 4.9-B). This is because conductance g_A in (4.11) determines the time constant of the response of bipolar cells, and that the mean level of g_A , dependent on the average of V_{Bip}^2 , is a growing value of contrast.

Similarly, the under-linearity of response amplitudes with contrast is also observed (successive curves spaced by less than $\log(2)$ in Figure 4.9-A). This is because g_A in (4.11) increases the leak in the bipolar membrane, and thus lowers the linear gain of bipolar transmission in the case of high input contrast.

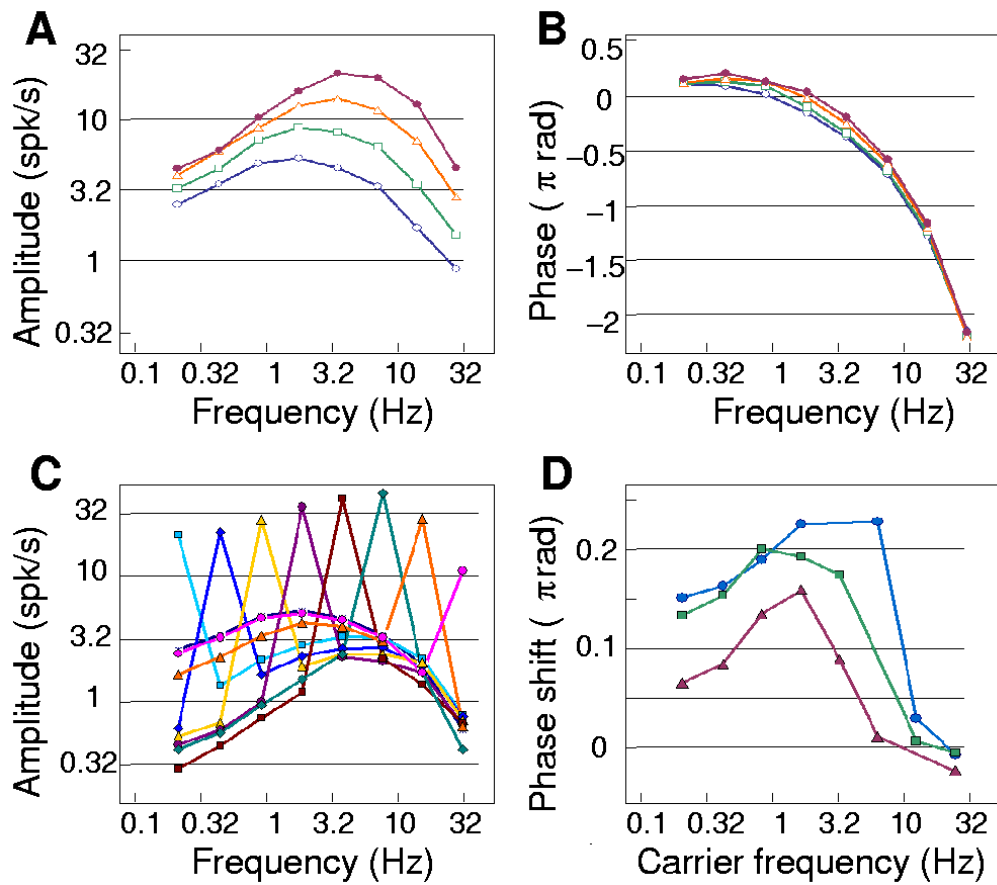


Figure 4.9: *Reproduction of the gain control effect by a model cat X cell.* A, B and D have same signification as in Figure 4.8 (including various curve markers). C represents the amplitude responses for the model cell in the 'carrier frequency' experiments (stimuli as in Figure 4.8, C-2). Contrast gain control is observed since the 'perturbation' kernels do not superimpose (see text). *Test grating:* mean luminance of 0.5, 0.2 cycles/deg. *X Cell parameters* as in Figure 4.7.

According to the preceding intuitive explanation, any shunting feedback loop necessarily implies a phase advance and an amplitude compression, and thus contrast gain control. However, reproducing the exact *shape* of the kernel, and how it varies with contrast, required more specific features from our model.

First, the feedback loop (4.11)-(4.13) is globally a low-pass setting, that can by no means reproduce the band-pass behavior observed in Figure 4.8-A. The band-pass behavior in our model arises *before* the feedback loop, through filter T_{w_U, τ_U} in (4.8) that accounts for temporal transients in the first layers of the retina, and *after* the feedback loop, through filter T_{w_G, τ_G} in (4.15) that accounts for temporal transients in the IPL.

Second, we found mandatory that function Q in (4.13) be *strictly convex* with a flat zone around $V_{\text{Bip}} = 0$, in order to reproduce the pronounced change in shape of the Wiener kernel between high and low contrast. If simulations are done with $Q(V_{\text{Bip}}) = \lambda|V_{\text{Bip}}|$, we obtain parallel amplitude curves spaced by less than $\log(2)$: Contrast gain control is thus present, but we are unable to reproduce the specific transformation of Wiener kernel shapes with contrast. The biological relevance of a strictly convex shape is discussed in Section 8.1.3.

‘Carrier’ protocol. The three measured phase differences $\phi_5(\xi_{i_0})$, $\phi_6(\xi_{i_0})$ and $\phi_7(\xi_{i_0})$ for our model are represented in Figure 4.9-D. We reproduce larger phase advances when the carrier frequency is in the range 1-10 Hz. This is due to the temporal band-pass filter T_{w_U, τ_U} in (4.8), that enhances the contributions of frequencies 1-10 Hz in the current I_{OPL} which is fed to the gain control mechanism (4.11).

In Figure 4.9-C we also provide the Wiener kernels associated to the experiment. Given a carrier frequency ξ_{i_0} , the interesting feature is the *perturbed kernel* measured at the remaining frequencies $\xi_i \neq \xi_{i_0}$. Perturbed kernels for different carriers ξ_{i_0} do not superimpose, because all carriers do not imply the same amount of gain control. Strong gain control translates in a Wiener kernel that is more cut at low temporal frequencies. For our set of parameters, we find that the carrier frequencies that elicit the most gain control are $\xi_{i_0} = 4, 8$ and 2 Hz, coherently with Figure 4.9-D.

6.3 LN analysis

Another way to compute Wiener kernels is Linear–nonlinear (LN) analysis, based on reverse correlation of the output signal with a white noise stimulus (Chapter 2, Section 5). It provides a way to measure the LN architecture (linear filtering followed by a static nonlinearity) that best fits the measured cell. This method has been recently applied to the retina to provide new measurements of contrast gain control (Chapter 3, Section 5.2.3).

Figure 4.10- A and B presents experimental results of Baccus and Meister 02 [5] on a salamander ganglion cell (already presented in Chapter 3, Figure 3.40).

They performed an LN analysis with white noise at two different contrasts, to measure the change in the filtering structure of the cell. The dual mark of contrast gain control is again observed: Time advance of the response (Figure 4.10-A) and decrease of the gain for high contrasts (slope of the nonlinear function in Figure 4.10-B).

LN analysis on a model cell is depicted in Figure 4.10- C and D. Our simulated cell is based on the X cell model of Figure 4.7, except for time scales which were fitted

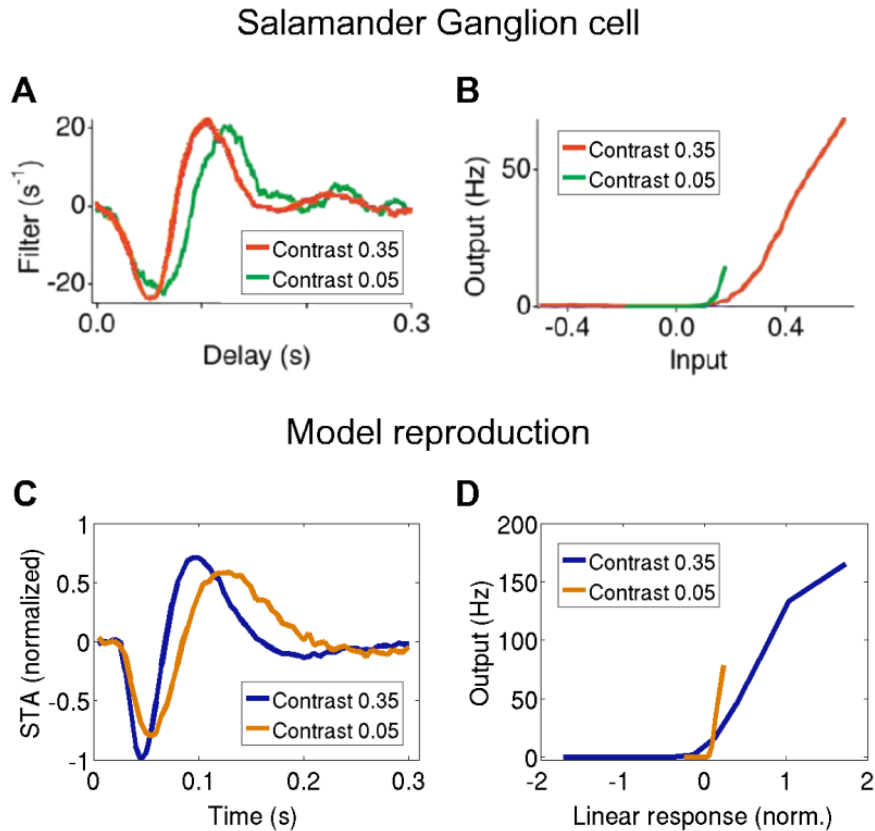


Figure 4.10: *A and B*: LN analysis by [5] on a salamander ganglion cell, revealing contrast gain control. Time advance can be observed (A), and decrease of the gain at high contrasts (B). *C and D*: LN analysis on a model cell, based on a spike-triggered average as in [31] (time bin 5 ms). Same parameters as the model X cell in Figure 4.7, except for slower time scales to account for the salamander retina: $\tau_C = 30$ ms, $\tau_S = 20$ ms, $\tau_G = 50$ ms, $i_G^0 = 0$ Hz, $\lambda_G = 300$ Hz.

to salamander retina time constants. The dependence on contrast of the linear filter and nonlinear curve is qualitatively similar to the original experiment. Such result is not surprising, since the LN analysis performed here has strong links with the multi-sinus contrast experiment of Section 6.2. Indeed, LN analysis is performed by measuring a response to white noise, and we have explained how the stimulus in Section 6.2 is closely related to a white noise signal.

Remark: When we first presented the results of Baccus and Meister 02 (Chapter 3, Figure 3.40), the distinction was made between ‘late’ and ‘early’ filters, to account for the effects of *slow* contrast adaptation. In our case, only the opposition between ‘*H*’ and ‘*L*’ filters is relevant, as arising from *fast* control gain control, which is the only effect reproduced in the current state of our model. The subject of slow adaptation is discussed in Section 8.1.3. ■

7 LARGE-SCALE SIMULATIONS

To conclude our presentation of *Virtual Retina*, we present simulations on whole images and sequences. We do not study quantitatively any retinal feature in this section: Our thesis did not aim at such study, but at creating a simulation tool. Rather, we illustrate qualitatively how large-scale simulations allow to link a model architecture with its perceptual consequences.

First, as a general illustration of the software, we present the complete simulation of a retina on a moving sequence, with spiking output and all intermediate signals involved. Second, we focus on two specific elements of the model and how they relate to a percept.

7.1 Large-scale simulation of the model

We show in Figure 4.11 the response of our model to an input video stimulation, with all intermediate signals represented at two instants of the simulation. To display all possibilities of *Virtual Retina*, we chose a hybrid retina, with cell properties being those of a cat retina (with X and Y cells), but that displays a radial structure as in a primate retina, with spatial precision maximum in the fovea, and decreasing towards the periphery. The simulated retina had a diameter of 50 deg, corresponding to 250 pixels. The input sequence lasted 1.4 s of ‘real time’, corresponding to 56 frames (each frame shown for 25 ms). There were three ganglion layers of 30,000 spiking cells each. On average, each cell fired approximately one spike per input frame. Total processing time was around 130 s (2 seconds per input frame).

The foveated structure, ruled by sampling scheme (4.17), can be observed on all retinal images (except for the input light): The periphery is more blurred than the central zone.

Signals C , S and I_{OPL} illustrate the properties of the OPL filter (4.8)-(4.10): It is the difference of two low-passed versions of the sequence, so it takes strong values on *image edges* and on *moving zones*. Its biggest response is thus located on the edges of the walking characters.

Second column corresponds to layers I_{OPL} , V_{Bip} and g_A which are involved in the contrast gain control scheme (4.11)–(4.13). The contrast gain control scheme enhances the linear contrast image I_{OPL} to produce V_{Bip} (which reveals better the details of contrast). This perceptual effect is detailed in the sequel.

Last column presents linear reconstructions from the output spike trains, respectively from X ON and OFF cells, and Y OFF cells. Each spike simply contributes to the reconstruction by adding a circular spot, whose diameter and intensity depend on the cell density in this region of the retina, and whose temporal profile is a decreasing exponential of time constant 20 ms. Thus, a reconstructed sequence displays in each pixel a quantity close to the ‘instantaneous firing rate for a cell located at this pixel’.

The positive and negative parts of signal V_{Bip} are coded respectively by ON and OFF ganglion cells. Y cells display a signal with less spatial precision than X cells, because of the supplementary synaptic pooling G_{σ_G} in (4.14). Second, Y cells are only sensitive to temporal changes, so they only detect the moving characters. This is obtained by making Y cells totally phasic with $w_G = 1$ in (4.14), and by lowering the spontaneous firing rate of Y cells, through parameter i_0^G in (4.15).

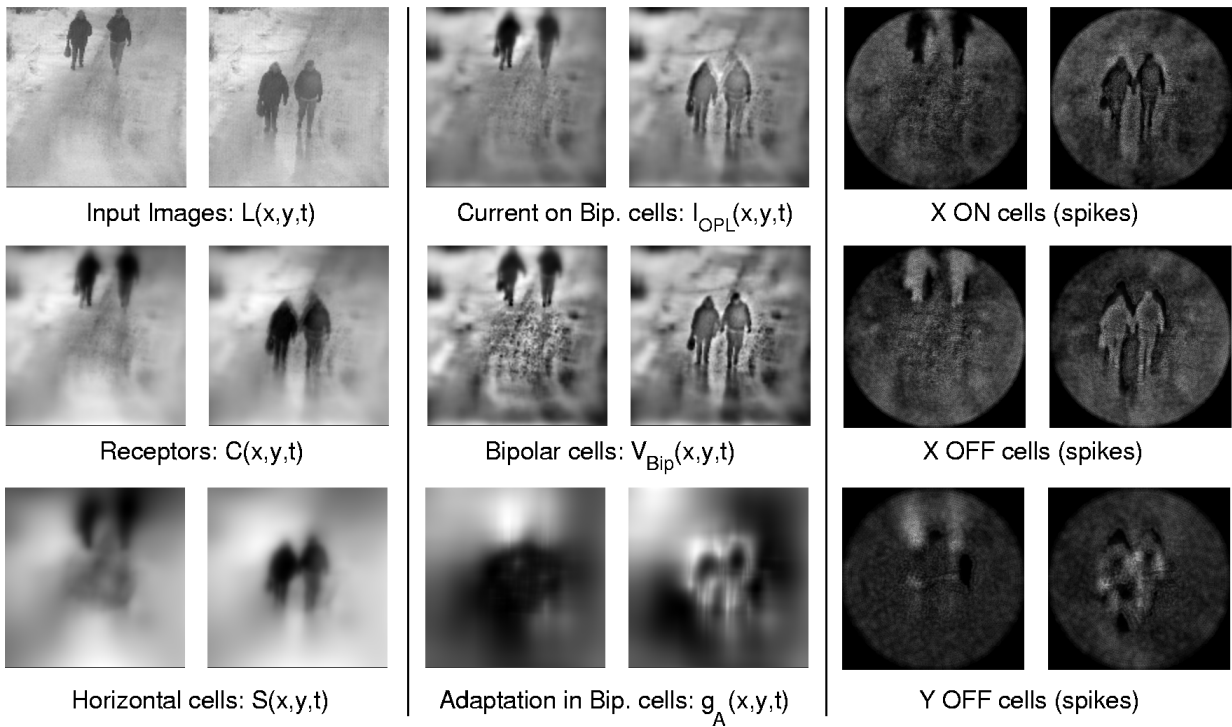


Figure 4.11: Large-scale simulation with cat X and Y cells. Image size: 50 deg (250 pixels). Same parameters as in Figure 4.7, except $\sigma_C = 0.3$ deg, $\sigma_S = 1$ deg, and for Y cells $\sigma_G = 1$ deg, $i_G^0 = 60$ Hz. Artificial radial structure as in primate retinas: $R_0 = 10$ deg (50 pix), $K = 0.2$ deg $^{-1}$. 90,000 spiking cells, simulation speed of around 1/100 real time (see text).

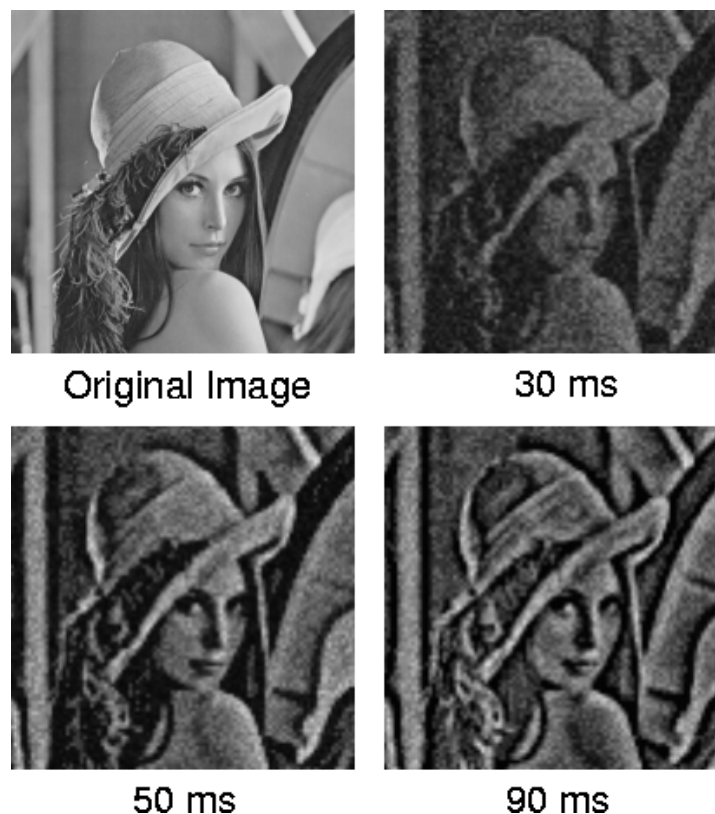


Figure 4.12: Spiking cells respond to the onset of a static image, after exposure to noise of similar luminance. First spikes code for a luminance signal (see reconstruction 30 ms after image onset). The ‘edge detection’ signal is coded only in the following spikes (see reconstruction at 90 ms), due to the non-separability of filtering in the OPL (see text). *Experimental procedure*: Primate ‘parvo’-like cells: $\sigma_C = 0.03$ deg, $\sigma_S = 0.1$ deg, $\sigma_A = 0.2$ deg; $\tau_S = 4$ ms, approximative delay measured between *center* and *surround* signal in cat [60] and primate [12]. Other parameters as in Figure 4.7. Input image 5 deg (500 pixels). Output array: 100x100 cells, one cell per pixel in the reconstruction.

7.2 Perceptual consequences of model architecture

7.2.1 Spiking pattern at image onset

It has long been known that the center-surround architecture of ganglion cells produces preferential responses to spatial or temporal change. Many subsequent modeling has considered the retina – or at least its center-surround ganglion cells pathway – as an *edge detector*. Here we suggest there could be another effect in the first milliseconds after image onset, due to the biologically observed delay of *surround* signal w.r.t *center* signal [60, 12].

Figure 4.12 presents a reconstruction from the spikes emitted by a square array of primate ‘parvo’-like cells, after onset of a static image (one cell per pixel, each spike adding an exponential contribution of latency 15 ms). To produce plausible initial conditions, the cells are previously exposed to Gaussian white noise of same luminance as the forthcoming image.

The first spikes coding for the image (observable from around 20 ms after image

onset) do not code for image edges, but only for the *center* signal, simply proportional to the input luminance: See reconstruction at time 30 ms. The following spikes progressively start coding for image edges, as the delayed *surround* signal (equation (4.9)) catches up. In the reconstruction of Figure 4.12, the transition is partly achieved at time 50 ms, totally achieved at time 90 ms. It is surprising, but verified, that the small supplementary delay of *surround* (here, $\tau_S = 4$ ms) has perceptual effects over several tens of milliseconds (likely, the supplementary transient T_{w_G, τ_G} helps to enhance the effect of the *surround*'s delay).

The subsequent ‘edge image’ is the *equilibrium* signal of the retina: It defines the ‘stabilized’ retinal output to the static image, after the initial luminance transient at onset (in fact, ‘stabilized’ is only an approximation, due to slow adaptation effects). But the initial ‘luminance transient’ probably has its importance for studies of spike-related information transmission. If it is true that the first emitted spikes carry the most information (Van Rullen and Thorpe 01 [148]), is the retina really an edge detector?

We believe that a large-scale, and relatively detailed simulator such as *Virtual Retina* might be of some help to theoreticians wishing to address this ‘image onset’ problem with quantitative tools such as information theory.

Remark: Using the basic microsaccade generator included in *Virtual Retina* (Chapter 6, Section 2.2.3), we also tested what signal is coded when the image is subject to small, regular displacements of frequency around 2 Hz (Martinez-Conde *et al.* 04 [106]). We found that the ‘microsaccade’-perturbed image remains perceptually close to the stabilized ‘edge image’. ■

7.2.2 Contrast enhancement through contrast gain control

As a second illustration of the relation between models and large-scale percepts, we present in Figure 4.13 how the gain control loop (4.11)–(4.13) enhances edges nonlinearly, in ways very similar to traditional image processing techniques.

The test image displays a flower with strong contrast, and smaller variations of contrast in the background. We only consider here the *equilibrium* ‘edge image’ of the retina, rather than the initial ‘luminance transient’ (as explained in the previous paragraph).

We compare the linear output of the retina I_{OPL} with two versions of V_{Bip} after contrast gain control. First version considers a purely temporal gain control loop, with no spatial extent for the measure of contrast by $g_A(x, y, t)$ (through $\sigma_A = 0$ in eq. (4.12)). Second version allows this spatial extent, with $\sigma_A = 0.2$ deg, a value comparable to the extent of our surround signal $\sigma_S = 0.1$ deg. We study these two cases distinctly because of the hypothetical nature of parameter σ_A in our retinal model (see Discussion in Section 8.2).

To produce comparable results, the three resulting images ($I_{\text{OPL}}(x, y)$ and the two $V_{\text{Bip}}(x, y)$) are normalized between -1 and 1 , and passed through an adimensional rectification N as in (4.15) (with $i^0 = 0.3$, $\lambda = 1$, $v^0 = 0$, see Figure 4.5) modeling ganglion rectification and spike generation.

Panel *B* presents the rectified version of $I_{\text{OPL}}(x, y)$, the linear response. In panels *C* and *D*, we present the interplay between the rectified nonlinear output $V_{\text{Bip}}(x, y)$ and the adapting conductance $g_A(x, y)$ that produced the nonlinear effect.

In the case of a purely temporal contrast gain control ($\sigma_A = 0$, panel *C*), one can observe a re-equilibrating of the contrast levels, as compared to the linear out-

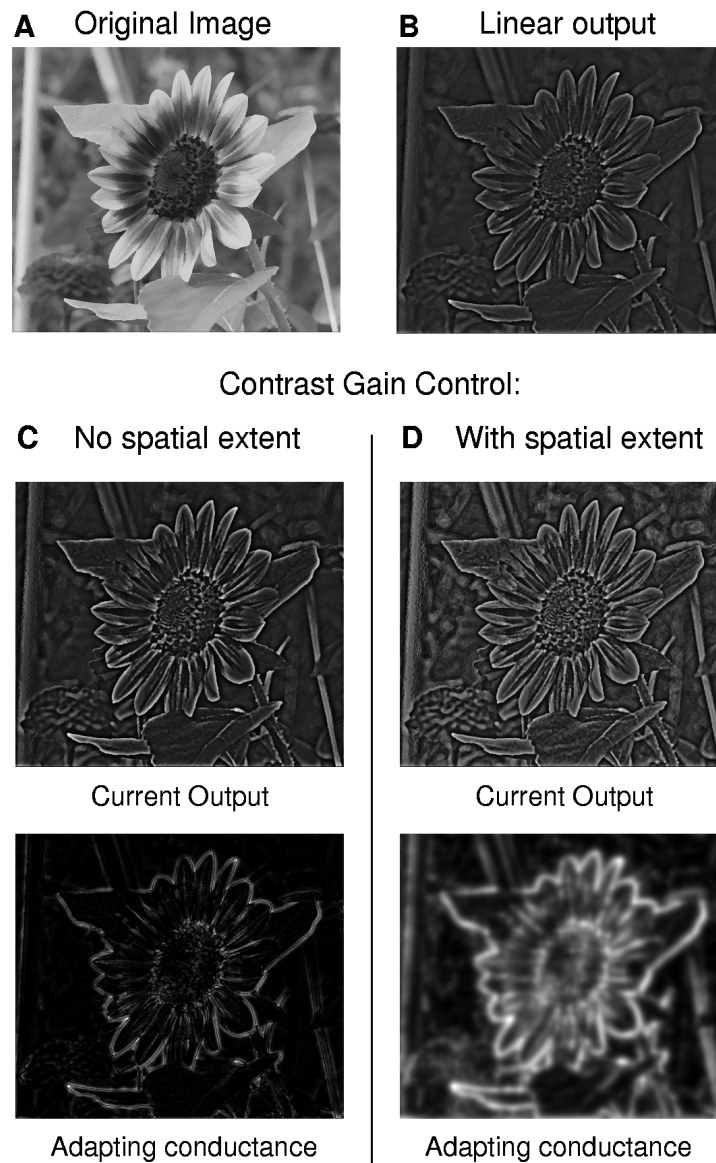


Figure 4.13: Perceptual comparison between a linear output (*B*) and two versions of the gain control mechanism. When the gain control is purely temporal ($\sigma_A=0$, panel *C*), it operates as a point-by-point Gamma transform on the image. When the gain control is allowed to have a spatial extent (*D*), it operates like a local histogram equalization on the contrast image. *B* to *D* are equilibrium responses, after the initial transient at image onset. Details and experimental procedure in the text. Flower photo courtesy of Marcello Moisan [114].

put (*B*). Intermediate contrast levels are enhanced as compared to high-contrast levels (see, e.g., the small flower at the bottom left). Mathematically, when equilibrium is reached in (4.11)–(4.13), one has the point-by-point relations $g_A(x, y) = Q(V_{\text{Bip}}(x, y)) = g_A^0 + \lambda_A V_{\text{Bip}}(x, y)^2$ and $I_{\text{OPL}}(x, y) = V_{\text{Bip}}(x, y)g_A(x, y)$, so that the nonlinear output can simply be understood as the static point-by-point compression

$$V_{\text{Bip}}(x, y) = L^{-1}(I_{\text{OPL}}(x, y)),$$

with $L(V) = V(g_A^0 + \lambda_A V^2)$. So in this case ($\sigma_A = 0$, on a static image), our gain control loop (4.11)–(4.13) is close to a Gamma-transform [71] on the original linear output.

In the case where contrast gain control mechanism includes a spatial extent σ_A (panel *D*), the equilibrium between $V_{\text{Bip}}(x, y)$ and $g_A(x, y)$ becomes dependent on the spatial structure of the input image and there is no analytical expression. Intuitively, $g_A(x, y)$ provides a divisive effect on $V_{\text{Bip}}(x, y)$ based on the contrast *in the neighborhood* of (x, y) , making $V_{\text{Bip}}(x, y)$ a measure of contrast that is *local* rather than absolute. This enhancement, which can be observed in the background in *D*, is very close to a local histogram equalization (see [71], chapter 3) on the linear contrast image.

These results are another example of link between physiological and perceptual features allowed by large-scale simulation. We wish to stress the *qualitative* nature of these perceptual results on contrast gain control. For example, one might argue that we humans do not see such an enhanced contrast as that displayed in Figure 4.13-*D*. It should not be forgotten that the Midget (‘parvo’) pathway of primates, which is supposed to be our primary source of precise form analysis, is very little subject to contrast gain control [13]. Besides, the problem of ‘double filtering’ (by the software, and by our visual system) raises other issues concerning what we see when looking at the reconstructions.

To conclude, note that physiological measurements such as those of Shapley and Victor 78 (Figure 4.8-*A*) demonstrate that there is under-linearity to contrast in cat ganglion cells, at least in specific spatio-temporal conditions (their experiments concerned sinusoidal stimulation, whereas here we simulate a totally static image). This necessarily implies a perceptual invariance, for all cells which display contrast gain control (cat cells, primate Parasol (‘magno’) cells): At least, a static compression effect as in Figure 4.13-*C*. Possibly, a local equalization as in Figure 4.13-*D*.

8 DISCUSSION

8.1 General discussion

8.1.1 Combining large-scale and plausibility

In this chapter we have presented the model that is implemented in our large-scale simulator *Virtual Retina*, whose usage and implementation are the subject of Chapter 6. Before going into the details of the underlying retina model, we wish to stress

that this model was designed to fit the requirements for software *Virtual Retina*: To achieve at the same time large-scale simulation and a relative biological plausibility, with an adaptable degree of complexity.

First of all, *Virtual Retina* is a *large-scale* simulator. It aims at providing input to neuroscientists who need this large-scale factor: Motion detection tasks in a natural scene, population coding by an assembly of spiking visual neurons, information-theoretic calculations on natural scenes. In this optic, it is being used by several research teams of the FACETS¹ European consortium as input to detailed models of primary visual cortex (V1). It can also serve as a demonstration tool in an educational framework.

As a large-scale simulator, we wished to reduce as much as possible the number of parameters used in the underlying model. This explains the simple form taken by our successive stages (OPL, contrast gain control, IPL and ganglion cells), that discard many effects known to occur in real retinas.

At the same time, *Virtual Retina* intends to be a *plausible* simulator, that can provide output spike trains reasonably close to those of real ganglion cells. The reproduction of a number of experimental recordings in Section 6 appeared a necessary step to prove the plausibility of the software.

As a plausible simulator, we wanted to keep specific properties of retinal processing that are often ignored by large-scale models. This includes: The non-separability of the OPL filter (4.10) that allows to detect both image edges and uniform flickering screens, the contrast gain control mechanism (4.11)–(4.13) that provides invariance to contrast in natural scenes, and the trial-to-trial variability in the emission of spike trains.

As a plausible simulator also, *Virtual Retina* uses an underlying model mostly based on prior, state-of-the-art knowledge on the retina, experimental results as well as models. This state-of-the-art knowledge has been thoroughly presented in Part I of this thesis. Our modeling task was to reduce this state-of-the-art knowledge to formulations as simple as possible, for inclusion in the software. As an exception, our contrast gain control mechanism in its precise form (4.11)–(4.13) is a more original contribution, although it also strongly relates to previous work. For this reason, the mechanism is specifically discussed in Section 8.2, and studied mathematically in Chapter 5.

The present model includes various functionally relevant features of real retinas (X and Y cells, contrast gain control, plausible spike generation), but also discards a number of features presented in Part I (other types of ganglion cells, light adaptation, spiking synchronies). However, the whole framework of the model (continuous convolutions and ODEs) and of the underlying implementation (Chapter 6) allows easy extensions (see Conclusion of the thesis).

Let us now discuss the general handling by our model of spatial (Section 8.1.2) and temporal (Section 8.1.3) interactions in the retina.

¹<http://facets.kip.uni-heidelberg.de/>

8.1.2 Spatial filtering in the model

The issue of continuous spatial filtering

A first question that may come to mind when considering our global modeling framework, is whether the use of a continuous formalism for spatial filtering is really justified. Indeed, we introduced continuous Gaussian kernels to model synaptic pooling and/or coupling through gap junctions, as the natural asymptotic limit when the typical spatial step δ between neighboring cells tends to zero (Chapter 2, 6). By proceeding to this continuous limit, we formalized our system in a functional, ‘image processing’ approach, and allowed a simple implementation of the first, ‘continuous’ retinal layers as 2D pixel maps. Could it be possible that some types of retinal interactions cannot be formalized in this framework?

Each of our 2D maps models a homogeneous layer of cells of the same nature, as we know it exists in the retina (Chapter 3, Section 3.1.2). A first limitation of ‘continuous modeling’ may arise if the cell mosaic is not dense enough, as compared to the typical spatial resolution of its ‘input current image’ (photocurrent, or synaptic inputs). But the spatial poolings and gap junction couplings precisely insure that the input current image is low-passed, thus avoiding any undesired aliasing.

But still, some synaptic interactions cannot be implemented in a ‘continuous’ framework:

1. *Inhibitory* interactions between neighboring cells of the same layer. If such interactions exist (likely, through chemical synapses), their modeling in a set of discrete equations cannot be extended to a continuous PDE form (the resulting PDE becoming unstable, e.g., like in the reverse heat equation). However, such interactions have not been reported in the retina (Part I). By opposition, we remind that inhibitory interactions between neighboring cells of *different* layers, very present in the retina, are naturally modelizable in our continuous framework as interactions between different 2D maps.
2. *Spiking* interactions in the IPL. It is difficult to convert a discrete array of spiking units to a spatially continuous framework. Such ‘continuous extensions’ exist in particular cases (e.g., in the case of spiking synchronies, by associating each image pixel to the local ‘phase of spiking’), but their formalism is too specific and restrictive for the general-purpose simulator that we are trying to produce.

For this reason, we naturally sampled our ‘ganglion current’ signal $I_{\text{Gang}}(x, y, t)$ to produce discrete sets of spike trains (Section 5.2). This amounts precisely to the generic ‘two-step’ models for spike emissions in the retina (1. continuous processing, 2. spike emission, Chapter 3, Section 4.1.3), and suffers from the same limitations: It can hardly model feedback influences of emitted spikes on the preceding ‘continuous’ layers. However, this sort of feedback, if it exists, is not well understood yet, and is not likely to be required from a general-purpose large-scale simulator.

In conclusion, the ‘continuous’ formalism for spatial filtering is well-suited for a large-scale retina model. It allows simple implementation and fast numerical schemes (spatial recursive filtering, Chapter 6, Section 3.2.2), without any severe aftermaths.

Spatial opposition in the IPL

Our model assumes that the center-surround behavior of bipolar cells arises mostly because of spatial oppositions in the OPL, due to horizontal cells. This allows to feed our contrast gain control stage (4.11) with an input current I_{OPL} which is already band-pass spatially.

This is in fact a strong assumption, as pieces of experimental evidence suggest a role of amacrine cells in the arousal of some ganglion cells' *surround*, possibly as feedback to bipolar cells (Chapter 3, Section 2.3.4). Inclusion of such a feedback would lead to a new model of bipolar integration, in which (4.11)-(4.12) is replaced by

$$\begin{aligned}\frac{dV_{\text{Bip}}}{dt} &= I_{\text{OPL}} - g_A V_{\text{Bip}} - w_{\text{Am}} V_{\text{Am}}, \\ V_{\text{Am}} &= G_{\sigma_{\text{Am}}} \overset{x,y}{*} E_{\tau_{\text{Am}}} \overset{t}{*} V_{\text{Bip}}, \\ g_A &= G_{\sigma_A} \overset{x,y}{*} E_{\tau_A} \overset{t}{*} Q(V_{\text{Bip}}),\end{aligned}$$

where V_{Am} provides a *surround* component to bipolar cells, of relative weight w_{Am} , modeling feedback from some amacrine cells, while g_A is still an adaptation conductance based on the recent values of V_{Bip} .

Formally, this set of equations includes a double feedback and is particularly hard to study. We do not know to what extent properties typical of contrast gain control would persist in this configuration. Likely, the temporal properties of contrast gain control would be little affected by the change, as long as I_{OPL} keeps the same temporal sensitivity (band-pass) as previously. By opposition, the perceptual effects of our original contrast gain control scheme (equalization of the levels of contrast in the image, as in Figure 4.13) would likely be affected, in a way which is hard to predict.

Studying this extended scheme with a feedback *surround* component from the IPL seems an interesting but challenging problem.

8.1.3 Temporal transients and adaptation in the model

'Adaptation' is a word widely used in neurophysiology, that can convey various meanings. When presenting the retina in Part I, we restricted this word to the description of nonlinear effects in retinal filtering. Conversely, we rather used the word 'transient' to define the temporal high-pass stages that we modeled through linear filters. Using this terminology, our simulator uses two linear transient filters T_{w_U, τ_U} and T_{w_G, τ_G} , and one contrast adaptation stage with the feedback loop (4.11)–(4.13). We designed the feedback loop (4.11)–(4.13) as a purely low-pass stage, by associating the adapting conductance g_A to a null Nernst potential. As a result, only the two linear filters T_{w_U, τ_U} and T_{w_G, τ_G} are in charge of temporal shaping in the system.

Slow adaptation is not modeled yet

Our adaptation scheme to contrast is discussed in Section 8.2. We wish to stress that this scheme only aims to reproduce *fast* gain control adaptation. Recent works

[5, 93] have revealed a second mechanism of gain control, on a much slower time scale (Chapter 3, Section 5.2.3). This secondary gain control enters the family of *slow adaptation* mechanisms in neurons, that we have not discussed nor included in our simulator. Likely, this slow adaptation is present simultaneously at different biological locations, both pre- and post-synaptically to ganglion cells (Chapter 3, Section 5.3).

For the moment, *Virtual Retina* ignores slow adaptation, although a very experimental spike-frequency adaptation scheme is available in the source code (as suggested to provide slow contrast gain control by Kim and Rieke 01 [93]). Note that if a slow adaptation was implemented in the model (spike-frequency adaptation or other), it would allow to account for the nonlinear variations of cat X cells in response to a uniform screen, according to their mean level of activity during the current stimulation (Section 6.1 and Figure 4.6-A).

Two temporal high-pass stages in the model

As for linear filters T_{w_U, τ_U} in (4.8) and T_{w_G, τ_G} in (4.14), they must be seen as a functionally convenient choice to reproduce high-pass behaviors in the retina. Their respective biological locations and time scales (100 ms for T_{w_U, τ_U} versus 10-30 ms for T_{w_G, τ_G}) do not intend to reproduce physiology with precision. We now detail the choice of location and time scale for these two transient filters.

Filter T_{w_U, τ_U} . This temporal transient is associated to filtering in the OPL. It can convey different physiological meanings. First, it can be seen as a crude approximation of the intrinsic undershoot occurring in cone phototransduction in the time scales of a few hundreds of milliseconds, as measured by Schnapf *et al.* 90 [151] (Figure 2.4, but see also Figure 3.3 A where no transient behavior is obvious). Second, it can account for the intrinsic transients in bipolar cells' synaptic receptors, which contribute to create 'sustained' and 'transient' subtypes of bipolar cells (work of De Vries *et al.*, Chapter 3, Section 2.4).

Filter T_{w_G, τ_G} . By opposition, this temporal transient is associated to filtering in the IPL. It accounts mostly for amacrine cells that provide a strong inhibition on some bipolar cells and/or ganglion cells at the level of synapses in the IPL (Chapter 3, Sections 2.4 and 3.1.3).

Slow and fast transients in our model. In a functional retina model, choosing the correct location for temporal transients is somewhat arduous. From the previous paragraphs, we have seen that such transients occur both prior and posterior to membranar integration in bipolar cells, where we have located our gain control mechanism. Also, the temporal scales at which both of these transients occur are not clear, due to their undefined physiological origin, and the natural variation from one cellular pathway to another. Because we wish that distinct elements of our model have distinct functionalities, we generally associated different time scales and roles to T_{w_U, τ_U} and T_{w_G, τ_G} .

Filter T_{w_U, τ_U} is thus generally taken as a rather *slow* transient, with τ_U in the order of a hundred of milliseconds, reflecting its possible signification as slow phototransduction transients. Filter T_{w_U, τ_U} serves as a way to correctly enhance the 1-10 Hz frequency range before application of the contrast gain control stage (Section 6.2

and Figure 4.8-D). At the same time, it provides a very simple linear equivalent to slow cellular adaptation described in the previous paragraph.

By opposition, filter T_{w_G, τ_G} is generally taken as the *fast* transient, with τ_G in the order of a few tens of milliseconds. As such, filtering by T_{w_G, τ_G} becomes the processing step where we can fix the balance between tonic and phasic cells, through parameter w_G (Section 5.1). Biologically, locating the tonic/phasic opposition at the level of the IPL is reasonable, since the IPL is the retinal location with the biggest variety of cell subtypes, by opposition with the OPL that involves only two types of light receptors (cones and rods) and three to four types of horizontal cells (as detailed in Chapter 3).

To sum up, our model takes the distributed nature of temporal transients into account thanks to two high-pass stages T_{w_U, τ_U} and T_{w_G, τ_G} , located prior and posterior to the gain control stage in bipolar cells. Associating T_{w_U, τ_U} to slow transients and T_{w_G, τ_G} to fast transients is an arbitrary choice to achieve a better functional repartition of tasks. However, the uncertainty in the choices of these two time scales remains a somewhat unsatisfactory element of our model, which should be better explored.

8.2 Contrast gain control mechanism

Although the gain control mechanism proposed here is close to existing models of gain control in the retina (Victor 87 [178], Chapter 3, Section 5.2.4), it is an original contribution in its precise form. Interestingly, because of its simple form, its gain control properties are justified mathematically (see the results in Chapter 5). We now discuss the biological relevance of our model, and relate it to other gain control models that have been proposed at the level of the retina.

8.2.1 Interpretation of the model

Shunt conductances

Our model assumes that fast contrast gain control is achieved by the divisive influence of conductances in the membrane of bipolar cells. When a conductance $g_j(t)$ opens in a cellular membrane, associated to *Nernst* potential E_j , it creates a synaptic current $g_j(t)(E_j - V(t))$ through the membrane, as detailed in equation (4.1). Such a current can be decomposed in a ‘linear contribution’ $g_j(t)E_j$ and a ‘shunt contribution’ $-g_j(t)V(t)$. If only the first term is taken into account, then $g_j(t)$ contributes linearly to $V(t)$. By opposition, the second term is independent of the *Nernst* potential and modifies nonlinearly the instantaneous gain of membranar integration, by contributing to reduce the total membranar resistance.

At the contrast gain control stage (4.11)–(4.13), our model focuses on the *shunting* impact of dynamic conductances onto bipolar cells: Only the term $-g_A(t)V(t)$ is present, as if our adapting conductance g_A was associated to a null *Nernst* potential (with the convention that $V_R = 0$ corresponds the neurons’ resting potential). We do not claim this to be the biological reality, but only a computational commodity to reduce the number of required parameters. First, it dispenses from fixing a value to the *Nernst* potential. More importantly, it allows the whole scheme (4.11)–(4.13) to display an ON-OFF symmetry, which provides a fair reduction in the number of parameters.

ON-OFF symmetry

In the retina, the positive and negative parts of visual signals are transmitted through two distinct pathways, ON and OFF, which imply different cells starting from bipolar cells (Chapter 1). By opposition, the distinction between ON and OFF cells arises only at the third stage of our model, right before spike generation by ganglion cells (Section 5, equation (4.14)). Before that, single signals ($I_{\text{OPL}}, V_{\text{Bip}} \dots$) are used, which code symmetrically for positive and negative values.

Our contrast gain control scheme (4.11)–(4.13), which is totally symmetric, is thus a consequent simplification of the biological reality, in order to reduce model complexity. This explains the symmetric shape of function Q , not often met in biological neurons: It is intended to encompass simultaneously gain controls on ON and OFF cells. The corresponding biological architecture, if it exists, is that of two distinct pathways which display:

- A gain control mechanism on their preferred contrast polarity (ON or OFF), similarly to (4.11)–(4.13), except for function Q that becomes a one-sided smooth rectification (similar to function N in the sequel - Figure 4.5).
- A signal compression on their non-preferred contrast polarity.

Convex activation function

The quadratic expression chosen here for Q is the simplest function to be both symmetric and flat around $V_{\text{Bip}} = 0$. This flatness around zero was found mandatory to reproduce the multi-sinus kernels of Section 6.2. For example, similar good reproduction was obtained when function Q was linear by parts with an activation threshold:

$$Q(V_{\text{Bip}}) = \begin{cases} g_A^0 & \text{if } 0 < V_{\text{Bip}} < v_0, \\ g_A^0 + \lambda_A(V_{\text{Bip}} - v_0) & \text{if } V_{\text{Bip}} > v_0, \end{cases} \quad (4.18)$$

and symmetrically in the negative range. But this required a supplementary parameter, and allowed a less well-defined mathematical analysis.

Biologically, the convex shape required for Q in our model might reflect the existence of voltage-gated conductances in bipolar cells, whose activation becomes significant only at high potentials V_{Bip} . Indeed, different voltage-gated inhibitory currents have been observed in bipolar cells of several species [36, 95] (Chapter 3, Section 5.2.3). Mathematically, the convexity of Q is also an important property to demonstrate the system's good behavior as a gain control mechanism (Chapter 5).

Physiological interpretation

It is natural to ask whether or not the present model of gain control can be attached to a physiological meaning. We know from different experiments that the *fast* gain control mechanism is already observed at the level of bipolar cells (Chapter 3, Section 5.2.3), which provides a first validation of our model.

But what could be the biological origin of conductances g_A in the membranes of bipolar cells, as in our model? We have seen that amacrine cells, which could have been candidates to provide the inhibitory conductance, are most likely not involved in the process. Instead, studies have suggested the possible role of voltage-gated

conductances, and more likely yet the role of calcium adaptation (Chapter 3, Section 5.2.3).

This suggests different possible biological explanations that can lead to equations (4.11)–(4.13) or close variants, as we present now. Let us remind that we are talking here about our presumed *biological* implementation of a ‘one-sided’ contrast gain control that would occur independently in ON and OFF cells, as proposed in the previous paragraph “ON-OFF symmetry”.

Voltage-gated conductances. A first possible explanation is that g_A might arise from voltage-gated conductances in the membranes of bipolar cells. This would explain the convex dependence of g_A on V_{Bip} , because the conductances only open strongly at high values of the membrane potential. It would also account well for the small time scale τ_A for the adaptation (almost no delay between a rise in potential and the subsequent conductance opening), that we found to produce the best results in our simulations ($\tau_A=5$ ms).

Calcium-dependent adaptation. A second, or simultaneous, explanation could imply calcium adaptation, in a way very similar to how it occurs during phototransduction (Chapter 3, Section 1.1): Synaptic currents in the bipolar cell’s dendrites may lead to an influx of calcium when the cell is stimulated (through the ionic channels opened by synaptic transmission – most likely from light receptors). In turn, calcium may be involved in a feedback reaction, through catalyzer equations (Chapter 3, Section 1.1.2) providing a divisive control on the synaptic channels, and thus on the membrane potential.

This alternative scheme could lead to a system formally close to (4.11)–(4.13), but where the involved variables would have a different signification:

- The ‘output’ variable, rather than directly being V_{Bip} , would be the synaptic current I_{Syn} flowing through the dendritic synaptic conductances from receptors and horizontal cells.
- The ‘control’ variable would be the concentration of some calcium-binding molecule $[M]$, whose concentration would depend on the inflow of calcium produced by I_{Syn} , and which would in turn regulate the ionic channels producing I_{Syn} , through a catalyzer equation of the form (3.1) (Chapter 3). The catalyzer equation, formally identical to the bipolar charging equation (4.11), would provide divisive control of $[M]$ over I_{Syn} (‘linear ODE’ framework, Chapter 2, Section 7).

Then, the other parameters of the model would also have equivalents: The control loop based on calcium inflow would occur with a characteristic time delay τ_A , and a convex nonlinearity Q may also be introduced for different reasons: Possibly, a Hill exponent in the binding of calcium to molecule $[M]$.

Pushing speculation further, the contrast gain control mechanism could also have a certain spatial extent σ_A , resulting from a diffusion of calcium between neighboring bipolar cells. Such diffusion is possible, due to the existence of gap junctions between neighboring bipolar cells (Dacey *et al.* 00 [38], Webvision [95]). We have seen in Section 7.2 how the presence of this diffusion through parameter σ_A would have interesting perceptual consequences on the output of the gain control model.

8.2.2 Other models of gain control

How does our model compare with other gain control models in the retina? The main influence of our gain control model is that of Victor 87 [178] (Chapter 3, Section 5.2.4). Our adapting conductance g_A , fixed by the recent values for $Q(V_{\text{Bip}})$, can be seen as a variation on the ‘neural measure of contrast’ $c(t)$ in Victor’s original model.

The main difference in our model is that we associate contrast gain control (4.11)–(4.13) to a *low-pass* scheme only (a simpler scheme which is also reminiscent of previous work, e.g., the Fuortes and Hodgkin 64 [68] model for light adaptation in photoreceptors). In our model, temporal high-pass is done through purely linear filters, before (slow transient T_{w_U, τ_U} in (4.8)) and after (fast transient T_{w_G, τ_G} in (4.14)) our gain control loop. Our gains by doing so are:

- Conceptual separation of two distinct effects, since a low-pass model is simpler, and sufficient to account for the contrast gain control.
- More biological plausibility, since our mechanism can be associated to (putative) biological interpretations.
- A mathematically tractable model, with available proofs concerning the behavior of the control loop (Chapter 5).

We also extended Victor’s concept of ‘neural measure of contrast’ to a possible spatial extent σ_A , and observed interesting consequences of this extension, on a perceptual level.

However, our gain control model remains the direct descent of the Victor model, one of the most accurate models of contrast gain control in the retina, that served as a direct influence to more recent models, such as the Y cell model of Enroth-Cugell and Freeman [58], or the Van Hateren model for primate Parasol cells [173] (Chapter 3, Section 5.2.4).

Another source of inspiration for our model can be found in models that propose *spatial* divisive effects in the retina. This is the case of the Bonin LGN model [17] which proposes the idea of a divisive *spatial* surround. But as such, it implements an invariance to local luminosity, so it accounts for different effects than our model which handles contrast gain controls.

By opposition, the Herault et al. retina model [79] allows at the same time for luminance and contrast invariance, through two successive divisive steps in retinal processing. Their model, strongly oriented towards fast image processing, displays purely analogical signals (no spikes), and does not focus on the temporal shaping of ganglion responses by temporal transients like our model. Neither Bonin nor Herault models are concerned with the dynamic change in the Wiener kernel induced by contrast gain control, but only by the *spatial* divisive influence of luminance and/or contrast on retinal outputs.

To summarize, two ‘trends’ of gain control models can be found: Those based on the temporal expression of the gain control and those based on its spatial expression. Here we proposed a framework where both effects can be accounted for, including a possible biological interpretation of the gain control phenomenon (voltage-gated conductances, or calcium adaptation).

CONCLUSION

In this chapter, we have described the retina model implemented in our simulation software *Virtual Retina*. The first stage of the model corresponds to the outer plexiform layer modeled as a non-separable spatio-temporal linear filter. The second stage is a functional implementation of contrast gain control through a shunting feedback mechanism. The third stage concerns further temporal shaping in the inner plexiform layer and spike generation in ganglion cells, to form the output spike trains.

Of course, this model remains an abstraction of the precise retinal mechanisms. It relies on assumptions and simplifications necessary to produce an efficient simulator. However, strong efforts were made to justify the modeling choices thanks to the physiology literature, as presented in Part I.

In particular, introducing relevant nonlinearities was one focus of the model. First, we included a model of the spatial nonlinearity of Y cells (Section 5.1), which plays an interesting role in the movement detection capabilities of these cells (Chapter 3, Section 3.2.2).

More importantly, we proposed an original nonlinear mechanism of contrast gain control, based on a dynamic feedback loop, which can implement both spatial and temporal invariance to contrast. The mechanism allows to reproduce well-known physiological expressions of contrast gain control (Section 6), and at the same time it yields an interesting perceptual effect of contrast enhancement (Figure 4.13). A mathematical analysis of this contrast gain control loop is the object of the next chapter.

The implementation of this model into software *Virtual Retina* is the object of Chapter 6. Future possible extensions and applications of the present model, based on the *Virtual Retina* library, are discussed in Conclusion to this thesis.

CHAPTER 5

A MATHEMATICAL STUDY OF THE GAIN CONTROL MECHANISM

In this chapter, we come back to the nonlinear feedback loop introduced in Chapter 4 to model dynamic contrast gain control. Our goal is to prove mathematically the good behavior of the system as a gain control device, producing under-linearity and phase advance at high input amplitudes.

Our gain control loop is the nonlinear extension of an ‘RC’ circuit. We thus start by studying this low-pass, linear filter, as a benchmark for comparison with our nonlinear system (Section 1). A necessary reduction of dimensionality leads us to the object of our study in this chapter, a 2-dimensional nonlinear control loop. We study its behavior through general properties and numerical simulation (Section 2).

Unfortunately, precise mathematical proofs are still out of reach in the general case of this 2D system. However, studying the phase portraits of the system for different sets of parameters reveals the existence of two asymptotic behaviors, at both extrema of one particular parameter’s definition domain, for which the dimensionality of the system is reduced to 1D. In Sections 3 and 4, we derive precise mathematical results for the two respective 1D asymptotic systems.

Finally, in Section 5, we give first hints of how perturbation analysis may allow to increase the range of parameters in which the system is mathematically tractable.

Contents

1	Introduction	223
1.1	The underlying low-pass linear system	223
1.2	Gain control through the nonlinear system	224
2	General study of the gain control system	226
2.1	System definition and first properties	226
2.2	Numerical simulation	231
3	Asymptotic behavior $b = 0$	237
3.1	System definition	237
3.2	Dependence of V_{\max} and ϕ_{\max} w.r.t. system parameters	238
4	Asymptotic behavior $b = +\infty$	240

4.1	System definition	240
4.2	Integral formulations for partial derivatives in the system . .	242
4.3	Dependence of V_{\max} and ϕ_{\max} w.r.t. system parameters	246
4.4	Local under-linearity of V_{\max} w.r.t. A	253
5	A track for the future: Perturbation analysis	255
5.1	Perturbation analysis near $b \rightarrow +\infty$	256
5.2	Perturbation analysis near $b \rightarrow 0$	259
	Conclusion	262
	Appendix: Periodic contracting system	262

1 INTRODUCTION

Here is the original gain control loop (4.11)-(4.13) used in our retina model (with somewhat simplified notations):

$$\frac{dV}{dt}(x, y, t) = I(x, y, t) - G(x, y, t)V(x, y, t) \quad (5.1)$$

$$G(x, y, t) = G_\sigma \overset{x,y}{*} E_\tau \overset{t}{*} Q(V)(x, y, t), \quad (5.2)$$

$$Q(v) = Q_0 + \lambda v^2, \quad (5.3)$$

where $G(x, y, t)$ is the simplified notation for the adapting conductance in this chapter (not to be confused with Gaussian kernel $G_\sigma(x, y)$, which is bound to disappear soon).

Because it is nonlinear, the response of such a system is not trivial, and a rigorous mathematical analysis appears difficult in the general case. Missing this mathematical analysis is problematic. Indeed, if the system is bound to be implemented in a bio-inspired model, one would like guarantees that it does not induce spurious effects (resonances, etc.) for certain sets of system parameters or input signals.

In fact, the gain control loop (5.1)-(5.3) appears to be very stable experimentally. Heuristically, the system is stable because it is a simple extension of a linear ‘RC’ circuit (a stable system if ever), only with a resistance R which varies dynamically. In this chapter, we try to provide a more rigorous explanation of the system’s stability, through a mathematical analysis of the system’s response to a simple type of input: Sinusoidal stimulation.

1.1 The underlying low-pass linear system

We start by making explicit the links of the gain control loop (5.1)-(5.3) with a simple ‘RC’ circuit. This analysis will help us to define a characterization of ‘good behavior’ for our nonlinear system.

The gain control loop (5.1)-(5.3) has been designed as an extension of a temporal *low-pass* system. Indeed, when the strength of the feedback in (5.3) is taken as $\lambda = 0$, (5.2) becomes the trivial relation $G(x, y, t) = Q_0$ (because filters $G_\sigma(x, y)$ and $E_\tau(t)$ both have a gain of 1), and in turn (5.1) writes:

$$\frac{dV}{dt}(x, y, t) = I(x, y, t) - Q_0 V(x, y, t), \quad (5.4)$$

which is a simple ‘RC’ low-pass temporal filter. Because system (5.4) is linear, it is completely described by its Fourier transform:

$$\tilde{H}(\omega) = 1/(Q_0 + \mathbf{j}\omega). \quad (5.5)$$

1.1.1 Characterizing the linear response to sinusoidal stimulation

A linear system is totally characterized by its response to a sinusoidal input:

$$\frac{dV}{dt}(t) = A \cos(\omega t) - Q_0 V(t). \quad (5.6)$$

When a solution $V(t)$ follows (5.6), its initial response depends on its initial conditions. But the initial conditions are forgotten asymptotically fast, and all solutions finally converge to a single trajectory which is also sinusoidal at pulsation ω , and hence fully described by two numbers:

1. Its maximum value V_{\max} , corresponding to the amplitude of $V(t)$, given by

$$V_{\max} = |\tilde{H}(\omega)|A. \quad (5.7)$$

2. The time t_{\max} when V_{\max} is reached (in each sinus cycle), which provides the phase difference of $V(t)$ with its input current:

$$\phi_{\max} = \omega t_{\max} = \arg(\tilde{H}(\omega)) \pmod{2\pi}. \quad (5.8)$$

Both formulas (5.7) and (5.8) rely on the Fourier transform (5.5).

Interestingly, V_{\max} and t_{\max} provide a good characterization of the dependence of system (5.6) w.r.t. parameters A and ω of the input current:

Dependence w.r.t. input frequency ω . The dependence of V_{\max} and t_{\max} w.r.t ω is typical of a *low-pass* system:

$$\partial_{\omega} V_{\max} < 0, \text{ and } \lim_{\omega \rightarrow +\infty} V_{\max} = 0, \quad (5.9)$$

$$\partial_{\omega} \phi_{\max} > 0, \text{ and } \lim_{\omega \rightarrow +\infty} \phi_{\max} = \pi/2 \pmod{2\pi}. \quad (5.10)$$

In words, (5.9) states that the response magnitude decreases with frequency towards 0 for large values, while (5.10) states that the phase delay of the response increases with frequency, towards phase quadrature.

Dependence w.r.t. input amplitude A . The dependence of V_{\max} and ϕ_{\max} w.r.t. A is trivial, since the system is linear:

$$\partial_A V_{\max} = |\tilde{H}(\omega)| > 0, \text{ and } \partial_A (V_{\max}/A) = 0 \quad (5.11)$$

$$\partial_A \phi_{\max} = 0 \quad (5.12)$$

In words, (5.11) states that the magnitude of response is simply proportional to the input amplitude, and (5.12) states that the phase (and thus, time of peak) of the response is independent of amplitude.

1.2 Gain control through the nonlinear system

1.2.1 Characterizing the nonlinear response to sinusoidal stimulation

In this chapter, we wish to study mathematically the *nonlinear* case, when feedback (5.2)-(5.3) has an effective strength $\lambda > 0$. For such a nonlinear system, Fourier analysis cannot be used simply anymore, so we cannot hope to fully characterize the system's response to *any* type of stimulus based only on the response to a sinus.

However, sinusoidal stimulation still has some descriptive power: It allows to test the system's response to stimuli of different amplitudes A , and different 'speeds of variation', as measured by the sinus' frequency ω . For this reason, our study of

the nonlinear system also focuses on input currents of the form $I(t) = A \cos(\omega t)$, and still uses V_{\max} and ϕ_{\max} as good indicators of the system's behavior.

More precisely, our ultimate goal is to find equivalents to formulas (5.9)-(5.12) in the nonlinear case, proving the good behavior of our system. Concerning the behavior w.r.t. to input frequency ω , we want to prove that formulas (5.9)-(5.10) still hold, meaning that our system is still 'low-pass', as measured by the amplitude V_{\max} of its response.

By opposition, concerning the behavior w.r.t. input amplitude A , we would like to prove a different behavior than (5.11)-(5.12) for our nonlinear system. Indeed, the system intends to be a *gain control* mechanism. Instead of (5.11), we would thus like to show that

$$\partial_A V_{\max} > 0, \text{ and } \partial_A (V_{\max}/A) < 0. \quad (5.13)$$

The first relation means that the system still responds with increasing amplitude to increasing contrasts (an important behavior to be verified!). However, the growth with A should be now *under-linear* (second relation), thus proving the presence of gain control.

Also, we would like to prove the phase advance at high amplitudes, which is a typical expression of contrast gain control in the retina (Chapter 3, Section 5.2). Instead of (5.12), we would thus like to show that

$$\partial_A \phi_{\max} < 0.$$

1.2.2 Reducing the system's dimensionality

In general, nonlinear systems get exponentially hard to study as the dimension of the space they live in increases. Systems of dimensions 1 and 2 are fairly understood, but chaotic behaviors and increased mathematical difficulty appear from dimension 3 on.

Unfortunately, the dimensionality of the original system (5.1)-(5.3) is particularly high, making mathematical analysis very difficult. As a consequence, we will proceed to successive simplifications of our system.

1. The spatial structure (x, y) of the equations, which is coupled with time by (5.2), provides an infinite dimensionality to system (5.1)-(5.3). To derive mathematical results, we must ignore this spatial structure, and study only the temporal evolution of two coupled variables $V(t)$ and $G(t)$, driven by an input current $I(t)$.
2. After the preceding simplification, we are left with a dynamic system (V, G) of dimension 2, but which is not *autonomous*, because the input current $I(t)$ varies in time. The equivalent autonomous system (by adding I , or t , to the system) is of dimension 3, and this is already a difficult dimensionality. We will see in the sequel how in particular limit cases, system (5.1)-(5.3) can further be simplified to a 1- (2- if autonomous) dimensional system.

For the moment, let us start by introducing our general 2D system (V, G) and its first properties.

2 GENERAL STUDY OF THE GAIN CONTROL SYSTEM

2.1 System definition and first properties

2.1.1 System definition

The system under study is that of a cell or population of cells with membrane potential $V(t)$, that integrates an input current $I(t) = A \cos(\omega t)$ under dynamic gain control from conductances $G(t)$ in its membrane. $(V(t), G(t))$ is driven by

$$\begin{cases} \dot{V}(t) = A \cos(\omega t) - G(t)V(t), & (a) \\ \dot{G}(t) = b(Q(V(t)) - G(t)), & (b) \end{cases} \quad (5.14)$$

where the dot denotes temporal derivation, b is a strictly positive parameter, and $Q(v)$ is a strictly positive, even and convex¹ function with sufficient regularity (see Figure 5.1). We note $Q_0 = Q(0) > 0$.

Leak function Q . We refer to $v \rightarrow Q(v)$ as the *leak function* of the system, because it defines the leaks $G(t)$ in the cellular membranes modeled by (5.14-a). More precisely, Q can always be decomposed as

$$Q(v) = \tilde{Q}(v) + Q_0,$$

with $\tilde{Q}(0) = 0$ and $Q_0 > 0$. Since equation (5.14-b) is linear with a gain of 1, this decomposition of Q translates to a decomposition of $G(t)$: $G(t) = \tilde{G}(t) + Q_0$, where $\tilde{G}(t)$ is the part of $G(t)$ linearly driven by $\tilde{Q}(V(t))$. Note that

$$G(t) \geq Q_0 > 0,$$

because $G(t)$ is a low-passed version of $Q(V(t))$. Note that mathematically, we must also *impose* this ‘physical’ property of $G(t)$ on our initial condition: $G(0) \geq Q_0$.

In turn, the leak current in (5.14-a) can be written

$$-G(t)V(t) = -\tilde{G}(t)V(t) - Q_0V(t),$$

so that Q_0 corresponds to the *static leaks* in the cellular membrane, and $\tilde{G}(t)$ to the ‘purely dynamic’ leaks.

Cut-off frequency for the adaptation b . As compared to (5.1)-(5.3), we have noted $b = \tau^{-1}$. Parameter b , expressed in Hertz, measures the rapidity with which $G(t)$ ‘sticks’ to its driving input $Q(V(t))$. This parameter will have a strong influence on the qualitative behavior of the system (Section 2.2.3).

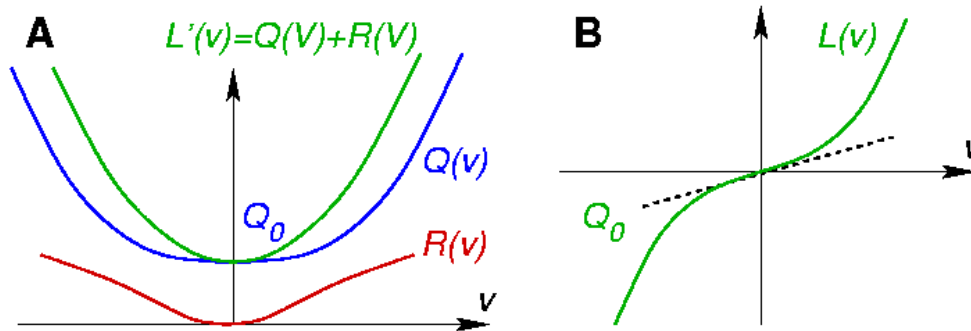


Figure 5.1: Schematic representations of functions $Q(v)$, $R(v) = vQ'(v)$ (panel A), $L(v) = vQ(v)$ (panel B), and $L'(v) = Q(v) + R(v)$ (panel A).

2.1.2 Notations

Various differentiations in the system. Throughout this chapter, we will encounter different types of differentiations and derivatives. Here are the general notations we will be using:

- Notation $\dot{f}(t)$ (or directly $\frac{df}{dt}$) represents the derivative w.r.t. time of function $f(t)$.
- Notation $F'(v)$ represents the derivative w.r.t. v of function $F(v)$, where v has the dimension of our variable $V(t)$ (originally, a membrane potential).
- Notation $\partial_p X$ represents the partial derivative of X (any scalar or vector) w.r.t. a parameter p of the system (typically, $p = A$).
- *Gâteaux derivatives.* Let a scalar/vector X depend on a particular function F (amongst other parameters):

$$X(F, \dots),$$

and let F_2 be a function of the same nature as F . If it exists, we will note $\partial_F^{(F_2)} X$ the *Gâteaux derivative* of X when F is modified along F_2 :

$$\partial_F^{(F_2)} X = \lim_{\varepsilon \rightarrow 0} \frac{X(F + \varepsilon F_2, \dots) - X(F, \dots)}{\varepsilon}.$$

Note that, for two well-defined Gâteaux derivatives $\partial_F^{(F_1)} X$ and $\partial_F^{(F_2)} X$, one has $\partial_F^{(F_1 + F_2)} X = \partial_F^{(F_1)} X + \partial_F^{(F_2)} X$.

- *Function derivatives.* If $X : t \in \mathbb{R} \rightarrow X(t)$ is a function of time, then $\partial_p X(t)$ represents the partial derivative along p of $X(t)$, t being held constant.

Remark: In all cases considered here, the function $t \rightarrow \partial_p X(t)$ so defined also corresponds to the partial derivative of *function* $t \rightarrow X(t)$ w.r.t. p for norm $\|\cdot\|_\infty$ over \mathbb{R} . This is because all partial derivatives considered will be T -periodic by construction, as stated in Point (iii) of Proposition 1. ■

¹For many results in this chapter, it is sufficient to consider Q strictly positive, even, and such that $\forall v, vQ'(v) \geq 0$. However, the supplementary requirement that Q be convex appears in some results. For simplicity, we prefer to assume it from the start.

Functions derived from $Q(v)$. Due to the intrinsic nature of system (5.14), we will repeatedly come across a number of algebraical expressions derived from function $v \rightarrow Q(v)$. For the sake of concision, we find it convenient to name these secondary functions.

We will first consider function

$$R(v) = vQ'(v) \geq 0, \quad (5.15)$$

which is always positive because $Q(v)$ is convex and even.

We will also consider the diffeomorphism from \mathbb{R} to itself:

$$L(v) = vQ(v), \quad (5.16)$$

which is indeed bijective since

$$L'(v) = Q(v) + R(v) \geq Q(v) \geq Q_0 > 0. \quad (5.17)$$

Functions $Q(v)$, $R(v)$, $L(v)$ and $L'(v)$ are schematically represented in Figure 5.1.

2.1.3 Periodic asymptotic solution of the system

We have seen in Section 1.1.1 that in the ‘linearized’ version of our system, $V(t)$ tends asymptotically fast to a sinusoidal response, possibly after some initial transient due to its initial conditions. The following proposition generalizes this behavior to nonlinear system (5.14).

Proposition 1 *Let A , ω and $b \in \mathbb{R}^{+*}$. Let $v \rightarrow Q(v)$ be an even, convex, strictly positive function with sufficient regularity, and $Q(0) = Q_0 > 0$. Let $T = 2\pi/\omega$.*

(i) *The following equation on $Z(t) = (X(t), Y(t))$:*

$$\dot{Z}(t) = \begin{pmatrix} \dot{X}(t) \\ \dot{Y}(t) \end{pmatrix} = \begin{pmatrix} A \cos(\omega t) - X(t)Y(t) \\ b(Q(X(t)) - Y(t)) \end{pmatrix} \quad (5.18)$$

admits a unique T -periodic solution that we note $W(t) = (V(t), G(t))$. All other solutions $Z(t)$ with initial condition $Y(0) \geq Q_0$ converge exponentially fast to $W(t)$.

(ii) *$V(t)$ is $T/2$ -antiperiodic, and $G(t)$ is $T/2$ -periodic:*

$$\begin{aligned} V(t) &= -V(t + T/2) \\ G(t) &= G(t + T/2). \end{aligned}$$

(iii) *Function $W : t \rightarrow W(t)$ admits C^1 differentiation w. r. t. parameters A and b and Gâteaux derivatives w.r.t. function Q , in the space of $(T/2$ -antiperiodic, $T/2$ -periodic) functions with norm $\|\cdot\|_\infty$.*

Remark: Differentiation w.r.t. parameter ω .

Concerning Point (iii), remark that parameter ω has not been included in the parameters with respect to which differentiation is possible. Indeed, even a small change of frequency $\omega \rightarrow \omega + \varepsilon$ leads to a strong divergence between the asymptotic trajectories $W_\omega(t)$ and $W_{\omega+\varepsilon}(t)$, since they have different periods!

However, the *scalar* quantities V_{\max} and ϕ_{\max} (defined on the asymptotic periodic solution $V(t)$) are differentiable w.r.t. ω . To study their dependence, a good solution is to introduce the change of parametrization $\phi = \omega t$, $\tilde{Y} = Y/\omega$, through which (5.18) becomes

$$\frac{d}{d\phi} \tilde{Z}(\phi) = \begin{pmatrix} \frac{d}{d\phi} X(\phi) \\ \frac{d}{d\phi} \tilde{Y}(\phi) \end{pmatrix} = \begin{pmatrix} \frac{A}{\omega} \cos(\phi) - X(\phi) \tilde{Y}(\phi) \\ b(\frac{1}{\omega} Q(X(t)) - \tilde{Y}(t)) \end{pmatrix}$$

In this new system, differentiation w.r.t. ω is possible (see the sequel). ■

The proof of Proposition 1 relies on the fact that system (5.18) is *contracting*, as defined in [100]. In the following paragraph, we remind the main properties of a contracting system. In a second paragraph, we present a general proposition on periodic contracting systems, which will apply to the system considered here. In a third paragraph, we show that system (5.18) is indeed contracting, and thus prove Proposition 1.

Contracting system

A dynamic system $\dot{Z}(t) = F(Z(t), t)$ defined in an open set Ω of a Banach E , is said to be *contracting* if $F(Z, t)$ admits a differential $dF(Z, t)$ w.r.t. its first variable, and a strictly negative upper bound $-\lambda_0 < 0$ can be found for the real parts of the eigenvalues of $dF(Z, t)$, independently of $t \in \mathbb{R}$ and $Z \in \Omega$ [100]. Or equivalently:

$$\forall t \in \mathbb{R}, \forall Z \in \Omega, \forall X \in E, \quad X^T dF(Z, t) X \leq -\lambda_0 \|X\|^2. \quad (5.19)$$

Such a system is characterized by an exponential convergence of all its solutions to a unique trajectory, independently of their initial condition [100]. Contraction is thus the warrant of a strong *stability* for the system.

We remind the main result when a system is contracting. If we consider two solutions $Z_1(t)$ and $Z_2(t)$, starting at time $t = 0$ with different initial conditions, then

$$\frac{d}{dt} (\|Z_1 - Z_2\|^2) = 2(Z_1 - Z_2)(F(Z_1, t) - F(Z_2, t)) \leq -\lambda_0 \|Z_1 - Z_2\|^2,$$

where the last inequality is a consequence of (5.19), when $dF(Z, t)$ is integrated between $Z_1(t)$ and $Z_2(t)$ along $Z_2(t) - Z_1(t)$. From Gronwall's Lemma, the last inequality can be integrated, yielding

$$\|Z_1(t) - Z_2(t)\|^2 \leq \|Z_1(0) - Z_2(0)\|^2 \exp(-\lambda_0 t). \quad (5.20)$$

So, after some initial transient that depends on their initial condition, all solutions $Z(t)$ converge to a 'unique' asymptotic trajectory.

Unique periodic solution of a contracting system

To prove Proposition 1, we must use the contracting properties of system (5.18), in the particular case of a periodic input $A \cos(\omega t)$. The following general proposition describes the asymptotic behavior of a periodic contracting system: The system's asymptotic response is also periodic, and depends continuously on the parameters of the system.

Proposition 2 (Periodic contracting system) *Consider a T -periodic contracting dynamic system defined on an open set $Z \in \Omega$:*

$$\frac{d}{dt}Z = F(Z(t), t, p), \quad (5.21)$$

where:

- p is any parameter of the system such that F has a C^1 dependence on p .
- Function F is T -periodic for a certain $T > 0$, in the sense that

$$\forall t, \forall p, \forall Z \in \Omega, \quad F(Z, t + T, p) = F(Z, t, p).$$

- Contraction property: F is C^1 w.r.t. Z , and its differential $dF(Z, t, p)$ admits a strictly negative upper bound $-\lambda_0 < 0$ on the real part of its eigenvalues, independently of t and $Z \in \Omega$ (possibly, λ_0 can depend on p).

Then, the asymptotic behavior of the system is characterized by the two following points:

- (i) For any value of parameter p , system (5.21) admits a unique T -periodic solution that we note $W(t, p)$ (or simply $W(t)$). Since the system is contracting, all other solutions of (5.21) converge exponentially fast to $W(t)$.
- (ii) Structural stability of the asymptotic solution: Function $W : (t, p) \rightarrow W(t, p)$ is C^1 .

Heuristically, Point (i) of this proposition states that any solution $Z(t)$ of a T -periodic contracting system rapidly becomes T -periodic itself, once that its initial conditions are forgotten and it is entirely driven by the nature of its input. Naturally, amongst the bundle of all solutions $Z(t)$ which are 'asymptotically periodic' (and converging to a 'unique' trajectory), there must exist a 'central' solution $W(t)$ that is *exactly* T -periodic.

As for Point (ii) of this proposition, it is strongly reminiscent of the local C^1 dependence of the solutions of an ODE w.r.t. to system parameters, as stated by the Cauchy-Lipschitz Theorem on the existence of local solutions to an ODE. The whole point here is to extend the *local* C^1 dependence, for any solution $Z(t)$, to a *global* C^1 dependence for the asymptotic trajectory, as 'materialized' by the unique periodic solution $W(t)$.

The results stated by Proposition 2 are quite natural, since a contracting system is precisely remarkable for its high stability, such that 'everything always works simply'. However, the rigorous proof is unnecessarily technical, so we only provide it in Appendix.

Proof of Proposition 1

Let us prove the contracting properties of system (5.18). In our case, $\Omega = \{Z = (X, Y) | Y \geq Q_0\}$ (by hypothesis for the initial condition $Y(0)$, and then because $Q(X(t)) \geq Q_0$). The system can be rewritten

$$\dot{Z}(t) = \begin{pmatrix} A \cos(\omega t) \\ 0 \end{pmatrix} - J(Z(t)), \quad (5.22)$$

with

$$J(Z) = \begin{pmatrix} XY \\ b(Y - Q(X)) \end{pmatrix}, \quad (5.23)$$

and the differential of J w.r.t. Z verifies the following property:

$$\det(dJ(Z) - \lambda \text{Id}) = \lambda^2 - (Y + b)\lambda + b[Y + R(X)],$$

with $R(v) = vQ'(v) \geq 0$ (from (5.15)). Then, if we denote λ_1 and λ_2 the two eigenvalues of $dJ(Z)$, straightforward calculus proves that:

$$\forall Z \in \Omega, \quad \max(\mathcal{R}(\lambda_1), \mathcal{R}(\lambda_2)) \geq \min(Q_0, b) \triangleq \lambda_0 > 0, \quad (5.24)$$

so that λ_0 , defined by (5.24), is a strictly positive lower bound for the real parts of the eigenvalues of $dJ(Z(t))$, independently of t and the solution $Z(t)$ considered. This proves that the system is contracting, following the definition given above.

Because system (5.18) is contracting and periodic, Proposition 2 directly provides Points (i) and (iii) of Proposition 1.

To prove Point (ii), note that the input sinus itself is $T/2$ -antiperiodic: $A \cos(\omega(t + T/2)) = -A \cos(\omega t)$, so that $(-V(t + T/2), G(t + T/2))$ is also a T -periodic solution of (5.18). By unicity of the periodic solution, $W(t) = (-V(t + T/2), G(t + T/2))$. \square

Remark: Note that Point (iii) of Proposition 2 also implies that the system ODE (5.18) can be differentiated w.r.t. any system parameter p , yielding a new ODE which drives $\partial_p W(t)$. We will often apply this technique in the sequel. \blacksquare

2.2 Numerical simulation

When it comes to quantitative analysis, such as characterizing the maximum V_{\max} of $V(t)$ over a cycle (the ultimate goal of the chapter, see Section 1.2), system (5.14) is particularly hard to study: Its complexity is equivalent to that of a 3-dimensional autonomous system (Section 1.2). As a result, we could not provide any quantitative mathematical results for the general case of system (5.14).

Instead, we simulated (5.14) for different sets of parameters, to gain a ‘heuristic’ understanding of the system. We thus found that, whatever set of parameters used, the under-linear dependence (5.13) of V_{\max} w.r.t. input amplitude A appears to hold. We also found that the shape of the phase portrait of $W(t) = (V(t), G(t))$ is strongly influenced by the value of the cut-off parameter b for the adaptation conductance. We now present these results.

2.2.1 General behavior of the system

Because system (5.14) is contracting, it reaches its asymptotic periodic trajectory $W(t)$ exponentially fast, with a typical time constant λ_0^{-1} , with $\lambda_0 = \min(b, Q_0)$. When the phase portrait of $W(t) = (V(t), G(t))$ is plotted, it displays a symmetric shape, because of the system's typical symmetry (Proposition 1, Point (ii)). The resulting curve, displayed² in Figure 5.2, can evoke different objects according to the viewer's frame of mind. In the scope of this thesis, we refer to it as a 'butterfly' curve...

Along with the evolution of $W(t)$, Figure 5.2 represents the evolution of some other 'relevant' 2D points (see legend).

For example, at each time t_0 , we define point $W_\infty(t_0) = (V_\infty(t_0), G_\infty(t_0))$ as the (unique) equilibrium point if the system was let to evolve for $t > t_0$ with an input current held constant at $I(t) = A \cos(\omega t_0)$ (Since the system is contracting, all other solutions would also converge exponentially fast to $W_\infty(t_0)$). This 'instantaneous' equilibrium point is computed by solving $(\dot{V} = 0, \dot{G} = 0)$, which has a unique solution:

$$\begin{cases} V_\infty(t)Q(V_\infty(t)) = A \cos(\omega t) \\ G_\infty(t) = Q(V_\infty(t)) \end{cases} \quad (5.25)$$

Graphically, $(V_\infty(t), G_\infty(t))$ is obtained as the intersection of the convex, symmetric curve $G = Q(V)$ with the branch of hyperbola $GV = I(t) = A \cos(\omega t)$ (Figure 5.3).

In linear systems, the 'instantaneous equilibrium point' plays the role of a *driving force* on the system (see next remark). Although there is no such well-defined role for $W_\infty(t)$ in the nonlinear system presented here, $W_\infty(t)$ still appears to act pretty much like a driving force on $W(t)$, as can be seen in Figure 5.2 (see legend).

Remark: Driving potential in stable linear systems

When a stable linear dynamic $\dot{Z}(t) = \mathbf{A}(t)Z(t) + B(t)$ is considered (such that $\forall t$, the two eigenvalues of $\mathbf{A}(t)$ have strictly negative real parts), the instantaneous equilibrium point is defined by $\mathbf{A}(t)Z_\infty(t) + B(t) = 0$. The system's driving equation can thus be re-written $\dot{Z}(t) = \mathbf{A}(t)(Z(t) - Z_\infty(t))$.

As a result, function $Z(t)$ depends linearly on function $Z_\infty(t)$. In particular, there exists a kernel $\mathbf{K}(t, u)$ (with the dimension of a matrix), depending only on the nature of function $t \rightarrow \mathbf{A}(t)$ (generally without any analytic expression), such that $\forall t$, $Z(t) = \mathbf{K}(t, t)Z(0) + \int_{u=0}^t \mathbf{K}(t, u)Z_\infty(t - u)du$ and $\int_{u=0}^{+\infty} \mathbf{K}(t, u)du = 1$, meaning that once initial conditions are forgotten, $Z(t)$ is obtained as a linear *average* over the recent values of $Z_\infty(t)$.

A typical example of such a linear system is the evolution of a conductance-driven membrane potential: See Chapter 2, Section 7. ■

2.2.2 Gain control on input amplitude

Now that we have described the typical behavior of $W(t)$, we can question more precisely the influence of the different parameters in the system. The dependence of $W(t)$ on amplitude A is particularly interesting to us, since we wish to prove the under-linearity of V_{\max} w.r.t. A (equation (5.13)).

And indeed, whatever set of parameters used in our simulations (b, ω and quadratic function $Q(v) = Q_0 + \lambda v^2$), we always found V_{\max} to be a growing function of A , and

²The corresponding animated movie can be found at www-sop.inria.fr/odyssee/team/Adrien.Wohrer/retina/other_files/CGC_movie.mpg.

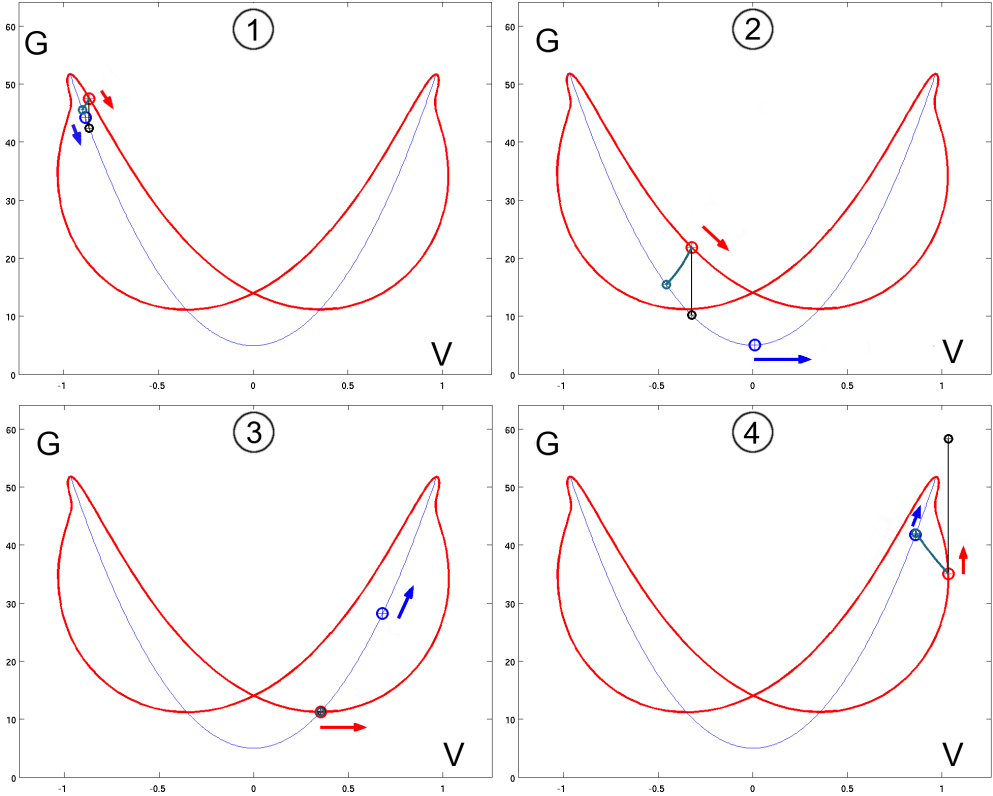


Figure 5.2: Evolution of system (5.14) over a half-period, for a typical set of parameters. The thick red curve is the phase portrait of $W(t) = (V(t), G(t))$: It typically revolves around the ‘driving curve’ defined by $G = Q(V)$ (thin blue curve). The current value of $W(t)$ is indicated by the large red dot, while the instantaneous equilibrium point $W_\infty(t)$ (see text) is indicated by the large blue dot. Although there is no trivial link between $W(t)$ and $W_\infty(t)$, the latter appears to ‘drive’ the former, since it is always ‘in advance’ in the phase portrait. Two other points are indicated in each figure: Point $(V(t), Q(V(t)))$ (small black dot) is coupled to the sign of $\dot{G}(t)$, whether it is over or under point $V(t)$ (vertical black line). See e.g. Panel 3 when $\dot{G}(t) = 0$. Point $(V_\pi(t), G_\pi(t))$ (small green dot) is the point on curve $G = Q(V)$ such that $V(t)G(t) = V_\pi(t)G_\pi(t)$. Its position relative to $W_\infty(t)$ is coupled to the sign of $\dot{V}(t)$. See e.g. Panel 4 when $\dot{V}(t) = 0$.

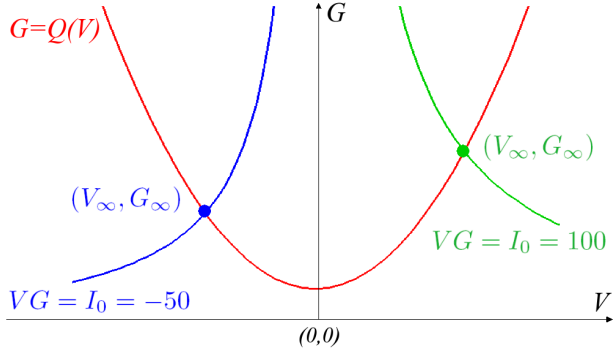


Figure 5.3: The instantaneous equilibrium point $W_\infty(t)$ of the system is graphically obtained at the intersection of curves $G = Q(V)$ and $GV = I(t) = A \cos(\omega t)$.

this growth to happen under-linearly.

A typical example of the system's dependence on input amplitude A is provided in Figure 5.4. Both $V(t)$ and phase portrait $(V(t), G(t))$ are represented, for different values of parameter A . The under-linearity w.r.t A can be observed, as well as the time advance of $V(t)$ as A increases (t_{\max} decreases with A). Note however that t_{\max} is not easily defined, as $V(t)$ can possibly display two maxima per cycle.

2.2.3 Parameter b defines the shape of the phase portrait

Parameter b defines the cut-off frequency for the integration of input $Q(V(t))$ by $G(t)$, through

$$\dot{G}(t) = b(Q(V(t)) - G(t)). \quad (5.26)$$

As a first remark, note that the value of b only has a 'secondary' effect on the typical *range of values* taken by $V(t)$ and $G(t)$. Indeed, the linear filter described by (5.26) has a gain of 1, so that $\widehat{G} = \widehat{Q(V)}$ independently of b , where the hat denotes averaging over one period of the system. As a result, the 'typical' orders of magnitude \tilde{V} and \tilde{G} of the system (a blurry notion if ever) can be defined by

$$\begin{cases} \tilde{V}Q(\tilde{V}) = A \\ \tilde{G} = Q(\tilde{V}), \end{cases}$$

independently of the value of parameter b .

A typical example of the system's dependence on parameter b is provided in Figure 5.5, where both $V(t)$ and phase portrait $(V(t), G(t))$ are represented for different values of b , all other parameters being held constant. It can be seen that, even if parameter b does not have a strong influence on the typical range of values taken by the system, it has a strong influence on the general *shape* of the phase portrait.

In particular, two asymptotic behaviors for the system can be observed, when $b \rightarrow 0$ and when $b \rightarrow +\infty$ (more precisely, the determinant factor is bT , comparing b to the intrinsic frequency of the system). Both asymptotic behaviors are characterized by a reduction of dimensionality, as the limit systems appear to live in a 1-dimensional space only:

'Flat' limit when $b = 0$. When b gets close to 0, the filtering of $Q(V(t))$ to produce $G(t)$ becomes more and more low-pass, implying that $G(t)$ becomes close to a *constant* function. In Figure 5.5 *B*, this translates in a progressive flattening of the phase diagram. In Section 3, we propose a suitable characterization of the asymptotic limit ' $b = 0$ ', in which $G(t) = G_0$ is imposed to be constant.

'Convex' limit when $b = +\infty$. When b gets close to $+\infty$, the filtering of $Q(V(t))$ to produce $G(t)$ becomes more and more high-pass, implying that $G(t)$ becomes close to $Q(V(t))$. In Figure 5.5 *B*, this translates in a phase diagram which 'sticks' to the driving curve $G = Q(V)$ (represented by a dotted line in the phase plane). In Section 4, we propose a suitable characterization of the asymptotic limit ' $b = +\infty$ ', in which relation $G(t) = Q(V(t))$ is imposed.

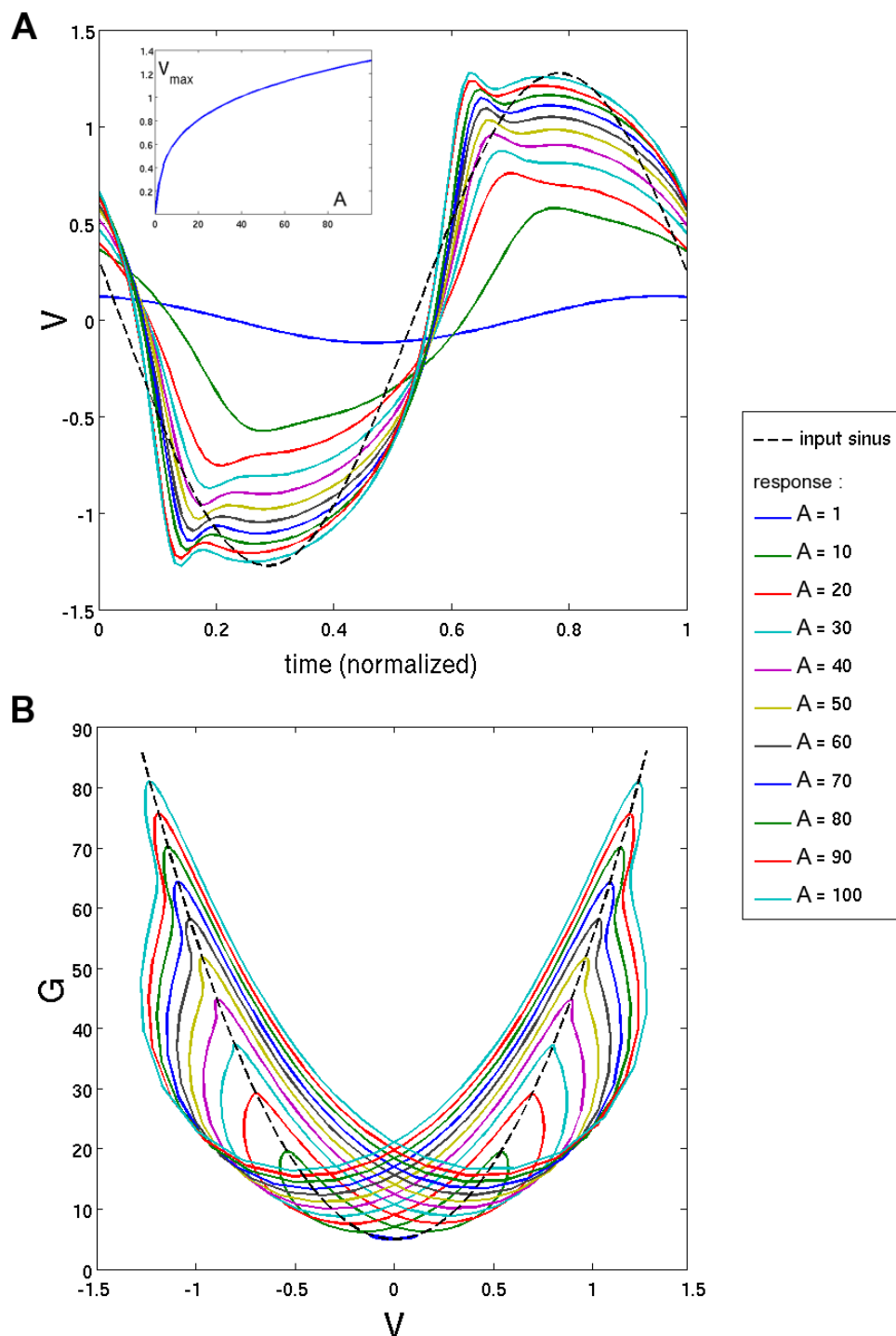


Figure 5.4: Response to an input sinusoidal current $I(t) = A \cos(\omega t)$ of increasing amplitude A . Panel A represents $V(t)$ over one period, and Panel B represents the phase portrait $(V(t), G(t))$. V_{\max} appears to be a growing function of A , but this growth is under-linear (inset curve plots V_{\max} against A). Also note the apparent phase advance for t_{\max} with increasing contrasts. At low input amplitudes (curve $A = 1$), the system behaves linearly, as the phase portrait remains in the zone ' $G \simeq Q_0$ '. Other simulation parameters: $\omega = 2\pi$ Hz, $b = 20$ Hz, $Q(V) = Q_0 + \lambda V^2$ with $Q_0 = 5$ Hz and $\lambda = 50$ Hz.

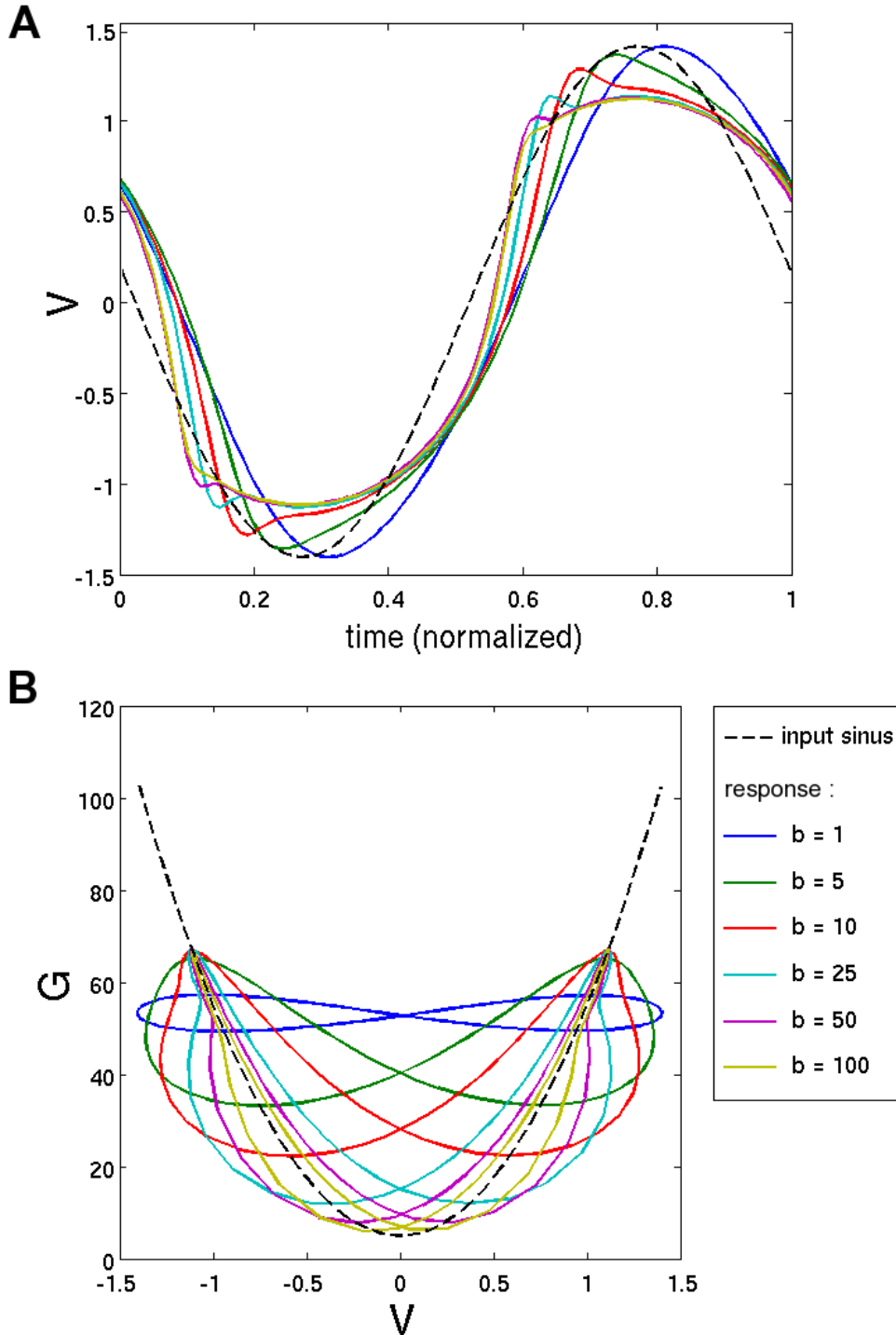


Figure 5.5: Response to an input sinusoidal current $I(t) = A \cos(\omega t)$, for different values of parameter b (typical frequency of the adaptation feedback). Panel A represents $V(t)$ over one period, and Panel B represents the phase portrait $(V(t), G(t))$. As b approaches the bounds of its definition domain, the system is constrained to 1D systems: 'Flat' system with $G(t) = \text{cst.}$ when $b \rightarrow 0$, and 'Convex' system with $G(t) = Q(V(t))$ when $b \rightarrow +\infty$. Other simulation parameters: $\omega = 2\pi$ Hz, $A = 75$ Hz, $Q(V) = Q_0 + \lambda V^2$ with $Q_0 = 5$ Hz and $\lambda = 50$ Hz.

Remark: Issues of continuity

In Sections 3 and 4, we propose characterizations and formulas for two respective regimes, which we term ‘ $b = 0$ ’ and ‘ $b = +\infty$ ’. However, it should be noted that the original 2D system (5.14) is *not* defined properly at these bounds (for $b = 0$ it is degenerated, and for $b = +\infty$ it is naturally undefined).

The 1-dimensional systems proposed in the sequel result from simple heuristics on the behavior of the 2D system (5.14) when parameter b gets close to the bounds of its domain. At the moment, we have no rigorous proof of continuity between the asymptotic 2D systems (e.g. $b = \varepsilon \rightarrow 0$ and $b = 1/\varepsilon \rightarrow +\infty$) and the proposed 1D systems (‘ $b = 0$ ’ and ‘ $b = +\infty$ ’).

The mathematical proof of continuity may be especially problematic in the particular case $b = \varepsilon \rightarrow 0$, since as b gets close to zero, the system takes infinite time to reach its periodic asymptote (the typical time constant being $0 < \lambda_0 \leq b$).

Possible keys for a further grounding of our 1D solutions as actual limits can be found in Section 5, where we sketch some results of perturbation analysis, near $b = 0$ and $b = +\infty$. ■

3 ASYMPTOTIC BEHAVIOR $b = 0$ _____

3.1 System definition

A heuristic definition of the asymptotic system

If the asymptotic behavior for $b = 0$ is directly considered by injecting relation ‘ $b = 0$ ’ into system (5.14), it yields:

$$\begin{cases} \dot{V}(t) = A \cos(\omega t) - G(t)V(t), & (a) \\ \dot{G}(t) = 0. & (b) \end{cases} \quad (5.27)$$

This happens to be a degenerate system, since (5.27-b) only indicates that $G(t) = G_0$ is a constant. In turn, (5.27-a) admits a valid solution for any possible value of G_0 .

A supplementary constraint must thus be found to fully define the system. And indeed, we have seen in Section 2.2.3 that once initial conditions are forgotten³, one always has $\widehat{G} = \widehat{Q(V)}$, independently of b , where the hat denotes averaging over one period.

It is natural to assume that in the ‘real’ asymptotic limit for $b = 0$, this relation still holds, so that the only ‘real’ value for G_0 is the one which satisfies

$$G_0 = \widehat{Q(V)}. \quad (5.28)$$

In turn, if $G(t) = G_0$ is constant, equation (5.27-a) that drives $V(t)$ becomes linear:

$$\dot{V}(t) = A \cos(\omega t) - G_0 V(t).$$

This is a simple low-pass linear filter, whose solution we have already described in (5.5) and (5.7)-(5.8). We are thus able to fully express the most plausible candidate

³Which takes an infinite time as $b \rightarrow 0$! See remark at the end of the preceding section.

for the ‘real’ asymptotic value when $b = 0$.

System definition, and proof of existence

In our asymptotic system $b = 0$, the state variable $W(t) = (V(t), G_0)$ is totally determined by a single number $G_0 > 0$, through the following hybrid system:

$$\begin{cases} V(t) = \frac{A}{\sqrt{G_0^2 + \omega^2}} \cos(\omega t - \arctan(\omega/G_0)), & (a) \\ G_0 = \frac{1}{T} \int_{u=t_0}^{t_0+T} Q(V(u)) du, & (b) \end{cases} \quad (5.29)$$

where t_0 can be any time, since $V(t)$ is T -periodic. The system is well defined, thanks to the following proposition.

Proposition 3 *System (5.29) forces a single possible value for G_0 , and thus for $W(t) = (V(t), G_0)$. Furthermore, G_0 is C^1 w.r.t. system parameters.*

Proof: Function $I(K) = \frac{1}{T} \int_{u=0}^T Q(K \cos(\omega u)) du$ is a continuous, growing function from \mathbb{R}^{+*} to $]Q_0, +\infty[$. Indeed, its derivative writes

$$I'(K) = \frac{1}{T} \int_{u=0}^T \cos(\omega t) Q'(K \cos(\omega u)) du = \frac{1}{TK} \int_{u=0}^T R(K \cos(\omega u)) du,$$

with $R(v) = vQ'(v) \geq 0$ (equation (5.15)).

As a result, (5.29-b) can rewrite $G_0 = I \circ K(G_0)$ where $K(G) = A/\sqrt{G^2 + \omega^2}$ is a decreasing function from \mathbb{R}^{+*} to $]0, A/\omega^2[$. $I \circ K$ is thus a positive decreasing function, whose graph $y = I \circ K(x)$ intersects once and only once the identity line $y = x$, defining a unique solution G_0 .

Furthermore, since functions $K(G)$ and $I(K)$ depend continuously on system parameters, so does G_0 . More precisely, for G_0 to have a C^k dependence on input parameters, it is sufficient that $v \rightarrow Q(v)$ be C^k . \square

Remark: Note that, even although equation (5.29-a) is obtained as the solution of a linear ODE, the whole system (5.29) is *not* linear with its input, since G_0 itself depends on parameters A and ω of the input current. \blacksquare

3.2 Dependence of V_{\max} and ϕ_{\max} w.r.t. system parameters

Because it has a reduced dimensionality, we are able to state precise results for system (5.29), concerning the dependence of V_{\max} and t_{\max} w.r.t. parameters A and ω of the input current. These results are summed up in the following theorem.

Theorem 1 *System (5.29) behaves as a low-pass filter with gain control on the input amplitude. First, here is how V_{\max} and ϕ_{\max} depend on input frequency ω :*

(i) *Low-pass setting*

$$\partial_{\omega} V_{\max} < 0 \text{ and } \lim_{\omega \rightarrow +\infty} V_{\max} = 0.$$

(ii) *Phase delay*

$$\partial_\omega \phi_{\max} > 0 \text{ and } \lim_{\omega \rightarrow +\infty} \phi_{\max} = \frac{\pi}{2} \pmod{2\pi}.$$

Second, here is how V_{\max} and ϕ_{\max} depend on input amplitude A :

(iii) *Growth of V_{\max}*

$$\partial_A V_{\max} > 0 \text{ and } \lim_{A \rightarrow +\infty} V_{\max} = +\infty.$$

(iv) *Phase advance*

$$\partial_A \phi_{\max} < 0 \text{ and } \lim_{A \rightarrow +\infty} \phi_{\max} = 0 \pmod{2\pi}.$$

(v) *Under-linearity*

$$\partial_A \frac{V_{\max}}{A} < 0 \text{ and } \lim_{A \rightarrow +\infty} \frac{V_{\max}}{A} = 0.$$

Proof:

To simplify further calculations, we express G_0 in a reduced time scale:

$$G_0 = \frac{1}{2\pi} \int_{\phi=0}^{2\pi} Q(V_{\max} \cos(\phi)) d\phi,$$

as obtained from (5.29-b) with the change of variable $\phi = \omega t - \arctan(\omega/G_0)$, and the choice of $t_0 = \arctan(\omega/G_0)/\omega$. Differentiating this expression w.r.t. parameter $p = A$ or ω (a valid operation thanks to Proposition 3), we get

$$\partial_p G_0 = \frac{\partial_p V_{\max}}{V_{\max}} \widehat{R(V)}, \quad (5.30)$$

where, again, $R(v) = vQ'(v)$ and the hat denotes average over one period.

We also remind the two expressions directly obtained from (5.29-a):

$$V_{\max} = A(G_0^2 + \omega^2)^{-1/2}. \quad (5.31)$$

$$\phi_{\max} = \arctan(\omega/G_0). \quad (5.32)$$

Dependence w.r.t. A (Points (iii)-(v)). Differentiation of (5.31) w.r.t. A yields

$$\partial_A V_{\max} = (G_0^2 + \omega^2)^{-3/2} (G_0^2 + \omega^2 - AG_0 \partial_A G_0), \quad (5.33)$$

which forms a coupled system with $\partial_A G_0$ (5.30). Solving this system provides

$$\partial_A V_{\max} = \left[\sqrt{G_0^2 + \omega^2} + \widehat{R(V)} \frac{G_0}{\sqrt{G_0^2 + \omega^2}} \right]^{-1}. \quad (5.34)$$

As a result, $\partial_A V_{\max} > 0$ (growth of system response with input amplitude) and $\partial_A G_0 > 0$ (with (5.30)). Then, because G_0 grows with A , (5.31) implies that $\partial_A (V_{\max}/A) < 0$ (under-linearity of system response with input amplitude), and (5.32) implies that $\partial_A \phi_{\max} < 0$ (phase advance with increasing amplitude).

To conclude the proof of Points (iii)-(v), we must find the respective limits of V_{\max} , ϕ_{\max} and V_{\max}/A when $A \rightarrow +\infty$. These three limits are determined by $G_{\infty} = \lim_{A \rightarrow +\infty} G_0 \in \mathbb{R}^+ \cup \{+\infty\}$, a number that must exist since G_0 grows with A .

Suppose $G_{\infty} \in \mathbb{R}$. Through (5.31) V_{\max} would also have a finite limit in \mathbb{R} , and necessarily $\lim_{A \rightarrow +\infty} \partial_A V_{\max} = 0$. This would be in contradiction with (5.34). As a result, $G_{\infty} = +\infty$, and (5.31)-(5.32) provide the limits stated by Points (iii)-(v).

Dependence w.r.t. ω (Points (i) and (ii)). In this case, equation (5.33) is replaced by

$$\partial_{\omega} V_{\max} = -A(G_0^2 + \omega^2)^{-3/2}(G_0 \partial_{\omega} G_0 + \omega). \quad (5.35)$$

The rest of the demonstration follows in a fashion similar to Points (iii)-(v). \square

4 ASYMPTOTIC BEHAVIOR $b = +\infty$ _____

4.1 System definition

We define our asymptotic system $b = +\infty$ as the following 1-dimensional ODE:

$$\dot{V}(t) = A \cos(\omega t) - V(t)Q(V(t)). \quad (5.36)$$

This system is the straightforward extension of the 2D system (5.14), when equation (5.14-b) is replaced by the asymptotic relation $G(t) = Q(V(t))$.

We will also consider the alternative formulation:

$$\dot{V}(t) = L(E(t)) - L(V(t)), \quad (5.37)$$

where $L(v) = vQ(v)$ is a diffeomorphism from \mathbb{R} to itself (as in (5.16)), and $E(t)$ defined as

$$E(t) = L^{-1}(A \cos(\omega t)) \quad (5.38)$$

acts as a driving potential on $V(t)$.

Remark: Letters L and E are chosen in link with their signification in a neuron membrane model. The term $L(V(t))$ in (5.37) is the instantaneous *Leak* current in the membrane, while $E(t)$ in (5.37) has the dimension of an attracting electrical potential, often noted E in neurophysiology. \blacksquare

The following Proposition insures that system (5.14) reaches exponentially fast a well-defined periodic solution $V(t)$ (as Proposition 1 in the 2D case). Furthermore, it states the existence of a single local maximum over each cycle.

Proposition 4

- (i) *Equation (5.36) admits a unique T -periodic solution that we note $V(t)$. All other solutions $W(t)$ to (5.36) converge asymptotically fast to $V(t)$.*

(ii) $V(t)$ is $T/2$ -antiperiodic: $V(t) = -V(t + T/2)$. Over one period, $V(t)$ has a single local maximum V_{\max} reached at time t_{\max} , and a single local minimum $V_{\min} = -V_{\max}$ reached at time $t_{\min} = t_{\max} - T/2$. Furthermore, $t_{\max} \in [0, T/4] \pmod{T}$.

(iii) Function $V : t \rightarrow V(t)$ admits C^1 differentiation w. r. t. parameter A and Gâteaux derivatives w.r.t. function Q , in the space of $T/2$ -antiperiodic functions with norm $\| \cdot \|_{\infty}$.

Proof:

The proof of all three Points relies on the same argument as Proposition 1 in the 2D case: System (5.36) is contracting. The whole demonstration is made in the same way⁴ and we will not repeat it here.

The only specific point left to prove here is the existence of a single local maximum in each cycle (Point (ii)). Note that this result does not hold in the general 2D case (see Figure 5.4). But in the present 1D system, equation (5.37) implies that local extrema of $V(t)$ correspond to points where $V(t)$ crosses $E(t)$.

More precisely, let us rewrite (5.37) and its derivative:

$$\begin{aligned}\dot{V}(s) &= L(E(s)) - L(V(s)) \\ \ddot{V}(s) &= \dot{E}(s)L'(E(s)) - \dot{V}(s)L'(V(s))\end{aligned}$$

Let s be a local maximum of V . One has $\dot{V}(s) = 0$ and $\ddot{V}(s) \leq 0$, so $V(s) = E(s)$ and $\dot{E}(s) = \ddot{V}(s)/L'(E(s)) \leq 0$. This last inequality can be made strict: Suppose $\ddot{V}(s) = 0$, then one must also have $\ddot{E}(s) = 0$ because s is a local extremum. So one must have at the same time $\dot{E}(s) = 0$ and $\ddot{E}(s) = 0$, which never happens.

In the end, for any time s :

$$\begin{aligned}s \text{ is a local maximum of } V &\iff \left(V(s) = E(s) \text{ and } \dot{E}(s) < 0 \right) \\ s \text{ is a local minimum of } V &\iff \left(V(s) = E(s) \text{ and } \dot{E}(s) > 0 \right)\end{aligned}$$

As any continuous function⁵, $V(t)$ necessarily displays an *alternation* of local maxima and local minima. As a result, the sign of $\frac{d}{dt}E(s)$ necessarily changes between two successive extrema, and $V(t)$ can only have one local maximum t_{\max} and one local minimum $t_{\min} = t_{\max} - T/2$ per cycle. The maximum is reached in the positive descending phase of $E(t)$, with t_{\max} comprised between 0 and $T/4$ (modulo T). The minimum is reached anti-symmetrically, in the negative ascending phase of $E(t)$. This is illustrated in Figure 5.6. \square

Before introducing our main result (Theorem 2, Section 4.3), we state two useful propositions in the next section, which provide integral expressions for the partial derivatives $\partial_p V(t)$ in the system.

⁴Note that rigorously, results for the 2D system cannot be directly applied here, because the 2D system is not defined for $b = +\infty$.

⁵save one which is locally constant. . .

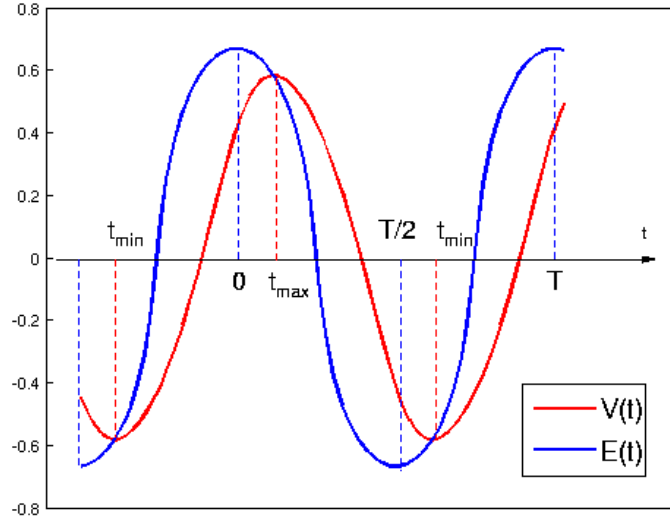


Figure 5.6: Driving potential $E(t) = L^{-1}(A \cos(\omega t))$, and periodic solution $V(t)$, represented for a particular set of parameters, and a quadratic leak function $Q(v) = Q_0 + \lambda v^2$.

4.2 Integral formulations for partial derivatives in the system

Proposition 5 (Integral formulation for partial derivatives)

Consider $V(t)$ the unique periodic solution of (5.36):

$$\dot{V}(t) = A \cos(\omega t) - L(V(t)),$$

and p a parameter of the system (e.g., A), for which $t \rightarrow \partial_p V(t)$ is well-defined. Then, for all t :

$$\partial_p V(t) = \frac{1}{1 + \exp\left(-\int_{s=t-T/2}^t L'(V(s)) ds\right)} \int_{u=t-T/2}^t Y_p(u) \exp\left(-\int_{s=u}^t L'(V(s)) ds\right) du, \quad (5.39)$$

with

$$Y_p(t) = \partial_p (A \cos(\omega t)) - V(t)(\partial_p Q)(V(t)),$$

and in particular:

$$\partial_p V_{\max} = \frac{1}{1 + \exp\left(-\int_{s=t_{\min}}^{t_{\max}} L'(V(s)) ds\right)} \int_{u=t_{\min}}^{t_{\max}} Y_p(u) \exp\left(-\int_{s=u}^{t_{\max}} L'(V(s)) ds\right) du. \quad (5.40)$$

A similar relation can be obtained if ∂_p is replaced by $\frac{d}{dt}$, or by a well-defined Gâteaux derivative for function Q along a symmetric function Q_2 .

Proof:

Differentiation of (5.36) leads to the following ODE on $\partial_p V(t)$:

$$\begin{aligned} \frac{d}{dt} \partial_p V(t) &= \partial_p (A \cos(\omega t)) - V(t)(\partial_p Q)(V(t)) - L'(V(t)) \partial_p V(t) \\ &= Y_p(t) - L'(V(t)) \partial_p V(t), \end{aligned}$$

with the definition for $Y_p(t)$ given in Proposition 5. This is a linear equation on function $t \rightarrow \partial_p V(t)$, so it can be integrated, starting from any initial condition t_0 :

$$\partial_p V(t) = \partial_p V(t_0) \exp\left(-\int_{s=t_0}^t L'(V(s)) ds\right) + \int_{u=t_0}^t Y_p(u) \exp\left(-\int_{s=u}^t L'(V(s)) ds\right) du. \quad (5.41)$$

But system (5.36) is $T/2$ -antiperiodic, and so is $V(t)$. So, $\partial_p V(t)$ is also $T/2$ -antiperiodic: $\partial_p V(t - T/2) = -\partial_p V(t)$. Taking $t_0 = t - T/2$ in (5.41) leads to expression (5.39).

Then, since $V_{\max} = V(t_{\max})$, we have:

$$\partial_p V_{\max} = (\partial_p V)(t_{\max}) + \dot{V}(t_{\max}) \partial_p t_{\max} = (\partial_p V)(t_{\max}), \quad (5.42)$$

since $\dot{V}(t_{\max}) = 0$. This proves (5.40). All the steps of this proof are similar if ∂_p is replaced by $\frac{d}{dt}$, or by a Gâteaux derivative for Q . \square

As a first application of Proposition 5, we present a proposition concerning the influence of the leak function Q on system (5.36). This proposition can be considered as a result by itself. Furthermore, we will use the calculations made here to prove Theorem 2 (Section 4.3).

Proposition 6 (Gâteaux derivative for leak function Q)

Consider $V(t)$ the unique periodic solution of (5.36):

$$\dot{V}(t) = A \cos(\omega t) - L(V(t)).$$

Let $v \rightarrow Q_2(v)$ be an even function with sufficient regularity, and such that $V(t)$ admits a Gâteaux derivative $\partial_Q^{(Q_2)} V(t)$ when the leak function Q is modified along Q_2 . Then:

(i) The variation of V_{\max} (maximum of $V(t)$) is given by:

$$\partial_Q^{(Q_2)} V_{\max} = -\frac{V_{\max} Q_2(V_{\max})}{L'(V_{\max})} + \frac{\int_{u=t_{\min}}^{t_{\max}} \frac{d}{dv} \left[\frac{v Q_2(v)}{L'(v)} \right] (V(u)) \dot{V}(u) \exp\left(-\int_u^{t_{\max}} L'(V)\right) du}{\left(1 + \exp\left(-\int_{t_{\min}}^{t_{\max}} L'(V)\right)\right)}. \quad (5.43)$$

(ii) The variation of t_{\max} (time for the maximum of $V(t)$) is given by:

$$\partial_Q^{(Q_2)} t_{\max} = -\frac{L'(V_{\max})}{A\omega \sin(\omega t_{\max})} \cdot \frac{\int_{u=t_{\min}}^{t_{\max}} \frac{d}{dv} \left[\frac{vQ_2(v)}{L'(v)} \right] (V(u)) \dot{V}(u) \exp\left(-\int_u^{t_{\max}} L'(V)\right) du}{\left(1 + \exp\left(-\int_{t_{\min}}^{t_{\max}} L'(V)\right)\right)}. \quad (5.44)$$

(iii) Generally, one has a time advance for increased leak: To have $\partial_Q^{(Q_2)} t_{\max} < 0$, a sufficient condition is that $Q_2(v)$ verifies:

$$\forall v, \quad \frac{d}{dv} \left[\frac{vQ_2(v)}{L'(v)} \right] > 0.$$

In (i)-(iii), notation $\frac{d}{dv}[\]$ denotes derivation of the function inside with respect to v . The expression $\int L'(V)$ stands for $\int L'(V(s)) ds$.

Proof:

Let us start by expressing $\partial_Q^{(Q_2)} V$ in the integral formulation of Proposition 5. When relation $\dot{V}(t) = A \cos(\omega t) - L(V(t))$ is differentiated along Q_2 , it yields:

$$\frac{d}{dt} \partial_Q^{(Q_2)} V(t) = -V(t) Q_2(V(t)) - L'(V(t)) \partial_Q^{(Q_2)} V(t). \quad (5.45)$$

The first term of the right-hand side is the Gâteaux derivative w.r.t. Q_2 of function $v \rightarrow L(v) = vQ(v)$, while the second term is the variation of $L(V(t))$ due to $\partial_Q^{(Q_2)} V(t)$. Applying formula (5.40) from Proposition 5 yields:

$$\begin{aligned} & \left(1 + \exp\left(-\int_{t_{\min}}^{t_{\max}} L'(V)\right)\right) \partial_Q^{(Q_2)} V_{\max} \\ &= -\int_{u=t_{\min}}^{t_{\max}} V(u) Q_2(V(u)) \exp\left(-\int_u^{t_{\max}} L'(V)\right) du \\ &= -\int_{u=t_{\min}}^{t_{\max}} \frac{V(u) Q_2(V(u))}{L'(V(u))} L'(V(u)) \exp\left(-\int_u^{t_{\max}} L'(V)\right) du \\ &= -\left[\frac{V(u) Q_2(V(u))}{L'(V(u))} \exp\left(-\int_u^{t_{\max}} L'(V)\right)\right]_{t_{\min}}^{t_{\max}} \\ & \quad + \int_{u=t_{\min}}^{t_{\max}} \left(\frac{d}{dt} \frac{V Q_2(V)}{L'(V)}\right)(u) \exp\left(-\int_u^{t_{\max}} L'(V)\right) du \\ &= -\left(1 + \exp\left(-\int_{t_{\min}}^{t_{\max}} L'(V)\right)\right) \frac{V_{\max} Q_2(V_{\max})}{L'(V_{\max})} \\ & \quad + \int_{u=t_{\min}}^{t_{\max}} \left[\frac{v Q_2(v)}{L'(v)}\right]' (V(u)) \dot{V}(u) \exp\left(-\int_u^{t_{\max}} L'(V)\right) du, \end{aligned}$$

using an integration by parts from line 3 to 4. From line 4 to last, we use the fact that $V(t_{\min}) = -V_{\max}$, and Q_2 and L' are even functions. Dividing the last line by $(1 + \exp(-\int_{t_{\min}}^{t_{\max}} L'(V)))$ yields Point (i) of the Proposition.

Now from another point of view, remark that $V(t)$ and driving potential $E(t)$ coincide at time t_{\max} , so we have:

$$\begin{aligned} V_{\max} &= E(t_{\max}) \\ \partial_Q^{(Q_2)} V_{\max} &= (\partial_Q^{(Q_2)} E)(t_{\max}) + \partial_Q^{(Q_2)} t_{\max} \dot{E}(t_{\max}). \end{aligned} \quad (5.46)$$

To calculate the right-hand side term, we differentiate relation $L(E(t)) = A \cos(\omega t)$ in two different ways: First along t , second along Q_2 . It yields

$$\begin{aligned} \dot{E}(t)L'(E(t)) &= -\omega A \sin(\omega t), \\ (\partial_Q^{(Q_2)} E)(t)L'(E(t)) + E(t)Q_2(E(t)) &= 0. \end{aligned}$$

The corresponding values for $\dot{E}(t_{\max})$ and $(\partial_Q^{(Q_2)} E)(t_{\max})$ can be deduced and injected into (5.46), yielding:

$$\partial_Q^{(Q_2)} V_{\max} = -\frac{V_{\max}Q_2(V_{\max})}{L'(V_{\max})} - \partial_Q^{(Q_2)} t_{\max} \frac{\omega A \sin(\omega t_{\max})}{L'(V_{\max})}. \quad (5.47)$$

Equations (5.43) and (5.47) provide two different expressions for $\partial_Q^{(Q_2)} V_{\max}$. By subtracting them, one gets the expression for $\partial_Q^{(Q_2)} t_{\max}$ proposed in Point (ii) of the Proposition.

To prove Point (iii), simply remark that if $[\frac{vQ_2(v)}{L'(v)}]' > 0$ for all v , then the integral in Point (ii) becomes trivially positive (since $\dot{V}(u) \geq 0$ over $[t_{\min}, t_{\max}]$), implying $\partial_Q^{(Q_2)} t_{\max} < 0$. \square

To illustrate this result, we give below two examples of application of Proposition 6, for different expressions of the leak functions Q .

Example 1: Constant leak function

If $Q(v) = Q_0$ and $Q_2(v) = 1$ are taken as constant functions, system (5.36) becomes the simple linear exponential filter (5.4), with time constant $1/Q_0$. In this case, Point (iii) can simply be reinterpreted as $\partial_{Q_0} t_{\max} < 0$, coherently with well-known results for the linear exponential filter. \blacksquare

Example 2: Quadratic leak function

To get more insight on the condition $[\frac{vQ_2(v)}{L'(v)}]' > 0$, required by Point (iii) of the Proposition, let us consider a function Q of the form

$$Q(v) = a + \lambda v^2.$$

First, if we take $Q_2(v) = v^2$, the Gâteaux derivative along Q_2 amounts to a partial

derivative when parameter λ is modified. And one has

$$[vQ_2(v)/L'(v)]' = [v^3/(a + 3\lambda v^2)]' = (3av^2 + 3\lambda v^4)/(a + 3\lambda v^2)^2 > 0,$$

meaning that $\partial_\lambda t_{\max} < 0$.

By opposition, if we take $Q_2(v) = 1$, the Gâteaux derivative along Q_2 amounts to a partial derivative when parameter a is modified. But there:

$$[vQ_2(v)/L'(v)]' = [v/(a + 3\lambda v^2)]' = (a - 3\lambda v^2)/(a + 3\lambda v^2)^2,$$

so Point (iii) *does not* apply. And indeed, numerical simulations (under Matlab) often reveal that as a augments, t_{\max} undergoes important fluctuations, and is highly non-monotonic with a .

The non-monotony of t_{\max} with a can be explained by the following heuristic argument: When the static leak a augments, it tends to make V_{\max} smaller, and thus the mean value of λV^2 gets smaller, which somehow compensates for the augmentation of a in the total leak $Q(V(t)) = a + \lambda V(t)^2$. ■

4.3 Dependence of V_{\max} and ϕ_{\max} w.r.t. system parameters

Because it has a reduced dimensionality, we are able to state precise results for system (5.36), concerning the dependence of V_{\max} and t_{\max} w.r.t. parameters A and ω of the input current. These results are summed up in the following theorem.

Theorem 2 *System (5.36) behaves as a low-pass filter with gain control on the input amplitude. First, here is how V_{\max} and ϕ_{\max} depend on input frequency ω :*

(i) *Low-pass setting*

$$\partial_\omega V_{\max} < 0 \text{ and } \lim_{\omega \rightarrow +\infty} V_{\max} = 0.$$

(ii) *Phase delay*

$$\partial_\omega(\phi_{\max}) > 0 \text{ and } \lim_{\omega \rightarrow +\infty} \phi_{\max} = \frac{\pi}{2} \pmod{2\pi}.$$

Second, here is how V_{\max} and ϕ_{\max} depend on the amplitude A :

(iii) *Growth of V_{\max}*

$$\partial_A V_{\max} > 0 \text{ and } \lim_{A \rightarrow +\infty} V_{\max} = +\infty.$$

(iv) *Phase advance*

$$\partial_A \phi_{\max} < 0 \text{ and } \lim_{A \rightarrow +\infty} \phi_{\max} = 0 \pmod{2\pi}.$$

(v) *Under-linearity*

$$\forall (\omega, Q), \text{ if } A \text{ is high enough, } \partial_A \frac{V_{\max}}{A} < 0.$$

$$\text{Also, } \lim_{A \rightarrow +\infty} \frac{V_{\max}}{A} = 0.$$

(vi) *Asymptotic equivalents*

$$V_{\max} \underset{A \rightarrow +\infty}{\sim} L^{-1}(A), \text{ and } \partial_A V_{\max} \underset{A \rightarrow +\infty}{\sim} \frac{1}{L'(V_{\max})}.$$

This theorem has the same form as Theorem 1 in the case $b = 0$, except for two details. First, there is an additional Point (vi) concerning equivalents for V_{\max} when $A \rightarrow +\infty$. Its results are more powerful than the simple asymptotic limits given in Points (iii) and (v).

Second, the under-linearity of V_{\max} w.r.t. A , stated in Point (v), also differs from Theorem 1 because we prove that $\partial_A(V_{\max}/A) < 0$ only asymptotically (if A is big enough). We were not able to fully prove that $\partial_A(V_{\max}/A) < 0$ for any set of parameters.

Experimentally, we always found the relation $\partial_A(V_{\max}/A) < 0$ to be true. Proposition 7 in Section 4.4 gives a non-differential equivalent to assertion $\partial_A(V_{\max}/A) < 0$, and provides a sufficient condition to have this inequality verified.

Proof:

We first demonstrate relations related to A (Points (iii)-(vi), Section 4.3.1), and then relations related to ω (Points (i)-(ii), Section 4.3.2), which are simpler and based on similar ideas. In both cases, it is convenient to first demonstrate all signs of variation of the form $\partial_p X$, and afterward to compute all the corresponding limits $\lim_{p \rightarrow +\infty} X$.

4.3.1 Dependence w.r.t. A (Points (iii)-(vi)).

Signs of variation

To prove $\partial_A V_{\max} > 0$, we use the integral formulation from Proposition 5. In this case, one has $Y_A(t) = \cos(\omega t)$, so (5.40) provides the formula:

$$\partial_A V_{\max} = \frac{1}{1 + \exp\left(-\int_{t_{\min}}^{t_{\max}} L'(V)\right)} \int_{u=t_{\min}}^{t_{\max}} \cos(\omega u) \exp\left(-\int_u^{t_{\max}} L'(V)\right) du. \quad (5.48)$$

One can easily get convinced that this integral is always positive (see Figure 5.7). Indeed, interval $[t_{\min}, -T/4]$, on which $\cos(\omega u)$ is negative, is smaller than interval $[-T/4, t_{\max}]$ on which $\cos(\omega u)$ is positive. Furthermore, function $u \rightarrow \exp(-\int_u^{t_{\max}} L'(V(s)) ds)$ is a positive growing function (schematically represented in green in Figure 5.7), that enhances even more the positive contribution of the cosine as compared to the negative contribution. As a result, one has indeed $\partial_A V_{\max} > 0$.

To prove $\partial_A \phi_{\max} < 0$, first note that

$$\partial_A \phi_{\max} = \partial_A(\omega t_{\max}) = \omega \partial_A t_{\max},$$

so we can rather focus on proving $\partial_A t_{\max} < 0$. Let us introduce the reduced variable

$$U(t) = \frac{V(t)}{A}, \quad (5.49)$$

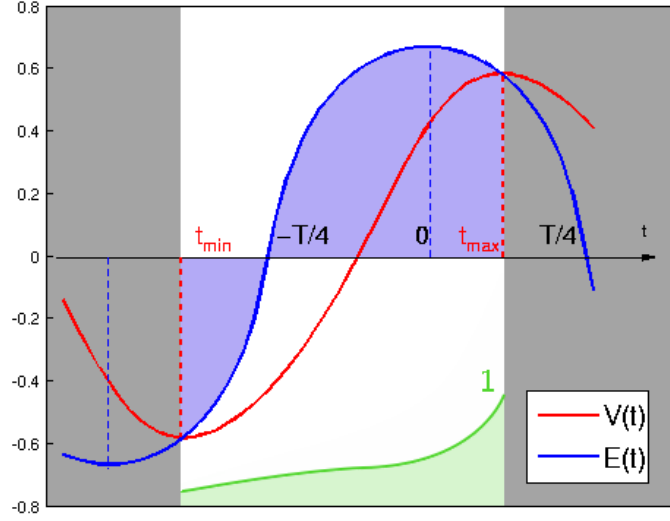


Figure 5.7: Zoom on $E(t)$ and $V(t)$ from t_{\min} to t_{\max} . The blue zone is a schematic view of the integral of $\cos(\omega u)$ over this interval. The green curve is a schematic view of function $u \rightarrow \exp(-\int_u^{t_{\max}} L'(V(s))ds)$, a growing function reaching value 1 in $u = t_{\max}$.

which is governed by the following ODE :

$$\dot{U}(t) = \cos(\omega t) - U(t)Q(AU(t)). \quad (5.50)$$

$U(t)$ is driven by an equation of the same nature as (5.36), except that its leak function is $Q_A : u \rightarrow Q(Au)$, having A as an internal parameter. Naturally, time t_{\max} also corresponds to the maximum of $U(t)$. Now, remark that for an infinitesimal $\varepsilon > 0$:

$$\begin{aligned} Q((A + \varepsilon)u) &= Q(Au) + \varepsilon u Q'(Au) + o(\varepsilon) \\ &= (Q + \varepsilon Q_2)(Au) + o(\varepsilon), \end{aligned}$$

with

$$Q_2(v) = \frac{vQ'(v)}{A} = \frac{R(v)}{A}.$$

So, from the point of view of system (5.50) on $U(t)$, a perturbation $A + \varepsilon$ has the same effect as replacing function Q by function $Q + \varepsilon Q_2$. This implies:

$$\partial_A t_{\max} = \partial_Q^{(Q_2)} t_{\max} = \frac{1}{A} \partial_Q^{(R)} t_{\max}. \quad (5.51)$$

We can then directly apply the results of Proposition 6, concerning Gâteaux derivatives. Indeed, function $v \rightarrow \frac{vR(v)}{L'(v)}$ is a growing function of v . Its derivative

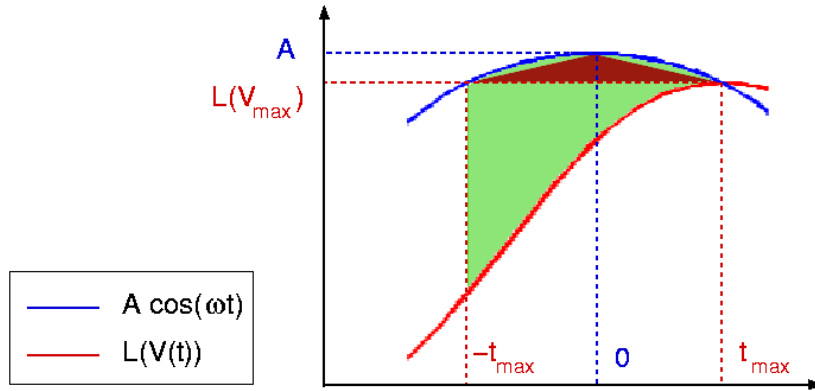


Figure 5.8: Functions $A \cos(\omega t)$ and $L(V(t))$, on interval $[-t_{\max}, t_{\max}]$. The integral $\int_{-t_{\max}}^{t_{\max}} (A \cos(\omega t) - L(V(t))) dt$, in green, can be minored by the area of the dark red triangle.

writes (we only provide the result):

$$\frac{d}{dv} \left[\frac{vR(v)}{L'(v)} \right] = \frac{2R(v)Q(v) + v^2Q''(v)}{L'(v)^2}, \tag{5.52}$$

which is positive because Q is convex ($Q''(v) \geq 0$). As a result, Point (iii) of Proposition 6 allows to directly conclude: $\partial_A t_{\max} < 0$, as stated by Point (iv) of the Theorem.

Remark: Naturally, this result could also be obtained without using Gâteaux derivatives, by direct differentiation of (5.50) along A , and calculations similar to the proof of Proposition 6. ■

Limits

We can now find the associated limits in Points (iii)-(v). Let us note $\phi_{\max} = \omega t_{\max}$ modulo 2π (so that $\phi_{\max} \in]0, \pi/2[$), and denote $\phi_{\infty} \geq 0$ the limit of ϕ_{\max} when $A \rightarrow +\infty$. We know this limit exists because we have just proved $\partial_A t_{\max} < 0$.

First, note that $L(V_{\max}) = A \cos(\phi_{\max})$. Since $\cos(\phi_{\infty}) > 0$, this implies

$$V_{\max} \underset{A \rightarrow +\infty}{\sim} L^{-1}(A \cos(\phi_{\infty})). \tag{5.53}$$

So, $\lim_{A \rightarrow +\infty} V_{\max} = +\infty$ and Point (iii) is proved. Also, since $L^{-1}(v)$ is under-linear, one has $\lim_{A \rightarrow +\infty} (V_{\max}/A) = 0$, as stated by Point (iv). Equation (5.53) will also provide the first asymptotic result in Point (v), once we show that $\phi_{\infty} = 0$.

To prove that $\phi_{\infty} = 0$, integrate the driving equation $\dot{V}(t) = A \cos(\omega t) - L(V)$ between $-t_{\max}$ and t_{\max} :

$$V_{\max} - V(-t_{\max}) = \int_{-t_{\max}}^{t_{\max}} (A \cos(\omega t) - L(V(t))) dt. \tag{5.54}$$

The integral on the right-hand side of (5.54) is schematically represented in Figure 5.8, in color green. Since function $t \rightarrow \cos(\omega t)$ is concave over $[-t_{\max}, t_{\max}]$, the integral term in (5.54) is bigger than the triangular area depicted in black red in

Figure 5.8. Which writes:

$$\int_{-t_{\max}}^{t_{\max}} (A \cos(\omega t) - L(V(t))) dt \geq t_{\max} (A - L(V_{\max})).$$

And since, trivially, $V_{\max} - V(-t_{\max}) \leq 2V_{\max}$, equation (5.54) implies the inequality:

$$2V_{\max} \geq t_{\max} (A - L(V_{\max})). \quad (5.55)$$

Now suppose that $\phi_{\infty} > 0$. In that case, (5.55) would imply that

$$2 \liminf_{A \rightarrow +\infty} V_{\max} \geq A \frac{\phi_{\infty}}{\omega} (1 - \cos(\phi_{\infty})), \quad (5.56)$$

because of (5.53), and the facts that $\phi_{\infty} > 0$ and $\cos(\phi_{\infty}) < 1$. But this is in contradiction with the fact that $\lim_{A \rightarrow +\infty} (V_{\max}/A) = 0$, as resulting from (5.53). So $\phi_{\infty} = 0$, which concludes the proof of Point (iv).

Equivalence relations

We finish by proving the equivalence relations in Point (vi). First, since $\phi_{\infty} = 0$, equation (5.53) gives us the stated equivalent to V_{\max} . Then, proceed to an integration by parts starting from (5.48):

$$\begin{aligned} & \left(1 + \exp\left(-\int_{t_{\min}}^{t_{\max}} L'(V)\right)\right) \partial_A V_{\max} \\ &= \int_{u=t_{\min}}^{t_{\max}} \frac{\cos(\omega u)}{L'(V(u))} L'(V(u)) \exp\left(-\int_u^{t_{\max}} L'(V)\right) du \\ &= \left(1 + \exp\left(-\int_{t_{\min}}^{t_{\max}} L'(V)\right)\right) \frac{\cos(\omega t_{\max})}{L'(V_{\max})} - \int_{u=t_{\min}}^{t_{\max}} \left(\frac{d}{dt} \frac{\cos(\omega t)}{L'(V(t))}\right)(u) \exp\left(-\int_u^{t_{\max}} L'(V)\right) du, \end{aligned}$$

using the fact that $\cos(\omega t_{\min}) = -\cos(\omega t_{\max})$ for the first term of the sum. And so

$$\partial_A V_{\max} = \frac{\cos(\phi_{\max})}{L'(V_{\max})} - \frac{\int_{u=t_{\min}}^{t_{\max}} \left(\frac{d}{dt} \frac{\cos(\omega t)}{L'(V(t))}\right)(u) \exp\left(-\int_u^{t_{\max}} L'(V)\right) du}{1 + \exp\left(-\int_{t_{\min}}^{t_{\max}} L'(V)\right)}. \quad (5.57)$$

We wish to prove that when $A \rightarrow +\infty$, $\partial_A V_{\max}$ is equivalent to the first term of the right-hand side in (5.57), itself equivalent to $1/L'(V_{\max})$ since $\phi_{\infty} = 0$. First, let us admit the simple convergence relation:

$$\forall t \in [t_{\min}, t_{\max}[, F(t) = \exp\left(-\int_t^{t_{\max}} L'(V)\right) \xrightarrow{A \rightarrow +\infty} 0, \quad (5.58)$$

which is intuitive since $L'(V_{\max}) \rightarrow +\infty$ when $A \rightarrow +\infty$. Proving rigorously this relation is tedious.

Then, prove that the second term on the right-hand side of (5.57) is a $o(1/L'(V_{\max}))$:

$$L'(V_{\max}) \frac{\int_{u=t_{\min}}^{t_{\max}} \left(\frac{d}{dt} \frac{\cos(\omega t)}{L'(V(t))} \right) (u) \exp \left(- \int_u^{t_{\max}} L'(V) du \right)}{1 + \exp \left(- \int_{t_{\min}}^{t_{\max}} L'(V) \right)}$$

$$\underset{A \rightarrow +\infty}{\sim} \int_{u=t_{\min}}^{t_{\max}} L'(V_{\max}) \left(\frac{d}{dt} \frac{\cos(\omega t)}{L'(V(t))} \right) (u) F(u) du \underset{A \rightarrow +\infty}{\rightarrow} 0.$$

where $F(t)$ is defined in (5.58). The limit comes from the fact that $F(t)$ converges simply to 0, and the integral term is dominated by

$$\int_{u=t_{\min}}^{t_{\max}} L'(V_{\max}) \left(\frac{d}{dt} \frac{\cos(\omega t)}{L'(V(t))} \right) (u) du = 2 \cos(\omega t_{\max}) < 2.$$

We thus found:

$$\partial_A V_{\max} \underset{A \rightarrow +\infty}{\sim} 1/L'(V_{\max}),$$

which finishes to prove Point (vi). But then,

$$\partial_A \frac{V_{\max}}{A} = \frac{A \partial_A V_{\max} - V_{\max}}{A^2} \underset{A \rightarrow +\infty}{\sim} \frac{L(V_{\max})/L'(V_{\max}) - V_{\max}}{A^2} = \frac{-V_{\max}^2 Q'(V_{\max})}{L'(V_{\max}) A^2},$$

using $L(v) = vQ(v)$ and $L'(v) = Q(v) + vQ'(v)$. This last result, which can also be found directly from (5.63), proves that $\partial_A \frac{V_{\max}}{A}$ becomes negative for A big enough. This concludes point (v) of the theorem.

4.3.2 Dependence w.r.t. ω (Points (i)-(ii))

The following results concern the dependence with respect to ω . They use similar arguments as Points (iii)-(v), with the supplementary problem that derivatives w.r.t. ω for $V(t)$ are ill-defined, because changing ω changes the period of the whole system. To solve this problem, we express our system in coordinates that make the period independent of ω : Set

$$\phi = \omega t,$$

and the system becomes ruled by:

$$\frac{d}{d\phi} V(\phi) = \frac{A}{\omega} \cos(\phi) - \frac{V(\phi)Q(V(\phi))}{\omega}. \quad (5.59)$$

Remark: This modification, although benign, makes notations and differentiations a bit more confusing (at least to us...). However, the underlying calculations are rather simpler here than for the amplitude-related differentiations of Points (iii)-(v). This simplicity reflects the fact that our gain control system (5.36) is the straightforward extension of a linear low-pass system. ■

Signs of variation

Differentiating (5.59) w.r.t ω leads to the following ODE:

$$\begin{aligned}\frac{d}{d\phi}(\partial_\omega V)(\phi) &= -\frac{A}{\omega^2} \cos(\phi) + \frac{L(V(\phi))}{\omega^2} - \frac{1}{\omega} L'(V(\phi)) \partial_\omega V(\phi) \\ &= -\frac{1}{\omega} \frac{d}{d\phi} V(\phi) - \frac{1}{\omega} L'(V(\phi)) \partial_\omega V(\phi),\end{aligned}$$

with $L(v) = vQ(v)$. We can again use Proposition 5 to obtain:

$$\begin{aligned}\partial_\omega V_{\max} &= \frac{1}{1 + \exp\left(-\int_{\phi_{\min}}^{\phi_{\max}} \frac{L'(V)}{\omega} d\phi\right)} \int_{\phi=\phi_{\min}}^{\phi_{\max}} \left(-\frac{1}{\omega} \frac{d}{d\phi} V(f)\right) \exp\left(-\int_{\phi}^{\phi_{\max}} \frac{L'(V)}{\omega}\right) d\phi \\ &= -\frac{1}{\omega} \frac{1}{1 + \exp\left(-\int_{t_{\min}}^{t_{\max}} L'(V)\right)} \int_{u=t_{\min}}^{t_{\max}} \dot{V}(u) \exp\left(-\int_u^{t_{\max}} L'(V)\right) du,\end{aligned}$$

where we have switched back to regular coordinates in the last line. Since \dot{V} is positive on the interval $[t_{\min}, t_{\max}]$, this formula proves $\partial_\omega V_{\max} < 0$.

Relation $\partial_\omega \phi_{\max} > 0$ can be proved without extra calculations, by using previous results. Consider a perturbation on the frequency: $\omega \rightarrow \omega + \varepsilon$. After first-order approximation of $1/(\omega + \varepsilon)$, we find that (5.59) is modified as follows:

$$\frac{d}{d\phi} V(\phi) = \frac{A(1 - \varepsilon/\omega)}{\omega} \cos(\phi) - \frac{VQ(V)(1 - \varepsilon/\omega)}{\omega} + o(\varepsilon). \quad (5.60)$$

As a result, the first-order perturbation on ϕ_{\max} induced by $\omega \rightarrow \omega + \varepsilon$ is the same as the first order perturbation induced by the simultaneous changes:

$$\begin{aligned}A &\rightarrow A - \frac{\varepsilon}{\omega} A \\ \text{and } Q(v) &\rightarrow Q(v) - \frac{\varepsilon}{\omega} Q(v).\end{aligned}$$

This writes:

$$\begin{aligned}\partial_\omega \phi_{\max} &= -\frac{A}{\omega} \partial_A \phi_{\max} - \frac{1}{\omega} \partial_Q^{(Q)} \phi_{\max} \\ &= -A \partial_A t_{\max} - \partial_Q^{(Q)} t_{\max} \\ &= -\partial_Q^{(Q+R)} t_{\max},\end{aligned}$$

because we know from (5.51) that $\partial_A t_{\max} = \partial_Q^{(R)} t_{\max}/A$. So in the end, since $L' = Q + R$:

$$\partial_\omega \phi_{\max} = -\partial_Q^{(L')} t_{\max}. \quad (5.61)$$

We then use Proposition 6 on Gâteaux derivatives, with $Q_2(v) = L'(v)$. Trivially,

$$\frac{d}{dv} [vQ_2(v)/L'(v)] = \frac{d}{dv} [v] = 1 > 0,$$

so that Point (iii) of Proposition 6 applies, and $\partial_\omega \phi_{\max} > 0$.

Limits

Finally, we find the associated limits for V_{\max} and ϕ_{\max} when $\omega \rightarrow +\infty$. Let us integrate (5.59) between $\phi_{\min} = \phi_{\max} - \pi$ and ϕ_{\max} :

$$\begin{aligned} 2V_{\max} &= \frac{2A \sin(\phi_{\max})}{\omega} - \int_{\phi_{\min}}^{\phi_{\max}} \frac{L(V(\phi))}{\omega} d\phi \\ &\leq \frac{2A}{\omega} + \frac{\pi A}{\omega} \\ V_{\max} &\leq \frac{A(1 + \pi/2)}{\omega}, \end{aligned}$$

where the integral term was majored using $|L(V)| \leq A$. So $\lim_{\omega \rightarrow +\infty} V_{\max} = 0$, and since $L(V_{\max}) = A \cos(\phi_{\max})$, $\lim_{\omega \rightarrow +\infty} \phi_{\max} = \pi/2$. This concludes the proof of the theorem. \square

4.4 Local under-linearity of V_{\max} w.r.t. A

To conclude this presentation of the asymptotic system $b = +\infty$, we present our tentative to show that the system is always locally under-linear with input amplitude:

$$\partial_A(V_{\max}/A) < 0.$$

This result would complete Theorem 2, by making the local variation property in Point (v) true for all A , and not only for A high enough.

Although we did not manage to prove that this relation is always true, we could find a simpler, and more intuitive equivalence to the relation. Using this equivalence, we could state a sufficient condition for $\partial_A(V_{\max}/A) < 0$ to be true.

Proposition 7 (Local under-linearity of V_{\max} w.r.t. A)

Consider $V(t)$ the unique periodic solution of (5.36):

$$\dot{V}(t) = A \cos(\omega t) - L(V(t)).$$

Then:

$$(i) \quad \partial_A \frac{V_{\max}}{A} < 0 \Leftrightarrow \left[\begin{array}{l} \int_{u=t_{\min}}^{t_{\max}} \left[\frac{v^2 Q'(v)}{L'(v)} \right]' (V(u)) \dot{V}(u) \exp\left(-\int_u^{t_{\max}} L'(V)\right) du \\ < \frac{V_{\max}^2 Q'(V_{\max})}{L'(V_{\max})} \left(1 + \exp\left(-\int_{t_{\min}}^{t_{\max}} L'(V)\right)\right) \end{array} \right.$$

(ii) A sufficient condition to have $\partial_A \frac{V_{\max}}{A} < 0$ is that the following, even function:

$$H(v) = \exp\left(-\int_{T(v)}^{t_{\max}} L'(V(s)) ds\right) + \exp\left(-\int_{T(-v)}^{t_{\max}} L'(V(s)) ds\right) \quad (5.62)$$

have its maximum over $[0, V_{\max}]$ reached in $v = V_{\max}$.

We have noted $T(v) : [-V_{\max}, V_{\max}] \rightarrow [t_{\min}, t_{\max}]$ the reciprocal function of $V(t)$ over $[t_{\min}, t_{\max}]$.

Point (i) allowed us to test under Matlab, in a simple fashion, whether or not $\partial_A \frac{V_{\max}}{A} < 0$ was true for the given set of parameters. We always found the inequality in Point (i) to be true.

Point (ii) states a sufficient condition for which the inequality in Point (i) can be easily proved true. We tried to prove this sufficient condition, but did not manage. Under simulation with Matlab, the sufficient condition was found true in all simulations, except when A was taken very close to zero (with value around $10^{-3}\omega$). But in these cases, $H(v) \simeq 2$ for all v , and at the same time Matlab calculated a whole period of $V(t)$ with less than ten sample points. So the exceptions found in these particular cases could very possibly be due to numerical imprecision.

Remark that the condition enunciated in Point (ii) appears plausible. The function

$$v \rightarrow \exp\left(-\int_{T(v)}^{t_{\max}} L'(V(s))ds\right)$$

decreases exponentially as v gets away from V_{\max} . So, from the moment that $L'(V(s))$ takes relatively large values, both terms in $H(v)$ become very small, unless v is close to V_{\max} .

We proved that, whatever set of parameters, V_{\max} is a *local* maximum for $H(v)$, because $H'(v) > 0$ near V_{\max} . More precisely, one has

$$H(V_{\max}) - H(V_{\max} - \varepsilon) = \sqrt{\frac{2}{A\omega \sin(\omega t_{\max})}} L'(V_{\max}) \left(1 - \exp\left(-\int_{t_{\min}}^{t_{\max}} L'(V)\right)\right) \varepsilon^{1/2} + o(\varepsilon^{1/2}),$$

so that $\lim_{v \rightarrow V_{\max}} H'(v) = +\infty$. This asymptotic relation is not proved here.

Proof of Proposition 7

Point (i) comes from the fact that

$$\partial_A \frac{V_{\max}}{A} = \frac{1}{A^2} \partial_Q^{(R)} V_{\max}, \quad (5.63)$$

with $R(v) = vQ'(v)$, a result proved exactly as (5.51). The expression of $\partial_Q^{(R)} V_{\max}$ is given by equation (5.43) of Proposition 6. Solving $\partial_A \frac{V_{\max}}{A} < 0$ then yields the inequality in Point (i).

To prove Point (ii), we re-express the integral term in Point (i) in terms of variable

V rather than t , by using the reciprocal function $T(v)$. We get:

$$\begin{aligned}
F &= \int_{u=t_{\min}}^{t_{\max}} \frac{d}{dv} \left[\frac{v^2 Q'(v)}{L'(v)} \right] (V(u)) \dot{V}(u) \exp \left(- \int_u^{t_{\max}} L' \right) du \\
&= \int_{V=-V_{\max}}^{V_{\max}} \frac{d}{dv} \left[\frac{v^2 Q'(v)}{L'(v)} \right] (V) \exp \left(- \int_{T(V)}^{t_{\max}} L' \right) dV \\
&= \int_{V=0}^{V_{\max}} \frac{d}{dv} \left[\frac{v^2 Q'(v)}{L'(v)} \right] (V) \left(\exp \left(- \int_{T(V)}^{t_{\max}} L' \right) + \exp \left(- \int_{T(-V)}^{t_{\max}} L' \right) \right) dV \\
&= \int_{V=0}^{V_{\max}} \frac{d}{dv} \left[\frac{v^2 Q'(v)}{L'(v)} \right] (V) H(V) dV
\end{aligned} \tag{5.64}$$

by symmetry of function $\frac{d}{dv} \left[\frac{v^2 Q'(v)}{L'(v)} \right]$. If the hypothesis $\forall v, H(v) \leq H(V_{\max})$ is verified, and since $\frac{d}{dv} \left[\frac{v^2 Q'(v)}{L'(v)} \right] > 0$ as proved before in (5.52), relation (5.64) can be continued into:

$$\begin{aligned}
F &< H(V_{\max}) \int_{V=0}^{V_{\max}} \frac{d}{dv} \left[\frac{v^2 Q'(v)}{L'(v)} \right] (V) dV \\
F &< \left(1 + \exp \left(- \int_{t_{\min}}^{t_{\max}} L'(V) \right) \right) \frac{V_{\max}^2 Q'(V_{\max})}{L'(V_{\max})},
\end{aligned}$$

which is precisely the equivalence condition stated in Point (i). \square

5 A TRACK FOR THE FUTURE: PERTURBATION ANALYSIS

To conclude this chapter, we report some preliminary results when perturbation analysis is applied near the boundaries of b 's domain of definition: $b \rightarrow 0$ and $b \rightarrow +\infty$.

The base assumption (verified experimentally) is that the 1D systems $b = 0$ and $b = +\infty$ presented in the preceding sections constitute natural *continuous* limits of the 2D system (5.14), so that the following expansion can be written:

$$\begin{cases} V^{(\varepsilon)}(t) = V_0(t) + \varepsilon V_1(t) + \dots + \varepsilon^k V_k(t) + o(\varepsilon^k), \\ G^{(\varepsilon)}(t) = G_0(t) + \varepsilon G_1(t) + \dots + \varepsilon^k G_k(t) + o(\varepsilon^k), \end{cases} \tag{5.65}$$

where:

- $(V_0(t), G_0(t))$ is the asymptotic 1D-system $b = 0$ (resp. $b = +\infty$).
- $(V^{(\varepsilon)}(t), G^{(\varepsilon)}(t))$ is the solution of 2D system (5.14) for parameter $b = b(\varepsilon)$, where $\varepsilon > 0$ and $b(\varepsilon)$ is a well-chosen decreasing (resp. increasing) function such that $\lim_{\varepsilon \rightarrow 0^+} b(\varepsilon) = 0$ (resp. $+\infty$).
- The coefficients $(V_k(t), G_k(t))$ of the expansion exist if and only if function $\varepsilon \rightarrow V^{(\varepsilon)}(t)$ admits a C^k extension in $\varepsilon = 0$.

In this section, we limit ourselves to C^1 expansions. We assume that a C^1 expansion is well defined in $b = 0$ for function $b(\varepsilon) = \varepsilon$, and in $b = +\infty$ for function $b(\varepsilon) = \varepsilon^{-1}$, and derive results from this assumption. We start by presenting the expansion near $b = +\infty$ (Section 5.1), which provides simpler calculations and higher hopes of generalization to the k -th order. We then present the expansion near $b = 0$ (Section 5.2).

5.1 Perturbation analysis near $b \rightarrow +\infty$

The simplest function $b(\varepsilon)$ tending to $+\infty$ is obviously $b(\varepsilon) = \varepsilon^{-1}$, and the consistency of the following results suggests that this is indeed the right choice, although we have not proved it.

As a result, the perturbed system $(V^{(\varepsilon)}(t), G^{(\varepsilon)}(t))$ is ruled by the following ODE:

$$\begin{cases} \dot{V}^{(\varepsilon)}(t) = A \cos(\omega t) - G^{(\varepsilon)}(t)V^{(\varepsilon)}(t), & (a) \\ \varepsilon \dot{G}^{(\varepsilon)}(t) = Q(V^{(\varepsilon)}(t)) - G^{(\varepsilon)}(t). & (b) \end{cases} \quad (5.66)$$

When development (5.65) is used up to order 1:

$$\begin{cases} \dot{V}_0(t) + \varepsilon \dot{V}_1(t) = A \cos(\omega t) - G_0 V_0 - \varepsilon(G_0 V_1 + G_1 V_0) + o(\varepsilon), & (a) \\ \varepsilon \dot{G}_0(t) = Q(V_0) - G_0 + \varepsilon(Q'(V_0)V_1 - G_1) + o(\varepsilon), & (b) \end{cases} \quad (5.67)$$

the zeroth-order terms annihilate each other, and the remaining first-order terms are ruled by

$$\begin{cases} \dot{V}_1(t) = -G_0 V_1 - G_1 V_0, & (a) \\ \dot{G}_0(t) = Q'(V_0)V_1 - G_1. & (b) \end{cases} \quad (5.68)$$

We have omitted to note the time dependence of all variables on the right-hand side, for the sake of readability.

Fast-slow dynamics. Note that, since parameter ε multiplies the left-hand side of (5.66-b), it annihilates the possible contribution of $\dot{G}_1(t)$ to the terms of first order in ε . As a consequence, $\dot{G}_1(t)$ is absent from (5.68-b), meaning that (5.68-b) is not a differential equation, but a simple equation which directly provides a formula for $G_1(t)$! This property is typical of systems with *fast-slow* dynamics (ε^{-1} being obviously the *fast* time constant), and it allows a considerable simplification of calculations.

Actually, we have already used this *fast-slow* property in Section 4, to define our 1D system $b = +\infty$. Indeed, the annihilation of zeroth-order terms in (5.67-b) implies that $(V_0(t), G_0(t))$ must verify $G_0(t) = Q(V_0(t))$, which is precisely the heuristic condition we used to derive our 1D system equation.

In other words, the 1D system ' $b = +\infty$ ' defined heuristically in Section 4 can be defined rigorously as the zeroth-order term of the perturbation expansion (5.65) for $b(\varepsilon) = \varepsilon^{-1}$, provided there is some guarantee of existence for the perturbation expansion. Most likely, the existence of such a perturbation expansion must be guaranteed by a theorem of the dynamic/control systems literature.

When system (5.68) is solved, it yields the following ODE for $V_1(t)$:

$$\dot{V}_1 + L'(V_0)V_1 = \dot{V}_0 R(V_0), \quad (5.69)$$

where $L(v) = vQ(v)$ and $R(v) = vQ'(v)$. As for $G_1(t)$, it is not an autonomous variable, its formula being imposed by the *fast-slow* dynamics:

$$G_1 = Q'(V_0)V_1 - \dot{G}_0. \quad (5.70)$$

Interestingly, $V_1(t)$ is ruled by a linear equation (5.69), so it can be derived from $V_0(t)$ through a close-form equation. Moreover, due to the symmetries of the system, $V_1(t)$ is necessarily $T/2$ -antiperiodic. We can thus apply the same type of integration (over a half-period) as we used to prove equation (5.39) in Proposition 5. This yields the formula:

$$V_1(t) = \frac{1}{1 + \exp\left(-\int_{t-T/2}^t L'(V_0)\right)} \int_{u=t-T/2}^t \dot{V}_0 R(V_0) \exp\left(-\int_u^t L'(V_0)\right) du, \quad (5.71)$$

where ' V_0 ' should be read ' $V_0(u)$ ', etc.

We could thus explicitly calculate $V_1(t)$ from our numerical approximation for $V_0(t)$. This allowed us to compare the real solution $(V^{(\varepsilon)}(t), G^{(\varepsilon)}(t))$ and its first order approximation $(V_0(t) + \varepsilon V_1(t), G_0(t) + \varepsilon G_1(t))$. An example is provided in Figure 5.9. For the given set of parameters, the first and second order approximations provided a relatively good fit up to $\varepsilon \simeq 0.01$ (corresponding to $b \simeq 100$). For higher ε , the approximations (especially second-order) quickly diverged (not shown).

Higher-order expansions. To conclude, we remark that the type of analysis produced here to derive the first-order expansion (V_1, G_1) applies similarly to all higher order expansions. Indeed, the multiplication by ε in the left-hand side of (5.66) (*fast-slow* dynamics) insures that, at any order k , function $G_k(t)$ is directly constrained by a formula involving only $V_k(t)$ (not its derivative!), and functions of previous orders. And in turn, $V_k(t)$ is always driven by a linear ODE of the form

$$\dot{V}_k + L'(V_0)V_k = \dots,$$

where the dots denote a combination of functions of previous orders.

This implies that all successive orders can be recursively calculated from the single solution $V_0(t)$ through close-form, linear equations. As a result, the 1D-solution $V_0(t)$ may possibly have a high descriptive power over the whole 2D system.

Because of the relative simplicity of the successive expansions, one could even investigate if some, or all, solutions $(V(t), G(t))$ of the 2D problem can be described by an infinite power series of extensions $(V_k(t), G_k(t))$.

Another question would be to investigate further characterizations of V_{\max} and ϕ_{\max} in the 2D case, and their dependence w.r.t. A , using perturbation analysis. However, even with a good theory for the successive expansions, such results still appear far away.

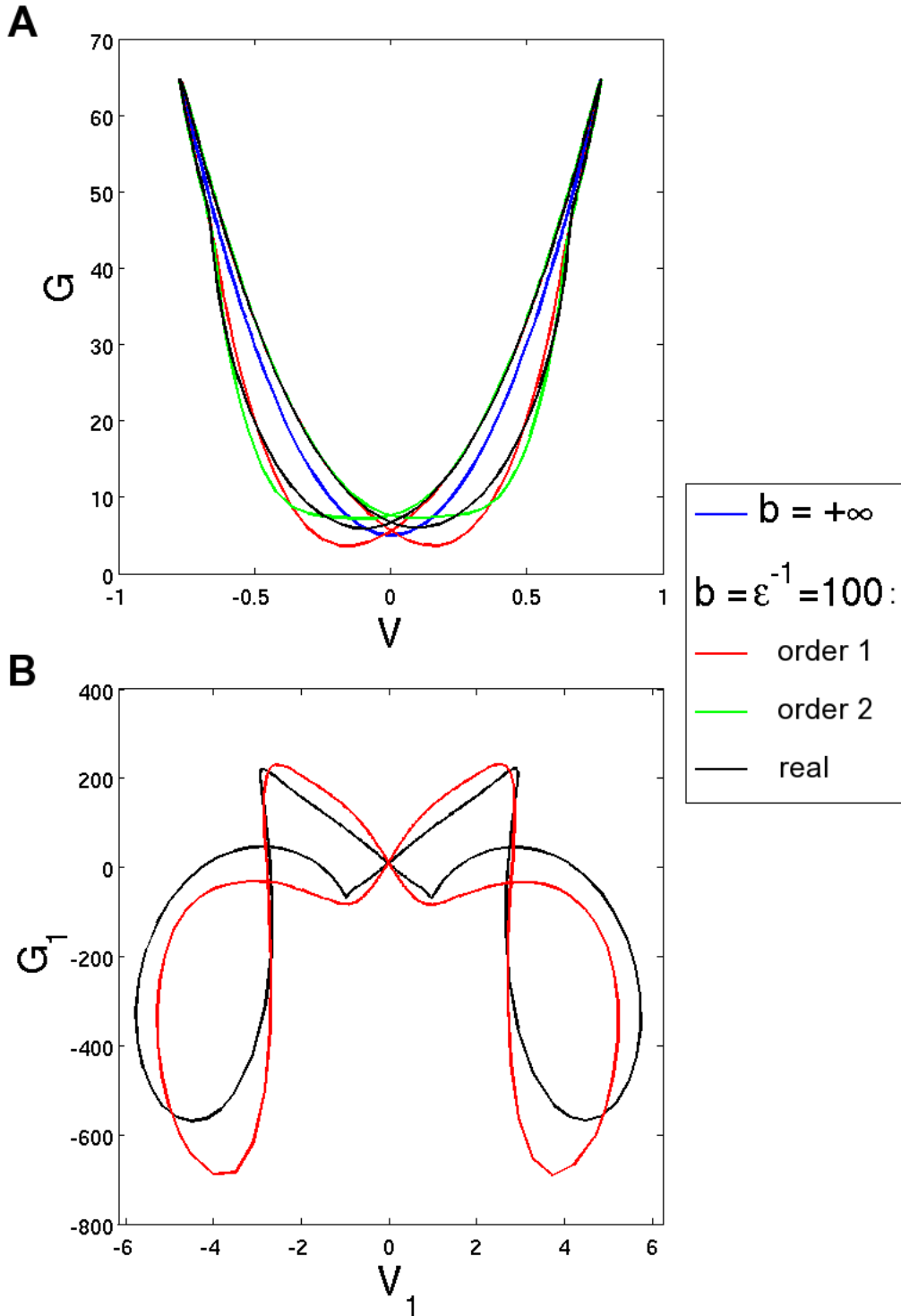


Figure 5.9: Perturbation analysis near $b = +\infty$. Panel A compares the real solution $(V^{(\varepsilon)}(t), G^{(\varepsilon)}(t))$ to its zeroth, first and second order approximations using perturbation analysis. Panel B compares more specifically the first-order expansion (V_1, G_1) to its approximation by $((V^{(\varepsilon)} - V_0)/\varepsilon, (G^{(\varepsilon)} - G_0)/\varepsilon)$. Perturbation parameter $b = \varepsilon^{-1} = 100$ Hz. Other simulation parameters: $\omega = 2\pi$ Hz, $A = 50$ Hz, $Q(V) = Q_0 + \lambda V^2$ with $Q_0 = 5$ Hz and $\lambda = 100$ Hz.

5.2 Perturbation analysis near $b \rightarrow 0$

Perturbation analysis is also possible near the boundary $b = 0$. The resulting equations for the successive expansions require a different treatment than in the case $b = +\infty$. Generally speaking, the equations are harder to solve near $b = 0$, especially for higher-order expansions. Also, the fact that the system's asymptotic periodic regime is reached within a time proportional to b^{-1} (thus tending to infinity) may raise some problems to rigorously prove the existence of an expansion.

For all these reasons, we spend less time on the case $b = 0$. We sketch the main principle to derive the successive expansions (based on what we term a 'binding condition'), and then provide a result obtained thanks to this 'binding condition', in the particular case where $Q(v) = Q_0 + \lambda v^2$ is quadratic.

The simplest function $b(\varepsilon)$ tending to 0 is obviously $b(\varepsilon) = \varepsilon$ and again, the following calculations tend to show that this is the right choice.

As a result, the perturbed system $(V^{(\varepsilon)}(t), G^{(\varepsilon)}(t))$ is ruled by the following ODE:

$$\begin{cases} \dot{V}^{(\varepsilon)}(t) = A \cos(\omega t) - G^{(\varepsilon)}(t)V^{(\varepsilon)}(t), & (a) \\ \dot{G}^{(\varepsilon)}(t) = \varepsilon(Q(V^{(\varepsilon)}(t)) - G^{(\varepsilon)}(t)). & (b) \end{cases} \quad (5.72)$$

When development (5.65) is used up to order 1:

$$\begin{cases} \dot{V}_0(t) + \varepsilon \dot{V}_1(t) = A \cos(\omega t) - G_0 V_0 - \varepsilon(G_0 V_1 + G_1 V_0) + o(\varepsilon), & (a) \\ \dot{G}_0(t) + \varepsilon \dot{G}_1(t) = \varepsilon(Q(V_0) - G_0) + o(\varepsilon), & (b) \end{cases} \quad (5.73)$$

the zeroth-order terms annihilate each other, and the remaining first-order terms are ruled by

$$\begin{cases} \dot{V}_1(t) = -G_0 V_1 - G_1 V_0, & (a) \\ \dot{G}_1(t) = Q(V_0) - G_0. & (b) \end{cases} \quad (5.74)$$

We have omitted to note the time dependence of all variables on the right-hand side, for the sake of readability. They all depend on time, except for $G_0(t) = G_0$ which is really a constant function (Section 3)!

Binding condition. The particularity of system (5.74) is that considered as such, it admits an infinity of solutions: Indeed, we have a choice in the integration constant K that will yield $G_1(t)$ from (5.74-b), and system (5.74-a) does not restrict our choice for K .

However, if we refer to the *asymptotic* periodic equilibrium of the *real* solution $(V^{(\varepsilon)}(t), G^{(\varepsilon)}(t))$, then (5.72-b) implies that

$$\widehat{G^{(\varepsilon)}} = \widehat{Q(V^{(\varepsilon)})}, \quad (5.75)$$

where the hat denotes averaging over one period. We denote this relation the 'binding condition' because it allows to bind the choice of constant K to the evolution of $V_1(t)$, and thus to determine $(V_1(t), G_1(t))$ unambiguously. Again, note that the binding condition itself is problematic because it is based on the asymptotic state of the system, which is reached with time constant $\varepsilon^{-1} \rightarrow +\infty$.

When applied to zeroth and first order, the binding condition yields:

$$\widehat{G}_0 = \widehat{Q}(V_0), \quad (5.76)$$

$$\widehat{G}_1 = \widehat{Q}'(V_0)V_1. \quad (5.77)$$

Note that we have already used this *binding* condition in Section 3, to define our 1D system $b = 0$. Indeed, zeroth-order approximation from (5.73-b) only yields $\dot{G}_0 = 0$, and we thus needed the binding condition (5.76) to fully describe our system.

Then, $(V_1(t), G_1(t))$ can be calculated according to the following procedure:

1. Integrate (5.74-b), yielding a function $G_1(t)$ where the integration constant K is left undetermined.
2. Insert the resulting expression for $G_1(t)$ into (5.74-a) and solve it formally (it is linear) with constant K still undetermined.
3. Use the binding condition (5.77) to finally determine K .
4. re-inject the value of K into the calculated expressions for $G_1(t)$ and $V_1(t)$.

We applied this procedure to the particular case where

$$Q(v) = Q_0 + \lambda v^2.$$

First, the zeroth-order binding condition (5.76) yields

$$(G_0 - Q_0)(G_0^2 + \omega^2) = \frac{\lambda A^2}{2},$$

which can be solved explicitly thanks to Cardan formulas, and from there

$$V_0(t) = \sqrt{\frac{2(G_0 - Q_0)}{\lambda}} \cos(\omega t - \arctan(\omega/G_0)).$$

Second, the procedure described in the previous paragraph yields the following first order expansions:

$$K = -\frac{(G_0 - Q_0)^3}{4G_0(G_0 - Q_0)^2 + \lambda A^2},$$

$$G_1(t) = \frac{G_0 - Q_0}{2\omega} \sin(2(\omega t - \arctan(\omega/G_0))),$$

$$\begin{aligned} V_1(t) &= \frac{(G_0 - Q_0)^2}{2\lambda A} \left(-\frac{1}{\omega} \sin(\omega t - 2\arctan(\omega/G_0)) + \frac{(G_0 - Q_0)^2}{\lambda A^2 + 2G_0(G_0 - Q_0)} \cos(\omega t - 2\arctan(\omega/G_0)) \right) \\ &\quad - \frac{\lambda(G_0 - Q_0)}{4\omega\sqrt{(G_0^2 + \omega^2)(G_0^2 + 9\omega^2)}} (\sin(3\omega t - 3\arctan(\omega/G_0) - \arctan(3\omega/G_0))). \end{aligned}$$

These zeroth and first order expansions are compared to the real trajectory in Figure 5.10.

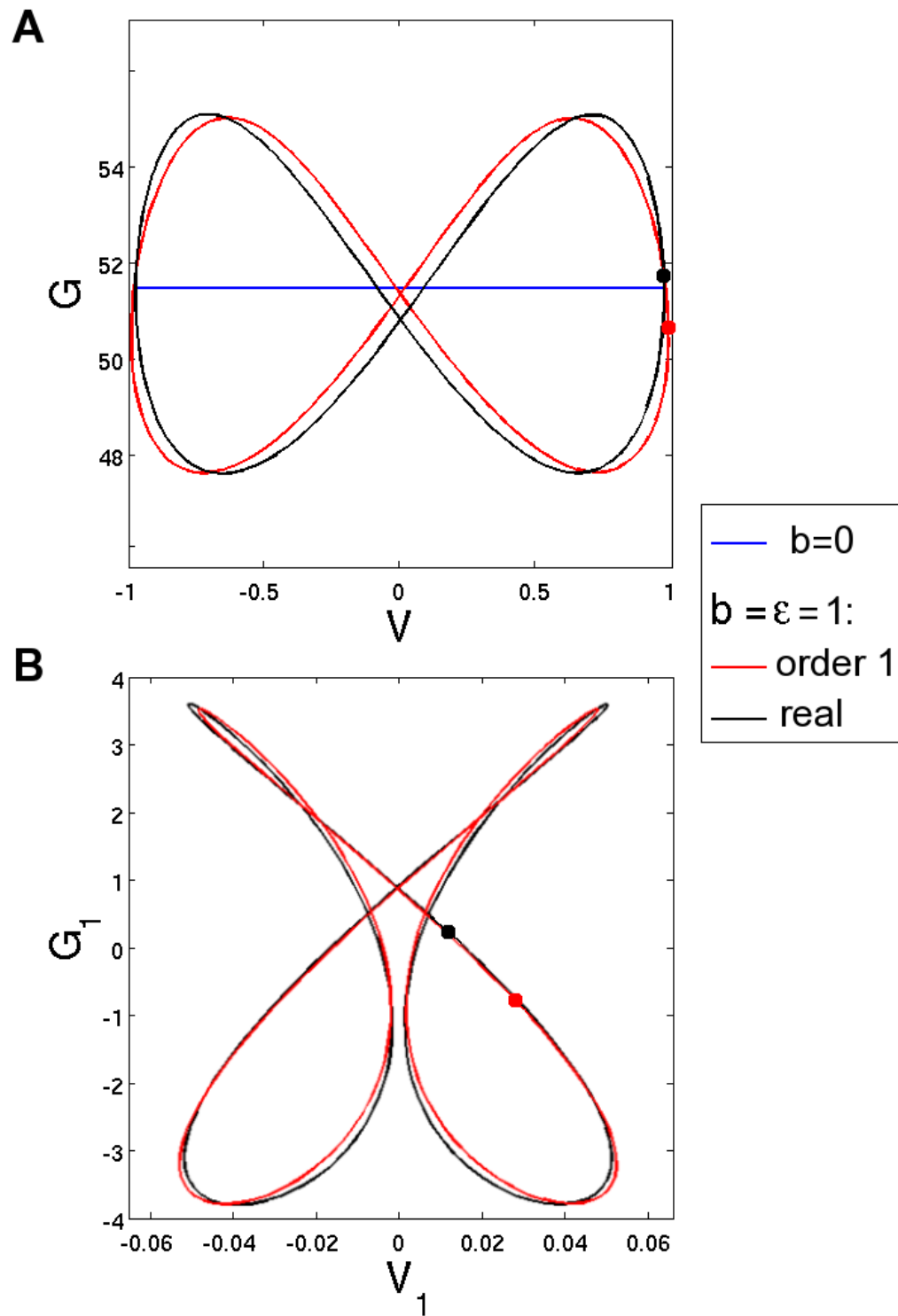


Figure 5.10: Perturbation analysis near $b = 0$. Panel A compares the real solution $(V^{(\varepsilon)}(t), G^{(\varepsilon)}(t))$ to its zeroth-, first- and second-order approximations using perturbation analysis. Panel B compares more specifically the first-order expansion (V_1, G_1) to its approximation by $((V^{(\varepsilon)} - V_0)/\varepsilon, (G^{(\varepsilon)} - G_0)/\varepsilon)$. The two dots mark the respective positions of the two variables at a given time. Perturbation parameter $b = \varepsilon = 1$ Hz. Other simulation parameters: $\omega = 2\pi$ Hz, $A = 50$ Hz, $Q(V) = Q_0 + \lambda V^2$ with $Q_0 = 5$ Hz and $\lambda = 100$ Hz.

CONCLUSION

As a conclusion, let us remind the practical reason for which we started to lead this study: We wanted to understand better the behavior of the amplitude V_{\max} and phase ϕ_{\max} of $V(t)$, output of our gain control loop, with respect to its input parameters.

The results presented herein prove, through theoretical results and simulations, that the following behavior can be considered true under virtually any sinusoidal stimulation:

1. The system acts as a temporal low-pass filter.
2. The system produces contrast gain control:

$$\begin{aligned} \partial_A V_{\max} &> 0 && \text{(growth with contrast),} \\ \partial_A \phi_{\max} &< 0 && \text{(phase advance with contrast),} \\ \partial_A \frac{V_{\max}}{A} &< 0 && \text{(under-linearity with contrast).} \end{aligned}$$

From a mathematical point of view, interesting asymptotic behaviors exist for the 2-dimensional system, which live on 1-dimensional spaces and are thus easier to study. Precise mathematical results are available for these 1D asymptotic systems. In the future, perturbation analysis might increase the extent of some results further into the realm of the general 2D system.

APPENDIX: PERIODIC CONTRACTING SYSTEM (PROPOSITION 2)

In this appendix, we prove Proposition 2, concerning the asymptotic behavior of periodic contracting systems. Let us thus consider a T -periodic contracting dynamic system, as defined in the hypothesis of Proposition 2:

$$\frac{d}{dt} Z = F(Z(t), t, p), \quad (5.78)$$

where F is C^1 w.r.t. p , T -periodic w.r.t. t , and contracting w.r.t. Z (differentiable, and associated to upper bound $-\lambda_0 < 0$ for the eigenvalues of dF).

We will use the generic notation $Z(t, k_0, p)$ to denote the solution of (5.78) with initial condition $Z(0) = k_0$ and parameter p . When it is possible, we will also use simplified expressions ($Z(t, k_0)$ if parameter p is unambiguous, etc.).

Since $F(Z, t, p)$ is C^1 w.r.t. Z , it is locally Lipschitz w.r.t. Z , so the Cauchy-Lipschitz (aka Picard-Lindelöf) Theorem (existence and unicity of ODE solutions) applies. In short form, the theorem insures that

$$(t, k_0, p) \rightarrow Z(t, k_0, p) \text{ is } C^1. \quad (5.79)$$

(Here and in the whole chapter, we are not preoccupied by any higher-order regularity than C^1 .)

Proof of Point (i) (unique periodic trajectory)

To prove Point (i), pick any particular solution $Z_0(t)$ of (5.78), and consider the following family of functions

$$\{Z_n : t \rightarrow Z_0(t + nT)\}_{n \in \mathbb{N}}.$$

Because F is T -periodic, all the $Z_n(t)$ are also solutions of (5.78).

Now fix $t \in \mathbb{R}^+$. For $k \in \mathbb{N}$, the contraction property (5.20) implies that

$$\|Z_{k+1}(t) - Z_k(t)\|^2 = \|Z_1(t + kT) - Z_0(t + kT)\|^2 \leq \|Z_1(t) - Z_0(t)\|^2 \exp(-kT\lambda_0),$$

and if this inequality is summed from $k = 0$ to $n - 1$,

$$\|Z_n(t) - Z_0(t)\|^2 \leq \|Z_1(t) - Z_0(t)\|^2 (1 - \exp(-nT\lambda_0)),$$

by triangular inequality, and majoration of $\sum_{k=0}^{n-1} \exp(-kT\lambda_0)$ by $(1 - \exp(-nT\lambda_0))$. This proves that $\|Z_n(t) - Z_0(t)\|$ is majored independently of n . Using this majoration, and applying again the contraction property (5.20), we can then write, for $n, m \in \mathbb{N}$:

$$\begin{aligned} \|Z_{n+m}(t) - Z_n(t)\|^2 &= \|Z_m(t + nT) - Z_0(t + nT)\|^2 \\ &\leq \|Z_m(t) - Z_0(t)\|^2 \exp(-nT\lambda_0) \\ &\leq \|Z_1(t) - Z_0(t)\|^2 (1 - \exp(-nT\lambda_0)) \exp(-nT\lambda_0) \end{aligned}$$

so that $\{Z_n(t) = Z_0(t + nT)\}$ is a Cauchy series. As a result it admits a limit, and we can define

$$W(t) \triangleq \lim_{n \rightarrow +\infty} Z_n(t). \quad (5.80)$$

Note that $W(t)$ actually depends on parameter p , so that the actual notation should be $W(t, p)$.

The resulting function $W(t)$ is periodic by construction. Because the system is contracting (5.20), $W(t)$ is unique and independent of the choice of solution $Z_0(t)$. Finally, remark that

$$Z(t, W(0)) = Z(t, \lim_{n \rightarrow \infty} Z_n(0)) = \lim_{n \rightarrow \infty} Z(t, Z_n(0)),$$

where the swapping of limits is licit, since the Cauchy-Lipschitz Theorem (5.79) states a continuous dependence on the system's initial conditions. In other words,

$$Z(t, W(0)) = \lim_{n \rightarrow \infty} Z_n(t) = W(t),$$

proving that $W(t)$ is indeed a solution of system (5.20). This concludes the proof of Point (i).

Remark: This proof to Point (i) is already sketched in [100] (their point 3.7-(vi)). ■

Proof of Point (ii) (regularity of the periodic trajectory)

Before starting the actual demonstration of Point (ii), we will need the following technical lemma:

Lemma 1 Consider a contracting system $\frac{d}{dt}Y(t) = G(Y, t, p)$ (associated to upper bound $-\lambda_0$ on the eigenvalues of dG), and a particular initial condition X_0 . We note $X(t) = Y(t, X_0, p)$. We are interested in the magnitudes of $\partial_p X$ when $p \in \Lambda$, a given set of the parameter space.

If there exists $M > 0$ such that

$$\forall t, \forall p \in \Lambda, \quad \|\partial_p G(X(t), t, p)\| < M$$

(bounded variation of G w.r.t. p on the trajectory of $X(t)$), then $\partial_p X$ is also bounded:

$$\forall t, \forall p \in \Lambda, \quad \|\partial_p X(t)\| < \frac{M}{\lambda_0}.$$

Proof:

Let us calculate the temporal derivative of $\|\partial_p X\|$ (supposed non-null, to simplify the calculation - but the final result is true anyway):

$$\begin{aligned} \frac{d}{dt}\|\partial_p X\| &= \frac{d}{dt}\sqrt{\|\partial_p X\|^2} \\ &= \frac{1}{2\|\partial_p X\|} \frac{d}{dt}\|\partial_p X\|^2 \\ &= \frac{\partial_p X}{\|\partial_p X\|} \partial_p(G(X(t))) \\ &= \frac{\partial_p X}{\|\partial_p X\|} (dG(X)\partial_p X + \partial_p G(X)) \\ &\leq -\lambda_0\|\partial_p X\| + M, \end{aligned}$$

Note that we have omitted to write parameter t in all variables, to simplify notations. Since $X(0) = X_0$ independently of p , $\partial_p X(0) = 0$. Then, Gronwall's Lemma implies that

$$\forall t, \forall p \in \Lambda, \quad \|\partial_p X\| \leq \frac{M}{\lambda_0}(1 - \exp(-\lambda_0 t)),$$

which can be trivially majored to prove the lemma. \square

We now come to Point (ii) of the Proposition: Proving that the unique periodic trajectory $W(t, p)$ is C^1 w.r.t. parameter p . Note that this result is very close to the Cauchy-Lipschitz Theorem. The only difference is that $W(t, p)$ can only be defined as an *asymptotic* trajectory, so that the local results of the Cauchy-Lipschitz Theorem have no reason to apply *a priori*. However, because the system is contracting (and thus very stable), we are indeed able to extend the results to $W(t, p)$.

In order to prove that $W(t, p)$ is C^1 w.r.t. p , we only need to prove that the initial condition $W(0, p)$ is C^1 w.r.t. p . Then, by composition with the flow in (5.79), the C^1 property will extend to all t .

Fix parameter p_0 , and $\bar{\varepsilon} > 0$. For $n \in \mathbb{N}$, $\varepsilon \in]0, \bar{\varepsilon}]$, we define the function

$$D(n, \varepsilon) \triangleq \frac{Z(nT, W(0, p_0), p_0 + \varepsilon) - W(0, p_0)}{\varepsilon}. \quad (5.81)$$

The particular solution $Z(t, W(0, p_0), p_0 + \varepsilon)$ used to define $D(n, \varepsilon)$ is an intermediate function between $W(t, p_0)$ and $W(t, p_0 + \varepsilon)$. It shares the former's initial condition (defined by parameter p_0), but it is driven by the same system as the latter (defined by parameter $p_0 + \varepsilon$). Through this intermediate function, we will be able to clarify the link between $W(t, p_0)$ and $W(t, p_0 + \varepsilon)$.

First, note that

$$D(n, \varepsilon) \xrightarrow{\varepsilon \rightarrow 0} \partial_p Z(nT, W(0, p_0), p_0), \quad (5.82)$$

as a consequence of (5.79) (Cauchy-Lipschitz Theorem).

Second, we can write

$$\begin{aligned} \left| D(n, \varepsilon) - \frac{W(0, p_0 + \varepsilon) - W(0, p_0)}{\varepsilon} \right| &= \frac{|Z(nT, W(0, p_0), p_0 + \varepsilon) - W(0, p_0 + \varepsilon)|}{\varepsilon} \\ &= \frac{|Z(nT, W(0, p_0), p_0 + \varepsilon) - Z(nT, W(0, p_0 + \varepsilon), p_0 + \varepsilon)|}{\varepsilon} \\ &\leq \frac{|W(0, p_0) - W(0, p_0 + \varepsilon)|}{\varepsilon} \exp(-nT\lambda_0) \end{aligned} \quad (5.83)$$

From first to second line, we use a simple re-writing of $W(t, p_0)$ as the unique T -periodic solution of (5.78). From second to third line, we use the contracting properties (5.20) of the system.

Let us now fix any initial condition $Z_0 \in \Omega$. We then apply Lemma 1 to $F(Z, t, p)$, initial condition Z_0 , and parameter space $\Lambda = [p_0, p_0 + \bar{\varepsilon}]$. Since we are in a periodic system, each trajectory $Z(t, Z_0, p)$ is bounded for $t \in \mathbb{R}^+$. We can thus find a strict upper bound $M > 0$ such that

$$\max_{p \in [0, \bar{\varepsilon}]} \sup_{t \in \mathbb{R}^+} \|\partial_p F(Z(t, Z_0, p), t, p)\| < M,$$

so the hypothesis of Lemma 1 are verified. As a result, there exists $M_1 > 0$ such that

$$\forall t, \forall p \in [p_0, p_0 + \bar{\varepsilon}], \quad \|\partial_p Z(t, Z_0, p)\| < M_1.$$

Then, for all $t > 0$ and $\varepsilon \in]0, \bar{\varepsilon}]$, we can write

$$\begin{aligned} \frac{|W(0, p_0) - W(0, p_0 + \varepsilon)|}{\varepsilon} &= \lim_{n \rightarrow \infty} \frac{|Z(nT, Z_0, p_0) - Z(nT, Z_0, p_0 + \varepsilon)|}{\varepsilon} \\ &= \lim_{n \rightarrow \infty} \frac{\left| \int_{\eta=0}^{\varepsilon} \partial_p Z(nT, Z_0, p_0 + \eta) d\eta \right|}{\varepsilon} \\ &\leq \max_{\eta \in [0, \bar{\varepsilon}]} \|\partial_p Z(nT, Z_0, p_0 + \eta)\| \\ &\leq M_1, \end{aligned}$$

When reinjected into (5.83), this last inequality provides:

$$\left| D(n, \varepsilon) - \frac{W(0, p_0 + \varepsilon) - W(0, p_0)}{\varepsilon} \right| \leq M_1 \exp(-nT\lambda_0).$$

Since the majoring term is independent of $\varepsilon \in]0, \bar{\varepsilon}]$, this implies that

$$D(n, \varepsilon) \xrightarrow[n \rightarrow +\infty]{} \frac{W(0, p_0 + \varepsilon) - W(0, p_0)}{\varepsilon}, \quad (5.84)$$

uniformly for ε over $]0, \bar{\varepsilon}]$.

Thanks to the uniform convergence of (5.84), we are allowed to swap limits in n and ε for $D(n, \varepsilon)$. This gives

$$\begin{aligned} \lim_{\varepsilon \rightarrow 0} \left(\lim_{n \rightarrow +\infty} D(n, \varepsilon) \right) &= \lim_{n \rightarrow +\infty} \left(\lim_{\varepsilon \rightarrow 0} D(n, \varepsilon) \right) \\ \lim_{\varepsilon \rightarrow 0} \frac{W(0, p_0 + \varepsilon) - W(0, p_0)}{\varepsilon} &= \lim_{n \rightarrow +\infty} \partial_p Z(nT, W(0, p_0), p_0), \end{aligned}$$

where these two limits are ensured to exist by the virtues of uniform convergence. So, $W(0, p)$ is differentiable w.r.t. p , and

$$\partial_p W(0, p_0) = \lim_{n \rightarrow +\infty} \partial_p Z(nT, W(0, p_0), p_0).$$

By composition with the flow (5.79), we get derivability w.r.t. p for all t , so that $t \rightarrow \partial_p W(t, p)$ is a well-defined function, C^1 in t thanks to the Cauchy-Lipschitz theorem (the derivative of the flow with respect to parameters is still derivable in time).

To conclude, we must prove that $W(t, p)$ is C^1 w.r.t. p , or in other words that $\partial_p W(t, p)$, just defined, is C^0 w.r.t. p . To do this, we simply derive the driving ODE (5.78) w.r.t. p , yielding

$$\frac{d}{dt} \partial_p W(t, p) = \partial_p F(W(t, p), t, p) + dF(W(t, p), t, p) \partial_p W(t, p).$$

As a result, $\partial_p W(t, p)$ is driven by a linear equation of the form

$$\frac{d}{dt} X = \mathbf{A}(t)X(t) + B(t),$$

where both $\mathbf{A}(t) = dF(W(t, p), t, p)$ and $B(t) = \partial_p F(W(t, p), t, p)$ are C^0 w.r.t. p (because $W(t, p)$ is derivable, so C^0 , w.r.t. p). By simple arguments on the general form of the solutions to linear ODEs (see the remark 'Driving potential in stable linear systems' at the end of Section 2.2.1), the solution $X(t) = \partial_p W(t, p)$ is also C^0 w.r.t. p .

□

VIRTUAL RETINA: A LARGE-SCALE SIMULATOR

In this chapter, we present in more details the software *Virtual Retina*, which implements on a large-scale the model presented in Chapter 4, in C++ language. Our goal is to provide a realistic retinal input to neuroscientists modeling low-level thalamo-cortical visual processing (typically, models of V1), which can at the same time offer some biological plausibility, allow large-scale simulations (up to around 100,000 cells), and display a modular structure allowing a better fit to potential users' requirements.

After a brief presentation of the software's goals and characteristics (Section 1), we explain its general organization and usage (Section 2), based on retina definition files in XML format. Then, we present the underlying C++ objects (Section 3), and how they can be used as building blocks to implement other retina models.

Contents

1	Introduction	268
2	Using <i>Virtual Retina</i>	269
2.1	The executables	270
2.2	The retina XML definition file	273
2.3	Installing <i>Virtual Retina</i>	279
3	Implementation details	280
3.1	Synaptic inputs and connections	282
3.2	Implementing a foveated structure	285
3.3	Continuous filtering	287
3.4	Spiking cells and arrays	297
3.5	<i>xmlParameters++</i> : Loading/saving parameters with XML	305
3.6	Assembling and simulating a retina	308

1 INTRODUCTION

*Virtual Retina*¹ was originally designed to provide a retinal input for modelers in our research team (Odyssee, INRIA laboratory). One strong initial requirement for the software was to produce *spikes* as output, because recent studies have suggested the potential importance of individual spikes in the cerebral code (as we have illustrated for the retina in Chapter 3, Section 4). For this reason, the software was developed on the basis of a library previously developed at INRIA labs, *MvaSpike*, which handles spikes in an event-driven formalism.

However, as opposed to cortical models that can be based only on spike exchanges inside a network, a model of retinal processing must also include a stage of continuous spatio-temporal filtering on the input visual sequence. This stage of continuous filtering is not only a modeling requirement, but also reflects the intrinsic nature of graded signal transmission in the first layers of the retina. We thus developed C++ objects to handle the linear and/or nonlinear differential equations which underly retinal filtering. For this purpose, we used the *CImg* image processing library, also developed in parts at INRIA Odyssee Lab.

The link between these objects in charge of continuous filtering, and the *MvaSpike* event-driven spiking formalism, was then done by implementing noisy integrate-and-fire neurons, following the model described in Chapter 4.

Also, we decided to store the various parameters of our model into a single XML architecture, whose tree structure reproduces the successive stages of filtering in the model (see Chapter 4). This allows an ordered storage of all the model's parameters in a single file, which is easily modifiable for programmers (changing names, adding parameters, etc.) and, more importantly, modular for users: Various stages of the model can be present or not in the test retina, by simple modifications in the architecture of the XML definition file. As a result, the output of the software can consist of spikes or continuous maps, the contrast gain control can be present or not, the retina can follow a log-polar scheme or a uniform scheme, etc.

To achieve this easy conversion from an XML architecture to C++ code, we designed a specific template library called *xmlParameters++*, which allows to save/load the relevant parameters of C++ objects to an XML file. Coding this library was not in the direct scope of the thesis, but it provided a very interesting discovery of advanced C++ programming, and a useful toolbox that can possibly be re-used.

Once the software *Virtual Retina* was finished in a somewhat stable version, we encapsulated it in a distribution for Linux, and provided it with a tutorial, for potential diffusion to interested neuroscientists. An archive with the distribution is now available for download from the *Virtual Retina* home page:

<http://www-sop.inria.fr/odyssee/software/virtualretina/>

Before entering the details, here is a summary of the software's characteristics:

- *Realistic model of retinal processing*: Following the model presented in Chapter 4. Also, the XML architecture of the parameter definition file is modular, allowing to use more simplified models if required.

¹Software under INRIA CeCILL C open-source license, IDD number IDD.FR.001.210034.000.S.P.2007.000.31235.

- *Possibility of large-scale simulations:* Up to 100,000 spiking cells can be simulated in a reasonable time (speed of around 1/100 real time).
- *Two possible sampling schemes:* First option is a uniform, square array of cells, associated to a uniform scaling function. In this case, all spatial filtering scales of the model (σ_C , σ_S , σ_A , σ_G) are constant throughout the whole image. Second option is a sampling of ganglion cells along concentric circles, associated to the radial scaling $s(r)$ in equation (4.17), to reproduce a foveated organization at the level of the whole retina. In that case, the Gaussian filters $G_\sigma(x, y)$ also have different scales according to the location in the retina, following radial scheme $s(r)$.
- *Fixation microsaccades:* Finally, the software allows to include a simple random microsaccades generator at the input of the retina, to account for fixation eye movements, as inspired from the review of Martinez-Conde *et al.* 04 [106].

This chapter is organized as follows. In Section 2, we present how to use software *Virtual Retina*: Organization of the package and usage of the programs, including how to write a retina definition file in XML. In Section 3, we enter the implementation of the software in more detail, through a presentation of the most important objects in the source code. These objects can be used as building blocks to implement other retina models than the one we have presented in Chapter 4.

2 USING *Virtual Retina*

In this first section, we describe how to use *Virtual Retina* in practice. We start by a general description of the programs available (Section 2.1). Most of these programs are based on the same retina definition file in XML: We describe this XML file in Section 2.2, and how it relates to the model presented in Chapter 4. Finally, Section 2.3 explains how to install the distribution. In this thesis chapter, we try to keep the description relatively short. A tutorial for the programs, included in the downloadable archive, contains most of the material presented here, plus additional examples.

Before starting, let us just present the organization of the *Virtual Retina* distribution, as it can be downloaded from the internet. The archive `Retina.Package` contains the root directory of *Virtual Retina*: `Retina.Package/VirtualRetina/`, and directory `Retina.Package/ExternalLibraries/`, which contains some required helper libraries (see installation in Section 2.3).

The root directory `Retina.Package/VirtualRetina/` is divided into five specific sub-directories:

- `src/` contains source codes for the `virtual_retina` library, for a library of general tools, and for the executables.
- `test/` contains some examples of retina definition files in XML (`retina_files/`), and visual input sequences to test the retina (`sequences/`).

- `local/` is the default directory for the compiled executables (`bin/`) and libraries (`lib/`).
- `tmp/` is the default output directory of all executables.
- `experiments/` contains some experiments on single cells, to validate the underlying retina model.

2.1 The executables

All executables have a `-h` command that provides the whole list of options for the executable. Here, we only present the most important options to run the executables.

2.1.1 The Retina executable

This is the main simulation executable. Input is a 3-dimensional sequence (space and time). Output is a set of spike trains or, if you did not ask for spikes, analog spatio-temporal sequences corresponding to the ‘activities’ of ganglion cells. It is typically called by:

```
Retina path/to/test_sequence*.pgm -ret path/to/retina.xml
      -r 10 -outD path/to/saving_directory
```

with possible options:

- input sequences can be passed as a series of 2d frames under any usual format (as here), or directly as a `.inr` 3d file.
- `-ret` gives the path to the retina definition file in XML format. This is the file containing the definition of the whole retinal architecture and parameters: See Section 2.2. Amongst other parameters, it fixes the retinal time step (let us say 5 ms, in this case).
- `-r 10` asks that each input frame be presented to the retina for a duration of $10 * (\text{retinal time step}) = 50$ ms in this case.
- `-outD` gives the path to the directory where all simulation files will be saved. By default, this directory is `VirtualRetina/tmp/`.
- Full list of options by typing `-h` when calling the executable. They include: position of the retina in the input sequence, saving options, display options, etc.

The executable has several output files:

simulation.txt is the main output file of the simulation, which can be used as input to executables who need to load an already existing simulation. It contains general information such as: input sequence, location of the `spikes.spk` file (see below), of the `retina.xml` file (see below), center of the retina in the input image, etc.

retina.xml is the file containing all characteristics of the retina used for the simulation. It has the same format as the input definition file (also in XML, see Section

2.2), except that it also contains the *positions and indexes of all ganglion cells created in the retina*, a necessary information to exploit the output spikes.

spikes.spk is an ASCII file containing all spikes emitted during the simulation, as generated by library *MvaSpike*. All spikes emitted by the retina are saved in a single file, ranked according to their emission time:

```
9128 0.0153717
9272 0.015372
7900 0.0153743
9332 0.015375
7692 0.0153755
etc.
```

The first number is an absolute index for the cell that emitted the spike. It can be linked to a spatial position thanks to the `retina.xml` file. Second number is the time of the spike. Alternatively, the emitted spikes can be retrieved in the binary `hdf5` format, by using option `-hdf5` when calling the executable (see Section 2.3).

Other output files are produced only if extra saving options are activated. Option `-savemap` saves all maps for intermediate signals (OPL current, bipolar cells, adaptation conductance, etc.), in specific directories termed `oplFrames/`, `bipolarFrames/`, etc. Option `-saveCP` only saves temporal courses for these signals at center pixel of the retina, in the form of 1-dimensional `.inr` images: `oplCP.inr`, etc. For both saving procedures, option `-nS` fixes the temporal frequency of saves, every `-nS` retinal time step.

2.1.2 The TestGanglionCell executable

This is a wrapper for program `Retina`, in the particular case where you want to test a *single*, spiking ganglion cell with noise in its spike generation, and reconstruct an averaged firing rate. This program can serve as a basis for simulating ‘physiological’ recordings on our model ganglion cells. Examples of use for this program can be found in directory `VirtualRetina/experiments/`.

Most important options:

- `-tr` fixes the number of trials used to reproduce a firing rate for the cell. It is meaningful only if you defined some intrinsic noise in the spike generation process for the cell (equation (4.16) of the model) in the retina definition file. If you set `-tr 0`, the cell does not fire spikes at all (only produces an analogical output).
- `-nodisp` to suppress displays (useful when automatically testing the program over many cells and/or stimuli). By default, the program displays the average firing rate over the trials (output of the program), and also displays two intermediate signals: OPL current (resulting from equation (4.10) of the model) and ganglion input current (resulting from equation (4.14) of the model).
- `-p` and `-lat` allow you to change the linear kernel used to reconstruct the average firing rate from the trains of spikes.

- etc. Full list of options by typing `-h` when calling the executable. In particular, most options for program `Retina` also work for program `TestGanglionCell`.

2.1.3 The ReconstructRetina executable

It allows to visualize the spiking output of the retina, by reconstructing a video sequence based on the spike trains emitted by program `Retina`.

The reconstruction process is a simple linear summation: Each emitted spike linearly contributes to the reconstruction by adding a spot, at the location of the emitting cell, for a particular length of time, expressed as a number of frames by option `-lat`. Spatially, the spot is a circle whose radius follows the radial scheme $s(r)$ of the retina (equation (4.17) of the model, if a foveated scheme was chosen). Option `-w` fixes the radius in pixels of a spot in the fovea. This defines the size of spots everywhere else, following the scaling function $s(r)$ of equation (4.17) (if a uniform scaling was chosen, $s(r) = 1$ everywhere).

So, in three dimensions, the spot has a certain volume `VolSpot` expressed in voxels (that depends on the radial position of the emitting cell). The intensity of the spot in each voxel is then chosen as

$$(\text{VolSpot} \cdot (d_0 s(r))^2)^{-1},$$

where $(d_0 s(r))^2$ is the local 2d density of cells in the region around the emitting cell. It is important to normalize our spot so that in the end, the number stocked in each pixel of the reconstructed sequence has the dimension of an *average firing rate per spiking cell*.

To avoid that the intensity of spots be divided by cell density $(d_0 s(r))^2$, write option `-nodn`. In which case the number stocked in each pixel of the reconstructed sequence has the dimension of an average firing rate *per pixel*, and you see nothing in peripheral regions where there are less cells...

Other important options:

- `-i path/to/simulation.txt` gives the path to the simulation file emitted by program `Retina`, that you want to reconstruct from.
- `-ch` fixes which layers of ganglion cells you want to represent (all ON channels, for example). It is used as follows: `-ch 2 0 3` means that you want to represent two channels, namely channels number 0 and 3. So if you had a single layer in your retina (most of the time!), you still have to write `-ch 1 0`.
- etc. Full list of options by typing `-h` when calling the executable.

2.1.4 Other executables

Some other executables that I wrote for my work (mostly, small utilities) have also been included in the distribution, since they can possibly be useful. Option `-h` can be used on each of them for more precisions.

`viewVideo` is a simple video viewer; useful to watch input sequences, or reconstructed sequences. You might also want to use `inrcast`, a much more complete application included in the *CImg* library, that is also copied in `VirtualRetina/local/bin`.

But unlike `inrcast`, `viewVideo` allows you to play the video (and at any speed you like, by using option `-s`).

`lumImage` allows to change the mean luminosity and contrast of a sequence before feeding it to the retina.

`Grating` creates a grating stimulus (!...).

`shapleyVictor` allows to test the responses of a single ganglion cell with contrast gain control, to multi-sinus stimuli (as in Chapter 4, Section 6.2).

2.2 The retina XML definition file

All retinal parameters, for a given simulation, are given to program `Retina` in the form of a single retina definition file in XML format. The XML logical structure syntax is a well diffused format. It allows us to store the numerous parameters in hierarchical structures which directly relate to the different stages of our model (Chapter 4).

In addition to what is presented here, more details about the XML files can be found in the *Virtual Retina* tutorial. There, the XML structure is presented along with its corresponding equations, and different example files are specifically commented.

2.2.1 General architecture of a file

The retina is described through a hierarchical XML structure, whose root element is simply termed `<retina/>`. As in every XML tree, an *element* has children *attributes* in the form `param-name="value"`, as well as children elements. The attributes correspond to *numerical parameters* of the model. The children elements allow to hierarchically define sub-structures, which themselves possess parameters in the form of attributes. This allows:

- A clearer organization of parameters for the retina, according to their location in the retinal model.
- An extended modularity of the retina, because sub-elements of node `<retina/>` are bricks that can be present or not in the architecture, making the resulting retinal model more or less complex.

Here is the general structure of the retina file, when only element `<retina/>` and its direct children are represented:

```
<retina-description-file>
  <retina  temporal-step__sec ="0.005"
          input-luminosity-range="255"
          pixels-per-degree="10.0">

    <log-polar-scheme/>
    <outer-plexiform-layer/>
    <contrast-gain-control/>
    <ganglion-layer/>
```

```

. . .
<ganglion-layer/>

</retina>
</retina-description-file>

```

The three first lines show attributes to element `<retina/>`. They are general parameters that concern the whole retinal scheme:

`temporal-step_sec` is the (simulated) time length of one discretization step for the retina. Note that this is not the precision of emitted spike trains! Rather, the spike trains are generated from a current that is constant within each bin of 5 ms (in this case).

`input-luminosity-range` is the intensity corresponding to color white in the input sequences fed to the retina. This allows not to change all subsequent amplitude parameters whenever the retina is fed images with another luminosity encoding.

`pixels-per-degree` is, in the same spirit, a conversion factor allowing to express all subsequent spatial scales of the retina in terms of visual degrees, rather than pixels. Which allows to change a single parameter (this one) when one wants to change how close the input image is to the simulated eye.

Note that, whenever a parameter is expressed in a unit that is not trivial, this unit is expressed in the XML name for the parameter, after a double underscore.

2.2.2 Sub-elements: Optional stages of the model

The sub-elements of node `<retina/>` correspond to various stages of the underlying retina model, as detailed in Chapter 4. Most of them are *optional* features of the retina, which can be added or removed, leading to different complexities for the retina model that will be used. Only element `<outer-plexiform-layer/>` is always necessary, as it implements the basic band-pass linear filtering typical of retinal filtering. We now briefly present the XML notations for the different stages of the model.

`<log-polar-scheme/>`

This XML node deals with the spatially non-uniform structure of the retina, as presented in Chapter 4, Section 5.3. If this node is absent, then the retina will have a uniform density of cells. If this node is present, its parameters define a central *fovea* with uniform density of cells, and then a radially decreasing density, following the model's equation (4.17). The node writes:

```

<log-polar-scheme  fovea-radius__deg="1.0"
                   scaling-factor-outside-fovea__inv-deg="1.0"/>

```

where the two parameters define respectively R_0 and K in (4.17).

`<outer-plexiform-layer/>`

This XML node defines the *center-surround* linear filter of the retina, as presented in Chapter 4, Section 3. It is the only block that must always be present in the retina definition file. In its most basic version, the node writes:

```

<outer-plexiform-layer>
  <linear-version
    center-sigma__deg="0.03"
    center-tau__sec="0.01"
    center-n="2"
    surround-sigma__deg="0.1"
    surround-tau__sec="0.01"
    opl-amplification="10"
    opl-relative-weight="1"
    leaky-heat-equation="1" />
</outer-plexiform-layer>

```

The different parameters correspond to the linear filter described in equations (4.8)–(4.10) of the model, but without the undershoot filter T_{w_U, τ_U} in equation (4.8).

In order to also include the undershoot filter T_{w_U, τ_U} in equation (4.8), another version of node `<outer-plexiform-layer/>` must be used:

```

<outer-plexiform-layer>
  <undershoot-version
    . . .

    undershoot-relative-weight="0.5"
    undershoot-tau__sec="0.2"
  />
</outer-plexiform-layer>

```

where the dots denote all the parameters already present in the `<linear-version/>` presented above. The existence of these two different versions for the OPL (‘linear’ and ‘undershoot’ –which is also linear!) mostly reflects the historical conception of the model. We kept both versions distinct because they can have different interests: The ‘linear’ version is simpler and can be sufficient for many large-scale simulations. The ‘undershoot’ version allows better reproduction of experimental curves (see Results in Chapter 4). Also, note that the ‘undershoot’ version allows potential users that need only a linear retina model (and thus, only the `<outer-plexiform-layer/>` node of the definition file) to include a linear temporal transient in their model.

Remark: Amplification parameter. The amplification parameter `opl-amplification` is designed for the output of the OPL stage to have *normalized* values, of order unity (the ‘typical’ range of output is [-1,1]). This is done in order to augment the modularity of the retina: It allows to easily remove the contrast gain control stage. See remark “Modularity and amplification parameters” in the description of node `<contrast-gain-control/>` (next section).

Also, note that `opl-amplification` is a *relative* term. It is always applied after a *first, automatic normalization* of input sequence $L(x, y, t)$ by its ‘typical’ range, given by attribute `input-luminosity-range` of node `<retina/>`. This automatic normalization may be removed in the future, if adaptation to light is explicitly modeled. ■

Remark: Leaky heat equation and gap junctions. We have seen in Chapter 2, Section 6 how the explicit modeling of gap junctions leads to a different expression for the low-pass filtering

occurring in a layer of cells (equation (2.21)). We kept a possibility to implement that type of filter.

If attribute `leaky-heat-equation` is set to 1 rather than 0, the *center* and *surround* signals in equations (4.8)-(4.9) are calculated following the alternative formula:

$$C(x, y, t) = T_{w_U, \tau_U} * K_{\sigma_C, \tau_C} * L(x, y, t), \quad (6.1)$$

$$S(x, y, t) = K_{\sigma_S, \tau_S} * C(x, y, t), \quad (6.2)$$

where T_{w_U, τ_U} remains the optional undershoot (according to the chosen version for the OPL), and filter

$$K_{\sigma, \tau}(x, y, t) = G_{\sigma} \sqrt{t/\tau} (x, y) \exp(-t/\tau)/\tau \quad (6.3)$$

is the typical ‘leaky heat equation’ filter resulting from electrical coupling through gap junctions. The relevance and interest of that type of filter have been rapidly discussed in Chapter 2, Section 6. It should be noted that this filter can be implemented in a particularly efficient way (Section 3.3), which provides another computational interest.

In the case where this alternative filtering scheme is chosen, all parameters of node `<outer-plexiform-layer/>` remain relevant, except for `center-n`, which becomes useless. ■

Remark: Nonlinear luminosity adaptation. Another alternative filtering for the OPL has been implemented that can provide invariance to luminance, on the same basis as the contrast gain control model presented in Chapter 4, Section 4 (through a dynamic adaptation conductance). This filtering scheme, termed `<luminance-gain-control-version/>`, remains very experimental and we do not present it here. Its attributes are described in the *Virtual Retina* tutorial. ■

`<contrast-gain-control/>`

This XML node defines parameters for the contrast gain control feedback mechanism, as presented in Chapter 4, Section 4. It writes:

```
<contrast-gain-control
  opl-amplification__Hz="150"
  bipolar-inert-leaks__Hz="5"
  adaptation-sigma__deg="0.5"
  adaptation-tau__sec="0.03"
  adaptation-feedback-amplification__Hz="100"/>
```

thus defining the parameters used in equations (4.11)-(4.13). All attributes have explicit names, except maybe for `bipolar-inert-leaks__Hz` which corresponds to parameter g_A^0 in (4.13).

Remark: Modularity and amplification parameters. According to the requirements of the user, the contrast gain control stage can easily be suppressed, simply by suppressing the `<contrast-gain-control/>` sub-element of element `<retina/>`. Indeed, the output of the OPL stage (preceding paragraph) and the output of this contrast gain control stage (V_{Bip} in (4.11)) both have dimensionless units, in the ‘typical’ range [-1,1]. So, the output of the OPL can directly be used, instead of V_{Bip} , as input to the next stage (ganglion cell, equation (4.14) of the model).

This explains the presence of parameter `opl-amplification_Hz` in the contrast gain control XML node, which has no correspondence in the model equations (4.11)-(4.13). This parameter insures the conversion from the dimensionless output of the OPL stage (preceding paragraph) to a current I_{OPL} in Hz, as used in (4.11). ■

`<ganglion-layer/>`

This XML node defines parameters for the third stage of the model: Ganglion cells (Chapter 4, Section 5). This includes both the additional signal transformation in (4.14), the spike generation parameters in (4.16), and the chosen ganglion cell sampling scheme (square or circular).

There can be as many ganglion layers as one desires, each with different filtering properties (X/Y, On/Off), all based on the same ‘bipolar’ signal: The output of the contrast gain control stage, or directly of the OPL stage if no contrast gain control scheme has been included.

In order to define different layers of ganglion cells, one just has to add different successive nodes `<ganglion-layer/>` of the same form in the retina file (as symbolized by the dots in the global architecture of the `<retina/>` node presented in Section 2.2.1).

The general structure for one `<ganglion-layer/>` node is the following:

```
<ganglion-layer
    sign="-1"
    transient-tau__sec="0.03"
    transient-relative-weight="0.75"
    bipolar-linear-threshold="0"
    value-at-linear-threshold__Hz="100"
    bipolar-amplification__Hz="300"
    sigma-pool__deg="0" >
    <spiking-channel>
        <circular-spiking-channel
            diameter__deg="10" fovea-density__inv-deg="1"
            g-leak__Hz="50" sigma-V="0.0" refr-mean__sec="0.003"
            refr-stdev__sec="0" random-init="1"/>
        </spiking-channel>
</ganglion-layer>
```

Additional filtering. The attributes of element `<ganglion-layer/>` deal with additional signal processing at the level of ganglion cells, corresponding to equations (4.14)-(4.15) of the model. Attribute `sign` corresponds to parameter ε in (4.14), set at 1 for ON cells and -1 for OFF cells. The two attributes `transient-tau__sec` and `transient-relative-weight` define the additional IPL transient T_{w_G, τ_G} in (4.14). Attribute `sigma-pool__deg` fixes the additional post-synaptic pooling σ_G in (4.14) which can be used to model Y cells.

In turn, parameters `bipolar-linear-threshold`, `value-at-linear-threshold_Hz` and `bipolar-amplification_Hz` fix the respective values of v_G^0 , i_G^0 and λ_G which define the shape of the transmission function N in (4.15).

Finally, sub-element `<spiking-channel/>` possibly defines a discrete array of spiking cells, with its own set of parameters. If this spiking element is present, the output of the retina is the set of emitted spike trains. If it is absent, the output of the retina is the continuous signal $I_{Gang}(x, y, t)$ in (4.14), which can be considered as an average firing rate since it is expressed in Hertz.

Two sampling schemes. As a first option, the spiking channel can be of subtype `<circular-spiking-channel/>` (as in the above example). This type of spiking channel is well suited when a foveated structure has been defined by introducing a `<radial-scheme/>` element. In that case, the sampling of ganglion cells is made along concentric circles, following the radial density $(d_0 s(r))^2$, where:

- $s(r)$ is the radial scaling function for the retina, defined by the sub-element `<radial-scheme/>` of element `<retina/>` (or by $s(r) = 1$, if there is no defined `<radial-scheme/>`).
- d_0 is the 1d density of cells in the fovea, defined by attribute `fovea-density_inv-deg`.

Finally, the total radius of the channel of ganglion cells is defined by attribute `diameter_deg`.

A second option is to use a square, uniform array of spiking cells, defined by the node:

```
<spiking-channel>
  <square-spiking-channel
    size-x_deg="10" size-y_deg="7.5" uniform-density_inv-deg="10"
    g-leak_Hz="50" sigma-V="0" refr-mean_sec="0.003"
    refr-stdev_sec="0" random-init="1" />
</spiking-channel>
```

In this case, three parameters `size-x_deg`, `size-y_deg` and `uniform-density_inv-deg` define respectively the size and the 1d density of cells in the array. Note that this sampling scheme cannot follow a foveated density, although it is still possible to define a `<radial-scheme/>` node for the retina: In this case, all spatial filtering scales will follow a foveated scheme with more precision in the center, but the subsequent sampling by ganglion cells will be square and uniform.

Spiking procedure. Both the `<circular-spiking-channel/>` and `<square-spiking-channel/>` have the same parameters for the spiking procedure of the ganglion cells, as defined by (4.16):

- Parameter `g-leak_Hz` fixes g^L in (4.16).
- Parameters `sigma-V`, `refr-mean_sec` and `refr-stdev_sec` fix the strengths of the two possible sources of noise in the spike generation (Section 5.2): Correlated Gaussian noise of standard deviation σ_V , and noisy refractory period following $\mathcal{N}(\text{refr-mean}, \text{refr-stdev})$.

2.2.3 Microsaccade generation

Aside from the node `<retina/>`, which describes the properties of retinal filtering, another node can be added in the definition file. This additional node allows a simple reproduction of fixation microsaccades, applied to the input image before it is passed to retinal treatment:

```
<retina-description-file>

  <basic-microsaccade-generator
    pixels-per-degree="10.0"
    temporal-step__sec ="0.005"

    angular-noise__pi-radians="0.3"
    period-mean__sec="1"
    period-stdev__sec="0.3"
    amplitude-mean__deg="0.3"
    amplitude-stdev__deg="0.1"
    saccade-duration-mean__sec="0.03"
    saccade-duration-stdev__sec="0.01"/>

  <retina. . ./>

</retina-description-file>
```

It implements straight microsaccades around the fixation point, with random amplitude, duration, and inter-saccadic interval (`period`). This object also expresses temporal scales in seconds and spatial scales in retinal degrees, with two conversion factors `pixels-per-degree` and `temporal-step__sec`. Make sure they are the same as for your retina! The whole retina itself must be described in node `<retina. . ./>`.

2.3 Installing *Virtual Retina*

To conclude this practical presentation, let us add a few words about the installation of the package. More details can be found in the *Virtual Retina* tutorial.

Virtual Retina compiles under Linux with `gcc`, version 3.4 or more. It has not been tested under Windows. The software requires several external C++ libraries:

- **CImg**², an image processing toolbox.
- **MvaSpike**³, an event-driven spike simulator.
- **libXML++**⁴, a C++ wrapper for *libXML2*, the GNU C interface to deal with XML files.
- **xmlParameters++**, a helper library I wrote to load/save parameters from an XML file in a flexible way.

²Author: David Tschumperlé, <http://cimg.sourceforge.net/>

³Author: Olivier Rochel, <http://www-sop.inria.fr/odyssee/software/mvaspike/>

⁴Authors: A. Johnson, C. de Vienne and M. Cumming, <http://libxmlplusplus.sourceforge.net/>

Amongst these libraries, *xmlParameters++* is also included in the downloadable archive. The two libraries I wrote, *VirtualRetina* and *xmlParameters++*, are compiled and installed thanks to **CMake**, a multi-platform Make tool. The other libraries must be downloaded and installed by the user with the traditional `configure/make install` commands.

Alternatively to manual installation, a shell code `download_build_all.sh` is included in the archive, which proceeds to automatic download and installation of all required libraries, and should greatly minimize installation efforts.

Finally, it is possible to save the emitted spikes in a special binary format called `hdf5`. The *hdf5* library, due to its size, is not required by the default installation procedure. Users interested by this facility must manually install `hdf5`, compile the wrapper library `mvaspike_hdf5`⁵ included in the package, and use a special compilation option to compile *Virtual Retina*. This procedure is described in more details in the tutorial.

3 IMPLEMENTATION DETAILS

Let us now enter the details of implementation. The goal of this section is to present the main classes that we have implemented, their principles, and how they relate to the XML definition file presented in Section 2.2. We chose an object-oriented language, C++, which allows the modularity required from the software: Independent objects are in charge of the different aspects of filtering, and can easily be assembled to produce various retinal architectures.

This lengthy section is quite important, as it introduces various classes which can be used, not only in the particular case of our model, but also as generic building blocks for other models of retina. In this spirit, we made *Virtual Retina* a fully open-source software.

Figure 6.1 presents an overview of the objects in *Virtual Retina*. Each different box in the figure indicates a functional unity of objects, and the associated number corresponds to the order in which the code is presented in this section.

We first introduce auxiliary objects, which allow us to handle synaptic inputs (Section 3.1), and the possible foveated structure of a whole retina (Section 3.2). We then present the two ‘basic’ types of signal processing objects used by *Virtual Retina*: Objects in charge of ‘continuous’ filtering (corresponding to spatio-temporal ODEs and convolutions in our model) are presented in Section 3.3. Objects in charge of spike emission are presented in Section 3.4. In Section 3.5, we present the principles of use of library *xmlParameters++*. In Section 3.6, we present how all these elements can be assembled to build retinal models of various complexities.

Amongst the various classes and tools presented here, some are particularly generic and prone to be reused and/or extended, so we mention them especially:

- The ‘BaseRecFilter’ object (Section 3.3.1) can handle recursive temporal filtering, including an easy implementation of convolution, sums, and other operations on recursive filters.

⁵Author: Olivier Rochel

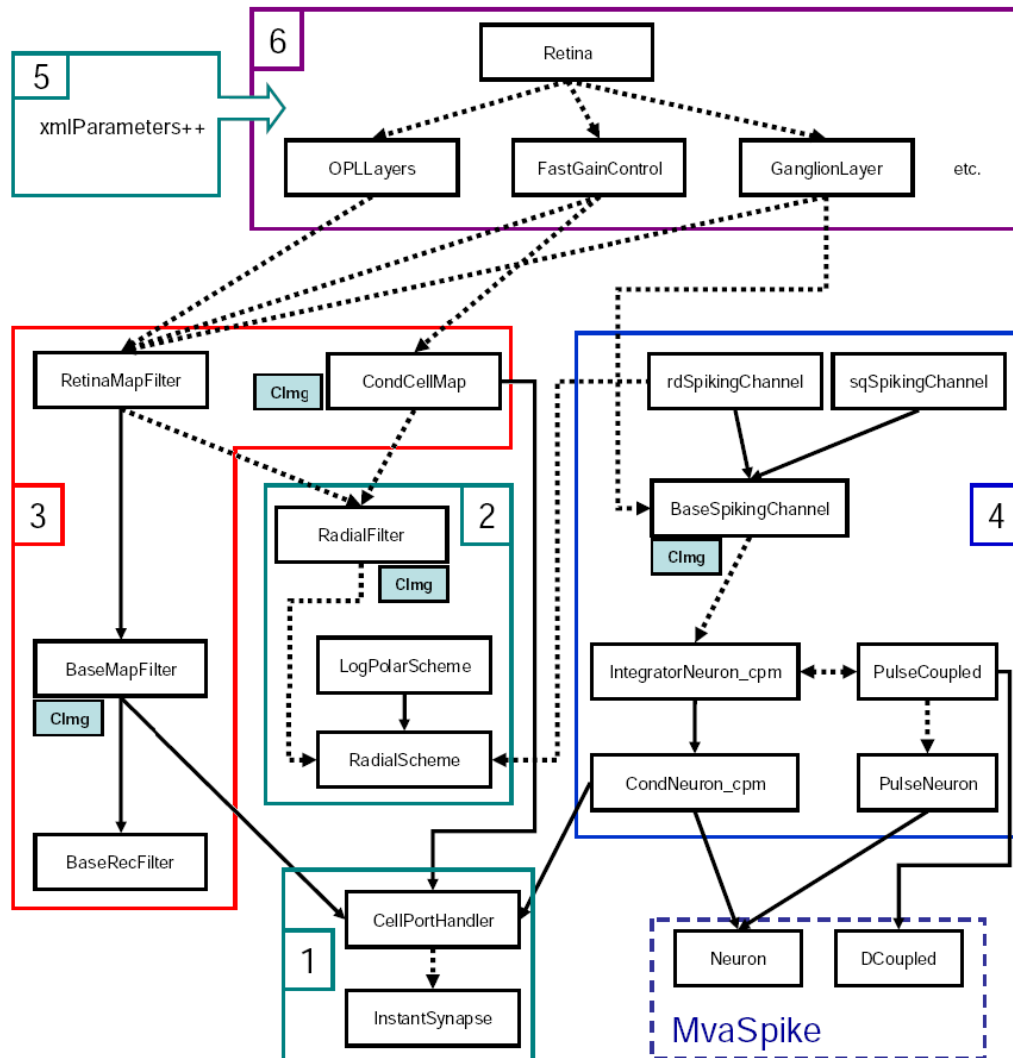


Figure 6.1: *Organization of the main objects in Virtual Retina.* Plain arrows indicate an inheritance relation. Dashed arrows represent a functional dependence: Single dashed arrows generally indicate the use of an object as a subfield, while double arrows indicate a cooperative functioning. Each box denotes a functional unity for a group of objects, and the associated number refers to the section where these objects are described. Our ‘spiking’ units (box 4) build up on the *MvaSpike* library. The *CImg* library is used whenever the object needs to handle 2d images.

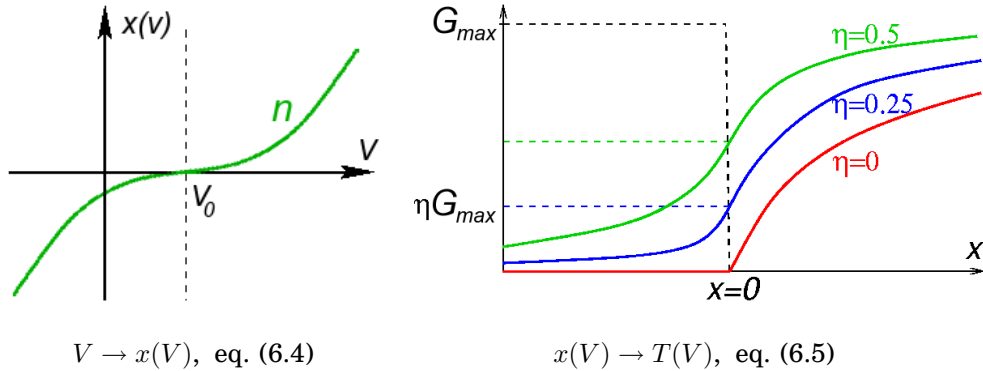


Figure 6.2: General form of the transmission implemented by the InstantSynapse (see text).

- The ‘CondCellMap’ object (Section 3.3.4) can implement any temporal ‘linear ODE’ (Chapter 2, Section 7), directly at the level of 2D spatial maps.
- The ‘RadialFilter’ object (Section 3.2.2) is a tool to implement radially-variant recursive spatial filters (e.g., as resulting from a foveated organization), following a fast, approximate algorithm.
- The ‘xmlParameters++’ template library (Section 3.5) allows serialization to XML of an object’s parameters and structure, including advanced operations such as pointer or vector initializations and polymorphism.

3.1 Synaptic inputs and connections

3.1.1 InstantSynapse: Model of synaptic transmission

We implemented the InstantSynapse object to handle the linear and nonlinear static functions used to model synaptic transmissions. The transmission $V \rightarrow T(V)$ implemented by the InstantSynapse relies on 5 parameters $(v_0, \lambda, n, G_{\max}, \eta)$, with the following general expression:

$$x(V) = \frac{\lambda}{G_{\max}} \text{sign}(V - v_0)(V - v_0)^n \quad (6.4)$$

$$T(V) = \begin{cases} G_{\max} \left(\eta + \frac{(1-\eta)x(V)}{1-\eta+x(V)} \right) & \text{if } x(V) > 0, \\ G_{\max} \frac{\eta^2}{\eta - x(V)} & \text{if } x(V) < 0. \end{cases} \quad (6.5)$$

Equation (6.4) calculates an ‘intermediate’ signal $x(V)$ (Figure 6.2, left). In turn, $x(V)$ defines the output value $T(V)$ after being passed through a sigmoid-like rectification function $T(x)$ ((6.5) and Figure 6.2, right), with two different regimes: Smooth rectification for $x < 0$, linear and/or compression for $x > 0$. Note that $T(x)$ is always positive, and that $T(x)$ is quasi-linear for $x \ll 1$.

The five parameters of the model are the following:

- v_0 defines the threshold between two different regimes: The ‘smooth rectification’ regime for $V < v_0$ (implying $x(V) < 0$), and the linear and/or compression

regime for $V > v_0$.

- λ is a linear amplification gain.
- n is an additional parameter that can be used to define convex shapes (typically, quadratic). It is also a way to introduce Hill coefficients in signal transmissions (see the Van Hateren and Lamb model for phototransduction, Chapter 3, Section 1.1.2).
- $G_{\max} > 0$ defines the maximum output value. The regime $x(V) > 0$ in (6.5) behaves as a smooth compression, or quasi-linearly if $G_{\max} \rightarrow +\infty$.
- $\eta \in [0, 1]$ defines the output value at threshold through $T(v_0) = G_{\max}\eta$. In the quasi-linear case where $G_{\max} \rightarrow +\infty$, η must tend to zero so that $T(v_0)$ remains bounded.

Here is a simplified header of the InstantSynapse object, where only most relevant fields are kept:

```

class InstantSynapse
{
public:

(1) Different ways to apply the transmission function
    double transmission(double inputValue);
    void apply(CImg<double>& input);
    CImg<double> transmission(const CImg<double>& input);
    void addTransmission(const CImg<double>& input, CImg<double>& output);

(2) Different pre-coded initializations of the parameters
    InstantSynapse& rectification(double v, double lam=1.0, double val_v=0.0); 10
    InstantSynapse& linearAmplification( double lam );

(3) Custom initialization of the parameters
    InstantSynapse& set_v0(double val);
    InstantSynapse& set_lambda(double val);
    InstantSynapse& set_power_exp(double val);
    InstantSynapse& set_Gmax(double val);
    InstantSynapse& set_eta(double val);
};

```

Point (1) shows that a synaptic transmission can be applied, either on single numbers, either on whole 2d images (retinal maps), stored in an image-handling type from library *CImg*.

Point (2) is an example of pre-coded initialization functions. Function `rectification(...)` implements the simplified case of (6.4)-(6.5) when $n = 1$, $G_{\max} \rightarrow +\infty$ and $G_{\max}\eta = \text{val}_v$ remains constant: The resulting function is similar to $N(V)$ in our model (equation (4.15)).

Note that, as implemented by (6.4)-(6.5), the output $T(V)$ is always positive. Function `linearAmplification(double lam)` allows an alternative usage of the `InstantSynapse` as a simple linear amplification: $T(V) = \lambda V$. In this case, all parameters other than λ become useless, and $T(V)$ can possibly take negative values.

The functions in point (3) allow to directly modify the parameters of the transmission. In this object and throughout the retina, most parameters are stored as

protected, and only accessible through **public** initialization functions of the form `set_xxx(...)`.

Future work

The `InstantSynapse` object tries to encompass different shapes of retinal transmission in a single object, and thus uses a single formula (6.4)-(6.5) which is often over-complicated, and yet limited (exponential transmissions, such as sigmoids, are impossible). The `InstantSynapse` should be modified to become a virtual base class, with different possible specializations implementing different synaptic transmissions (`LinearSynapse`, `QuadraticSynapse`, etc.).

3.1.2 CellPortHandler: Synaptic inputs to a cell

The `CellPortHandler` object is implemented to encompass the different types of synaptic inputs that can be received by a retinal neuron. Several other implemented objects presented in the sequel (modeling a layer of cells, a spiking neuron, etc.) inherit from a `CellPortHandler`. Here is a simplified header, where only most relevant fields are kept:

```

class CellPortHandler
{
protected:
    vector<InstantSynapse*> inputSynapses;
    vector<double*> inputNernst;
    int lastPort;

public:
    int new_currentInput( InstantSynapse *syn=0 ) ;
    int new_ionicChannel( double valNernst, InstantSynapse *syn=0 ) ;
    InstantSynapse& inputSynapse(int port=0) ;
};

```

This small interface allows to register a number of synaptic inputs, either currents or conductances, each associated to a different input synapse. Both vectors `inputNernst` and `inputSynapses` are of size `lastPort+1`, `lastPort` being the index of the last synaptic input created. Synaptic ports are created with either functions `new_currentInput(...)` or `new_ionicChannel(...)`, which return the index for the newly created port.

The synapse associated to a port can either be an already created `InstantSynapse`, whose address is then specified by the `new_xxx(...)` function, or be created at the call of the function (if no `InstantSynapse` address is specified), and initialized as ‘transparent’ (with a linear amplification of 1).

The distinction between current and conductance currents is made thanks to the vector<**double***> `inputNernst`. Consider port number i , with $i \leq \text{lastPort}$:

- If `inputNernst(i)=0` (not initialized), port i is a current.
- If `inputNernst(i)` is initialized, port i is a conductance, associated to Nernst potential $\ast(\text{inputNernst}(i))$.

In the default constructor, a CellPortHandler is associated to a single, current port, with a ‘transparent’ inputSynapse.

3.2 Implementing a foveated structure

Another family of auxiliary objects is dedicated to handling the possible non-homogeneous scaling scheme of the whole retina (function $s(r)$ in (4.17)). The scaling function itself is implemented in a RadialScheme object, designed as a singleton. Then, RadialFilter objects implements recursive spatial filters that can follow the scaling function $s(r)$.

3.2.1 RadialScheme and LogPolarScheme: defining the retinal scaling function

The RadialScheme interface

The class RadialScheme is intended to serve as a base class, to define any desired radial scaling function $s(r)$ through derived objects. Here is a simplified header for the class:

```
class RadialScheme
{
public:
    static RadialScheme * instance();
    static void dontUse();

    virtual double density(double r);
    virtual double integratedDensity(double r);
    virtual double findRadius(double integrated_density);
};
```

Any specialization of RadialScheme must override the three virtual functions density(...), integratedDensity(...) and findRadius(...), which define respectively the three functions $s(r)$, $I(r) = \int_0^r s(u)du$, and $I^{-1}(x)$.

Our model retina has a single scaling function, so it needs a single RadialScheme object. This is likely to often be the case in future usages of this object. As a result, the class possesses a static function RadialScheme::instance(), designed to give access to a ‘privileged’ RadialScheme object. It returns whether NULL (if no RadialScheme was defined), or the address of a the ‘privileged’ RadialScheme (by default, the only existing one!). Function RadialScheme::dontUse() (which we never use!) is designed to ‘free’ the RadialScheme instance.

This small trick simplifies the use of other objects (RadialFilter and rdSpikingChannel). that need to know which radial scheme they should follow.

LogPolarScheme: Log-polar scaling function

This object is our (only) specialization of a RadialScheme, which overrides functions density(...) following the log-polar scaling used in our model:

$$s(r) = \begin{cases} 1 & \text{if } r < R_0, \\ 1/(1 + K(r - R_0)) & \text{if } r > R_0. \end{cases}$$

The respective formulas for $I(r) = \int_0^r s(u)du$, and $I^{-1}(x)$ are straightforward, and implemented respectively in `integratedDensity(...)` and `findRadius(...)`.

3.2.2 RadialFilter: spatially-variant recursive filtering

If a `RadialScheme` has been defined in the program, it influences the spatial filtering properties of the ‘continuous’ maps: In our model, when a retinal map $Y(x, y)$ performs a Gaussian pooling on its input $X(x, y)$, the standard deviation of the pooling at each location is as defined $\sigma(r) = \sigma_0/s(r)$, depending on the eccentricity r from the center of the retina:

$$Y(x, y) = \iint G_{\sigma(r)}(u, v)X(x - u, y - u) du dv, \quad (6.6)$$

with $r = \sqrt{(x - x_0)^2 + (y - y_0)^2}$. This filter, although linear, is not a convolution anymore, since filter $G_{\sigma(r)}$ is not spatially uniform.

A real Gaussian convolution is well approximated by recursive Deriche filters, which allow a very fast implementation, with a well-defined mathematical framework (see Deriche 87 [51], and Section 3.3 for an introduction to recursive filtering).

By opposition, there is no mathematically well-defined recursive scheme to perform the linear transformation (6.6). It can only be applied as a straightforward convolution, calculated point by point. This is problematic, because a straightforward calculation is very long, especially when the standard deviation $\sigma(r)$ becomes large, at high eccentricities.

We thus decided to implement an alternative algorithm, as proposed by Tan *et al.* 03 [165], which uses a recursive scheme inspired by Deriche filters. In a Deriche filter, a set of recursive coefficients (a_1, a_2, b_0) is calculated to implement the convolution by G_σ . Here instead, a set of coefficients $(a_1(x, y), a_2(x, y), b_0(x, y))$ is calculated *at each pixel*, corresponding to the Deriche coefficients for filter $G_{\sigma(r)}$. Then, when the recursive loop is made along lines and columns of the image, the used recursive coefficients change at each pixel.

Such a scheme is still linear, and can still be written

$$Y(x, y) = \iint F_{x,y}(u, v)X(x - u, y - u) du dv,$$

but there is no mathematical expression for $F_{x,y}(u, v)$ anymore, nor any guarantee that it approximates well the Gaussian filter $G_{\sigma(r)}(u, v)$. However, experiments reveal that the approximation remains good, as long as the spatial variation of $s(r)$ is slow as compared to the extent defined by $\sigma(r)$, as is indeed the case in the retina (the receptive fields are small enough for the filtering scheme to be considered uniform on small patches of retina).

Practically, the gain of computational speed largely compensates the small mathematical incertitude. Also, note that this filter amounts to a classical Deriche filter if one chooses a uniform scaling function $s(r) = 1$ for the retina.

Here is a simplified header for the RadialFilter object:

```

class RadialFilter
{
protected:
    void allocateValues();

public:
    RadialFilter& set_sizeX(int x);
    RadialFilter& set_sizeY(int y);
    RadialFilter& set_sigma0(double sigma);

    void radiallyVariantBlur(CImg<double>& image);
    CImg<double> get_radiallyVariantBlur(const CImg<double>& image); 10
};

```

The object is initialized by setting parameter σ_0 , but also the size of the images to which the filter will apply. By opposition, the radial scheme is not passed to the filter, but automatically detected according to the (unique) `RadialScheme::instance()`⁶.

The effective filtering functions, `radiallyVariantBlur(...)` and `get_radiallyVariantBlur(...)`, are directly adapted from function `deriche(...)` in the `CImg` library. All recursive coefficients ($a_1(x, y)$, $a_2(x, y)$, $b_0(x, y)$) for the filter are automatically allocated at the first call to a filtering function, with a call to protected function `allocateValues()`. Once this is done, the `RadialFilter` cannot be re-initialized to a different set of parameters.

Remark: Other recursive filters. The generic algorithm of Tan *et al.* 03 [165] applies to virtually any spatial recursive filter. For example, first and second derivatives of a Gaussian are also implementable in the same framework, providing a good approximation of Gabor filters. ■

3.3 Continuous filtering

Our retina model (Chapter 4) relies on successive spatio-temporal filtering stages, both linear (exponential temporal filters, Gaussian spatial filters) and nonlinear (the contrast gain control scheme).

To handle linear filtering, we designed a succession of inheriting objects: `BaseRecFilter`, `BaseMapFilter` and `RetinaMapFilter`, this last object being a ‘generic’ model for a retinal layer performing spatio-temporal linear filtering on its inputs. To handle the nonlinear conductance-driven scheme used in our gain control mechanism, we designed the `CondCellMap` object, which models a layer of retinal cells integrating synaptic conductances and/or current inputs. In both linear and conductance-driven objects, the possible influence of linear coupling through gap junctions is taken into account, through a very simple computational scheme.

3.3.1 BaseRecFilter: Recursive temporal filtering

Recursive filtering

Recursive filtering is a computationally efficient way to model many types of linear filters. It allows the conversion of an input signal $\{X(k)\}_{k \in \mathbb{N}}$ to an output signal

⁶This architecture based on a singleton `RadialScheme` is well-suited for our programs, but could easily be modified to a more classical system, where each `RadialFilter` has a pointer to its own `RadialScheme`.

$\{Y(k)\}_{k \in \mathbb{N}}$ through the generic calculation:

$$Y(k) = \sum_{j=0}^{M-1} b_j X(k-j) - \sum_{i=1}^N a_i Y(k-i). \quad (6.7)$$

The particularity of this type of filter is that its preceding output values, the $Y(k-i)$, are used in the calculation of the new output value at each time step, hence the name ‘recursive’. N is termed the *order* of the recursive filter. The case $N = 0$ corresponds to a classical, non-recursive, finite impulse response (FIR) filter. By opposition, when $N \geq 1$, the resulting filter has an infinite impulse response (IIR).

The number of operations per time step, and thus the rapidity of the filter, is roughly proportional to $M + N$. This is precisely the interest of recursive filters, which allow to implement IIR filters very rapidly. By opposition, approximating an IIR filter through a classical FIR filter generally requires a very large M , and thus much slower calculations.

We note A and B the respective polynomes $A(Z) = 1 + \sum_{i=1}^N a_i Z^i$ and $B(Z) = \sum_{j=0}^{M-1} b_j Z^j$. In terms of Laplace transform, one gets the relation:

$$Y(Z) = \frac{\sum_{j=0}^{M-1} b_j Z^j}{1 + \sum_{i=1}^N a_i Z^i} X(Z) = \frac{B(Z)}{A(Z)} X(Z). \quad (6.8)$$

The Laplace transform of the filter is non-polynomial whenever $N \geq 1$, implying an infinite impulse response. Also, the filter is stable if all roots of the denominator polynome are smaller than one in norm. This condition often sets a limitation on recursive filters in practice, causing the filter to become instable for large values of N , as one of the roots becomes larger than one: This reflects the intuitive notion that a filter which calculates its new value from a large number of its own past values can easily amplify numerical errors.

The BaseRecFilter object

Temporal recursive filtering, following (6.7), can apply to a simple numerical signal ($X(k)$ and $Y(k)$ being real numbers of type **float** or **double**), to complex numbers, or even to whole images - the case we are really interested in. We thus implemented a generic object, the BaseRecFilter, which allows to handle and initialize the recursive polynomes $A(Z)$ and $B(Z)$, but without performing any actual filtering. Here is a simplified header of the BaseRecFilter object:

```

class BaseRecFilter
{

protected:
    int M, N;
    double* a, b;
    double step;

public:
    BaseRecFilter& Exp(double tau);
    BaseRecFilter& ExpCascade(double tau,int n);
    BaseRecFilter& Cascade(const BaseRecFilter &second);

```

```

friend BaseRecFilter operator+(const BaseRecFilter &first, const BaseRecFilter &second);
BaseRecFilter& operator+=(const BaseRecFilter &secondFilt);
friend BaseRecFilter operator*(double lambda, const BaseRecFilter &filt);
:
:
virtual void feedInput(void){}
virtual void tempStep(void){}
};

```

The recursive coefficients $A(Z)$ and $B(Z)$ are stored in two arrays `a` and `b` of respective sizes `M` and `N+1`. `step` is the temporal length associated to one discretization step, which allows to make a conversion to some underlying ‘continuous’ time. This value will be shared by all retinal objects in charge of ‘continuous’ filtering, and fixed by the XML attribute `temporal-step_sec` of node `<retina/>` (see Section 2.2). It defines the precision of filtering in the tested retina, but not the precision of the *spiking* procedure, which is event-driven (see Section 3.4).

The default constructor (not shown) initializes the coefficients at $A(Z) = 1$ and $B(Z) = 1$, corresponding to a ‘transparent’ filtering.

Hard-coded initialization functions

```

BaseRecFilter& Exp(double tau);
BaseRecFilter& ExpCascade(double tau,int n);

```

These two functions define the values of $A(Z)$ and $B(Z)$ in the respective cases of an exponential filter ($E_\tau(t)$ in (4.4)) and a Gamma filter ($E_{n,\tau}(t)$ in (4.5)). We only implemented these two ‘basic’ filters because, coupled with band-pass differences, they define all temporal filtering required by our model (Chapter 4). Naturally, other hard-coded initialization functions could be defined by the user if required.

Coefficients for the exponential filter are taken as

$$B(Z) = 1 - \exp(-\text{step}/\tau) \quad \text{and} \quad A(Z) = 1 - Z \exp(-\text{step}/\tau),$$

corresponding to the exact solution of a continuous ‘RC’ circuit when the input is constant by parts over the time steps. Coefficients for the Gamma filter are directly calculated from the cascade of n exponential filters, using the `Cascade()` operator described in the sequel.

Customizable initialization functions

In order to build more complicated temporal filters (such as band-pass differences) from simple filtering bricks (exponential filters), we also implemented generic composition functions between filters, defining a sort of ‘arithmetic’ over the space of our `BaseRecFilters`.

The `Cascade()` operator. This function allows to transform a filter $X(k) \rightarrow Y(k)$, of coefficients $A_1(Z)$ and $B_1(Z)$, into a new filter $X(k) \rightarrow Z(k)$, by composition with a second filter $Y(k) \rightarrow Z(k)$ of coefficients $A_2(Z)$ and $B_2(Z)$. The composition rule is

very simple, as can be calculated from the Laplace transform expression (6.8):

$$\begin{aligned} A_1(Z)A_2(Z) &\rightarrow A_1(Z) \\ B_1(Z)B_2(Z) &\rightarrow B_1(Z). \end{aligned}$$

At the level of coefficient vectors \mathbf{a} and \mathbf{b} , this transformation amounts to a convolution.

The `Cascade()` function is useful, since it allows to create complex filters $X(k) \rightarrow Y_1(k) \rightarrow \dots \rightarrow Y_{n-1}(k) \rightarrow Z(k)$ (such as Gamma functions resulting from the composition of exponential filters) in a single `BaseRecFilter` object, without needing any explicit formulas.

From a computational standpoint, the `Cascade()` operator is always optimal: The single cascaded filter $X(k) \rightarrow Z(k)$ results in the same number of operations as would be obtained if several `BaseRecFilter` objects $Y_i(k) \rightarrow Y_{i+1}(k)$ were explicitly serialized. Furthermore, using a single cascaded filter allows to copy each intermediate signal $Y_i(k)$ only once in memory, which provides a sensible gain of time when the signals $Y_i(k)$ consist of large 2d images.

Arithmetic operators (+, -, *, /). We also implemented arithmetic operators on the `BaseRecFilters`. The *multiplicative* operators are simply between a filter and a scalar, creating filter $X(k) \rightarrow \lambda Y(k)$ from filter $X(k) \rightarrow Y(k)$.

The *additive* operators, directly between two filters, allow to create the coefficients for filter $X(k) \rightarrow Y(k) = Y_1(k) + Y_2(k)$, starting from the two filters $X(k) \rightarrow Y_1(k)$ and $X(k) \rightarrow Y_2(k)$. In this case, the implemented rule, derived from (6.8), is the following:

$$\begin{aligned} A_1(Z)A_2(Z) &\rightarrow A(Z) \\ A_1(Z)B_2(Z) + A_2(Z)B_1(Z) &\rightarrow B(Z). \end{aligned}$$

This operator is interesting because it limits the number of `BaseRecFilter` that need to be created in a program. Furthermore, it can often lead to a reduction in the total number of required operations. However, the use of the additive operator may also often be problematic. We present these issues in the next paragraph.

Limitations of the additive operators. Unlike the `Cascade()` and multiplicative operators, the additive operator is not always optimal, because the resulting ‘summed’ `BaseRecFilter` does not compare trivially to the case where two filters $X(k) \rightarrow Y_1(k)$ and $X(k) \rightarrow Y_2(k)$ are kept separated, and their two outputs summed externally afterward. Indeed, the recursive coefficients $A(Z)$ and $B(Z)$ of the ‘summed’ `BaseRecFilter` have orders $M = \max(N_1 + M_2, N_2 + M_1)$ and $N = N_1 + N_2$.

From a computational standpoint (number of required operations), it is interesting to use the ‘summed’ `BaseRecFilter` rather than two separated filters if $N + M \leq N_1 + M_1 + N_2 + M_2$. This is the case only if the two separated filters both verify $N_1 \leq M_1$ and $N_2 \leq M_2$.

More importantly, from a numerical standpoint, the ‘summed’ filter always has a higher (or equal) recursive order N than any of the two individual filters, and this can easily raise severe issues of convergence, and exactitude of the resulting filtering.

For these two reasons (computational and numerical), ‘summed’ filters can be used, but with care. In particular, when compositions (symbolized by sign $*$) and sums are mixed to build complex filters, the factorized implementation $(F_1 + F_2) * G$ should always be preferred to $F_1 * G + F_2 * G$. This is illustrated through the following example of use.

An example of use: The Adelson-Bergen filter. The Adelson-Bergen filter (Adelson and Bergen 85 [1]) was proposed as a good estimator for the temporal responses of V1 cells. In our terminology, it is a DOE filter (Chapter 2, Section 3) that depends on a unique parameter τ , through the formula:

$$AB(t) = E_{5,5\tau}(t) - w E_{7,7\tau}(t). \quad (6.9)$$

Let us present three possible implementations using BaseRecFilters, which lead to different computational speeds.

1. The separated implementation makes no use of additive operators. It simply initializes two exponential cascades:

```
BaseRecFilter fast(step), slow(step);
fast.ExpCascade(5*tau,5);
slow.ExpCascade(7*tau,7);
```

The difference of the two filters being made externally when running the simulation. For exponential cascade of order n , one has $M=1$ and $N=n$. So in this scheme, the total number of operations will be $1+5+1+7=14$ (plus the external summation).

2. The *factorial* implementation, using additive operators, is the optimal solution:

```
BaseRecFilter AB(step), trs(step);
trs.ExpCascade(2*tau,2);
AB -= w*trs;
AB.ExpCascade(5*tau,5);
```

Note that this initialization is based on the factorial expression

$$AB(t) = (\delta_0(t) - w E_{2,2\tau}(t)) * E_{5,5\tau}(t).$$

Using the results above, one easily finds that in this case, the final recursive coefficients for BaseRecFilter AB are $M=3$ and $N=7$. The total number of operations is thus $3+7=10$, markedly optimized as compared to the separated implementation.

3. By opposition, the *developed* implementation, using additive operators, is utterly non-optimal:

```
BaseRecFilter AB(step), trs(step);
AB.ExpCascade(5*tau,5);
trs.ExpCascade(7*tau,7);
AB -= w*trs;
```

In this case, the recursive orders of the ‘summed’ filter are $M=8$ and $N=12$, implying a computational loss ($8+12=20$) and above all a very *unstable* filter ($N=12$). The problem here is well expressed in terms of Laplace transform: $A(Z)$ and $B(Z)$ share common root of order 5, so that their ratio (6.8) is not a reduced fraction.

Additive operators are thus an interesting feature, but to be handled with care. ■

Derived objects are in charge of the actual filtering

```
virtual void feedInput(void){}
virtual void tempStep(void){}
```

These two last lines are not necessary to the object's function, but illustrate the principle of use of the BaseRecFilter: It does not perform any linear filtering by itself. This task is left to its derived types, through implementation of the two virtual functions `feedInput(<input-type>)` and `tempStep()`.

Function `feedInput(<input-type>)` will allow to pass a new input $X(k)$, of whatever type is handled by the particular derived object. Then, function `tempStep()` will implement the calculation (6.7) for the new time step.

Future work: Strengthen the link with continuous ODEs

Because it involves the output values $Y(k - i)$ at preceding time steps, recursive filtering can be seen as the 'discretized' version of a linear ODE. More precisely, when a continuous linear ODE of the form

$$\sum_{i=0}^n c_i y^{(i)}(t) = x(t), \quad (6.10)$$

is solved by using a fixed discretization step ($X(k) = x(k\Delta t)$, $Y(k) = y(k\Delta t)$) and a numerical scheme which respects the linearity from $X(k)$ to $Y(k)$, the discretized problem can be expressed as a linear recursive filtering relation (possibly with the apparition of a time delay $X(k + D)$ if the numerical scheme looks in the 'future' of $x(t)$ to determine the present values of $y(t)$).

For the moment, we directly consider our input and output signals as being discrete, without making an explicit link to some underlying continuous signal. However, because real retinal time is continuous, the link to continuous filtering should be thought of more thoroughly. Very likely, our present 'discretized' approach has links with first-order Euler methods, but we have no mathematical certitude of this fact for the moment.

Exploring the relation between 'discrete' and 'continuous' filtering may also help us to implement more complex numerical schemes in the BaseRecFilter: Typically, a fourth-order Runge-Kutta method, associated to a linear interpolation of $X(k)$ between time steps. Because it remains linear, such a numerical scheme would still amounts to discrete recursive filtering, but with more complex coefficients $A(Z)$ and $B(Z)$.

3.3.2 BaseMapFilter: Spatio-temporal filtering

For the retina programs, we must perform temporal filtering on signals $X(k)$ consisting of 2d images. We thus specialize the BaseRecFilter into a BaseMapFilter. Here is a simplified header for this new object:

```
class BaseMapFilter: public BaseRecFilter, public CImgReader, public CellPortHandler
{
protected:
    int sizeX, sizeY;
    CImg<double>** last_inputs, last_values;
```

```

public:
    virtual void feedInput(const CImg<double>& new_input, int port=0);
    virtual void tempStep(void);

    virtual void allocateValues(void);
    virtual void spatialFiltering(CImg<double>* image){}
};

```

10

Unlike the BaseRecFilter, this object *can* filter actual inputs, consisting of 2d images stored as CImg<**double**> objects. It must store $N + M$ images in memory, corresponding to the last M inputs $X(k)$ and N outputs $Y(k)$ which have passed through the filter. These are stored respectively in two arrays CImg<**double**>* last_inputs(M) and CImg<**double**>* last_values(N+1), where each *(last_xxx(i)) is a CImg<**double**> image of size (sizeX, sizeY). We use pointers on the images, to allow a simple rotation of pointers after each time step, rather than a full circular copy of the stored images (see the sequel).

The memory required to store the images is allocated by function allocateValues(), which must be called once the filtering properties ($A(Z)$, $B(Z)$ and image sizes) have been set, and before the filter is actually used.

Use of the BaseMapFilter

Once it has been allocated, the filter is ready for use thanks to the ‘driving’ functions feedInput(...) and tempStep(). The feedInput(...) function, which must be called once or more at each time step, linearly adds contributions to the new input image $X(k)$ (which is re-initialized at zero after a new time step). The contributions can come from different ports, with different intrinsic linear amplification factors, as inherited from the CellPortHandler interface (only through *current* ports, which are linear - see Section 3.1).

Then, exactly once per time step, the new input $X(k)$ is integrated by function tempStep(), to produce the new output $Y(k)$ following (6.7). Afterward, the output image of the filter is easily accessible through function read() (as inherited from the CImgReader object, a simple read-only interface to access protected CImg fields).

In the end, the typical usage of a BaseMapFilter is the following:

```

BaseMapFilter bm ;

(1) Initialization of the filter's characteristics
bm.ExpCascade(4,0.05)
:
bm.allocateValues();

(2) Using the filter
for ( int t=0; t<end_time ; t++){
    bm.feedInput( new_input_image(s) ) ;
    bm.tempStep() ;
    bm.read().do_something_with_the_output() ;
}

```

Implementation

At each new time step, the values fed with `feedInput()` are stored in the image `*(last_inputs(0))`⁷. These values are integrated only at the call to function `tempStep()`, whose global organization is the following:

```

void BaseMapFilter::tempStep(void)
{
(1) Automatic allocation at first call
    if(!done)
        allocateValues();

(2) Possible spatial filtering on the input image
    this->spatialFiltering(last_inputs(0));

(3) Rotation on addresses of the last_values, to kick out the oldest map
    CImg<double>* fakepoint=last_values(N) ;
    for( int i=1 ; i<N+1 ; ++i)
        last_values(N+1-i) = last_values(N-i);
    last_values(0)=fakepoint;
(4) Calculate the new output Y(k), based on equation (6.7)
    *(last_values(0)) = . . .
(5) Reinitialization procedure: Rotation on last_inputs as in point (3),
    and reinitialization of image *(last_inputs(0)) at zero.
    . . .
}

```

Spatio-temporal separable filtering

Remark that, at step (2) of the preceding listing, a function `spatialFiltering()` can possibly be applied on the new input image $X(k)$. This virtual function, which is empty by default in the `BaseMapFilter` object, can be implemented in derived types of the `BaseMapFilter`. Typically, it can consist of a spatial linear filtering on the input image, in which case the derived object will implement a *separable* spatio-temporal filtering of the type:

$$Y(x, y, t) = K_{\text{temp}}(t) * L_{\text{spat}}(X(x, y, t)), \quad (6.11)$$

where $K_{\text{temp}}(t)$ is any temporal impulse response coded by the `BaseRecFilter` part of the object, and L_{spat} is any spatial linear operator: Convolution by a Gaussian, by a DOG, or even by a Gabor function (for models of V1), etc.

3.3.3 RetinaMapFilter: Specific retinal specialization

The `RetinaMapFilter`, a specialization of the `BaseMapFilter`, can implement two distinct types of spatio-temporal linear filters, typical of retinal layers. In both cases, the spatial filtering can eventually follow a global scaling scheme, because it is implemented by `RadialFilter` objects (Section 3.2). Here is a simplified header of the

⁷Under special circumstances (a single input per time step, fed without amplification to a filter with $M = 0$), an optimization enables to not copy the new input image, but directly read from its source thanks to a constant pointer.

RetinaMapFilter object:

```

class RetinaMapFilter: public BaseMapFilter
{
protected:
    RadialFilter sigmaPoolFilter, leakyHeatFilter;
    void spatialFiltering( CImg<double>* image );

public:
    void set_sigmaPool( double sigma );
    void leakyHeatEquation( double tauLeak , double sigmaHeat );
    void allocateValues();
    void tempStep();
};

```

10

Separable spatio-temporal filtering

The BaseMapFilter virtual function spatialFiltering(...) is specialized to implement a Gaussian blur, using the RadialFilter sigmaPoolFilter. The overall filtering operation of the RetinaMapFilter, written as in (6.11), is then:

$$Y(x, y, t) = K_{\text{temp}}(t) * G_{\sigma_P}(x, y) * X(x, y, t) \quad (6.12)$$

Here and in the sequel, we only present the equation in the case of a uniform scaling, but remember that RadialFilters can also follow any non-uniform scaling scheme.

Non-separable electrical coupling filter

As an alternative possibility, the RetinaMapFilter can be initialized to perform the 'leaky heat equation' resulting from a linear model of electrical coupling by gap junctions between neighboring cells (Chapter 2, Section 6):

$$Y(x, y, t) = G_{\sigma_H \sqrt{t/\tau}}(x, y) E_\tau(t) * X(x, y, t), \quad (6.13)$$

which is non-separable because of the presence of time t in the Gaussian part of the filter. This particular initialization is called with function leakyHeatEquation(**double** tauLeak, **double** sigmaHeat).

There is a numerically efficient way⁸ to implement the coupling filter (6.13), through the following scheme in discrete time:

$$Y(x, y, k) = [(1 - a)X(x, y, k) + aY(x, y, k - 1)] * G_\delta, \quad (6.14)$$

with

$$\begin{aligned}
 a &= 1 - \exp(-\text{step}/\tau) \\
 \delta &= \sigma_H \sqrt{\text{step}/\tau}.
 \end{aligned}$$

The Gaussian filter G_δ , whose standard deviation gets asymptotically small as the time step tends to zero, encompasses the effects of the 'heat equation'-like diffusion

⁸Communicated to us by Jeanny Herault.

process, over one time step. Unlike G_{σ_P} in (6.12), which is applied to the input image before temporal filtering, G_δ is applied to the output image, *after* the temporal filtering. G_δ is implemented by a second RadialFilter object, called leakyHeatFilter. The virtual functions allocateValues() and tempStep(), inherited from the BaseMapFilter, are overridden to include this possibility of ‘leaky heat’ model of gap junction coupling.

Note that it is possible to implement a filter which has both a separable Gaussian of value σ_P applied on its input, and a non-separable coupling of value σ_H applied on its output. However, if the ‘leaky heat’ filter is used, there is no choice anymore in the initialization of the BaseRecFilter component: It is necessarily set to a simple Exponential filter of order $N = 1$, following the numerical scheme in (6.14).

3.3.4 CondCellMap: nonlinear, conductance-driven filtering

The ‘RetinaMapFilter’ presented in the preceding section handles different linear filters on retinal maps. But our model also uses a nonlinear, conductance-driven filtering scheme, at the level of its contrast gain control stage (Chapter 4, Section 4). To implement this, we designed another object which can integrate both currents and conductances, possibly also with electrical coupling through gap junctions: The CondCellMap.

The underlying continuous equation implemented by a CondCellMap is the following:

$$\frac{dV}{dt}(x, y, t) = \sum_i I_i(x, y, t) + \sum_j g_j(x, y, t)(E_j - V) - g^L V(x, y, t) + \mathcal{G} \Delta V(x, y, t), \quad (6.15)$$

where Δ is the Laplacian operator modeling the electrical coupling of gap junctions, with strength \mathcal{G} (see Chapter 2, Section 6). It allows to integrate any number synaptic inputs, as currents or as conductances, directly at the level of 2d continuous maps.

Equation (6.15) is integrated with a basic Euler scheme, identical to (6.14) but with a ‘time constant’ a which now changes at each pixel:

$$V(x, y, k) = [(1 - a(x, y, k))X(x, y, k) + a(x, y, k)V(x, y, k - 1)] \overset{x,y}{*} G_\delta, \quad (6.16)$$

with

$$\begin{aligned} X(x, y, k) &= \sum_i I_i(x, y, t) + \sum_j g_j(x, y, t)E_j \\ a(x, y, k) &= 1 - \exp\left(-\text{step}\left(g^L + \sum_j g_j(x, y, t)\right)\right) \\ \delta &= \sqrt{2\mathcal{G}\text{step}}. \end{aligned}$$

Here is a simplified header of the CondCellMap object:

```

class CondCellMap : public CImgReader, public CellPortHandler
{
protected:
    double step;
    int sizeX, sizeY;
    double g_leak, G;
    RadialFilter gapJunctionFilter;

public:
    vector<CImgReader> readInputs;
    CondCellMap& feedInput(const CImg<double>& input, int port=0, bool shutUp=false); 10
    void tempStep(void);
    void allocateValues(void);
};

```

The implementation and usage are very close to that of a RetinaMapFilter: Functions feedInput(...) and tempStep() are used in alternation at each time step. The synaptic inputs (currents and/or conductances) are dealt through the CellPortHandler interface (Section 3.1). A RadialFilter allows the electrical coupling through gap junctions to follow the retina's log-polar scaling. The vector<CImgReader> readInputs allows a read-only access to the different input components of the map.

Remark: Linear ODE Note that the CondCellMap, through equation (6.15), can in fact implement any temporal linear ODE of the general form (2.28) (Chapter 2), directly for each pixel of 2D spatial maps. As a result, the CondCellMap can be used to implement, not only conductance-driven neurons, but any linear ODE, such as the catalyzer equations occurring during phototransduction. Implementing models such as Van Hateren and Lamb's model of phototransduction [175] (Chapter 3, Section 1.1.2) is thus straightforward in the scope of *Virtual Retina*. ■

3.4 Spiking cells and arrays

Other 'basic' objects have been created to produce a spiking output for the retina. These spiking objects are based on the *MvaSpike* library, and consist of spiking conductance-driven integrate-and-fire neurons, which can be assembled in arrays of spiking cells.

3.4.1 *MvaSpike* in a nutshell

Event-driven formalism

Our spiking objects build up on the *MvaSpike* library. In *MvaSpike*, the whole evolution of the simulated system relies solely on the exchange of events between objects. Each event i (typically, a spike) is associated to a precise time t_i , and is exchanged between one emitting object O_i (typically, a neuron) and one or several receiving objects (typically, other neurons, or the emitting neuron itself).

The fundamental assumption of event-driven simulation is that at any time t , any object is capable of knowing with precision the time of its next emitted event, if nothing was to change in its internal state until that emission time. If this (strong)

assumption is respected, then an assembly of connected objects (a network) can be simulated following the simple algorithmic loop:

```
while (simulation is not over)
{
  1. Ask all objects for the time of their next event, and pick the earliest one:
      $i_{\text{next}}=(O_{\text{next}},t_{\text{next}})$ .
  2. Propagate  $i_{\text{next}}$  to all its receiving objects (including  $O_{\text{next}}$  itself), and incorporate the resulting changes in their internal state.
}
```

This loop naturally produces the whole series of events which successively occur during the simulation. Interestingly, this type of simulation is totally asynchronous: All events are calculated with an ‘infinite’ precision (up to computer’s numerical precision), without any required discretization of the time line.

Event-driven simulation in neuroscience

In neuroscience, the event-driven formalism appears an interesting way to simulate spiking neural networks -the events being spikes- since it allows an ‘infinite’ temporal precision in the times of the spikes, unlike a classical incremental simulation (with an underlying discretization of time).

Event-driven simulation can also become more interesting than incremental simulation in terms of computation times, although the computational complexities of both algorithmic schemes are generally hard to compare (the complexity of incremental simulation depends a lot on the required *precision* for the event times, while that of event-driven simulation depends a lot on the *number* of emitted events - see e.g. Brette 06 [21]). Brette 06 [21] proves that event-driven simulation has at worst the same complexity (up to a multiplicative factor) as incremental simulation, and can have a smaller complexity in some favorable cases (basically, when the modeled neurons have small firing rates).

However, event-driven simulation suffers from a strong limitation: The fundamental assumption, that each neuron is able to calculate the time of its next spike in the absence of any external event, is rarely met when the internal model for the neuron becomes too complicated. For integrate-and-fire (IF) neurons with synaptic inputs (conductance or currents) that are *constant by parts*, the formulas giving the time of next spike are straightforward. For IF neurons with *exponential* synaptic currents, there is generally no close form anymore for the time of next spike, but efficient numerical schemes still exist under several conditions (Brette 06 [21], 07 [22]). For more complicated models of neurons (e.g. with quadratic [84] or exponential [20] currents), numerical schemes become yet harder, thus reducing the computational efficiency of the whole simulation.

Event-driven simulation in the retina

When it comes to modeling a retina, using an event-driven formalism may appear a bit awkward at first sight since, in order to model continuous filtering in the first layers of the retina, a temporal discretization step must be introduced anyway. However, the following argument suggests that event-driven simulation can also be useful in the retina.

The time scales involved in continuous filtering and spike generation are fundamentally different: The typical time scales for continuous retinal filtering are in the magnitudes of 10-100 ms, as measured e.g. through reverse correlation techniques (Chapter 2, Section 5). By opposition, the precision of emitted spike trains can reach the magnitude of 1 ms, especially if spike synchronies between neighboring cells are considered (Chapter 3, Section 4). As a result, any incremental model wishing to correctly encompass the precision of retinal spike trains must use a discretization time step of order 1 ms, which is probably over-precise as far as continuous filtering in the first layers is concerned.

By opposition, the hybrid scheme using an event-driven spiking generation that we have implemented allows to use larger discretization time steps (5 ms or more), sufficient to model continuous filtering in the first retinal layers, and this without impeding the precision of the subsequent spike trains. In turn, the spike generation procedure is very fast (it always accounts for a minority of the total processing time, even with 100,000 spiking neurons), thanks to the optimized implementation of *MvaSpike*. As a result, for comparable precisions in the output spike trains, the hybrid scheme leads to calculation times several times smaller than a purely incremental scheme.

The price to pay for this computational advantage of the hybrid scheme is a number of limitations in the choice of models. First, the model neurons cannot get too complicated, as explained previously. Second, the hybrid scheme sets a barrier between the ‘continuous’ and ‘spiking’ parts of the simulation, that forbids the precise modeling of some spike-driven interactions in the IPL (e.g. feedbacks from ganglion cells to bipolar cells, via amacrine cells).

In the present state of our model, event-driven simulation remains a computational advantage without severe drawbacks, but we are aware of its potential limitations. If ever it was found necessary to switch back to another spiking formalism, the change would be reasonably easy and limited to the ‘spiking’ objects, thanks to the modular organization of our library.

The *MvaSpike* library

In the *MvaSpike* library, class *Devs* is the virtual base for any object capable of emitting/receiving events. This class has three main virtual functions, which must be overridden in derived objects, to implement the two points in the basic event-driven simulation loop described previously:

1. Function **double** *ta*(**void**) can be called at any time, and must return the time of the *Devs*’s next event if no external event is received in between.
2. If a *Devs* receives an event *i* from *Devs* *O* at time *t*, there are two possibilities:
 - If *O* is the emitting *Devs* itself, which has just emitted the event, function **int** *delta_int*(**double** *t*) is called, proceeding to possible re-initializations of the internal state.
 - If *O* is another *Devs*, function **void** *delta_ext*(**double** *t*, **int** *x*) is called: It can perform various changes of internal state, according to the input port *x* (e.g. excitatory or inhibitory in a neuron) by which the new event was received.

Other important classes of *MvaSpike* are the following:

- Class `Neuron`, a specialization of `Devs`, implements an ‘individual spiking unit’.
- By opposition, class `DCoupled`, another specialization of `Devs`, is designed to handle an *assembly* of ‘contained’ `Devs` (some of whom can already be `DCoupled` objects, defining a tree organization). Its functions `ta()`, `delta_int()` and `delta_ext()` make recursive calls to those of the contained `Devs` (using priority queues). The `DCoupled` has a function `connect(...)` which allows to build the spiking interactions in the network of its contained `Devs`.
- Finally, each program must contain a single `Root` object, in charge of actually *running* the simulation. A `Root` is designed to simulate a single `Devs` object. To simulate an assembly of `Devs` objects, they must all be included in a single `DCoupled`, which is itself simulated by the `Root` of the program.

3.4.2 CondNeuron_cpm: Event-driven GIF neuron

To implement the spiking neurons of *Virtual Retina*, we have specialized base class `Neuron` into the `CondNeuron_cpm` object, which can handle the following conductance-driven integrate-and-fire (GIF) scheme:

$$\left\{ \begin{array}{l} \frac{dV}{dt} = \sum_i I_i(t) + \sum_j g_j(t)(E_j - V(t)) - g^L V(t) \\ \text{Spike when threshold } \theta \text{ is reached: } V(t_{\text{spk}}) = \theta, \\ \text{Reset and possible refractory period: } V(t) = V_R \text{ while } t < t_{\text{spk}} + \eta_{\text{refr}}, \\ \text{and (6.17) again,} \end{array} \right. \quad (6.17)$$

where:

- The synaptic inputs $I_i(t)$ and $g_j(t)$ are supposed *constant by parts*⁹.
- The refractory period η_{refr} can possibly be stochastic, drawn following a (rectified) normal law.

Here is a simplifier header for class `CondNeuron_cpm`:

```
class CondNeuron_cpm : public Neuron, public Warray, public CellPortHandler
{
protected:
    double tl, V, g_infini, I_tot, E_infini;
    double* inputValues;

    void add_inputValue(double newAddVal, int cellPort);
    void change_inputValue(double newVal, int cellPort);

public :
    double Vreset, thres, g_leak;
    double tau_refr, noise_refr;
```

10

⁹‘cpm’ in the object’s name stands for the French ‘*constante par morceaux*’.

```

double ta(void);
void advance(double t);
int delta_int(double t);
void init(void);
};

```

In our simplified header, the neuron's parameters are noted as **public double** fields. They define the values for leak conductance g^L , reset potential V_R , spiking threshold θ and mean and variance of the refractory period η_{refr} , in the spiking scheme (6.17).

Internal state of the neuron

The **protected** variables define the present *internal state* of the neuron. **double** `tl` is the present internal time of the neuron. Due to the properties of the event-driven simulation scheme, `tl` always corresponds to the last time at which the neuron has received an event. **double** `V` stores the value of the neuron's potential at time `tl`.

Synaptic input ports are defined thanks to the `CellPortHandler` interface (Section 3.1). The input values for each port are stored in an array **double**(`inputValues`) of size `lastPort+1` (number of input ports in the `CellPortHandler`), and they can be modified at any time by functions `add_inputValue(...)` and `change_inputValues(...)`. Note that values corresponding to a *conductance* port must always be positive.

Every time one of these functions is called, it changes `inputValue(cellPort)` accordingly, and updates the following internal variables:

$$\begin{aligned}
 g^\infty(t) &= g^L + \sum_j g_j(t) \\
 I_{\text{tot}}(t) &= \sum_i I_i(t) + \sum_j g_j(t)E_j \\
 E^\infty(t) &= I_{\text{tot}}(t)/g^\infty(t).
 \end{aligned}$$

Using these variables, (6.17) rewrites

$$\frac{dV}{dt} = I_{\text{tot}}(t) - g^\infty(t)V(t), \quad (6.18)$$

which bears an analytical solution if $I_{\text{tot}}(t)$ and $g^\infty(t)$ are constant by parts.

Note that, in order to be suitable with the event-driven simulation, functions `add_inputValue(...)` and `change_inputValue(...)` cannot be called directly by the user, as this would imply modifying the neuron's internal state without warning the simulator in charge of the event-driven simulation loop. Instead, these two functions must only be triggered by received events, being called internally by functions `delta_int(...)` and/or `delta_ext(...)`. As a result, the `CondNeuron_cpm` cannot be directly used in simulations: It must first be specialized.

Event-driven functions

- Function **double** `ta()` returns the analytical solution of equation (6.18), knowing that $I_{\text{tot}}(t)$ and $g^\infty(t)$ will remain constant until a new event is received by the neuron.

- Function `delta_int(double t)` performs to the reset procedure in (6.17), including the drawing of a new stochastic refractory period.
- Function `delta_ext(double t, int x)` is not overridden. Its specialization is left to derived objects of `CondNeuron_cpm`, that will specify how the synaptic inputs $I_i(t)$ and $G_j(t)$ must be changed according to the events received by the neuron.
- Function `void advance(double t)` is a helper function for `delta_int(...)` and `delta_ext(...)`: It advances the internal state of the neuron from time `tl` (last event) to time `t` (new received event), knowing that no other event has been received during interval `[tl,t]`. In the `CondNeuron_cpm` object, this amounts to integrating (6.18) between `tl` and `t`.

Function `init()` is called just before starting the simulation, to initialize specific internal variables and possibly allocate working memory: It is the equivalent, in the *MvaSpike* nomenclature, of functions `allocateValues()` used elsewhere in our library.

3.4.3 IntegratorNeuron_cpm: ‘Pulsed’ integration of a time-varying signal

The `CondNeuron_cpm` has been designed as a general event-driven implementation of a GIF neuron. By opposition, its derived type `IntegratorNeuron_cpm` is designed more precisely to generate spikes from time-continuous pre-synaptic signals, providing the link between the ‘continuous’ and ‘spiking’ parts of our model.

PulseCoupled and PulseNeuron

The implementational difficulty is that the discrete values resulting from continuous filtering must be fed to the neuron *in the scope of the event driven simulation*, because the resulting change of internal state must be made under control of the event-driven simulator (the `Root` object). Also, the continuous values at each new time step k must be integrated by the spiking neuron exactly at time $k\Delta t$.

In order to solve these problems, we created a particular specialization of a `DCoupled`, termed the `PulseCoupled`, in which we can include `IntegratorNeuron_cpm` objects. Aside from its traditional role as a `DCoupled` (handle the spike times of contained `Devs` in a priority queue), the `PulseCoupled` contains a supplementary `Devs`, the `PulseNeuron`, which fires an event at the beginning of each new time step, thus marking the time at which the new continuous values must be integrated by the `IntegratorNeuron_cpm` objects.

Functioning of the IntegratorNeuron_cpm

Let us now present the implementation and usage of class `IntegratorNeuron_cpm`. Here is a simplified header for this class:

```
class IntegratorNeuron_cpm : public CondNeuron_cpm
{
protected :
    double step;
    double** stockPulsedInput;
    void delta_ext(double t, int port);
```

```

public :
    int pulsed_MvaspikePort;

    void set_step( double stepp );
    void set_noiseV( double sigma );
    virtual void add_in_coupled( PulseCoupled & daCoupled );
    void feedInput( double val, int cellPort=0 );
};

```

Before it can be used, the `IntegratorNeuron_cpm` must be included in a `PulseCoupled` which will synchronize it in the event-driven simulation. This is done simply by a call to the following function.

```

void IntegratorNeuron_cpm::add_in_coupled( PulseCoupled & daCoupled )
{
    int localId = daCoupled.add_component(*this);
    daCoupled.connect( 0, 0 , localId, pulsed_MvaspikePort, 0.0 );
    addedInCoupled=true;
}

```

It adds the `IntegratorNeuron_cpm` inside the `PulseCoupled`, and then creates an internal connection from the `PulseCoupled`'s `PulseNeuron` (the two first 0's in the 'connect' line) to a dedicated *MvaSpike* in-port¹⁰ in the `IntegratorNeuron_cpm` class, identified by index `pulsed_MvaspikePort`.

At each time step, 'continuous' synaptic signals can be fed to the neuron by the user thanks to function `feedInput(...)`. These values are simply stored into the array `*stockPulsedInput`, of size `lastPort+1` (number of synaptic in-ports as inherited from the `CellPortHandler` object). When the `IntegratorNeuron_cpm` receives an event from the `PulseNeuron`, marking the beginning of the new time step, it automatically integrates the values stored in array `*stockPulsedInput` into its *effective* internal state, thanks to function `CondNeuron_cpm::add_inputValue(...)`. This procedure, coded in function `IntegratorNeuron_cpm::delta_ext(dots)`, allows all neurons in the retina to integrate their new 'continuous' inputs exactly at the same time.

In the end, the typical simulation loop of an `IntegratorNeuron_cpm` is the following:

```

(1) Definition of the different MvaSpike objects
IntegratorNeuron_cpm neur1(step), neur2(step);
PulseCoupled pc(step);
neur1.add_in_coupled(pc);
neur2.add_in_coupled(pc);

```

```

Root simulator;
simulator.set_system(pc);

```

```

(2) Initialize internal variables, allocate memory, etc.
simulator.init();

```

¹⁰a generic in-port for *MvaSpike* events, inherited from the `Devs` class; not to be confused with the synaptic in-ports handled by the `CellPortHandler` class!

```

(3) Launch the simulation
for ( int k=0; k<end_time/step ; k++){
    neur1.feedInput( new_continuous_input1(k) ) ;
    neur2.feedInput( new_continuous_input2(k) ) ;
    simulator.run( (k+0.5)*step ) ;
}

```

Function `Root::run(double t)` runs the event-driven simulation until time t . Note that we must run the simulation by chunks of length ‘step’, in order to specify the new continuous inputs at each time step. Thanks to the `PulseCoupled`, these new inputs are not integrated in the neurons’ internal equations at the call to `feedInput(...)`, but exactly at time $k \cdot \text{step}$, simultaneously for all neurons present.

Remark: Other spiking interactions. Note that in addition to their continuous inputs, `IntegratorNeuron_cpm` neurons can also receive ‘normal’ events from other neurons. Spiking interactions between neighboring cells, as present in the retina, can thus be implemented by specializing class `IntegratorNeuron_cpm`. In the derived class, a new `MvaSpike` in-port will have to be added, corresponding to input from neighboring cells, and its effects defined accordingly in function `delta_ext(...)`. ■

Remark: Gaussian auto-correlated noise. Function `set_noiseV(...)` allows to add a noise current I_{noise} to the neuron’s integration equation (6.17), as proposed in our model (Chapter 4, Section 5.2). At each new time step, the neuron adds to $I_{\text{tot}}(t)$ a number ΔI stochastically drawn along $\mathcal{N}(0, \sigma(t))$, where

$$\sigma(t) = \sigma_V \sqrt{1 - \exp(-2\Delta t g^\infty(t))} \simeq \sigma_V \sqrt{2\Delta t g^\infty(t)}, \quad (6.19)$$

Δt being the length of one time step. Note that the `IntegratorNeuron_cpm` must know the value of Δt , which explains why it also has a field termed `step`.

In the case of a linear ‘LIF’ neuron which only integrates *currents*, one always has $g^\infty(t) = g^L$. Then, in the limit $\Delta t \rightarrow 0$, $\Delta I(t)$ tends towards a white noise, and the whole process is equivalent to adding a Gaussian auto-correlated noise $V_{\text{noise}}(t)$ to $V(t)$, of standard deviation σ_V and correlation time $1/g^L$ (as in the model of Keat *et al.* 01).

In the case of a nonlinear ‘GIF’ neuron which also integrates *conductances*, the noise source’s effect is better seen using the reduced time $u = \int g^\infty(t) dt$: In this time scale, $V_{\text{noise}}(u)$ is still a Gaussian auto-correlated noise, of standard deviation σ_V and correlation time 1.

The exact formula implemented in (6.19) is derived from the discrete, recursive implementation of filtering by an exponential kernel (the solution to (6.18) when $g^\infty(t) = g^L$ remains constant). It partly compensates for the fact that Δt is in fact a non-infinitesimal time step. ■

3.4.4 Various SpikingChannel objects

Individual `IntegratorNeuron_cpm` objects can then be assembled into arrays, to define retinal layers of ganglion cells. In the present state, these arrays are straightforward structures, which only perform the two basic tasks:

1. Create an array of neurons, each associated to a different position (`xOffset,yOffset`), following a sampling which can be square or circular.
2. When fed with a new image, feed each `IntegratorNeuron_cpm` with the image’s value at position (`xOffset,yOffset`) (precise value obtained by linear interpolation).

BaseSpikingChannel is the base class implementing this simple interface. It is further derived into two specialized classes:

- Class sqSpikingChannel implements the square array of cells, corresponding to a node `<square-spiking-channel/>` in the retina XML definition file.
- Class rdSpikingChannel implements the circular array of cells, corresponding to a node `<circular-spiking-channel/>` in the retina XML definition file. In this particular case, small helper functions are required to handle efficiently cell indexes. Also, the noiseless sampling scheme is the following: (i) Define a series of radii for the circles where the cells will be located; (ii) For each circle, determine the number of cells in the circle, and space them uniformly along the circle.

Remark: Position noise. In both types of spiking channel, the units can possibly be disposed with noise around their ‘theoretical’ position. If variable noisePos is different than zero, the real position for each unit is randomly drawn uniformly in a circle around the theoretical position, of radius: $\text{noisePos}/(d_0s(r))$ (local 1d density of cells). For the rdSpikingChannel, the angular offset of each circle of units is also chosen randomly, to avoid the artificial presence of a line of cells at angle $\theta = 0$. ■

Remark: Reverse spatial access. A future extension of our model would be to include spiking interactions between neighboring cells. If such a model is implemented, one will have to handle distances between different neurons, to define spatial neighborhoods, etc. The SpikingChannel objects, which are in charge of the spatial repartition of the different units, will then have to be enhanced with a reverse access to the neurons contained in any spatial area. ■

3.5 *xmlParameters++*: Loading/saving parameters with XML

3.5.1 Goals

Library *xmlParameters++* was written in order to save/load the many parameters of the retina from an XML tree. More precisely, to fit the modular structure required from our simulated retinas, we designed a library with the following characteristics:

1. Generally speaking, *xmlParameters++* assumes a one-to-one correspondence between C++ objects and XML nodes. An object of class ‘Toto’ can be saved/loaded from an XML element with a particular chosen name (say, "toto") and structure. In the XML element "toto", the object’s numerical parameters are stored as attributes, and sub-field objects are stored as sub-elements.
2. *Pointers* Toto* can also be initialized from the XML structure, *if* an element coding for a Toto object is present in the XML file. If no such element is present, the pointer is left uninitialized.
3. *Polymorphism* of pointers is possible: A given pointer Toto* can be initialized into different specializations of a Toto (say, Toto and Tata), according to the type of element ("toto" or "tata") present in the XML file.
4. *Standard template containers* such as `vector<Toto>` or `list<Toto>` can simply be initialized by writing successive nodes "toto" in the definition file.

5. All the preceding features can be combined at will, so that one can for example initialize a vector<Toto*> from an XML file, by writing a succession of "toto" and "tata" nodes.

Library *xmlParameters++* relies strongly on template code. It can be used independently of *Virtual Retina*, in any piece of code requiring the definition of several parameters organized in logical structures. With respect to existing serialization tools, this small library is tuned to the sole definition of *numerical parameters* for a model/simulation.

A precise documentation of this library is not in the scope of this thesis. Interested readers will find supplementary examples and documentation included in the archive for *Virtual Retina*. Let us simply review here the basic principles of use of the library, as it is used in the code for *Virtual Retina*.

3.5.2 Usage

xmlClass and function xml_ize()

In order to be serializable to XML, an object Toto must inherit from a particular class termed xmlClass:

```
class Toto: virtual public xmlClass
{
    double d ;
    int i ;
    SomeClass sc ;
};
```

An xmlClass possesses a virtual function xml_ize(), which must be overridden in the Toto to define how it can be loaded from an XML element:

```
void Toto::xml_ize()
{
    add_param (d , "name-for-d");
    add_param (i , "name-for-i");
    add_child (sc , "some-name-for-my-child");
}
```

Note that the inclusion of sub-field sc implies that class SomeClass is also serializable from XML.

Registration of pointers and/or containers

A strong feature of *xmlParameters++* is its possibility to initialize pointers and vectors from the XML structure, including polymorphism. In order to do so, one must register the XML element names for the whole chain of inclusion, from pointer and/or container to the name of the derived objects themselves.

As a single example of use, consider again class Toto and its derived class Tata, and an xml_ized class SomeClass that needs to initialize a particular sub-field:

`vector<Toto*> glub`. This can be done by writing in function `SomeClass::xml_ize()`:

```
add_child (glub,"my-pointer-vector") ;
xmlRegister <2,Toto> (glub , xml_names("name-of-a-pointer","toto")) ;
```

The first template index (here, 2) indicates the ‘depth’ of the chain of containers and pointers before reaching the actual object. In this particular case, element `glub` will be correctly initialized by an XML element of the form

```
<my-pointer-vector>
  <name-of-a-pointer>
    <toto . . ./>
  </name-of-a-pointer/>

  <name-of-a-pointer>
    <toto . . ./>
  </name-of-a-pointer/>

  etc.
</my-pointer-vector/>
```

Now, consider the alternative definition in function `SomeClass::xml_ize()`:

```
add_child (glub,"") ;
xmlRegister <2,Toto> (glub , xml_names("","toto")) ;
xmlRegister <2,Tata> (glub , "tata") ;
```

In that case, element `glub` will be correctly initialized by XML elements of the form

```
<toto . . ./>
<toto . . ./>
<tata . . ./>
etc.
```

This alternative scheme illustrates two distinct notions:

1. Containers and/or pointers can be associated to no explicit XML element, by setting their registration name to the empty string `" "`.
2. Once the whole chain of names has been registered once, other derived types can be registered at the end of the chain, by changing the second template parameter of function `xmlRegister<...>(...)`, and adding only the new registration name as second argument to the function.

Concluding remarks

Usage in executable code. Once an XML architecture has been defined in a set of objects by overriding their functions `xml_ize(...)`, the structure can simply be saved/loaded from an XML structure, thanks to two functions `xmlParam::save(...)` and `xmlParam::load(...)`. The XML structure must first have been parsed thanks to library `libxml++`. An example of use is provided with the `xmlParameters++` library.

Custom definition of an XML architecture. It is also possible to define various parameters from XML without an underlying correspondence to real C++ objects, if base `xmlClass` objects are directly used to define the elements of the XML structure. Parameters and filiation between `xmlClass` objects can directly be defined (outside of any function `xml_ize()`), by using the ‘external’ functions `xmlParam::add_param_custom(...)` and `xmlParam::add_child_custom(...)`.

3.6 Assembling and simulating a retina

All ‘basic’ objects of the *Virtual Retina* library have now been described. We conclude this presentation by rapidly showing how these objects have been assembled to build our retina model, and how this retina model is simulated in effect, in the code for our executables. The interest here is not to re-describe our model, but rather to provide examples of use of our library, which can possibly be used to build other models than ours.

3.6.1 The Retina object

Objects reproducing our retinal structure are declared in header `retina.h`, and implemented in `retina.cc`. Logically enough, the main object is called `Retina`. Here is a simplified header:

```

struct Retina: virtual public xmlClass
{
    XML_IZE_MACRO;
    double step , input_luminosity_range, pixels_per_degree ;

    Retinal_LogPolarScheme* radScheme;
    OPLLayers* outerPlexiformLayer;
    FastGainControl* contrastGainControl;
    vector<GanglionLayer*> ganglionLayers;

    int sizeX, sizeY;
    void degToPix();
    void adjustSizes(int imX, int imY);
    void allocateValues(bool verbose=true);

    void feedInput(const CImg<double>& image);
    void tempStep();
};

```

Notice that `Retina` inherits from an `xmlClass`: As a result, it possesses a function `xml_ize()` (automatically declared by macro `XML_IZE_MACRO`) which allows to define its serialization to an XML file (Section 3.5).

The structure of object `Retina` is exactly that of node `<retina/>` in the XML definition file (Section 2.2.1), very logically since library `xmlParameters++` defines a parallel between C++ objects and XML architecture. It possesses:

- Three general **double** parameters (step, luminosity range and conversion pix/deg).
- Four sub-fields corresponding to the three stages of the model, plus the log-polar scheme. Note that these subfields are *pointers*, that can be initialized or not, and possibly specialized with polymorphism, from the XML file. This

allows the modularity of the software, concerning the underlying retina model (Section 2.2.1).

Simulating the retina. Usage of the whole retina is very similar to that of its individual components: At each time step, a new input image is fed with `feedInput(...)`, the continuous filtering is performed by calling `tempStep()`, and the possible spikes are emitted thanks to an *MvaSpike* Root object.

Remark: Spatial sizes and scales In the XML definition file, spatial parameters are passed in visual *degrees*. To convert these to pixels, we had to specialize some objects with prefix ‘Retinal.’ (e.g., the ‘Retinal_LogPolarScheme’ in the header), with an added function `degToPix()` in charge of the conversion.

Also, note that the size (`sizeX,sizeY`) of the various retinal continuous maps is *not* specified in the XML definition file. Internal function `Retina::adjustSizes(...)` automatically sets these two numbers, based on the minimum of two possible sizes:

- Size of the input image.
- User’s size requirements for spiking arrays, if defined.



3.6.2 Example of sub-stage object: The GanglionLayer

It would be tiresome and uninteresting to describe the various specializations of objects `OPLayers`, `FastGainControl` and `GanglionLayer`, which implement the different sub-stages of our retina model. Instead, to conclude this chapter, we provide a single example illustrating how our basic retinal objects can be combined in retinal objects. We show code extracts from the `GanglionLayer` object, which performs the successive operations:

1. High-pass, rectify, and possibly pool the input bipolar signal, following (4.14)–(4.15).
2. Generate sets of spike train, following (4.16).

Retinal maps are initialized in function `GanglionLayer::allocateValues(...)`

```
void GanglionLayer::allocateValues(int sx, int sy, double st, bool verbose)
{
(1) RetinaMapFilter `supplementaryTransient':
    BaseRecFilter amacrineCuttingInGanglion(st);
    amacrineCuttingInGanglion.Exp(tauTransient).warningVerbose=false;
    amacrineCuttingInGanglion*=wTransient;

    supplementaryTransient.set_sizeX(sx).set_sizeY(sy).set_step(st);
    supplementaryTransient-=amacrineCuttingInGanglion;
    supplementaryTransient.allocateValues();

(2) RetinaMapFilter `inputCurrent':
    sign=(sign<0)? -1.0:1.0;
    inputCurrent.set_sizeX(sx).set_sizeY(sy).set_step(st);
    inputCurrent.inputSynapse().rectification( sign*vThresh, sign*ampInputCurrent, valThresh);
    inputCurrent.set_sigmaPool( sigmaPool*fatherRetina->pixels_per_degree );
    inputCurrent.allocateValues();
```

(3) If spiking channels have been defined:

```

if(spikingChannel)
{
    spikingChannel->set_step(st);
    spikingChannel->allocateValues();
}

```

20

Here is the link with equations (4.14)–(4.15): `RetinaMapFilter supplementaryTransient` implements the partially high-pass filter $T_{w_G, \tau_G}(t)$ (as resulting from amacrine inhibition of the ganglion cells), while `RetinaMapFilter inputCurrent` implements $I_{Gang}(x, y, t)$ (rectification and possible synaptic pooling), which will be used to generate the spike trains.

Retinal connections are coded in function `GanglionLayer::feedInput(...)`

```

void GanglionLayer::feedInput(const CImg<double>& image)
{
    supplementaryTransient.feedInput( image );
    inputCurrent.feedInput( supplementaryTransient.read() );
    if(spikingChannel)
        spikingChannel->feedInput( inputCurrent.read() );
}

```

Note that read-only access to retinal maps is done thanks to function `read()`, inherited from the `CImgReader` interface (read-only pointers to protected `CImg<double>` images, not described in this chapter). In the executable code also, the `read()` functions must be used to access the retinal maps (e.g. for saving, displaying, etc.).

Synchronous temporal steps

```

void GanglionLayer::tempStep()
{
    supplementaryTransient.tempStep();
    inputCurrent.tempStep();
}

```

Synchronous `tempStep()` of all objects in the retina is important to respect the causality in the underlying ‘continuous’ ODEs and avoid artificial oscillations, especially when feedback loops are considered (contrast gain control mechanism).

Conclusion and perspectives

Summary and main contributions

The retina is a complex neural structure, which does not only detect an incoming light signal, but also proceeds to many complex signal transformations. The characteristics of retinal processing have been reviewed extensively in Part I of this work: It is a very ordered structure, which proceeds to band-pass spatio-temporal enhancements of the incoming light, along different parallel output pathways with distinct spatio-temporal properties. The spike trains emitted by the retina have a complex statistical structure, such that precise spike timings may play a role in the code conveyed by each ganglion cell, and even more in the code conveyed by a cell population, due to stimulus-driven spike synchronizations. Finally, several mechanisms of gain control, with different time scales, provide a constant adaptation of the retina to the input levels of luminosity and contrast, and even to more complex spatio-temporal correlations in the input.

The retina model that we have defined and implemented in Part II can account for a good part of this complexity. It can model spatio-temporal band-pass behavior with adjustable filtering scales, with the inclusion of plausible mechanisms of contrast gain control and spike generation. The two best-known types of retinal cells, X and Y, are reproduced in their general characteristics, including Y cells' spatial nonlinearity. The gain control mechanism proposed in the model provides a good fit to experimental data, and it can induce interesting effects of local renormalization in the output retinal image. Furthermore, a mathematical analysis confirms that the gain control behaves well under simple sinusoidal stimulation. Finally, the simulator *Virtual Retina* implements the model on a large-scale, so that it can emulate up to around 100,000 cells with a processing speed of about 1/100 real time. It is ready for use in various applications, while including a number of advanced retinal functionalities which are too often overlooked. Model parameters are defined in a modular XML file which insures an easy manipulation. The underlying C++ objects implement generic signal processing tools which can be reused in other models of retina or other low-level cortical areas.

To conclude this thesis, let us discuss the perspectives of future work from this point on. Mainly, these perspectives are of two types. First, the software *Virtual Retina* can be used in its present state for various research applications. Second, the model and software can undergo a number of extensions towards other interesting retinal features which are not implemented yet, and may be functionally relevant.

Applications of the simulator

First, we discuss possible applications of software *Virtual Retina* to future research. Some of these applications are personal projects for the future, while others are concrete, already ongoing uses of the software.

Retinal input to thalamo-cortical models. The first obvious application of *Virtual Retina* is that for which it was designed: Provide input to models of higher-level processing areas. Originally designed for internal use in our lab, the software has started to spread amongst other partners of the FACETS¹¹ European consortium. It has thus been tested as input to detailed models of V1 at the *Computational Biology*

¹¹<http://facets.kip.uni-heidelberg.de/>

& *Neurocomputing* group at KTH University (Stockholm). We hope that such dissemination will continue, in parallel with possible future extensions of the software.

Simplified models of low-level visual areas. As a close but alternative possibility, the computer tools that we have implemented can be directly used as building blocks to produce simplified models of the first thalamo-cortical visual areas: LGN naturally, but also possibly V1. The models that could be produced in this scope would be ‘enhanced’ LN models (often used as simplified models of low-level areas, e.g., with Gabor filters in the case of V1), but inheriting from the nonlinear tools that we have developed for the retina model: Contrast gain control is known to be very present in the cortex (Ohzawa *et al.* 85 [125]), while the rectification/pooling scheme used to model Y cells has strong links with models for V1 complex cells.

This could allow easily to ‘shift’ the present issue (build a plausible retinal input for models of low-level visual areas) to a higher level (build simplified V1/LGN models as input to higher-level cortical areas).

Coding and information theory. Our personal hope is that *Virtual Retina* can be a useful tool for studying the links between efficient coding and large-scale percepts in the retina. In Chapter 4, Section 7.2, we have shown first qualitative examples of how the constitutive elements of the model (nature of the linear filter, contrast gain control) have a strong influence on large-scale percepts, as assessed from a simple linear reconstruction from the spike trains. We would be interested in *quantifying* the impact of these various constitutive elements on the nature of retinal coding.

More precisely, we would like to derive some statistical measure of coding efficiency (possibly, an information-theoretic measure), and use the modularity of our retina software to test the impact of different retinal features, simply by adding or removing them from our model. The impact of a non-separable center-surround filtering (Chapter 4, Section 3), of contrast gain control (Chapter 4, Section 4), or of the non-Poisson spiking statistics induced by the nLIF model (Chapter 4, Section 5) could thus be quantified. Ideally, a scheme for stimulus-driven spike synchronies (Chapter 3, Section 4.3) could also be implemented and tested with the same procedure, as in Kenyon *et al.* 04 [90]. Implementing stimulus-driven synchronies is but one of possible extensions from the current model, as we present now.

Possible extensions of the model

To conclude this discussion, we mention the possibilities of extension of our model, and especially their feasibility in the computational framework that we have developed for *Virtual Retina*. Indeed, as compared to the complexity of retinal processing presented in Part I, our present model discards many features with a potentially strong functional impact. The ‘missing’ features that we discuss here are: Adaptation to light (Chapter 3, Section 5.1), the variety of ganglion cell output pathways (Chapter 3, Section 3.2), color vision (Chapter 3, Section 3.2.3) and spike correlations between neighboring cells (Chapter 3, Section 4.3).

We argue here that the formalism used in our model, and the way it has been implemented into generic tools (Chapter 6, Section 3), allows relatively easy extensions for many of these features. We remind that *Virtual Retina* has an open-source license, allowing free use and improvements from any interested user.

Light adaptation. Light adaptation has not been implemented in the ‘stable’ version of our model and simulator. Instead, our simulator (Chapter 6) automatically proceeds to a renormalization of the input sequence, based on the direct indication of the sequence’s ‘typical’ range by the user. Such a simple scheme seemed sufficient for most potential applications of the software.

However, we have also noted (Chapter 3, Section 1.1.2) that catalyzer equations and calcium adaptation in photoreceptors use a very similar mathematical framework as the one used in our contrast gain control stage (‘linear ODE’ framework, Chapter 3, Section 7), implying that a model of light adaptation could easily be implemented (e.g., the Van Hateren and Lamb 06 [175] model), with already existing C++ objects (CondCellMap, Chapter 6, Section 3.3.4).

‘Other’ ganglion cells. We discussed in Chapter 3, Section 3.2 the existence of various output pathways for the retina, through numerous subtypes of different ganglion cells. Our model focuses on X and Y cells, which are by far the most documented cells. Here, we suggest the simplest modifications which could be performed to implement other, less well-known types of cells. These suggestions are really minimal, and we do not claim that the resulting models would indeed perform well in reproducing (the rare) physiological data. However, they illustrate well how easily new models can be implemented with our present computational tools.

- Q cells (Chapter 3, Section 3.2.7), which have properties similar to X cells (center-surround architecture, linear behavior) but with larger receptive fields and less emitted spikes, could very likely be modeled in the existing framework, but with modified parameters.
- Orientation-selective cells (Chapter 3, Section 3.2.7) and their elongated receptive fields, could be modeled simply by changing the Gaussian kernels to asymmetric, oriented Gaussian kernels. However, it is not clear whether these asymmetric kernels can still be implemented by recursive filtering, the fast method used in our present model (Deriche filters, as presented in Chapter 6, Section 3.2.2).
- Local edge detectors (LEDs, Chapter 3, Section 3.2.6) could be modeled taking into account the suggestion of Levick 67 [99], that the inhibitory *surround* itself is sensitive to image edges. An easy way to introduce this behavior would be to add an inhibitory current or conductance to the LED, sensitive to a rectified and spatially low-passed version of the bipolar signal (typically, the inhibitory signal on LEDs would resemble the excitatory signal on Y cells).
- Suppressed-by-contrast cells (Chapter 3, Section 3.2.7) could be implemented as the ‘negative’ of the LED, that would typically fire when the LED is silent, and reciprocally.
- Direction-selective cells (DS, Chapter 3, Section 3.2.5) would be more difficult to implement. More exactly, the difficulty would be to model starburst (Sb) amacrine cells, suspected of being the actual movement detectors. Indeed, the process through which Sb cells gain a centrifugal motion sensitivity in their different dendrites is not fully known. The easiest approximation would likely be to implement four layers of Reichardt movement detectors [130], each layer modeling the dendrites of Sb cells in one cardinal direction.

Color cells. At present state, our simulator only deals with gray level signals, and this may be a real limitation for certain applications. Although the exact biological implementation of color-coded cells is still controversial (Chapter 3, Section 3.2.3), we have reviewed how color-coded cells possibly arise simply from the opposition between a *center* signal with given spectral sensitivity (red, green or blue) and an undifferentiated *surround* with generic sensitivity (red+green, consisting mostly of an unspecific pooling of the two dominant types of cones).

So, likely, only the OPL filter should be re-implemented with an added spectral sensitivity, before using the same following mechanisms for contrast gain control (optionally) and spike generation. From an implementation point of view, this would require the use of a third dimension in the input images, which is already implemented in the *CImg* image processing library (Chapter 6, Section 3).

Spike correlations. Implementing stimulus-driven correlations in the output spike trains of neighboring cells (Chapter 3, Section 4.3) is presumably a harder work starting from the present model, but also one of the most promising extensions. The main problem in this case is the relative rarity of effective functional models reproducing the phenomenon. As a matter of fact, the only effective model we know is that of Kenyon *et al.* 03 [91], which involves a complex interplay between Y ganglion cells and two different populations of amacrine cells. This sort of model is quite distant from our present framework.

The easiest extension from our present framework would be a model where no amacrine cells are explicitly modeled, but only direct, possibly inhibitory, interactions between ganglion cells. From the physiological standpoint, we have reviewed evidence that the statistical structure of correlations in the retina (stimulus-driven or not) is well accounted for by pairwise interactions directly between ganglion cells (Chapter 3, Section 4.3.3). From the computational standpoint, this sort of model could be implemented and simulated very efficiently with the *MvaSpike* spiking library used by our simulator (Chapter 6, Section 3.4). However, including such a simplified model of correlations in the software would first require a strong, preliminary theoretical study. We view such a study as a particularly interesting track for the future.

Conclusion générale (en Français)

La rétine est une structure neurale complexe, qui non seulement capte la lumière incidente au fond de l'œil, mais procède également à des transformations importantes du signal lumineux. Dans la Partie I de ce travail, nous avons résumé en détail les caractéristiques fonctionnelles de la rétine: Il s'agit d'une structure très ordonnée, qui réalise un filtrage passe-bande du stimulus visuel, selon différents canaux parallèles d'information aux propriétés spatio-temporelles distinctes. Les trains de potentiels d'action émis par la rétine ont une structure statistique complexe, où les temps précis d'émission de potentiels d'action sont susceptibles de véhiculer une information importante, tant au niveau des cellules individuelles que des *populations* de cellules, au sein desquelles des synchronisations apparaissent en réponse à certains stimuli. Enfin, de nombreux mécanismes de contrôle de gain, avec différentes échelles temporelles, permettent à la rétine d'adapter ses caractéristiques de filtrage en fonction de la luminosité et du contraste ambiants, et même en fonction de statistiques plus complexes du stimulus.

Le modèle de rétine défini et implémenté dans la Partie II de ce travail prend en compte une part importante de cette complexité. Il reproduit le comportement passe-bande, à l'aide de filtres linéaires spatio-temporels appropriés. Des mécanismes non-linéaires d'adaptation au contraste et de génération de potentiels d'action sont également inclus, qui possèdent à la fois une expression simple et une bonne capacité à reproduire les données biologiques. Les deux types de cellules ganglionnaires les plus connues, les types 'X' et 'Y', peuvent être simulées, y compris la non-linéarité spatiale typique des cellules 'Y'.

Le mécanisme de contrôle du gain au contraste que nous avons proposé permet une bonne reproduction des données expérimentales, et peut également véhiculer d'importants effets d'égalisation spatiale des contrastes en sortie de rétine. De plus, une analyse mathématique confirme que notre mécanisme a le comportement escompté en réponse à une stimulation sinusoïdale.

Enfin, le simulateur *Virtual Retina* implémente le modèle à grande échelle, permettant la simulation d'environ 100 000 cellules en un temps raisonnable (100 fois le temps réel). L'attrait premier de ce simulateur est le fait qu'il est prêt à l'emploi, tout en incluant des fonctionnalités souvent négligées par les modèles à grande échelle. De plus, les paramètres du modèle sont définis dans une structure au format XML qui permet une manipulation simple. Les objets informatiques sous-jacents, implémentés en C++, offrent des outils de filtrage et de traitement du signal neuronal qui peuvent aisément être réutilisés dans d'autres modèles de rétine, voire d'autres aires visuelles de bas-niveau.

Le simulateur *Virtual Retina* pourra être utilisé pour différentes applications futures. Premièrement, comme entrée de modèles d'aires visuelles thalamo-corticales. Deuxièmement, comme outil d'estimation des capacités de codage de la rétine elle-même, à travers ses différentes étapes de filtrage. Par ailleurs, le simulateur offre de bonnes possibilités d'évolution, que ce soit vers une plus grande complexité rétinienne, avec la modélisation d'adaptations supplémentaires, de synchronisations entre cellules voisines, ou de types plus rares de cellules ganglionnaires, ou vers des modèles simplifiés d'autres aires visuelles de bas niveau, telles que le corps genouillé latéral (LGN) ou le cortex visuel primaire (V1).

Appendix

CONVOLUTION OF EXPONENTIAL FILTERS

In the retina, the transmission of visual signal through multiple layers of cell membranes and through chemical synapses induces a series of low-pass convolutions of the signal with decaying exponential filters. If linear, the related delays can be accounted for through a single filter, resulting from the convolution of many exponential filters, possibly with different characteristic times. This annex proposes a generic approximation for the resulting filter, depending on two time parameters τ_{\max} and τ_{dec} .

In this annex, we deal with normalized decaying exponential filters:

$$E_{\tau}(t) = \frac{1}{\tau} \exp\left(-\frac{t}{\tau}\right), \quad (20)$$

as that of Figure 3 (A), and try to calculate or approximate the filter resulting from a cascade of such exponential decays, whose convolution kernel is:

$$F_{\tau_1, \tau_2, \dots, \tau_N}(t) = E_{\tau_1} * E_{\tau_2} * \dots * E_{\tau_N}(t), \quad (21)$$

with some of the $\{\tau_n\}$ possibly being equal one to another.

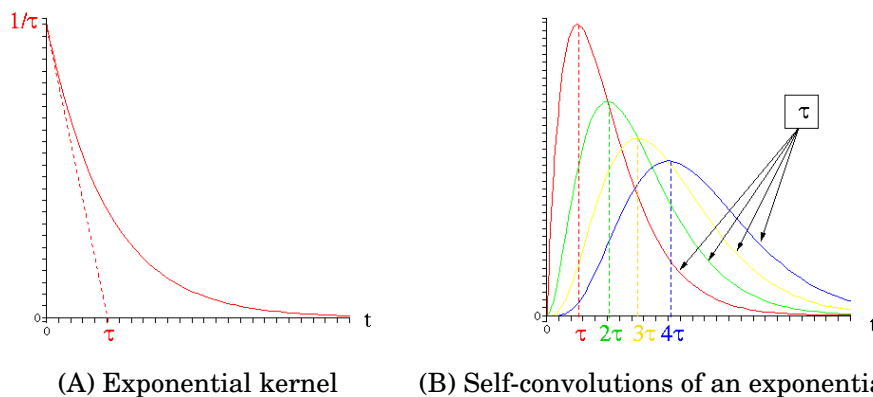


Figure 3: An exponential kernel and its four first self-convolutions. All filters decay with the same characteristic time τ . Note that when n self-convolutions occur, the resulting filter peaks at time $n\tau$.

1. Exact calculations

Self-convolution of a filter. From a few algebra, it appears that when one exponential filter is convolved with itself k times, the resulting filter is:

$$F_{\underbrace{\tau, \tau, \dots, \tau}_{k+1}}(t) = E_{k, \tau}(t) = \frac{t^k}{\tau^{k+1} k!} \exp\left(-\frac{t}{\tau}\right). \quad (22)$$

This function is a positive 'blob' that reaches its maximum value at time $k\tau$ and then decays exponentially with a time constant τ (Figure 3 (B)). Note that (22) for $k = 0$

gives the filter in (20), meaning

$$E_{0,\tau} = E_\tau.$$

Remark: Different notations. As opposed to the body of the thesis, notation $E_{k,\tau}$ here defines the k -fold convolution of filter $E_\tau(t)$, peaking at time $k\tau$. In the body of the thesis, we had defined it as the k -fold convolution of filter $E_{\tau/k}(t)$, peaking at time τ . ■

Convolution of different filters. Another derivable case is when exponential filters with different scales are convolved one to another. If N exponential filters E_{τ_n} are convolved, *with each τ_n being different from all the others*, the resulting filter writes:

$$F_{\tau_1, \tau_2, \dots, \tau_N}(t) = \sum_{n=1}^N \gamma_n E_{\tau_n}(t), \quad \text{with:} \quad (23)$$

$$\gamma_n = \prod_{p \neq n} \frac{\tau_n}{\tau_n - \tau_p}.$$

This function is also a positive 'blob' (Figure 4), but its peak time is not calculable anymore. Neither is its 'apparent' decay time, as defined by the strength of the decrease after the peak of the filter.

General case. Merging (22) and (23) should lead to a formula for the general case when N different exponential filters E_{τ_n} are convolved, with each filter n being cascaded K_n times. This most general case can be seen as a degenerated limit of (23) when different times get very close one to another. As a result, it also possesses the typical 'blobby' shape (Figure 4). It corresponds to a pondered sum of E_{k,τ_n} filters, with $k \in \{0, K_n\}$, but the corresponding coefficients $\gamma_{n,k}$ do not bear any simple expression anymore.

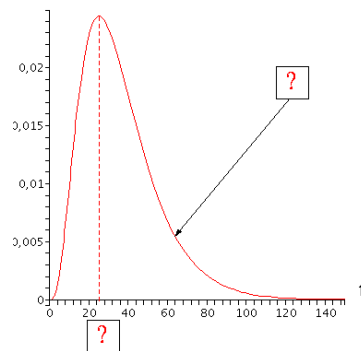


Figure 4: Convolution of exponential kernels with different decay times. Four filters were convolved here, with characteristic times of 5, 6, 10 and 15 ms, which are characteristic times for retinal low-pass filters (see report). Visually, the resulting filter still has typical rising time and decay time, but their exact calculation is impossible in general.

Calculating the transfer function. An alternative approach is to obtain the transfer function in the Fourier domain. This is straightforward, since convolution in the time domain corresponds to the multiplication in the Fourier domain. As a result, in the Fourier domain, any convolution of exponential filters has the following transfer function:

$$\tilde{F}_{\tau_1, \tau_2, \dots, \tau_N}(\xi) = \prod_{n=1}^N \frac{1}{1 - \mathbf{j}\tau_n \xi}, \quad (24)$$

where some of the $\{\tau_n\}$ can possibly be equal one to another (general case).

Equation (24) is a more convenient way to work on the filter, since its properties are now described by a simple equation. Note also that coefficients γ_n in (23) can be obtained by reducing the total fraction of (24) in its simple elements. Similarly, one can derive the coefficients $\gamma_{n,k}$ for the general case, but the degenerated times τ_n lead to a term $1/(1 - \mathbf{j}\tau_n \xi)^{K_n}$ in (24) that yields harder calculations for the simple elements' coefficients.

2. An approximate two-parameter filter

How can such an exponential cascade be described by few parameters? We believe that in the case of biological systems where all equations are approximate, a two-parameter model defined by a rising time τ_{\max} and a decay time τ_{dec} is a sufficient fit for any low-pass cascade.

The parametric function we use is defined by:

$$E_{\alpha, \tau}(t) = \frac{t^\alpha}{\tau^{\alpha+1} \Gamma(\alpha+1)} \exp\left(-\frac{t}{\tau}\right), \quad (25)$$

where α and τ are any real positive numbers. Γ is the mathematical Gamma function; it only serves as a normalization factor. Its most classical definition is precisely as being the integral of function $t^{\alpha-1}e^{-t}$ over \mathbb{R}^+ , when $\alpha > 0$. Here again, notations are coherent. Indeed, function $x \rightarrow \Gamma(x+1)$ is an interpolation of the integer 'factorial' function. This means that (25) defines the same function as (22), when $\alpha \in \mathbb{N}$.

$E_{\alpha, \tau}$ is a function that reaches its maximum at time $\alpha\tau$, before decaying with time constant τ (Figure 5). Thus α and τ govern the two parameters we have chosen to describe our exponential 'blobs', with:

$$\begin{cases} \tau_{\max} = \alpha\tau, \\ \tau_{\text{dec}} = \tau. \end{cases} \quad (26)$$

Empirically one finds that any convolution of exponential filters is always well approached by some function $E_{\alpha, \tau}(t)$, except in its initial rising phase when the best fitting α is smaller than 1 (Figure 6). For this reason, we describe all retinal low-pass filters by appropriate functions $E_{\alpha, \tau}(t)$. However, one last question should be addressed. What links are there between the values for (α, τ) found empirically, and the times $(\tau_1, \tau_2, \dots, \tau_n)$ of the original exponential filters that generated the blob?

Deriving parameters α and τ . We generated exponential cascades, numerically calculated the corresponding kernel, and looked for the visually best-fitting pair

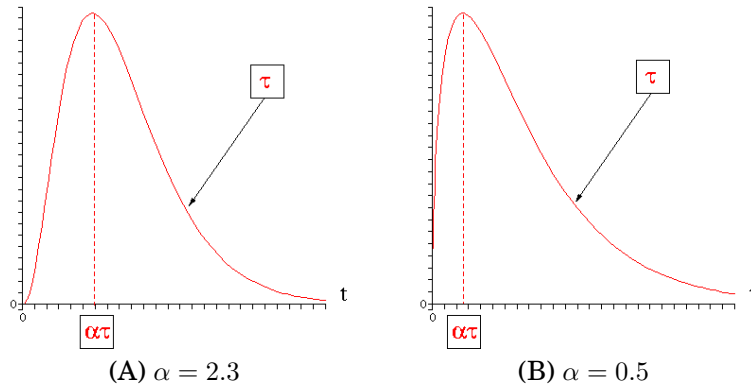


Figure 5: Two examples of kernel $E_{\alpha, \tau}$. Note that when $\alpha < 1$ (case (B)), the derivative of the kernel in $t = 0$ is always infinite. This is the main limitation for visual fitting of kernel $F_{\tau_1, \tau_2, \dots, \tau_n}$ with a function $E_{\alpha, \tau}$ in some cases (see Figure 6).

(α, τ) . Empirically, we find out that for our best-fitting (α, τ) , the sum of time-to-peak $\tau_{\max} = \alpha\tau$ and of decay time $\tau_{\text{dec}} = \tau$ is always close to the sum of all generating times. That is:

$$(1 + \alpha)\tau \simeq \sum_{n=1}^N \tau_n. \quad (27)$$

Empirically still, the visually best-fitting decay time τ for the whole cascade is a pondering of all individual exponential decay times, but with a pass filtersative contribution of big (slow) exponential filters. That big time constants have a bigger impact on the decay time of the cascade is intuitive: a fast filter i in the cascade, with characteristic time $\tau_i \simeq 0$, does not modify the signal at all, so it cannot influence the visually best-fitting decay time. The simplest way to do this is to have each term in the sum pondered by its own value. And indeed, we find

$$\tau = \frac{\sum_{n=1}^N \tau_n^2}{\sum_{n=1}^N \tau_n} \quad (28)$$

to be a suitable choice for the decay time in most cases. Then, according to observation (27), we chose:

$$\alpha = \frac{\sum_{n=1}^N \tau_n}{\tau} - 1 \quad (29)$$

as our value for α . Using these approximations always provides a relatively correct fit of the real cascaded filter, as shown in Figure 6.

These empirical choices for (α, τ) can actually be justified in the Fourier domain. Indeed, one can check easily that the general Fourier transform of function $E_{\alpha, \tau}$ is given by:

$$\tilde{T}_{\alpha, \tau}(\xi) = \frac{1}{(1 - \mathbf{j}\tau\xi)^{\alpha+1}}. \quad (30)$$

Then, developing the actual transfer function $\tilde{F}_{\tau_1, \tau_2, \dots, \tau_N}(\xi)$ of (24) and its ap-

proximation $\tilde{T}_{\alpha,\tau}(\xi)$, both at the second order in ξ , provides:

$$\left\{ \begin{array}{l} \tilde{F}_{\tau_1,\tau_2,\dots,\tau_N}(\xi) = 1 + \mathbf{j} \left(\sum_{n=1}^N \tau_n \right) \xi - \frac{1}{2} \left(\left(\sum_{n=1}^N \tau_n \right)^2 + \sum_{n=1}^N \tau_n^2 \right) \xi^2 + o(\xi^2), \\ \text{and:} \\ \tilde{T}_{\alpha,\tau}(\xi) = 1 + \mathbf{j}((\alpha + 1)\tau) \xi - \frac{1}{2} (\tau^2(\alpha + 1)(\alpha + 2)) \xi^2 + o(\xi^2). \end{array} \right. \quad (31)$$

As a result, imposing that $\tilde{T}_{\alpha,\tau}(\xi)$ be equal to $\tilde{F}_{\tau_1,\tau_2,\dots,\tau_N}(\xi)$ as far at the second order in ξ yields the approximation for α and τ that was empirically proposed in (28,29).

Best approximation with an integer α . Kernels $E_{\alpha,\tau}$ for which $\alpha \in \mathbb{N}$ have the computational advantage to be implementable through recursive filtering. Hence we also tested visual differences between the best-fitting $E_{\alpha,\tau}$ as described through (28,29) and its “integer alpha” approximation as defined by:

$$\left\{ \begin{array}{l} \alpha_{\mathbb{N}} = \text{round}(\alpha) \\ \tau_{\mathbb{N}} = \tau \frac{1 + \alpha}{1 + \alpha_{\mathbb{N}}}. \end{array} \right. \quad (32)$$

Function *round* returns the closest integer to α . $\tau_{\mathbb{N}}$ is still any real number, but it is calculated so as for $(\alpha_{\mathbb{N}}, \tau_{\mathbb{N}})$ to verify observation (27), or equivalently, to fit the first-order developments of Fourier transforms in (31). This procedure still yields visually satisfying kernels, as illustrated in Figure 6.

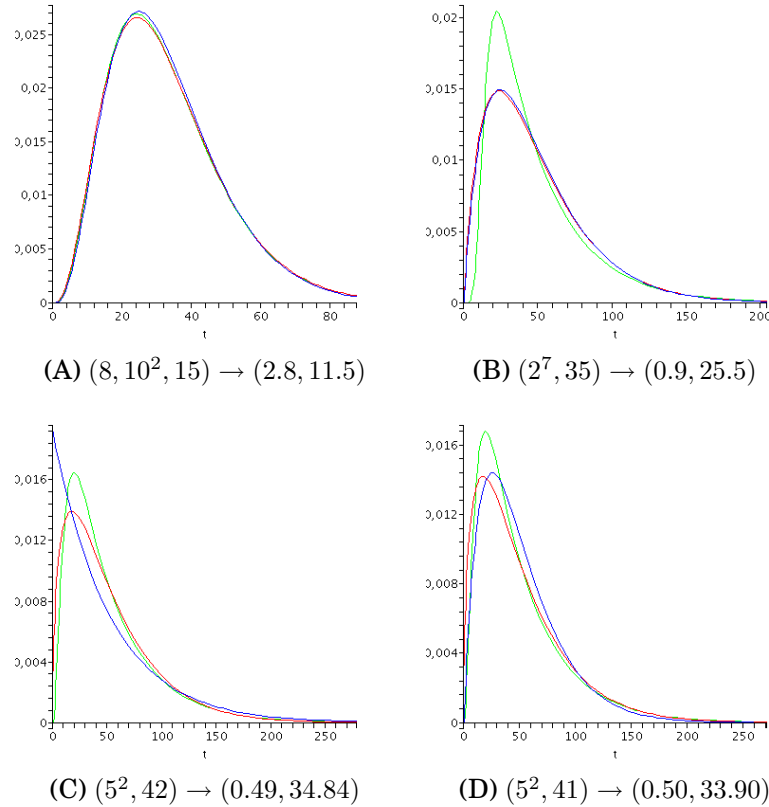


Figure 6: Four approximations of exponential cascades by $E_{\alpha, \tau}$ kernels. Notation is $(\tau_1, \tau_2, \dots, \tau_N) \rightarrow (\alpha, \tau)$ using formulas (28,29). *Green Curve*: original cascade kernel. *Red Curve*: best approximation as described through (28,29). *Blue Curve*: Best approximation with integer α , as in (32). Figures comment: (A) very good fitting case. (B) problematic fitting case. The 7-fold repetition of exponential kernel $\tau = 2$ provides the real kernel with null derivatives in $t = 0$ at the 5 first orders, whereas the derivative of the approximate kernel is infinite, since $\alpha < 1$. (C) and (D) worst-case scenario for the fitting of best kernel $E_{\alpha, \tau}$ with an “integer α ” kernel, through equation (32). A slight change of one of the original exponential times makes the best-fitting α cross value 0.5, yielding two different approximations for the Blue curve.

Bibliography

- [1] E.H. Adelson and J.R. Bergen. Spatiotemporal energy models for the perception of motion. *Journal of the Optical Society of America A*, 2:284–299, 1985.
- [2] D. Alleysson, S. Susstrunk, and J. Hérault. Linear demosaicing inspired by the human visual system. *Image Processing, IEEE Transactions on*, 14(4):439–449, 2005.
- [3] F.R. Amthor, E.S. Takahashi, and C.W. Oyster. Morphologies of rabbit retinal ganglion cells with complex receptive fields. *Journal of comparative neurology*, 280(1):97–121, 1989.
- [4] J.J. Atick. Could information theory provide an ecological theory of sensory processing? *Network: Computation in Neural Systems*, 3(2):213–251, 1992.
- [5] S. Baccus and M. Meister. Fast and slow contrast adaptation in retinal circuitry. *Neuron*, 36(5):909–919, 2002.
- [6] D. Bálya, B. Roska, T. Roska, and F. S. Werblin. A CNN framework for modeling parallel processing in a mammalian retina. *International Journal of Circuit Theory and Applications*, 30(2–3):363–393, 2002.
- [7] H.B. Barlow, R.M. Hill, and W.R. Levick. Retinal ganglion cells responding selectively to direction and speed of image motion in the rabbit. *The Journal of Physiology*, 173(3):377, 1964.
- [8] H.B. Barlow and W. R. Levick. The mechanism of directionally selective units in rabbit’s retina. *J Physiol*, 178:477–504, 1965.
- [9] D.A. Baylor, B.J. Nunn, and J.L. Schnapf. The photocurrent, noise and spectral sensitivity of rods of the monkey macaca fascicularis. *The Journal of Physiology*, 357(1):575–607, 1984.
- [10] D.L. Beaudoin, B.G. Borghuis, and J.B. Demb. Cellular basis for contrast gain control over the receptive field center of mammalian retinal ganglion cells. *Journal of Neuroscience*, 27:2636–2645, 2007.
- [11] WHA Beaudot. *The neural information processing in the vertebrate retina: A melting pot of ideas for artificial vision*. PhD thesis, PhD Thesis in Computer Science, INPG (France), dec 1994.
- [12] E. A. Bernadete and E. Kaplan. Dynamics of primate P retinal ganglion cells: responses to chromatic and achromatic stimuli. *Journal of Physiology*, 519(3):775–790, 1999.

- [13] E.A. Bernadete, E. Kaplan, and B.W. Knight. Contrast gain control in the primate retina: P cells are not X-like, some M cells are. *Visual Neuroscience*, 8(5):483–486, 1992.
- [14] M.J. Berry, I.H. Brivanlou, T.A. Jordan, and M. Meister. Anticipation of moving stimuli by the retina. *Nature*, 398(6725):334–8, 1999.
- [15] M.J. Berry, D.K. Warland, and M. Meister. The structure and precision of retinal spike trains. *Proc Natl Acad Sci USA*, 94:5411–5416, 1997.
- [16] G.G. Blasdel. Orientation selectivity, preference, and continuity in monkey striate cortex. *Journal of Neuroscience*, 12(8):3139–3161, 1992.
- [17] V. Bonin, V. Mante, and M. Carandini. The suppressive field of neurons in Lateral Geniculate Nucleus. *Journal of Neuroscience*, 25(47):10844–10856, November 2005.
- [18] B.B. Boycott and H. Wassle. The morphological types of ganglion cells of the domestic cat’s retina. *The Journal of Physiology*, 240(2):397–419, 1974.
- [19] B.B. Boycott and H. Wassle. Morphological classification of bipolar cells of the primate retina. *Eur J Neurosci*, 3(11):1069–1088, 1991.
- [20] R. Brette and W. Gerstner. Adaptive exponential integrate-and-fire model as an effective description of neuronal activity. *Journal of Neurophysiology*, 94:3637–3642, 2005.
- [21] Romain Brette. Exact simulation of integrate-and-fire models with synaptic conductances. *Neural Computation*, 18(8):2004–2027, 2006.
- [22] Romain Brette. Exact simulation of integrate-and-fire models with exponential currents. *Neural Computation*, 19(10):2604–2609, 2007.
- [23] I. H. Brivanlou, D. K. Warland, and M. Meister. Mechanisms of concerted firing among retinal ganglion cells. *Neuron*, 20:527–529, March 1998.
- [24] ME Burns and TD Lamb. *Visual transduction by rod and cone photoreceptors*, chapter 16, pages 215–233. In Chalupa and Werner [30], 2004.
- [25] J.J. Bussgang. Crosscorrelation functions of amplitude-distorted gaussian signals. *Research Laboratory of Electronics, Massachusetts Institute of Technology, Tech Report*, (216), 1952.
- [26] D. Cai, G. C. Deangelis, and D. Freeman. Spatiotemporal receptive field organization in the lateral geniculate nucleus of cats and kittens. *Journal of Neurophysiology*, 78(2):1045–1061, August 1997.
- [27] J.H. Caldwell and N.W. Daw. New properties of rabbit retinal ganglion cells. *The Journal of Physiology*, 276(1):257–276, 1978.
- [28] J.H. Caldwell, N.W. Daw, and H.J. Wyatt. Effects of picrotoxin and strychnine on rabbit retinal ganglion cells: lateral interactions for cells with more complex receptive fields. *The Journal of Physiology*, 276:277, 1978.

- [29] M. Carandini, J. B. Demb, V. Mante, D. J. Tollhurst, Y. Dan, B. A. Olshausen, J. L. Gallant, and N. C. Rust. Do we know what the early visual system does? *Journal of Neuroscience*, 25(46):10577–10597, November 2005.
- [30] L. M. Chalupa and J.S. Werner, editors. *The visual neurosciences*. MIT Press, 2004.
- [31] E. J. Chichilnisky. A simple white noise analysis of neuronal light responses. *Network: Comput. Neural Syst.*, 12:199–213, 2001.
- [32] E. J. Chichilnisky and R. S. Kalmar. Temporal resolution of ensemble visual motion signals in primate retina. *The Journal of Neuroscience*, 17:6681–6689, 2003.
- [33] B.G. Cleland and W.R. Levick. Brisk and sluggish concentrically organized ganglion cells in the cat's retina. *The Journal of Physiology*, 240(2):421–456, 1974.
- [34] B.G. Cleland and W.R. Levick. Properties of rarely encountered types of ganglion cells in the cat's retina and an overall classification. *The Journal of Physiology*, 240(2):457–492, 1974.
- [35] D. Colella. Web : http://www.mitre.org/news/the_edge/september_99/fifth.html, 1999.
- [36] V. P. Connaughton and G. Maguire. Differential expression of voltage-gated K⁺ and Ca²⁺ currents in bipolar cells in the zebrafish retinal slice. *European Journal of Neuroscience*, 10(4):1350–1362, apr 1998.
- [37] L. J. Croner and E. Kaplan. Receptive fields of P and M ganglion cells across the primate retina. *Vision Research*, 35(1):7–24, jan 1995.
- [38] D. Dacey, O. S. Packer, L. Diller, D. Brainard, B. Peterson, and B. Lee. Center surround receptive field structure of cone bipolar cells in primate retina. *Vision Research*, 40:1801–1811, 2000.
- [39] D. Dacey and M. Petersen. Dendritic field size and morphology of midget and parasol ganglion cells of the human retina. *Proc Natl Acad Sci*, 89:9666–70, 1992.
- [40] D.M. Dacey. Primate retina: cell types, circuits and color opponency. *Progress in Retinal and Eye Research*, 18(6):737–763, 1999.
- [41] D.M. Dacey and B.B. Lee. The 'blue-on' opponent pathway in primate retina originates from a distinct bistratified ganglion cell type. *Nature*, 367(6465):731–735, 1994.
- [42] D.M. Dacey, B.B. Peterson, F.R. Robinson, and P.D. Gamlin. Fireworks in the primate retina in vitro photodynamics reveals diverse LGN-projecting ganglion cell types. *Neuron*, 37(1):15–27, 2003.
- [43] R.F. Dacheux and E. Raviola. Horizontal cells in the retina of the rabbit. *Journal of Neuroscience*, 2(10):1486, 1982.

- [44] R.F. Dacheux and E. Raviola. The rod pathway in the rabbit retina: a depolarizing bipolar and amacrine cell. *Journal of Neuroscience*, 6(2):331, 1986.
- [45] P. Dayan and L. F. Abbott. *Theoretical Neuroscience : Computational and Mathematical Modeling of Neural Systems*. MIT Press, 2001.
- [46] F.M. De Monasterio and P. Gouras. Functional properties of ganglion cells of the rhesus monkey retina. *The Journal of Physiology*, 251(1):167–195, 1975.
- [47] A. Delorme, J. Gautrais, R. VanRullen, and S. J. Thorpe. Spikenet: A simulator for modeling large networks of integrate and fire neurons. *Neurocomputing*, 26:989–996, 1999.
- [48] J. B. Demb, K. Zaghloul, L. Haarsma, and P. Sterling. Bipolar cells contribute to nonlinear spatial summation in the brisk-transient (Y) ganglion cell in mammalian retina. *Journal of Neuroscience*, 21(19):7447–7454, October 2001.
- [49] J.B. Demb and E.N. Pugh. Connexin36 forms synapses essential for night vision. *Neuron*, 36(4):551–553, 2002.
- [50] J.B. Demb, K. Zaghloul, and P. Sterling. Cellular basis for the response to second-order motion cues in Y retinal ganglion cells. *Neuron*, 32(4):711–721, 2001.
- [51] R. Deriche. Using Canny’s criteria to derive a recursively implemented optimal edge detector. *International Journal of Computer Vision*, 1(2):167–187, may 1987.
- [52] A. Destexhe, M. Rudolph, and D. Paré. The high-conductance state of neocortical neurons in vivo. *Nature Reviews Neuroscience*, 4:739–751, 2003.
- [53] S.H. DeVries. Correlated firing in rabbit retinal ganglion cells. *Journal of Neurophysiology*, 81(2):908–920, 1999.
- [54] S.H. DeVries. Bipolar cells use kainate and AMPA receptors to filter visual information into separate channels. *Neuron*, 28(3):847–856, 2000.
- [55] S.H. Devries and D.A. Baylor. Mosaic arrangement of ganglion cell receptive fields in rabbit retina. *Journal of Neurophysiology*, 78(4):2048–2060, 1997.
- [56] S.H. DeVries and E.A. Schwartz. Kainate receptors mediate synaptic transmission between cones and ‘off’ bipolar cells in a mammalian retina. *Nature*, 397(6715):157–60, 1999.
- [57] N.K. Dhingra and R.G. Smith. Spike generator limits efficiency of information transfer in a retinal ganglion cell. *J. Neuroscience*, 24:2914–2922, 2004.
- [58] C. Enroth-Cugell and A. W. Freeman. The receptive-field spatial structure of cat retinal Y cells. *Journal of Physiology*, 384(1):49–79, 1987.
- [59] C. Enroth-Cugell and J. G. Robson. The contrast sensitivity of retinal ganglion cells of the cat. *J Physiol*, 187:517–552, 1966.
- [60] C. Enroth-Cugell, J. G. Robson, D. E. Schweitzer-Tong, and A. B. Watson. Spatio-temporal interactions in cat retinal ganglion cells showing linear spatial summation. *J Physiol*, 341:279–307, 1983.

- [61] H. Erwin. Web : <http://scat-he-g4.sunderland.ac.uk/harry-erw/phpwiki/index.php/tonicphasic>, 2004.
- [62] T. Euler, P.B. Detwiler, and W. Denk. Directionally selective calcium signals in dendrites of starburst amacrine cells. *Nature*, 418:845–852, 2002.
- [63] T. Euler and R. H. Masland. Light-evoked responses of bipolar cells in a mammalian retina. *J. Neurophysiology*, 83(4):1817–1829, April 2000.
- [64] D.J. Field. Relations between the statistics of natural images and the response properties of cortical cells. *J. Opt. Soc. Am. A*, 4(12):2379–2394, 1987.
- [65] N. Flores-Herr, D. A. Protti, and H. Wässle. Synaptic currents generating the inhibitory surround of ganglion cells in the mammalian retina. *Journal of Neuroscience*, 21(13):4852–4863, jul 2001.
- [66] S.I. Fried, T.A. Muench, and F.S. Werblin. Mechanisms and circuitry underlying directional selectivity in the retina. *Nature*, 420(6914):411–414, 2002.
- [67] K. Funke and U. Eysel. Inverse correlation of firing patterns of single topographically matched perigeniculate neurons and cat dorsal lateral geniculate relay cells. *Visual Neuroscience*, 15(04):711–729, 1998.
- [68] M.G.F. Fuortes and A.L. Hodgkin. Changes in time scale and sensitivity in the ommatidia of limulus. *The Journal of Physiology*, 172(2):239, 1964.
- [69] N. Gazeres, L. Borg-Graham, and Y. Fregnac. A model of non-lagged X responses to flashed stimuli in the cat lateral geniculate nucleus. *Visual Neuroscience*, 1998.
- [70] K.R. Gegenfurtner. Cortical mechanisms of colour vision. *Nature Reviews Neuroscience*, 4(7):563–572, 2003.
- [71] Rafael C. Gonzalez and Richard E. Woods. *Digital Image Processing*. Addison Wesley, 3 edition, 1992.
- [72] W. Hare and W. Owen. Spatial organization of the bipolar cell's receptive field in the retina of the tiger salamander. *J Physiol*, 421:223–245, 1990.
- [73] W.A. Hare and W.G. Owen. Receptive field of the retinal bipolar cell: a pharmacological study in the tiger salamander. *Journal of Neurophysiology*, 76(3):2005–2019, 1996.
- [74] S.H.C. Hendry and R.C. Reid. The koniocellular pathway in primate vision. *Annual Review of Neuroscience*, 23(1):127–153, 2000.
- [75] M. H. Hennig, K. Funke, and F. Wörgötter. The influence of different retinal subcircuits on the nonlinearity of ganglion cell behavior. *Journal of Neuroscience*, 22(19):8726–8738, oct 2002.
- [76] J. Héroult. A model of colour processing in the retina of vertebrates: from photoreceptors to colour opposition and colour constancy phenomena. *Neurocomputing*, 12:113–129, 1996.
- [77] J. Héroult. *De la rétine biologique aux circuits neuromorphiques*, chapter 3. Hermès science publications, 2001.

- [78] J. Héroult, editor. *Vision: Signals, Images and Neural Networks*. World Scientific Publications, 2008.
- [79] J. Héroult and B. Durette. Modeling visual perception for image processing. In F. Sandoval, A. Prieto, J. Cabestany, and M. Graña, editors, *Computational and Ambient Intelligence : 9th International Work-Conference on Artificial Neural Networks, IWANN 2007*, 2007.
- [80] S. Hochstein and R. M. Shapley. Linear and nonlinear spatial subunits in Y cat retinal ganglion cells. *J Physiol*, 262:265–284, 1976.
- [81] T. Hosoya, S. A. Baccus, and M. Meister. Dynamic predictive coding by the retina. *Nature*, 436:71–77, 2005.
- [82] D. H. Hubel and T. N. Wiesel. Receptive fields of optic nerve fibres in the spider monkey. *J. Physiol.*, 154:572–80, December 1960.
- [83] M. Hubener, D. Shoham, A. Grinvald, and T. Bonhoeffer. Spatial relationships among three columnar systems in cat area 17. *Journal of Neuroscience*, 17(23):9270–9284, 1997.
- [84] E. Izhikevich. Simple model of spiking neurons. *IEEE Transactions on Neural Networks*, 14(6):1569–1572, 2003.
- [85] A. L. Jacobs and F. S. Werblin. Spatiotemporal patterns at the retinal output. *Journal of Neurophysiology*, 80(1):447–451, jul 1998.
- [86] M. Kamermans, I. Fahrenfort, K. Schultz, U. Janssen-Bienhold, T. Sjoerdsma, and R. Weiler. Hemichannel-mediated inhibition in the outer retina. *Science*, 292(5519):1178–1180, 2001.
- [87] E.R. Kandel, J.H. Schwartz, and T.M. Jessel. *Principles of Neural Science*. McGraw-Hill, 4th edition, 2000.
- [88] P. Kara, P. Reinagel, and R. C. Reid. Low response variability in simultaneously recorded retinal, thalamic, and cortical neurons. *Neuron*, 27(3):635–646, 2000. Poisson, retina, spike variability.
- [89] J. Keat, P. Reinagel, R. C. Reid, and M. Meister. Predicting every spike: a model for the responses of visual neurons. *Neuron*, 30:803–817, 2001.
- [90] G. T. Kenyon, J. Theiler, J. S. George, B. J. Travis, and D. W. Marshak. Correlated firing improves stimulus discrimination in a retinal model. *Neural Computation*, 16:2261–2291, 2004.
- [91] G.T. Kenyon, B. Moore, J. Jeffs, K.S. Denning, G.J. Stephens, B.J. Travis, J.S. George, J. Theiler, and D.W. Marshak. A model of high-frequency oscillatory potentials in retinal ganglion cells. *Visual Neuroscience*, 20(05):465–480, 2003.
- [92] G.T. Kenyon, B.J. Travis, J. Theiler, J.S. George, G.J. Stephens, and D.W. Marshak. Stimulus-specific oscillations in a retinal model. *Neural Networks, IEEE Transactions on*, 15(5):1083–1091, 2004.

- [93] K. J. Kim and F. Rieke. Temporal contrast adaptation in the input and output signals of salamander retinal ganglion cells. *Journal of Neuroscience*, 21(1):287–299, jan 2001.
- [94] H. Kolb. The inner plexiform layer in the retina of the cat: electron microscope observation. *Journal of Neurocytology*, 8:295–329, 1979.
- [95] H. Kolb, E. Fernandez, and R. Nelson. Webvision : the Organization of the Retina and Visual System. Web : <http://webvision.med.utah.edu/>, 2001.
- [96] S. W. Kuffler. Discharge patterns and functional organization of mammalian retina. *Journal of Neurophysiology*, 16:37–68, 1953.
- [97] T. D. Lamb. Spatial properties of horizontal cell responses in the turtle retina. *J Physiol*, 263(2):239–55, 1976.
- [98] M. Laufer and M. Verzeano. Periodic activity in the visual system of the cat. *Vision Res*, 7(3):215–29, 1967.
- [99] W.R. Levick. Receptive fields and trigger features of ganglion cells in the visual streak of the rabbits retina. *The Journal of Physiology*, 188(3):285–307, 1967.
- [100] W. Lohmiller and J. J. Slotine. On contraction analysis for non-linear systems. *Automatica*, 34(6):683–696, jun 1998.
- [101] M. A. Mahowald and C. Mead. The silicon retina. *Sci. Am.*, 264(5):76–82, 1991.
- [102] V. Mante, R. A. Frazor, V. Bonin, W. S. Geisler, and M. Carandini. Independence of luminance and contrast in natural scenes and in the early visual system. *Nature Neuroscience*, 2005.
- [103] B.U.Q. Mao, P.R. Macleish, and J.D. Victor. The intrinsic dynamics of retinal bipolar cells isolated from tiger salamander. *Visual Neuroscience*, 15(03):425–438, 1998.
- [104] D. Marr. *Vision*. W.H. Freeman and Co., 1982.
- [105] P.R. Martin. Colour processing in the primate retina: recent progress. *The Journal of Physiology*, 513(3):631–638, 1998.
- [106] Susana Martinez-Conde, Stephen L. Macknik, and David H. Hubel. The role of fixational eye movements in visual perception. *Nature Reviews Neuroscience*, 5:229–240, 2004.
- [107] R. Masland. The fundamental plan of the retina. *Nature neuroscience*, 4(9), September 2001.
- [108] R.H. Masland. Neuronal diversity in the retina. *Current Opinion in Neurobiology*, 11(4):431–436, 2001.
- [109] D.N. Mastronarde. Correlated firing of cat retinal ganglion cells. I. Spontaneously active inputs to X-and Y-cells. *Journal of Neurophysiology*, 49(2):303–324, 1983.

- [110] B.A. McGuire, J.K. Stevens, and P. Sterling. Microcircuitry of bipolar cells in cat retina. *Journal of Neuroscience*, 4(12):2920, 1984.
- [111] M. J. McMahon, M. J. M. Lankheet, P. Lennie, and D. R. Williams. Fine structure of parvocellular receptive fields in the primate fovea revealed by laser interferometry. *Journal of Neuroscience*, 20(5):2043–2053, mar 2000.
- [112] M. J. McMahon, O. S. Packer, and D. M. Dacey. The classical receptive field surround of primate Parasol ganglion cells is mediated primarily by a non-GABAergic pathway. *Journal of Neuroscience*, 24(15):3736–3745, apr 2004.
- [113] SL Mills and SC Massey. Distribution and coverage of A-and B-type horizontal cells stained with neurobiotin in the rabbit retina. *Vis Neurosci*, 11(3):549–60, 1994.
- [114] M. Moisan. <http://www.flickr.com/photos/marchelino/>.
- [115] D. Weedman Molavi, J. Price, H. Burton, and D. Van Essen. The W.U.S.M Neuroscience Tutorial. Web : <http://thalamus.wustl.edu/course/>, 1997.
- [116] K. I. Naka and W. A. Rushton. The generation and spread of s-potentials in fish (cyprinidae). *J Physiol*, 192(2):437–61, September 1967.
- [117] S. Nawy. Regulation of the On bipolar cell mGluR6 pathway by Ca²⁺. *Journal of Neuroscience*, 20(12):4471, 2000.
- [118] R. Nelson, E.V. Famiglietti, and H. Kolb. Intracellular staining reveals different levels of stratification for on-and off-center ganglion cells in cat retina. *Journal of Neurophysiology*, 41(2):472–483, 1978.
- [119] R. Nelson and H. Kolb. Synaptic patterns and response properties of bipolar and ganglion cells in the cat retina. *Vision Res*, 23(10):1183–95, 1983.
- [120] S. Neuenschwander, M. Castelo-Branco, and W. Singer. Synchronous oscillations in the cat retina. *Vision Research*, 39(15):2485–2497, 1999.
- [121] S. Neuenschwander and W. Singer. Long-range synchronization of oscillatory light responses in the cat retina and lateral geniculate nucleus. *Nature*, 379(6567):728–732, February 1996.
- [122] S. Nirenberg and M. Meister. The light response of retinal ganglion cells is truncated by a displaced amacrine circuit. *Neuron*, 18:637–650, 1997.
- [123] R.A. Normann and I. Perlman. The effects of background illumination on the photoresponses of red and green cones. *The Journal of Physiology*, 286(1):491–507, 1979.
- [124] B.J. O'Brien, T. Isayama, R. Richardson, and D.M. Berson. Intrinsic physiological properties of cat retinal ganglion cells. *The Journal of Physiology*, 538(3):787–802, 2002.
- [125] I. Ohzawa, G. Sclar, and D. Freeman. Contrast gain control in the cat's visual cortex. *J. Neurophysiol.*, 54:651–667, 1985.
- [126] B.P. Ölveczky, S.A. Baccus, and M. Meister. Segregation of object and background motion in the retina. *Nature*, 423:401–408, 2003.

- [127] G. Osterberg. Topography of the layer of rods and cones in the human retina. *Acta Ophthalmol.*, suppl. 6:1–103, 1935.
- [128] C.W. Oyster, E. Takahashi, and H. Collewijn. Direction-selective retinal ganglion cells and control of optokinetic nystagmus in the rabbit. *Vision Res*, 12(2):183–93, 1972.
- [129] I. Perlman and J. Ammermuller. Receptive-field size of L1 horizontal cells in the turtle retina: effects of dopamine and background light. *Journal of Neurophysiology*, 72(6):2786–2795, 1994.
- [130] T. Poggio and W. Reichardt. Considerations on models of movement detection. *Biological Cybernetics*, 13(4):223–227, 1973.
- [131] A. Polans, W. Baehr, and K. Palczewski. Turned on by Ca^{2+} ! The physiology and pathology of Ca^{2+} -binding proteins in the retina. *Trends in Neurosciences*, 19(12):547–554, December 1996.
- [132] M. Pu, D.M. Berson, and T. Pan. Structure and function of retinal ganglion cells innervating the cat's geniculate wing: an in vitro study. *Journal of Neuroscience*, 14(7):4338, 1994.
- [133] J.L. Puchalla, E. Schneidman, R.A. Harris, and M.J. Berry. Redundancy in the population code of the retina. *Neuron*, 46(3):493–504, 2005.
- [134] EN Pugh and TD Lamb. Amplification and kinetics of the activation steps in phototransduction. *Biochim Biophys Acta*, 1141(2-3):111–49, 1993.
- [135] E.N. Pugh, S. Nikonov, and T.D. Lamb. Molecular mechanisms of vertebrate photoreceptor light adaptation. *Current Opinion in Neurobiology*, 9(4):410–418, 1999.
- [136] D. Purves, G.J. Augustine, D. Fitzpatrick, W.C. Hall, LaMantia A-S., McNamara J.O., and Williams S.M. *Neuroscience*. Sinauer Associates, Inc, 3rd edition, 2004.
- [137] E. Raviola and N. B. Gilula. Gap junctions between photoreceptor cells in the vertebrate retina. *Proceedings of the National Academy of Sciences*, 70(6):1677–1681, jun 1973.
- [138] D.S. Reich, J.D. Victor, and B.W. Knight. The power ratio and the interval map: Spiking models and extracellular recordings. *Journal of Neuroscience*, 18(23):10090, 1998.
- [139] F. Rieke. Temporal contrast adaptation in salamander bipolar cells. *Journal of Neuroscience*, 21(23):9445–9454, dec 2001.
- [140] F. Rieke, D. Warland, R. de Ruyter van Steveninck, and W. Bialek. *Spikes: Exploring the Neural Code*. Bradford Books, 1997.
- [141] D. Ringach and R. Shapley. Reverse correlation in neurophysiology. *Cognitive Science*, 28(2):147–16620, 2004.
- [142] R.L. Rockhill, F.J. Daly, M.A. MacNeil, S.P. Brown, and R.H. Masland. The diversity of ganglion cells in a mammalian retina. *Journal of Neuroscience*, 22(9):3831, 2002.

- [143] R.W. Rodieck. Quantitative analysis of cat retinal ganglion cell response to visual stimuli. *Vision Research*, 5:583–601, 1965.
- [144] R.W. Rodieck and M. Watanabe. Survey of the morphology of macaque retinal ganglion cells that project to the pretectum, superior colliculus, and parvicellular laminae of the lateral geniculate nucleus. *The Journal of Comparative Neurology*, 338(2):289–303, 1993.
- [145] B. Roska, A. Molnar, and F.S. Werblin. Parallel processing in retinal ganglion cells: How integration of space-time patterns of excitation and inhibition form the spiking output. *Journal of Neurophysiology*, 95(6):3810–3822, 2006.
- [146] B. Roska and F. Werblin. Vertical interactions across ten parallel, stacked representations in the mammalian retina. *Nature*, 410:583–7, mar 2001.
- [147] M.H. Rowe and J. Stone. Properties of ganglion cells in the visual streak of the cat’s retina. *J Comp Neurol*, 169(1):99–125, 1976.
- [148] R. Van Rullen and S. Thorpe. Rate coding versus temporal order coding: What the retina ganglion cells tell the visual cortex. *Neural Computing*, 13(6):1255–1283, 2001.
- [149] H.M. Sakai and K.I. Naka. Dissection of the neuron network in the catfish inner retina. IV. Bidirectional interactions between amacrine and ganglion cells. *Journal of Neurophysiology*, 63(1):105–119, 1990.
- [150] H.M. Sakai and K.I. Naka. Dissection of the neuron network in the catfish inner retina. V. Interactions between NA and NB amacrine cells. *Journal of Neurophysiology*, 63(1):120–130, 1990.
- [151] J. L. Schnapf, B. J. Nunn, M. Meister, and D. A. Baylor. Visual transduction in cones of the monkey macaca fascicularis. *J Physiol*, 427(1):681–713, 1990.
- [152] D.M. Schneeweis and J.L. Schnapf. Photovoltage of rods and cones in the macaque retina. *Science*, 268(5213):1053–1056, 1995.
- [153] E. Schneidman, M.J. Berry, R. Segev, and W. Bialek. Weak pairwise correlations imply strongly correlated network states in a neural population. *Nature*, 440(7087):1007–1012, 2006.
- [154] R. Shapley and C. Enroth-Cugell. Visual adaptation and retinal gain controls. *Progress in retinal research*, 3:263–346, 1984.
- [155] R. M. Shapley and J. D. Victor. The effect of contrast on the transfer properties of cat retinal ganglion cells. *The Journal of Physiology*, 285(1):275–298, 1978.
- [156] R. M. Shapley and J. D. Victor. How the contrast gain control modifies the frequency responses of cat retinal ganglion cells. *The Journal of Physiology*, 318(1):161–179, 1981.
- [157] L.T. Sharpe and A. Stockman. Rod pathways: the importance of seeing nothing. *Trends in Neurosciences*, 22(11):497–504, 1999.
- [158] S.M. Sherman and R.W. Guillery. *The Visual Relays in the Thalamus*, chapter 35, pages 565–591. In Chalupa and Werner [30], 2004.

- [159] R.A. Shiells and G. Falk. A rise in intracellular Ca^{2+} underlies light adaptation in dogfish retinal 'on' bipolar cells. *The Journal of Physiology*, 514(2):343–350, 1999.
- [160] J. Shlens, G.D. Field, J.L. Gauthier, M.I. Grivich, D. Petrusca, A. Sher, A.M. Litke, and E.J. Chichilnisky. The structure of multi-neuron firing patterns in primate retina. *Journal of Neuroscience*, 26(32):8254, 2006.
- [161] W. Singer. Neuronal synchrony: a versatile code for the definition of relations? *Neuron*, 24(1):49–65, 1999.
- [162] M.V. Srinivasan, S.B. Laughlin, and A. Dubs. Predictive coding: A fresh view of inhibition in the retina. *Proceedings of the Royal Society of London. Series B, Biological Sciences*, 216(1205):427–459, 1982.
- [163] J. Stone and Y. Fukuda. Properties of cat retinal ganglion cells: a comparison of W-cells with X-and Y-cells. *Journal of Neurophysiology*, 37(4):722–748, 1974.
- [164] G. Svaetichin. The cone action potential. *Acta Physiol. Scand*, 29(suppl 106):565–599, 1953.
- [165] S. Tan, J. Dale, and A. Johnston. Performance of three recursive algorithms for fast space-variant gaussian filtering. *Real-Time Imaging*, 2003.
- [166] L. Tao, M. Shelley, D. McLaughlin, and R. Shapley. An egalitarian network model for the emergence of simple and complex cells in visual cortex. *Proc Natl Acad Sci*, 101(1):366–371, January 2004.
- [167] W.R. Taylor and D.I. Vaney. New directions in retinal research. *Trends in Neurosciences*, 26(7):379–385, 2003.
- [168] R. Tootell, E. Switkes, M. Silverman, and S. Hamilton. Functional anatomy of the macaque striate cortex. ii. retinotopic organization. *Journal of neuroscience*, 8(5):1531–1568, 1988.
- [169] V. Torre, HR Matthews, and TD Lamb. Role of Calcium in regulating the cyclic GMP cascade of phototransduction in retinal rods. *PNAS*, 83(18):7109–7113, 1986.
- [170] J.B. Troy, G. Einstein, J.G. Schuurmans, R.P. and Robson, and C. Enroth-Cugell. Responses to sinusoidal gratings of two types of very nonlinear retinal ganglion cells of cat. *Vis Neurosci*, 3(3):213–23, 1989.
- [171] J.B. Troy and T. Shou. The receptive fields of cat retinal ganglion cells in physiological and pathological states: where we are after half a century of research. *Progress in Retinal and Eye Research*, 21(3):263–302, 2002.
- [172] J.M. Valetton and D. Van Norren. Light adaptation of primate cones : An analysis based on extracellular data. *Vision Research*, 23(12):1539–1547, 1983.
- [173] J. H. van Hateren, L. Rüttiger, H. Sun, and B. B. Lee. Processing of natural temporal stimuli by macaque retinal ganglion cells. *J. Neuroscience*, 22(22):9945–9960, 2002.

- [174] J.H. van Hateren. A cellular and molecular model of response kinetics and adaptation in primate cones and horizontal cells. *Journal of Vision*, 5(4):5, 2005.
- [175] J.H. van Hateren and T.D. Lamb. The photocurrent response of human cones is fast and monophasic. *BMC Neuroscience*, 7(1):34, 2006.
- [176] F.L. Van Nes, J.J. Koenderink, H. Nas, and M.A. Bouman. Spatiotemporal modulation transfer in the human eye. *J Opt Soc Am*, 57(9):1082–8, 1967.
- [177] M. van Wyk, W.R. Taylor, and D.I. Vaney. Local edge detectors: A substrate for fine spatial vision at low temporal frequencies in rabbit retina. *Journal of Neuroscience*, 26(51):13250, 2006.
- [178] J. D. Victor. The dynamics of the cat retinal X cell centre. *The Journal of Physiology*, 386(1):219–246, 1987.
- [179] J.D. Victor. Spike train metrics. *Current Opinion in Neurobiology*, 15(5):585–592, 2005.
- [180] H. Wassle. Parallel processing in the mammalian retina. *Nat Rev Neurosci*, 5(10):747–57, 2004.
- [181] F. S. Werblin and J. E. Dowling. Organization of the retina of the mudpuppy. *Journal of Neurophysiology*, 32(3):339–355, 1969.
- [182] A. Wohrer. Mathematical study of a neural gain control mechanism. Research report 6327, INRIA, 2007.
- [183] Y. Xu, N.K. Dhingra, R.G. Smith, and P. Sterling. Sluggish and brisk ganglion cells detect contrast with similar sensitivity. *Journal of Neurophysiology*, 93(5):2388–2395, 2005.
- [184] G.M. Zeck, Q. Xiao, and R.H. Masland. The spatial filtering properties of local edge detectors and brisk-sustained retinal ganglion cells. *Eur J Neurosci*, 22(8):2016–26, 2005.